SUBDUCTION AND COLLISION DYNAMICS OF TECTONIC PLATES

EDITED BY: Zhong-Hai Li, Jie Liao, Lijun Liu and Manuele Faccenda
PUBLISHED IN: Frontiers in Earth Science

frontiers Research Topics

ISSN 1664-8714
ISBN 978-2-83250-298-3
DOI 10.3389/978-2-83250-298-3

About Frontiers

Frontiers is more than just an open-access publisher of scholarly articles: it is a pioneering approach to the world of academia, radically improving the way scholarly research is managed. The grand vision of Frontiers is a world where all people have an equal opportunity to seek, share and generate knowledge. Frontiers provides immediate and permanent online open access to all its publications, but this alone is not enough to realize our grand goals.

Frontiers Journal Series

The Frontiers Journal Series is a multi-tier and interdisciplinary set of open-access, online journals, promising a paradigm shift from the current review, selection and dissemination processes in academic publishing. All Frontiers journals are driven by researchers for researchers; therefore, they constitute a service to the scholarly community. At the same time, the Frontiers Journal Series operates on a revolutionary invention, the tiered publishing system, initially addressing specific communities of scholars, and gradually climbing up to broader public understanding, thus serving the interests of the lay society, too.

Dedication to Quality

Each Frontiers article is a landmark of the highest quality, thanks to genuinely collaborative interactions between authors and review editors, who include some of the world's best academicians. Research must be certified by peers before entering a stream of knowledge that may eventually reach the public - and shape society; therefore, Frontiers only applies the most rigorous and unbiased reviews.
Frontiers revolutionizes research publishing by freely delivering the most outstanding research, evaluated with no bias from both the academic and social point of view. By applying the most advanced information technologies, Frontiers is catapulting scholarly publishing into a new generation.

What are Frontiers Research Topics?

Frontiers Research Topics are very popular trademarks of the Frontiers Journals Series: they are collections of at least ten articles, all centered on a particular subject. With their unique mix of varied contributions from Original Research to Review Articles, Frontiers Research Topics unify the most influential researchers, the latest key findings and historical advances in a hot research area! Find out more on how to host your own Frontiers Research Topic or contribute to one as an author by contacting the Frontiers Editorial Office: frontiersin.org/about/contact

SUBDUCTION AND COLLISION DYNAMICS OF TECTONIC PLATES

Topic Editors:
Zhong-Hai Li, University of Chinese Academy of Sciences, China
Jie Liao, Sun Yat-sen University, Zhuhai Campus, China
Lijun Liu, University of Illinois at Urbana-Champaign, United States
Manuele Faccenda, Università Padova, Italy

Citation: Li, Z.-H., Liao, J., Liu, L., Faccenda, M., eds. (2022). Subduction and Collision Dynamics of Tectonic Plates. Lausanne: Frontiers Media SA.
doi: 10.3389/978-2-83250-298-3

Table of Contents

frontiers | Frontiers in Earth Science

TYPE Editorial
PUBLISHED 09 September 2022
DOI 10.3389/feart.2022.1023604

EDITED AND REVIEWED BY
Derek Keir,
University of Southampton,
United Kingdom

*CORRESPONDENCE
Zhong-Hai Li,
li.zhonghai@ucas.ac.cn

SPECIALTY SECTION
This article was submitted to Solid Earth Geophysics,
a section of the journal
Frontiers in Earth Science

RECEIVED 19 August 2022
ACCEPTED 24 August 2022
PUBLISHED 09 September 2022

CITATION
Li Z-H, Liao J, Liu L and Faccenda M (2022), Editorial: Subduction and collision dynamics of tectonic plates.
Front. Earth Sci. 10:1023604.
doi: 10.3389/feart.2022.1023604

Editorial: Subduction and collision dynamics of tectonic plates

Zhong-Hai Li[1]*, Jie Liao[2], Lijun Liu[3] and Manuele Faccenda[4]

[1]Key Laboratory of Computational Geodynamics, College of Earth and Planetary Sciences, University of Chinese Academy of Sciences, Beijing, China, [2]School of Earth Sciences and Engineering, Sun Yat-Sen University, Zhuhai, China, [3]University of Illinois at Urbana-Champaign, Urbana, IL, United States, [4]Dipartimento di Geoscienze, Università di Padova, Padova, Italy

KEYWORDS

oceanic subduction, continental collision, lithospheric deformation, mantle flow, numerical modeling

Editorial on the Research Topic
Subduction and collision dynamics of tectonic plates

Plate subduction and collision zones are some of the most active tectonic regions on the Earth, which control the mass and energy exchange between the Earth's surface and interior, produce volcanism and the majority of great earthquakes, and are strongly correlated with the generation of mineral resources. The subducting oceanic slab penetrates through the mantle, interacts with multiple phase transition layers and results in variable slab morphologies and complex mantle flow. On the other hand, the continental plate subduction and collision generally follow the closure of oceanic subduction and lead to formation of great mountain belts on the Earth. The subduction/collision zone is a key element of plate tectonics and geodynamics, involving multiple processes and multi-scale mechanisms; however, many problems in this research field remain unclear and widely debated. The set of 14 studies in this special Research Topic aimed to bring together multi-scale geodynamic modeling studies, with the general goal of understanding the processes, dynamics, and effects of plate subduction and collision, as well as providing a general framework for future research efforts.

Normal subduction

For a normal oceanic subduction zone, a narrow, linear trough (trench) is produced in front of the overriding plates. The trenches may have a wide variation in their topographic characteristics, such as width, depth, and bounding surface slopes. What are the controlling factors? Dasgupta and Mandal showed that the mechanical coupling between the subducting and overriding plates, expressed by the maximum depth of decoupling, is a leading factor controlling the topographic evolution of a trench.

Unusual subduction

In addition to the normal oceanic plate subduction, there are also unusual subduction geometries that challenge our understanding of subduction dynamics. A typical and important case is the mid-ocean ridge (MOR) subduction, including the trench-parallel and trench-perpendicular/oblique regimes. For the trench-parallel MOR subduction, Shen and Leng numerically investigated the dynamics and effects of three MOR types (fast spreading, slow spreading, and extinction modes), and find that the key factor controlling these subduction modes is the relative motion between the foregoing and the following oceanic plates, separated by the MOR. For the trench-perpendicular/oblique MOR subduction, Guo et al. numerically studied the effects of the unusual subduction around the Chile Triple Junction (CTJ), showing that the CTJ is not only a wedge subduction boundary but also an important factor controlling the lithospheric thermal structure and seismogenic zone of the overriding plate. The subduction of aseismic ridges or other positively buoyant features may lead to the development of flat and shallow dipping slabs, the formation of cusps in trench geometry, and the cessation of associated arc magmatism. Using a series of 3-D simulations of free subduction, Suchoy et al. examined the effects of downgoing plate age (affecting buoyancy and strength), ridge buoyancy, and ridge location along the trench, and found that the buoyant aseismic ridges can locally change slab sinking and trench retreat rates, in turn modifying the evolution of slab morphology at depth and trench shape at the surface.

Multiple-subduction system

On the natural Earth, several subduction zones may locate closely and interact with each other. For example, the New Guinea region is a widely accepted example of the parallel triple subduction system, including a northward dip at the New Britain Trench (NBT), a southward dip at the Trobriand Trough (TT), and North Solomon Trench (NST). Using systematic numerical models, Wang et al. deciphered the formation mechanisms of these three correlated subduction zones, as well as their interactions in the complex parallel subduction system. Numerical tests on model parameters suggest that the initiation and development of triple subduction are rather difficult, and the presence of pre-existing weakness and the length of the ocean-continental transition zone are the key parameters. The multiple subduction zones can also be oblique or perpendicular to each other, in which the trenches will be intersected to generate a corner, with the formation of a subduction cusp. Using 3-D numerical models with imposed two subduction zones that formed an initial subduction cusp, Zhao et al. showed that the subduction cusps have a tendency to become smooth and disappear during the subduction process. The asymmetric distribution of the overriding plate strength and initial slab-pull force determines the asymmetric evolutionary pathway of subduction cusps.

Deep subduction and mantle flow

The interaction of subducting slab and mantle transition zone results in contrasting slab morphologies. The mechanism of slab stagnation and the formation of a big mantle wedge are widely debated. Using 3-D global convection models, Wu et al. proposed that all subducted Izanagi slabs have completely fallen into the lower mantle until the late Cenozoic and the stagnant slabs currently observed at the mantle transition zone depth beneath Eastern Asia are entirely from the Pacific Plate. They also find that multiple slab stagnation events have occurred during the subduction of the Izanagi Plate in the Mesozoic, each lasting for tens of millions of years. The complex and long history of Western Pacific subduction has greatly modified and characterized the East Asian tectonics. Brown et al. proposed a solution to decipher the Cenozoic intraplate tectonism of this region, where hot Pacific asthenospheric material flows into East Asia through the slab window opened by the subduction of the Izanagi–Pacific ridge during the early Cenozoic. They find that this process significantly affects the topography and volcanic history of the backarc and hinterland regions.

Continental collision patterns

Continental collision generally occurs following the closure of oceanic subduction and leads to the formation of mountain belts. The collision pattern varies among different mountain ranges; even the same collision zone shows significant lateral tectonic variations along its strike. Using systematic numerical models, Liu et al. showed that slowdown of plate velocities after the closure of ocean basins strongly influences continental collision evolution. The decreasing convergent velocity promotes the extension inside the slab by decreasing the movement of the surface plate, which will contribute greatly to the subducting slab break-off. Li et al. further integrated the reconstruction-based, time-dependent convergence rate of the India–Asia collision into a large-scale thermomechanical numerical model, showing that the collision mode selection, deformation partition, and continental mass conservation are greatly controlled by the rheological strength of the overriding plate. The strain localization and shortening of the rheologically weak Tibetan plate hinder subduction transference to the Indian Ocean during the India–Asia collision but instead results in lithospheric shortening and delamination of the overriding plate.

Post-collision processes

When the collision slows down or terminates, it often leads to the detachment of earlier subducted oceanic lithosphere, which changes the subsequent dynamics of the orogenic system. Using visco-elasto-plastic models, Van Agtmaal et al. investigated the conditions for post-collisional slab steepening versus shallowing. The results show a two-stage elastic and viscous slab rebound process lasting tens of millions of years, which is associated with slab unbending and eduction that together generates orogenic widening and trench shift toward the foreland. On the other hand, the lithosphere delamination generally results during or after continental collision, which occurs not only along the Moho, but also along the mid-lithospheric discontinuity. Qi et al. numerically investigated the dynamics of intra-crustal continental delamination along the base of the upper crust, featured by decoupled crustal deformation, that is, the lower crust subducts attached to the mantle lithosphere while the upper crust shortens at shallow depth. The intra-crustal strength decoupling and continental delamination are controlled by the upper crustal thickness, lower crustal rheology and initial Moho temperature.

Himalayan–Tibetan system

As one of the most important continental collisional belts on the present Earth, the Himalayan–Tibetan system plays a key role in understanding the plate collision dynamics. Using 3D thermo-mechanical modeling, Zhang et al. investigated the effects of hinterland basins on the detailed topography evolution of the Tibetan Plateau and found that a strong hinterland basin develops into a lowland with respect to the surrounding plateau, but a weak hinterland basin forms a highland after ~20 Myr of convergence, which explains the Tibetan topography evolution. After the uplift of the Tibetan Plateau, the resulting great potential energy will lead to a strong push on the neighboring blocks. The rheologically strong Sichuan Basin is located to the east of the Tibetan Plateau, with a remarkable mountain range, that is, Longmen Shan, in between. Shen et al. revealed that the rigid Ruoergai block resists the formation of a weak layer in the northern Longmen Shan block, resulting in the observed difference in lithospheric properties between the northern and southern Longmen Shan blocks, and thus constraining the eastern Tibetan evolution.

The studies in this Research Topic collection cover a whole chain of plate convergent processes. We hope that the reader will find it a useful reference for future research on plate subduction and collision tectonics and dynamics.

Author contributions

Z-HL, JL, LL, and MF edited the Research Topic of Subduction and Collision Dynamics of Tectonic Plates. Z-HL wrote the manuscript, and JL, LL, and MF revised the manuscript.

Funding

This work was supported by the NSFC Tethys project (91855208).

Conflict of interest

The authors declare that the research was conducted in the absence of any commercial or financial relationships that could be construed as a potential conflict of interest.

Publisher's note

frontiers in Earth Science

ORIGINAL RESEARCH
published: 01 November 2021
doi: 10.3389/feart.2021.781117

The Mode of Trench-Parallel Subduction of the Middle Ocean Ridge

Xiaobing Shen[1] *and Wei Leng*[1,2]*

[1]*Laboratory of Seismology and Physics of Earth's Interior, School of Earth and Space Sciences, University of Science and Technology of China, Hefei, China,* [2]*CAS Center for Excellence in Comparative Planetology, Hefei, China*

Trench-parallel subduction of mid-ocean ridges occurs frequently in plate motion history, such as along the western boundary of the Pacific plate in the early Cenozoic and along the eastern boundary of the Pacific plate at present. Such subduction may strongly alter the surface topography, volcanic activity and slab morphology in the mantle, whereas few studies have been conducted to investigate its evolutionary process. Here, we construct a 2-D viscoelastoplastic numerical model to study the modes and key parameters controlling trench-parallel subduction of mid-ocean ridges. Our model results show that the subduction modes of mid-ocean ridges can be primarily categorized into three types: the fast spreading mode, the slow spreading mode, and the extinction mode. The key factor controlling these subduction modes is the relative motion between the foregoing and the following oceanic plates, which are separated by the mid-ocean ridge. Different subduction modes exert different surface geological expressions, which may explain specific evolutionary processes related to mid-ocean ridge subduction, such as topographic deformation and the eruption gap of volcanic rocks in East Asia within 55–45 Ma and in the western North American plate during the late Cenozoic.

Keywords: mid-ocean ridge, trench-parallel subduction, spreading velocity, viscosity, fast mode, slow mode, extinction mode, volcanism gap

Edited by:
Zhong-Hai Li,
University of Chinese Academy of Sciences, China

Reviewed by:
Jiashun Hu,
Southern University of Science and Technology, China
Jie Liao,
Sun Yat-sen University, Zhuhai Campus, China

Correspondence:
Wei Leng
wleng@ustc.edu.cn

Specialty section:
This article was submitted to Solid Earth Geophysics, a section of the journal Frontiers in Earth Science

Received: *22 September 2021*
Accepted: *19 October 2021*
Published: *01 November 2021*

Citation:
Shen X and Leng W (2021) The Mode of Trench-Parallel Subduction of the Middle Ocean Ridge. Front. Earth Sci. 9:781117. doi: 10.3389/feart.2021.781117

INTRODUCTION

A mid-ocean ridge (MOR) is a divergent boundary of plate tectonics where new plates are continuously generated (Turcotte and Schubert, 2002). Although MORs are generally located at the centers of ocean basins, such as the present mid-Atlantic ridge, they may subduct into the deep mantle when tectonic environments cause MORs to move to ocean trenches (Georgieva et al., 2019). Typical examples include the subducted MOR between the Izanagi plate and the Pacific plate, which subducted at 55–45 Ma (Müller et al., 2016) and the subducted MOR between the Farallon plate and the Pacific plate, which subducted at 30–0 Ma (Ferrari et al., 2018). According to the contact angle between the MOR and the trench, MOR subduction can be divided into high-angle (trench-vertical) subduction and low-angle (trench-parallel) subduction (Wu and Wu, 2019).

Different methods of MOR subduction may cause different evolutionary pathways and surface expression. On the one hand, for trench-vertical MOR subduction, large-scale MORB-like igneous rocks erupt at the intersections between MORs and trenches, which have a small influence range but a long duration. Symmetrical igneous rock sequences, such as adakite-granitoid-adakite sequences, along the MOR are formed on the overriding plate (Ling et al., 2009; Isozaki et al., 2010). Analog model experiments further show that ridge subduction has a strong impact on the accumulation and migration of the accretionary wedge and the shape of the subduction zone edge (Wang et al., 2019). On the other hand, for trench-parallel MOR subduction, large-scale MORB-like igneous rocks erupt at the trench, which has a large influence range but a relatively short duration (Gutiérrez et al., 2005; Müller et al., 2016; Liu et al., 2020). For instance, early Cenozoic MORB bedrocks have also been found in Hokkado, Japan (Maeda and Kagami, 1996; Nanayama et al., 2019). The seafloor age can also affect the local morphology of the slab (Hu et al., 2016).

Many numerical studies have focused on the subduction evolution of a continuous oceanic plate (e.g., Gurnis and Hager, 1988; Christensen, 1996; Torii and Yoshioka, 2007; Čížková and Bina, 2013; Garel et al., 2014; King et al., 2015; Yang et al., 2018), whereas only a few studies have been conducted on MOR subduction at plate boundaries. Trench-vertical aseismic ridge subduction can affect the slab geometry and the deformation of the overriding continental plate based on analog model results (Martinod et al., 2013). Specifically, aseismic ridge subduction can provide extra buoyancy to reduce the dip angle of the slab, such as flat slab subduction beneath the South American plate (van Hunen et al., 2002; Gutiérrez et al., 2005; Rosenbaum et al., 2005; Espurt et al., 2008; Hu et al., 2016). Furthermore, when an active ridge subducts into the mantle, a slab window forming strong magmatism can be generated (Li et al., 2020). Groome and Thorkelson, (2009) showed that the slab window migrates with the subduction of an active ridge. Moreover, the spreading velocity and cooling age of ridges have a strong influence on ridge-inversed subduction (Qing et al., 2021). Burkett and Billen (2009) suggested that the change in buoyancy of the weakened zone of lithosphere close to the MOR causes the slab detachment from the subducting plates. The morphology of the MOR is affected by the MOR spreading speed (Püthe and Gerya, 2014). Overall, since much attention has been given to MOR subduction, the specific mode of trench-parallel subduction of the MOR needs to be thoroughly analyzed.

MOR subduction along the western boundary of the Pacific plate in the early Cenozoic and along the eastern boundary of the Pacific plate at present is primarily viewed as trench-parallel (Seton et al., 2015; Müller et al., 2016; Tang et al., 2018; Liu et al., 2020). In this study, we focus on the different modes of trench-parallel MOR subduction and the related key controlling parameters. Specifically, the pulling force from the slab connecting to the foregoing oceanic plate and the motion of the following oceanic plate may play important roles in MOR subduction. The initial dip angle of the slab and the viscosity structure of the mantle also affect the plate movement. Therefore, we investigate the effects of foregoing slab length, the following plate speed, the initial dip angle of the slab and the viscosity structure of the mantle on the modes of MOR subduction and analyze the surface expression, including the topography and volcanic activity, on the overriding plate.

METHODS

We construct a 2-D Cartesian viscoelastoplastic model to study the evolution of plate movement during MOR subduction based on the finite element method. We use the Ellipsis approach (Moresi et al., 2003) to solve the governing equations of mass, momentum and energy. The movement and deformation of the lithosphere and mantle are tracked by Lagrangian particles (Moresi et al., 2003; Leng and Gurnis, 2015; Chen et al., 2020).

TABLE 1 | Physical parameters in the model.

Parameters	Values
Reference density ρ_0	3,300 kg/m^3
Crust density ρ_c	2,800 kg/m^3
Air density ρ_{Air}	0 kg/m^3
Box thickness D	1,000 km
Gravitational acceleration g	9.8 m/s^2
Coefficient of thermal expansion α	$3 \times 10^{-5}/K$
Thermal diffusivity κ	1×10^{-6} m^2/s
Specific heat C_p	1000 J/(kg·K)
Reference viscosity η_0	1×10^{20} Pa·s
Reference Temperature T_0	1,500°C
Shear modulus G	30 GPa
Activation energy E	540 kJ/mol
Gas constant R	8.31 J/mol
Strain exponent n	3.5
Minimum cohesion C_f	4.4 MPa
Reference strain rate $\dot{\varepsilon}_0$	10^{-15}/s
Maximum viscosity	1×10^{24} Pa·s
Minimum viscosity	1×10^{19} Pa·s

An incompressible Maxwell material body is used to describe the viscoelasticity of the model composition. The deformation rate of the material composition is described by the viscous part and elastic part:

$$\dot{\varepsilon}_{ij} = \frac{1}{2G}\dot{\tau}_{ij} + \frac{1}{2\eta}\tau_{ij}$$

where $\dot{\varepsilon}_{ij}$ is the strain rate, G is the shear modulus, $\dot{\tau}_{ij}$ is the time variation rate of deviatoric stress, η is the viscosity, and τ_{ij} is the deviatoric stress. i and j represent spatial indices.

The viscosity equation we use is non-Newtonian and is temperature- and depth-dependent (Karato and Wu, 1993):

$$\eta = \eta_0\left(\frac{\dot{\varepsilon}_{\mathrm{II}}}{\dot{\varepsilon}_0}\right)^{\left(\frac{1}{n}-1\right)} exp\left[\eta_z\left(\frac{z}{d}\right) + \frac{E}{nR}\left(\frac{1}{T} - \frac{1}{T_0}\right)\right]$$

where η_0 is the reference viscosity, $\dot{\varepsilon}_{\mathrm{II}}$ is the second invariant of the deviatoric strain rate tensor, $\dot{\varepsilon}_0$ is the reference strain rate, n is the strain exponent, E is the activation energy, R is the gas constant, T is the absolute temperature (in Kelvin), T_0 is the reference temperature, η_z is the pre-exponential factor of depth-dependent viscosity, d is the model box thickness, and z is the depth (**Table 1**). The depth-dependent mantle viscosity structure in the upper mantle is variable with uncertainties (Steinberger and Calderwood, 2006; Čížková et al., 2012). Therefore, we consider two possible viscosity structures: Temperature-dependent viscosity (ViscT) versus Temperature- and depth-dependent viscosity (ViscT&D). For the ViscT viscosity structure, $\eta_z = 0$. For the ViscT&D viscosity structure, $\eta_z = \ln(50) = 3.912$.

The plasticity of the material is applied with the Drucker-Prager criterion through the yield stress:

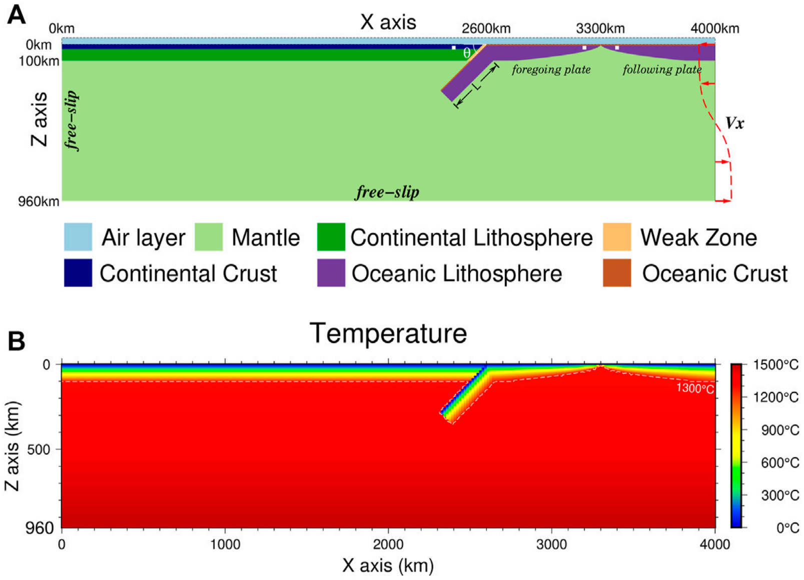

FIGURE 1 | Model initial setting and boundary conditions. **(A)** The 2-D model is 4,000 × 1,000 km with an air layer 40 km thick at the top. At 3,300 km in the horizontal direction, we set up an MOR structure, and the two sides of the MOR are the foregoing oceanic plate and the following oceanic plate. The three white squares represent the sampling points placed in the model. Different colors in the model represent different lithologies, as shown at the bottom. θ is the initial dip angle of the foregoing plate. The initial slab length (L) and the imposed velocity (V_x) at the right boundary are the main control parameters in our model. **(B)** Initial temperature field. The white dashed line is the 1,300°C isotherm, which represents the bottom boundary of the lithosphere.

$$\tau_y = \mu P + C$$

where τ_y is the yield stress, μ is the coefficient of friction, P is the pressure and C is the cohesion, which is the strength of the material at zero hydrostatic pressure. As the plastic strain increases, the mantle material becomes weaker (Buck and Poliakov, 1998; Poliakov and Buck, 1998). Therefore, both μ and C linearly decrease when the accumulated plastic strain increases:

$$\mu = \mu_0 \left[1 - \min\left(1, \frac{\varepsilon_p}{\varepsilon_f}\right)\right]$$

$$C = C_f + \left(C_0 - C_f\right)\left[1 - \min\left(1, \frac{\varepsilon_p}{\varepsilon_f}\right)\right]$$

where μ_0 is the initial coefficient of friction, ε_p is the accumulated plastic strain, ε_f is the reference plastic strain, C_0 is the initial cohesion and C_f is the minimum cohesion (**Table 1**). The material no longer weakens when ε_p becomes larger than the reference plastic strain. To decouple the overriding plate and the subducting plate, we placed a long strip of weak zones along the interface between the continental lithosphere and the subducted oceanic plate (28 km in width, **Figure 1**). The plastic parameters of the weak zone, μ_0, ε_f, C_0 and C_f, are set to 0.0, 0.01, 0.6 and 0.6 MPa, respectively (Muhuri et al., 2003; Leng and Gurnis, 2011; Leng and Gurnis, 2015).

Our 2-D Cartesian model has a length of 4,000 km and a depth of 1,000 km (**Figure 1**). To simulate the top free-surface boundary, we set a sticky air layer 40 km thick at the top with zero density and minimum viscosity (Leng and Gurnis, 2011, 2015; Chen et al., 2020). The grid of our model is 513 × 129, which gives a resolution of 7.8 km in both the horizontal and vertical directions. To track the evolution and migration of the materials accurately, at the beginning of the model, we placed 32 particles uniformly distributed in each cell. Since our integration points for the finite element method are put on these tracking particles, our model can well resolve the compositional boundaries during model evolution (Moresi et al., 2003).

The upper, lower and left boundaries of the model are all set as free-slip boundary conditions, while at the right boundary, we impose a velocity boundary condition. A *tanh* function of horizontal velocities is applied from the plate upper surface to the bottom of the model to ensure the conservation of mass during the evolutionary process of the model. The top and bottom boundary temperatures of the model are fixed at 0°C and the reference temperature (**Table 1**), respectively.

We divide the lithosphere into three parts in the model, i.e., the continental plate (x = 0–2,600 km), the foregoing oceanic plate (x = 2,600–3,300 km) and the following oceanic plate (x = 3,300–4,000 km) (**Figure 1A**). For the continental plate, the thickness of the lithosphere is 100 km with a 30-km thick crust. The initial temperature field of the continental lithosphere increases linearly from the surface to the bottom (**Figure 1B**). For the foregoing and following oceanic plates, the oceanic crust thickness is 7 km. The density of the continental and oceanic crust is 2,800 kg/m^3, and the density of the lithosphere is uniformly 3,300 kg/m^3. We set an initial slab with a length of L connecting to the foregoing oceanic plate, which has subducted into the mantle. The foregoing and the

TABLE 2 | Case parameters and resulting modes of MOR subduction.

Case	Slab length L (km)	Imposed velocity V_x (cm/yr)	Dip angle θ (º)	Viscosity structure	Mode
RS01	600	3	45	ViscT	Fast
RS01_HR	600	3	45	ViscT	Fast
RS02	400	3	30	ViscT&D	Extinction
RS03	600	3	30	ViscT&D	Extinction
RS04	600	2	30	ViscT&D	Extinction
RS05	600	1	30	ViscT&D	Extinction
RS06	800	1	30	ViscT&D	Fast
RS07	600	1	60	ViscT&D	Slow
RS08	400	3	60	ViscT&D	Extinction
RS09	400	1	45	ViscT&D	Extinction
RS10	600	1	45	ViscT&D	Fast
RS11	700	1	45	ViscT&D	Fast
RS12	700	3	45	ViscT&D	Slow
RS13	600	3	45	ViscT&D	Slow
RS14	600	5	45	ViscT&D	Extinction
RS15	800	3	45	ViscT&D	Slow
RS16	400	3	45	ViscT&D	Extinction
RS17	400	5	45	ViscT&D	Extinction
RS18	200	3	45	ViscT&D	Extinction
RS19	600	3	60	ViscT&D	Extinction
RS20	200	5	45	ViscT&D	Extinction
RS21	600	5	60	ViscT&D	Extinction
RS22	200	2	45	ViscT&D	Extinction
RS23	500	2	45	ViscT&D	Slow
RS24	700	2	45	ViscT&D	Fast
RS25	400	3	60	ViscT&D	Extinction
RS26	800	5	30	ViscT&D	Extinction
RS27	800	5	45	ViscT&D	Extinction
RS28	600	5	30	ViscT&D	Extinction
RS29	800	1	45	ViscT&D	Fast
RS30	200	1	45	ViscT&D	Extinction
RS31	800	3	30	ViscT&D	Extinction
RS32	600	2	45	ViscT&D	Fast
RS33	600	2	60	ViscT&D	Extinction
RS34	200	5	45	ViscT	Extinction
RS35	600	5	45	ViscT	Fast
RS36	600	1	45	ViscT	Fast
RS37	400	1	45	ViscT	Fast
RS38	200	1	45	ViscT	Extinction
RS39	500	3	45	ViscT&D	Extinction
RS40	600	3	30	ViscT	Fast
RS41	600	3	60	ViscT	Fast
RS42	600	10	45	ViscT	Slow
RS43	600	8	45	ViscT	Fast
RS44	400	2	45	ViscT&D	Extinction
RS45	800	2	45	ViscT&D	Fast

Here, L is the initial slab length connected to the foregoing oceanic plate. V_x is the magnitude of the imposed velocity at the right boundary. θ is the initial dip angle of the slab. The mantle viscosity structure includes the ViscT and ViscT&D viscosity structures, as indicated in the Methods section. In the "Mode" column, "Fast" represents the fast spreading mode, "Slow" represents the slow spreading mode, and "Extinction" represents the extinction mode. For case RS01_HR, we refine the mesh grid and achieve a higher resolution (2 × 2 km).

following oceanic plates are separated by the MOR at 3,300 km in the horizontal direction. We set the age of the oceanic plate at the MOR to 0 Myr, which linearly increases to 80 Myrs at both ends of the foregoing and following oceanic plates (i.e., at x = 2,600 and 4,000 km, respectively) (**Figure 1B**). The purple color in **Figure 1A** shows the oceanic plate thickness, which is determined by the thermal boundary layer thickness y_L (Turcotte and Schubert, 2002):

$$y_L = 2.32\,(\kappa t)^{1/2}$$

where κ is the thermal diffusivity and t is the oceanic plate age. The initial temperature fields of the oceanic plate are computed with the half-space cooling model (Turcotte and Schubert, 2002). We take the 1,300°C isotherm as the boundary between the lithosphere and the mantle. The initial temperature field of the mantle increases linearly from 1,300°C at the bottom of the lithosphere to T_0 = 1,500°C at the bottom of the box (**Figure 1B**).

We use a simple model to estimate the mantle melting extent (Katz et al., 2003). The degree of mantle melting $F\left(P, T, X_{H_2O}^{bulk}\right)$ is calculated based on the temperature, pressure and water content:

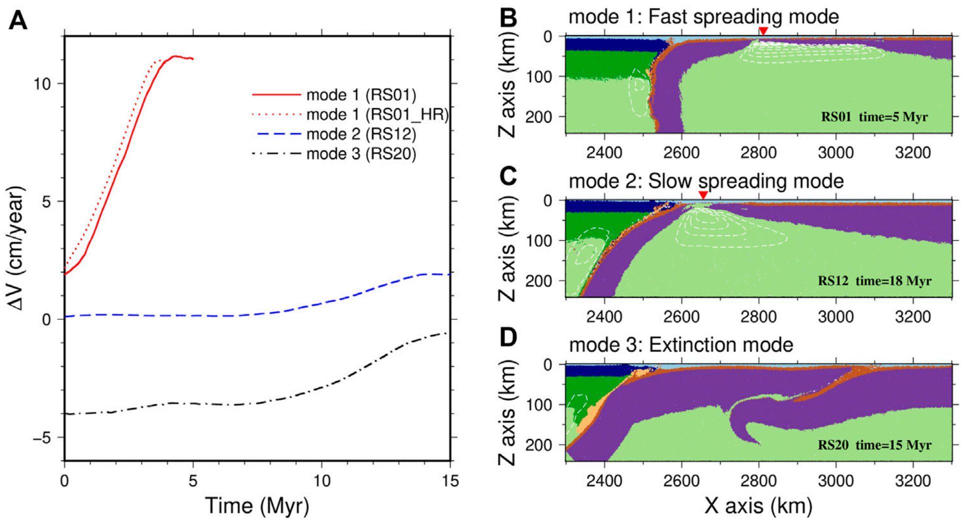

FIGURE 2 | (A) Time evolution of Δ*v* for cases RS01, RS12 and RS20 with different MOR subduction modes. **(B–D)** show the zoomed-in area of the MOR for case RS01 at 5 Myrs, case RS12 at 18 Myrs and case RS20 at 15 Myrs. The white dashed lines represent the extent of melting with an interval of 5%. The red inverted triangle represents the location of the MOR.

$$F\left(P,T,X_{H_2O}^{bulk}\right)=\left[\frac{T-\left(T_{solidus}-\Delta T\left(X_{H_2O}\left(X_{H_2O}^{bulk},P,T\right)\right)\right)}{T_{liquidus}^{lherz}-T_{solidus}}\right]^{1.5}$$

$$\mathrm{T}_{\mathrm{solidus}}=1358.7+132.9P-5.1P^2$$

$$T_{liquidus}^{lherz}=1748.0+80P-3.2P^2$$

where T is the temperature, P is the pressure, $X_{H_2O}^{bulk}$ is the weight fraction of bulk water, X_{H_2O} is the weight fraction of water in liquid phase, $T_{solidus}$ is the solidus temperature, $\Delta T\,(X_{H_2O}(X_{H_2O}^{bulk},P,T))$ is the temperature decrease in the solidus at a water content and $T_{liquidus}^{lherz}$ is the lherzolite liquidus temperature.

For the water content part, we consider that the mantle area within 60 km above the slab surface is wet, and the water content of this layer is assumed to be 0.3% (Rüpke et al., 2004; Leng et al., 2012).

RESULTS

The slab morphology is mainly affected by ridge push, slab pull, friction resistance, cohesion, among which the ridge push and slab pull force are the two main driving forces (Turcotte and Schubert, 2002). The slab pull force increases with the slab length. The imposed velocity is the main driving force of the following plate motion. So we run a total of 46 cases (**Table 2**) to study the effects of the initial slab length, imposed velocity, initial subduction angle and mantle viscosity structure on the evolution of trench-parallel MOR subduction. The initial length of the slab varies in the range of 200–800 km; the imposed velocity varies in the range of 1–10 cm/yr; the subduction angles are 30°, 45°, and 60°, respectively; and the depth-dependent viscosity structure includes the ViscT viscosity structure and ViscT&D viscosity structure, as indicated in the Methods section. We placed sampling points in the lithosphere of the foregoing and following oceanic plates to detect the relative motion of the two oceanic plates. To quantify the relative motion between the foregoing and following oceanic plates, we define the velocity difference dv between the two oceanic plates as (the velocity direction is positive to the left):

$$\Delta v=v_1-v_2$$

where v_1 is the velocity of the foregoing oceanic plate and v_2 is the velocity of the following oceanic plate. $\Delta v=0$ indicates that the foregoing and the following oceanic plates have the same speed, whereas $\Delta v>0$ or $\Delta v<0$ indicates that the speed of the foregoing oceanic plate is greater or less than that of the following oceanic plate. Based on our model results, we find that Δv is a key factor influencing the mode of trench-parallel subduction of the MOR.

By analyzing and comparing all the model results, we divide the trench-parallel subduction of the MOR into three modes: 1) In the fast spreading mode, where the Δv value is positive (case RS01, the red line in **Figure 2A**), representing a much faster velocity of the foregoing oceanic plate than that of the following oceanic plate. The MOR region experiences rapid expansion, and the melting area becomes wider (**Figure 2B**). 2) In the slow spreading mode, the Δv value is close to 0 (case RS12, the blue dashed line in **Figure 2A**), indicating that the motion speed of the foregoing oceanic plate is almost the same as that of the following oceanic plate. The MOR area expands slowly, and the melting area is basically unchanged (**Figure 2C**). 3) In the extinction mode, the Δv value is negative (case RS20, the black dot-dash line in **Figure 2A**). The following oceanic plate moves much faster than the foregoing oceanic plate, such that the following oceanic plate collides with the foregoing oceanic plate, causing the MOR

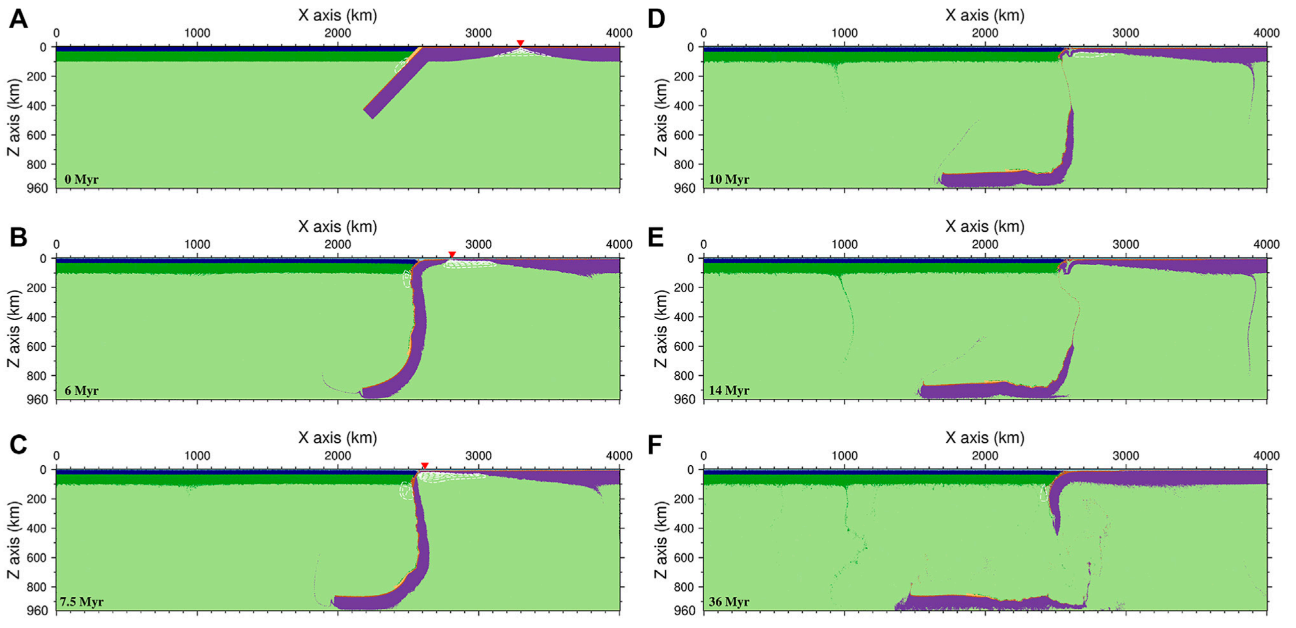

FIGURE 3 | Model evolution of case RS01 (L = 600 km, V_x = 3 cm/yr, θ = 45°) with the ViscT viscosity structure. **(A–F)** Snapshots at 0, 6, 7.5, 10, 14 and 36 Myrs. The white dashed line represents the extent of melting with an interval of 5%. The red inverted triangle represents the location of the MOR.

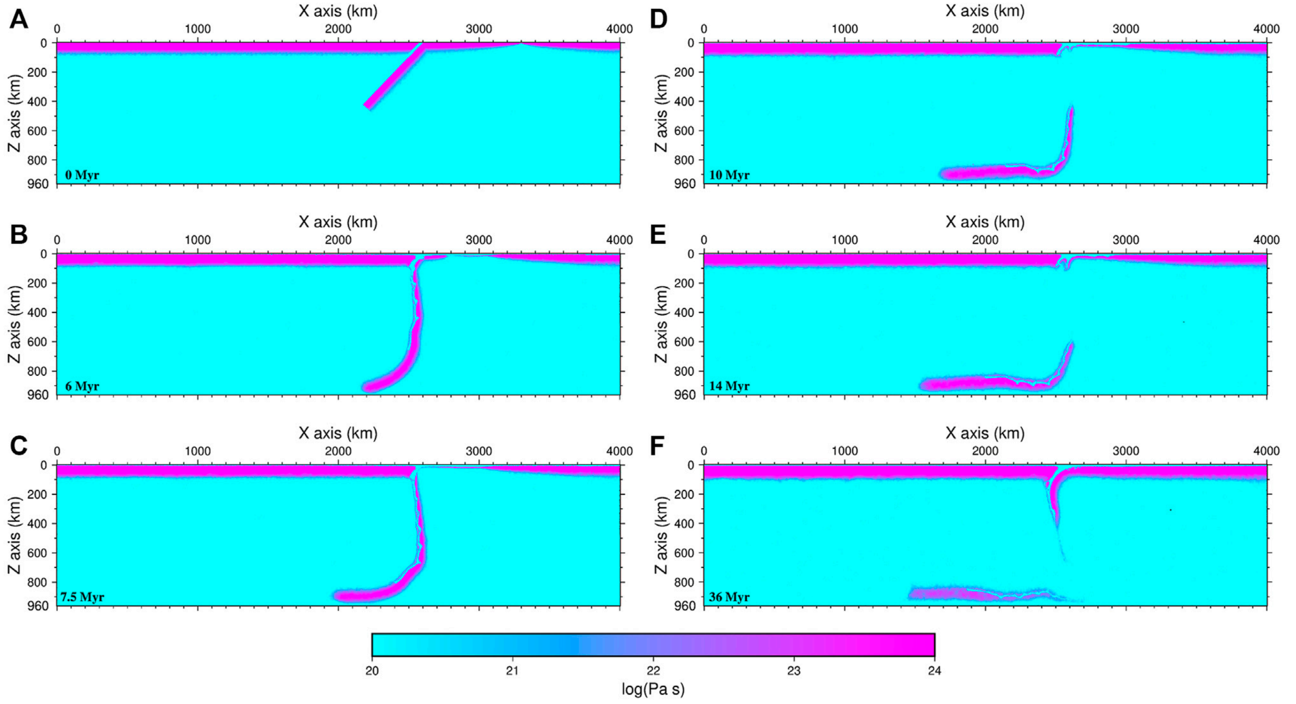

FIGURE 4 | The viscosity structure for case RS01 (L = 600 km, V_x = 3 cm/yr, θ = 45°) with the ViscT viscosity structure. **(A–F)** Snapshots at 0, 6, 7.5, 10, 14 and 36 Myrs.

structure to disappear. After ~13.0 Myrs, the Δv value increases to nearly 0, indicating that the foregoing and following oceanic plates merge and move at the same speed.

According to the results of the model, the main factor controlling the subduction of the following plate is the imposed velocity V_x. Even if V_x is a small value, such as V_x =

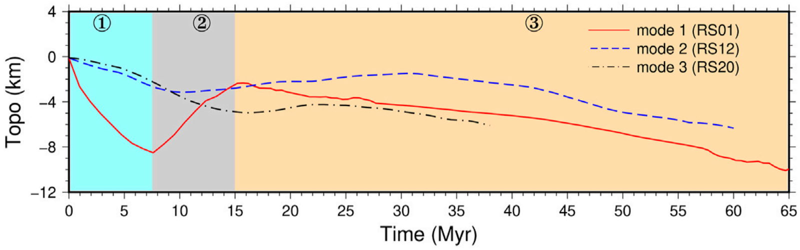

FIGURE 5 | Time evolution of the topography on the overriding continental plate for case RS01 (the fast spreading mode), case RS12 (the slow spreading mode) and case RS20 (the extinction mode). Three different background colors show the three stages for case RS01 of the fast spreading mode. Stage 1 is 0–7.5 Myrs, when the foregoing oceanic plate subducts into the mantle; stage 2 is 7.5–14 Myrs, when the MOR subducts; stage 3 is 14–65 Myrs, when the following oceanic plate subducts into the mantle.

1 cm/yr, the following plate can continue to subduct (e.g. cases RS10, RS11). However, when there are oceanic plateaus or microcontinents on the following plate, the imposed velocity V_x can be reduced to 0 because of the negative density anomaly of the oceanic plateaus or microcontinent-arc collision. Therefore, when V_x value is 0, the following plate lacks driving force and cannot subduct. For example, the Palawan subduction stopped at ~20 Ma because of the microcontinent-arc collision (Keenan et al., 2016). This situation can be considered as a special case of the extinction mode. Later, we will discuss the other situation in detail where V_x is greater than 0, that is, the following oceanic plate can subduct into the mantle.

The Fast Spreading Mode

Case RS01 represents a typical example of the fast spreading mode of MOR trench-parallel subduction. In this case, the length of slab L, the imposed velocity V_x, the initial dip angle of the slab θ and the viscosity structure of the mantle are set to 600 km, 3 cm/yr, 45° and the ViscT viscosity structure, respectively. **Figure 3** shows the evolutionary process of case RS01. Due to the reference plastic strain and yield stress, the oceanic plate experiences strong weakening (**Figures 4A–F**). Within 0–6 Myrs (**Figures 3A,B**), the negative buoyancy of the slab is strong such that the foregoing oceanic plate is dragged by the subducted slab and quickly sinks into the mantle. Due to the release of water carried by the slab, the mantle wedge area experiences intense melting and weakening (**Figures 3B**, **4B**). Therefore, the overriding continental plate experiences intense magmatic events. The topography of this area rapidly decreases due to slab subduction (the red line in **Figure 5**, 0–7 Myrs).

In this case, the speed of the foregoing oceanic plate is much faster than that of the following oceanic plate; therefore, the MOR (the red inverted triangle in **Figures 3B,C**) has always been at the right boundary of the foregoing oceanic plate and moved forward with the foregoing oceanic plate. The rapidly expanding area between the MOR and the following oceanic plate is filled by the newly formed oceanic plate (Figures 3B, 4B, X = 2,800–3,100 km). The thickness of the newly formed oceanic plate is relatively thin because of the rapid extension of this area.

At 7.5 Myrs (**Figures 3C**, **4C**), the foregoing oceanic plate has completely subducted into the mantle. The front segment of the following oceanic plate starts to contact the continental plate, marking the beginning of the subduction of the MOR. The buoyant MOR was strongly compressed with the overriding continental plate during the subduction process, resulting in a significant uplift of the continental plate near the trench (the red line in **Figure 5, 7.5–14** Myrs). With the subduction of the MOR and the continuous forward movement of the following oceanic plate, the melting area of the mantle below the MOR gradually cools down, and the degree of melting decreases until melting disappears (**Figures 3C–E**).

From 10 to 14 Myrs (**Figures 3D,E**, **4D,E**), the following oceanic plate starts to subduct, generating a new subduction zone. The thickness of the newly formed oceanic plate by the rapid expansion of the MOR is small, and the strength of the plate is weak; therefore, under the dual effect of the continuous compression of the following ocean plate and the obstruction of the front continental plate, the newly formed thin oceanic plate near the trench ruptures and gradually forms a new subduction (**Figures 3E**, **4E**).

After 36 Myrs, a new subduction zone eventually forms. Mantle wedge melting resumes due to water transport from the following oceanic plate (**Figures 3F**, **4F**). The continuous subduction of the following oceanic plate since 14 Myrs also results in the continuous reduction in the topography of the continental plate near the trench (the red line in **Figure 5**, 14–60 Myrs). During active MOR subduction, a gap of melting events and rapid topographic uplift occurs on the overriding continental plate. This melting gap divides the igneous events on the overriding plate into two separate periods.

The Slow Spreading Mode

Case RS12 is a typical case of the slow spreading mode, which has the same parameters as case RS01 except that the viscosity structure becomes a ViscT&D viscosity profile and the slab length increases to 700 km. Similar to case RS01, the foregoing oceanic plate in case RS12 continuously subducts due to slab pull. However, because of the change in the viscosity structure, the mantle resistance to the subducted plate increases, resulting in the decreased velocity of the foregoing oceanic plate. Therefore, the expansion of the MOR between the foregoing and following oceanic plates becomes slow, and the melting region of mantle beneath the MOR maintains a triangular

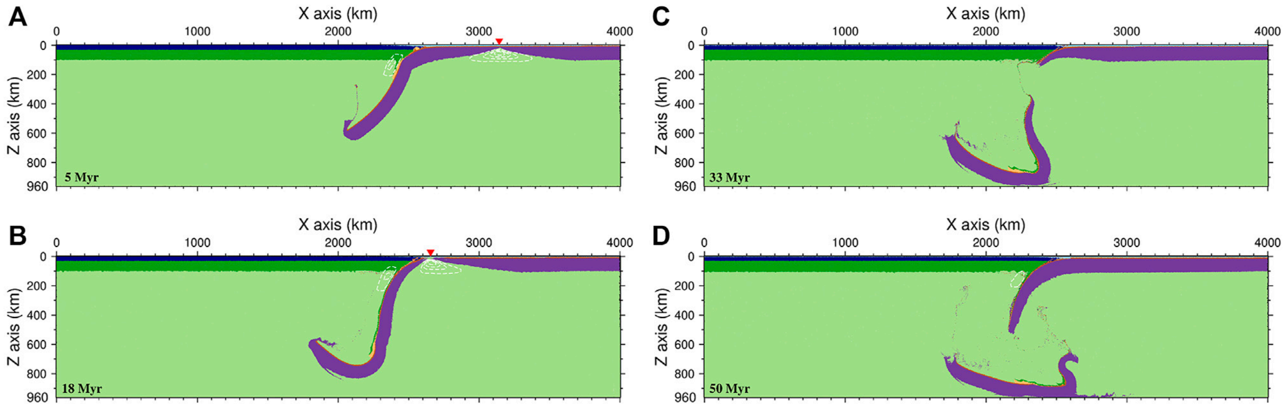

FIGURE 6 | Model evolution of case RS12 (L = 700 km, V_x = 3 cm/yr, θ = 45°) with the ViscT&D mantle viscosity structure. **(A–D)** Snapshots at 5, 18, 33 and 50 Myrs. The white dashed line represents the extent of melting with an interval of 5%. The red inverted triangle represents the location of the MOR.

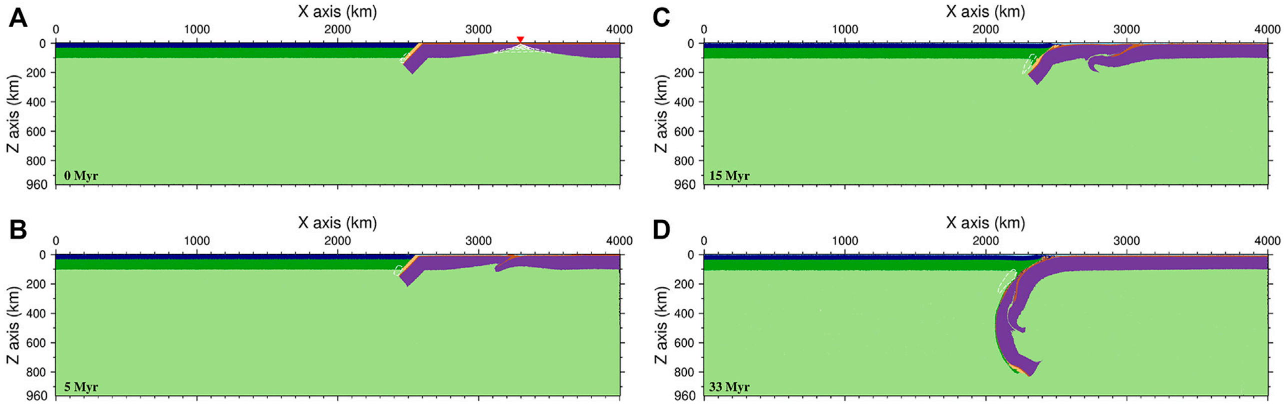

FIGURE 7 | Model evolution of case RS20 (L = 200 km, V_x = 5 cm/yr, θ = 45°) with the ViscT&D viscosity structure. **(A–D)** Snapshots at 0, 5, 15 and 33 Myrs. The white dashed line represents the extent of melting with an interval of 5%. The red inverted triangle represents the location of the MOR.

shape (**Figures 6A,B**). Similar to case RS01, the topography on the continental plate near the trench also continuously decreases due to the subduction of the foregoing oceanic plate, except that the magnitude of the topography change is much smaller than that in case RS01 (the blue dashed line in **Figure 5**). At 18 Myrs (**Figure 6B**), the foregoing oceanic plate completely subducts into the mantle, and the MOR begins to contact the continental plate. Correspondingly, the topography of the overriding continental plate begins to rise due to the subduction of the buoyant MOR. Nevertheless, unlike case RS01, the newly formed oceanic plate is relatively thick and strong, and no fractures or distortions are observed during the formation of the new subduction zone (**Figures 6C,D**). With the continuous subduction of the following oceanic plate, the topography of the overriding continental plate changes from uplift to subsidence (the blue dashed line in **Figure 5**). The melting in case RS12 also experiences a gap during MOR subduction (**Figures 6C,D**), which divides the surface volcanism into two time periods.

The Extinction Mode

Case RS20 represents a typical example of the extinction mode (**Figure 7**). In this case, the length of slab L, the imposed velocity V_x, the initial dip angle of the slab θ and the viscosity structure of the mantle are set to 200 km, 5 cm/yr, 45° and the ViscT&D viscosity structures, respectively. At the beginning, the length of the slab connecting to the foregoing oceanic plate is short (L = 200 km). The resulting negative buoyancy from the slab pull is less than the resistance force. Therefore, the foregoing plate cannot proceed to subduct into the mantle. On the other hand, the following oceanic plate is pushed to move under the imposed velocity boundary condition. Because the MOR has the characteristics of high temperature and low viscosity, the following oceanic plate starts to form new subduction at the MOR zone under strong compression, resulting in the closure and cooling of the MOR region (**Figures 7A,B**). The subducted part of the following oceanic plate is the youngest and thinnest plate; therefore, before it subducts into the deep mantle, it is coupled with the foregoing oceanic plate. The extinction of the

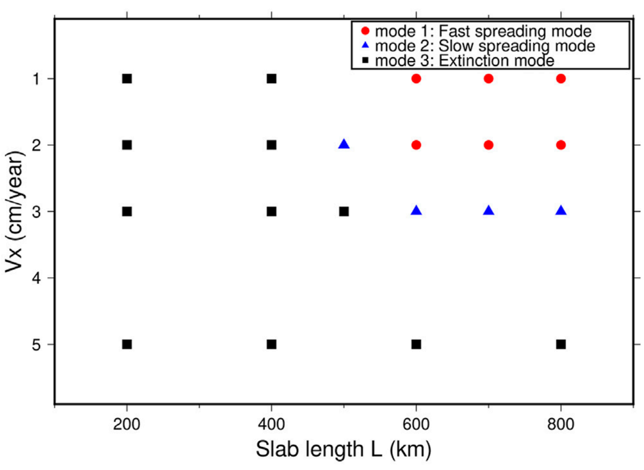

FIGURE 8 | Influences of the slab length L and the imposed velocity V_x on the modes of trench-parallel MOR subduction. All of these cases have a ViscT&D mantle viscosity structure and an initial slab dip angle of $\theta = 45^\circ$.

original MOR forms a new plate with a thick coupled region (**Figure 7C**), which is driven by the velocity boundary condition to move forward as a whole and to subduct beneath the overriding continental plate (**Figures 7C,D**).

The subduction of the extinct MOR does not show a melting gap, as in case RS01 and case RS12 (**Figure 7**). The topography of the overriding plate has experienced continuous subsidence, and only a slight uplift occurs during the collision between the coupled region and the overriding plate (the black dotted-dashed line in **Figure 5**).

The Role of Slab Length (L) and the Imposed Velocity (V_x)

The negative buoyancy of the slab connecting to the foregoing oceanic plate and the imposed velocity at the right boundary are the key driving factors for MOR subduction. We investigate the effects of different L and V_x values on the MOR subduction (cases RS09, RS10, RS11, RS12, RS13, RS14, RS15, RS16, RS17, RS18, RS20, RS22, RS23, RS24, RS27, RS29, RS30 and RS32).

We run three cases (RS22, RS23 and RS24) with the same V_x of 2 cm/yr but different initial slab lengths L of 200, 500 and 700 km. The model results show that when L becomes larger, the increased negative buoyancy of the slab leads to a larger subduction velocity of the foregoing plate. Consequently, the subduction mode of the MOR changes from the extinction mode to the slow spreading mode and eventually to the fast spreading mode (**Figure 8**). The oceanic plate age is also an important factor affecting the motion of plate. For the foregoing oceanic plate, the old plate can provide more negative buoyancy and drive the foregoing plate to subduct at a fast speed. The influence of old plate is similar to that of long initial slab length L. Therefore, we do not quantitatively explain the effect of oceanic plate age.

On the other hand, we fix the slab length L to 600 km and vary the imposed velocity V_x from 1 to 3 cm/yr and 5 cm/yr for cases RS54, RS58 and RS60, respectively. The results show that the subduction mode of the MOR changes from the fast spreading mode to the slow spreading mode and then to the extinction mode (**Figure 8**). Therefore, the increased L and decreased V_x effectively increase the magnitude of Δv, making the trench-parallel subduction of MOR move to the fast spreading mode. In contrast, the decreased L and increased V_x decrease the magnitude of Δv, leading to the slow spreading mode of MOR subduction. When Δv is small enough, we even observe shrinkage and extinction of the MOR. The following and foregoing oceanic plates strongly collide and merge into a coupled and thickened region (**Figure 7C**).

The Role of Other Parameters

Using case RS01 as a reference case, we refine the grid of our model to achieve a resolution of 2.0 km in both the horizontal and vertical directions. The results show that there is only a small difference from the previous model (**Figure 2A**). Then, we test the influence of the initial dip angle of the slab and the initial viscosity structure profile of the model on MOR subduction (cases RS02, RS03, RS04, RS05, RS06, RS07, RS08, RS19, RS21, RS25, RS26, RS28, RS31, RS33, RS34, RS35, RS36, RS37, RS38, RS40, RS41, RS42 and RS43). Cases RS40 and RS41 have the same parameters as case RS01 except that the initial dip angle θ changes to 30° and 60°, respectively. From the model results, the evolutionary processes of cases RS40, RS01, and RS41 are only slightly different from each other (**Figure 9**). These results indicate that under the same initial viscosity structure profile, even if the initial dip angles of the three models are different, the subduction angle of the slab becomes nearly vertical in a very short time. Therefore, the initial dip angle of the slab has little effect on the evolution of the subduction mode of the MOR.

We then vary the mantle viscosity structure between ViscT and ViscT&D and run case RS58. Cases RS01 and RS58 have the same parameters except for the initial viscosity structure. Since the change in the viscosity structure significantly affects the sinking velocity of the slab, the subduction mode of the MOR changes from the fast spreading mode (case RS01, **Figure 9B**) to the slow spreading mode (case RS58, **Figure 9E**). For the initial dip angle θ of 30°, when the mantle viscosity structure changes from ViscT to ViscT&D, the subduction mode of the MOR changes from the fast spreading mode to the extinction mode (**Figures 9A,D**). This similar variation also appears when the initial dip angle θ is 60° (**Figures 9C,F**). Therefore, the mantle viscosity structure may greatly affect the mode of trench-parallel subduction of the MOR.

DISCUSSION

Implications for the Subduction of the Eastern and Western Ridges of the Pacific Plate

From our model results, for the fast-spreading subduction and slow-spreading modes, igneous rock event gaps and rapid topographic uplift on the overriding continental plate occur during active MOR subduction. Two typical subduction events

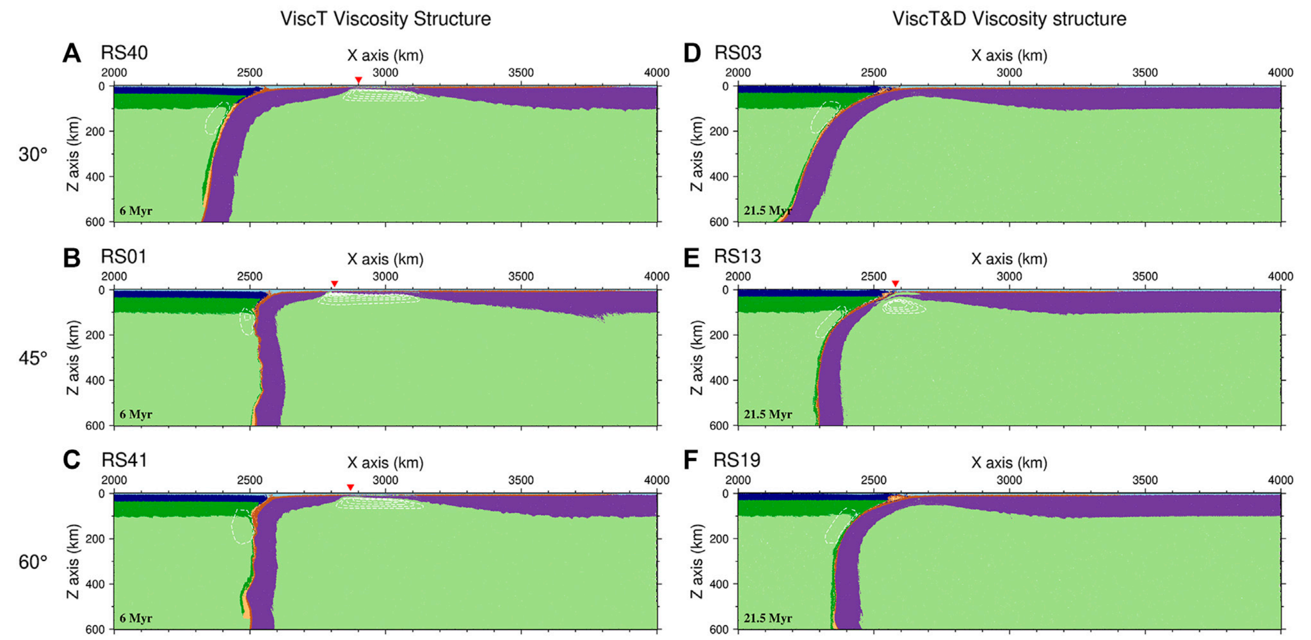

FIGURE 9 | The effects of different initial slab dip angles θ and mantle viscosity structures on the subduction of the MOR. We choose to show snapshots of the model when the foregoing oceanic plate is about to completely subduct. **(A–C)** show cases RS40, RS01 and RS41 at 6 Myrs when θ values are 30°, 45° and 60°, respectively, with the ViscT mantle viscosity structure. **(D–F)** show cases RS47, RS58 and RS19 at 21.5 Myrs when θ values are 30°, 45° and 60°, respectively, with the ViscT&D mantle viscosity structure.

of MORs are the subduction of the Western Pacific ridge (Izanagi-Pacific MOR) in the Late Cretaceous (Müller et al., 2016) and the subduction of the Eastern Pacific ridge (Pacific-Farallon MOR) from 30 Ma to the present (Ferrari et al., 2018).

The Izanagi-Pacific MOR that subducted toward the eastern Eurasian lithosphere underwent trench-parallel subduction at 55–43 Ma, as shown in **Figure 10A** (Müller et al., 2016). During the Late Cretaceous, the velocity of the Izanagi plate was 20 cm/yr, which was much larger than that of the Pacific plate moving at a speed of 7 cm/yr on the other side of the MOR (Wu and Wu, 2019). Similar to the model of the fast spreading mode, the velocity difference Δv between the two sides of the MOR was much greater than 0. In this period, the young, hot and high-topographic MOR subducted under the Eurasian plate, which had strong positive buoyancy and enhanced coupling with the eastern edge of the Eurasian plate. The eastern Eurasian margin changed from regional extension to local compression (Liu et al., 2020; Zhang et al., 2020). During this period, the Northeast China regional topography also experienced obvious tectonic uplift (Wang et al., 2013; Song et al., 2014), similar to case RS01 at 7.5–14 Myrs when the overriding continental plate experienced rapid uplift (the red line in **Figure 5**). The distribution of igneous rocks since the Late Cretaceous is shown in **Figures 10A,B**. Based on the eruption time of the igneous rocks, the active volcanic activities in eastern Eurasia since the Late Cretaceous can be divided into two time periods: event 1 (100–55 Ma) and event 2 (45 Ma–present). Late Cretaceous igneous rocks are more widely distributed in NE Asia, but there are fewer igneous rocks after the Cenozoic. From the relationship between the $\varepsilon Nd\,(t)$ values and $^{87}Sr/^{86}Sr$ values over time (**Figures 10D,E**), there is an obvious quiet igneous period between 55 and 45 Ma and a lack of igneous rock activity (Tang et al., 2018; Wu and Wu, 2019; Liu et al., 2020). Interestingly, the igneous rocks that formed before 55 Ma are significantly different from those formed after 45 Ma in terms of geochemical properties. The igneous rocks that formed before 55 Ma have low $\varepsilon Nd\,(t)$ values and high $^{87}Sr/^{86}Sr$ values. The $\varepsilon Nd\,(t)/(^{87}Sr/^{86}Sr)$ values are mostly less than 0 (**Figure 10E**). The igneous samples that formed after 45 Ma have high $\varepsilon Nd\,(t)$ values and low $^{87}Sr/^{86}Sr$ values, and the $\varepsilon Nd\,(t)/(^{87}Sr/^{86}Sr)$ ratios are mostly greater than 0 (**Figure 10E**). The difference in the geochemical properties of the igneous rocks in these two periods may be due to the change in the source of molten mantle material caused by the transformation of the subducting plate from the Izanagi plate to the Pacific plate. The quiet igneous period between 55 and 45 Ma in NE Asia can be compared to the disappearance of mantle melting above the subducting slab in our modeled case RS01 (**Figures 3A–D**).

On the other side of the Pacific plate, East Pacific ridge subduction began at 30 Ma and has continued to the present. The MOR has not yet fully subducted into the North American plate. We can observe that the East Pacific ridge is approximately parallel to the subduction zone (**Figure 10C**). In this period, the Sierra Madre Occidental silicic large igneous province with crustal melting and the Comondú Group of Baja California were formed, and resulting mafic magmas are widely distributed in western North America (Ferrari et al., 2018). However, the age of the subduction-related igneous rocks since 24 Ma can be divided into two stages (24–12 Ma and

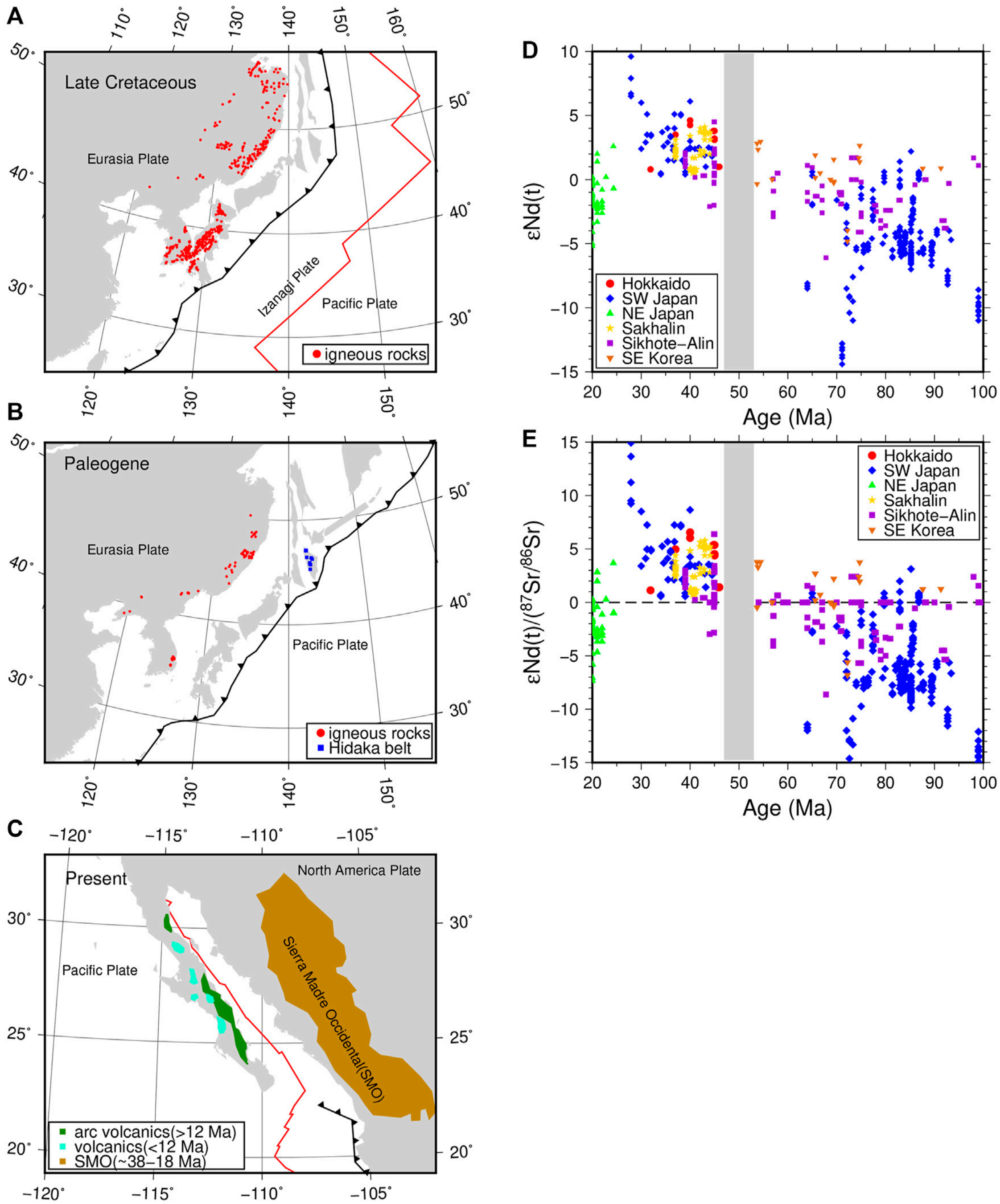

FIGURE 10 | Reconstructed model of the NE Eurasian plate and the West American plate and the $\varepsilon Nd(t)$ and $\varepsilon Nd(t)/(^{87}Sr/^{86}Sr)$ versus ages for the NE Eurasian igneous rocks. **(A,B)** show the distribution maps of igneous rocks in northeastern Eurasia during the Late Cretaceous and Paleogene, respectively. The red dots show the locations of igneous rocks. The blue squares show the Hidaka belt where MORB-type basaltic rocks are dominant (Nanayama et al., 2019). The black lines with triangles are the subduction zones at that time. The red line is the MOR between the Izanagi plate and the Pacific plate. **(C)** Locations of the volcanic rocks after the Oligocene and the Sierra Madre Occidental silicic large igneous province (Ferrari et al., 2018). Plate reconstruction topologies are derived from Müller et al. (2016) and Vaes et al. (2019). **(D,E)** show $\varepsilon Nd(t)$ and $\varepsilon Nd(t)/(^{87}Sr/^{86}Sr)$ values versus age for the northeast Eurasian igneous rocks from 100 to 20 Ma. The gray zone is a gap of continuous igneous events. Different color symbols [in **(D,E)**] represent igneous rock samples in different regions. Igneous rock data are from Wu and Wu (2019) and Tang et al. (2018).

12 Ma–present) (**Figure 10C**). There is also a short gap in the subduction-related igneous rocks at approximately 12 Ma (Martı´n et al., 2000; Pallares et al., 2007).

The magmatic activity gap in East Asia is longer than that in western North America (**Figures 10A–C**). We think it probably has two factors: the dip angle of the slab and the MOR subduction pattern, whether it is monolithic or segmented. The Western Pacific plate subducted under the East Asian plate at a high dip angle, caused strong backarc expansion, and formed a series of extensional basins on the edge of East Asia (e.g., Japan sea basin and Philippine basin). It maked the East Asian continent far away from the trench. The igneous rocks produced by oceanic plate subduction need a long time to migrate to the East Asian continent. As for the Farallon plate, it subducted under the North American plate with a low dip angle, and did not form extensional basins. In addition, the Izanagi-Pacific MOR is roughly parallel to the edge of the East Asian plate. The Izanagi-Pacific MOR subduction as a monolithic in a short period of time (within a few million years), while there was a small angle between the Farallon-Pacific MOR and the North American plate boundary. So the Farallon-Pacific MOR gradually subducted in segments. And the MOR subduction lasted for a long time (more than ten million years). This situation caused the lateral magmatic flow and resulted in a short igneous events gap.

Plate Coupling and Thickening in the Extinction Mode

From the results of the extinction mode, when the speed of the foregoing oceanic plate is much smaller than that of the following oceanic plate, the latter may be coupled with the foregoing oceanic plate. The extinction of the original MOR forms a new plate with a thickened coupling region, and the thickness of the coupling region can reach 150 km (**Figures 7C,D**). Therefore, the coupling region can be clearly distinguished from the normal thickness of the oceanic plate by seismic methods. Since the geological sequence of the coupling region is crust-lithosphere-crust-lithosphere (**Figure 7C**), the seismic waveform of this region can be relatively complicated. Moreover, the high temperature and high pressure applied to the coupled crustal region may generate metamorphic rocks and ophiolites, e.g., the Palawan ophiolite (Keenan et al., 2016). Due to the extinction of the active MOR, the following oceanic plate follows the foregoing oceanic plate to form continuous subduction. Therefore, a melting gap will not appear in the mantle wedge (**Figures 7B–D**). Continuous oceanic plate subduction causes continuous subsidence of the overriding continental plate topography (**Figure 5**).

The Shape and Mode of the MOR Subduction

Based on our results, the velocity difference Δv between the foregoing and following oceanic plates determines the evolutionary modes and the shape of the MOR during its subduction. When Δv is greater than 0, the velocity of the foregoing oceanic plate is much faster than that of the following oceanic plate, and the MOR region expands rapidly with a wide melting area (**Figure 3B**). When Δv is close to 0, the foregoing and following oceanic plates move synchronously, the MOR area expands slowly, and the melting area appears to be normal and triangular. The center of the MOR is located in the center of the melting area (**Figures 6A,B**). However, when the MOR area is close to the trench, we find that the center of the MOR moves forward toward the left oceanic plate. This result occurs because when the foregoing oceanic plate is pulled by the slab and begins to subduct, due to the distance from the MOR, the age of the subducted foregoing oceanic plate gradually becomes younger and the density decreases as subduction continues. Because of continuous subduction, the length of the slab entering the mantle becomes longer, and the length of the unsubducted part of the foregoing oceanic plate becomes shorter. Therefore, the subduction velocity of the foregoing oceanic plate increases rapidly after a period of subduction (as shown in **Figure 2A** at 10–15 Myrs), resulting in the rapid forward movement of the center of the MOR, which is no longer at the center of the melting region. When Δv is less than 0, the speed of the following oceanic plate is faster than that of the foregoing oceanic plate, and the MOR region gradually disappears (**Figure 7B**). Then, the foregoing and the following oceanic plates collide and merge into one plate with a thickened coupling region.

Nevertheless, previous studies have shown that many of the MORs are not completely parallel to the trench (Van Hunen et al., 2002; Gutiérrez et al., 2005; Rosenbaum et al., 2005; Espurt et al., 2008; Seton et al., 2015; Hu et al., 2016; Müller et al., 2016; Tang et al., 2018; Liu et al., 2020). The nonparallel subduction of MORs or asymmetric ridges may show different temporal and spatial distributions of igneous events and topographic evolution on the overriding plate. For these situations, our 2-D model has limitations, and 3-D models are required in future studies.

CONCLUSION

We construct a 2-D viscoelastoplastic model to study the modes and key parameters controlling the trench-parallel subduction of the mid-ocean ridge. Our model results show that the subduction modes of mid-ocean ridges can be primarily categorized into three types: the fast spreading mode, the slow spreading mode, and the extinction mode. The key factor controlling these subduction modes is the relative motion between the foregoing and following oceanic plates, which are separated by the mid-ocean ridge. The viscosity structure of the mantle significantly affects the sinking velocity of the preceding slab; therefore, the mantle viscosity structure may greatly affect the mode of trench-parallel subduction of the MOR. The volcanic gap and the topographic evolution observed in our model may successfully explain the geological observations for the subduction of the Izanagi-Pacific ridge at 55–45 Ma and the Pacific-Farallon ridge from 30 Ma to the present.

DATA AVAILABILITY STATEMENT

The raw data supporting the conclusion of this article will be made available by the authors, without undue reservation.

AUTHOR CONTRIBUTIONS

XS and WL contributed to conception and design of the study. XS and WL designed the model. XS ran the model and analyzed the results. XS wrote the first draft of the manuscript. All authors contributed to manuscript revision, read, and approved the submitted version.

FUNDING

This work is supported by the National Natural Science Foundation of China (41820104004, 41774105, 41688103) and the Fundamental Research Funds for the Central Universities (WK2080000144).

ACKNOWLEDGMENTS

We thank Jie Tang for providing igneous rock data in northeast Eurasia.

REFERENCES

Buck, W. R., and Poliakov, A. N. B. (1998). Abyssal hills Formed by Stretching Oceanic Lithosphere. *Nature* 392 (6673), 272–275. doi:10.1038/32636

Burkett, E. R., and Billen, M. I. (2009). Dynamics and Implications of Slab Detachment Due to ridge-trench Collision. *J. Geophys. Res. Solid Earth* 114, B12402. doi:10.1029/2009jb006402

Chen, M., Shen, X., Leng, W., and Chen, L. (2020). Destruction of Cratonic Lithosphere Induced by Oceanic Subduction Initiation. *Geophys. Res. Lett.* 47 (15), e2020GL089140. doi:10.1029/2020GL089140

Christensen, U. R. (1996). The Influence of Trench Migration on Slab Penetration into the Lower Mantle. *Earth Planet. Sci. Lett.* 140 (1-4), 27–39. doi:10.1016/0012-821x(96)00023-4

Čížková, H., and Bina, C. R. (2013). Effects of Mantle and Subduction-Interface Rheologies on Slab Stagnation and Trench Rollback. *Earth Planet. Sci. Lett.* 379, 95–103. doi:10.1016/j.epsl.2013.08.011

Čížková, H., van den Berg, A. P., Spakman, W., and Matyska, C. (2012). The Viscosity of Earth's Lower Mantle Inferred from Sinking Speed of Subducted Lithosphere. *Phys. earth Planet. Interiors* 200, 56–62. doi:10.1016/j.pepi.2012.02.010

Espurt, N., Funiciello, F., Martinod, J., Guillaume, B., Regard, V., Faccenna, C., et al. (2008). Flat Subduction Dynamics and Deformation of the South American Plate: Insights from Analog Modeling. *Tectonics* 27 (3), TC3011. doi:10.1029/2007tc002175

Ferrari, L., Orozco-Esquivel, T., Bryan, S. E., López-Martínez, M., and Silva-Fragoso, A. (2018). Cenozoic Magmatism and Extension in Western Mexico: Linking the Sierra Madre Occidental Silicic Large Igneous Province and the Comondú Group with the Gulf of California Rift. *Earth-Science Rev.* 183, 115–152. doi:10.1016/j.earscirev.2017.04.006

Garel, F., Goes, S., Davies, D. R., Davies, J. H., Kramer, S. C., and Wilson, C. R. (2014). Interaction of Subducted Slabs with the Mantle Transition-zone: A Regime Diagram from 2-D Thermo-mechanical Models with a mobile Trench and an Overriding Plate. *Geochem. Geophys. Geosyst.* 15 (5), 1739–1765. doi:10.1002/2014gc005257

Georgieva, V., Gallagher, K., Sobczyk, A., Sobel, E. R., Schildgen, T. F., Ehlers, T. A., et al. (2019). Effects of Slab-Window, Alkaline Volcanism, and Glaciation on Thermochronometer Cooling Histories, Patagonian Andes. *Earth Planet. Sci. Lett.* 511, 164–176. doi:10.1016/j.epsl.2019.01.030

Groome, W. G., and Thorkelson, D. J. (2009). The Three-Dimensional Thermo-Mechanical Signature of ridge Subduction and Slab Window Migration. *Tectonophysics* 464 (1-4), 70–83. doi:10.1016/j.tecto.2008.07.003

Gurnis, M., and Hager, B. H. (1988). Controls of the Structure of Subducted Slabs. *Nature* 335 (6188), 317–321. doi:10.1038/335317a0

Gutiérrez, F., Gioncada, A., Ferran, O. G., Lahsen, A., and Mazzuoli, R. (2005). The Hudson Volcano and Surrounding Monogenetic Centres (Chilean Patagonia): an Example of Volcanism Associated with ridge–trench Collision Environment. *J. Volcanology Geothermal Res.* 145 (3-4), 207–233. doi:10.1016/j.jvolgeores.2005.01.014

Hu, J., Liu, L., Hermosillo, A., and Zhou, Q. (2016). Simulation of Late Cenozoic South American Flat-Slab Subduction Using Geodynamic Models with Data Assimilation. *Earth Planet. Sci. Lett.* 438, 1–13. doi:10.1016/j.epsl.2016.01.011

Isozaki, Y., Aoki, K., Nakama, T., and Yanai, S. (2010). New Insight into a Subduction-Related Orogen: A Reappraisal of the Geotectonic Framework and Evolution of the Japanese Islands. *Gondwana Res.* 18 (1), 82–105. doi:10.1016/j.gr.2010.02.015

Karato, S.-i., and Wu, P. (1993). Rheology of the Upper Mantle: A Synthesis. *Science* 260 (5109), 771–778. doi:10.1126/science.260.5109.771

Katz, R. F., Spiegelman, M., and Langmuir, C. H. (2003). A New Parameterization of Hydrous Mantle Melting. *Geochem. Geophys. Geosystems* 4 (9), 1–9. doi:10.1029/2002gc000433

Keenan, T. E., Encarnación, J., Buchwaldt, R., Fernandez, D., Mattinson, J., Rasoazanamparany, C., et al. (2016). Rapid Conversion of an Oceanic Spreading center to a Subduction Zone Inferred from High-Precision Geochronology. *Proc. Natl. Acad. Sci. USA* 113 (47), E7359–E7366. doi:10.1073/pnas.1609999113

King, S. D., Frost, D. J., and Rubie, D. C. (2015). Why Cold Slabs Stagnate in the Transition Zone. *Geology* 43 (3), 231–234. doi:10.1130/g36320.1

Leng, W., Gurnis, M., and Asimow, P. (2012). From Basalts to Boninites: The Geodynamics of Volcanic Expression during Induced Subduction Initiation. *Lithosphere* 4 (6), 511–523. doi:10.1130/l215.1

Leng, W., and Gurnis, M. (2011). Dynamics of Subduction Initiation with Different Evolutionary Pathways. *Geochem. Geophys. Geosystems* 12 (12), Q12018. doi:10.1029/2011gc003877

Leng, W., and Gurnis, M. (2015). Subduction Initiation at Relic Arcs. *Geophys. Res. Lett.* 42 (17), 7014–7021. doi:10.1002/2015gl064985

Li, S. M., Wang, Q., Zhu, D. C., Cawood, P. A., Stern, R. J., Weinberg, R., et al. (2020). Reconciling Orogenic Drivers for the Evolution of the Bangong-Nujiang Tethys during Middle-Late Jurassic. *Tectonics* 39 (2), e2019TC005951. doi:10.1029/2019TC005951

Ling, M.-X., Wang, F.-Y., Ding, X., Hu, Y.-H., Zhou, J.-B., Zartman, R. E., et al. (2009). Cretaceous ridge Subduction along the Lower Yangtze River belt, Eastern China. *Econ. Geology.* 104 (2), 303–321. doi:10.2113/gsecongeo.104.2.303

Liu, K., Zhang, J., Xiao, W., Wilde, S. A., and Alexandrov, I. (2020). A Review of Magmatism and Deformation History along the NE Asian Margin from Ca. 95 to 30 Ma: Transition from the Izanagi to Pacific Plate Subduction in the Early Cenozoic. *Earth-Science Rev.* 209, 103317. doi:10.1016/j.earscirev.2020.103317

Maeda, J. I., and Kagami, H. (1996). Interaction of a Spreading ridge and an Accretionary Prism: Implications from MORB Magmatism in the Hidaka Magmatic Zone, Hokkaido, Japan. *Geol* 24 (1), 31–34. doi:10.1130/0091-7613(1996)024<0031:ioasra>2.3.co;2

Martinod, J., Guillaume, B., Espurt, N., Faccenna, C., Funiciello, F., and Regard, V. (2013). Effect of Aseismic ridge Subduction on Slab Geometry and Overriding Plate Deformation: Insights from Analogue Modeling. *Tectonophysics* 588, 39–55. doi:10.1016/j.tecto.2012.12.010

Martı´n, A., Fletcher, J. M., López-Martı´nez, M., and Mendoza-Borunda, R. (2000). Waning Miocene Subduction and Arc Volcanism in Baja California: the San Luis Gonzaga Volcanic Field. *Tectonophysics* 318 (1-4), 27–51.

Moresi, L., Dufour, F., and Mühlhaus, H.-B. (2003). A Lagrangian Integration point Finite Element Method for Large Deformation Modeling of Viscoelastic Geomaterials. *J. Comput. Phys.* 184 (2), 476–497. doi:10.1016/s0021-9991(02)00031-1

Muhuri, S. K., Dewers, T. A., Scott, T. E., Jr, and Reches, Z. E. (2003). Interseismic Fault Strengthening and Earthquake-Slip Instability: Friction or Cohesion? *Geol* 31 (10), 881–884. doi:10.1130/g19601.1

Müller, R. D., Seton, M., Zahirovic, S., Williams, S. E., Matthews, K. J., Wright, N. M., et al. (2016). Ocean basin Evolution and Global-Scale Plate Reorganization Events since Pangea Breakup. *Annu. Rev. Earth Planet. Sci.* 44, 107–138. doi:10.1146/annurev-earth-060115-012211

Nanayama, F., Yamasaki, T., Iwano, H., Danhara, T., and Hirata, T. (2019). Zircon U-Pb Ages of Sedimentary Complexes in the Hidaka Belt. *Jour. Geol. Soc. Jpn.* 125 (6), 421–438. doi:10.5575/geosoc.2019.0011

Pallares, C., Maury, R. C., Bellon, H., Royer, J. Y., Calmus, T., Aguillón-Robles, A., et al. (2007). Slab-tearing Following ridge-trench Collision: Evidence from Miocene Volcanism in Baja California, México. *J. Volcanology Geothermal Res.* 161 (1-2), 95–117. doi:10.1016/j.jvolgeores.2006.11.002

Poliakov, A. N., and Buck, W. R. (1998). Mechanics of Stretching Elastic-Plastic-Viscous Layers: Applications to Slow-Spreading Mid-ocean Ridges. *Geophys. Monogr. Ser.* 106, 305–324. doi:10.1029/GM106p0305

Püthe, C., and Gerya, T. (2014). Dependence of Mid-ocean ridge Morphology on Spreading Rate in Numerical 3-D Models. *Gondwana Res.* 25 (1), 270–283. doi:10.1016/j.gr.2013.04.005

Qing, J., Liao, J., Li, L., and Gao, R. (2021). Dynamic Evolution of Induced Subduction through the Inversion of Spreading Ridges. *J. Geophys. Res. Solid Earth* 126 (3), e2020JB020965. doi:10.1029/2020JB020965

Rosenbaum, G., Giles, D., Saxon, M., Betts, P. G., Weinberg, R. F., and Duboz, C. (2005). Subduction of the Nazca Ridge and the Inca Plateau: Insights into the Formation of Ore Deposits in Peru. *Earth Planet. Sci. Lett.* 239 (1-2), 18–32. doi:10.1016/j.epsl.2005.08.003

Rüpke, L. H., Morgan, J. P., Hort, M., and Connolly, J. A. (2004). Serpentine and the Subduction Zone Water Cycle. *Earth Planet. Sci. Lett.* 223 (1-2), 17–34. doi:10.1016/j.epsl.2004.04.018

Seton, M., Flament, N., Whittaker, J., Müller, R. D., Gurnis, M., and Bower, D. J. (2015). Ridge Subduction Sparked Reorganization of the Pacific Plate-mantle System 60-50 Million Years Ago. *Geophys. Res. Lett.* 42 (6), 1732–1740. doi:10.1002/2015gl063057

Song, Y., Ren, J., Stepashko, A. A., and Li, J. (2014). Post-rift Geodynamics of the Songliao Basin, NE China: Origin and Significance of T11 (Coniacian) Unconformity. *Tectonophysics* 634, 1–18. doi:10.1016/j.tecto.2014.07.023

Steinberger, B., and Calderwood, A. R. (2006). Models of Large-Scale Viscous Flow in the Earth's Mantle with Constraints from mineral Physics and Surface Observations. *Geophys. J. Int.* 167 (3), 1461–1481. doi:10.1111/j.1365-246x.2006.03131.x

Tang, J., Xu, W., Wang, F., and Ge, W. (2018). Subduction History of the Paleo-Pacific Slab beneath Eurasian Continent: Mesozoic-Paleogene Magmatic Records in Northeast Asia. *Sci. China Earth Sci.* 61 (5), 527–559. doi:10.1007/s11430-017-9174-1

Torii, Y., and Yoshioka, S. (2007). Physical Conditions Producing Slab Stagnation: Constraints of the Clapeyron Slope, Mantle Viscosity, Trench Retreat, and Dip Angles. *Tectonophysics* 445 (3-4), 200–209. doi:10.1016/j.tecto.2007.08.003

Turcotte, D. L., and Schubert, G. (2002). *Geodynamics*. Cambridge: Cambridge University Press.

Vaes, B., Hinsbergen, D. J. J., and Boschman, L. M. (2019). Reconstruction of Subduction and Back-Arc Spreading in the NW Pacific and Aleutian Basin: Clues to Causes of Cretaceous and Eocene Plate Reorganizations. *Tectonics* 38 (4), 1367–1413. doi:10.1029/2018tc005164

van Hunen, J., van den Berg, A. P., and Vlaar, N. J. (2002). The Impact of the South-American Plate Motion and the Nazca Ridge Subduction on the Flat Subduction below South Peru. *Geophys. Res. Lett.* 29 (14), 35–41. doi:10.1029/2001gl014004

Wang, C., Ding, W., Li, J., Dong, C., Fang, Y., Tang, L., et al. (2019). Effects of Trench-perpendicular ridge Subduction on Accretionary Wedge Deformation: Clues from Analogue Modelling. *Geol. J.* 54 (4), 2665–2678. doi:10.1002/gj.3317

Wang, C., Feng, Z., Zhang, L., Huang, Y., Cao, K., Wang, P., et al. (2013). Cretaceous Paleogeography and Paleoclimate and the Setting of SKI Borehole Sites in Songliao Basin, Northeast China. *Palaeogeogr. Palaeoclimatol. Palaeoecol.* 385, 17–30. doi:10.1016/j.palaeo.2012.01.030

Wu, J. T.-J., and Wu, J. (2019). Izanagi-Pacific ridge Subduction Revealed by a 56 to 46 Ma Magmatic gap along the Northeast Asian Margin. *Geology* 47 (10), 953–957. doi:10.1130/g46778.1

Yang, T., Moresi, L., Zhao, D., Sandiford, D., and Whittaker, J. (2018). Cenozoic Lithospheric Deformation in Northeast Asia and the Rapidly-Aging Pacific Plate. *Earth Planet. Sci. Lett.* 492, 1–11. doi:10.1016/j.epsl.2018.03.057

Zhang, B., Liu, S., Lin, C., Shen, W., and Li, X. (2020). Reconstruction of the Stress Regime in the Jiaolai Basin, East Asian Margin, as Decoded from Fault-Slip Analysis. *J. Struct. Geology.* 141, 104190. doi:10.1016/j.jsg.2020.104190

Conflict of Interest: The authors declare that the research was conducted in the absence of any commercial or financial relationships that could be construed as a potential conflict of interest.

frontiers
in Earth Science

ORIGINAL RESEARCH
published: 17 November 2021
doi: 10.3389/feart.2021.783409

Evolution of Subduction Cusps From the Perspective of Trench Migration and Slab Morphology

Hui Zhao [1,2], *Xiaobing Shen* [1,2] *and Wei Leng* [1,2]*

[1] *Laboratory of Seismology and Physics of Earth's Interior, School of Earth and Space Sciences, University of Science and Technology of China, Hefei, China,* [2] *CAS Center for Excellence in Comparative Planetology, Zhuhai, China*

The geometries of trenches vary worldwide due to continuous plate boundary reorganization. When two trenches intersect to generate a corner, a subduction cusp is formed. Although subduction cusps are frequently observed throughout historical plate movement reconstructions, few studies have been conducted to explore the controlling factors of trench migration and slab morphology along subduction cusps. Here, we use a 3-D dynamic subduction model to explore the influence of the overriding plate strength, initial slab-pull force, and initial cusp angle on the evolution of subduction cusps. Our numerical model results suggest the following: 1) subduction cusps have a tendency to become smooth and disappear during the subduction process; 2) the slab dip angle is smallest in the diagonal direction of the subduction cusp, and a larger cuspate corner angle leads to a larger slab dip angle; 3) the asymmetric distribution of the overriding plate strength and initial slab-pull force determine the asymmetric evolutionary pathway of subduction cusps. Our results provide new insights for reconstructing the evolution of subduction cusps from seismological and geological observations.

Keywords: subduction cusp, trench migration, slab morphology, oceanic subduction, numerical simulation

Edited by:
Jie Liao,
Sun Yat-sen University, China

Reviewed by:
Liming Dai,
OUC, China
Quan Zhou,
Facebook, United States

Correspondence:
Wei Leng
wleng@ustc.edu.cn

Specialty section:
This article was submitted to
Solid Earth Geophysics,
a section of the journal
Frontiers in Earth Science

Received: *26 September 2021*
Accepted: *01 November 2021*
Published: *17 November 2021*

Citation:
Zhao H, Shen X and Leng W (2021)
Evolution of Subduction Cusps From
the Perspective of Trench Migration
and Slab Morphology.
Front. Earth Sci. 9:783409.
doi: 10.3389/feart.2021.783409

INTRODUCTION

During the evolution of plate tectonics, trenches located at the junction of subducting and overriding plates can develop various kinds of geometries (Schellart et al., 2007; Müller et al., 2016). When two trenches intersect with each other to form a corner, we define it as a subduction cusp. For example, at 40 Ma, the trenches along the Kurile Islands and northeast Japan intersected and formed a subduction cusp (**Figure 1A**) (Vaes et al., 2019). At 35 Ma, the Pacific plate subducted beneath the Eurasian and Philippine Sea plates, and the trenches along the Eastern Japan and Izu-Bonin arc were generally perpendicular to each other, forming a subduction cusp (**Figure 1D**) (Hall, 2002; Ma et al., 2019).

Subduction cusps can be generated under various tectonic settings. For example, a series of numerical models and analog models have shown that a subduction cusp can be formed by aseismic ridge or plateau subduction (Martinod et al., 2005; Martinod et al., 2013; Zeumann and Hampel, 2016). It is possible that the cusps linking the Kurile Islands and northeast Japan trenches and the Izu-Bonin arc and East Japan trenches (**Figure 1**) were generated by the subduction of oceanic plateaus that have since been entirely consumed (Rosenbaum and Mo, 2011).

Once a subduction cusp is formed, its evolutionary pathway is of particular interest in terms of trench migration and slab morphology. The evolution of the Kurile cusp and Izu-Bonin cusp has some common features regarding their trench migration. At 40 Ma, the angle between the trenches

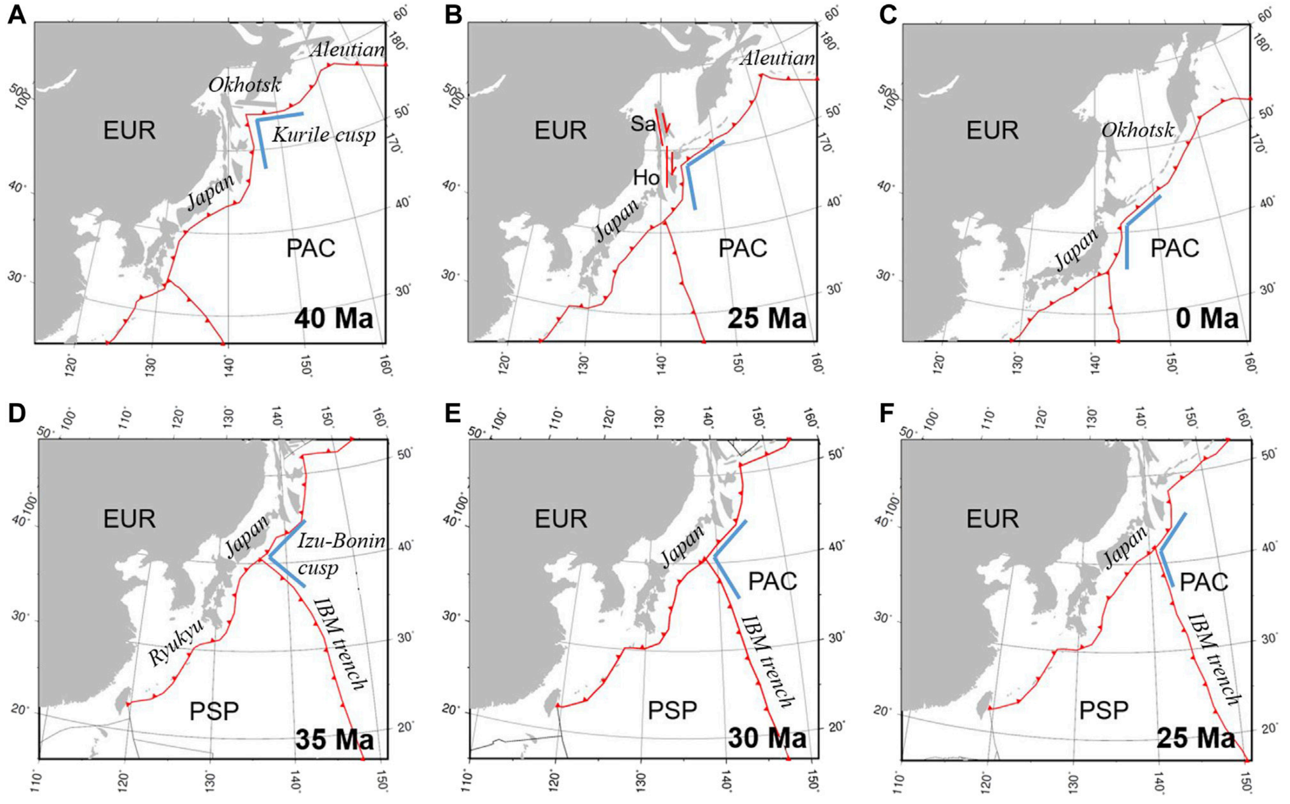

FIGURE 1 | (A), **(B)**, and **(C)** show the plate boundary configurations near the Kurile Islands at **(A)** 40 Ma, **(B)** 25 Ma, and **(C)** 0 Ma (after Vaes et al., 2019). **(D)**, **(E)**, and **(F)** show plate reconstruction results near the Philippine Sea plate at **(D)** 35 Ma, **(E)** 30 Ma, and **(F)** 25 Ma (after Müller et al., 2016). Red lines with filled triangles and arrows represent trenches and strike-slip faults, respectively. The Kurile and Izu-Bonin cusps are represented by blue angles. Abbreviations: PAC = Pacific plate; EUR = Eurasian plate; PSP = Philippine Sea plate; Sa = Sakhalin; and Ho = Hokkaido.

along northeast Japan and the Kurile Islands was ~90° (**Figure 1A**). Then, the trench along the Kurile Islands began to retreat and rotate counterclockwise, forming a dextral strike-slip fault between Sakhalin and central Hokkaido (**Figure 1B**). After that, the trench along northeast Japan began to retreat at approximately 25 Ma. The retreat of these two trenches facilitated the opening of the Kurile and Japan Sea basins. The trench retreated faster at the subduction cusp, causing an increasing angle between these two trenches (**Figures 1A–C**) (Vaes et al., 2019). Similarly, at 35 Ma, the Pacific plate subducted beneath the Philippine Sea plate and East Asian margin. The trenches along these two overriding plates were almost perpendicular to each other (**Figure 1D**). The Philippine Sea plate moved northward and rotated clockwise, with the subduction of the Pacific plate, thereby forcing the triple junction (between the Pacific plate, Philippine Sea plate and Eurasian plate) to move northeastward, and the angle between the Izu-Bonin arc and Japan trench gradually became larger (**Figures 1D–F**) (Hall, 2002; Ma et al., 2019).

The Kurile cusp and Izu-Bonin cusp also show similar characteristics in slab morphology. From seismic tomography results, we can find that the slab dip angle varies along these two subduction zones and reaches its minimum beneath the cuspate area (Miller and Kennett, 2006; Zhang et al., 2019). Along the Kurile trench, the subducting slab steepens gradually from the cuspate area to the northeast Kurile and Kamchatka (Miller and Kennett, 2006), and the slab dip angle along the Izu-Bonin subduction zone increases southward (Zhang et al., 2019). Such variations in slab dip angle have formed a unique slab morphology beneath the Kurile Islands and Izu-Bonin arc. Part of the subducting slab penetrates into the lower mantle through the mantle transition zone, while other parts of the slab remain stagnant in the mantle transition zone (Torii and Yoshioka, 2007; Zhao et al., 2012; Zhang et al., 2019).

The 3-D evolution of subduction zones has been studied before using numerical models. For example, Bengtson and van Keken (2012) and Kneller and van Keken (2008) used a 3-D subduction model to investigate the influence of slab geometries on mantle flow, shear wave anisotropy, and temperature structure. Morishige and Honda (2013) focused on the influence of rheology on mantle flow, slab morphology and seismic anisotropy in a subduction model with a triple junction. However, few studies have investigated the evolution of subduction cusps and related trench migration patterns and slab morphologies.

In this paper, we explore the evolution of subduction cusps using a 3-D dynamic subduction model. In particular, we systematically investigate the controlling effects of the

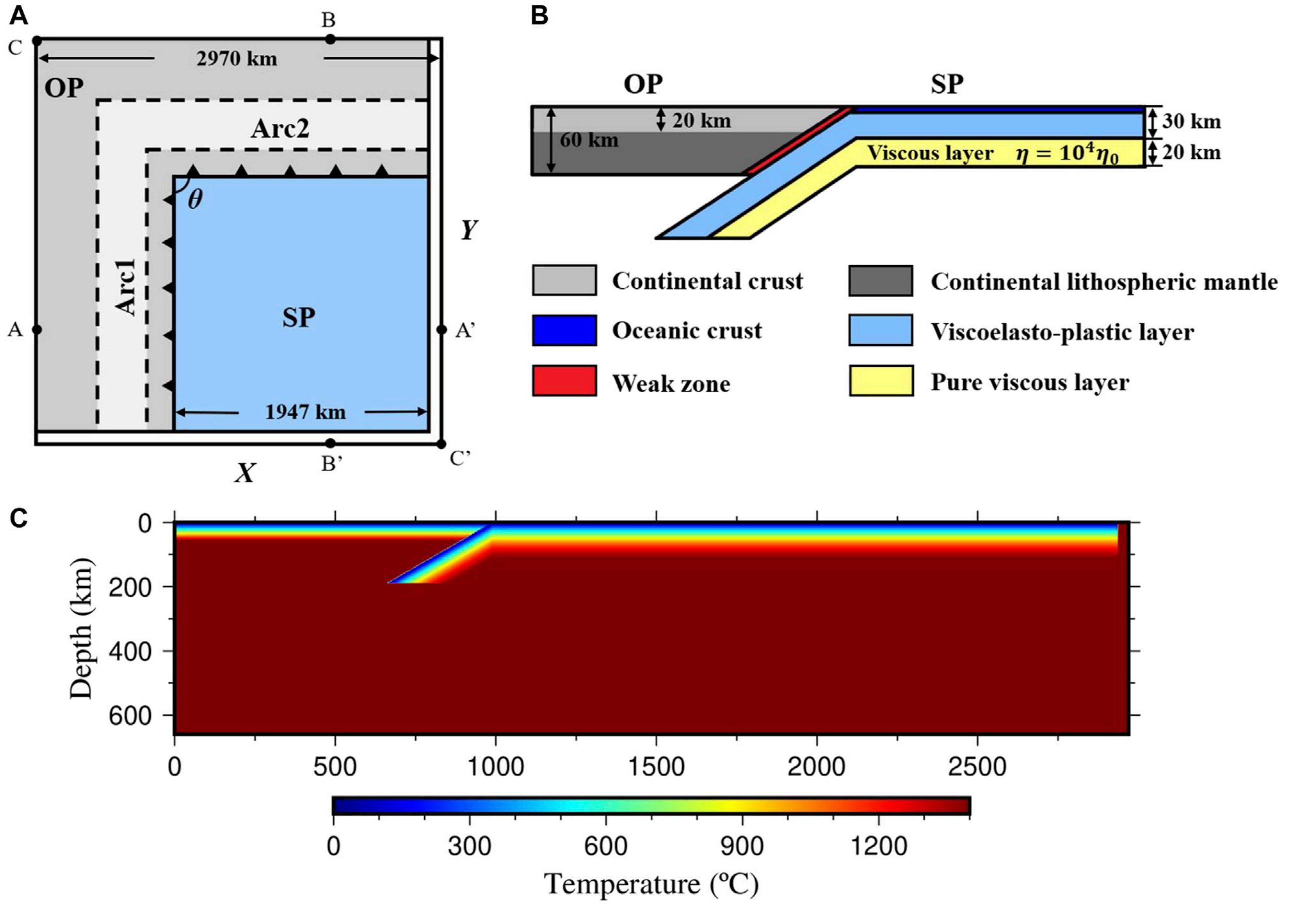

FIGURE 2 | (A) Top view of our geodynamic model, including a subducting oceanic plate and an overriding continental plate. We select profiles *AA'* (*Y*=1,155 km), *BB'* (*X*=1815 km), and *CC'* (diagonal direction) to show slab morphology and quantify the distance of trench migration. *θ* represents the initial angle of the subduction cusp. **(B)** Schematic diagram of the compositional field near the trench. On the left is the layered overriding plate (OP), which consists of 20-km-thick continental crust (light gray) and 40-km-thick continental lithospheric mantle (deep gray). On the right is the subducting plate (SP), where deep blue, light blue, and yellow colors represent oceanic crust and two layers of oceanic lithospheric mantle with different rheological properties. The red zone is a weak zone at the interface between the overriding and subducting plates. **(C)** The initial temperature field of our model along profile *AA'*. We use a linear temperature profile for the overriding continental plate and a half-space cooling model for the subducting oceanic plate.

overriding plate strength, initial slab-pull force, and initial cusp angle on trench migration and slab morphology in subduction cusps.

MATERIALS AND METHODS

To investigate the trench migration process and slab morphology of subduction cusps, a 3-D dynamic subduction model is developed. Leng and Gurnis (2015) modified CitcomCU (Zhong, 2006) by adding viscoelastic and material tracking methods. Our calculation method follows Leng and Gurnis (2015) to solve the mass, momentum, and energy conservation equations. Here, only the basic model setup and material rheology are introduced. For more details on the methodology, please refer to Leng and Gurnis (2011) and Leng and Gurnis (2015).

The model domain is 660 km deep, 2,970 km wide and 2,970 km in length. The "particle in cell" method makes it possible to calculate a 3-D numerical model with a relatively low resolution. We use a uniform grid of $256 \times 256 \times 64$ (X, Y, and Z directions) in our model, leading to a resolution of $11.6 \times 11.6 \times 10.3$ km (X, Y, and Z directions). We set 27 particles in each element. Our model includes a square subducting oceanic plate and an overriding continental plate (**Figure 2A**). The subducting plate (1947 × 1947 km) is located 33 km away from the lateral boundaries of the model to ensure that the subducting plate can be detached from the lateral model boundaries and subduct freely. The overriding plate is attached to the lateral boundaries (**Figure 2A**) and remains stable during the subduction process. Thus, trench retreat is mainly caused by the extension of the weak back-arc region (Arc1 and Arc2 in **Figure 2A**). The overriding plate thickness is 60 km and consists of a 20-km-thick continental crust and a 40-km-thick continental lithospheric mantle. A 7-km-thick oceanic crust overlies the subducting plate (**Figure 2B**). To induce subduction at the initial time step, the tip of the oceanic

TABLE 1 | Model constants.

Parameter names	Symbols	Values
Reference mantle density	ρ_0	3,300 kg m^{-3}
Crust density	ρ_c	2,800 kg m^{-3}
Gravitational acceleration	g	9.81 m s^{-2}
Shear modulus	G	30 GPa
Thermal expansivity	α	3 × 10^{-5} K^{-1}
Reference temperature	T_0	1,400℃
Reference viscosity	η_0	10^{20} Pa s
Gas constant	R	8.31 J mol^{-1}
Activation energy	E	540 kJ mol^{-1}
Strain exponent	n	3.5
Reference strain rate	$\dot{\varepsilon}_0$	10^{-15} s^{-1}
Minimum cohesion	C_f	0.6 MPa
Maximum viscosity	η_{max}	10^{24} Pa s
Minimum viscosity	η_{min}	10^{20} Pa s

lithosphere is bent to reach a certain depth (165 km in the reference model) with a dip angle of 30°.

We impose isothermal boundary conditions with a fixed temperature at 0°C at the top boundary and 1,400°C at the bottom ignoring adiabatic heating. A half-space cooling model with an age of 60 Ma is imposed as the initial temperature field of the subducting plate, and a linear temperature field is employed on the overriding continental plate (**Figure 2C**). The influences of the subducting plate age and overriding plate thickness on subduction dynamics have been discussed previously (Holt et al., 2015; Agrusta et al., 2017). A thick overriding plate prevents trench retreat and has the tendency to develop a large slab dip angle (Holt et al., 2015), whereas old plate subduction promotes trench retreat and usually develops a small slab dip angle, leading to a stagnant slab in the mantle transition zone (Agrusta et al., 2017). Therefore, we fix the overriding plate thickness to 60 km and the subducting plate age to 60 Ma in our model. We apply free-slip boundary conditions to all model boundaries.

An incompressible Maxwell body is used to describe the viscoelasticity of the material in our model. The following equation is employed to calculate the contribution of viscous and elastic components to the strain rate (Moresi et al., 2002):

$$\dot{\varepsilon}_{ij} = \frac{1}{2G}\dot{\tau}_{ij} + \frac{1}{2\eta}\tau_{ij} \tag{1}$$

where $\dot{\varepsilon}_{ij}$, G, η, τ_{ij}, and $\dot{\tau}_{ij}$ represent the strain rate, shear modulus, dynamic viscosity, deviatoric stress, and time rate of deviatoric stress, respectively. The non-Newtonian viscosity is temperature- and stress-dependent and can be expressed by:

$$\eta = \eta_0\left(\frac{\dot{\varepsilon}_{II}}{\dot{\varepsilon}_0}\right)^{\left(\frac{1}{n}-1\right)} exp\left[\frac{E}{nR}\left(\frac{1}{T}-\frac{1}{T_0}\right)\right] \tag{2}$$

where η_0, $\dot{\varepsilon}_{II}$, $\dot{\varepsilon}_0$, n, E, R, T, and T_0 represent the reference viscosity, second invariant of the deviatoric strain rate tensor, reference strain rate, strain exponent, activation energy, gas constant, absolute temperature, and reference temperature, respectively. We set an upper limit, η_{max}, and a lower limit, η_{min}, for viscosity to guarantee the convergence and efficiency of our model. The values of the model constraints can be found in **Table 1**.

The yielding stress, τ_y, is expressed as:

$$\tau_y = \mu P + C \tag{3}$$

where μ, P, and C represent the coefficients of friction, pressure, and cohesion, respectively. In our model, μ and C decrease with increasing accumulated plastic strains ε_p following these equations:

$$\mu = \mu_0\left[1 - min\left(1, \frac{\varepsilon_p}{\varepsilon_f}\right)\right] \tag{4}$$

$$C = C_f + \left(C_0 - C_f\right)\left[1 - min\left(1, \frac{\varepsilon_p}{\varepsilon_f}\right)\right] \tag{5}$$

where μ_0, C_0, C_f, and ε_f represent the initial coefficients of friction, initial cohesion, minimum cohesion, and reference plastic strain, respectively. In our model, μ_0, C_0, and ε_f are set as 0.5, 40 MPa, and 0.3, respectively. A 22.8-km-thick pure viscous weak zone is imposed at the interface between the subducting and overriding plates (**Figure 2B**), and we set the viscosity of the weak zone as 10^{20} Pa s for plate decoupling. To prevent plate rupture during the subduction process, we also set a 20-km-thick pure viscous layer at a depth of 30 km in the subducting oceanic plate (**Figure 2B**) (Stegman et al., 2010; Schellart and Moresi, 2013). By systematically comparing their model results with interseismic deformation, Itoh et al. (2019) suggested that the Southern Kurile arc and its back-arc areas are weak. Here, we set the initial value of ε_p to 0.2 to reflect the weak rheology in the back-arc area.

RESULTS

The Reference Model

We first run a reference case_ref (**Table 2**), with two weak arc regions (Arc1 and Arc2) in the overriding continental plate. The

TABLE 2 | Parameter values for cases in this study. ε_{p1} and ε_{p2} represent the initial plastic strains of Arc1 and Arc2, respectively. d_y represents the maximum depth that the front of the subducting plate can reach initially and the unit of d_y is km. θ is the initial angle of subduction cusp (**Figure 2A**). All parameters in case_r320 are same to case_ref, except a higher model resolution, which is 320 × 320 × 80 (X, Y, and Z directions) in case_r320.

case	ε_{p1}	ε_{p2}	d_y	θ
Case_ref	0.2	0.2	165	90°
Case_r320*	0.2	0.2	165	90°
Case_ss	0.0	0.0	165	90°
Case_sw	0.0	0.2	165	90°
Case_d215	0.2	0.2	215	90°
Case_d265	0.2	0.2	265	90°
Case_a120	0.2	0.2	165	120°
Case_a180	0.2	0.2	165	180°

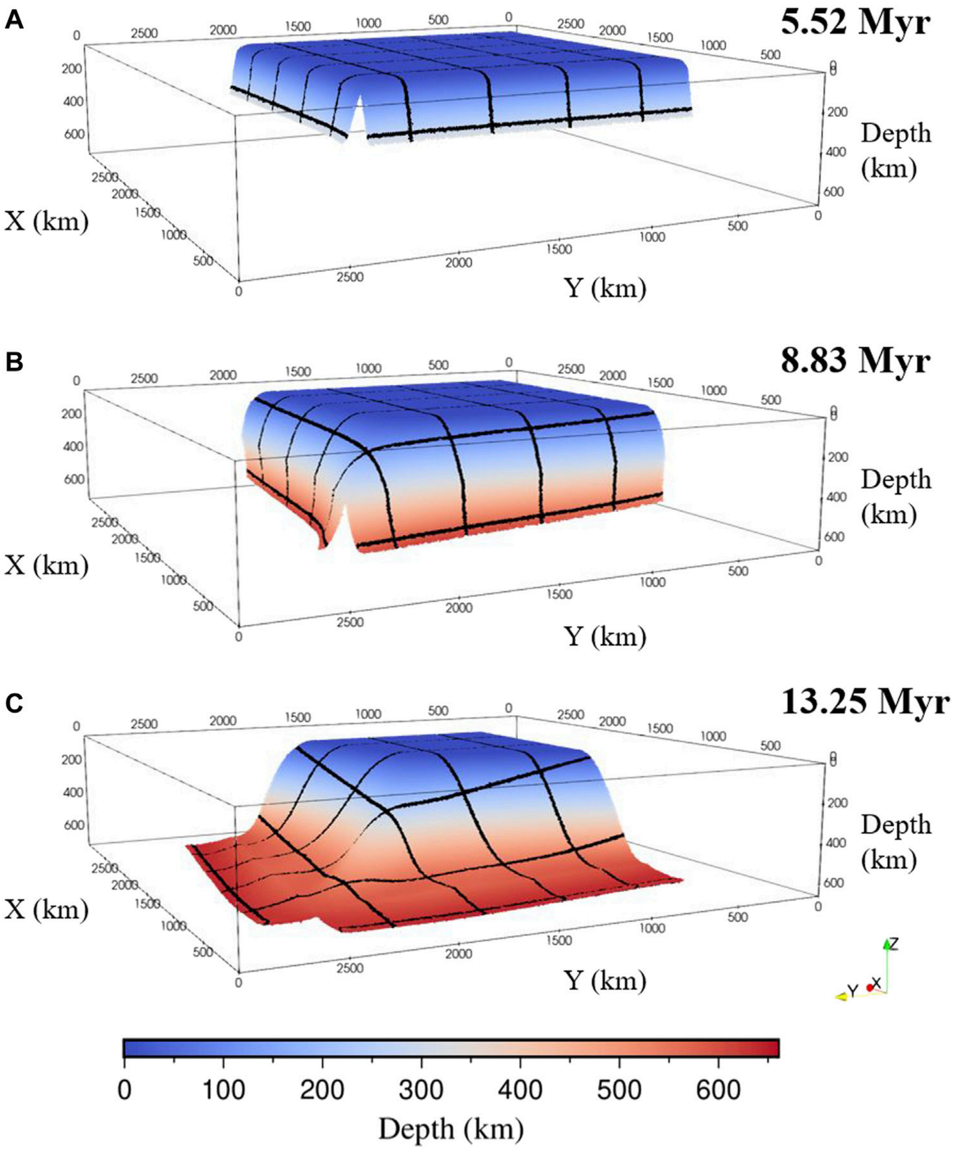

FIGURE 3 | The evolution of slab morphology at 5.52 **(A)**, 8.83 **(B)**, and 13.25 **(C)** Myr in the reference model. The color indicates the depth of the slab. We put some black tracking lines on the slab surface to better display the three-dimensional structure of the slab.

weak region is 297 km wide and 165 km away from the trench (**Figure 2A**). The tip of the subducting slab is bent to reach a depth of 165 km, which can provide enough initial slab-pull force to initiate subduction.

At the beginning of the subduction process, the tip of the subducting slab changes its dip angle from 30° to nearly 90°, and the subducting plate begins to move slowly trenchward due to a relatively small slab-pull force (**Figure 3A**). Then, as the subduction process continues, the subducting plate begins to accelerate, reaching the bottom boundary of the model domain after 8.83 million years (Myr) of subduction (**Figure 3B**). Finally, the subducting slab stagnates on the bottom boundary after 13.25 Myr (**Figure 3C**). The subducting slab develops different dip angles in different directions. Here, we select profiles *AA*', *BB*', and *CC*' in **Figure 2A** to show the variation in slab dip angle in the X, Y, and diagonal directions (**Figure 4**). At 13.25 Myr, the slab stagnates on the bottom boundary and develops a similar morphology along profiles *AA*' and *BB*' due to the symmetric model set up in the X and Y directions. However, in the diagonal direction along profile *CC*', the slab dip angle is much smaller than that of profiles *AA*' and *BB*' (**Figure 4C**). Such a small slab dip angle can resist mantle flow reaching the corner of mantle wedge, thus causing a cold mantle wedge (**Figure 4C**).

We placed tracking tracers at the end of the subducting plate (66 km away from the plate edge) to obtain its velocity.

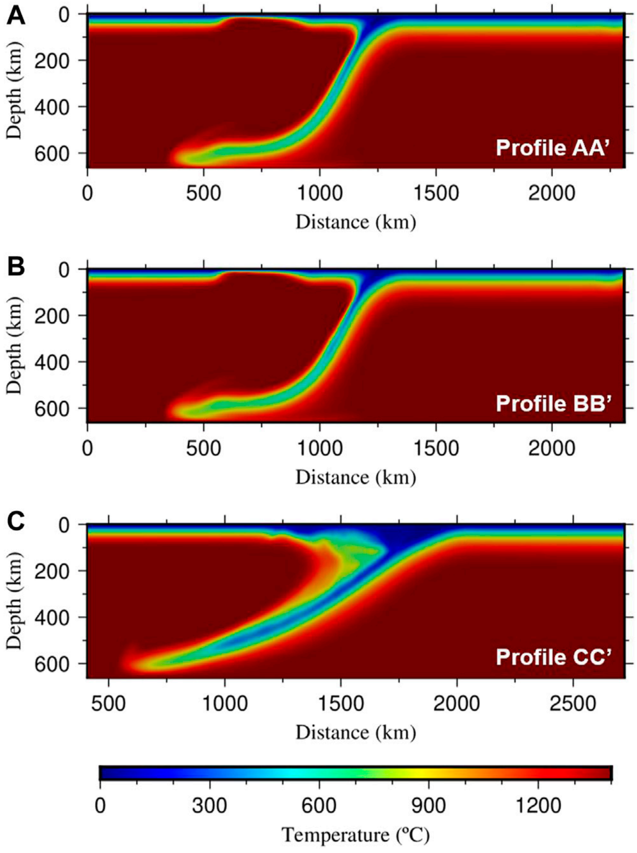

FIGURE 4 | Temperature field along the profiles of *AA*' **(A)**, *BB*' **(B)**, and *CC*' **(C)** at 13.25 Myr in the reference model. The locations of the *AA*', *BB*', and *CC*' profiles are shown in **Figure 2A**.

Figure 5A shows that the subducting velocity (red lines in **Figure 5A**) is almost the same in the X and Y directions. The slab-pull force becomes larger because of a longer slab tip as the subduction process proceeds, and the velocity of the subducting plate shows a significant increase (**Figure 5A**). After approximately 8 Myr of subduction, the subduction velocities v_x and v_y increase from 0 to 8 cm/yr (**Figure 5A**). Then, the tip of the subducting slab reaches the bottom boundary, which resists the subduction process. After ~4 Myr of fluctuation, the velocity of the subducting plate begins to decrease (**Figure 5A**). **Figure 5B** shows the corresponding trench locations at different times. It can be noted that the trench retreats faster in the diagonal direction than in the X and Y directions, leading to an increase in the cuspate corner angle from 90° to ~150° (**Figure 5B**). However, the trench retreat speed and the angular speed of opening of subduction cusp doesn't have a proportional relationship to subducting velocity (**Figure 5B**), because trench retreat can be influenced by many factors (Holt et al., 2015; Agrusta et al., 2017).

Resolution test has been made to determine the proper resolution required to resolve the subduction zone accurately (case_r320 in **Table 2**). The results show that the velocities of subducting plate are very comparable for a resolution of 256 × 256 × 64 (red lines in **Figure 5A**) and 320 × 320 × 80 (orange lines in **Figure 5A**). Thus, we choose a resolution of 256 × 256 × 64 for other models presented in this paper, considering both calculation accuracy and efficiency.

Influence of the Overriding Plate Strength

The overriding plate is relatively weak due to the existence of weak arc regions in the reference model. Previous 2-D studies have shown that the overriding plate strength has great influences on subduction dynamics (Garel et al., 2014; Holt et al., 2015; Yang et al., 2018). Here, we investigate the influence of the asymmetry of the weak arc region on the evolution of subduction cusps (case_sw and case_ss in **Table 2**). In our reference model case_ref, the overriding plate is weak in both the Arc1 and Arc2 regions (**Figure 2A**). In case_sw, only the Arc2 region is weak, whereas in case_ss, both weak arc regions are removed.

Figure 5C–E shows the influence of the overriding plate strength on the trench retreat process. **Figures 5C, D** show the evolution of trench geometries in case_ss and case_sw, respectively. In case_ss, the trench retreats slightly in the diagonal direction, changing the sharp subduction cusp to a gentle curvature locally. Nevertheless, the trench positions are generally stable in both the X and Y directions, and the intersection angle of these two trenches remains ~90° throughout the whole subduction process (**Figure 5C**). In case_sw, the trench position remains stable in the X direction generally; however, the trench retreats significantly in the Y direction, causing an increasing cusp angle during the subduction process (**Figure 5D**). Such an asymmetric trench geometry is completely different from the symmetric subduction regime in case_ref and case_ss (**Figures 5B,C**). It can be observed that the trench retreats symmetrically in both case_ref and case_ss, with similar retreating distances in the X and Y directions but a larger retreating distance in the diagonal direction (**Figure 5E**). Comparing case_ss to case_ref, we can find that the trench retreat distance is smaller in case_ss because of the strong overriding plate, which makes it difficult for the trench to retreat (**Figure 5E**). In case_sw, the overriding plate is strong in Arc1 but weak in the Arc2 region; thus, the trench retreats asymmetrically. A larger retreat distance appears in the Y direction, while in the X direction, the trench retreat distance is similar to the results in case_ss (**Figure 5E**). Together, the results of these three cases (case_ref, case_ss, and case_sw) suggest that the weakening of the overriding plate promotes trench retreat, which is consistent with the results of previous studies (Holt et al., 2015; Agrusta et al., 2017). Thus, the asymmetric distribution of weak regions in the overriding continental plate can cause asymmetric trench migration processes. It can also be noted that the trench retreats more significantly in the diagonal direction regardless of the overriding plate strength, which typically causes the subduction cusp to become smooth and disappear during the subduction process (**Figures 5B–E**).

Figure 6 shows the morphology of the subducting slab in the X, Y, and diagonal directions in case_ss and case_sw. In case_ss,

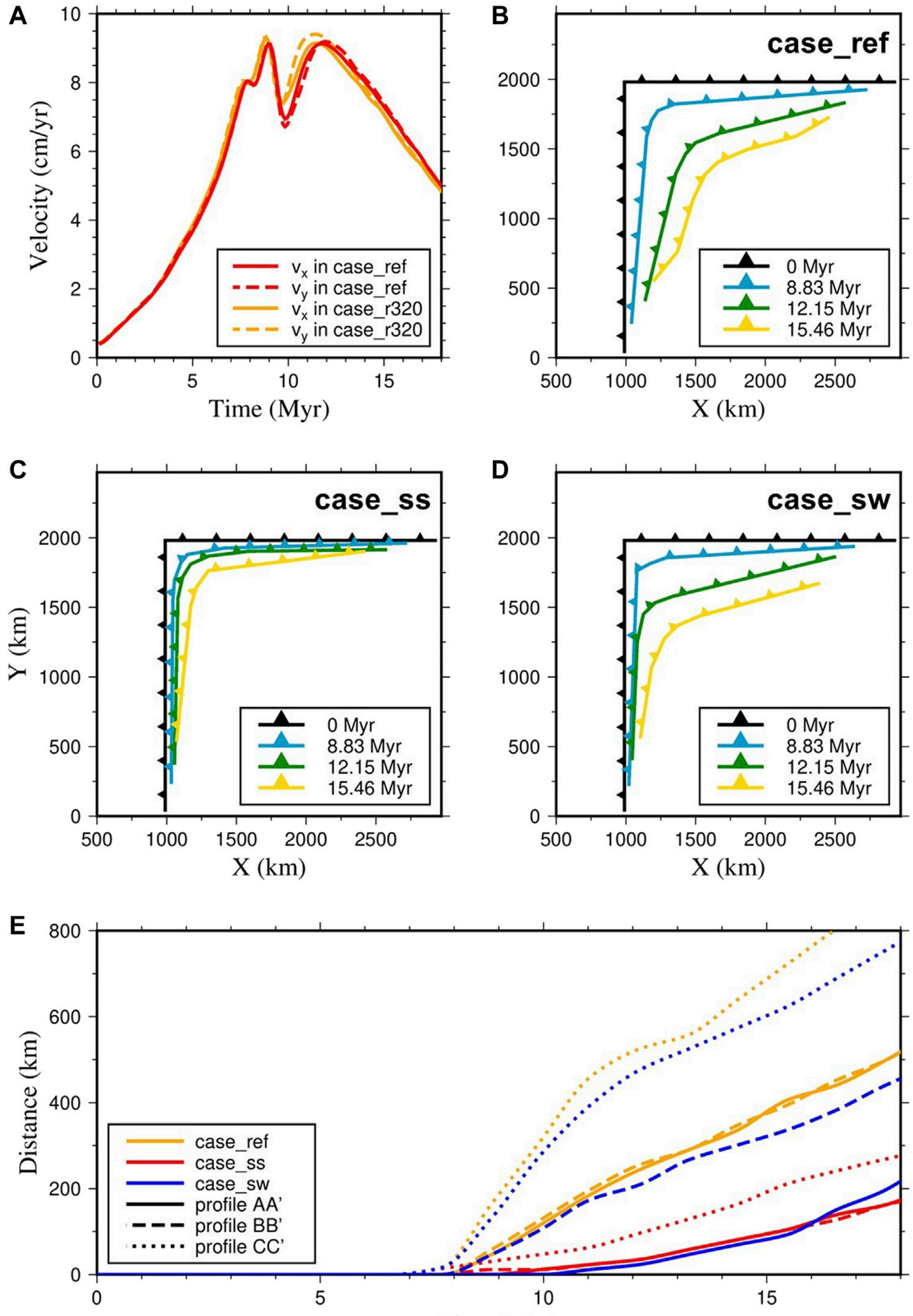

FIGURE 5 | (A) The velocities of the subducting plate in the *X* (v_x, solid line) and *Y* (v_y, dashed line) directions. Red and orange colors show the results of case_ref and case_320, respectively. **(B)**, **(C)**, and **(D)** show the trench migration history in case_ref, case_ss, and case_sw, respectively. **(E)** The migration distances of the trench along profiles *AA*' (solid line), *BB*' (dashed line), and *CC*' (dotted line) in **Figure 2A**. Orange, red, and blue colors show the results of case_ref, case_ss, and case_sw, respectively.

the slab subducts nearly vertically with a slab dip angle of ~80° in the *X* and *Y* directions (**Figures 6A, C**). In case_sw, the subducting slab subducts asymmetrically; the slab dip angle is smaller in the *Y* direction with the weak Arc2 region, while in the *X* direction, the slab subducts nearly vertically (**Figures 6B, D**). A weak overriding plate is easier to deform and thus promotes

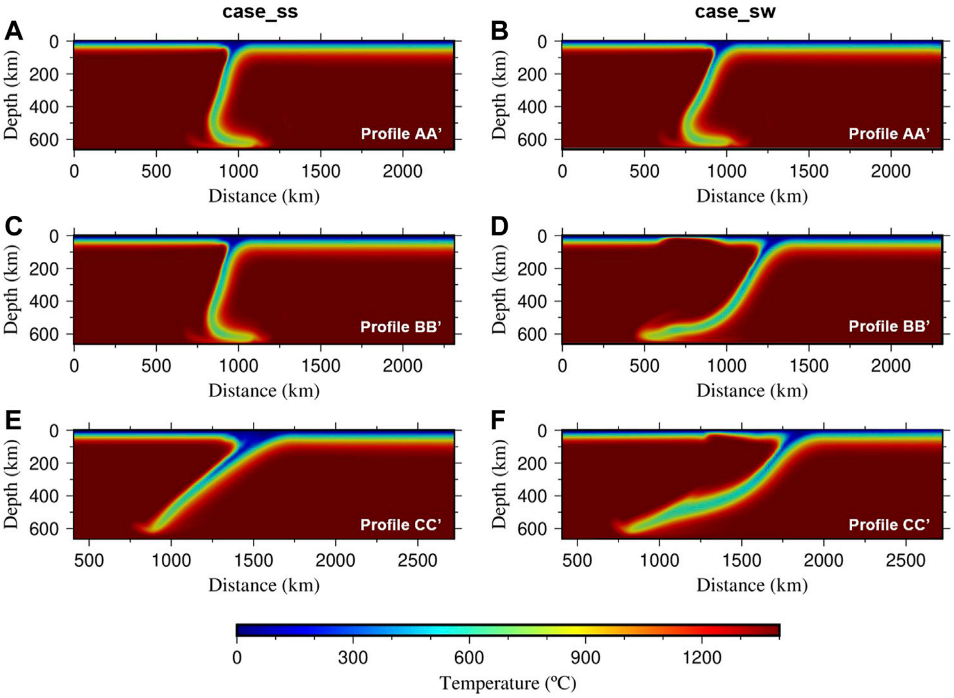

FIGURE 6 | Temperature field along the profiles of *AA*', *BB*', and *CC*' at 12.15 Myr in case_ss **(A–E)** and case_sw **(B–F)**. The locations of the *AA*', *BB*', and *CC*' profiles are shown in **Figure 2A**.

trench retreat, which forms a smaller dip angle in the subducting slab (Holt et al., 2015). In the diagonal direction, the slab dip angle is smallest regardless of how we change the overriding plate strength (**Figures 6E, F**).

Influence of the Initial Slab-Pull Force

The slab-pull force is considered to be the main driving force behind subduction (Schellart, 2004). Here, we change the initial length of the bending tip of the subducting slab to control the initial slab-pull force (case_d215 and case_d265 in **Table 2**). A longer bending tip of the subducting slab provides a larger slab-pull force. In the reference case_ref, the tip of the subducting slab reaches 165 km depth beneath both the Arc1 and Arc2 regions. For the cases of case_d215 and case_d265, we keep the slab tip at 165 km depth beneath the Arc1 region but increase the slab tip to 215 and 265 km depths beneath the Arc2 region.

Figure 7A shows the influence of the initial slab-pull force on the velocities of the subducting plate in the *X* and *Y* directions. In case_ref, the velocities of the subducting plate are similar in the *X* and *Y* directions, and the slab subducts symmetrically (**Figure 7A**). However, when the initial slab-pull force becomes larger beneath the Arc2 region (**Figure 2A**) for case_d215 and case_d265, the subducting velocity in the *Y* direction becomes significantly larger than that in the *X* direction (**Figure 7A**), causing the subducting plate to rotate counterclockwise, and the subduction becomes asymmetric.

Figure 7B shows the influence of the initial slab-pull force on trench migration. When the initial slab-pull force in the *Y* direction becomes larger, the trench migration distance becomes larger in the *X* direction. Meanwhile, in the *Y* direction, the trench migration distance becomes smaller (**Figure 7B**) and (**Figures 8A,B**). Previous studies have pointed out that when the subducting velocity increases, it becomes more difficult for the trench to retreat (Schellart, 2005). Our results confirm this point in subduction cusp evolution (**Figure 7B**) and (**Figures 8A,B**). Regardless of how we change the initial slab-pull force, the trench retreats more significantly in the diagonal direction, causing a smaller slab dip angle (**Figure 7B**) and (**Figures 8A,B**).

Influence of the Initial Cusp Angle

In the previous cases, the slab dip angle remains smallest in the diagonal direction, even for case_ss, in which the trench retreats a very limited distance (**Figures 5C**) and (**Figure 6E**). Therefore, the overriding plate strength and the initial slab-pull force cannot be the key controlling factors driving the slab dip angle in the diagonal direction. On the other hand, the initial cusp angle may play important roles in the resulting slab morphology. We run case_a120 and case_a180 with different initial cusp angles of 120° and 180° to test this point (**Table 2**).

With increasing initial cusp angles, the subducting plate becomes smaller. The subduction process continues for only ~12 Myr in case_a180 (**Figure 8D**). Comparing case_ref, case_a120, and case_a180 (**Figures 5B**) and (**Figures 8C,D**), it can be observed that the trench only retreats insignificantly when the initial cusp angle is large. When the initial cusp angle

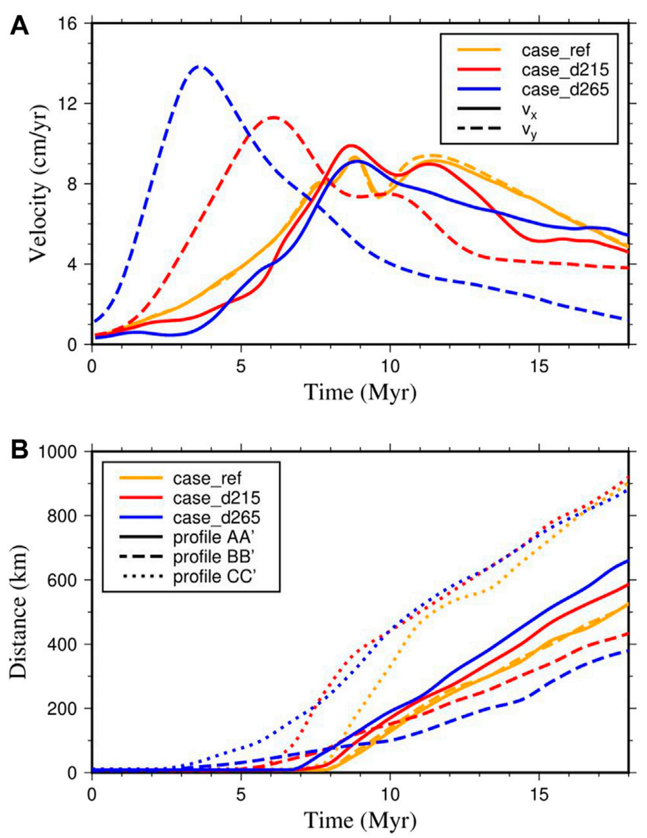

FIGURE 7 | (A) The velocities of the subducting plate in case_ref (orange), case_d215 (red), and case_d265 (blue). The solid line and dashed line represent the velocities of the subducting plate in the *X* and *Y* directions, respectively. **(B)** The migration distances of the trench along profiles *AA*' (solid line), *BB*' (dashed line), and *CC*' (dotted line) in **Figure 2A**. Orange, red, and blue colors show the results of case_ref, case_d215, and case_d265, respectively.

becomes smaller than 120°, the trench retreat distance in the diagonal direction increases drastically (**Figures 5B**) and (**Figures 8C,D**). Therefore, a smaller cusp angle leads to a faster trench retreat in the diagonal direction, which eventually smooths and destroys the cusp. **Figure 9** shows the slab dip angle in the diagonal direction for case_ref, case_a120, and case_a180. With increases in the initial cusp angle from 90° to 120° and 180°, the slab dip angle in the diagonal direction increases from ~30° to ~45° and ~90°. Thus, a larger cuspate corner angle causes a larger slab dip angle.

DISCUSSION

Evolution of the Kurile and Izu-Bonin Cusps

Plate reconstruction results suggest that the Pacific plate began to subduct beneath Kurile and Japan at ~60 Ma, following the subduction of the Izanagi plate (**Figure 1A**) (Müller et al., 2016; Vaes et al., 2019). The cuspate corner angle at the Kurile Islands was approximately 90° at 40 Ma and it became increasingly larger during the subduction of the Pacific plate (**Figures 1A–C**), which is consistent with our model results (**Figures 5B–D**). The trench along the Kurile Islands retreated faster near the cuspate corner, developing a wedge-shaped extensional basin in the back-arc area (Schellart et al., 2003), which is also in high agreement with the results of our model (**Figures 8A,B**). The morphology of the subducting slab beneath the Kurile Islands can be obtained from seismic tomography results. Our results show that the slab dip angle is smallest in the diagonal direction and becomes increasingly larger toward two lateral edges when the initial cusp angle is relatively small (**Figure 3**). Seismic tomography shows similar results beneath the Kurile Islands in which the slab dip angle is small beneath the cuspate corner area and becomes larger northeastward (Miller and Kennett, 2006).

One interesting observation for the Kurile cusp is that the retreat distance of the Kurile trench is larger than that along the northeast Japan trench, suggesting asymmetric subduction. Both the overriding plate strength and initial slab-pull force may cause asymmetric cusp subduction (**Figure 5D**) and (**Figure 8A**). Many geological observations suggest that the overriding Okhotsk and northeast Japan plates both experienced extensive tectonic events before the subduction of the Pacific plate (Itoh et al., 2019; Vaes et al., 2019); therefore, the strength of both plates were likely weak. As a result, the asymmetric subduction of the Kurile cusp may have been caused by different initial slab-pull forces. According to the results of our model, we suggest that the initial slab-pull force beneath northeast Japan is larger than that beneath the Kurile Islands. After the Izanagi plate subducted beneath the Eurasian plate, the Pacific plate began to subduct, and the two plates broke up at the mid-ocean ridges (Thorkelson, 1996; Seton et al., 2015). If the plates broke earlier beneath northeast Japan, the early subduction of the Pacific plate would have caused a larger slab-pull force beneath northeast Japan than beneath the Kurile Islands.

At the Izu-Bonin cusp, the trench migration history and slab morphology are similar to those of the Kurile cusp. The angle of the cuspate corner changed from ~90° to ~120° between 35 Ma and 25 Ma (**Figures 1D–F**). The Izu-Bonin trench retreated faster near the cuspate corner and formed a wedge-shaped extensional basin in the back-arc region on the Philippine Sea plate (Hall, 2002; Ma et al., 2019). Seismic tomography results show that the slab dip angle becomes larger southward (Zhang et al., 2019). In our model, the overriding plate is a continental plate that is different from the Izu-Bonin cusp. Nevertheless, the Philippine Sea plate is a young oceanic plate, which is presumably weaker than a weak continental plate. Thus, based on our model results, it is reasonable to assume that the Izu-Bonin trench retreats dominantly due to a weak overriding plate.

Evolution of Other Cusps

Aside from the Kurile and Izu-Bonin cusps, we can find another cusp located at Solomon Sea in plate tectonic history. The Pacific plate was subducting beneath Philippine Sea plate and Solomon Sea plate, and the cusp

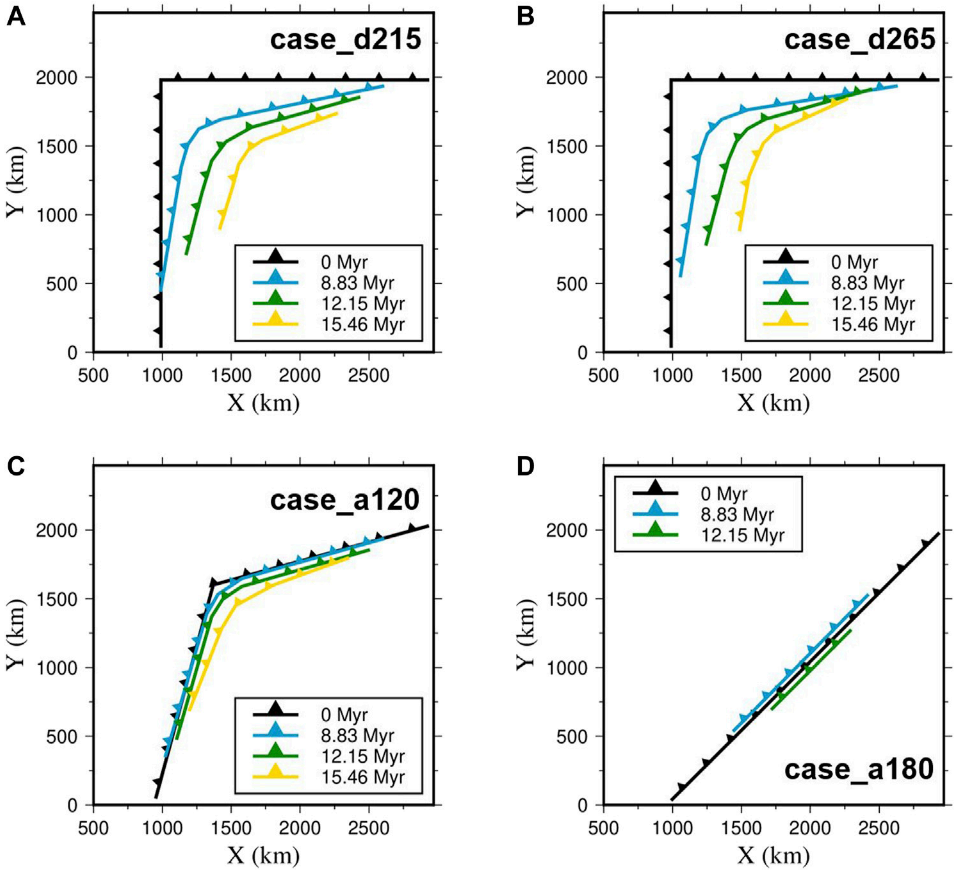

FIGURE 8 | Trench migration history in case_d215 **(A)**, case_d265 **(B)**, case_a120 **(C)**, and case_a180 **(D)**.

angle became smaller continuously between 35 Ma and 20 Ma (Zahirovic et al., 2014; Seton et al., 2016). There are many other cusps on the Earth's surface, such as the Kamchatka cusp and Alaskan cusp, whose cusp angles have remained small during the last several million years (Müller et al., 2016). These cusps have strong correlations to the subduction of aseismic ridges or buoyant blocks (Rosenbaum and Mo, 2011). At the Kamchatka cusp, the Hawaii-Emperor seamount trail subducts beneath the overriding continental plate, possibly causing a subduction cusp at the collision area. The angle of the cuspate corner remains small at the Gulf of Alaska, where the collision of the Yakutat block and Kodiak and Cobb seamount trails occurs (Mazzotti and Hyndman, 2002; Rosenbaum and Mo, 2011). Comparing the Kamchatka and Alaskan cusps with the Kurile and Izu-Bonin cusps, it should be noted that the ongoing subduction of buoyant seamount trails beneath the Kamchatka and Alaskan cusps corresponds to small cusp angles, whereas the Kurile and Izu-Bonin cusps have a tendency to become smooth and disappear. Thus, we can speculate that the subduction process of aseismic ridges or buoyant blocks causes the formation of subduction cusps. Once the subduction of aseismic ridges or buoyant blocks terminates, the subduction cusp tends to be smooth and disappear, as shown in our model results.

3-D Effects of the Trench Retreat and Slab Dip Angle

In previous 2-D studies, it has been proposed that trench retreat can strongly influence the dip angle of subducting slabs (Agrusta et al., 2017). When the trench retreats fast, the subducting slab has a small dip angle. When the trench retreats slowly, it is difficult for the subducting slab to incline, and it prefers to subduct vertically with a large slab dip angle. Here, in our 3-D subduction cusp model, we can see from **Figure 5C** and **Figure 6** that the trench retreating distance is limited in case_ss, but the slab dip angle is still small in the diagonal direction, showing that the 3-D effects of a subduction cusp are important for slab geometry.

Effects of the Lower Mantle

Here, we did not include the lower mantle in our model for computational efficiency. Since both the viscosity jump and endothermic phase transition at a depth of 660 km could make the slab stagnate in the mantle transition zone (Torii

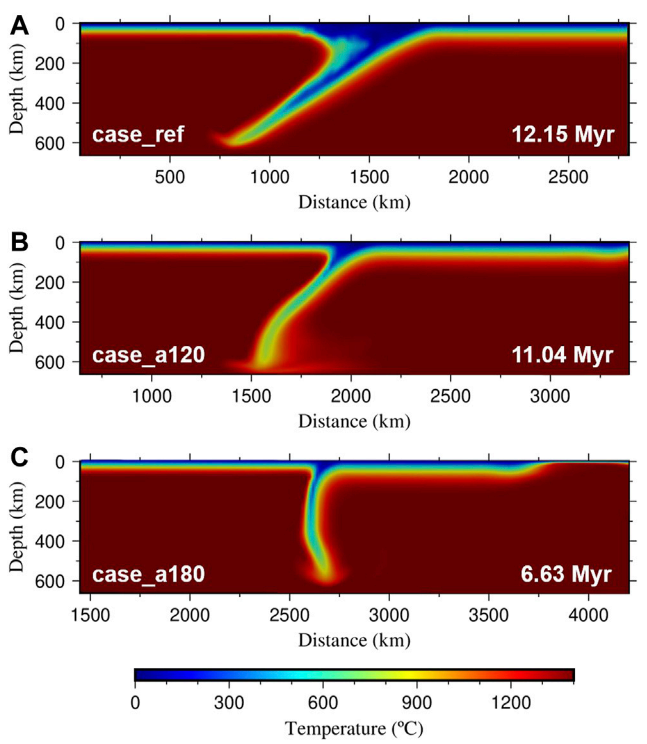

FIGURE 9 | Temperature field along profile *CC'* (**Figure 2A**) in case_ref (at 12.15 Myr) **(A)**, case_a120 (at 11.04 Myr) **(B)**, and case_a180 (at 6.63 Myr) **(C)**.

and Yoshioka, 2007; Yoshida, 2013; Agrusta et al., 2017), such a simplification is probably reasonable. Nevertheless, a larger box with a lower mantle included is helpful for future studies of subduction cusp evolution. Moreover, our model results show that the slab dip angle in the diagonal direction is the smallest compared with that in the *X* and *Y* directions. Thus, the subducting slab in the diagonal direction more easily stagnates in the mantle transition zone, whereas the subducting slab with a larger dip angle in the *X* and *Y* directions tends to roll back or subduct vertically into the lower mantle. Seismic tomography results have shown that the subducting Pacific slab stagnates on the mantle transition zone beneath Izu-Bonin cusp, and the south part of it rolls back beneath Izu-Bonin-Mariana trench, indicating a tear of Pacific plate (Zhang et al., 2019). The special slab morphology from subduction cusp evolution may be employed to better explain seismic tomography results, especially at Kurile cusp and Izu-Bonin cusp (Miller and Kennett, 2006; Zhang et al., 2019).

CONCLUSION

In summary, using a 3-D dynamic subduction model, we investigate the influence of overriding plate strength, initial slab-pull force, and initial cusp angle on slab morphology and trench migration of subduction cusps. Following conclusions are obtained:

Subduction cusps have the tendency to become smooth and disappear during the subduction process.

The slab dip angle is the smallest in the diagonal direction of subduction cusps, and a larger cuspate corner angle leads to a larger slab dip angle.

The asymmetric distribution of the overriding plate strength and initial slab-pull force determines the asymmetric evolutionary pathway of subduction cusps.

DATA AVAILABILITY STATEMENT

The raw data supporting the conclusion of this article will be made available by the author, without undue reservation.

AUTHOR CONTRIBUTIONS

HZ and WL contributed to conception and design of this study. XS found plate reconstruction data and plot them. HZ wrote the first draft of the manuscript. All authors contributed to manuscript revision, read, and approved the submitted version.

FUNDING

This work is supported by the National Natural Science Foundation of China (41774105, 41820104004, 41688103) and the Fundamental Research Funds for the Central Universities (WK2080000144).

REFERENCES

Agrusta, R., Goes, S., and van Hunen, J. (2017). Subducting-slab Transition-Zone Interaction: Stagnation, Penetration and Mode Switches. *Earth Planet. Sci. Lett.* 464, 10–23. doi:10.1016/j.epsl.2017.02.005

Bengtson, A. K., and van Keken, P. E. (2012). Three-dimensional thermal Structure of Subduction Zones: Effects of Obliquity and Curvature. *Solid Earth* 3 (2), 365–373. doi:10.5194/se-3-365-2012

Garel, F., Goes, S., Davies, D. R., Davies, J. H., Kramer, S. C., and Wilson, C. R. (2014). Interaction of Subducted Slabs with the Mantle Transition-zone: A Regime Diagram from 2-D Thermo-mechanical Models with a mobile Trench and an Overriding Plate. *Geochem. Geophys. Geosyst.* 15 (5), 1739–1765. doi:10.1002/2014gc005257

Hall, R. (2002). Cenozoic Geological and Plate Tectonic Evolution of SE Asia and the SW Pacific: Computer-Based Reconstructions, Model and Animations. *J. Asian Earth Sci.* 20 (4), 353–431. Article Pii s1367-9120(01)00069-4. doi:10.1016/s1367-9120(01)00069-4

Holt, A. F., Becker, T. W., and Buffett, B. A. (2015). Trench Migration and Overriding Plate Stress in Dynamic Subduction Models. *Geophys. J. Int.* 201 (1), 172–192. doi:10.1093/gji/ggv011

Itoh, Y., Wang, K., Nishimura, T., and He, J. (2019). Compliant Volcanic Arc and Backarc Crust in Southern Kurile Suggested by Interseismic Geodetic Deformation. *Geophys. Res. Lett.* 46 (21), 11790–11798. doi:10.1029/2019gl084656

Kneller, E. A., and van Keken, P. E. (2008). Effect of Three-Dimensional Slab Geometry on Deformation in the Mantle Wedge: Implications for Shear Wave Anisotropy. *Geochem. Geophys. Geosyst.* 9, a–n. Article Q01003. doi:10.1029/2007gc001677

Leng, W., and Gurnis, M. (2011). Dynamics of Subduction Initiation with Different Evolutionary Pathways. *Geochem. Geophys. Geosyst.* 12, a–n. Article Q12018. doi:10.1029/2011gc003877

Leng, W., and Gurnis, M. (2015). Subduction Initiation at Relic Arcs. *Geophys. Res. Lett.* 42 (17), 7014–7021. doi:10.1002/2015gl064985

Ma, P., Liu, S., Gurnis, M., and Zhang, B. (2019). Slab Horizontal Subduction and Slab Tearing beneath East Asia. *Geophys. Res. Lett.* 46 (10), 5161–5169. doi:10.1029/2018gl081703

Martinod, J., Funiciello, F., Faccenna, C., Labanieh, S., and Regard, V. (2005). Dynamical Effects of Subducting Ridges: Insights from 3-D Laboratory Models. *Geophys. J. Int.* 163 (3), 1137–1150. doi:10.1111/j.1365-246X.2005.02797.x

Martinod, J., Guillaume, B., Espurt, N., Faccenna, C., Funiciello, F., and Regard, V. (2013). Effect of Aseismic ridge Subduction on Slab Geometry and Overriding Plate Deformation: Insights from Analogue Modeling. *Tectonophysics* 588, 39–55. doi:10.1016/j.tecto.2012.12.010

Mazzotti, S., and Hyndman, R. D. (2002). Yakutat Collision and Strain Transfer across the Northern Canadian Cordillera. *Geol* 30 (6), 4952–5498. doi:10.1130/0091-7613(2002)030<0495:Ycasta>2.0.Co;2

Miller, M. S., and Kennett, B. L. N. (2006). Evolution of Mantle Structure beneath the Northwest Pacific: Evidence from Seismic Tomography and Paleogeographic Reconstructions. *Tectonics* 25 (4), a–n. Article Tc4002. doi:10.1029/2005tc001909

Moresi, L., Dufour, F., and Mühlhaus, H.-B. (2002). Mantle Convection Modeling with Viscoelastic/brittle Lithosphere: Numerical Methodology and Plate Tectonic Modeling. *Pure Appl. Geophys.* 159 (10), 2335–2356. doi:10.1007/s00024-002-8738-3

Morishige, M., and Honda, S. (2013). Mantle Flow and Deformation of Subducting Slab at a Plate junction. *Earth Planet. Sci. Lett.* 365, 132–142. doi:10.1016/j.epsl.2013.01.033

Müller, R. D., Seton, M., Zahirovic, S., Williams, S. E., Matthews, K. J., Wright, N. M., et al. (2016). "Ocean Basin Evolution and Global-Scale Plate Reorganization Events since Pangea Breakup," in *Annual Review of Earth and Planetary Sciences*. Editors R. Jeanloz and K. H. Freeman, 44, 107–138. doi:10.1146/annurev-earth-060115-012211

Rosenbaum, G., and Mo, W. (2011). Tectonic and Magmatic Responses to the Subduction of High Bathymetric Relief. *Gondwana Res.* 19 (3), 571–582. doi:10.1016/j.gr.2010.10.007

Schellart, W. P., Freeman, J., Stegman, D. R., Moresi, L., and May, D. (2007). Evolution and Diversity of Subduction Zones Controlled by Slab Width. *Nature* 446 (7133), 308–311. doi:10.1038/nature05615

Schellart, W. P. (2005). Influence of the Subducting Plate Velocity on the Geometry of the Slab and Migration of the Subduction Hinge. *Earth Planet. Sci. Lett.* 231 (3-4), 197–219. doi:10.1016/j.epsl.2004.12.019

Schellart, W. P., Jessell, M. W., and Lister, G. S. (2003). Asymmetric Deformation in the Backarc Region of the Kuril Arc, Northwest Pacific: New Insights from Analogue Modeling. *Tectonics* 22 (5), a–n. doi:10.1029/2002tc001473

Schellart, W. P., and Moresi, L. (2013). A New Driving Mechanism for Backarc Extension and Backarc Shortening through Slab Sinking Induced Toroidal and Poloidal Mantle Flow: Results from Dynamic Subduction Models with an Overriding Plate. *J. Geophys. Res. Solid Earth* 118 (6), 3221–3248. doi:10.1002/jgrb.50173

Schellart, W. P. (2004). Quantifying the Net Slab Pull Force as a Driving Mechanism for Plate Tectonics. *Geophys. Res. Lett.* 31 (7), a–n. Article L07611. doi:10.1029/2004gl019528

Seton, M., Flament, N., Whittaker, J., Müller, R. D., Gurnis, M., and Bower, D. J. (2015). Ridge Subduction Sparked Reorganization of the Pacific Plate-mantle System 60-50 Million Years Ago. *Geophys. Res. Lett.* 42 (6), 1732–1740. doi:10.1002/2015gl063057

Seton, M., Mortimer, N., Williams, S., Quilty, P., Gans, P., Meffre, S., et al. (2016). Melanesian Back-Arc basin and Arc Development: Constraints from the Eastern Coral Sea. *Gondwana Res.* 39, 77–95. doi:10.1016/j.gr.2016.06.011

Stegman, D. R., Schellart, W. P., and Freeman, J. (2010). Competing Influences of Plate Width and Far-Field Boundary Conditions on Trench Migration and Morphology of Subducted Slabs in the Upper Mantle. *Tectonophysics* 483 (1-2), 46–57. doi:10.1016/j.tecto.2009.08.026

Thorkelson, D. J. (1996). Subduction of Diverging Plates and the Principles of Slab Window Formation. *Tectonophysics* 255 (1-2), 47–63. doi:10.1016/0040-1951(95)00106-9

Torii, Y., and Yoshioka, S. (2007). Physical Conditions Producing Slab Stagnation: Constraints of the Clapeyron Slope, Mantle Viscosity, Trench Retreat, and Dip Angles. *Tectonophysics* 445 (3-4), 200–209. doi:10.1016/j.tecto.2007.08.003

Vaes, B., Hinsbergen, D. J. J., and Boschman, L. M. (2019). Reconstruction of Subduction and Back-Arc Spreading in the NW Pacific and Aleutian Basin: Clues to Causes of Cretaceous and Eocene Plate Reorganizations. *Tectonics* 38 (4), 1367–1413. doi:10.1029/2018tc005164

Yang, T., Moresi, L., Zhao, D., Sandiford, D., and Whittaker, J. (2018). Cenozoic Lithospheric Deformation in Northeast Asia and the Rapidly-Aging Pacific Plate. *Earth Planet. Sci. Lett.* 492, 1–11. doi:10.1016/j.epsl.2018.03.057

Yoshida, M. (2013). The Role of Harzburgite Layers in the Morphology of Subducting Plates and the Behavior of Oceanic Crustal Layers. *Geophys. Res. Lett.* 40 (20), 5387–5392. doi:10.1002/2013gl057578

Zahirovic, S., Seton, M., and Müller, R. D. (2014). The Cretaceous and Cenozoic Tectonic Evolution of Southeast Asia. *Solid Earth* 5 (1), 227–273. doi:10.5194/se-5-227-2014

Zeumann, S., and Hampel, A. (2016). Three-dimensional Finite-Element Models on the Deformation of Forearcs Caused by Aseismic ridge Subduction: The Role of ridge Shape, Friction Coefficient of the Plate Interface and Mechanical Properties of the Forearc. *Tectonophysics* 684, 76–91. doi:10.1016/j.tecto.2015.12.022

Zhang, H., Wang, F., Myhill, R., and Guo, H. (2019). Slab Morphology and Deformation beneath Izu-Bonin. *Nat. Commun.* 10, 1310, 2019 . Article. doi:10.1038/s41467-019-09279-7

Zhao, D., Yanada, T., Hasegawa, A., Umino, N., and Wei, W. (2012). Imaging the Subducting Slabs and Mantle Upwelling under the Japan Islands. *Geophys. J. Int.* 190 (2), 816–828. doi:10.1111/j.1365-246X.2012.05550.x

Zhong, S. (2006). Constraints on Thermochemical Convection of the Mantle from Plume Heat Flux, Plume Excess Temperature, and Upper Mantle Temperature. *J. Geophys. Res.* 111 (B4), B04409, 2006 . Article. doi:10.1029/2005jb003972

Conflict of Interest: The authors declare that the research was conducted in the absence of any commercial or financial relationships that could be construed as a potential conflict of interest.

frontiers in Earth Science

ORIGINAL RESEARCH
published: 21 December 2021
doi: 10.3389/feart.2021.782458

Numerical Simulation of the Effects of Wedge Subduction on the Lithospheric Thermal Structure and the Seismogenic Zone South of Chile Triple Junction

Changsheng Guo[1,2], *Pengchao Sun*[1,2] *and Dongping Wei*[1,2]*

[1]*College of Earth and Planetary Science, University of Chinese Academy of Sciences, Beijing, China,* [2]*Key Laboratory of Computational Geodynamics, Chinese Academy of Sciences, Beijing, China*

In contrast to common subduction, the young and thin part of the Antarctic Plate subducts first to the south of the Chile Triple Junction (CTJ), followed by the old and thick part, corresponding to wedge subduction. A finite element model was used to simulate the wedge subduction of the Antarctic Plate and to compare it with the slab subduction of the Nazca Plate. The results show that the CTJ is not only a wedge subduction boundary but also an important factor controlling the lithospheric thermal structure of the overriding plate. The computed heat flow curves are consistent with the data observed near the trench of the two selected profiles. The different slab dips to the north and south of the CTJ are considered to be caused by wedge subduction. When the slabs are young and at the same age, the deep dip of the Antarctic slab is 22° smaller than the Nazca slab. Southward from the CTJ, the slab age of the wedge subduction increases, which leads to a larger slab dip, a colder slab, and a wider seismogenic zone. The effect of the slab age of wedge subduction on the focal depth is smaller than that of the convergence rate. A 4.8-cm/year difference in convergence rate of the wedge subduction results in an 11-km difference in the width of the seismogenic zone and a 10-km difference in the depth of the downdip limit. Among these controlling factors, the convergence rate plays a major role in the different focal depths south and north of the CTJ.

Keywords: Chile Triple Junction, wedge subduction, seismogenic zone, plate age, thermal structure, numerical simulation

OPEN ACCESS

Edited by:
Lijun Liu,
University of Illinois at Urbana-Champaign, United States

Reviewed by:
Lin Chen,
Institute of Geology and Geophysics (CAS), China
Wei Leng,
University of Science and Technology of China, China

***Correspondence:**
Dongping Wei
dongping@ucas.ac.cn

Specialty section:
This article was submitted to Solid Earth Geophysics, a section of the journal Frontiers in Earth Science

Received: *24 September 2021*
Accepted: *09 November 2021*
Published: *21 December 2021*

Citation:
Guo C, Sun P and Wei D (2021) Numerical Simulation of the Effects of Wedge Subduction on the Lithospheric Thermal Structure and the Seismogenic Zone South of Chile Triple Junction. Front. Earth Sci. 9:782458. doi: 10.3389/feart.2021.782458

INTRODUCTION

Fewer earthquakes occur to the south than the north of the Chile Triple Junction (CTJ) (**Figure 1A**), and the focal depths south of CTJ are much shallower. A common hypothesis is that the position of the interplate seismogenic zone is mainly controlled by temperature (Tichelaar and Ruff, 1991; Oleskevich et al., 1999; Völker et al., 2011). Temperature is typically lower in the subduction zone, except for the spreading ridge entering subduction zones. Generally, the spreading-ridge subduction is accompanied by several phenomena, such as surface heat flow anomalies, earthquakes, and high geothermal gradients in the lithosphere (Hamza et al., 2005; Agurto-Detzel et al., 2014). Therefore, it is important to study the lithospheric thermal structure of the area in which the ridge is subducting beneath the continental plate.

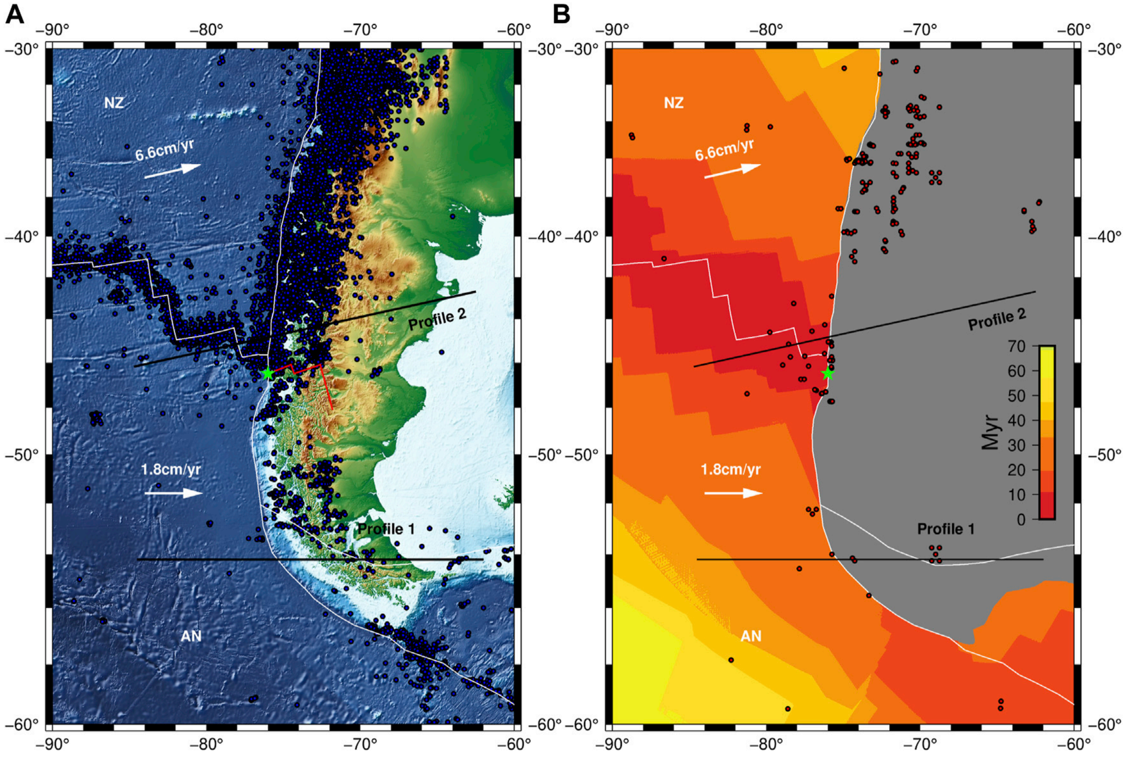

FIGURE 1 | Topographic map of the Chile Triple Junction (CTJ). NZ, Nazca plate; AN, Antarctic plate. The CTJ is indicated by the green five-pointed star. White lines are plate boundaries. Subduction vectors (white arrow) are according to Cande and Leslie (1986) and Maksymowicz et al. (2012). The profiles are indicated by the black solid lines. **(A)** Earthquakes in the area of CTJ. The seismicity data (1906–2021) from the ISC [International Seismological Centre (2021), On-line Bulletin, https://doi.org/10.31905/D808B830] (Bondár and Storchak, 2011; Storchak et al., 2017; Storchak et al., 2020) are symbolized by the blue dots. The location of ridge and transform fault subducted in the past 5.3 Ma is indicated by the red solid line (Maksymowicz et al., 2012). **(B)** The oceanic crustal age (seton et al., 2020) in the area of CTJ. The heat flow data (Lucazeau, 2019) are symbolized by the red dots.

The CTJ is located at the junction of the Nazca, Antarctic, and South American plates (**Figure 1A**). It is formed by the subduction of the spreading Chile ridge into the Chile trench (Forsythe and Nelson, 1985). Because of the ridge subduction, the age distributions on the northern and southern sides of the CTJ notably differ. To the north of the CTJ, the Nazca Plate subducts beneath the South American Plate. The oceanic crust age of the Nazca plate increases northward from the CTJ along the Chile trench and eastward from the Chile ridge. To the south of the CTJ, the Antarctic plate subducts beneath the South American Plate after the spreading ridge. The oceanic crust age of the Antarctic Plate increases southward from the CTJ along the trench and decreases from west to east (**Figure 1B**) (Seton et al., 2020). In other words, to the north of the CTJ, the old and thick part of the Nazca Plate subducts first, followed by the young and thin part, constituting slab subduction. The ridge subduction to the south of the CTJ, however, leads the young and thin part of the Antarctic Plate to subduct first, and should be considered as wedge subduction. As is shown in **Figure 1**, the CTJ is the wedge subduction boundary, and wedge subduction generally occurs after ridge subduction.

Previous studies of subduction zones have considerably advanced research on oceanic and continental subduction zones (Völker et al., 2011; Leng and Sun, 2019; Liu et al., 2019; Chen et al., 2020; Tang et al., 2020). Relevant research mainly focused on common slab subduction, whereas little attention had been paid to wedge subduction, which may significantly affect the slab dip, lithospheric thermal structure, and seismicity of areas in which spreading ridges are subducted such as the CTJ area. Based on the kinematic history and the oceanic plate age distribution (**Figure 1B**) south of the CTJ, wedge subduction is common in the south of the CTJ (from 46°30′S to 55°S and farther south) and exhibits similar tectonic characteristics (Breitsprecher and Thorkelson, 2009). Wedge subduction may also have an impact on the thermal structure of the continental lithosphere farther south of the CTJ, which is little affected by the spreading ridge or slab window. In addition to the spreading ridge, factors in the thermal structure of subduction zones include the plate age, convergence rate, the slab dip, rheological properties of the mantle wedge, thickness of the overlying plate, and frictional heating (Leng and Sun, 2019; Tang et al., 2020), the most important of which are the plate age and convergence rate (Leng and Sun, 2019).

We made two profiles to compare the wedge subduction process of the Antarctic Plate with the slab subduction of the Nazca Plate in the south and north of the CTJ, respectively

TABLE 1 | Slab age and seismogenic zones.[a]

	Model 1	Model 2	Model 3	Model 4	Model 5	Model 6	Model 7
Convergence rate (cm/year)	1.8	6.6	6.6	6.6	6.6	1.8	6.6
Slab age at trench of the initial model (Ma)	20	20	50	20	50	20	20
Slab age of the initial model (Ma)	5–20	5–20	35–50	20–35	50–65	5–20	20–35
Slab age at trench after 11 Ma (Ma)	25	35	65	5	35	25	5
Slab age after 11 Ma (Ma)	5–25	5–35	35–65	5–35	35–65	5–25	5–35
Corresponding Profile	1	—	—	2	—	—	—
100°C(*x*) (km)	28	15	17	17	22		
150°C(*x*) (km)	44	28	34	25	38		
350°C(*x*) (km)	91	87	97	92	99		
450°C(*x*) (km)	109	109	121	116	122		
100°C(*y*) (km)	20	12	13	12	10		
150°C(*y*) (km)	30	27	25	22	24		
350°C(*y*) (km)	56	63	63	62	62		
450°C(*y*) (km)	64	76	80	76	79		
Length locked zone[b](km)	63	72	80	75	77		
Length transition zone[c] (km)	18	22	24	24	23		
Length seismogenic zone[d] (km)	72	83	92	87	89		

Note. [a]*Definitions of locked zone, transition zone, and seismogenic zone are from Klotz et al. (2006) (Völker et al., 2011).*

[b]*x (350°C) −x (100°C).*

[c]*x (450°C) −x (350°C).*

[d]*x (350°C) −x (100°C) + 0.5 × (x(450°C) −x (350°C)).*

(**Figure 1**). We selected the two profiles because the slab ages of two plates are similar near the trench (**Table 1**), but for one, the young part of the plate subducts first; for the other, the old part subducts first. To the south of the CTJ, we selected profile 1 far away from the CTJ. Note that little data have been obtained south of the CTJ, and there is a lack of observations of the slab dip of the Antarctica Plate. The small slab dip of the Antarctic Plate is only kinematically inferred (Breitsprecher and Thorkelson, 2009; Agurto-Detzel et al., 2014). We selected profile 1 south of the CTJ for the following reasons:

First, no significant change has been observed in the relative velocities of the Antarctic–South America plates since 6 Ma, and their directions and convergence rates are similar along the strike (Cande and Leslie, 1986; Bourgois et al., 2016).

Second, according to the boundary of the slab window inferred based on kinematics (Breitsprecher and Thorkelson, 2009), the slab window and subducted ridge should exert very limited influence far away from the CTJ. Therefore, the tectonic setting along the strike is similar and can be simplified and analyzed as wedge subduction. In addition, the oceanic crust age of the Antarctic Plate increases southward along the strike (**Figure 1B**) (Seton et al., 2020).

Although the sediment distribution of the Nazca Plate differs, parameters including the geometry, slab dip, etc., north of the CTJ are similar (Bohm et al., 2002; Lange et al., 2007; Völker et al., 2011). The thermal state of the incoming Nazca Plate significantly varies with the plate age (Völker et al., 2011).

Based on these characteristics, a finite element model was used to simulate the two-dimensional (2D) wedge subduction process of the Antarctic Plate and compare it with the subduction of the Nazca Plate. The effects of the plate age, wedge subduction, and convergence rate on the lithospheric thermal structure and the seismogenic zone of the CTJ area were studied.

TECTONIC SETTING

Geological and geophysical data for the CTJ, which is in a typical ridge subduction zone, have been gradually accumulated in recent years, providing a basis for numerical simulations (Völker et al., 2011; Ji et al., 2019; Liu et al., 2019; Xu et al., 2019). Due to the ridge subduction and other factors, the thermal anomaly to the south of the CTJ is more significant than that to the north (Hamza et al., 2005; Rotman and Spinelli, 2014). Based on the drilling data, Lagabrielle et al. (2000) inferred that the temperature of the area between the CTJ and about 50 km south of it may reach 800–900°C at a depth from 10 to 20 km.

Wang and Wei (2018) classified the triple junctions worldwide and analyzed their evolutionary characteristics. The three boundaries of the CTJ are a ridge and two trenches, forming an RTT-type (ridge–trench–trench) triple junction (**Figure 1**). The convergence rate of the Nazca–South America plates is about 6.6 cm/year to the north of the CTJ in the direction almost parallel to transform faults, whereas the convergence rate of the Antarctic–South America is around 1.8 cm/year to the south of the CTJ approximately in the E–W direction (Cande and Leslie, 1986; Angermann et al., 1999; Maksymowicz et al., 2012; Wang et al., 2018) (**Figure 1**). Compared with other active tectonic regions in the world, little geological data are available for the south of the CTJ. In addition, the crustal structure of South America is among the least studied continental areas on Earth. According to gravity data obtained for the Moho, the depth of the Moho below South America varies greatly. The thickness of the crust in the Andes is more than 65 km, whereas the average thickness of the crust in the northern and eastern parts of South America is around 40 km (van der Meijde et al., 2013).

The CTJ is located at 46°30′S, where the Chile ridge axis is about 10° oblique to the Chile trench (Cande et al., 1987). A series of transform faults divide the Chile ridge into several segments. These ridge segments and transform faults alternately subduct beneath the South American plate (Tebbens et al., 1997). Because of its special geometric structure, the CTJ moves northward when a ridge segment is subducted, representing an RTT-type triple junction. The CTJ moves southward slowly when a transform fault is subducted, representing an FTT-type (fault–trench–trench) triple junction (Forsythe et al., 1986; Maksymowicz et al., 2012). Ridge subduction commonly occurred from 46°30′S to farther than 55°S south of the CTJ in the past 16 Ma (Breitsprecher and Thorkelson, 2009). North of the CTJ, the oceanic crust age of the Nazca Plate increases from 0 Ma at the CTJ to about 37 Ma at 32.8°S along the trench (Tebbens et al., 1997; Flueh et al., 1998; Zelt et al., 2003). South of the CTJ, the age of the Antarctic Plate increases to about 30 Ma along the trench (Seton et al., 2020) (**Figure 1B**).

Statistics show that few earthquakes occur south of the CTJ, whereas more earthquakes can be observed in the north (Murdie et al., 1993) (**Figure 1A**). South of 43°S, the focal depths are generally shallow, and the Wadati–Benioff (WB) plane is not observable because of the lack of interplate seismic data. This may be due to the subduction of very young lithosphere (Kirby et al., 1996; Lange et al., 2007; Agurto-Detzel et al., 2014). The WB plane is well constrained north of 43°S (Agurto-Detzel et al., 2014). Between 36°and 43.5°S, the WB plane has a dip ranging from around 30–33 (Bohm et al., 2002; Lange et al., 2007).

NUMERICAL MODEL

Basic Equations

In this paper, numerical models were built by the 2D finite element method “ASPECT” (Kronbichler et al., 2012), which solves the three conservation equations of, respectively, momentum, mass, and heat.

1) Stokes equation:

$$-\nabla \cdot \left[2\eta\left(\varepsilon(\boldsymbol{u})\right)\right] + \nabla P = \rho \boldsymbol{g} \quad \text{in}\, \Omega, \tag{1}$$

where η is the viscosity, $\varepsilon(\boldsymbol{u})$ is the strain rate, $\boldsymbol{u}$ is the velocity, P is the pressure, $\boldsymbol{g}$ is the gravitational acceleration, and ρ is the density in Boussinesq approximation.

2) Conservation of mass is approximated by the incompressible continuity equation:

$$\nabla \cdot \boldsymbol{u} = 0 \quad \text{in}\, \Omega, \tag{2}$$

3) Heat conservation equation:

$$\rho \mathrm{C}_p \left(\frac{\partial T}{\partial t} + \boldsymbol{u} \cdot \nabla T\right) - \nabla \cdot k \nabla T = \rho H \;\; \text{in}\, \Omega, \tag{3}$$

where $\partial T/\partial t$ is the time derivative of temperature, C_p is the isobaric heat capacity, k is the thermal conductivity, and H is the radioactive heat production.

Visco-Plastic Rheology

ASPECT regards the mantle as a high-viscosity fluid. The common rheological criteria used in geodynamics are adopted in this paper (Billen and Gurnis, 2001; Lallemand et al., 2005; Jadamec et al., 2013; Holt et al., 2015; Leng and Gurnis, 2015). The viscosity for dislocation or diffusion creep is defined as:

$$\eta = \frac{1}{2} A^{-\frac{1}{n}} d^{\frac{m}{n}} \dot{\varepsilon}_l^{\frac{1-n}{n}} \exp\left(\frac{E + PV}{n\mathrm{R}T}\right), \tag{4}$$

where η is the viscosity, A is the prefactor, n is the stress exponent, $\dot{\varepsilon}_l$ is the second invariant of the deviatoric strain rate tensor, d is the grain size, m is the grain size exponent, E is the activation energy, V is the activation volume, R is the gas exponent, and T is the absolute temperature.

In case of diffusion creep, m ≠ 0 and n = 1, the viscosity coefficient in 4) is η_{diff}. While dislocation creep m = 0 and n > 1, the viscosity coefficient in 4) is η_{disl}. So the contributions of diffusion and dislocation creep to the effective viscosity are harmonically averaged into a composite viscosity:

$$\eta_{\mathrm{comp}} = \left(\frac{1}{\eta_{\mathrm{diff}}} + \frac{1}{\eta_{\mathrm{disl}}}\right)^{-1}, \tag{5}$$

Thus, the viscous stress is defined as:

$$\sigma_{\mathrm{visco}} = 2 \times \eta_{\mathrm{diff,disl,comp}} \times \dot{\varepsilon}_l, \tag{6}$$

where $\eta_{\mathrm{diff,\,disl,comp}}$ is one of η_{diff}, η_{disl}, and η_{comp} according to different rheologies (Glerum et al., 2018; Liu et al., 2019).

The ductile rheology is combined with a brittle/plastic rheology to yield an effective visco-plastic rheology. In our implementation, it is defined by the Drucker–Prager criterion (Davis and Selvadurai, 2002):

$$\eta_{\mathrm{Drucker-Prager}} = \begin{cases} \eta_{\mathrm{diff,disl,comp}}, \sigma_{\mathrm{visco}} < \sigma_{\mathrm{yield}} \\ \dfrac{\sigma_{\mathrm{yield}}}{2\dot{\varepsilon}_l}, \sigma_{\mathrm{visco}} \geq \sigma_{\mathrm{yield}} \end{cases}, \tag{7}$$

σ_{yield} is the yield value:

$$\sigma_{\mathrm{yield}} = C \cos\phi + P \sin\phi, \tag{8}$$

where ϕ is the internal friction angle, P is the pressure, and C is the cohesion.

The final effective viscosity η_{eff} is capped by the defined minimum viscosity η_{min} (10^{20} Pas) and maximum viscosity η_{max} (10^{25} Pas) to avoid extremely low or high viscosity values (Glerum et al., 2018):

$$\eta_{\mathrm{eff}} = \min\left(\max\left(\eta_{\mathrm{Drucker-Prager}}, \eta_{min}\right), \eta_{max}\right). \tag{9}$$

Model Set-Ups

Based on the geological background of the CTJ, we built a series of 2D geodynamic numerical models, which fall into Antarctic models and Nazca models, respectively, corresponding to wedge and slab subduction.

Model 1, which simulates the wedge subduction of the Antarctic Plate, corresponds to profile 1 with the convergence

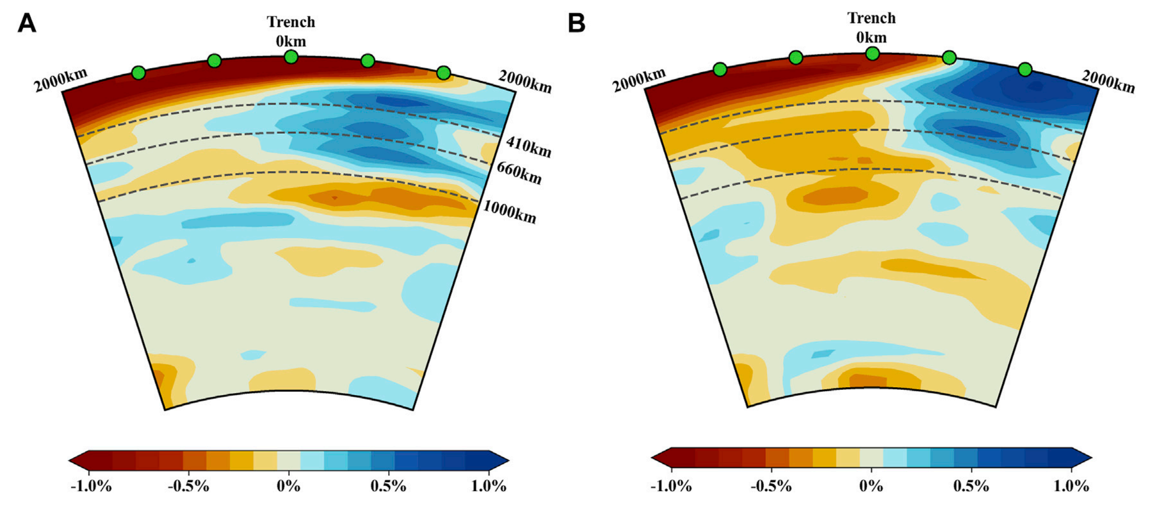

FIGURE 2 | Vertical cross sections of *P* wave velocity perturbations (Simmons et al., 2010) along the profiles shown in **Figure 1**. **(A)** Profile 1 (at 54°12′S). **(B)** Profile 2 (at 44°48′S).

rate set as 1.8 cm/year (**Figure 1**) (Cande and Leslie, 1986; Maksymowicz et al., 2012). The other four models, i.e., Models 2–5, were built to investigate the effect of the slab age and wedge subduction on the lithospheric thermal structure with a set convergence rate of 6.6 cm/year. Models 2 and 3 correspond to wedge subduction, and Models 4 and 5 represent slab subduction. The slab of Model 3 is older than that of Model 2, and the slab of Model 5 is older than that of Model 4. When the calculation finishes, the slab age of Model 4 is the same as that of Model 2 and the slab age of Model 5 is the same as that of Model 3. The slab ages of Models 1–5 are shown in **Table 1**. Model 4 is a simplification based on profile 2.

The computational domain is 2,500 × 660 km; the continental and oceanic plates are 1,500- and 1,000-km long, respectively. To our knowledge, there is a lack of direct observation of the slab dip of Antarctic plate, which is only inferred to be smaller than that of the Nazca Plate (Breitsprecher and Thorkelson, 2009; Agurto-Detzel et al., 2014). Since there are rarely earthquakes south of CTJ, there have been many different tomographic models depending on the various cases in reality. These models differ greatly for this area. On the basis of the tomography (**Figure 2**) and previous numerical model settings for the CTJ (van der Hilst and de Hoop, 2005; Scherwath et al., 2006, 2009; Simmons et al., 2010; Völker et al., 2011; Maksymowicz et al., 2012) and the comparison of different initial slab dips (***Surface Heat Flow*** and ***Seismogenic Zone and Seismicity Data***), the initial slab dips of Models 1–5 were set in a way in which it gradually increases with the depth from 0° at the trench to 30° at about 120-km deep.

The initial temperature field and the boundary conditions were set as follows: The upper boundary was maintained at a constant temperature of 0°C. The temperature at the lithosphere–asthenosphere boundary was set as 1,300°C (Tetreault and Buiter, 2012). An initial geothermal gradient of 0.25°C/km was set for the asthenosphere; thus, the temperature at the lower boundary was set as 1,440°C (Tetreault and Buiter, 2012). A plate cooling model was used for the oceanic plate with a maximum plate thickness of 95 km. The thickness and initial temperature field of the oceanic lithosphere were calculated according to the plate age (Stein and Stein 1992; Richards et al., 2018):

$$T(x,y) = T_{\mathrm{m}}\left[\frac{y}{a} + \sum_{n=1}^{\infty}\frac{2}{n\pi}\exp\left(-\frac{\beta_n x}{a}\right)\sin\left(\frac{n\pi y}{a}\right)\right], \tag{10}$$

where a is the asymptotic thermal plate thickness, T_{m} is the basal temperature, $\beta_{\mathrm{n}} = \sqrt{R^2 + n^2\pi^2} - R, R = va/(2\kappa)$, κ is the thermal diffusivity, and v is the half-spreading rate. x and y denote the horizontal and vertical coordinates. The lithosphere thickness of the continental plate was set as 100 km, and the thickness of the upper and lower crust was both 20 km (Assumpção et al., 2013; Bagherbandi et al., 2017; Liu et al., 2019). A linear interpolation method was used for the initial temperature field of the continental plate (Li and Shi, 2016). The thickness of each layer is listed in **Table 2.**

A constant velocity was applied to the upper part of the left boundary to simulate the convergence of the plates and also applied to the lower part in the opposite direction (Liu et al., 2019). The upper boundary was a free surface and the right and lower boundaries were set to be free slip (**Figure 3**). The parameters obtained in relevant studies are listed in **Table 2** (Tetreault and Buiter, 2012; Liu et al., 2019). For the radioactive heat production, this study refers to Xu et al. (2019) and, for the viscosity values, Glerum et al. (2018) and Liu et al. (2019).

According to the initial slab length, a calculation of 5.5 Ma was needed to obtain the initial temperature field of the slab. The calculation process is as follows: First, the boundary velocity was set as 0, and a calculation of 5.5 Ma was carried out. Subsequently, a boundary velocity corresponding to the actual convergence rate was applied to the left boundary, and another calculation of 5.5 Ma was done. In total, the model was run for 11 Ma. After that, the plate ages of Models 1 and 4 match those of profiles 1 and 2, respectively, in **Figure 1**. The slab ages of the models and the

TABLE 2 | Relevant parameters of numerical model.

Material	Unit	Asthenospheric mantle	Upper continentalcrust	Lower continentalcrust	Lithospheric mantle	Sediments	Oceanic crust	Weak zone
Thickness	km	to 660	20	20	0–88	4	0–8	—
Thermal diffusivity (κ)	$m^2 \cdot s^{-1}$	9.89×10^{-7}	1.21×10^{-6}	1.15×10^{-6}	9.87×10^{-7}	1.21×10^{-6}	1.15×10^{-6}	1.21×10^{-6}
Specific heat (C_p)	$J \cdot kg^{-1} \cdot K^{-1}$	750	750	750	750	750	750	750
Reference density (ρ)	$kg \cdot m^{-3}$	3,300	2,800	2,900	3,300	3,000	3,100	3,300
Thermal expansivity (α)	K^{-1}	2×10^{-5}	2×10^{-5}	2×10^{-5}	2×10^{-5}	2×10^{-5}	2×10^{-5}	2×10^{-5}
Internal friction angle (ϕ)	°	20	20	20	20	5	10	0.03
Cohesion (C)	Pa	20×10^6	20×10^6	20×10^6	20×10^6	10×10^6	10×10^6	1×10^6
Radioactive heat production (A)	$W \cdot m^{-3}$	—	10^{-6}	4×10^{-7}	—	—	—	—
Rheological criterion[a]	—	Dry olivine	Wet quartzite	Wet anorthite	Dry olivine	Gabbro	Gabbro	gabbro
Prefactor[b]	$Pa^{-n} \cdot m^{-p} \cdot s^{-1}$	2.37×10^{-15}	1×10^{-50}	1×10^{-50}	2.37×10^{-15}	1×10^{-50}	1×10^{-50}	1×10^{-50}
diff/disl		6.52×10^{-16}	8.57×10^{-28}	7.13×10^{-18}	6.52×10^{-16}	1.12×10^{-10}	1.12×10^{-10}	1.12×10^{-10}
Stress exponent (n)	—	1	1	1	1	1	1	1
diff/disl		3.5	4.0	3	3.5	3.4	3.4	3.4
Activation energy (E)	$J \cdot mol^{-1}$	375×10^3	0	0	375×10^3	0	0	0
diff/disl		530×10^3	223×10^3	345×10^3	530×10^3	497×10^3	497×10^3	497×10^3
Activation volume (V)	$m^3 \cdot mol^{-1}$	4×10^{-6}	0	0	4×10^{-6}	0	0	0
diff/disl		13×10^{-6}	0	0	18×10^{-6}	0	0	0
Grain size exponent (m)	—	3	1	1	3	1	1	1

[a] *Note. Rheological criterion: for dry olivine, refer to Hirth and Kohlstedt (2003); for wet olivine, refer to Gleason and Tullis (1995); for wet anorthite, refer to Rybacki et al. (2006); for gabbro, refer to Wilks and Carter (1990).*

[b] *For prefactor, refer to Johnson (1997), Naliboff and Buiter (2015).*

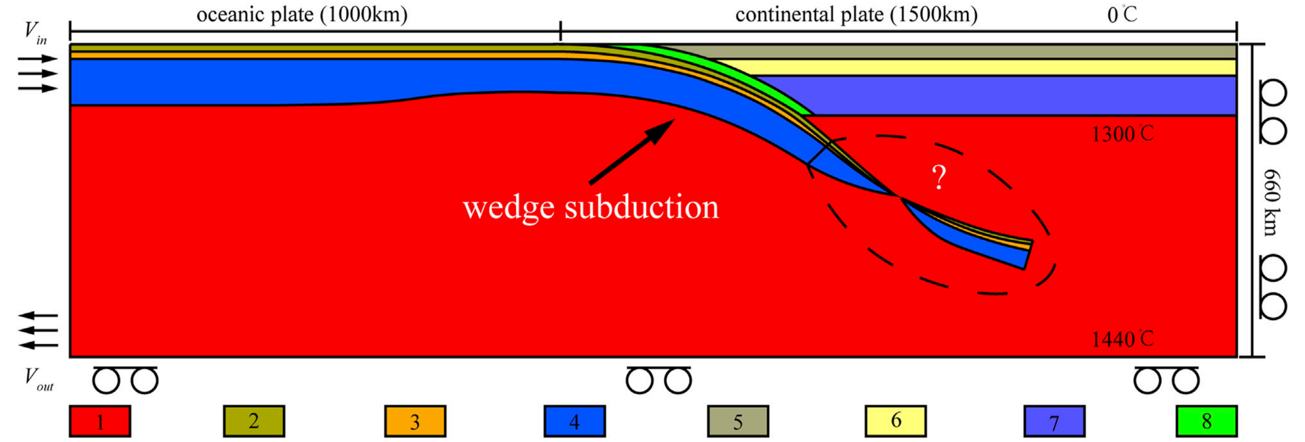

FIGURE 3 | Initial setups and boundary conditions of the wedge subduction. Wedge subduction is a type of subduction in which the young and thin part of the slab subducts first, and the old and thick part subducts later. Surrounded by the dotted line is the truncated part with unclear tectonic structure indicated by the question mark. Colors are used to indicate different compositional fields: 1, asthenospheric mantle; 2, sediments; 3, oceanic crust; 4, lithospheric mantle; 5, upper continental crust; 6, lower continental crust; 7, lithospheric mantle; 8, weak zone. Viscosity of mantle can be calculated with relevant parameters (**Table 2**). All these parameters come from the rheological experiments on dislocation creep and diffusion creep of dry olivine (Hirth and Kohlstedt, 2013).

corresponding relationship between the models and profiles are shown in **Table 1**.

RESULTS

We built a series of models to investigate the effects of wedge subduction (**Table 1**). Due to the lack of observations of the slab dip south of the CTJ, we focused, in ***Slab Dip***, on the effect of wedge subduction on slab dip. In ***Surface Heat Flow*** and ***Seismogenic Zone and Seismicity Data***, the computed heat flow and seismogenic zones of the models, which had different initial slab dips, were compared with the observed data. We chose the initial slab dip, which is more consistent with the observed data to determine the effect of wedge subduction on the seismogenic zone (***Seismogenic Zone and Seismicity Data***) and the temperature field (***Temperature Field***). The effects of slab age and convergence rate are discussed in ***Slab Dip***, ***Temperature Field***.

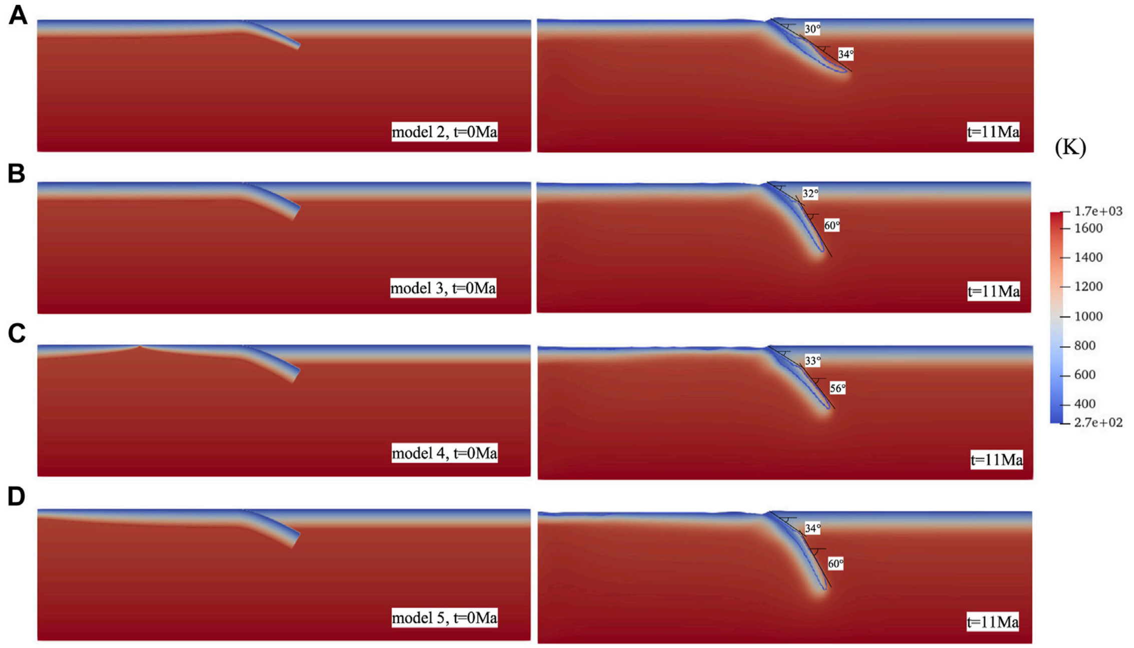

FIGURE 4 | Temperature fields and slab dips of Models 2–5; convergence rate = 6.6 cm/year. On the left and right are, respectively, the initial and final temperature fields. The upper and lower dips on the right are the mean shallow dips and the mean deep dips according to Lallemand et al. (2005). Sediment contours are indicated by the solid blue lines in right models, and the upper parts of the outlines are the upper surface of the slabs **(A)** Model 2, wedge subduction with a young slab. **(B)** Model 3, wedge subduction with an old slab. **(C)** Model 4, slab subduction with a young slab. **(D)** Model 5, slab subduction with an old slab.

Slab Dip

The Nazca model in which the old part subducted first corresponded to slab subduction, whereas the Antarctic model in which the young part subducted first corresponded to wedge subduction. Typically, the slab dip gradually increases with the depth and stops growing at about 80–150 km deep. Beneath this depth, it remains almost constant down to the boundary between the upper and lower mantle (Lallemand et al., 2005). According to the definition of the shallow dip and the deep dip of Lallemand et al. (2005), the mean shallow dips and mean deep dips of Models 2, 3, 4, and 5 are given in **Figure 4**.

The solid blue lines in **Figures 4** and **5** are the sediment contours. **Figure 5** shows the evolution of the sediment outlines. The upper parts of the outlines are the upper surface of the slabs. As is shown in **Figure 4**, the older the slab, the greater the slab dip. In the Antarctic models, for example, the slab of Model 2 is younger than that of Model 3 and the mean shallow dip and mean deep dip of Model 2 are about 2° and 26° smaller than those of Model 3 (**Figure 4A, B**). In the Nazca models, the slab of Model 4 is younger than that of Model 5, and the mean shallow dip and mean deep dip of Model 4 are around 1° and 4° smaller than those of Model 5 (**Figure 4C, D**).

When the slab ages of the wedge subduction and the slab subduction are the same, the slab dip of wedge subduction is smaller than that of slab subduction. For example, the mean shallow dip and mean deep dip of Model 2 (Antarctic model, **Figure 4A**) are, respectively, about 3° and 22° smaller than that of Model 4 (Nazca model, **Figure 4C**). The slabs of Model 3 and Model 5 are too old for their thickness to increase with age, so they have similar slap dips (**Figure 4B, D**). Among Models 2, 3, 4 and 5, Model 2 has the smallest slap dip. Based on the results above, the slab dip differences of the areas north and south of the CTJ are considered a consequence of the wedge subduction.

Surface Heat Flow

In the effort to obtain a more reasonable initial slab dip, an initial slab dip of 15° was applied to Models 6 and 7. Except for the initial slab dip, the other settings of Models 6 and 7 were the same as those of Models 1 and 4. **Figure 6** shows the observed surface heat flow (Lucazeau, 2019) and computed surface heat flow of the different models. In the Antarctic models, the observed heat flow data is too limited to constrain the initial slab dip (**Figure 6A**). In the Nazca models, the heat flow of Model 4 with an initial slab dip of 30°is more consistent with observed data in the vicinity of the trench than that of Model 7 (**Figure 6B**).

The larger the convergence rate, the higher the maximum heat flow in the vicinity of the trench. The convergence rate of Model 1 is smaller than that of Model 2, and the maximum heat flow of Model 1 is 133.7°mW/m^2 lower than that of Model 2 in the oceanic plate and 23.7°mW/m^2 lower in the forearc (**Figure 6C**).

The surface heat flow, including the oceanic surface heat flow and forearc heat flow, is generally high in the vicinity of the trench (**Figure 6**). The surface heat flow in the forearc is complex and depends on several factors such as the topography of the overlying plate or the different slab dips. As is shown in **Figure 6D**, the forearc heat flow of Model 2 is high, and the heat flow values of Models 3, 4, and 5 gradually stabilize and are almost the same far away from the trench.

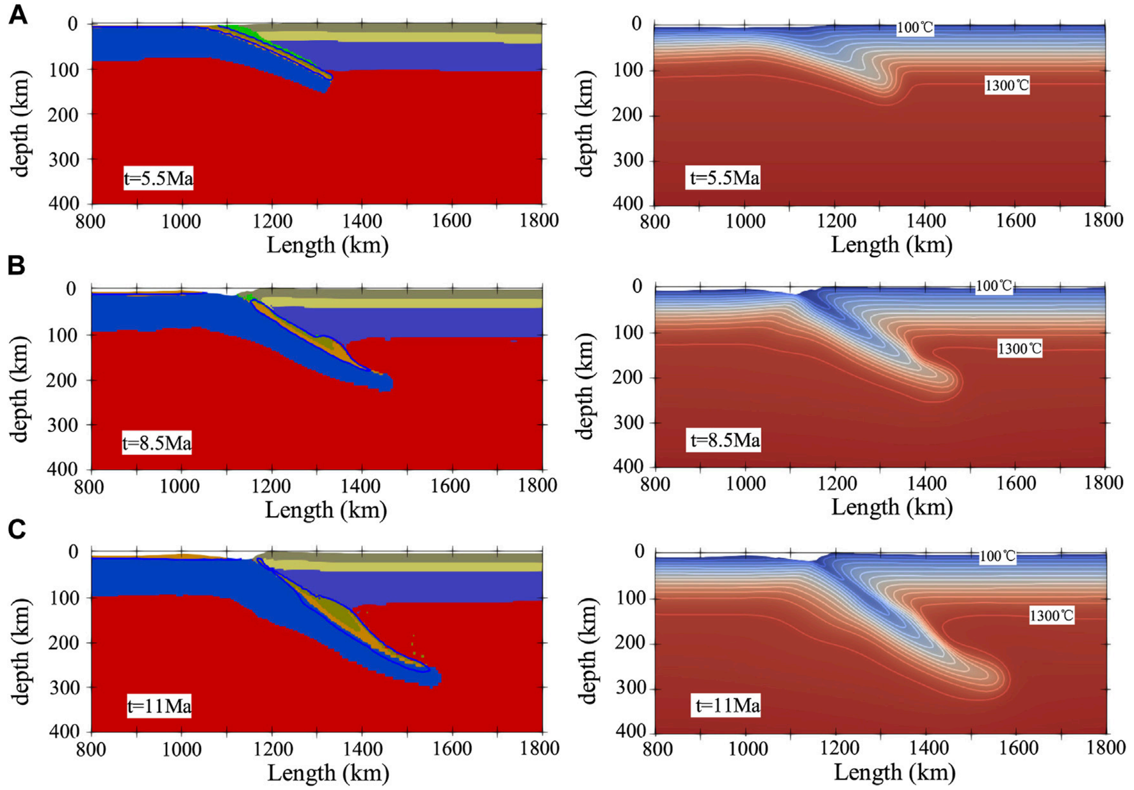

FIGURE 5 | Evolution of material field **(left)** and temperature field **(right)** of Model 2 (wedge subduction with a young slab). **(A)** t = 5.5 Ma. **(B)** t = 8.5 Ma. **(C)** t = 11 Ma. Sediment contours are indicated by the solid blue lines in the material field. The solid white lines indicate isotherms in the temperature field **(right)**, with a minimum of 100°C and a maximum of 1,300°C.

Generally, the younger the plate is, the higher the maximum oceanic surface heat flow is in the vicinity of the trench (**Figure 6D**). In the Antarctic models, the oceanic plate of Model 2 is younger than that of Model 3, and the maximum oceanic heat flow of Model 2 (300.8 mW/m^2) is higher. The maximum forearc heat flow of Model 2 (70.8mW/m^2) is higher than that of Model 3 (59.2°mW/m^2; **Figure 6D**), which is related to the young slab and small slab dip. In the Nazca models, the oceanic plate of Model 4 is younger than that of Model 5, and the maximum oceanic heat flow of Model 4 is higher (427.0 mW/m^2) in the vicinity of the trench, which is related to the young plate and adjacent ridge. However, the maximum forearc heat flow of Model 5 (94.7 mW/m^2) is higher than that of Model 4 (73.2 mW/m^2).

Seismogenic Zone and Seismicity Data

The position of the interplate seismogenic zone is related to the interplate seismicity and primarily controlled by temperature (Tichelaar and Ruff, 1991; Oleskevich et al., 1999; Völker et al., 2011). The earthquake distribution in Chile (Tichelaar and Ruff, 1991; Oleskevich et al., 1999; Völker et al., 2011) and in the Nazca subduction zone is consistent with this hypothesis. Klotz et al. (2006) generally defines 1) the interseismic locked zone as the region in which the plate contact is at temperatures from 100°C to 350°C, 2) the temperature range from 350°C to 450°C as the transition zone from full locking to full slip, and 3) the seismogenic zone as the width of the locked zone plus half the width of the transition zone (Völker et al., 2011).

The seismicity data (1906–2021) in the vicinity of the profiles from the ISC (International Seismological Centre (2021), On-line Bulletin, https://doi.org/10.31905/D808B830) (Bondár and Storchak, 2011; Storchak et al., 2017; 2020) were projected to profile 1 and profile 2 to contrast with seismogenic zones of our models (**Figure 7**).

The seismicity data of profile 1 is too little to constrain the seismogenic zone south of the CTJ. In the north of the CTJ, the seismicity data of profile 2 are more consistent with Model 4 than with Model 7 in the seismogenic zone. However, the observed deep seismic events within the slab of profile 2 are more consistent with Model 7 than with Model 4. This is due to the shallow and deep dip of the slab increase during the subduction in Model 4. In the *Slab dip* section, it is found that the different slab dips of the areas north and south of the CTJ are due to the wedge subduction. Therefore, the initial slab dip of profile 1 and profile 2 were set to be the same. Based on the comparison of the seismogenic zone and heat flow, the numerical models with an initial slab dip that gradually increases from 0° to 30° (Models 1–5) better reflect the interplate seismogenic zone and surface heat flow than those with a dip of 15° (Models 6–7). The widths of the seismogenic zones of Models 1–5 according to the definitions of Klotz et al. (2006) are shown in **Table 1**.

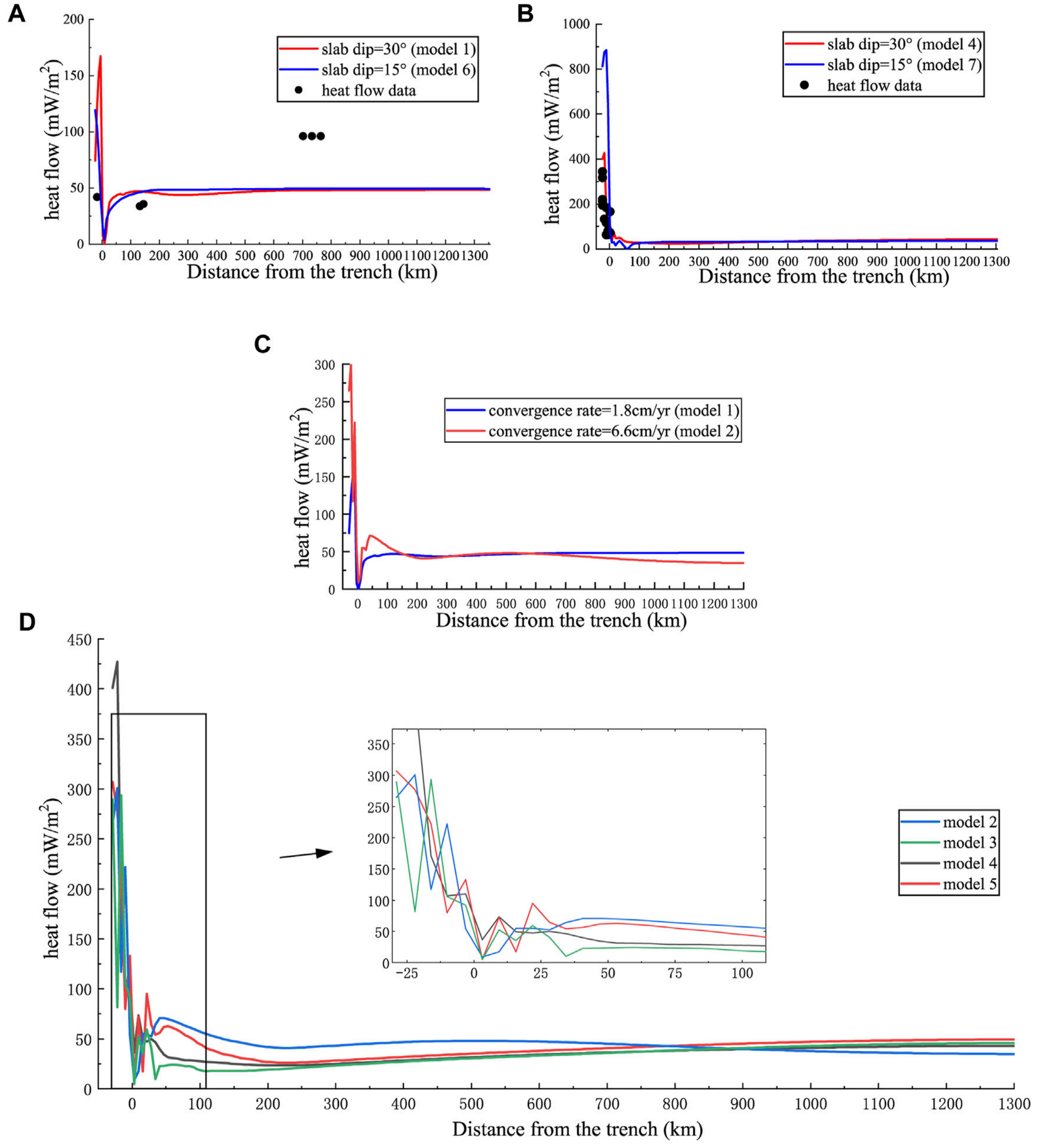

FIGURE 6 | Results of the surface heat flow ahead of the trench. Observed heat flow is marked by the black dots. Solid lines correspond to heat flow results of different models. **(A)** Profile 1. **(B)** profile 2. **(C)** Comparison between heat flow results of different convergence rates. **(D)** Comparison between heat flow results of Models 2, 3, 4, and 5. Model 2, wedge subduction with a young slab; Model 3, wedge subduction with an old slab; Model 4, slab subduction with a young slab; Model 5, slab subduction with an old slab.

When the slab subduction and wedge subduction are of the same, old slab age and convergence rate, the width of the seismogenic zone of the former is smaller than that of the latter. As **Table 1** shows, the width of the seismogenic zone of Model 5 is 3 km narrower than that of Model 3. The opposite results were obtained for slabs with the same young age and convergence rate, as is illustrated by the 4-km-wider seismogenic zone in Model 4 compared with Model 2. Generally, the widths of the locked zone, transition zone, and seismogenic zone of Model 2 are smaller than those of the other models when the convergence rate is 6.6 cm/year (**Table 1**).

The older the slab, the wider the seismogenic zone. For instance, the slab of Model 5 is older than that of Model 4, and the seismogenic zone of Model 5 is 2 km wider than that of Model 4. The slab of Model 3 is older than that of Model 2, and the seismogenic zone of Model 3 is 9 km wider than that of Model 2.

The seismogenic zone related to wedge subduction widens with the increase in the convergence rate. The convergence rate of

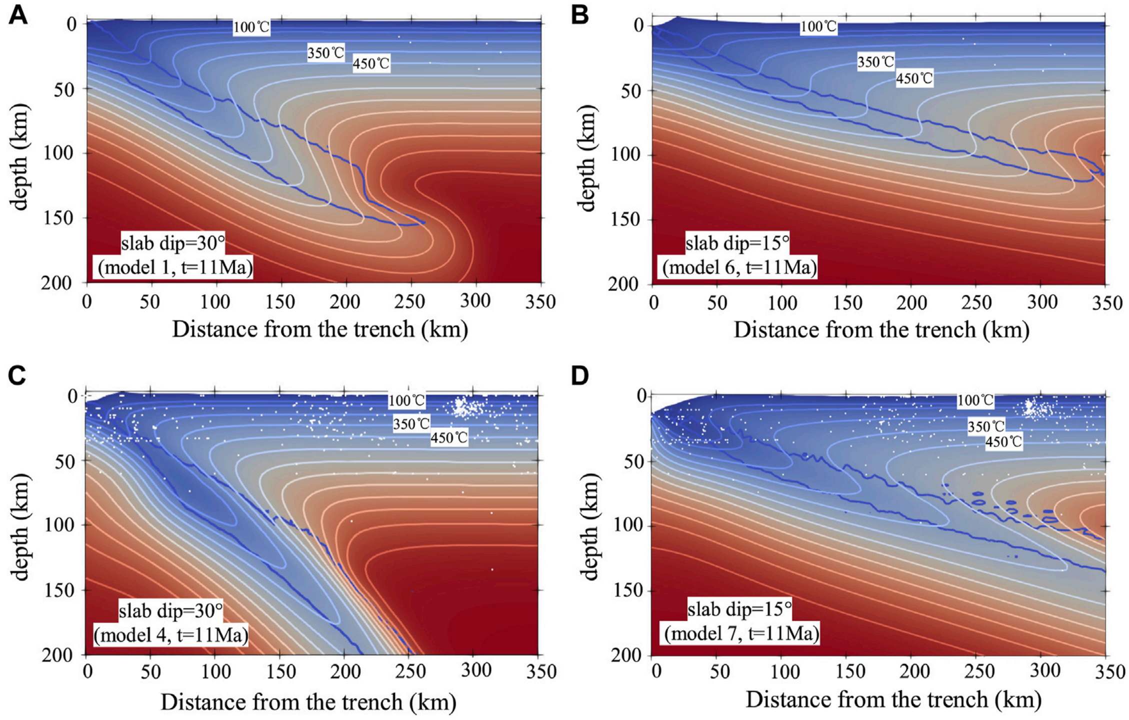

FIGURE 7 | Earthquakes in the vicinity of the trench. Earthquakes of profile 1 and profile 2 are indicated by the white circles. **(A)** Profile 1, initial slab dip = 30°, convergence rate = 1.8 cm/yr (Model 1) **(B)** profile 1, initial slab dip = 15°, convergence rate = 1.8 cm/yr (Model 6) **(C)** profile 2, initial slab dip = 30°, convergence rate = 6.6 cm/yr (Model 4) **(D)** profile 2, initial slab dip = 15°, convergence rate = 6.6 cm/yr (Model 7).

Model 2 is larger than that of Model 1, and the seismogenic zone of Model 2 is 11 km wider than that of Model 1 (**Table 1**). Besides, as is shown in **Table 1**, the intersections of the slab surface with the 350°C and 450°C isotherms of Model 2 are much deeper than those of Model 1. The depth of the downdip limit of the seismogenic zone of Model 2 is about 10 km deeper than that of Model 1.

Temperature Field

Figure 8 shows the temperature field within 350 km ahead of the trench. Affected by the subduction of the cold slab, the temperature in the vicinity of the upper surface of the slab is low. In contrast, the overlying plate far away from the slab is only slightly affected. The x- and y-coordinates at the intersections of the upper surface of the slab with the isotherms of 100°C, 150°C, 350°C, and 450°C (**Figure 8**) are shown in **Table 1**.

At the same age, the slab of wedge subduction tends to be hotter than that of slab subduction horizontally. As **Table 1** shows, the slab ages of Models 4 and 2 are the same, and the x-coordinates of Model 4 at intersections of the slab surface with the 100, 350, and 450°C isotherms are larger than those of Model 2. Compared with the differences between their x-coordinates, the differences between the y-coordinates of Models 2 and 4 are much smaller.

Generally, the older the slab is, the lower the temperature is in the vicinity of the upper surface of the slab in the horizontal direction. In the Antarctic models, for example, the slab of Model 2 is younger than that of Model 3. The x-coordinates of Model 2 at the intersections of the slab surface with the isotherms of 100, 150, 350, and 450 °C are smaller than those of Model 3. For Models 2–5, the difference in the y-coordinates is much smaller than the difference in the x-coordinates (**Table 1**). For example, the maximum difference in the x-coordinates between Models 4 and 5 is 13 km at the 150°C isotherm, whereas the maximum difference in the y-coordinates is 3 km at the 450°C isotherm.

The temperature in the vicinity of the slab surface lowers with a decrease in the convergence rate horizontally. In the Antarctic models, the convergence rate of Model 1 is smaller than that of Model 2. The x-coordinates of Model one at the intersections of the slab surface with the isotherms of 100, 150, 350, and 450°C are larger than or equal to those of Model 2 (**Table 1**). In addition, the y-coordinates of Model 1 at the intersections of the slab boundary with the 100°C and 150°C isotherms are 8 and 3 km, respectively, deeper than those of Model 2, whereas at the intersections of the slab boundary with the 350 and 450°C isotherms, the y-coordinates of Model 1 are, respectively, 7 and 12 km shallower than those of Model 2. This means that the convergence rate has a more significant effect on the temperature field than the slab age in the vertical direction.

DISCUSSIONS

There are significant differences in seismicity and slab dip between the south and north of the CTJ. According to our results and the inference of Breitsprecher and Thorkelson

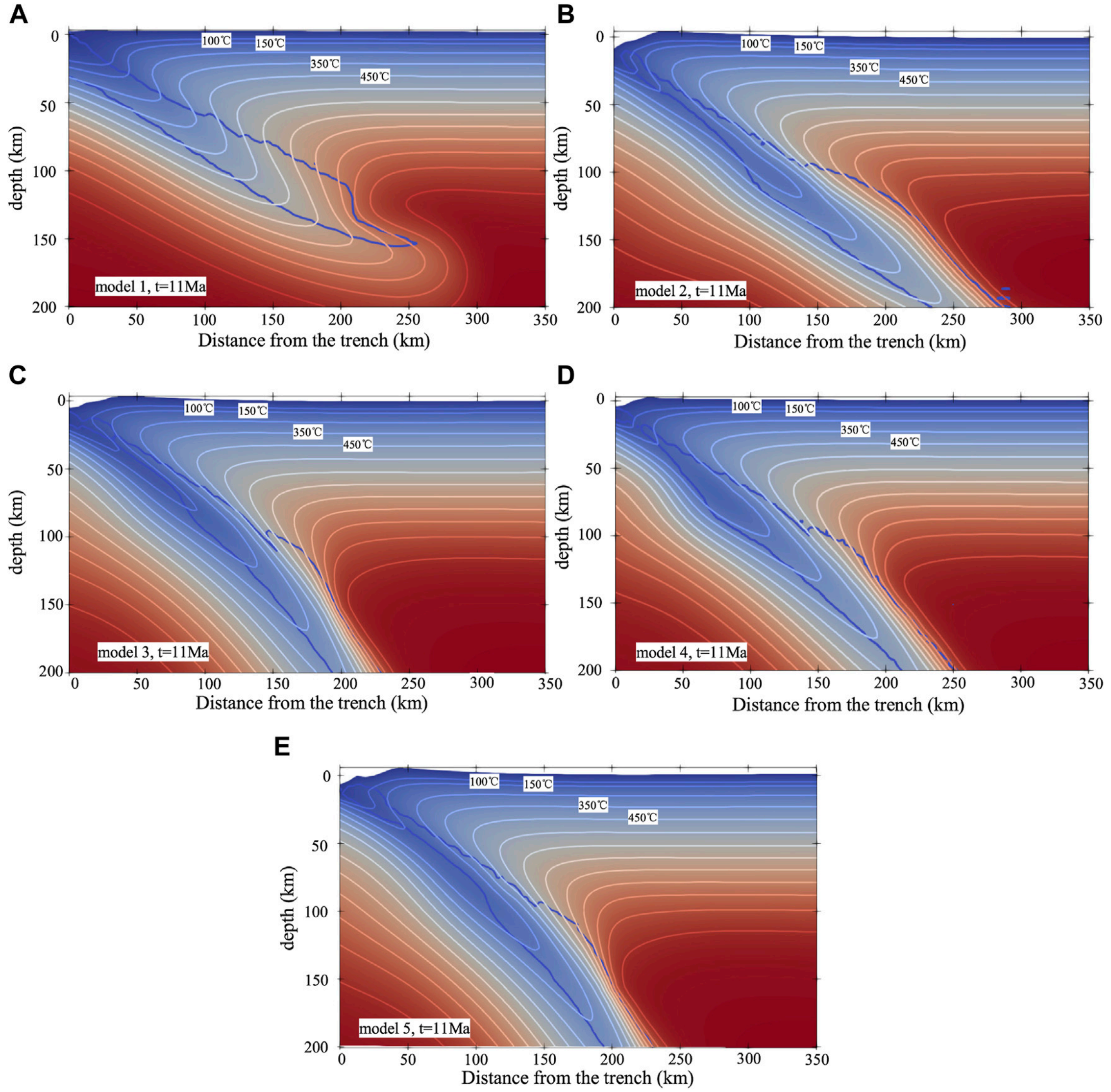

FIGURE 8 | Temperature fields within 350 km ahead of the trench. Sediment contours are indicated by the solid blue lines. **(A)** Model 1, wedge subduction with a young slab, convergence rate = 1.8 cm/yr **(B)** Model 2, wedge subduction with a young slab, convergence rate = 6.6 cm/yr **(C)** Model 3, wedge subduction with an old slab, convergence rate = 6.6 cm/yr **(D)** Model 4, slab subduction with a young slab, convergence rate = 6.6 cm/yr **(E)** Model 5, slab subduction with an old slab, convergence rate = 6.6 cm/yr.

(2009), the slab dip of the wedge subduction zone should be small south of the CTJ. The slab dip (*Slab dips between the south and north of the Chile Triple Junction* section) and the seismogenic zone (*Seismogenic zones between the south and north of the Chile Triple Junction* section) are controlled by the slab age, wedge subduction, and convergence rate.

Slab Dips Between the South and North of the Chile Triple Junction

Our simulations show that the slab dip of the Antarctic Plate, which increases southward from the CTJ, is smaller than that of the Nazca Plate when the same slab age is chosen. To the south of the CTJ, the slab between the CTJ and profile 1 is younger than that of profile 1 and, thus, its slab dip is smaller than that of profile 1. It is also smaller than the dip of the Nazca slab (profile 2) because the slab dip of profile 2 is almost the smallest to the north of the CTJ (***Slab Dip***). This is consistent with the tomography of the area south of the CTJ in the vicinity of 47°30S, which shows a smaller slab dip compared with the Nazca Plate (Maksymowicz et al., 2012). However, there is a lack of evidence farther south, But the results are consistent with the inference of Breitsprecher and Thorkelson (2009) based on kinematics. In addition, the slab age is generally considered to be the main factor in the change of the slab dip. The older the oceanic plate age, the greater the slab dip (Jarrard, 1986; Stern, 2002). Tomographic evidence, the tomography in the vicinities of 45°30′S, 44°30′S (Maksymowicz et al., 2012), 43°S (Scherwath et al., 2006; 2009), 38°S (Contreras-Reyes, et al., 2008), and farther north (van der Hilst and de Hoop, 2005), shows that the slab dip increases northward from the CTJ. Our results show that, with the slab age, the slab dip increases when the slabs are young but remains almost unchanged when the slabs are old. The results in ***Slab Dip*** show that the slab age and slab dip increase northward from profile 2, which is also consistent with the tomographic evidence above.

Seismogenic Zones Between the South and North of the Chile Triple Junction

If we adopt the definitions of Klotz et al. (2006), the simulation results of Models 2 and 3 show that the temperature of the Nazca slab decreases, and the width of the seismogenic zone increases northward from the CTJ (***Seismogenic Zone and Seismicity Data***, ***Temperature Field***). This is consistent with the numerical simulation results of Völker et al. (2011), the width of the seismogenic zone Wang et al. (2007) inferred from GPS measurements, and the earthquake distribution to the north of the CTJ (**Figure 1**).

Wedge subduction significantly affects the seismogenic zone. Our simulation results show that the seismogenic zone of the Antarctic slab is narrower than that of the Nazca slab when the slabs are young. The seismogenic zone of profile 1 is 15 km narrower than that of profile 2 (**Table 1**). Then the seismogenic zone of profile 1 is narrower than that of the Nazca slab because the seismogenic zone of profile 2 is almost the narrowest to the north of the CTJ. The slab between the CTJ and profile 1 is younger than that of profile 1, so its seismogenic zone is narrower than that of profile 1 and much narrower than that of the Nazca Plate. Our simulations by considering exclusively the slab age and convergence rate show that the width of the seismogenic zone increases southward from the CTJ to profile 1. In addition, a few earthquakes occur to the south of the CTJ according to statistics (Murdie et al., 1993). South of 43°S, the WB plane is not observable for the young age of the Antarctic slab, as proposed by Kirby et al. (1996), Lange et al. (2007), and Agurto-Detzel et al. (2014). This hypothesis is also supported by our finding that the younger slab corresponds to a narrower seismogenic zone. Besides, the oldest slab age of the Antarctic Plate (at the trench) is around 30 Ma, as **Figure 1** shows. Therefore, old slabs do not exist south of the CTJ. In fact, the spreading ridge raises the temperature of the South America Plate to a much higher degree and leads to a much narrower seismogenic zone in the vicinity of the CTJ than our simulation results indicate. This may cause difficulties in observing the WB plane, while wedge subduction is not conducive to this phenomenon. Thus, the wedge subduction, slab age, and convergence rate have weaker effects than ridge subduction on the width of the seismogenic zone.

The focal depth is generally shallower south of, than north of, the CTJ (Agurto-Detzel et al., 2014). Because of the wedge subduction, the slab dip of the Antarctic Plate is smaller than that of the Nazca Plate (*Slab dip* section). Although the Antarctic slab is hotter and has a smaller dip than the Nazca slab, our results suggest that there is little difference between the depths of the seismogenic zones of wedge subduction and slab subduction (**Table 1**). The downdip limit depth of the seismogenic zone of Model 2 is approximately 1 km deeper than that of profile 2 (Model 4), but 10 km deeper than that of profile 1 (Model 1). Therefore, the effects of slab age and wedge subduction on the focal depth are smaller than that of convergence rate, and the difference between the convergence rate of the Antarctic Plate and that of the Nazca Plate is a main cause of the different focal depths to the south and north of the CTJ. To the north of the CTJ, slip distributions of a 900-km-long rupture zone terminate at a similar depth were inversed by Barrientos and Ward (1990) and Moreno et al. (2009) (Völker et al., 2011). Our results show that the downdip limit of the seismogenic zone increases by only about 2 km, while the slab age increases by 30 Ma, which is consistent with the results of Barrientos and Ward (1990) and Moreno et al. (2009). However, this is inconsistent with the statistics related to the focal depths of the area between 36°S and 40°S (Bohm et al., 2002). In conclusion, the CTJ is not only a wedge subduction boundary but also an important factor controlling the lithospheric thermal structure of the overriding plate. Without considering the spreading ridge beneath the South American plate, the differences in the slab dip, seismic distribution, and focal depth between the northern and southern sides of the CTJ are consistent with the results of our simulation controlled by the plate age, the wedge subduction, and the convergence rate.

Effect of dehydration and other processes

Several processes that occur in the subduction zone, such as shear heating, partial melting, hydrothermal cooling, and dehydration, were not covered in this study. Dehydration and partial melting are related to element recycling, intermediate and deep earthquakes, and double seismic zones (Seno et al., 2001; Li and Ni, 2020). Dehydration is essentially a result of the slab responding to the temperature and pressure change during subduction. Dehydration has significantly different effects in cold and hot subduction zones (Li and Ni, 2020). The subduction zone to the north of the CTJ is cold and that to the south is hot. The slab north of the CTJ can, thus, retain more water at greater depths, whereas the slab south of the CTJ dehydrates extensively at shallower depths. Shear heating and hydrothermal cooling are related to the thermal structure of the subduction zone. These processes and their occurrences north of the CTJ are discussed in Völker et al. (2011). The shear heating may give rise to a higher heat flow and a hotter slab south of the CTJ, corresponding to a narrower seismogenic zone; in contrast, the effect of hydrothermal circulation is the opposite of it, leading to a lower heat flow and a colder slab.

Complexity of the Subduction Process South of the Chile Triple Junction

The observed data of the area to the south of the CTJ are scant. In this paper, effects of the wedge subduction of Antarctica plate are determined based on 2D numerical simulations. However, south of the CTJ, the thermal structure and seismicity near the CTJ are mainly affected by the spreading ridge subduction, which is a very complex 3D process. In this study, we discuss the effect of wedge subduction on the vicinity of the CTJ only based on the results obtained for the area far away from the CTJ.

The geological conditions in the CTJ area are complex, particularly the lithospheric thermal structure, and the distribution of seismogenic zones are affected by a series of factors such as the ridge subduction, the slab window, the plate age, the slab dip, the hydrothermal circulation, volcanic activities, and the uneven thickness of the lithosphere. With the ridge subduction and other factors ruled out, the effects of the slab age and convergence rate on the lithospheric thermal structure and seismogenic zone were investigated in this paper. The results of our simulations, however, are still complex, especially those obtained for the forearc heat flow. In fact, compared with the plate age and convergence rate, the ridge subduction and the slab window have greater effects of on the thermal structure of the lithosphere of the area south of the CTJ, where the WB plane cannot be observed. Although a series of studies showed that the definition of the seismogenic zone in Klotz et al. (2006) is in good agreement with geological observations on the north of the CTJ, several limitations and uncertainties remain with respect to the mechanism controlling interplate earthquakes. For future research, we will consider the effects of the different factors during the ridge subduction in the CTJ area.

CONCLUSION

1) The difference between the slab dip north and south of the CTJ is considered due to wedge subduction. When the slabs are old and at the same age, the slab dips of slab subduction and wedge subduction are similar. When the slabs are young and at the same age, the Antarctic slab has a deep dip 22° smaller, a temperature higher, and a seismogenic zone 4 km narrower than those of the Nazca slab.
2) The slab age of the wedge subduction southward from the CTJ increases and leads to a larger slab dip, a colder slab in the horizontal direction, and a wider seismogenic zone.
3) The effect of the slab age of wedge subduction on the focal depth is smaller than that of the convergence rate. The difference between the convergence rate of the Antarctic and that of the Nazca plates plays a major role in the different focal depths to the south and north of the CTJ. The smaller the convergence rate, the shallower the seismogenic zone. A difference of 4.8 cm/year in the convergence rate of the wedge subduction processes results in an 11-km difference in the width of the seismogenic zone and a 10-km difference in the depth of the downdip limit.
4) The computed heat flow curves are consistent with the data obtained in the vicinity of the trench. The younger the plate is, the higher the maximum oceanic heat flow is in the vicinity of the trench. The oceanic heat flow reaches up to 427.0 mW/m^2. The larger the convergence rate, the higher the maximum heat flow. A difference of 4.8 cm/year in the convergence rate of the wedge subduction processes leads to a heat flow difference of 133.7 mW/m^2 in the oceanic plate and one of 23.7 mW/m^2 in the forearc.

DATA AVAILABILITY STATEMENT

Publicly available datasets were analyzed in this study. These data can be found here: The seismic data (1906–2021) for this study can be found in the ISC [International Seismological Centre (2021), On-line Bulletin (Bondár and Storchak, 2011; Storchak et al., 2017; 2020)] (https://doi.org/10.31905/D808B830). The heat flow data for this study can be found in Lucazeau (2019) (https://agupubs.onlinelibrary.wiley.com/doi/10.1029/2019GC008389).

AUTHOR CONTRIBUTIONS

CG conceptualized the study, developed the methodology, performed the numerical simulation and validation, and wrote the manuscript. PS performed the investigation, data curation, and validation. DW acquired the funding and supervised the study.

FUNDING

This work was supported by the National Natural Science Foundation of China (41874115).

ACKNOWLEDGMENTS

We would like to thank Dr. Lin Chen and Dr. Wei Leng for their constructive suggestions and comments. Some of the figures were generated using the Generic Mapping Tools (GMT) (Wessel et al., 2019).

REFERENCES

Agurto-Detzel, H., Rietbrock, A., Bataille, K., Miller, M., Iwamori, H., and Priestley, K. (2014). Seismicity Distribution in the Vicinity of the Chile Triple Junction, Aysén Region, Southern Chile. *J. South Am. Earth Sci.* 51, 1–11. doi:10.1016/j.jsames.2013.12.011

Angermann, D., Klotz, J., and Reigber, C. (1999). Space-geodetic Estimation of the Nazca-South America Euler Vector. *Earth Planet. Sci. Lett.* 171, 329–334. doi:10.1016/S0012-821X(99)00173-9

Assumpção, M., Feng, M., Tassara, A., and Julià, J. (2013). Models of Crustal Thickness for South America from Seismic Refraction, Receiver Functions and Surface Wave Tomography. *Tectonophysics* 609, 82–96. doi:10.1016/j.tecto.2012.11.014

Bagherbandi, M., Bai, Y., Sjöberg, L. E., Tenzer, R., Abrehdary, M., Miranda, S., et al. (2017). Effect of the Lithospheric thermal State on the Moho Interface: A Case Study in South America. *J. South Am. Earth Sci.* 76, 198–207. doi:10.1016/j.jsames.2017.02.010

Barrientos, S. E., and Ward, S. N. (1990). The 1960 Chile Earthquake: Inversion for Slip Distribution from Surface Deformation. *Geophys. J. Int.* 103, 589–598. doi:10.1111/j.1365-246x.1990.tb05673.x

Billen, M. I., and Gurnis, M. (2001). A Low Viscosity Wedge in Subduction Zones. *Earth Planet. Sci. Lett.* 193 (1-2), 227–236. doi:10.1016/S0012-821X(01)00482-4

Bohm, M., Lüth, S., Echtler, H., Asch, G., Bataille, K., Bruhn, C., et al. (2002). The Southern Andes between 36° and 40°S Latitude: Seismicity and Average Seismic Velocities. *Tectonophysics* 356 (4), 275–289. doi:10.1016/S0040-1951(02)00399-2

Bondár, I., and Storchak, D. (2011). Improved Location Procedures at the International Seismological Centre. *Geophys. J. Int.* 186, 1220–1244. doi:10.1111/j.1365-246X.2011.05107.x

Bourgois, J., Lagabrielle, Y., Martin, H., Dyment, J., Frutos, J., and Cisternas, M. E. (2016). A Review on Forearc Ophiolite Obduction, Adakite-like Generation, and Slab Window Development at the chile Triple junction Area: Uniformitarian Framework for Spreading-ridge Subduction. *Pure Appl. Geophys.* 173 (10-11), 3217–3246. doi:10.1007/978-3-319-51529-8_2

Breitsprecher, K., and Thorkelson, D. J. (2009). Neogene Kinematic History of Nazca-Antarctic-Phoenix Slab Windows beneath Patagonia and the Antarctic Peninsula. *Tectonophysics* 464 (1-4), 10–20. doi:10.1016/j.tecto.2008.02.013

Cande, S. C., and Leslie, R. B. (1986). Late Cenozoic Tectonics of the Southern Chile Trench. *J. Geophys. Res.* 91, 471–496. doi:10.1029/JB091iB01p00471

Cande, S. C., Leslie, R. B., Parra, J. C., and Hobart, M. (1987). Interaction between the Chile Ridge and Chile Trench: Geophysical and Geothermal Evidence. *J. Geophys. Res.* 92 (B1), 495–520. doi:10.1029/JB092iB01p00495

Chen, L., Liu, L., Capitanio, F. A., Gerya, T. V., and Li, Y. (2020). The Role of Pre-existing Weak Zones in the Formation of the Himalaya and Tibetan Plateau: 3-D Thermomechanical Modelling. *Geophys. J. Int.* 221, 1971–1983. doi:10.1093/gji/ggaa125

Contreras-Reyes, E., Grevemeyer, I., Flueh, E. R., and Reichert, C. (2008). Upper Lithospheric Structure of the Subduction Zone Offshore of Southern Arauco peninsula, Chile, at ~38°S°. *J. Geophys. Res.*, 113(B07303), 1–19. doi:10.1029/2007JB005569

Davis, R. O., and Selvadurai, A. P. S. (2002). *Plasticity and Geomechanics*. Cambridge University Press.

Flueh, E. R., Vidal, N., Ranero, C. R., Hojka, A., von Huene, R., Bialas, J., et al. (1998). Seismic Investigation of the continental Margin off- and Onshore Valparaiso, Chile. *Tectonophysics* 288, 251–263. doi:10.1016/S0040-1951(97)00299-0

Forsythe, R. D., Nelson, E. P., Carr, M. J., Kaeding, M. E., Herve, M., Mpodozis, C., et al. (1986). Pliocene Near-Trench Magmatism in Southern Chile: A Possible Manifestation of ridge Collision. *Geol* 14, 3–27. doi:10.1130/0091-7613(1986)14<23:PNMISC>2.0.CO;2

Forsythe, R., and Nelson, E. (1985). Geological manifestations of ridge collision: evidence from the Golfo de Penas-Taitao Basin, southern Chile. *Tectonics* 4, 477–495. doi:10.1029/TC004i005p00477

Gleason, G. C., and Tullis, J. (1995). A Flow Law for Dislocation Creep of Quartz Aggregates Determined with the Molten Salt Cell. *Tectonophysics* 247 (1-4), 1–23. doi:10.1016/0040-1951(95)00011-B

Glerum, A., Thieulot, C., Fraters, M., Blom, C., and Spakman, W. (20182018). Nonlinear Viscoplasticity in ASPECT: Benchmarking and Applications to Subduction. *Solid Earth* 9 (2), 267–294. doi:10.5194/se-9-267-2018

Hamza, V. M., Dias, F. J. S. S., Gomes, A. J. L., and Terceros, Z. G. D. (2005). Numerical and Functional Representations of Regional Heat Flow in South America. *Phys. Earth Planet. Interiors* 152, 223–256. doi:10.1016/j.pepi.2005.04.009

Hirth, G., and Kohlstedt, D. (2003). Rheology of the Upper Mantle and the Mantle Wedge: A View from the Experimentalists. *Geophys. Monogr.*, 83–105. doi:10.1029/138GM06

Holt, A. F., Buffett, B. A., and Becker, T. W. (2015). Overriding Plate Thickness Control on Subducting Plate Curvature. *Geophys. Res. Lett.* 42 (10), 3802–3810. doi:10.1002/2015GL063834

Jadamec, M. A., Billen, M. I., and Roeske, S. M. (2013). Three-dimensional Numerical Models of Flat Slab Subduction and the Denali Fault Driving Deformation in South-central Alaska. *Earth Planet. Sci. Lett.* 376, 29–42. doi:10.1016/j.epsl.2013.06.009

Jarrard, R. D. (1986). Relations Among Subduction Parameters. *Rev. Geophys.* 24 (2), 217–284. doi:10.1029/RG024i002p00217

Ji, Y., Yoshioka, S., Manea, V. C., Manea, M., and Suenaga, N. (2019). Subduction thermal Structure, Metamorphism and Seismicity beneath north-central Chile. *J. Geodynamics* 129, 299–312. doi:10.1016/j.jog.2018.09.004

Johnson, C. (1997). RANALLI, G. 1995. Rheology of the Earth, 2nd Ed. Xv + 413 Pp. London, Glasgow, Weinheim, New York, Tokyo, Melbourne, Madras: Chapman & Hall. Price £29.95 (Paperback). ISBN 0 412 54670 1, 2nd Ed. London. *Geol. Mag.Geological Mag.* 134 (3), 409–421. doi:10.1017/S0016756897226981

Kirby, S., Engdahl, E. R., and Denlinger, R. (1996). *Geophysical Monograph Series*. Washington D.C: American Geophysical Union, 195–214.Intermediate-depth Intraslab Earthquakes and Arc Volcanism as Physical Expressions of Crustal and Uppermost Mantle Metamorphism in Subducting Slabs

Klotz, J., Abolghasem, A., Khazaradze, G., Heinze, B., Vietor, T., Hackney, R., et al. (2006). *The Andes-Active Subduction Orogeny*, 65–89. doi:10.1007/978-3-540-48684-8_4Long-Term Signals in the Present-Day Deformation Field of the Central and Southern Andes and Constraints on the Viscosity of the Earth's Upper Mantle

Kronbichler, M., Heister, T., and Bangerth, W. (2012). High Accuracy Mantle Convection Simulation through Modern Numerical Methods. *Geophys. J. Int.* 191 (1), 12–29. doi:10.1111/j.1365-246X.2012.05609.x

Lagabrielle, Y., Guivel, C., Maury, R. C., Bourgois, J., Fourcade, S., and Martin, H. (2000). Magmatic-tectonic Effects of High thermal Regime at the Site of Active ridge Subduction: the Chile Triple Junction Model. *Tectonophysics* 326, 255–268. doi:10.1016/S0040-1951(00)00124-4

Lallemand, S., Heuret, A., and Boutelier, D. (2005). On the Relationships between Slab Dip, Back-Arc Stress, Upper Plate Absolute Motion, and Crustal Nature in Subduction Zones. *Geochem. Geophys. Geosyst.* 6, a–n. AGU Fall Meeting Abstracts. doi:10.1029/2005GC000917

Lange, D., Rietbrock, A., Haberland, C., Bataille, K., Dahm, T., Tilmann, F., et al. (2007). Seismicity and Geometry of the South Chilean Subduction Zone (41.5°S-43.5°S): Implications for Controlling Parameters. *Geophys. Res. Lett.* 34, L06311. doi:10.1029/2006GL029190

Leng, W., and Gurnis, M. (2015). Subduction Initiation at Relic Arcs. *Geophys. Res. Lett.* 42 (17), 7014–7021. doi:10.1002/2015GL064985

Leng, W., and Sun, Y. D. (2019). Numerical Studies of thermal Structure for the continental Subduction Zones. *Earth Sci.* 44 (12), 3993–3997 [in Chinese with English abstract]. doi:10.3799/dqkx.2019.253

Li, W., and Ni, H. (2020). Dehydration at Subduction Zones and the Geochemistry of Slab Fluids. *Sci. China Earth Sci.* 63 (12), 1925–1937. doi:10.1007/s11430-019-9655-1

Li, Z. H., and Shi, Y. L. (2016). Constraints of 3-D Plate Geometry on the Dynamics of continental Deep Subduction. *Chin. J. Geophys.* 59 (8), 2806–2817. (in Chinese with English abstract). doi:10.6038/cjg20160808

Liu, M. X., Wei, D. P., and Shi, Y. N. (2019). Effect of Plate Interface Geometry on the Evolution of Subduction. *Chin. J. Geophys.* 62 (1), 78–87. (in Chinese with English abstract).

Lucazeau, F. (2019). Analysis and Mapping of an Updated Terrestrial Heat Flow Data Set. *Geochem. Geophys. Geosyst.* 20 (8), 4001–4024. doi:10.1029/2019GC008389

Maksymowicz, A., Contreras-Reyes, E., Grevemeyer, I., and Flueh, E. R. (2012). Structure and Geodynamics of the post-collision Zone between the Nazca-Antarctic Spreading center and South America. *Earth Planet. Sci. Lett.* 345-348, 27–37. doi:10.1016/j.epsl.2012.06.023

Moreno, M. S., Bolte, J., Klotz, J., and Melnick, D. (2009). Impact of Megathrust Geometry on Inversion of Coseismic Slip from Geodetic Data: Application to the 1960 Chile Earthquake. *Geophys. Res. Lett.* 36, L16310. doi:10.1029/2009GL039276

Murdie, R. E., Prior, D. J., Styles, P., Flint, S. S., Pearce, R. G., and Agar, S. M. (1993). Seismic Responses to ridge-transform Subduction:Chile Triple junction. *Geol* 21, 1095–1098. doi:10.1130/0091-7613(1993)021<1095:srtrts>2.3.co;2

Naliboff, J., and Buiter, S. J. H. (2015). Rift Reactivation and Migration during Multiphase Extension. *Earth Planet. Sci. Lett.* 421, 58–67. doi:10.1016/j.epsl.2015.03.050

Oleskevich, D. A., Hyndman, R. D., and Wang, K. (1999). The Updip and Downdip Limits to Great Subduction Earthquakes: Thermal and Structural Models of Cascadia, South Alaska, SW Japan, and Chile. *J. Geophys. Res.* 104, 14965–14991. doi:10.1029/1999JB900060

Richards, F. D., Hoggard, M. J., Cowton, L. R., and White, N. J. (2018). Reassessing the Thermal Structure of Oceanic Lithosphere with Revised Global Inventories of Basement Depths and Heat Flow Measurements. *J. Geophys. Res. Solid Earth* 123, 9136–9161. doi:10.1029/2018JB015998

Rotman, H. M. M., and Spinelli, G. A. (2014). Remarkably Consistent thermal State of the South central Chile Subduction Zone from 36°S to 45°S. *J. Geophys. Res. Solid Earth* 119, 3503–3516. doi:10.1002/2013JB010811

Rybacki, E., Gottschalk, M., Wirth, R., and Dresen, G. (2006). Influence of Water Fugacity and Activation Volume on the Flow Properties of fine-grained Anorthite Aggregates. *J. Geophys. Res.* 111, a–n. doi:10.1029/2005JB003663

Scherwath, M., Contreras-Reyes, E., Flueh, E. R., Grevemeyer, I., Krabbenhoeft, A., Papenberg, C., et al. (2009). Deep Lithospheric Structures along the Southern central Chile Margin from Wide-angleP-Wave Modelling. *Geophys. J. Int.* 179, 579–600. doi:10.1111/j.1365-246X.2009.04298.x

Scherwath, M., Flueh, E., Grevemeyer, I., Tillman, F., Contreras-Reyes, E., and Weinrebe, W. (2006). Investigating Subduction Zone Processes in Chile. *Eos Trans. AGU* 87 (27), 265. doi:10.1029/2006EO270001

Seno, T., Zhao, D., Kobayashi, Y., and Nakamura, M. (2001). Dehydration of Serpentinized Slab Mantle: Seismic Evidence from Southwest Japan. *Earth Planet. Sp* 53, 861–871. doi:10.1186/BF03351683

Seton, M., Müller, R. D., Zahirovic, S., Williams, S., Wright, N. M., Cannon, J., et al. (2020). A Global Data Set of Present-Day Oceanic Crustal Age and Seafloor Spreading Parameters. *Geochem. Geophys. Geosyst.* 21, 1–15. doi:10.1029/2020GC009214

Simmons, N. A., Forte, A. M., Boschi, L., and Grand, S. P. (2010). GyPSuM: A Joint Tomographic Model of Mantle Density and Seismic Wave Speeds. *J. Geophys. Res.* 115, B12310. doi:10.1029/2010JB007631

Stein, C. A., and Stein, S. (1992). A Model for the Global Variation in Oceanic Depth and Heat Flow with Lithospheric Age. *Nature* 359 (6391), 123–129. doi:10.1038/359123a0

Stern, R. J. (2002). Subduction Zones. *Rev. Geophys.* 40 (4), 3–1. doi:10.1029/2001RG000108

Storchak, D. A., Harris, J., Brown, L., Lieser, K., Shumba, B., and Di Giacomo, D. (2020). Rebuild of the Bulletin of the International Seismological Centre (ISC)-part 2: 1980-2010. *Geosci. Lett.* 7, 18. doi:10.1186/s40562-020-00164-6

Storchak, D. A., Harris, J., Brown, L., Lieser, K., Shumba, B., Verney, R., et al. (2017). Rebuild of the Bulletin of the International Seismological Centre (ISC), Part 1: 1964-1979. *Geosci. Lett.* 4, 32. doi:10.1186/s40562-017-0098-z

Tang, J., Chen, L., Meng, Q., and Wu, G. (2020). The Effects of the thermal State of Overriding continental Plate on Subduction Dynamics: Two-Dimensional thermal-mechanical Modeling. *Sci. China Earth Sci.* 63, 1519–1539. doi:10.1007/s11430-019-9624-1

Tebbens, S. F., Cande, S. C., Kovacs, L., Parra, J. C., LaBrecque, J. L., and Vergara, H. (1997). The Chile ridge: A Tectonic Framework. *J. Geophys. Res.* 102, 12035–12059. doi:10.1029/96JB02581

Tetreault, J. L., and Buiter, S. J. H. (2012). Geodynamic Models of Terrane Accretion: Testing the Fate of Island Arcs, Oceanic Plateaus, and continental Fragments in Subduction Zones. *J. Geophys. Res.* 117 (B8), a–n. doi:10.1029/2012JB009316

Tichelaar, B. W., and Ruff, L. J. (1991). Seismic Coupling along the Chilean Subduction Zone. *J. Geophys. Res.* 96 (B7), 11997. doi:10.1029/91JB00200

van der Hilst, R. D., and de Hoop, M. V. (2005). Banana-doughnut Kernels and Mantle Tomography. *Geophys. J. Int.* 163, 956–961. doi:10.1111/j.1365-246X.2005.02817.x

van der Meijde, M., Julià, J., and Assumpção, M. (2013). Gravity Derived Moho for South America. *Tectonophysics* 609, 456–467. doi:10.1016/j.tecto.2013.03.023

Völker, D., Grevemeyer, I., Stipp, M., Wang, K., and He, J. (2011). Thermal Control of the Seismogenic Zone of Southern central Chile. *J. Geophys. Res.* 116, 1–20. doi:10.1029/2011JB008247

Wang, K., Hu, Y., Bevis, M., Kendrick, E., Jr., Smalley, R., Vargas, R. B., et al. (2007). Crustal Motion in the Zone of the 1960 Chile Earthquake: Detangling Earthquake-Cycle Deformation and Forearc-Sliver Translation. *Geochem. Geophys. Geosyst.* 8, a–n. doi:10.1029/2007GC001721

Wang, S., Yu, H., Zhang, Q., and Zhao, Y. (2018). Absolute Plate Motions Relative to Deep Mantle Plumes. *Earth Planet. Sci. Lett.* 490, 88–99. doi:10.1016/j.epsl.2018.03.021

Wang, Z. S., and Wei, D. P. (2018). Research Progress on the Formation and Evolution of Triple Junctions of Global Plate Motions. *Prog. Geophys.* 33 (5), 1834–1843 [in Chinese with English abstract]. doi:10.6038/pg2018BB0286

Wessel, P., Luis, J. F., Uieda, L., Scharroo, R., Wobbe, F., Smith, W., et al. (2019). The Generic Mapping Tools Version 6. *Geochem. Geophys. Geosyst.* 20, 5556–5564. doi:10.1029/2019GC008515

Wilks, K. R., and Carter, N. L. (1990). Rheology of Some continental Lower Crustal Rocks. *Tectonophysics* 182 (1-2), 57–77. doi:10.1016/0040-1951(90)90342-6

Xu, J. J., Wang, Z. S., Wang, S. P., and Wei, D. P. (2019). Numerical Simulation of the Lithospheric thermal Structure in the Subduction Zone of the South Chile Triple junction. *Chin. J. Geophys.* 62 (12), 4729–4737. [in Chinese with English abstract]. doi:10.6038/cjg2019M0592

Zelt, C. A., Sain, K., Naumenko, J. V., and Sawyer, D. S. (2003). Assessment of Crustal Velocity Models Using Seismic Refraction and Reflection Tomography. *Geophys. J. Int.* 153, 609–626. doi:10.1046/j.1365-246X.2003.01919.x

Conflict of Interest: The authors declare that the research was conducted in the absence of any commercial or financial relationships that could be construed as a potential conflict of interest.

frontiers in Earth Science

ORIGINAL RESEARCH
published: 22 February 2022
doi: 10.3389/feart.2022.814710

Effects of Plate Velocity Slowdown on Altering Continental Collision Patterns and Crustal-Lithospheric Deformation During the Collision Process

Mengxue Liu[1], Dinghui Yang[1] and Pengpeng Huangfu[2]*

[1]Department of Mathematical Sciences, Tsinghua University, Beijing, China, [2]Key Laboratory of Computational Geodynamics, College of Earth and Planetary Sciences, University of Chinese Academy of Sciences, Beijing, China

Continental collision zones are widely distributed across the earth's surface with diverse types of tectonic processes. Even the same collision zone shows significant lateral tectonic variations along its strike. In this study, we systematically investigated how plate velocity slowdown after the closure of the ocean influences the continental collision evolution, as well as the effects of kinematic characteristics and continental rheology on varying the continental collision modes in a plate velocity slowdown model. From the comparison between the constant plate velocity system (CVS) and the plate velocity-dropping system (VDS), we can conclude the following: Plate velocity dropping promotes the extension inside the slab by decreasing the movement of the surface plate, whereas slab pull increases as subduction continues. The timing of the subducting slab break-off and the polarity alteration was initiated earlier in the plate velocity drop models than in the constant plate velocity models, and fast convergence may have triggered multiple episodes of slab break-off and caused strong deformation adjacent to the collision zone. Parametric tests of the initial subducting angle, plate convergence velocity, and continental crustal rheological strength in VDS indicated the following: (1) Three end members of the continental lithospheric mantle deformation modes were identified from the VDS; (2) models with a low subducting angle, fast continental convergence velocity, and medium-strength overriding crust were more likely to evolve into a polarity reversed mode, whereas steep-subducting-angle, slow-plate-velocity, weak-overriding-crust models tended toward a two-sided mode; (3) a strong overriding continent is more liable to develop a stable mode; and (4) overriding crustal rheological strength plays a significant role in controlling changes in continental collision modes.

Keywords: numerical modeling, Alpine-Himalayan Tethyan belt, continental collision, various continental collision mode, plate velocity slowdown

Edited by:
Jie Liao,
Sun Yat-sen University, Zhuhai Campus, China

Reviewed by:
Quan Zhou,
Facebook, United States
Lin Chen,
Institute of Geology and Geophysics (CAS), China

****Correspondence:***
Dinghui Yang
ydh@mail.tsinghua.edu.cn

Specialty section:
This article was submitted to Solid Earth Geophysics, a section of the journal Frontiers in Earth Science

Received: *14 November 2021*
Accepted: *06 January 2022*
Published: *22 February 2022*

Citation:
Liu M, Yang D and Huangfu P (2022) Effects of Plate Velocity Slowdown on Altering Continental Collision Patterns and Crustal-Lithospheric Deformation During the Collision Process. Front. Earth Sci. 10:814710. doi: 10.3389/feart.2022.814710

INTRODUCTION

Continental collision is an important process for regional tectonic evolution. It is widely distributed across the earth, ranging from the Mediterranean Sea to southwestern China (**Figure 1A**) (Li et al., 2011; Handy et al., 2010, 2015; Roda et al., 2010, 2012), significantly affecting the climate, resource reallocation, surface topography construction process, and deep mantle spatial–temporal evolution

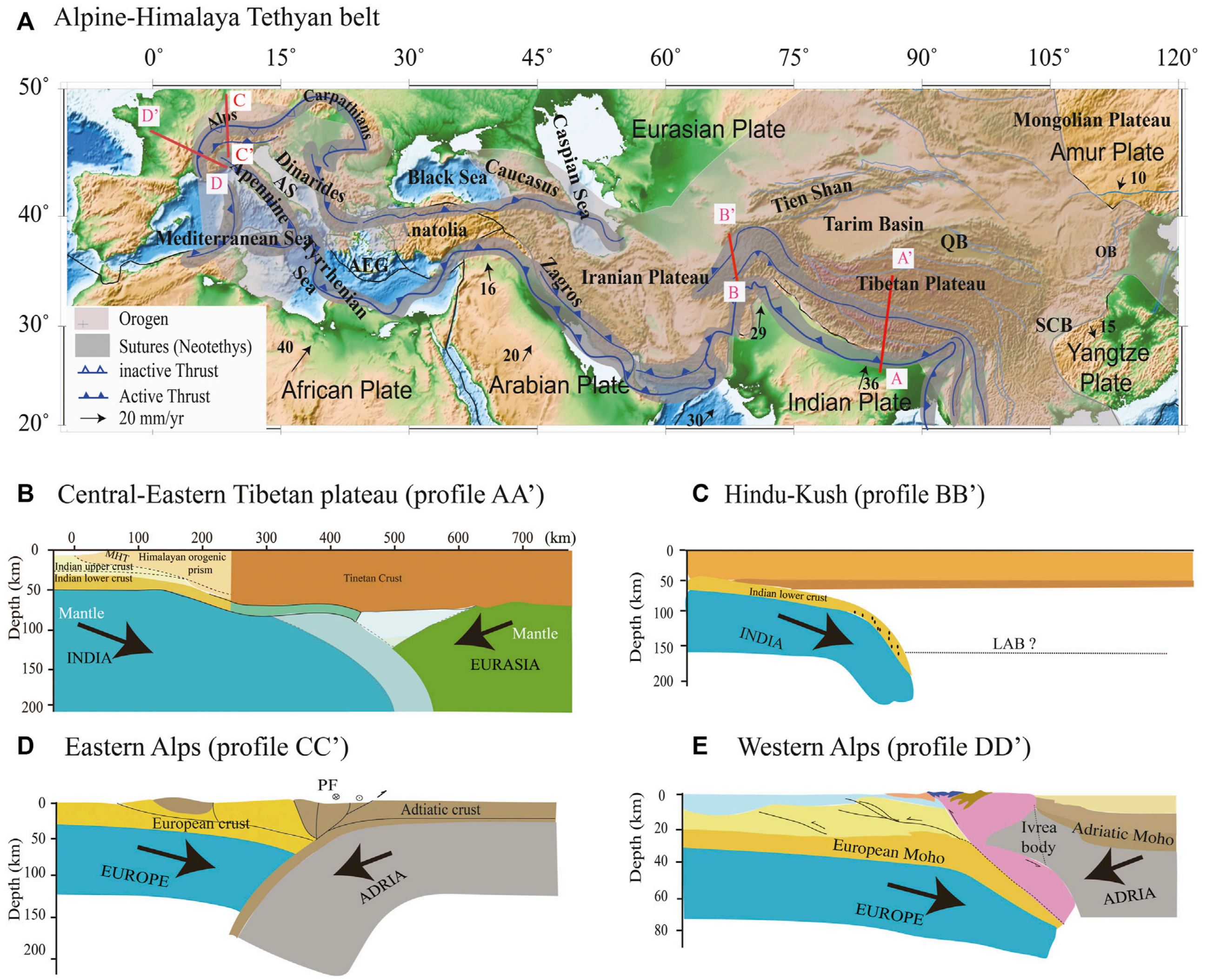

FIGURE 1 | (A) The Alpine–Himalayan Tethyan belt and main tectonic units along the collisional orogens. White and black lines outline the orogens and plate convergence boundary, respectively. Gray shadows mark the continental sutures since Cenozoic. Dark sawtooth blue lines show the main thrust belts, and light blue lines delineate the first-order block boundaries around Tibet. Black arrows refer to the plate convergence direction with numbers denoting plate velocity. AS: Adria Sea, AEG: Aegean Sea, QB: Qaidam Basin, SCB: Sichuan Basin, OB: Ordos Basins (Bird, 2003; Li et al., 2011; Saein and Afzal 2017). A simplified schematic diagram of the lithospheric structure of the collisional orogens is shown across **(B)** central-eastern Tibetan Plateau (AA′) (Owens and Zandt, 1997; Tilmann and Ni, 2003; Nabelek et al., 2009; Mechie et al., 2012; Mechie and Kind, 2013; Ye et al., 2015; Huangfu et al., 2018), **(C)** Hindu Kush (BB′) (Liang et al., 2020; Kufner et al., 2021), **(D)** eastern Alps (CC′) (Lippitsch et al., 2003; Kissling et al., 2006; Handy et al., 2015), and **(E)** Austroalpine of the western Alps (DD′) (Lippitsch et al., 2003; Kissling et al., 2006; Handy et al., 2010; Roda et al., 2010, 2012; Zhao et al., 2015).

(Wang et al., 2014; Li et al., 2015). Complex discrepant tectonic evolution exists among different continental convergence zones (Negredo et al., 2007; Chertova et al., 2014; Spakman et al., 2018), and even the same collision zone also shows evident lateral variations of tectonic characters along its strike direction (Chen et al., 2015; Liang et al., 2016); in particular, along the Himalaya orogen, tomographic images have recognized distinct east–west inhomogeneous subducting angles and horizontal slip distances (**Figures 1B,C**) there. For example, Nabelek et al. (2009) used the receiver function method to construct an image of the crust and upper mantle beneath the Himalayas and the southern Tibetan Plateau; they argued that the Indian mantle lithosphere has not extended significantly beyond 31°N. Mechie et al. (2011a, 2011b, 2012) also adopted receiver function method to identify Moho characters across Tibet Plateau and recognized that Indian lithospheric mantle extends northwards until about the Banggong-Nujiang suture, where it steeply sinks to 350–400 km depth. Based on seismic anisotropy characters, Chen et al. (2015) suggested that the geometry of Indian lithosphere underthrusting beneath South Tibet is characterized by lateral variations. Kufner et al. (2021) presented finite-frequency tomography in Hindu Kush; they interpreted their high-velocity anomalies as crustal subduction on top of a northwards-subducting Indian lithosphere, and its penetration depth increases along-strike while thinning and steepening. By contrast, Alpine orogen exhibits several distinct lithospheric mantle deformation features (Kissling et al., 2006; Roda et al., 2010, 2012; Handy et al., 2015; Zhao et al., 2015); e.g., under the central and eastern Alps, subductions operate in an opposite polarity (**Figure 1D**, profile CC′), while in the western Alps, the overriding Adriatic lithospheric mantle seemed to delaminate and was dragged down by the subducting European lithosphere (**Figure 1E**, profile DD’).

In recent years, a number of numerical simulations have been conducted to investigate the essential process and controlling parameters of different continental convergence processes, and prominent progress has been achieved in our understanding of these dynamic processes. Although previous studies have recognized kinematic characters (like subducting angle and plate velocity) and plate rheology can highly influence the fate of plates when they do meet each other, further efforts are still needed to better understand the geodynamic controls and styles of post-subduction collisional orogenic processes (Faccenda et al., 2008). According to the differential dynamic processes controlled by different plate kinematic characters and lithospheric deformation among the various continental convergent boundaries, conceptual models that account for the behavior of continental lithospheric mantle, proposed thus far, can be summarized as follows: (1) pure shear thickening, (2) folding and buckling, (3) one-sided underthrusting or subduction (steep/flat), (4) two-sided/ablative plate consumption, and (5) subducting slab break-off (Pysklywec, 2001; Li et al., 2011; Li, 2014; Yang et al., 2019; Chen, 2021). Pysklywec et al. (2000) suggested that according to their modeling results, continental convergence is such a complicated process that it needs to be illustrated through a combination of several modes, rather than using a single model. Little work, however, has focused on such a combined effect.

Slowdown of plate motion after continental collision, following the oceanic subduction, is a common process that has already been recognized by previous geological and geophysical measurements. For example, plate reconstruction has shown that the convergence velocity between India and Asia experienced a dramatic decrease from ~18 to ~3.5 cm/year (Patriat and Achache, 1984; Wang et al., 2001, 2014; Copley et al., 2010) at 50–35 Ma, started from the initial contact of margins between Indian and Asian continents, and continued as the Himalayan orogeny developed and the Tibetan Plateau uplifted (Guillot et al., 2003; Copley et al., 2010). Although numerous numerical simulations have been conducted to study the evolution of continental collision, most of them have adopted a constant plate velocity through the plate convergence process (oceanic subduction and continental collision) for simplification (Burg and Gerya, 2005; Warren et al., 2008; Yamato et al., 2008; Duretz et al., 2012; Liao and Gerya, 2017), and little attention has been given to the influence of plate velocity slowdown (Faccenda et al., 2008; Li et al., 2013; Capitanio et al., 2015).

In this study, we conducted a series of two-dimensional (2D) numerical experiments that integrated both oceanic subduction and the following continental convergence process to systematically investigate differences between a constant velocity system (CVS; a constant plate velocity is incorporated through oceanic subduction and continental convergence) and a velocity-dropping system (VDS; plate velocity decreases after continental collision), as well as the influences of various kinematic characters (e.g., convergence velocity and subducting angle) and continental crustal rheological strength on diverse continental convergence styles in VDS, by following the evolutionary trajectory of plates, analyzing the results of different model series, exploring the potential relationships, or even transitions, among the various continental collision modes to better understand the evolution of continental convergence, and, finally, applying it to explain dynamic processes of related natural cases. This study shed new light on the study of continental collision differentiation.

MATERIALS AND METHODS

Governing Equation

We conducted numerical experiments with a 2D finite element code [**A**dvanced **S**olver for **P**roblems in **E**arth’s **C**onvec**T**ion (ASPECT); Kronbichler et al., 2012]. ASPECT is an extensible code of the C++ program library deal.ii (Differential Equations Analysis Library, https://www.dealii.org/) targeted at the computational solution of partial differential equations using adaptive finite elements (Arndt et al., 2021). It solves regional thermal convection problems and incorporates the use of complex boundary conditions, large variations in rheological parameters, and localized mesh refinement. The viscous-plastic rheology used in this study satisfied the equations of the conservation of mass (**Eq. 1**), momentum (**Eq. 2**), and internal energy (**Eq. 3**) for an incompressible medium and adopted the Boussinesq approximation.

$$-\nabla \cdot 2\eta\varepsilon(\mathbf{u}) + \nabla p = \rho\mathbf{g} \qquad \text{in } \Omega, \tag{1}$$

$$\nabla \cdot \mathbf{u} = 0 \qquad \text{in } \Omega, \tag{2}$$

$$\begin{aligned}\rho_0 C_p\left(\frac{\partial T}{\partial t} + \mathbf{u}\cdot\nabla T\right) - \nabla\cdot k\nabla T &= \rho_0 H \\ &\quad + 2\eta\,\varepsilon(\mathbf{u}) : \varepsilon(\mathbf{u}) \\ &\quad + \alpha T\,(\mathbf{u}\cdot\nabla p) \quad \text{in } \Omega\end{aligned} \tag{3}$$

The right-hand-side terms of **Eq. 3** correspond to internal heat production, for example, due to radioactive decay, friction heating, and adiabatic compression of material. η is the viscosity, $\varepsilon(\mathbf{u}) = \frac{1}{2}(\nabla\mathbf{u} + \nabla\mathbf{u}^T)$ is the symmetric gradient of the velocity (often called the strain rate), $\mathbf{u}$ is the velocity, p is the pressure, $\mathbf{g}$ is the gravitational acceleration, Ω is the interesting domain, C_p is the heat capacity, k is heat conductivity, H is the intrinsic specific heat production, α is the thermal expansion coefficient, and ρ_0 is the adiabatic reference density. We consider that the density satisfies the equation

$$\rho = \rho_0(1 - \alpha\,(T - T_0)) \tag{4}$$

where ρ_0 is the reference density at reference temperature T_0 (293 K).

TABLE 1 | Parameter list of the numerical experiments.

Material parameters	Units	Sub-lithospheric mantle	Upper continental crust	Lower continental crust^c	Lithospheric mantle	Sediments	Oceanic crust	Weak zone
Thermal diffusivities (κ)	$m^2\ s^{-1}$	9.89^{-7}	1.21^{-6}	1.15^{-6}	9.87^{-7}	1.21^{-6}	1.21^{-6}	1.21^{-6}
Heat capacity (C_p)	$J\ kg^{-1} K^{-1}$	750	750	750	750	750	750	750
Density (ρ)	$kg\ m^{-3}$	3,300	2,800	2,900	3,300	3,000	3,000	3,300
Thermal expansivity (α)	K^{-1}	2^{-5}	2^{-5}	2^{-5}	2^{-5}	2^{-5}	2^{-5}	2^{-5}
Angle of internal friction (ϕ)	°	20	20	20	20	5	10	2
Cohesion (C)	Pa	2×10^7	2×10^7	2×10^7	2×10^7	10^6	10^6	10^6
Flow law^a	–	Dry olivine	Wet quartzite	Wet anorthite (varies)^c	Dry olivine	Gabbro	Gabbro	Gabbro
Visc. prefactor (A^*)^b Diff/Disl	$Pa^{-n}\ S^{-1}$	$2.37^{-15}/6.52^{-16}$	$10^{-50}/8.57^{-28}$	$10^{-50}/7.13^{-18}$	$2.37^{-15}/6.52^{-16}$	$10^{-50}/1.12^{-10}$	$10^{-50}/1.12^{-10}$	$10^{-50}/1.12^{-10}$
Stress exponent (n)	–	1/3.5	1/4.0	1/3	1/3.5	1/3.4	1/3.4	1/3.4
Activation energy(E)	$J\ mol^{-1}$	$375^3/530^3$	$0/\ 223^3$	$0/\ 345^3$	$375^3/530^3$	$0/\ 497^3$	$0/\ 497^3$	$0/\ 497^3$
Activation volume (V)	$m^3\ mol^{-1}$	$4^{-6}/18^{-6}$	0/0	0/0	$4^{-6}/18^{-6}$	0/0	0/0	0/0
Grain size exponent (m)	–	3	1	1	3	1	1	1

[a] *Flow law is taken from Hirth and Kohlstedt (2003) for dry olivine, Gleason and Tullis (1995) for wet quartzite, Rybacki et al. (2006) for wet anorthite, and Wilks and Carter (1990) for gabbro.*

[b] *The viscosity pre-factor, A^*, is scaled from uniaxial experiments for plane strain as in Ranalli (1995) and Tetreault and Buiter (2012).*

[c] *Flow law for retrocontinental lower crust are taken from Chen et al. (2017) for mafic granulite (for weak crust) and Maryland diabase (for strong crust).*

Eq. 5 is used to describe the evolution of a set of variables c_i (X, t), I = C named compositional fields here. Compositional fields were designed to track the chemical composition of the convecting medium. Thus, the composition is a non-diffusive quantity (Kronbichler et al., 2012).

$$\frac{\partial \boldsymbol{c}}{\partial t} + \boldsymbol{u} \cdot \nabla \boldsymbol{c} = 0 \tag{5}$$

Rheology

Like other geodynamics codes, ASPECT assumes that the solid Earth materials can be treated as a highly viscous fluid, its deformation is predominantly defined by brittle fracture or viscous creep; thus, we apply three basic rheological characters: plastic yielding, diffusion creep, and dislocation creep. Diffusion and dislocation creep can be conveniently formulated with **Eq. 6** (Karato and Wu, 1993; Karato, 2008).

$$\eta_{\mathrm{diff/disl}} = \frac{1}{2} \mathrm{A}^{-\frac{1}{\mathrm{n}}}\, \mathrm{d}^{\frac{m}{n}}\, \dot{\varepsilon}_e^{\frac{1-n}{n}} \exp\left(\frac{Q + PV}{nRT}\right) \tag{6}$$

Where the effective deviatoric strain rate is defined as $\dot{\varepsilon}_e = \sqrt{\frac{1}{2}\dot{\varepsilon}_{ij}^{'}\, \dot{\varepsilon}_{ij}^{'}}$. For diffusion creep, $n = 1$, $m > 0$, while in the case of dislocation creep $n > 1$, $m = 0$. Definition and values of other symbols are shown in **Table 1**. Surface erosion and sedimentation are neglected.

We implemented composite viscosity combining diffusion creep (η_{diff}) and dislocation creep (η_{disl}) for both lithospheric mantle and sub-lithospheric mantle as shown in **Eq. (7)**.

$$\eta_{\mathrm{comp}} = \left(\frac{1}{\eta_{\mathrm{diff}}} + \frac{1}{\eta_{\mathrm{disl}}}\right)^{-1} \tag{7}$$

The effective viscosity in the viscous stress is defined for the power law creep based on the temperature and the strain rate tensor (Glerum et al., 2018; Karato, 2008). The plastic yielding is defined by the Drucker–Prager criterion **Eq. 8** (Davis and Selvadurai, 2002):

$$\sigma_{\mathrm{yield}} = C \cos(\phi) + P \sin(\phi) \tag{8}$$

When the viscous stress 2 $\eta_{\mathrm{diff/disl/comp}}\ \dot{\varepsilon}_{\mathrm{ii}}$ exceeds the yield stress, the viscosity is rescaled to the yield surface:

$$\eta_{yield} = \frac{\sigma_{\mathrm{yield}}}{2 \cdot \dot{\varepsilon}_e} \tag{9}$$

After giving the maximum ($\eta_{\max}$) and minimum ($\eta_{\min}$) viscosity cutoffs, the viscosity is then given by **Eq. (10)**:

$$\eta_{\mathrm{eff}} = \min(\max(\eta_{\mathrm{i}}, \eta_{\min}), \eta_{\max}) \tag{10}$$

where i is one of the subscripts among diff, disl, comp, and yield.

Initial Model Configuration and Boundary Conditions

The model is 2,000 km long and 660 km deep in the *x*- and *z*-directions, respectively. The resolution of finite element mesh consists of three parts, in the upper 2,000 km × 200 km domain is 2 km × 2 km, then it is decreased to 4 km × 4 km in the following 2,000 km × 100 km, while resolution of the rest domain is 8 km × 8 km. In the context, we adopted terminology from Jamieson et al. (1998) to distinguish different parts of the adjacent convergent plates, a plate with an initial oceanic subduction on the left is defined as the "pro" side, an overriding plate on the right is defined as the "retro" side. The initial model consists of three plates: procontinental plate (length of 600 km), oceanic plate (length of 400 km), and retrocontinental plate (length of

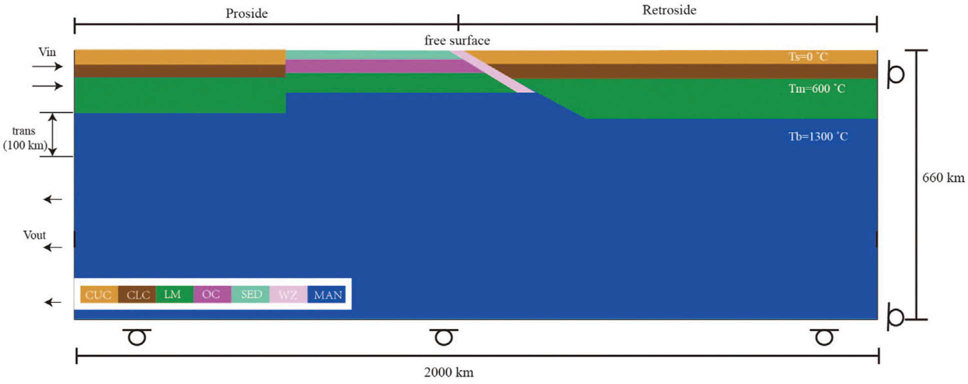

FIGURE 2 | Configuration of the reference model. The size of the numerical box is 2000 × 660 km, and an oceanic plate is integrated with a continental plate on the proside (left). The retroside (right) is an overriding continental plate. Various colors reflect to different lithologies, CUC: continental upper crust, CLC: continental lower crust, LM: lithospheric mantle, OC: oceanic crust, SED: sediment, WZ: weak zone, and MAN: sub-lithospheric mantle. Ts is surface temperature, Tmn is the Moho temperature of normal continent, Tmc stands for the Moho temperature of continental Craton, Tb is the bottom temperature of lithosphere. V_{in} and V_{out} denote where material flow in and out, and V_{trans} denotes the transition zone from flow in to flow out.

TABLE 2 | Viscous flows used for retrocontinental lower crust.

Symbol	Flow laws	E (J/mol)	V (m³/mol)	n –	A* $Pa^{-n}\ s^{-1}$
Weak	Mafic granulite	244 × 103	0	3.2	1.58×10^{-21}
Medium	Wet anorthite	345 × 103	0	3.0	7.13×10^{-18}
Strong	Maryland diabase	485 × 103	0	4.7	1.98×10^{-27}

1,000 km). An inclined 10-km-width weak zone (**Table 1**) sits between the retro and pro sides, and various angles (30°, 45°, and 60°) are designed to test their effects on model evolutions. The continental lithosphere is 140 km thick, with an upper crust (20 km thick), a lower crust (20 km thick), and a 100-km-thick lithospheric mantle, while the oceanic lithosphere (~80 Ma) comprises of a sediment layer (4 km thick), crust (8 km thick), and lithospheric mantle of 68 km thick (**Figure 2**). Continental upper crustal and procontinental lower crustal rheological properties are defined as wet quartzite (Gleason and Tullis, 1995) and wet anorthite (Rybacki et al., 2006), respectively, while different flow laws for retrocontinental lower crust are applied to explore their effects on model results, mafic granulite (Chen et al., 2017) for a relatively weak lower crust compared to wet anorthite, and Maryland diabase (Chen et al., 2017) for a relatively strong one. In addition, sediment and oceanic crust are both represented by gabbro (Wilks and Carter, 1990). Dry olivine (Hirth and Kohlstedt, 2003) is used for lithospheric mantle and sub-lithospheric mantle (see **Tables 1**, **2** for more details).

The initial surface temperature is 0°C, the initial Moho temperature of the oceanic lithosphere and retrocontinent is 600°C, while it is 400°C for the procontinent. The initial Lithosphere–Asthenosphere Boundary (LAB) temperature is defined as 1,300°C, below which an adiabatic thermal gradient of 0.5°C/km is assumed. Both side walls are thermal insulated boundaries.

The initial temperature structure of continental lithosphere follows a steady-state geotherm from Chapman (1986) that considers the thickness of each compositional layer, shown as Eqs. (11), (12), and (13). The initial oceanic lithospheric temperature distribution follows the plate cooling model (Turcotte and Schubert, 2002).

$$\mathrm{T_Z} = \mathrm{T_T} - \frac{q_T}{k} \times Z - \frac{A \times Z^2}{2k} \tag{11}$$

$$\mathrm{T_B} = \mathrm{T_T} + \frac{q_T}{k} \times \Delta Z - \frac{A \times \Delta Z^2}{2k} \tag{12}$$

$$\mathrm{q_B} = \mathrm{q_T} - \mathrm{A} \times \Delta \mathrm{Z} \tag{13}$$

Where T_Z denotes the temperature of the depth Z, T_T is the top surface temperature of each layer, T_B denotes the bottom temperature of each layer, and the heat flows at the top and bottom of each layer are denoted as q_T and q_B, respectively. ΔZ is the thickness of the layer, A is volumetric heat production, and k is thermal conductivity.

Mechanical boundary conditions are free slip at both the retroside and bottom boundaries; the top boundary used a true free-surface condition to account for topography evolution. Inflow velocity at the procontinental lithosphere wall, it is the approximation of an integration of three major forces in nature, i.e., slab pull, ridge push, and convection drag, and equivalently balanced outflow velocity on the same sidewall across the sub-lithospheric mantle. Besides, there is a velocity transition zone between flow-in and flow-out zones (thickness of 100 km) (**Figure 2**).

RESULTS

Comparison of CVS and VDS

Previous studies have indicated that the force equilibrium state and thermal structure of plate, and lithospheric deformation styles during subduction, are related to the convergence

TABLE 3 | Model list of parametric tests.

Velocity system	Model name	Convergence velocity V_{os} – > V_{cc} (cm/year)	Angle α (°)	Continental crustal strength (CCS)
VDS (MSI)	v1a1	10–>3	30	Medium
	v1a2	10–>3	45	Medium
	v1a3	10–>3	60	Medium
	v2a1	10–>5	30	Medium
	v2a2	10–>5	45	Medium
	v2a3	10–>5	60	Medium
	v3a1	10–>7	30	Medium
	v3a2	10–>7	45	Medium
	v3a3	10–>7	60	Medium
	s1a1	10–>3	30	Weak
	s1a2	10–>3	45	Weak
	s1a3	10–>3	60	Weak
	s2a1	10–>3	30	Strong
	s2a2	10–>3	45	Strong
	s2a3	10–>3	60	Strong
CVS (MSII)	ca1	3–>3	30	Medium
	ca2	5–>5	30	Medium
	ca3	7–>7	30	Medium

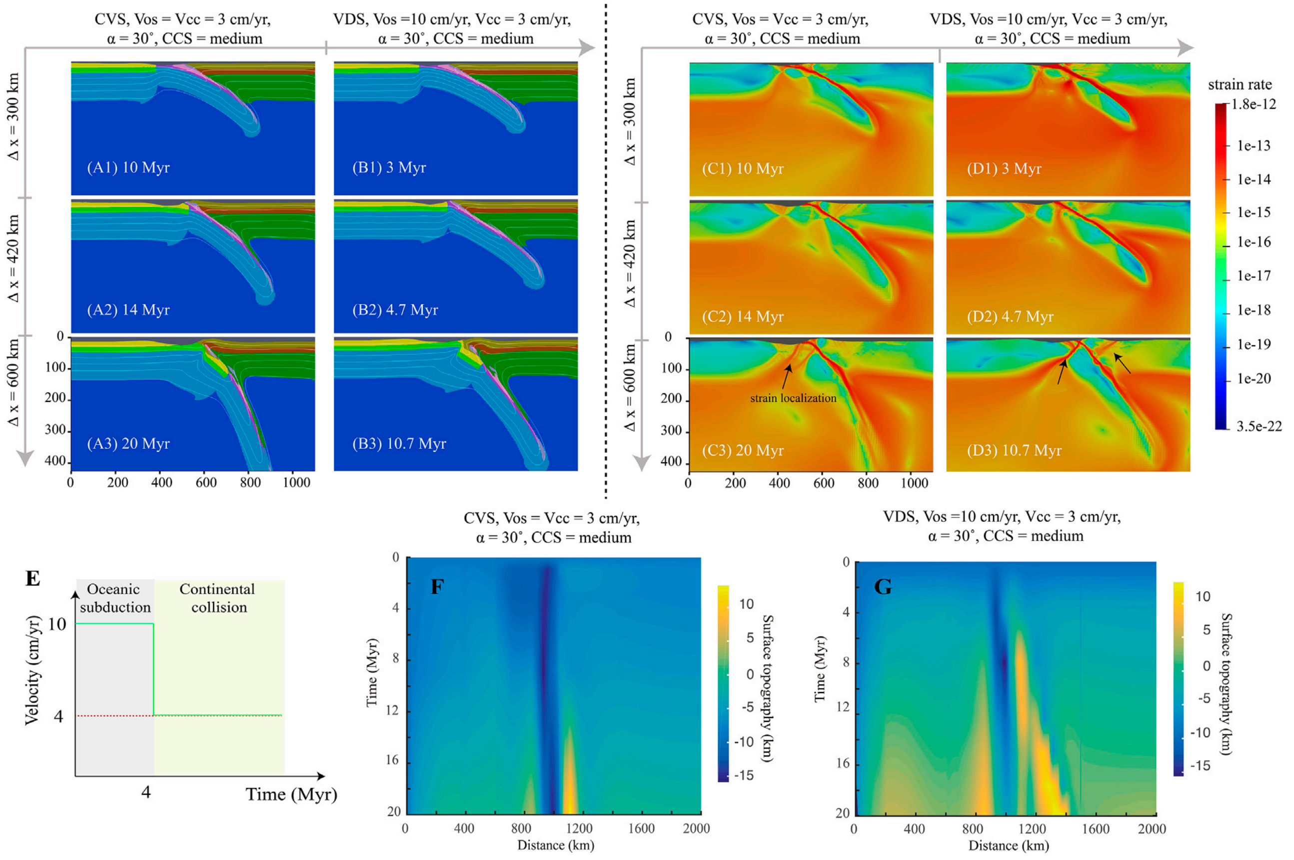

FIGURE 3 | The upper left panel shows the snapshots of compositional fields from models MSII-ca1 (CVS) **(A1–A3)** and MSI-v1a1 (VDS) **(B1–B3)**, respectively. Different colors denote different lithologies (see **Figure 2**). White lines denote isotherm with 200°C increment that start from 200°C to 1,200°C. The upper right panel shows the snapshots of strain rate from models MSII-ca1 **(C1–C3)** and MSI-v1a1 **(D1–D3)**. Δx is the amount of convergence. **(E)** shows the velocity boundary conditions of CVS (red dotted line) and VDS (green dotted line). **(F)** and **(G)** show the topography evolution of both models.

velocity (Li et al., 2002). It has also been recognized that dramatic plate velocity slowdown after continental collision following oceanic subduction is a general phenomenon, but little work has been done using numerical modeling to systematically investigate how such a convergence velocity drop influences the spatial–temporal evolution of crustal-lithospheric deformation during continental collision. Thus, we started with the comparison of CVS and VDS.

First, we constructed two series of numerical models using (1) MSII-ca1, -ca2, and -ca3 and (2) MSI-v1a1, -v2a1, and -v3a1 that belong to CVS and VDS, respectively (**Table 3**). All models shared the same initial subducting angle (α = 30°) and continental crustal rheological strength (medium).

Take MSII-ca1 as an example (**Figure 3**). In this model, we push from the proside with a constant velocity. This velocity during oceanic subduction is equal to that in the continental convergence phase, and both are constant ($V_{os} = V_{cc}$ = 3 cm/year) (**Figure 3E**). During the initial stage of oceanic subduction, relatively dense oceanic plate subducted along a prescribed slope weak zone, and little sediment and oceanic crust was scraped off and rested in site (**Figure 3A1**). Excess negative buoyancy is attributed to the prior oceanic plate subduction and then dragged the trailing continental plate downward though it is buoyant, accompanied by the steepening of subducting angle. Note that, as procontinent arrived at trench, collision started, characterized by a notable upbending of the leading edge of retrocontinent. Besides, slow pushing led to a slow proplate motion, which resulted in relatively strong coupling between plates, as a portion of the retrocontinental lithospheric mantle was dragged down and sank together with the subducting slab (**Figure 3A2**). At the early stage of continental collision, combined effects from continuous pushing from the proside trailing edge and slab downward dragging maintained the downward movement of the continental lithospheric mantle. However, as more buoyant continental crust resisted sinking, it accumulated at shallow. Later, pushing from prescribed velocity competed with the crust's buoyance. The process gave rise to strain localization (**Figure 3C3**), especially in the proside ocean-continent transition zone, and then generated a rupture there, along which temperature abnormally increased (**Figure 3A3**). In addition, we can recognize significant uplift of both plates adjacent to the collision zone, especially the retroside that formed a narrow and almost stationary orogen (**Figure 3F**).

MSI-v1a1 from VDS, on the other hand, was applied with a 10 cm/year plate velocity during oceanic subduction (V_{os} = 10 cm/year) for ~4 Myr, followed by a much slower continental convergence (V_{cc} = 3 cm/year). Though a higher V_{os} was applied to MSI-v1a1 than to MSII-ca1, the main process of oceanic subduction proceeded in a similar way except for two differences: (1) Little material from the retrocontinental lithospheric mantle was dragged down by the slab due to plates' relative weaker coupling resulting from fast subduction (**Figure 3B1**). (2) The subducting angle was slightly gentle (**Figures 3A2,3B2**). After the continents' initial contact, convergence velocity decreased to 3 cm/year. Similar to the process in MSI-ca1, accumulation of buoyant continental crust at the plate interface occurred, and local crustal rupture developed in the proplate through which an anomalous temperature increasing occurred (**Figure 3B3**). At shallow depth, dramatic strain localization developed in the proside ocean-continent transition zone (**Figure 3D3**). Besides, under the increased pulling from the slab in depth, the subducting angle gradually steepened (**Figures 3D2,3D3**). It is worth noting that the subducting angle in model MSI-ca1 is much steeper than the one in MSI-v1a1. We supposed that, as the prior oceanic subduction was prescribed a higher plate convergence velocity in the latter model, during the early stage of continental collision, plates were still weakly coupled. The subducting plate could keep cold and maintain its strength, which facilitated the lithosphere sinking integrally with a nearly steady dipping angle. At the same time, prior fast plate convergence velocity could cause tense compression in the collision zone and result in severe deformation at the front edge of the retrocontinent. A new shear zone at shallow was then formed retroside (**Figures 3D2,3D3**). Finally, compared with the nearly fixed narrow orogen in the MSII-ca1, orogen in MSI-v1a1 showed a prominent retroward advance, and eventually developed into a relatively wider orogen (**Figures 3F,G**).

To further investigate the effects of plate velocity on the continental collision pattern in both systems, we varied the continental convergence velocity (V_{cc}) (**Table 3**). As is shown in **Figure 4**: (1) Increasing V_{cc} could get a relatively gentle subducting angle in both series of models (**Figures 4A,B**). (2) All models tended to generate plate polarity reversal, while the time of slab break-off and polarity alteration was initiated earlier in the VDS than in the CVS (**Figure 4C**). In addition, fast V_{cc} always causes severe deformation of both plates adjacent to the collision zone.

Controlling Parameters of Altering the Continental Collision Mode in VDS

According to the foregoing numerical experiment results, VDS showed conspicuous differences from the normally used CVS. By varying the continental convergence velocity, the dip angle of the initial weak zone, and retrocontinental crustal rheological strength, we then examined how these parameters influence the spatial–temporal evolution of the continental collision process in VDS. Three end members of the continental collision mode can be obtained according to the model results from parametric sensitive tests: (1) polarity reversed mode, (2) oceanic-type stable mode, and (3) two-sided/ablative mode

The polarity reversed continental collision mode is not a new concept model. Numerous geological and geophysical records have recognized this type of collision mode and referred to these collisions between volcanic arcs and ocean–continent subduction zones or those with subducting ridges (Clift et al., 2003; Brown et al., 2011; Handy et al., 2015; von Hagke et al., 2016). Take the model MSI-v1a1 as an example (**Figure 5**). The whole evolution process includes oceanic subduction (OS) and continental collision (CC). Considering the negative buoyance of cool oceanic plate, fast plate convergence velocity (10 cm/year) was prescribed during the whole OS. At the early stage, little sediment and crust material was scraped off from the lower plate because of

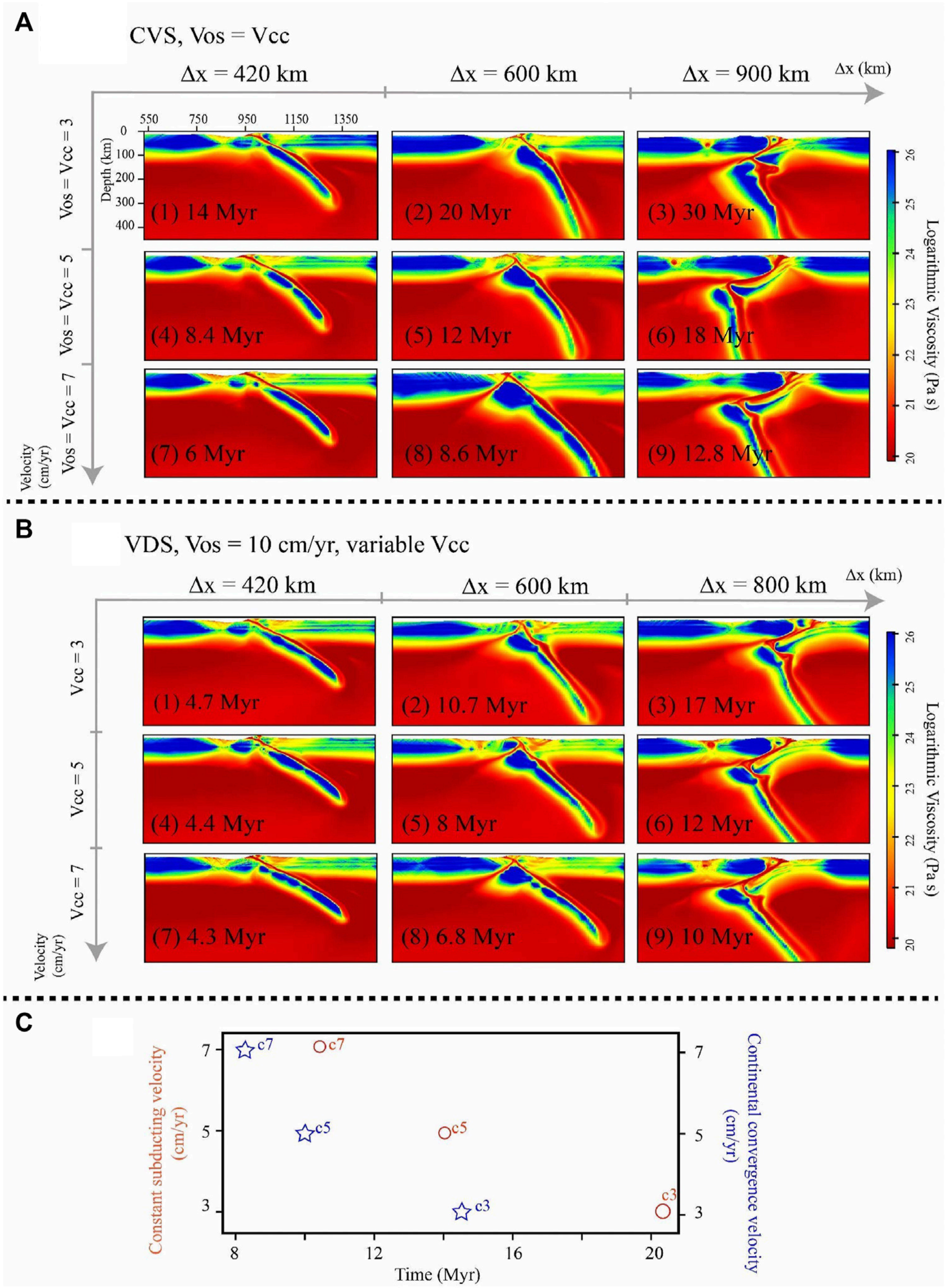

FIGURE 4 | (A) shows the viscosity field of models with variable plate velocity in CVS ($V_{os} = V_{cc}$), (1)–(3) are the snapshots of model with a 3 cm/year constant plate velocity, and (4)–(9) correspond to the snapshots of models with 5 cm/year and 7 cm/year constant plate velocity, respectively. **(B)** shows the viscosity field of models with variable plate velocity in VDS ($V_{os} > V_{cc}$), (1)–(3) show the snapshots of model with a 3 cm/year continental convergence velocity (V_{cc}), and (4)–(9) correspond to the snapshots of the model with 5 cm/year and 7 cm/year continental convergence velocity, respectively. Δx is the amount of convergence. **(C)** The start time of slab break-off. Red notes and circles denote the results of CVS; blue notes and stars denote the VDS results.

weak coupling between plates under fast plate convergence. The scraped-off material then rested in site, accumulated, and accreted to the adjoining retroplate. Meanwhile, distinct subsidence occurred as slab bended and promoted to the formation of a foreland basin (**Figure 5A**). When the ocean closed (during CC), the prescribed plate convergence velocity slowed down (3 cm/year). Continuous compression, along with the accumulation of scraped-off material at shallow, uplifted the collision zone rapidly, producing a narrow orogen, underneath which the slab dipping angle gradually steepened (**Figures 5B,C**). The model results also showed that a small portion of the retrocontinental lithospheric mantle was dragged down by the

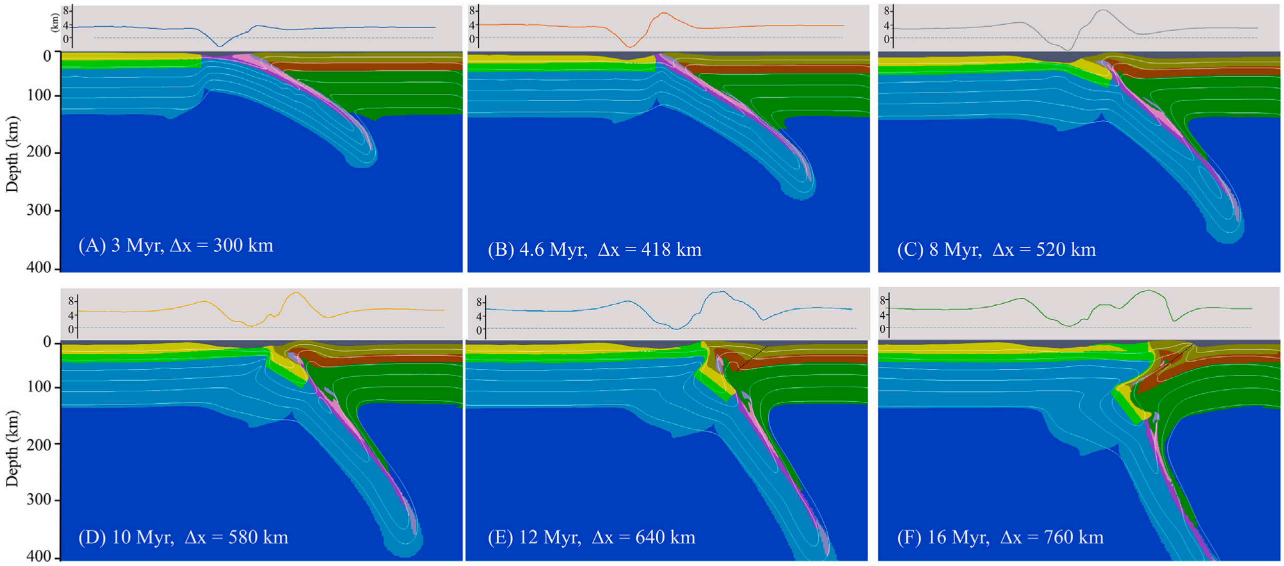

FIGURE 5 | Evolution of polarity reversed mode. Panels above each snapshot with gray shading show the corresponding topography. Δx is the amount of convergence. Different colors in **(A–F)** denote different lithologies (same as **Figure 2**).

slab as plates' strong coupling under slow convergence (**Figure 5C**). As continental convergence continued, on the retroside around orogen, a slight subsidence happened at almost the symmetric place to the proside foreland basin with respect to the axis of orogenic belt. On the proside, foreland basin broadened slightly, with its proside flank slightly uplifted. It is worth noting that temperature increased abnormally at the retroplate leading edge (**Figure 5C**). The reasons for this may come from two aspects: (1) The compression from continental collision resulted in crustal thickening (**Figure 5D**), which may increase the radioactive heat from the continental crust. (2) A portion of hot retrocontinental lithospheric material moved upward along the plates' interface (**Figure 5D**). Following that, procontinental crust ruptured, leaving the surface crust indented to the orogenic wedge and causing the wedge to grow retroward along the reversed shear zone on the retroplate (**Figure 5E**). Eventually, the procontinent plate obducted onto the retroplate. The retrocontinent then delaminated, accompanied by parts of the lower crust and lithospheric mantle underthrusted beneath the procontinent, leaving a gentle uplift and widening of the foreland basin on the proside. Meanwhile, a new narrow retroside subsidence generated behind orogenic wedge (**Figure 5F**). To conclude, from OS to the early stage of CC, topography building up was relatively concentrated on the collision zone, followed by a broad surface uplift and a retroward movement of the orogenic wedge.

The most common mode is the stable continental collision mode, which has been confirmed by geological and geophysical observations as well as numerical models (Chemenda et al., 2000; Yin and Harrison, 2000; Li et al., 2011; Huangfu et al., 2018). It has a one-sided asymmetric type with a stable plate polarity and can be further divided into flat and steep subtypes.

The model MSI-s2a3 was an example of a steep subtype (**Figure 6**). The general process of OS in this model was similar to that in model MSI-v1a1 (**Figure 5**), while much more sediment and oceanic crust were scraped off (**Figure 6A**). During CC, a relative slow continental convergence velocity of 3 cm/year compared to the OS was prescribed. Initially, accumulated oceanic crust at shallow detached from its deeper part. After that, temperature abnormally increased along the gap. The accumulation then contributed to the growth of the orogen wedge and the notable uplift (**Figure 6B**). As the procontinental lithosphere arrived at the collision zone, the subducting angle gradually steepened, accompanied by a slight slab roll-over. At ~8 Myr, a second proside crustal rupture happened at the place where slab necking occurred. During this period, both the proside and the retroside around the collision zone experienced uplift (**Figures 6C,D**). Meanwhile, the break-off procontinental crust moved downward, persisted at approximately 130–180 km because of its intrinsic buoyancy, and partly intruded into the bottom of the adjacent retrocontinental lithosphere. Contemporary decoupling between the procontinental upper and lower crust occurred, leaving the upper crust stacked at the surface, while the lower crust started to sink with the lithospheric mantle. The retrocontinental leading end near the surface was warped slightly upward, followed by a proward advance of the orogeny wedge (**Figures 6E,F**).

The ablative/two-sided continental collision mode (Tao and O'connell, 1992; Faccenda et al., 2008; Warren et al., 2008) was the third mode obtained from the model results. This mode can be further divided into symmetric and polarity-reversed subtypes. The model MSI-s1a2 consisted of a weaker retrocontinental lower crust and a 45° subducting angle. It yielded a similar oceanic subduction process as MSI-v1a1 (**Figure 5**) did. However, it

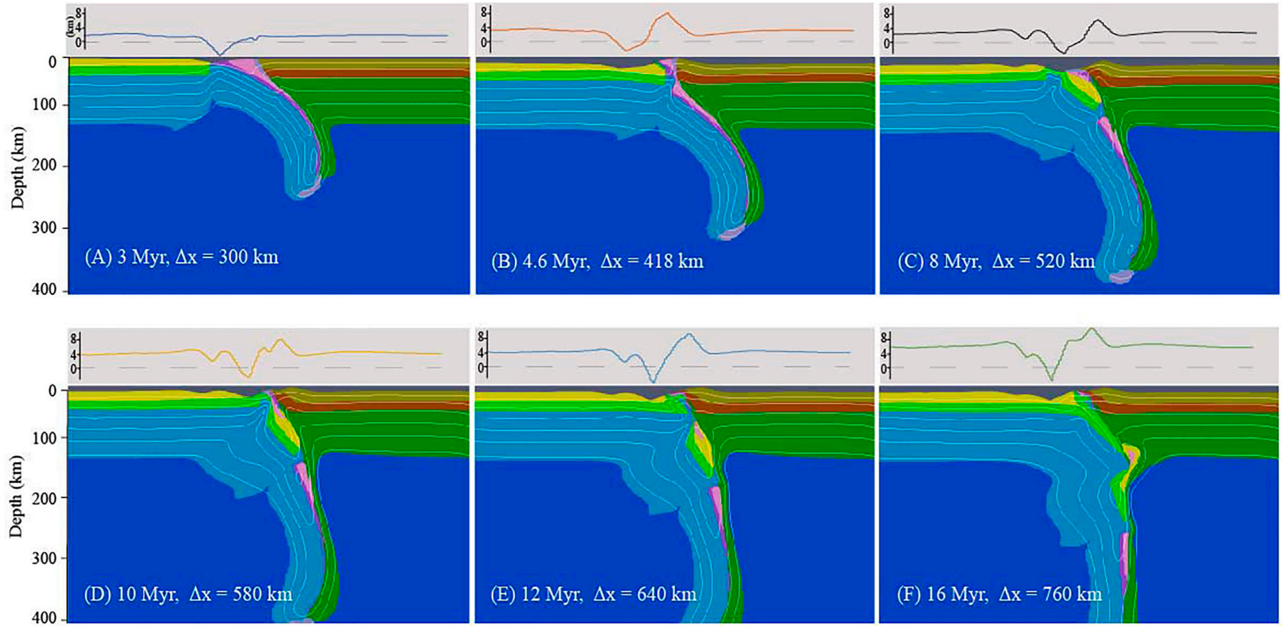

FIGURE 6 | Evolution of the stable continental collision mode. Panels above each snapshot with gray shading show the corresponding topography. Δx is the amount of convergence. Different colors in **(A–F)** denote different lithologies (same as **Figure 2**).

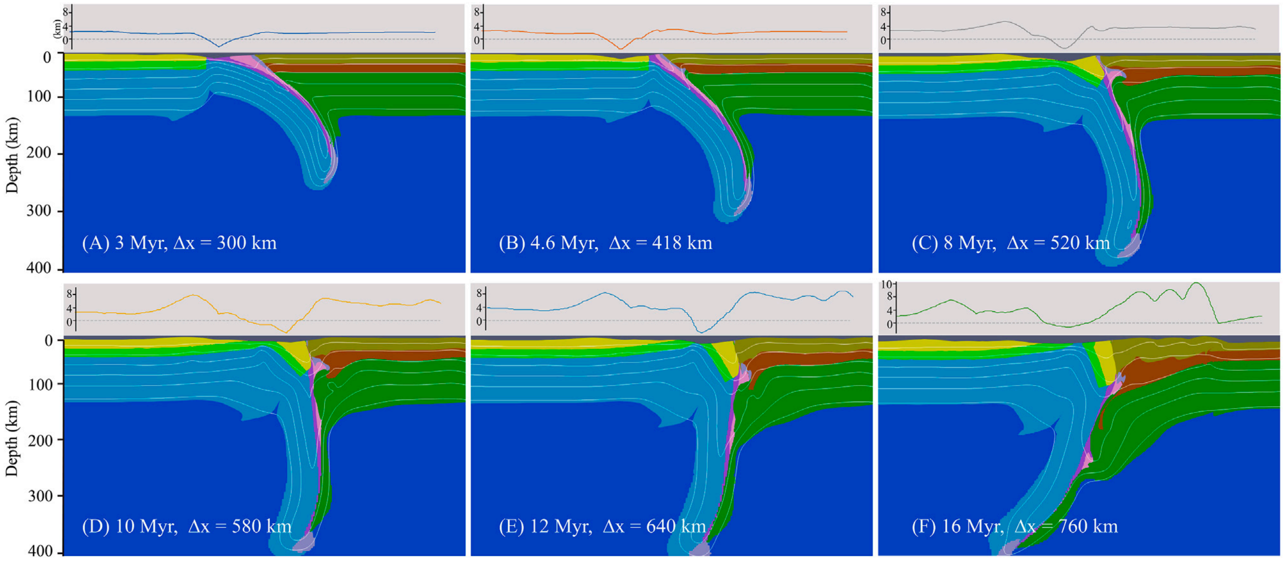

FIGURE 7 | Evolution of the ablative/two-sided continental collision mode. Panels above each snapshot with gray shading show the corresponding topography. Δ x is the amount of convergence. Different colors in **(A–F)** denote different lithologies (same as **Figure 2**).

generated a relatively gentle topographic uplift (**Figures 7A,B**). Thereafter, it became extremely distinct as the continents ran into each other. As the retrocontinental lower crust was designed to be rheologically weak, the sediment and procrustal rocks accumulated at shallow could easily cause an indention without creating significant orogen wedge rising. In contrast, under the obstruction from a buttress that consisted of the scraped-off material and the upward retrolithospheric mantle, the procontinental leading edge uplifted instead (**Figure 7C**). Continuous horizontal proside pushing gave rise to a thick and quasi-symmetric collision zone with a thickened crust, which caused a wide retroside topographic growth. As the procontinental crust is intrinsically buoyant, it resisted going downward. The competition between continuous proside

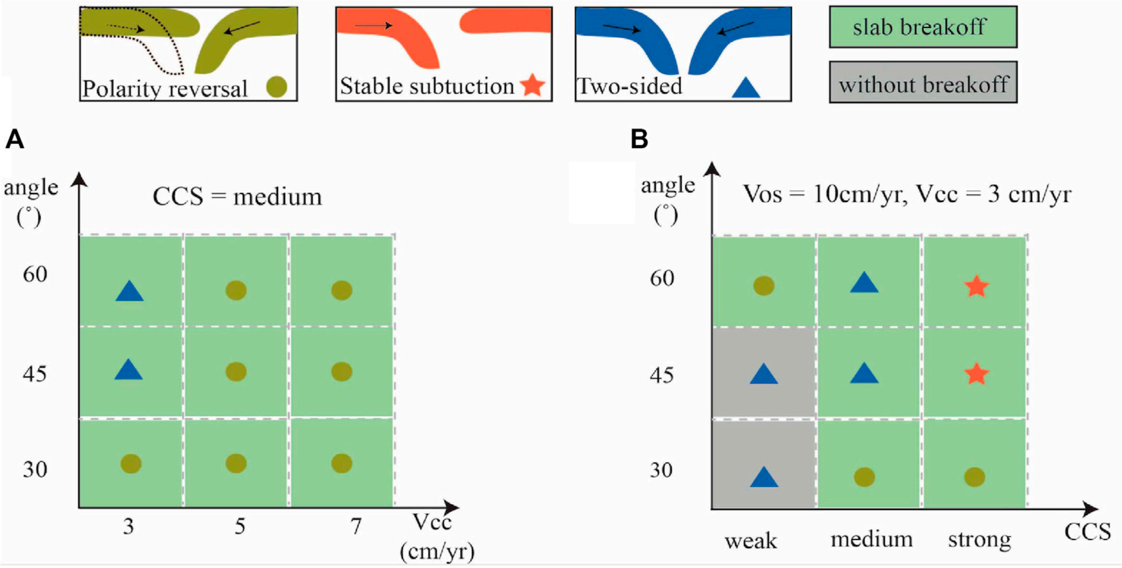

FIGURE 8 | Schematic figures of continental collision modes depending on **(A)** subducting angle and plate velocity, and **(B)** subducting angle and crustal rheological strength. Different symbols denote different collision modes.

pushing and the resistance from the retrocontinent then resulted in strain localization of the proplate leading edge, after which the procontinental crust ruptured (**Figures 7D,E**). Later on, the subducting slab gradually turned over and changed its polarity, indented into the retrocontinent, peeled off the retrocontinental upper crust, and started to subduct with the delaminated retrocontinental lithospheric mantle, leaving a retrocrustal fold at the surface (**Figure 7F**).

In this study, an important aspect of our effort to differentiate the models from previous experiments was conducting a parametric study in VDS. Three distinct end members of continental collision modes were obtained. The regime diagram (**Figure 8**, **Supplementary Material**) shows the dependence of continental collision evolution on the continental convergence rate, initial subducting angle, and continental crustal rheological strength.

Among models that used a medium retrocontinental crustal strength, the ones with a gentle subducting angle (30°) always exhibited polarity-reversed mode. In the same time frame, increasing continental convergence velocity resulted in an earlier break-off of the proplate as well as a longer retrocontinental delamination (**Figure 4B**). In contrast, models with a slightly steeper subducting angle (45°) and slow continental convergence (3 cm/year) evolved into the ablative continental collision mode, whereas models with fast convergence velocity (≥ 5 cm/year) evolved into the two-sided mode (**Figure 8A**). Although increasing the subducting angle to a steeper degree (60°) has little influence on the tendency of continental convergence modes transition, fast continental convergence may result in a second or even multiple fractures in procontinental forepart adjacent to the collision zone, as Model v3a2 (**Table 1**) indicated.

In the weak continental crustal regime (CCS = weak), the retrocontinental lower crust had relatively low viscosity in favor of the decoupling between the retrocontinental crust and the underlying mantle lithosphere. Such models were more liable to evolve polarity reversals. Differences existed, however, between models with a relatively gentle subducting angle (≤ 45°) and those with a steep angle (>45°). The former corresponded to the two-sided mode, while the latter refers to the process that occurred as the slab first broke off, and then the detached retro lithospheric mantle began to sink and formed a one-sided polarity reversed mode (**Figure 8B**).

As we applied a strong retrocontinental crustal strength (CCS = strong), the retroplate seemed to be strong enough to resist intense deformation and delamination. It was then more inclined to deform as an integrated plate, which produced a stable continental collision mode (**Figure 8B**).

To conclude, these numerical results indicate that continental convergence velocity, initial subducting angle, and retrocontinental crustal rheological strength are three crucial first-order controlling parameters that have significant influences on the continental collision process in VDS, and the crustal strength is especially important for the alteration of continental collision patterns among them. As illustrated in **Figure 8**, in models with medium crustal strength, slow convergence velocity and steep subducting angle tended to evolve into a two-sided/ablative continental collision mode. Fast convergence and gentle subducting angles always developed into a polarity reversal mode. Models with a weak continental lower crust were more likely to form a two-sided reversed mode. Further enhancing crustal strength contributed to a strong, coherent retrocontinental lithosphere and tended to evolve into a stable mode. Note that a weak retrocontinental lower crust with a gentle subducting angle accommodated continental convergence with a two-sided reversed mode characterized by rolling over of the proplate, rather than breaking off.

DISCUSSION

The Effects of Plate Velocity Slowdown on the Continental Collision Process

The most crucial setup that differentiates VDS models from CVS is decreasing plate convergence velocity from 10 cm/year during oceanic subduction to the slower ones (3/5/7 cm/year) after the onset of continental collision. **Figure 4** shows that the polarity reversal mode dominated the continental collision style in both VDS and CVS, while the time of polarity reversal in VDS is always earlier than in CVS. This phenomenon arises from the change of both net force and temperature field in VDS: On one hand, during oceanic subduction, fast plate convergence velocity caused fast slab sinking that led to an increase in negative buoyancy. When sharply decreasing the continental convergence velocity after the continental collision, surface lithospheric motion notably slowed down, with slab in depth continuing its downward dragging. The net effect from the forces acting in opposite directions could trigger tension and localized strain in the slab interior. In addition, the foregoing fast oceanic subduction could aggravate the plates' relative motion and increase shear heating on the plates' interface, which may also warm and weaken the plates from the surface. As a consequence, the subducting slab may weaken in certain zones. On the other hand, fast plate convergence velocity corresponded to high horizontal compression. Intense compression between plates could result in severe deformation in and around the collision zone, providing ideal conditions for the formation of a new fault, along which a new subduction may develop.

Besides, slab break-off always results in a sudden removal of downward slab pulling. After that, the following continental forepart could rebound upward due to its buoyancy. In our models, such a process may facilitate the obduction of procontinent along the newly developed fault, and contribute to the evolution of plate polarity reversal (**Figure 5**).

Continental Collision Modes in the Plate Velocity Slowdown Model

Parametric sensitive tests revealed that kinematic characteristics (including plate convergence velocity and subducting angle), as well as the rheological strength of continental crust, had strong influences on continental collision evolution in a plate velocity slowdown model, which has also been confirmed by previous studies that adopted a constant plate velocity model (Pysklywec, 2001; Faccenda et al., 2008; Yang et al., 2019). However, it has its own characteristics. Except for models with slow continental convergence velocity (3 cm/year) and steep subducting angles (>45°), which result in a quasisymmetric ablative mode, the polarity-reversed mode dominated the continental collision style in models with medium overriding crustal strength. When we fixed the plate convergence velocity but altered the subducting angle and retrocontinental crustal strength, three end members of the collision modes were observed under specific parameter ranges: Models with a weak crust and low subducting angles (<45°) showed a reversed ablative mode whereas models with a strong crust always demonstrated a stable mode. In addition, with the exception of a weak crust group, the others evolved into slab necking or slab break-off. Thus, we can infer that plate velocity slowdown after continents meet can break the force equilibrium of the slab by increasing resistance to subduction and then intensifying the extension of the slab, especially in the transition zone between the oceanic and continental plates. This extension is responsible for the local weakening and subsequent break-off of the subducting plate. The shallower the slab that breaks off, the much easier it is for the adjacent overriding plate to switch its polarity. Overriding crustal strength is crucial to altering continental collision modes among these three parameters. A weak overriding continental crust could partially or completely decouple the crust from the lithospheric mantle and facilitate the proplate's indention, resulting in the sinking of the delaminated lithospheric mantle. On the contrary, a strong overriding crust could hamper further deformation and maintain its polarity to form a stable mode inherited from the foregoing oceanic subduction.

Geological Implications for Different Continental Collision Modes

Plate convergence involving oceanic lithosphere is always characterized by one plate that descends beneath the other at the plate's boundary (namely, subduction). The nature of lithospheric deformation during continental plate convergence, however, is still ambiguous. Continental crust generally resists subduction because of its buoyancy, and consequently, it is more liable to deform, thicken, and uplift at a collision zone. These orogenic events significantly contribute to cover up the nature of the underlying lithospheric mantle dynamics. Evidence supports the subduction of the lithospheric mantle at continental collision boundaries. This process is not as steady or coherent as it is in oceanic subduction; instead, it is characterized by diverse tectonic complexities. Our numerical experiments are not prescribed to certain specific orogeny; thus, snapshots mainly show the general process of lithospheric scale deformation at collisional margins. However, numerous seismic images conducted in the active continental collision zones enable the division of continental collision modes into three end members.

Hindu Kush

The Hindu Kush region, located in the western syntaxis of the Tibetan plateau, is the westernmost part of the India-Eurasia collision system and a prominent site to study ongoing continental collision. The comparison of the geodynamic conditions and evolution of Hindu Kush with the stable continental collision mode exhibited good consistency (**Figures 1C**, **6F**). In the Hindu Kush region, the lower plate has been interpreted to be the Indian craton lithosphere, and the overriding plate as the Tajik Basin (TB). The TB is formed by accreted continental terrane during the late Carboniferous to Early Permian, and its crust experienced limited extension. Thus, it is reasonable to presume TB to be a strong overriding lithosphere, which is the favored condition to develop a stable continental collision mode according to the model predictions (**Figure 8**). Seismic tomographic and seismological studies

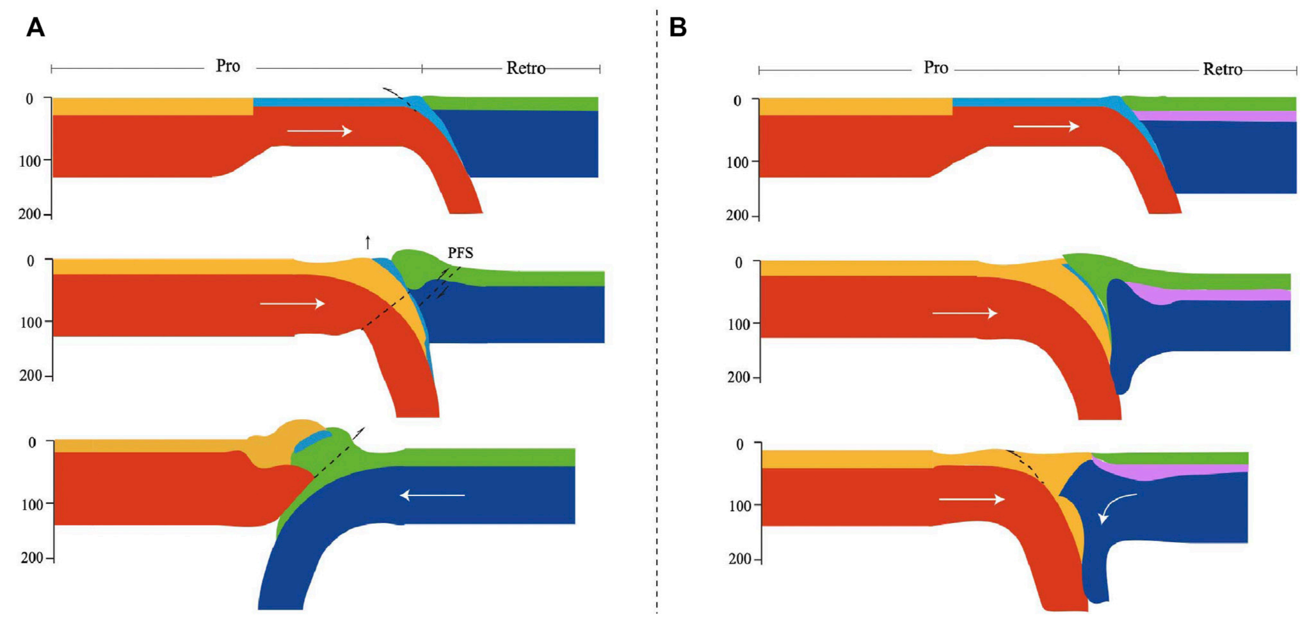

FIGURE 9 | Schematic diagram of the evolution of **(A)** polarity reversed mode in eastern Alps and **(B)** ablative mode in the Austroalpine of the western Alps. PFS is Periadriatic Fault System (Handy et al., 2015; Zhao et al., 2015).

indicated a steep northward dipping High Velocity Zone (HVZ) underneath the HK. The HVZ was interpreted as the subducting Indian lithosphere, along the surface of which is a thin intermediate-depth seismic belt that was interpreted as the subducting lower crust; these slab geometry and lithospheric deformation features are well consistent with the results of stable collision models (**Figure 6F**). In addition, a slab necking was observed in seismic images, the structure of which was also indicated by the model results (**Figure 6F**).

Eastern Alps

Geophysical and geologic evidence has suggested that switches in subduction polarity, either in time (at a given location) or in space, along the plate convergent boundaries are ubiquitous (von Hagke et al., 2016). Polarity reversed mode has been recognized in both subduction orogenies (e.g., Taiwan) and collisional mountain belts (e.g., Pamir-Hindu-Kush, circum-Mediterranean Alpine mountain belt) (Faccenna et al., 2004; Handy et al., 2015; von Hagke et al., 2016). Teleseismic tomographic images have indicated that two + VP anomalies with disparate orientations exist beneath the Alps (Handy et al., 2015): one of them beneath the western and central parts subducts southeastward to ~200 km (Schmid et al., 1996), and the other one beneath the eastern part directs to the opposite side for European subduction and inclines northward to ≥210 km (Kissling et al., 2006; Dando et al., 2011). Mitterbauer et al. (2011) considered the high-velocity anomaly beneath the Eastern Alps to be a vertical to steeply northeast-dipping subducting plate that represented European lithosphere, which originally subducted southward and then steepened and overturned. Handy et al. (2015) have described the polarity reversal process in detail through plate reconstruction based on measurements. According to their concept model, in the late Cretaceous time, the eastern part of the Alpine orogeny underwent Alpine Tethys subduction. During this period, scraped-off oceanic crust from the downward slab accumulated in the collision zone, followed by the entering of the margin of the European plate into the Alpine trench at ~45 Ma, which was recorded by Priabonian flysch in distal Ultra-helvetic units. Calc-alkaline magmatism along the Periadriatic Fault System indicated that the European slab subducts beneath the Alps ruptured in the Oligocene, and the slab gap between the recent Central and Eastern parts of the Alps experienced a vertical tear in the downward European slab that nucleated during Early Oligocene–Early Miocene (Kissling et al., 2006). They proposed that when collision happened in the Alps, the convergence rate between Adria and Europe then dropped from 15 mm/year (before 35 Ma) to 6 mm/year; lateral decoupling occurred between the Eastern Alps and adjacent Adriatic lithosphere. This process led to the subduction of Adriatic slab fragments beneath the Eastern Alps in early Miocene. In this study, we observed similar processes in the models that belong to the polarity reversal continental collision mode (**Figure 5**): They both experienced an oceanic subduction stage, accompanied by oceanic material scraped off, moving upward, and then accreting. The continental collision was followed by slab necking and detachment. A temperature anomaly resulted from asthenosphere upwelling from the slab tearing window. Eventually, polarity reversal was realized.

Furthermore, the evolution of surface topography in our model is coincidental with the results of analogue modeling (Willingshofer and Sokoutis, 2009), as well as the evolution of the eastern Alps based on geological data (Genser et al., 2007). Willingshofer and Sokoutis (2009) once pointed out that plates experienced weakly coupling during the consumption of Alpine

Tethys as calcareous clays and silts from sediment and oceanic crust worked as decoupling materials, after which the European continental margin started underthrusting (late Eocene). During the late Eocene–early Oligocene, strong subsidence occurred to form a foreland basin (Genser et al., 2007). The above process is compatible with our polarity-reversed models (**Figures 5A–C**) with fast oceanic subduction. From Oligocene to Miocene, strong internal deformation and vertical motion occurred in the wedge, followed by the switch of thrusting of the orogenic wedge from north-directed onto the European plate to south-directed. During Middle-late Miocene, cooling of the orogenic wedge strengthened it to facilitate the transmission of stress to the northern plate, which may have led to the late-stage uplift of foreland basin. First-order characteristics of topographic evolution from our model with slow convergence (**Figures 5C–F**) are also consistent with the evolution of the above continental collision stage.

On the basis of model results, we can conclude that the following conditions are favorable for the development of the polarity reversed mode: (1) slab break-off at shallow, after which the remaining strong surface proplate moves upward; and (2) newly developed reversed fault (in this case, the Periadriatic Fault System) working as a weak zone in the leading edge of the overriding plate contiguous to the collision zone, along which the pre-subducting plate would readily slide and facilitate its obduction (**Figure 9A**).

The Austroalpine of the Western Alps

Ablative/two-sided plate consumption model was first introduced by Tao and O'Connell (1992), they interpreted the process based on the dynamics of fluids, which suggests that the viscous lower lithosphere flows downward, and the brittle upper lithosphere deforms in a passive response as it is dragged downward by a dense, descending neighbor. Roda et al. (2012) once verified that the statistical data of the natural P–T peak assemblages coming from the Austroalpine of the Western Alps and the simulated P-T data from the continental upper and lower crust are in good agreement; they proposed that the structural, metamorphic setting, and exhumation of HP/UHP rocks in the Austroalpine Domain could be interpreted as episodic oceanic subduction and orogenic processes that might be manifested by an ablative mode induced by strong coupling of adjacent converged plates. As in model MSI-s1a2, continuous indention of the prolithosphere peeled off the upper crust from the weaker lower lithosphere, leaving a notable shallow converge deformation and an uplift of the collision zone; meanwhile retrocrust accreted to the orogenic wedge (**Figure 9B**). These features are in accordance with certain tectonic characters of the western Austroalpine, for example, the double-verged accretion in the region (Handy et al., 2010; Roda et al., 2012). Although it might not totally explain tectonic evolution of the Austroalpine, the results of our ablative model could shed new light on our understanding of the tectonic evolution of this region.

Ivrea body, once recognized as a slice of the Adriatic mantle exhumed during Mesozoic extension (Nicolas et al., 1990; Zhao et al., 2015), is a special tectonic unit that shapes the recent orogenic structure and crust–mantle deformation pattern of the western Alps. It can work as a buttress between lower and upper plates, impedes pro-upper crustal material from retroward advancing, constrains crustal shortening in the subducting plate, and generates high surface elevation (Liao et al., 2018). Our ablative models also showed the similar characteristics of a lithospheric structure and topography evolution (**Figure 7C**).

MODEL LIMITATIONS

Though our models can reconcile important first-order continental collision characteristics, as well as topographic responses, limitations still exist and hamper the reproduction of detailed orogenic process. Because it is based on a 2D model, it cannot reproduce tectonic processes, such as extrusion tectonics and highly curved collision front and lateral mantle flow; however, the formation of the natural orogens is intrinsically 3D; therefore, 3D modeling approach is required in the future for a better simulation. **Figure 3F** exhibited a surface uplift of ~10 km, which is not observed on earth. This extremely high value in 2D models may be due in part to the lateral extrusion deformation. Besides, in the models, the flow-in and flow-out were prescribed on the same wall, which is not strictly consistent with the mantle flow pattern, and may introduce differences in the model results.

To simplify the model, we neglected mineral phase changes. However, it would modify density. For example, eclogitization in subducted oceanic crust can influence the slab pull and help change the continental collision regime, and control slab break-off. Partial melting is not included either, which can reduce the effective viscosity (strength) of crustal rocks. Besides, no plastic weakening occurs, which is related to the strength of lithosphere, topography evolution, and slab break-off.

CONCLUSION

Plate velocity slowdown between the transition from oceanic subduction to continental convergence, along with continental convergence velocity, subducting angle, and continental crustal rheological strength, are first-order controlling parameters that have significant influences on the fate of the oceanic and continental lithosphere, as well as on the whole evolution of the continental convergence system.

Three different deformation modes of the lithospheric mantle can be obtained through conducting a series of numerical experiments: polarity-reversed mode, two-sided/ablative mode, and stable mode. In addition, by comparing models with distinct configurations, we can conclude the following:

1) A dramatic decrease in plate convergence velocity when continents meet facilitated the extension in the interior of the subducting plate, as the surface plate's motion was slower than the slab's downward sinking, which may have resulted in the slab break-off after certain localized strain accumulation.
2) Fast continental convergence velocity in VDS helps the acceleration of continental collision processes and results in earlier slab break-off. In contrast, in models with a slow continental convergence velocity and a steep subducting angle, the overriding lithospheric mantle tended to delaminate and was dragged down by the subducting plate.

3) Increasing overriding crustal strength produces a stable collision zone. Such a strong crust can limit the development of strain localization in the overriding plate, making the model more likely to evolve into a stable continental convergence mode. Applying a medium or even weak overriding continental crust may more easily produce crust–mantle decoupling, after which the lithospheric mantle may sink in either a reversed mode or a two-sided mode.
4) Favorable conditions for the development of a polarity reversed mode are as follows: (i) a shallow slab break-off, after which the remaining surface subducting plate would move upward, and (ii) a newly developed reversed fault (in this case, the Periadriatic Fault System) contiguous to the collision zone would act as a weak zone at the leading edge of the overriding plate, along which the presubducting plate would readily slide and facilitate its obduction. Decoupling between the upper and middle/lower crust could decrease the influence of downward slab pull and facilitate the scrape-off and accumulation of crustal material at surface. Continuous pulling down of the deeper slab can then dragged the delaminated overriding lithospheric mantle downward.

DATA AVAILABILITY STATEMENT

The original contributions presented in the study are included in the article/**Supplementary Material**, further inquiries can be directed to the corresponding author.

AUTHOR CONTRIBUTIONS

ML performed numerical modeling and wrote the manuscript. DY contributed to the writing and revision of the manuscript. PH contributed to the revision of the manuscript. All authors contributed to scientific interpretations and commented on the manuscript.

FUNDING

This work is supported by the National Key Research and Development Program on Monitoring, Early Warning and Prevention of Major Natural Disaster (No. 2017YFC1500301) and the National Natural Science Foundation of China (Grant Nos. U1839206 and 42104097). The figures in this paper are produced by the Generic Mapping Tools V5.4.2 (Wessel et al., 2013), Python V3.6.7, and Paraview V5.7.0, and then compiled by Adobe Illustrator.

ACKNOWLEDGMENTS

We thank the Computational Infrastructure for Geodynamics for supporting the development of ASPECT (https://aspect.geodynamics.org).

SUPPLEMENTARY MATERIAL

The Supplementary Material for this article can be found online at: https://www.frontiersin.org/articles/10.3389/feart.2022.814710/full#supplementary-material

Supplementary Figure S1 | Viscosity fields of models in VDS with variable subducting angle (30°, 45°, 60°) and continental convergence velocity (3 cm/year, 5 cm/year, 7 cm/year) correspond to Figure 8.

Supplementary Figure S2 | Viscosity fields of models in VDS with variable retrocontinental lower crustal strength (weak, medium, strong) and dip angle (30°, 45°, 60°) correspond to Figure 8.

REFERENCES

Arndt, D., Bangerth, W., Blais, B., Fehling, M., Gassmöller, R., Heister, T., et al. (2021). The deal.II Library, Version 9.3. *J. Numer. Math.* 29, 171–186. doi:10.1515/jnma-2021-0081

Bird, P. (2003). An Updated Digital Model of Plate Boundaries. *Geochem. Geophys. Geosyst.* 4 (3), 1027. doi:10.1029/2001GC000252

Brown, D., Ryan, P. D., Afonso, J. C., Boutelier, D., Burg, J. P., Byrne, T., et al. (2011). "Arc–Continent Collision: The Making of an Orogen," in *Arc-Continent Collision* (Berlin, Heidelberg: Springer Berlin Heidelberg), 477–493. doi:10.1007/978-3-540-88558-0_17

Burg, J.-P., and Gerya, T. V. (2005). The Role of Viscous Heating in Barrovian Metamorphism of Collisional Orogens: Thermomechanical Models and Application to the Lepontine Dome in the Central Alps. *J. Metamorph. Geol.* 23 (2), 75–95. doi:10.1111/j.1525-1314.2005.00563.x

Capitanio, F. A., Replumaz, A., and Riel, N. (2015). Reconciling Subduction Dynamics during Tethys Closure with Large-Scale Asian Tectonics: Insights from Numerical Modeling. *Geochem. Geophys. Geosyst.* 16, 962–982. doi:10.1002/2014gc005660

Chapman, D. S. (1986). Thermal Gradients in the continental Crust. *Geol. Soc. Lond. Spec. Publ.* 24 (1), 63–70. doi:10.1144/GSL.SP.1986.024.01.07

Chemenda, A. I., Burg, J. P., and Mattauer, M. (2000). Evolutionary Model of the Himalaya–Tibet System: Geopoembased on New Modelling, Geological and Geophysical Data. *Earth Planet. Sci. Lett.* 174 (3-4), 397–409. doi:10.1016/S0012-821X(99)00277-0

Chen, Y., Li, W., Yuan, X., Badal, J., and Teng, J. (2015). Tearing of the Indian Lithospheric Slab beneath Southern Tibet Revealed by SKS-Wave Splitting Measurements. *Earth Planet. Sci. Lett.* 413, 13–24. doi:10.1016/j.epsl.2014.12.041

Chen, L., Capitanio, F. A., Liu, L., and Gerya, T. V. (2017). Crustal Rheology Controls on the Tibetan Plateau Formation during India-Asia Convergence. *Nat. Commun.* 8, 15992–15998. doi:10.1038/ncomms15992

Chen, L. (2021). The Role of Lower Crustal Rheology in Lithospheric Delamination during Orogeny. *Front. Earth Sci.* 9. doi:10.3389/feart.2021.755519

Chertova, M. V., Spakman, W., Geenen, T., Van Den Berg, A. P., and Van Hinsbergen, D. J. J. (2014). Underpinning Tectonic Reconstructions of the Western Mediterranean Region with Dynamic Slab Evolution from 3-D Numerical Modeling. *J. Geophys. Res. Solid Earth* 119 (7), 5876–5902. doi:10.1002/2014JB011150

Clift, P. D., Schouten, H., and Draut, A. E. (2003). A General Model of Arc-Continent Collision and Subduction Polarity Reversal from Taiwan and the Irish Caledonides. *Geol. Soc. Lond. Spec. Publ.* 219, 81–98. doi:10.1144/GSL.SP.2003.219.01.04

Copley, A., Avouac, J.-P., and Royer, J.-Y. (2010). India-Asia Collision and the Cenozoic Slowdown of the Indian Plate: Implications for the Forces Driving Plate Motions. *J. Geophys. Res.* 115 (B3). doi:10.1029/2009JB006634

Dando, B. D. E., Stuart, G. W., Houseman, G. A., Hegedüs, E., Brückl, E., and Radovanović, S. (2011). Teleseismic Tomography of the Mantle in the

Carpathian-Pannonian Region of central Europe. *Geophys. J. Int.* 186 (1), 11–31. doi:10.1111/j.1365-246X.2011.04998.x

Davis, R. O., and Selvadurai, & A. P. S. (2002). *Plasticity and Geomechanics*. Cambridge: Cambridge University Press.

Duretz, T., Schmalholz, S. M., and Gerya, T. V. (2012). Dynamics of Slab Detachment. *Geochem. Geophys. Geosyst.* 13 (3), a–n. doi:10.1029/2011GC004024

Faccenda, M., Gerya, T. V., and Chakraborty, S. (2008). Styles of post-subduction Collisional Orogeny: Influence of Convergence Velocity, Crustal Rheology and Radiogenic Heat Production. *Lithos* 103 (1-2), 257–287. doi:10.1016/j.lithos.2007.09.009

Faccenna, C., Piromallo, C., Crespo-Blanc, A., Jolivet, L., and Rossetti, F. (2004). Lateral Slab Deformation and the Origin of the Western Mediterranean Arcs. *Tectonics* 23. doi:10.1029/2002tc001488

Genser, J., Cloetingh, S. A. P. L., and Neubauer, F. (2007). Late Orogenic Rebound and Oblique Alpine Convergence: New Constraints from Subsidence Analysis of the Austrian Molasse basin. *Glob. Planet. Change* 58, 214–223. doi:10.1016/j.gloplacha.2007.03.010

Gleason, G. C., and Tullis, J. (1995). A Flow Law for Dislocation Creep of Quartz Aggregates Determined with the Molten Salt Cell. *Tectonophysics* 247, 1–23. doi:10.1016/0040-1951(95)00011-b

Glerum, A., Thieulot, C., Fraters, M., Blom, C., and Spakman, W. (2018). Nonlinear Viscoplasticity in ASPECT: Benchmarking and Applications to Subduction. *Solid Earth* 9, 267–294. doi:10.5194/se-9-267-2018

Guillot, S., Garzanti, E., Baratoux, D., Marquer, D., Mahéo, G., and de Sigoyer, J. (2003). Reconstructing the Total Shortening History of the NW Himalaya. *Geochem. Geophys. Geosyst.* 4 (7). doi:10.1029/2002GC000484

Handy, M. R., M. Schmid, S. S., Bousquet, R., Kissling, E., and Bernoulli, D. (2010). Reconciling Plate-Tectonic Reconstructions of Alpine Tethys with the Geological-Geophysical Record of Spreading and Subduction in the Alps. *Earth-Science Rev.* 102 (3-4), 121–158. doi:10.1016/j.earscirev.2010.06.002

Handy, M. R., Ustaszewski, K., and Kissling, E. (2015). Reconstructing the Alps-Carpathians-Dinarides as a Key to Understanding Switches in Subduction Polarity, Slab Gaps and Surface Motion. *Int. J. Earth Sci. (Geol Rundsch)* 104 (1), 1–26. doi:10.1007/s00531-014-1060-3

Hirth, G., and Kohlstedt, D. (2003). "Rheology of the Upper Mantle and the Mantle Wedge: A View from the Experimentalists," in *Geophysical Monograph Series* (Washington DC: American Geophysical Union), 138, 83–105. doi:10.1029/138gm06

Huangfu, P., Li, Z.-H., Gerya, T., Fan, W., Zhang, K.-J., Zhang, H., et al. (2018). Multi-terrane Structure Controls the Contrasting Lithospheric Evolution beneath the Western and central-eastern Tibetan Plateau. *Nat. Commun.* 9 (1), 3780. doi:10.1038/s41467-018-06233-x

Jamieson, R. A., Beaumont, C., Fullsack, P., and Lee, B. (1998). Barrovian Regional Metamorphism: Where's the Heat? *Geol. Soc. Lond. Spec. Publ.* 138 (1), 23–51. doi:10.1144/GSL.SP.1996.138.01.03

Karato, S.-i., and Wu, P. (1993). Rheology of the Upper Mantle: A Synthesis. *Science* 260, 771–778. doi:10.1126/science.260.5109.771

Karato, S.-i. (2008). *Deformation of Earth Materials: An Introduction to the Rheology of Solid Earth*. Cambridge: Cambridge University Press.

Kissling, E., Schmid, S. M., Lippitsch, R., Ansorge, J., and Fügenschuh, B. (2006). Lithosphere Structure and Tectonic Evolution of the Alpine Arc: New Evidence from High-Resolution Teleseismic Tomography. *Geol. Soc. Lond. Mem.* 32 (1), 129–145. doi:10.1144/GSL.MEM.2006.032.01.08

Kronbichler, M., Heister, T., and Bangerth, W. (2012). High Accuracy Mantle Convection Simulation through Modern Numerical Methods. *Geophys. J. Int.* 191 (1), 12–29. doi:10.1111/j.1365-246X.2012.05609.x

Kufner, S.-K., Kakar, N., Bezada, M., Bloch, W., Metzger, S., Yuan, X., et al. (2021). The Hindu Kush Slab Break-Off as Revealed by Deep Structure and Crustal Deformation. *Nat. Commun.* 12, 1685. doi:10.1038/s41467-021-21760-w

Li, L., Liao, X., and Fu, & R. (2002). Slab Breakoff Depth: A Slowdown Subduction Model. *Geophys. Res. Lett.* 29 (3), 11–111113. doi:10.1029/2001GL013420

Li, Z. H., Xu, Z. Q., and Gerya, T. V. (2011). Flat versus Steep Subduction: Contrasting Modes for the Formation and Exhumation of High- to Ultrahigh-Pressure Rocks in continental Collision Zones. *Earth Planet. Sci. Lett.* 301 (1-2), 65–77. doi:10.1016/j.epsl.2010.10.014

Li, Z.-H., Xu, Z., Gerya, T., and Burg, J.-P. (2013). Collision of continental Corner from 3-D Numerical Modeling. *Earth Planet. Sci. Lett.* 380, 98–111. doi:10.1016/j.epsl.2013.08.034

Li, Y., Wang, C., Dai, J., Xu, G., Hou, Y., and Li, X. (2015). Propagation of the Deformation and Growth of the Tibetan-Himalayan Orogen: A Review. *Earth-Sci. Rev.* 143, 36–61. doi:10.1016/j.earscirev.2015.01.001

Li, Z. (2014). A Review on the Numerical Geodynamic Modeling of continental Subduction, Collision and Exhumation. *Sci. China Earth Sci.* 57 (1), 47–69. doi:10.1007/s11430-013-4696-0

Liang, X., Chen, Y., Tian, X., Chen, Y. J., Ni, J., Gallegos, A., et al. (2016). 3D Imaging of Subducting and Fragmenting Indian continental Lithosphere beneath Southern and central Tibet Using Body-Wave Finite-Frequency Tomography. *Earth Planet. Sci. Lett.* 443, 162–175. doi:10.1016/j.epsl.2016.03.029

Liang, Y., Li, L., Liao, J., and Gao, R. (2020). Interaction of the Indian and Asian Plates under the Pamir and Hindu-Kush Regions: Insights from 3-D Shear Wave Velocity and Anisotropic Structures. *Geochem. Geophys. Geosyst.* 21, e2020GC009041. doi:10.1029/2020gc009041

Liao, J., and Gerya, T. (2017). Partitioning of Crustal Shortening during continental Collision: 2-D Thermomechanical Modeling. *J. Geophys. Res. Solid Earth* 122 (1), 592–606. doi:10.1002/2016JB013398

Liao, J., Gerya, T., and Malusà, M. G. (2018). 3D Modeling of Crustal Shortening Influenced by Along-Strike Lithological Changes: Implications for continental Collision in the Western and Central Alps. *Tectonophysics* 746, 425–438. doi:10.1016/j.tecto.2018.01.031

Lippitsch, R., Kissling, E., and Ansorge, J. (2003). Upper Mantle Structure beneath the Alpine Orogen from High-Resolution Teleseismic Tomography. *J. Geophys. Res.* 108. doi:10.1029/2002JB002016

Mechie, J., and Kind, R. (2013). A Model of the Crust and Mantle Structure Down to 700 Km Depth beneath the Lhasa to Golmud Transect across the Tibetan Plateau as Derived from Seismological Data. *Tectonophysics* 606, 187–197. doi:10.1016/j.tecto.2013.04.030

Mechie, J., Kind, R., and Saul, J. (2011a). The Seismological Structure of the Tibetan Plateau Crust and Mantle Down to 700 Km Depth. *Geol. Soc. Lond. Spec. Publ.* 353, 109–125. doi:10.1144/sp353.7

Mechie, J., Yuan, X., Schurr, B., Schneider, F., Sippl, C., Ratschbacher, L., et al. (2011b). Crustal and Uppermost Mantle Velocity Structure along a Profile across the Pamir and Southern Tien Shan as Derived from Project TIPAGE Wide-Angle Seismic Data. *Geophys. J. Int.* 188, 385–407. doi:10.1111/j.1365-246x.2011.05278.x

Mechie, J., Zhao, W., Karplus, M., Wu, Z., Meissner, R., Shi, D., et al. (2012). Crustal Shear (S) Velocity and Poisson's Ratio Structure along the INDEPTH IV Profile in Northeast Tibet as Derived from Wide-Angle Seismic Data. *Geophys. J. Int.* 191, 716. doi:10.1111/j.1365-246x.2012.05616.x

Mitterbauer, U., Behm, M., Brückl, E., Lippitsch, R., Guterch, A., Keller, G. R., et al. (2011). Shape and Origin of the East-Alpine Slab Constrained by the ALPASS Teleseismic Model. *Tectonophysics* 510 (1), 195–206. doi:10.1016/j.tecto.2011.07.001

Nábelek, J., Hetényi, G., Vergne, J., Sapkota, S., Kafle, B., Jiang, M., et al. (2009). Underplating in the Himalaya-Tibet Collision Zone Revealed by the Hi-CLIMB experiment. *Science* 325, 1371–1374. doi:10.1126/science.1167719

Negredo, A. M., Replumaz, A., Villaseñor, A., and Guillot, S. (2007). Modeling the Evolution of continental Subduction Processes in the Pamir-Hindu Kush Region. *Earth Planet. Sci. Lett.* 259 (1-2), 212–225. doi:10.1016/j.epsl.2007.04.043

Nicolas, A., Hirn, A., Nicolich, R., and Polino, R. (1990). Lithospheric Wedging in the Western Alps Inferred from the ECORS-CROP Traverse. *Geol* 18, 587–590. doi:10.1130/0091-7613(1990)018<0587:lwitwa>2.3.co;2

Owens, T. J., and Zandt, G. (1997). Implications of Crustal Property Variations for Models of Tibetan Plateau Evolution. *Nature* 387, 37–43. doi:10.1038/387037a0

Patriat, P., and Achache, J. (1984). India-Eurasia Collision Chronology Has Implications for Crustal Shortening and Driving Mechanism of Plates. *Nature* 311 (5987), 615–621. doi:10.1038/311615a0

Pysklywec, R. N., Beaumont, C., and Fullsack, P. (2000). Modeling the Behavior of the continental Mantle Lithosphere during Plate Convergence. *Geology* 28 (7), 655. doi:10.1130/0091-7613(2000)028<0655:mtbotc>2.3.co;2

Pysklywec, R. N. (2001). Evolution of Subducting Mantle Lithosphere at a continental Plate Boundary. *Geophys. Res. Lett.* 28 (23), 4399–4402. doi:10.1029/2001gl013567

Roda, M., Marotta, A. M., and Spalla, M. I. (2010). Numerical Simulations of an Ocean-Continent Convergent System: Influence of Subduction Geometry and Mantle Wedge Hydration on Crustal Recycling. *Geochem. Geophys. Geosyst.* 11 (5). doi:10.1029/2009GC003015

Roda, M., Spalla, M. I., and Marotta, A. M. (2012). Integration of Natural Data within a Numerical Model of Ablative Subduction: a Possible Interpretation for the Alpine Dynamics of the Austroalpine Crust. *J. Metamorph. Geol.* 30 (9), 973–996. doi:10.1111/jmg.12000

Rybacki, E., Gottschalk, M., Wirth, R., and Dresen, G. (2006). Influence of Water Fugacity and Activation Volume on the Flow Properties of fine-grained Anorthite Aggregates. *J. Geophys. Res. Solid Earth* 111. doi:10.1029/2005jb003663

Saein, L. D., and Afzal, P. (2017). Correlation between Mo Mineralization and Faults Using Geostatistical and Fractal Modeling in Porphyry Deposits of Kerman Magmatic Belt, SE Iran. *J. Geochem. Explor.* 181, 333–343. doi:10.1016/j.gexplo.2017.06.014

Schmid, S. M., Pfiffner, O. A., Froitzheim, N., Schönborn, G., and Kissling, E. (1996). Geophysical-geological Transect and Tectonic Evolution of the Swiss-Italian Alps. *Tectonics* 15 (5), 1036–1064. doi:10.1029/96TC00433

Spakman, W., Chertova, M. V., van den Berg, A. P., and van Hinsbergen, D. J. J. (2018). Publisher Correction: Puzzling Features of Western Mediterranean Tectonics Explained by Slab Dragging. *Nat. Geosci.* 11 (5), 374. doi:10.1038/s41561-018-0096-6

Tao, W. C., and O'connell, R. J. (1992). Ablative Subduction: A Two-Sided Alternative to the Conventional Subduction Model. *J. Geophys. Res.* 97 (B6), 8877–8904. doi:10.1029/91JB02422

Tetreault, J. L., and Buiter, S. J. H. (2012). Geodynamic Models of Terrane Accretion: Testing the Fate of Island Arcs, Oceanic Plateaus, and continental Fragments in Subduction Zones. *J. Geophys. Res.* 117 (B8). doi:10.1029/2012JB009316

Tilmann, F., and Ni, J. (2003). Seismic Imaging of the Downwelling Indian Lithosphere Beneath Central Tibet. *Science* 300, 1424–1427. doi:10.1126/science.1082777

Turcotte, D. L., and Schubert, G. (2002). *Geodynamics*. Cambridge: Cambridge University Press. doi:10.1017/CBO9780511807442

von Hagke, C., Philippon, M., Avouac, J.-P., and Gurnis, M. (2016). Origin and Time Evolution of Subduction Polarity Reversal from Plate Kinematics of Southeast Asia. *Geology* 44 (8), 659–662. doi:10.1130/G37821.1

Wang, Q., Zhang, P.-Z., Freymueller, J. T., Bilham, R., Larson, K. M., Lai, X. a., et al. (2001). Present-Day Crustal Deformation in China Constrained by Global Positioning System Measurements. *Science* 294 (5542), 574–577. doi:10.1126/science.1063647

Wang, C., Dai, J., Zhao, X., Li, Y., Graham, S. A., He, D., et al. (2014). Outward-growth of the Tibetan Plateau during the Cenozoic: A Review. *Tectonophysics* 621, 1–43. doi:10.1016/j.tecto.2014.01.036

Warren, C. J., Beaumont, C., and Jamieson, R. A. (2008). Modelling Tectonic Styles and Ultra-high Pressure (UHP) Rock Exhumation during the Transition from Oceanic Subduction to continental Collision. *Earth Planet. Sci. Lett.* 267 (1-2), 129–145. doi:10.1016/j.epsl.2007.11.025

Wessel, P., Smith, W. H. F., Scharroo, R., Luis, J., and Wobbe, F. (2013). Generic Mapping Tools: Improved Version Released. *Eos Trans. AGU* 94, 409–410. doi:10.1002/2013eo450001

Wilks, K. R., and Carter, N. L. (1990). Rheology of Some continental Lower Crustal Rocks. *Tectonophysics* 182, 57–77. doi:10.1016/0040-1951(90)90342-6

Willingshofer, E., and Sokoutis, D. (2009). Decoupling along Plate Boundaries: Key Variable Controlling the Mode of Deformation and the Geometry of Collisional Mountain Belts. *Geology* 37, 39–42. doi:10.1130/g25321a.1

Yamato, P., Burov, E., Agard, P., Le Pourhiet, L., and Jolivet, L. (2008). HP-UHP Exhumation during Slow continental Subduction: Self-Consistent Thermodynamically and Thermomechanically Coupled Model with Application to the Western Alps. *Earth Planet. Sci. Lett.* 271 (1), 63–74. doi:10.1016/j.epsl.2008.03.049

Yang, T., Huangfu, P., and Zhang, Y. (2019). Differentiation of Continental Subduction Mode: Numerical Modeling. *J. Earth Sci.* 30 (4), 809–822. doi:10.1007/s12583-017-0946-y

Ye, Z., Gao, R., Li, Q., Zhang, H., Shen, X., Liu, X., et al. (2015). Seismic Evidence for the North China Plate Underthrusting beneath Northeastern Tibet and its Implications for Plateau Growth. *Earth Planet. Sci. Lett.* 426, 109–117. doi:10.1016/j.epsl.2015.06.024

Yin, A., and Harrison, T. M. (2000). Geologic Evolution of the Himalayan-Tibetan Orogen. *Annu. Rev. Earth Planet. Sci.* 28, 211–280. doi:10.1146/annurev.earth.28.1.211

Zhao, L., Paul, A., Guillot, S., Solarino, S., Malusà, M. G., Zheng, T., et al. (2015). First Seismic Evidence for continental Subduction beneath the Western Alps. *Geology* 43, 815–818. doi:10.1130/g36833.1

Conflict of Interest: The authors declare that the research was conducted in the absence of any commercial or financial relationships that could be construed as a potential conflict of interest.

frontiers in Earth Science

ORIGINAL RESEARCH
published: 09 March 2022
doi: 10.3389/feart.2022.829163

Dynamics of the Subducted Izanagi-Pacific Plates Since the Mesozoic and Its Implications for the Formation of Big Mantle Wedge Beneath Eastern Asia

Bingcheng Wu[1], Yongming Wang[2] and Jinshui Huang[1]**

[1]Mengcheng National Geophysical Observatory, School of Earth and Space Sciences, University of Science and Technology of China, Hefei, China, [2]School of Earth Sciences, Yunnan University, Kunming, China

The slab dynamics of the subducted Izanagi-Pacific plate is still a subject of controversy and its relationship with the tectonic evolution of Eastern Asia remains not well explored. Here, we perform 3-D global convection models to investigate the slab dynamics of the Izanagi-Pacific plate beneath Eastern Asia since the Mesozoic time. We introduce a tracking technique in numerical models to explicitly distinguish the Izanagi slab and the Pacific slab during their subduction processes. We find that all subducted Izanagi slabs have completely fallen into the lower mantle until the late Cenozoic and the stagnant slabs currently observed at the mantle transition zone depth beneath Eastern Asia are entirely from the Pacific plate. We also find that multiple slab stagnation events have occurred during the subduction of the Izanagi plate in the Mesozoic time (~150–120 Ma, 90–70 Ma) with a timescale of tens of million years. The stagnation of the subducted slabs facilitates the formation of a big mantle wedge beneath the overriding lithosphere and the time periods of the mantle wedge are consistent with the episodes of magmatic activities in Eastern Asia.

Keywords: Izanagi-Pacific plate, Eastern Asia, big mantle wedge, slab stagnation, numerical modelling

Edited by:
Lijun Liu,
University of Illinois at Urbana-Champaign, United States

Reviewed by:
Jiashun Hu,
Southern University of Science and Technology, China
Nicolas Flament,
University of Wollongong, Australia

Correspondence:
Yongming Wang
ymwang@ynu.edu.cn
Jinshui Huang
jshhuang@ustc.edu.cn

Specialty section:
This article was submitted to Solid Earth Geophysics, a section of the journal Frontiers in Earth Science

Received: *05 December 2021*
Accepted: *09 February 2022*
Published: *09 March 2022*

Citation:
Wu B, Wang Y and Huang J (2022) Dynamics of the Subducted Izanagi-Pacific Plates Since the Mesozoic and Its Implications for the Formation of Big Mantle Wedge Beneath Eastern Asia. Front. Earth Sci. 10:829163. doi: 10.3389/feart.2022.829163

INTRODUCTION

The tectonic units in East Asia mainly consist of four terrain blocks: the Siberia Craton to the north, the North China Craton (NCC) in the middle, the South China Block (SCB) on the south and the Central Asian Orogenic Belt (CAOB) in between (Domeier and Torsvik, 2014; **Figure 1**). These four blocks were separately drifting on their own at least before the Triassic (e.g., Domeier and Torsvik, 2014; Matthews et al., 2016). Since the Late Paleozoic, the NCC amalgamated with the CAOB during the Late Permian to Early Triassic and collided with the SCB in the Triassic, while the northeast China combined with the Siberia Craton during the Jurassic to Early Cretaceous, and these four terrains converged together to become part of the Eurasian plate (e.g., Sorokin et al., 2020). To the east, the western Pacific plate is actively subducting along the Kuril, Japan and Mariana trenches, whereas the Philippine Sea Plate is descending along the Nankai trough and the Ryukyu trench (e.g., Matthews et al., 2016; **Figure 1**).

Since the early Mesozoic, extensive tectonic deformations have occurred in Eastern Asia (Zhu et al., 2012; Wang et al., 2018; Li et al., 2019). The northeast China experienced intensive extensional

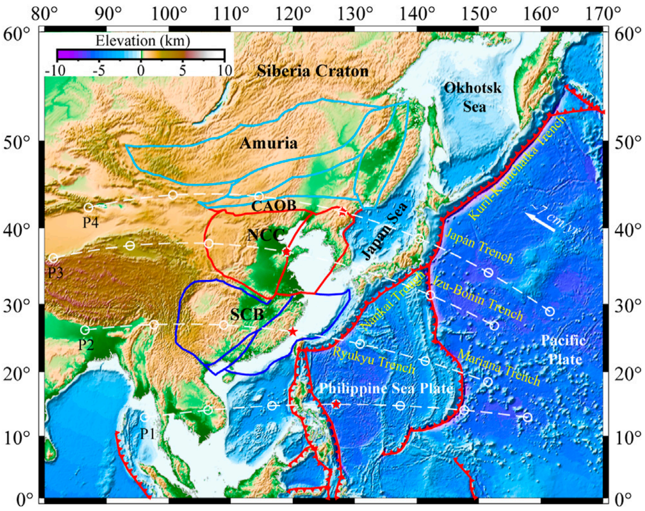

FIGURE 1 | Major tectonic settings of Eastern Asia. The blue, red and cyan lines denote the shapes of South China Block (SCB), North China Craton (NCC) and Amuria Block, respectively. The red lines with triangles denote the subduction zones. The white dashed lines denote locations of the vertical cross-sections P1-P4 shown in **Figure 2**. The start, center (red star) and end coordinates with a great circle distance of 10° for each profile are marked (white circle) on each cross-section.

deformations in the Early Cretaceous which are characterized by widespread volcanism and extensional basins (Meng, 2003; Wu et al., 2005; Wang et al., 2006). The interior of the NCC had undergone extensive modification and reactivation from Mesozoic to Cenozoic as indicated by large-scale deformation, magmatic activities, and basin formation (Zhu et al., 2012; Wu et al., 2019). The mantle xenoliths studies show that the ancient lithospheric mantle of the SCB was replaced by the newly accreted mantle through lithospheric extension and asthenosphere upwelling during the Meso-Cenozoic time (Li et al., 2014a; Li et al., 2014b). The tectonic evolution of the Eastern Asia area has been suggested to be closely related to the subduction history of the Paleo-Pacific plate (i.e., the Izanagi plate) and the west Pacific plate (e.g., Zhu and Xu, 2019 and references therein). The large-scale extension and volcanic activities in northeast China are supposed to be associated with the slab rollback of the subducted Izanagi plate (e.g., Xu and Zheng, 2017; Li et al., 2019; Ma and Xu, 2021), and many researchers regard Izanagi-Pacific subduction as one of the principal triggers for the reactivation and destruction of the NCC (e.g., Zhu and Xu, 2019; Liu et al., 2021). It has also been proposed that the Pacific subduction influenced the SCB mainly during the middle to late Mesozoic and produced large-scale granitoid and volcanic rocks (Sun et al., 2007; Liu et al., 2012).

However, the subduction history of the Izanagi-Pacific plate is poorly constrained and remains controversial (e.g., Sun et al., 2007; Yang, 2013; Domeier and Torsvik, 2014; Matthews et al., 2016; Müller et al., 2019). The link between the Izanagi-Pacific plate subduction and the tectonic evolution of Eastern Asia has not been fully explored, especially lack of geodynamical verifications for the Mesozoic time. Based on seismic tomography studies many scholars have argued that the Pacific slab, and perhaps the older Paleo-Pacific slab are stagnant in the mantle transition zone beneath Eastern Asia (Fukao et al., 2009; Zhao et al., 2011) to form a "big mantle wedge" (BMW) that the overriding lithosphere evolved in response to subduction dynamics of the BMW (Zhao et al., 2011; Xu et al., 2018; Zhu and Xu, 2019). Some recent studies on magmatic activities in Eastern Asia have also indicated the development of a big mantle wedge between 145–120 Ma (e.g., Ma and Xu, 2021). On the other hand, recent studies have proposed that the present-day stagnant slab in the mantle transition zone beneath Eastern Asia is the subducted Pacific slab rather than the Izanagi slab (Ma et al., 2019). In addition, global mantle convection models show that the stagnant slab under Eastern Asia largely results from subduction in the past 20–30 Myr (Mao and Zhong, 2018). The stagnation of the Izanagi-Pacific slab beneath Eastern Asia has been investigated in many numerical experiments (e.g., Seton et al., 2015; Peng et al., 2021a; Liu et al., 2021). However, most of these studies have focused on the stagnation of the Pacific slab in the Cenozoic time, while whether the Izanagi slab in the Mesozoic time could be stagnant or not remains unclear. Therefore, some remaining questions that 1) how does the Izanagi-Pacific plate evolve beneath Eastern Asia since the Mesozoic time, and 2) how its subduction dynamics would potentially affect the formation of the BMW, especially in the Mesozoic time, deserve to be well explored from a geodynamical perspective.

In this study, we perform 3-D global mantle convection models to study the slab dynamics of the subducted Izanagi-Pacific plate and its influence on the tectonic evolution of Eastern Asia. In numerical models, the plate motion history is incorporated to 1) constrain the boundary conditions and 2) track the Izanagi and the Pacific plate separately to distinguish their evolutionary processes.

METHODS

The dynamical evolution of the mantle convection system is governed by partial differential equations for conservation of mass, momentum and energy and advection of composition (McNamara and Zhong, 2004). We assume the mantle is incompressible and solve the governing equations under the Boussinesq approximation with modified numerical code CitcomS (Zhong et al., 2008) and the non-dimensional governing equations are:

$$\nabla \cdot \vec{u} = 0 \tag{1}$$

$$-\nabla P + \nabla \cdot (\eta \dot{\varepsilon}) + \left(RaT - \sum_{k} Rb^{k} \Gamma_{k} \right) \hat{e_r} = 0 \tag{2}$$

$$\frac{\partial T}{\partial t} + \left(\vec{u} \cdot \nabla \right) T = \nabla^{2} T + Q \tag{3}$$

where $\vec{u}$ is the velocity, P is the dynamic pressure, η is the viscosity, $\dot{\varepsilon}$ is the strain rate, Ra is the Rayleigh number, T is the temperature, $\hat{e_r}$ is the unit vector in the radial direction, t is the

TABLE 1 | Physical parameters of numerical models.

Parameter	Symbol	Value
Earth radius	R_0	6370 km
Gravitational acceleration	g	9.81 m/s^2
Reference density	ρ	3300 kg/m^3
CMB radius	r_i	3504 km
Rayleigh number	Ra	5.0×10^7
Reference temperature	ΔT	2500 K
Reference viscosity	η	1.25×10^{22} Pa s
Thermal expansivity	α	3.0×10^{-5}/K
Thermal diffusivity	κ	10^{-6} m^2/s
Gas constant	R_{gas}	8.314 J/(K mol)
Clapeyron slope at 670-km depth	γ	−2.0 MPa/K
Density changes at 670-km depth	$\Delta\rho/\rho$	8%
Reference temperature at 670-km depth	T_k	1573 K
Phase change width at 670-km depth	δ	40 km

time, Q is the internal heating. The thermal Rayleigh number Ra and the phase-change Rayleigh number Rb^k are defined as:

$$Ra = \frac{\alpha\rho g_0 \Delta T R^3}{\kappa\eta_0} \tag{4}$$

$$Rb^k = \frac{\Delta\rho_k g_0 R^3}{\kappa\eta_0} \tag{5}$$

where $\alpha, \rho, g_0, \Delta T, \kappa, \eta_0$ are dimensional parameters for the reference thermal expansivity, density, gravitational acceleration, temperature difference between the bottom and the surface, thermal diffusivity and viscosity, respectively. $\Delta\rho_k$ is the density jump for the kth phase change and R is the radius of the Earth. Notice that the Rayleigh number is defined using the radius of the Earth and is ~10 times larger than that defined using the mantle thickness.

A phase-change function formulation is used here to represent phase changes as in earlier studies (Christensen and Yuen, 1985; Zhong and Gurnis, 1994). Γ_k is defined in dimensionless form as:

$$\Gamma_k = \frac{1}{2}\left[1 + \tanh\left(\frac{\pi_k}{\delta}\right)\right] \tag{6}$$

where δ is the phase change width that measures the depth segment of phase change, and π_k is the dimensionless “excess pressure” as

$$\pi_k = d - d_k - \gamma_k (T - T_k) \tag{7}$$

where d is the depth, d_k and T_k are the reference depth and temperature of phase change k, and γ_k is the Clapeyron slope. The Clapeyron slope is normalized by $\rho g R/\Delta T$. The phase change at 670 km depth from spinel to post-spinel changes is included in our models. All relevant physical parameters are listed in **Table 1**.

The models have a dimensionless radius of 0.55 and 1.0 at the CMB and the surface, respectively. The computational domain is divided into 12 caps with each cap containing 128 × 128 × 80 elements and employs grid refinements near the surface (~25 km), the phase transition (~25 km) and the CMB (~25 km) in the radial direction. The surface temperature is constant with nondimensional $T = 0$ (i.e., 273 K), whereas the CMB is thermally insulating (i.e., zero heat flux boundary condition) to prohibit the formation of upwelling plumes. The heat flux that is expected to come out of the core in our models is smaller due to the relatively small temperature drop (i.e., 2500 K, **Table 1**) than estimated constraints (Lay et al., 2008). However, since we focus on upper mantle slab dynamics and do not consider the bottom thermal boundary layer above the CMB, we, therefore, use a zero heat flux instead of isothermal condition for the bottom boundary and a relatively smaller temperature drop. Models are internally heated with a nondimensional internal heating rate of $Q = 100$ (i.e., ~6×10^{-12} W/kg). The velocity boundary condition for the top boundary is time-dependent by imposing the plate velocity history from the reconstruction model (e.g., Matthews et al., 2016), while the CMB is free-slip. The initial temperature for the lithosphere (e.g., above 150 km) is obtained by following the half-space cooling model with a plate age of 100 Ma and below the lithosphere is 0.52 (or 1573 K) everywhere, respectively (**Supplementary Figure S1**).

The viscosity structure in our models is both depth and temperature-dependent, expressed as $\eta(T,r) = \eta_r exp[A(0.5 - T)]$, where η_r is the depth-dependent pre-factor and A is the activation coefficient which is 9.21 in all cases (e.g., equivalent to ~190 kJ/mol of activation energy dimensionalized by $R_{gas}\Delta T$), leading to a maximum of 4 orders of viscosity change due to variation of temperature. The viscosity pre-factor η_r is 1.0, 0.02, 2.0 for the lithosphere, asthenosphere and the lower mantle, respectively. All cases in this study include a thin (~60 km) weak layer (η_r is set to 0.002) below the phase change boundary to simulate the rheological effects of the phase change (e.g., Mitrovica and Forte, 2004), which is suggested to play an important role in producing horizontally deflected slabs in the transition zone (Mao and Zhong, 2018) (**Supplementary Figure S1**). Our models also include a linear increase of thermal diffusivity and a decrease of thermal expansivity from the surface to the CMB, as indicated from mineral physics experiments (Gibert et al., 2003; Katsura et al., 2009), by a factor of 2.18 and 2.5, respectively (e.g., Mao and Zhong, 2018).

In this study, we use ~315 million tracers (20 per element) in numerical models to track the Izanagi plate and the Pacific plate separately. We introduce a tracking technique by which we can explicitly distinguish the evolution of the Izanagi slab and the Pacific slab in the mantle. The general tracking procedure is as follows: firstly, a time-dependent plateID that represents different plates at the surface is obtained by extracting the plateID information from the reconstruction model with a time interval of 1 Myr using the GPlates software (Müller et al., 2018); secondly, at each timestep, 1) we choose the closest time point to assign the plateID for each surface node, 2) for each tracer in an element above a given depth (e.g., above 150 km), and determine the corresponding surface element that is in the same vertical column with this tracer's element; if the nodal plateID of this surface element matches the plate that we want to track, then we remark the tracer as the target plate with a given flavor, 3) for tracers below the given depth, we do not

TABLE 2 | Numerical model parameters.

Case name	Start age	Plate model[a]	Weak layer
Case1	410 Ma	Ma2016	Yes
Case2	410 Ma	Yo2019	Yes
Case3	410 Ma	Ma2016 + Ya 2013[b]	Yes
Case4	300 Ma	Ma2016	Yes
Case5	410 Ma	Ma2016	No

[a] *Ma2016 refers to plate model from Matthews et al. (2016), Yo2019 refers to plate model from Young et al. (2019), Ya2013 refers to plate model from Yang (2013).*

[b] *For case 3, the plate history is from a combination of Ma 2016 (410–90 Ma) and Ya 2013 (90–0 Ma).*

remark the tracers and leave the flavors of the tracers as they are and move to next timestep.

RESULTS

We present five models that differ in plate motion history model, initial setup and the presence of weak layer in the transition zone and use case 1 as reference (**Table 2**). Case 1 uses the plate model of Matthews et al. (2016) and starts to run from 410 Ma. Case 2 uses the plate reconstruction model of Young et al. (2019) and starts to run from 410 Ma. Case 3 is similar to case 1, except that the plate motion history after 90 Ma is replaced by that from Yang (2013), while the plate motion history before 90 Ma is the same as case 1 from Matthews et al. (2016). In case 3, the moving direction of the Izanagi plate was rotated by ~20° clockwise after 90 Ma so that the plate moved north-northwestward at around 84 Ma. The average moving speed of the Izanagi plate during 90–77 Ma is ~20 cm/yr. After 77 Ma the Izanagi plate subducted beneath northeast Asia and totally fell into the mantle around 55 Ma. Case 4 uses the plate model of Matthews et al. (2016) but starts to run from 300 Ma. Case 5 is the same as case 1 but without the weak layer at 670-km transition zone.

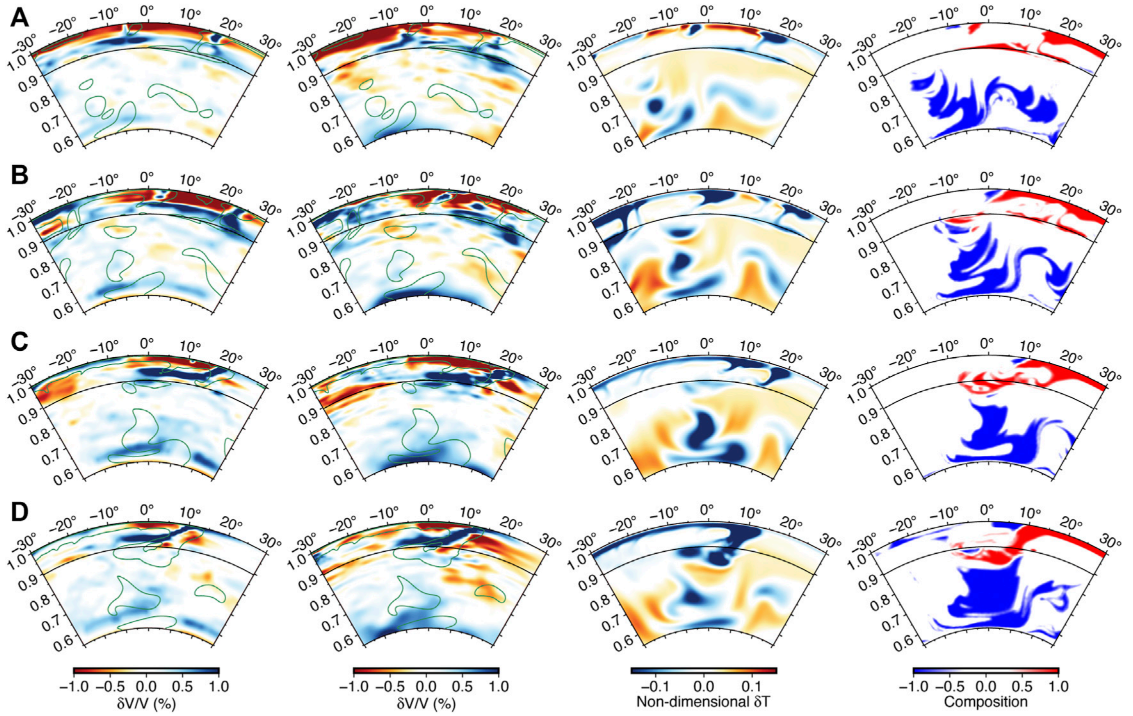

FIGURE 2 | Cross-sections of P-wave velocity perturbations from seismic tomography models TX2019slab (first column) (Lu et al., 2019) and GAP_P4 (second column) (Fukao and Obayashi, 2013), and the present-day non-dimensional residual temperature (third column) and composition (last column) from numerical model case 1. The black line in each cross-section corresponds to the 670-km depth. The locations of **(A–D)** correspond to profiles P1-P4 as shown in **Figure 1**, respectively. In figures of tomography models (i.e., first and second columns) the green lines indicate contours of non-dimensional residual temperature *δT* of −0.05 from the third columns, i.e., material 5% colder than the ambient mantle that supposed to be associated with subducted slabs. In figures of compositional field, the blue and red colors represent the Izanagi Plate and the Pacific Plate, respectively.

Slab Structure of the Izanagi-Pacific Plate

We first show the results of case 1 which uses the plate model of Matthews et al. (2016) started from 410 Ma. **Figure 2** shows several cross-sections of the temperature and compositional fields at different locations for this case at t = 0.0 Ma, i.e., present-day time. The P-wave velocity perturbations from two seismic tomography models TX2019slab (Lu et al., 2019) and GAP_P4 (Fukao and Obayashi, 2013) are also shown in **Figure 2**. The slabs

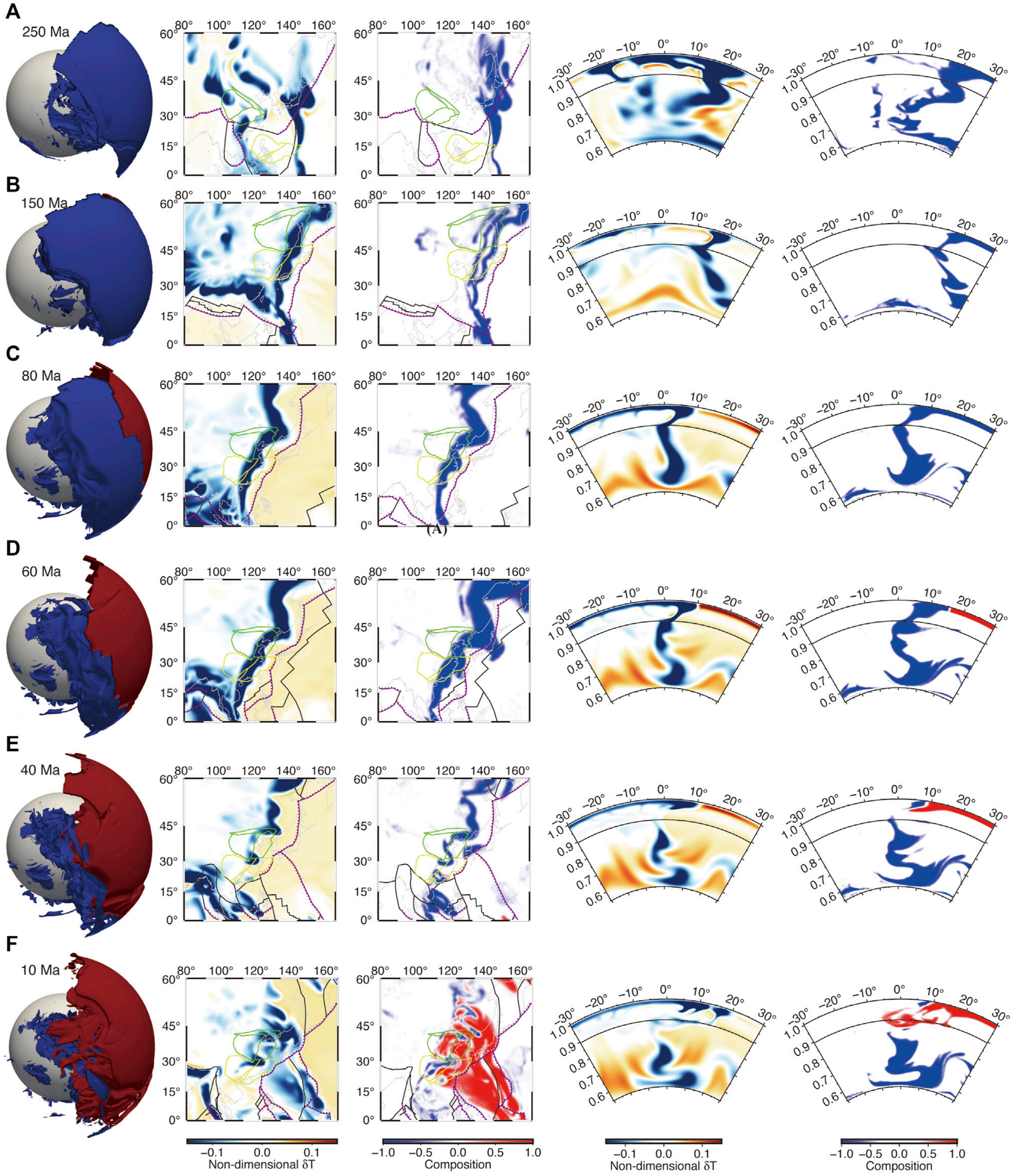

FIGURE 3 | Slab structures of the Izanagi-Pacific plate from case 1 at **(A)** 250 Ma, **(B)** 150 Ma, **(C)** 80 Ma, **(D)** 60 Ma, **(E)** 40 Ma and **(F)** 10 Ma. The first column shows the 3D slab structures of the Izanagi plate (blue) and the Pacific plate (red) at the Eastern Aisa region. The second and third columns show the residual temperature and composition fields at 670 km depth, respectively. Convergent and ridge and transform boundaries are represented by magenta and black lines, respectively. The fourth and fifth columns show the cross-section of residual temperature and composition fields at section P3 as shown in **Figure 1**. In figures of compositional fields, the blue and red colors denote the Izanagi plate and the Pacific plate, respectively. A full-time evolution of the slab structures is provided in **Supplementary Figure S2**.

show a variety of morphologies at different locations beneath Eastern Asia. The slab subducts nearly vertically into the transition zone depth along the Mariana Trench in southeast Asia (**Figures 2A,B**, columns 1 and 2). However, beneath the north and northeast Asia, the slabs are horizontally deflected and tend to stagnate near the transition zone depth (**Figures 2C,D**, columns 1 and 2). The general slab structures in the upper mantle beneath Eastern Asia are quite similar for different seismic models (**Figure 2**, columns 1 and 2). For case 1, the structures of the subducted slabs as represented by the cold thermal anomalies and the compositional fields show good first-order consistency with the structures of fast velocity anomalies in seismic models, especially the existence of stagnant slabs beneath Eastern Asia in the mantle transition zone (**Figure 2**, columns 3 and 4).

However, although the seismic observations show fast velocity anomalies beneath Eastern Asia, they do not tell whether the velocity anomalies are associated with the Izanagi plate or the Pacific plate. By tracking the Izanagi plate and the Pacific plate separately in our models (*Methods*), we find that at the present-day time, most of the Izanagi slabs beneath the Eastern Asia region have entered the lower mantle, except a few regional slab fragments left near the 670-km depth (**Figure 2**, column 4). The fast velocity anomalies at the 670-km transition zone are associated with the new Pacific plate rather than the old Izanagi plate (**Figure 2**, column 4), which is consistent with other previous studies (Ma et al., 2019; Liu et al., 2021).

Figure 3 shows some snapshots of the temperature and composition fields at 670 km depth for case 1 together with a cross-section showing slab structures beneath Eastern Asia, and a full-time evolution is provided in **Supplementary Figure S2**. In the early Mesozoic (e.g., 250 Ma), the mantle structure beneath Eastern Asia is rather complex and abundant Izanagi slabs are trapped and accumulate at 670 km depth before falling into the lower mantle (**Figure 3A** and **Supplementary Figure S2**). The subducted slabs distribute not only at the leading edge of the trench but also at the trailing edge due to slab rollback (**Figure 3A** and **Supplementary Figure S2**). From early to middle Mesozoic (~150 Ma), the Izanagi plate continues to subduct westward beneath the Eurasian plate and the slabs mostly distribute at the leading edge of the trench, while many of the previously accumulated Izanagi slabs have fallen into the lower mantle (**Figure 3B** and **Supplementay Figure S2**). To the late Mesozoic, the subducted slabs generally first accumulate at the transition zone depth before entering the lower mantle, which results in a buckling morphology when they sink to greater depths (**Figures 3C,D** and **Supplementary Figure S2**). Meanwhile, the middle ocean ridge of the Izanagi-Pacific plate also moves westward closely to the Eurasian plate while no subduction initiates for the Pacific plate (**Figure 3D** and **Supplementary Figure S2**).

To the early Cenozoic (~40 Ma), the entire Izanagi plate has subducted to the mantle including the ridge and the subduction of the Pacific plate has initiated (**Figure 3E** and **Supplementary Figure S2**). Although most Izanagi slabs have fallen to the lower mantle, some remnants are still preserved in the upper mantle at transition zone depth, while the slabs of the Pacific plate remain at a shallower depth (**Figure 3E** and **Supplementary Figure S2**). Since then, the residuals of the Izanagi slabs continue to sink from the transition zone until they have completely entered the lower mantle at the present-day time (**Figure 3F** and **Supplementary Figure S2**). Meanwhile, the subduction of the Pacific plate has fully developed, and the slabs are mostly trapped or flattened above the transition zone instead of penetrating to the lower mantle (**Figure 3F** and **Supplementary Figure S2**).

Time-Dependent Slab Structure Beneath the NCC and the SCB

Here, we present the slab structures of the Izanagi-Pacific plate beneath the NCC and the SCB. **Figure 4** shows some snapshots of the temperature and composition fields beneath the NCC and the SCB from case 1, in which the locations of the cross-sections are not fixed but move along with the NCC and SCB over time. The fully-time evolution of slab structures is provided in **Supplementary Figures S3, S4**, respectively. From early to middle Mesozoic, the slab structures beneath the NCC and the SCB are quite similar, that is the subducted slabs of the Izanagi plate mostly directly pass through the 670-km boundary into the lower mantle and tend to be stirred into small pieces by mantle convection (e.g., 250–180 Ma, **Figure 4A**, **Supplementary Figures S3, S4**). From middle to late Mesozoic, instead of directly penetrating to the lower mantle, some of the subducted slabs of the Izanagi plate are trapped or stagnant above the mantle transition zone depth beneath the NCC and spread westward to the central part of the NCC (e.g., ~130 Ma, **Figure 4B**, left columns). Similar slab structures are also observed beneath the SCB at this stage but with a different time of slab stagnation (e.g., ~140 Ma, **Figure 4B**, right columns). The stagnation of the subducted slabs which extends with a horizontal length of 800–1,000 km facilitates the formation of a big mantle wedge beneath the lithosphere of the NCC and the SCB (**Figure 4B**).

With time, more and more slab materials accumulate at the transition zone depth and eventually they pass through the 670-km boundary to sink into the lower mantle (e.g., **Figure 4C**). The mantle wedge is thus destroyed due to this subsequent accumulation and sinking of Izanagi slabs in the middle Mesozoic (~110 Ma, **Figure 4C**). From the middle to the late Mesozoic (~70 Ma), another slab stagnation event has developed beneath both the NCC and the SCB, although the duration times are somewhat different beneath these two blocks (**Figure 4D**, **Supplementary Figures S3, S4**). The timescales of these multiple slab stagnation events, however, are quite similar with a magnitude on the order of tens of million years (**Supplementary Figures S3, S4**). In the early Cenozoic (~40 Ma), most of the Izanagi slabs beneath the NCC and the SCB have completely fallen into the lower mantle (**Figure 4E**). From the middle Cenozoic to the present, the subducted slabs of the Pacific plate are mostly trapped and lie horizontally at the 670-km mantle transition zone depth (**Figure 4F**, **Supplementary Figures S3, S4**). However, abundant slabs of the Pacific plate have subducted and spread to the center part of the NCC which promotes the formation of a big mantle wedge

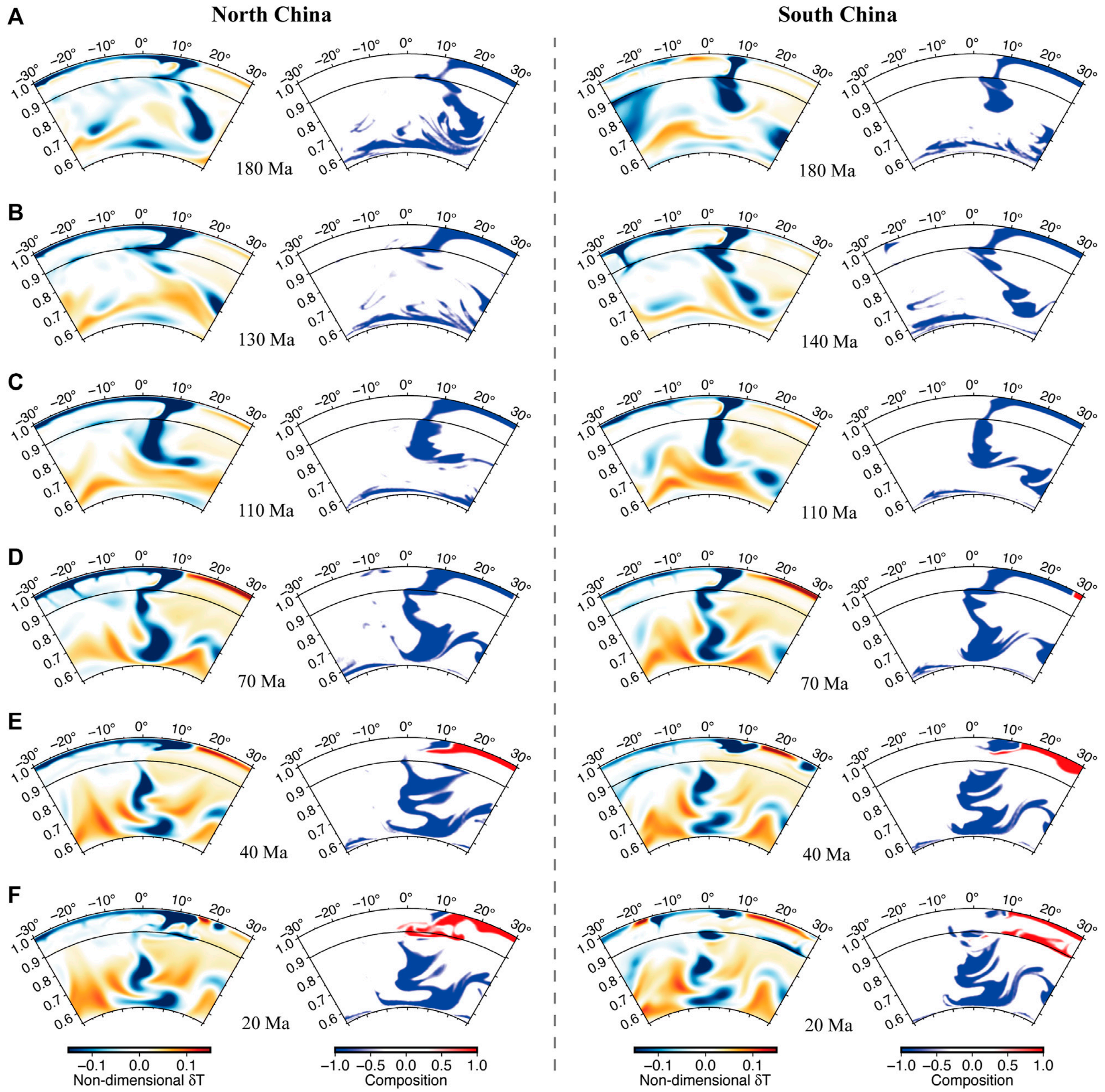

FIGURE 4 | Slab structures of the Izanagi-Pacific plate beneath the North China Craton (left columns) and the South China Block (right columns) at some time snapshots from case 1. In **(A–F)**, the left and right columns are cross-sections of the residual temperature and composition fields across the NCC and the SCB, respectively. The fully-time evolution of the slab structures for the NCC and the SCB are provided in **Supplementary Figures S3, S4**, respectively.

beneath the lithosphere, while there are fewer Pacific slabs beneath the SCB due to the block of the Philippine plate (**Supplementary Figures S3, S4**).

Effect of Plate Reconstruction Models and Model Setup

The motion histories of many plates at the early stage have been destroyed, and the reconstructions of the plate motion history remain under debate. Here we test the influences of different plate motion history models on our results. Case 2 uses the same model setup as case 1 but with surface plate motion history from a different plate reconstruction model of Young et al. (2019). The present-day upper mantle slab structures beneath Eastern Asia in case 2 are quite similar to case 1, although some differences exist for slab morphologies in the lower mantle depths (**Figures 2A–D, 5A–D**). However, the slab dynamics of the Izanagi plate for case 2 reveal some significant differences in the Mesozoic time

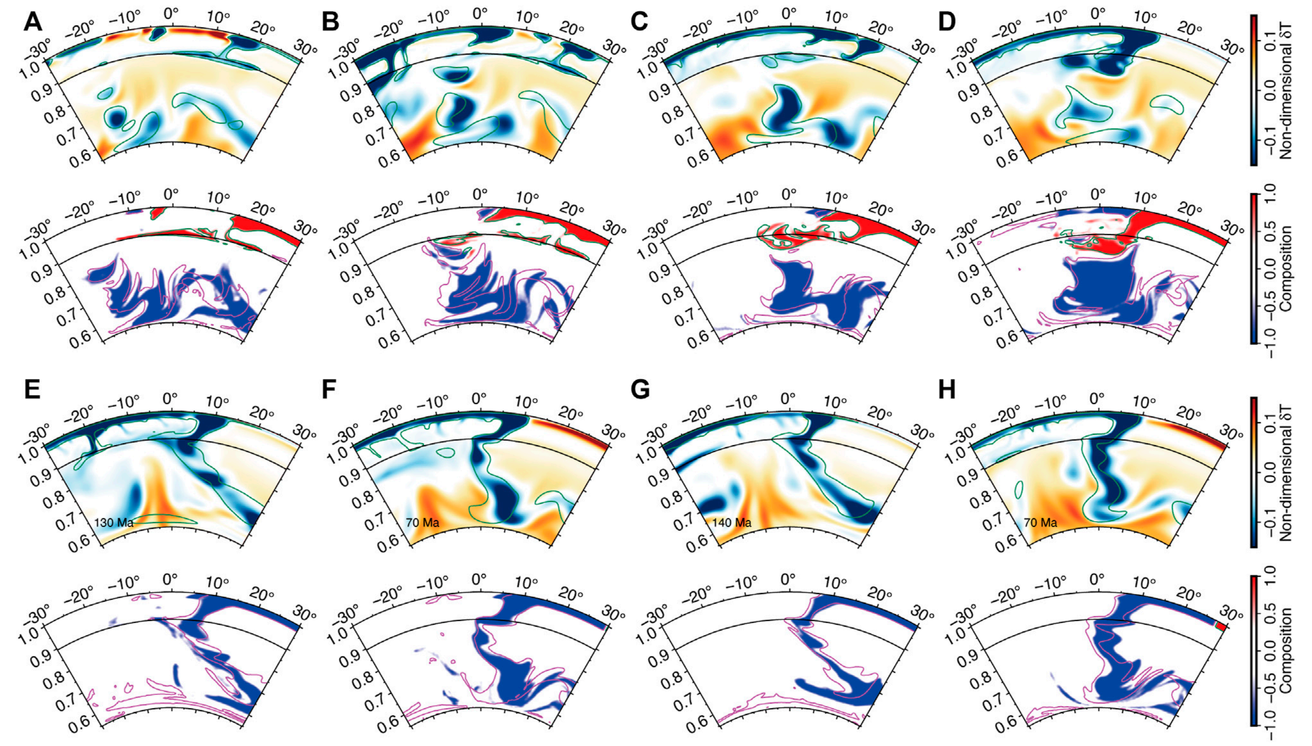

FIGURE 5 | Slab structures of the Izanagi-Pacific Plate beneath the Eastern Aisa for case 2 in which the plate motion history is from Young et al. (2019). **(A–D)** are present-day temperature and composition of slab structures for cross-sections P1-P4 in **Figure 1**, respectively. **(E,F)** are temperature and compositional fields from cross-sections through the NCC at 130 Ma and 70 Ma, respectively. **(G,H)** are temperature and compositional fields from cross-sections through the SCB at 140 Ma and 70 Ma, respectively. In panels of temperature fields, the green lines indicate contours of non-dimensional residual temperature δT of -0.05 from case 1 at the same time and cross-section. In panels of compositional fields, the magenta and green lines indicate compositional contours of -0.5 and 0.5 from case 1 which associated with the Izanagi slab and the Pacific slab, respectively.

compared to case 1. For example, there is no slab stagnation in the middle Mesozoic (~130 Ma) beneath the NCC for case 2 to facilitate the formation of a big mantle wedge (**Figure 5E**), while the horizontal extent of the stagnant slabs beneath the SCB (~140 Ma) in case 2 seems to be also smaller than that in case 1 (**Figures 4B**, **5G**). On the other hand, the slab dynamics of the Izanagi plate in the late Mesozoic time in case 2 is similar to case 1, in which the slabs tend to be temporarily stagnant above the transition zone beneath both the NCC and the SCB (**Figures 5F,H**).

There are also some debates on the subduction history on the Izanagi-Pacific plate: one view suggests that the ridge system of the Izanagi plate is parallel to the coastline and subducts to the west together with the Izanagi plate (e.g., Matthews et al., 2016), whereas another view suggests that the ridge system is perpendicular to the coastline, and the Izanagi plate subducts to the north and finally extinct (e.g., Yang, 2013). Case 3 uses the same model setup as case 1, except that the plate motion history after 90 Ma is replaced by that from Yang (2013), while the plate motion history before 90 Ma is the same as case 1 from Matthews et al. (2016). The general slab structures beneath Eastern Asia at present-day for case 3 are consistent with case 1, especially in the upper mantle depths (**Figures 6A–D**). However, from the late Mesozoic to early Cenozoic, the slabs of the Izanagi plate in case 3 tend to only subduct to the northern part of Eastern Asia, while in the southern part (e.g., beneath the SCB) there are no remnants of the Izanagi slabs left at the transition zone depths (**Figures 6E,F**). To the middle Cenozoic, there are no Izanagi slabs left in the upper mantle beneath the NCC and SCB in case 3 and the subducted slabs of the Pacific plate have reached the margin of the Eastern Asia region, which is earlier than that in case 1 (**Figures 3E**, **6G**). The slabs of the Pacific plate in the late Cenozoic for case 3 are similar to case 1 while all Izanagi slabs have sunk to the lower mantle (**Figures 3F**, **6H**).

In this study, we use a simple initial temperature condition and let the model run very earlier to obtain well-developed mantle convection and subduction pattern before the Mesozoic. To justify this model setup we also run another case, case 4, which uses the same initial condition as case 1 except that the model runs starting at 300 Ma with plate motion history from Matthews et al. (2016). In the Mesozoic time, the slab structures of the subducted Izanagi plate beneath the NCC and SCB are quite similar between case 4 and case 1, both in the upper mantle and in the lower mantle, except that there are some remnants of the Izanagi slabs near the core-mantle boundary in case 1 rather than in case 4 (**Figures 4**, **7**). The slab stagnation events of the Izanagi plate beneath the NCC (~130 Ma) and the SCB (~140 Ma) are also observed in case 4 which are consistent

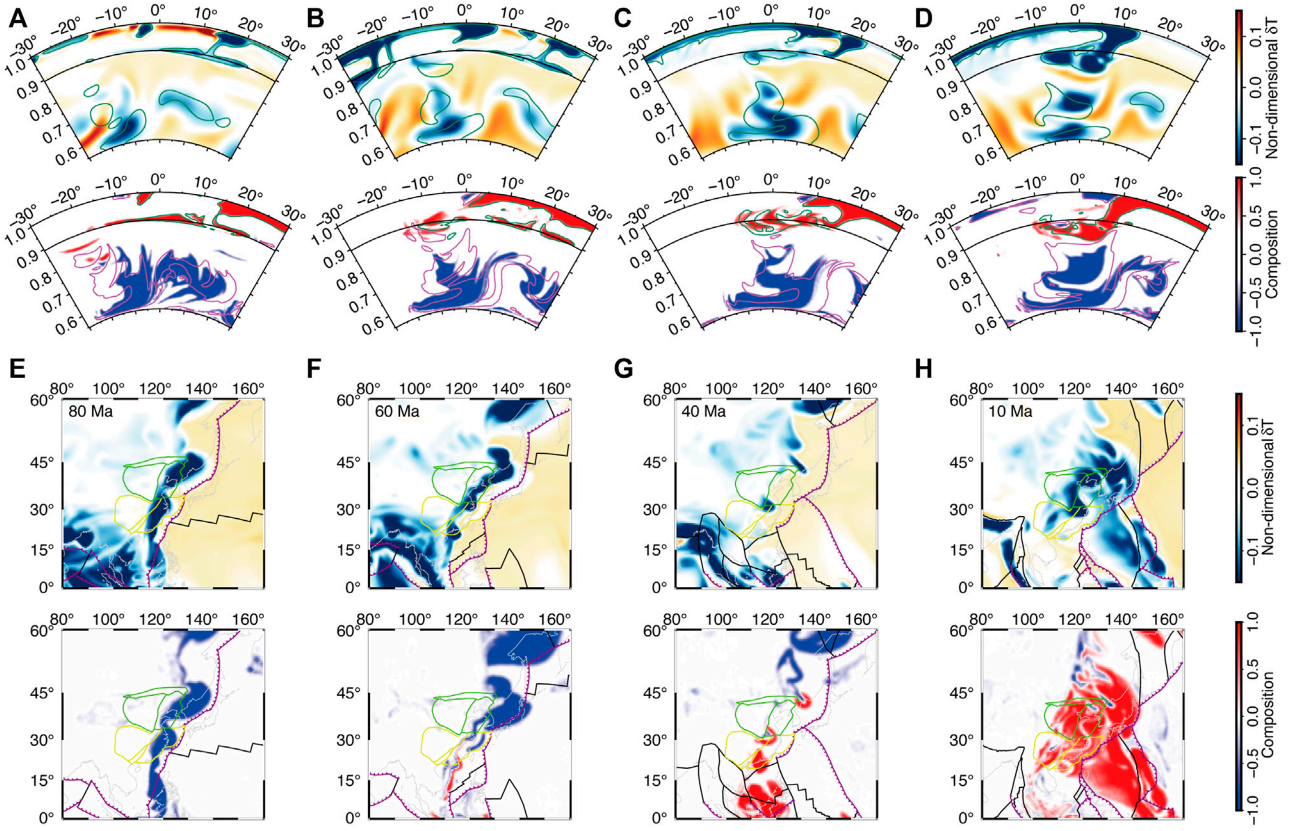

FIGURE 6 | Slab structures of the Izanagi-Pacific Plate beneath the Eastern Aisa for case 3 in which the plate motion history after 90 Ma is from Yang (2013). **(A–D)** are present-day temperature and composition of slab structures for cross-sections P1-P4 in **Figure 1**, respectively. **(E–H)** are some time snapshots of the residual temperature and composition fields at 670 km depth, respectively. Line descriptions are the same as that in **Figure 5**.

with that in case 1 (**Figure 7**). To the Cenozoic, the slab structures beneath the NCC and the SCB in case 4 are nearly identical to case 1 (**Figures 4**, **7**).

In most of our models, we include a weak viscosity layer that is associated with the phase transition at 670 km depth, which has been suggested to be crucial for slab stagnation in the mantle transition zone (e.g., Mao and Zhong, 2018). Case 5 uses the same model setup as case 1 except that the weak layer due to phase transition at 670 depth is removed. Although in case 5 the slab structures in the upper mantle beneath the NCC and SCB are similar with case 1, the slab stagnation of the subducted slabs has not well developed as prominent as that in case 1, especially for the Izanagi slabs in the Mesozoic time (**Figure 8**). However, the Pacific slabs are still mostly stagnant in the mantle transition zone even without the presence of the weak layer which is consistent with that in case 1 (**Figures 4**, **8**).

DISCUSSIONS

In this study, we perform global mantle convection models to examine the behaviors of the Izanagi plate and the Pacific plate since the Mesozoic time. We introduce a tracking procedure in numerical models to explicitly distinguish the slab materials of the two plates, which provides a more robust demonstration of slab dynamics in their evolutionary processes than identifying slabs solely from thermal structures as in many previous studies (e.g., Seton et al., 2015; Peng et al., 2021a; Liu et al., 2021). Our results show a general match of present-day slab structures beneath Eastern Asia with those inferred from seismic tomography observations, especially in the upper-to-middle mantle depths. Although a quantitative comparison between the predicted and seismic imaged slabs (e.g., Seton et al., 2015; Flament, 2019) could be helpful, our models still show a first-order consistency which is valid for the current study. There may be uncertainties in plate reconstruction models which could affect the structures of the subducting slabs, such as the poor-constrained motion history of the Izanagi plate, but the one we used here (i.e., Matthews et al., 2016) has reproduced the consistent mantle structures. In addition, in our models we use a uniform upper thermal boundary layer as the initial condition and let the models run fully self-consistent, rather than constraining the thermal structure of the lithosphere and the slabs in the upper mantle through data assimilation (e.g., Bower et al., 2015). However, we have performed models with different initial conditions which show little difference in the time evolution of slab structures in the upper mantle beneath Eastern Asia. Moreover, although double-sided subduction

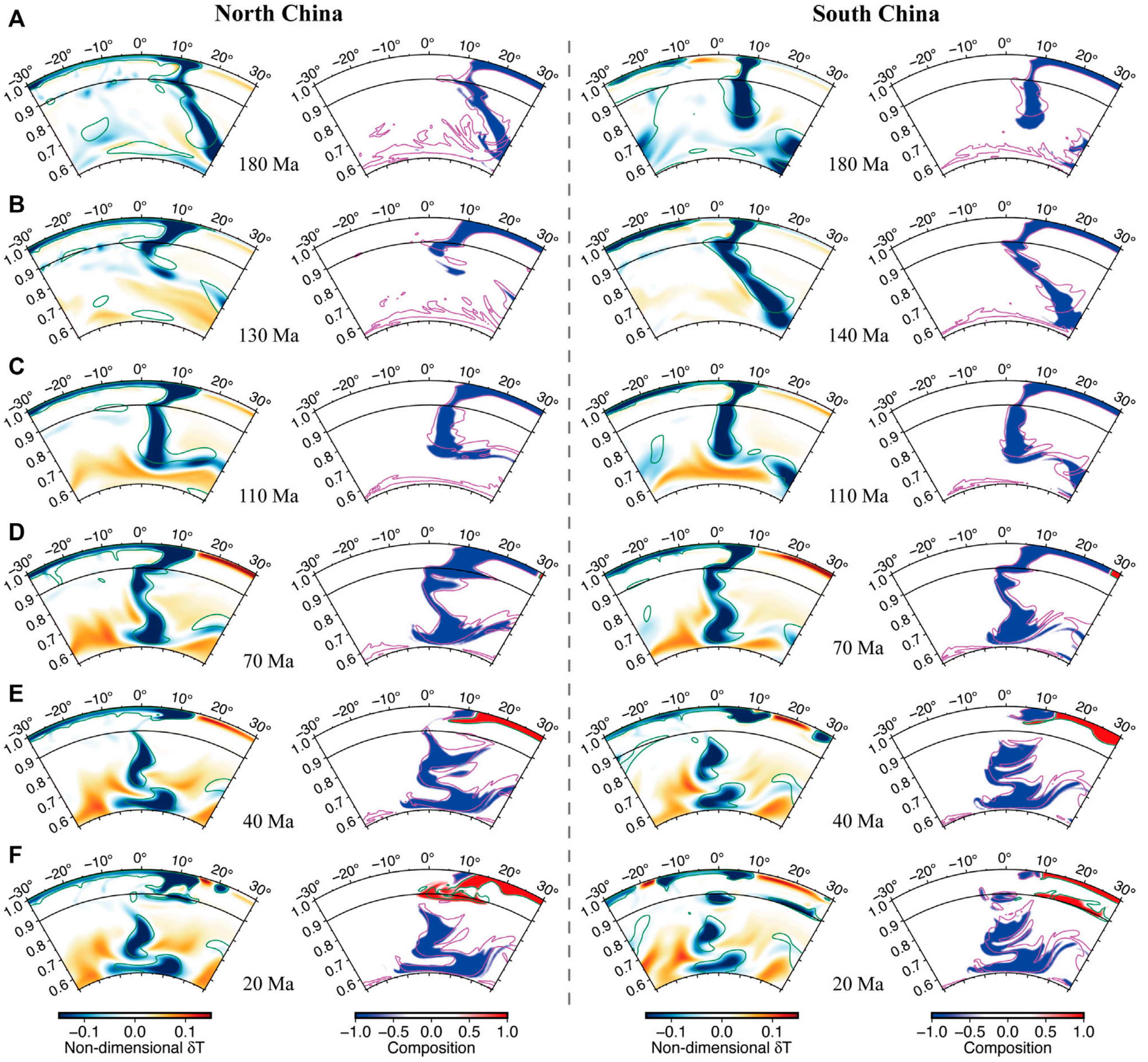

FIGURE 7 | Slab structures of the Izanagi-Pacific Plate beneath the North China Craton (left columns) and the South China Block (right columns) at some time snapshots for case 4. In **(A–F)**, the left and right columns are cross-sections of the residual temperature and composition fields across the NCC and the SCB, respectively. Line descriptions are the same as those in **Figure 5**.

could potentially develop in our models which can be restrained by imposing slab dip in shallower depths (e.g., Bower et al., 2015) or a lubricating oceanic crust (e.g., Hu et al., 2018) as in data assimilation method, our models have revealed a more fully self-consistent mantle convection system without introducing other artificial constraints.

We show that the subducted slabs of the Izanagi plate and the Pacific plate beneath Eastern Asia exhibit different slab behaviors since the Mesozoic time. In the Mesozoic, the subducted slabs of the Izanagi plate do not always directly pass through the 670-km boundary into the lower mantle, and sometimes they tend to first accumulate and spread laterally above the boundary before falling to the lower mantle. In some cases, the stagnation of the slabs promotes the formation of a big mantle wedge beneath the overriding lithosphere. In particular, we find that multiple stagnation events of the Izanagi slabs have occurred in the Mesozoic time beneath Eastern Asia, e.g., beneath the NCC at 150–120 Ma and 90–70 Ma, and beneath the SCB at 160–140 Ma and 90–70 Ma, respectively. These two stages of slab stagnation events correspond to the episodes of trench advance (170–150 Ma and 120–100 Ma) in plate reconstruction model (Matthews et al., 2016). Since the Mesozoic time, multistaged magmatism activities have been identified in Eastern Asia. For example, three main periods of magmatism formation are identified in NCC, e.g.,

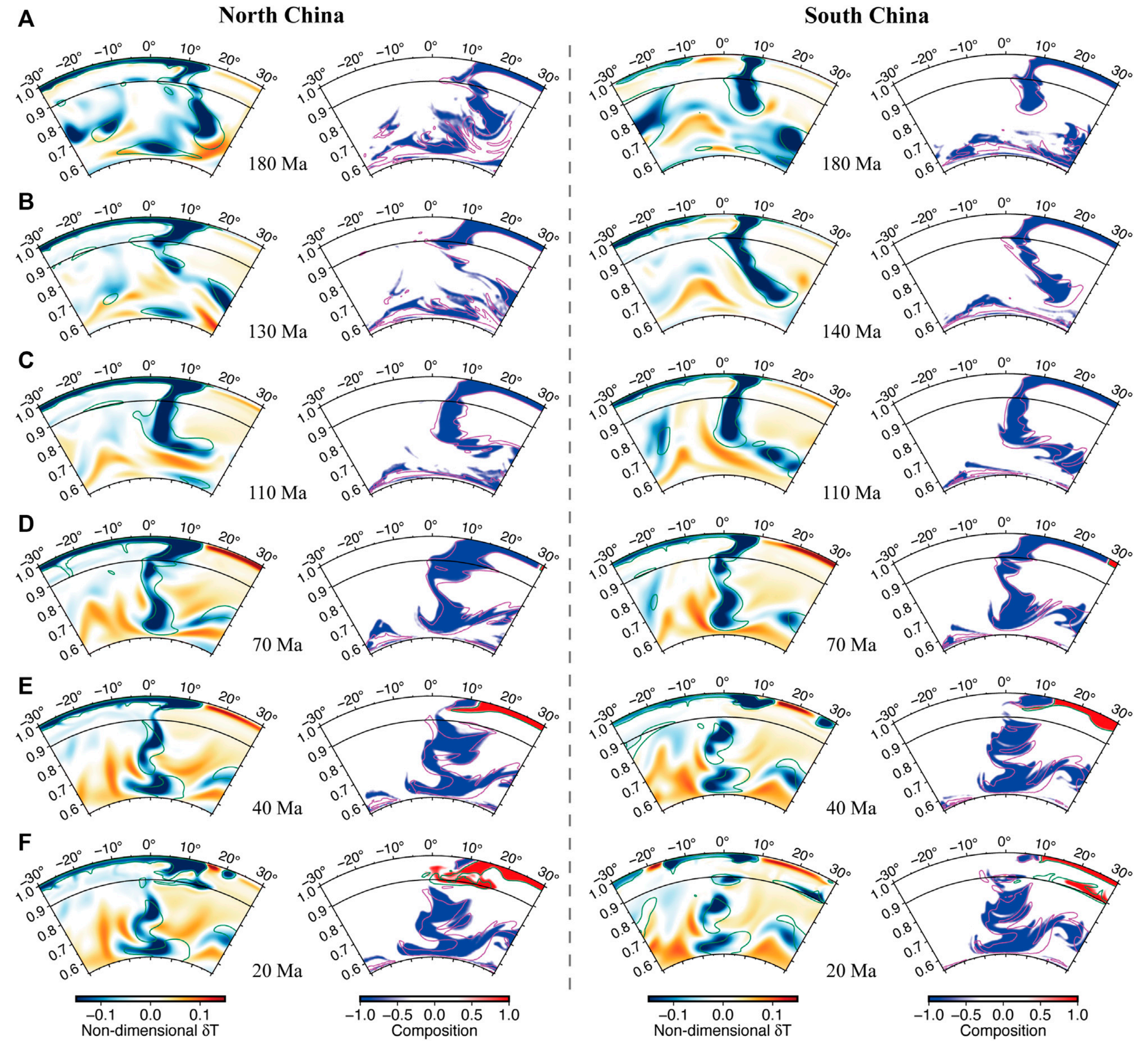

FIGURE 8 | Slab structures of the Izanagi-Pacific Plate beneath the North China Craton (left columns) and the South China Block (right columns) at some time snapshots for case 5. In **(A–F)**, the left and right columns are cross-sections of the residual temperature and composition fields across the NCC and the SCB, respectively. Line descriptions are the same as those in **Figure 5**.

160–140 Ma, 130–110 Ma and 100–80 Ma, with the peak period at ~125 Ma (Zhai et al., 2016). Regional igneous rocks in the SCB have been divided into four major emplacement episodes: 190–175 Ma, 165–155 Ma, 145–125 Ma and 105–95 Ma (Cao et al., 2021). The magmatism from Jurassic to Early Cretaceous in NCC has been attributed to flat-slab subduction followed by a rollback of the Izanagi plate during the late Mesozoic (Wu et al., 2019). However, the time periods of slab stagnation events beneath Eastern Asia in our numerical models also generally coincide with the episodes of magmatic activities in this region. The formation of such mantle wedge, which may lead to slab-triggered water release and vigorous mantle convective flow that could potentially weaken the lithosphere (e.g., Wang et al., 2016; Yang et al., 2017), is therefore supposed to be responsible for the Mesozoic evolution of the overriding plate that are characterized by magmatic activities and/or lithospheric instabilities in Eastern Asia (Ma and Xu, 2021). The intraplate magmatism along East Asia has disappeared in the Late Mesozoic (~80 Ma) and a flat slab model has been proposed to explain this magmatic termination (Peng et al., 2021b). In contrast, our numerical results still show a stagnation event at 90–70 Ma, but the resultant mantle wedge seems to be smaller than that in the middle Mesozoic (~130 Ma) which might be insufficient to cause large-scale magmatism. Moreover, the mantle wedge is later destroyed due to the subsequent sinking of the stagnant slabs within a duration timescale of ~10–20 Myrs, suggesting a transient nature of slab stagnation which has also been revealed by previous global mantle convection studies (Mao and Zhong, 2018). To the middle Cenozoic, most slabs of the Izanagi plate have fallen into the lower mantle and currently, there are few remnants preserved in the upper mantle beneath the Eastern Asia region, which is consistent with recent studies (Liu et al., 2017). In comparison, the subducted slabs of the Pacific plate mostly lie horizontally in the mantle transition zone depth beneath Eastern Asia, which is supposed to be responsible for the Cenozoic magmatic activities and lithosphere evolution in this area (e.g., Zhu et al., 2012; Liu et al., 2017).

In this study, we apply a weak viscosity layer associated with the 670-km phase transition in our models, in which the stagnant slabs remain coherent as they spread horizontally along the 670-km boundary rather than dissolve in the weak viscosity layer (**Supplementary Figure S5**). Although some regional models have suggested that the weak layer has a small effect on slab stagnation (e.g., Li et al., 2019), global models have demonstrated that the weak layer is crucial to explain not only the stagnant slabs in the transition zone (e.g., East Asia) but also other slab structures (e.g., North America) that are observed in seismic tomography studies (Mao and Zhong, 2018). Recent numerical studies, on the other hand, have argued that a pressure-driven Cenozoic mantle wind is the dominant mechanism for the formation of the stagnant slabs beneath East Asia (Peng et al., 2021a). The linkage between the Izanagi plate subduction and the tectonic evolution of East Asia is still controversial because the slab dynamics of the Izanagi plate have not been well resolved. Previous studies have proposed flat-slab subduction of the Izanagi plate to be responsible for the East Asian lithospheric evolution in Mesozoic time (Liu et al., 2021; Peng et al., 2021b). Our numerical results, which reveal multiple stagnation events of the Izanagi slab in Mesozoic time as an alternative mechanism, provide new insight into the Izanagi slab dynamics and its relation with the East Asian tectonics. On the other hand, there are some potential limitations in our models. We assume an incompressible mantle under the Boussinesq approximation which may overpredict slab volumes particularly in the lower mantle (Flament, 2019). In this study, we focus on slab dynamics in the upper mantle and we suspect mantle compressibility may have a small effect on upper mantle slab dynamics.

CONCLUSION

Our 3-D global geodynamic model reproduces the typical slab structures as observed by seismic tomographic imaging beneath Eastern Asia. Our model also shows that multiple slab stagnation events, which facilitate the formation of big mantle wedge beneath Eastern Asia, have developed during the subduction of the Izanagi plate in Mesozoic time with a timescale on the order of tens of million years. Importantly, the duration times of those slab stagnation events generally coincide with the episodes of magmatic activities in Eastern Asia. Our model provides an attractive relationship between the subduction of the Izanagi-Pacific plate and the tectonic evolution of Eastern Asia.

DATA AVAILABILITY STATEMENT

The seismic tomography models GAP_P4 and TX2019slab are available at the websites http://d-earth.jamstec.go.jp/ and IRIS website http://ds.iris.edu/ds/products/emc-tx2019slab/, respectively. The numerical models are performed using modified CitcomS (www.geodynamics.org) that is available at https://github.com/bchwu/plate_tracer.

AUTHOR CONTRIBUTIONS

BW, JH, and YW contributed to the conception and design of the study. BW, JH, and YW designed the model. BW ran the model and analyzed the results. All authors contributed to writing the manuscript and approved the submitted version.

FUNDING

The work is supported by National Natural Science Foundation of China (42074105; 41674096; 41764004) and the National Key Scientific and Technological Infrastructure project “Earth System Science Numerical Simulator Facility” (EarthLab).

ACKNOWLEDGMENTS

We thank Editor Lijun Liu, Jiashun Hu and Nicolas Flament for their insightful and constructive reviews and comments that significantly improve the paper. We also thank Profs. Mingming Li and Yang Li for helping improve the paper a lot. Figures are drawn using the Generic Mapping Tools (GMT, www.soest.hawaii.edu/gmt/).

SUPPLEMENTARY MATERIAL

The Supplementary Material for this article can be found online at: https://www.frontiersin.org/articles/10.3389/feart.2022.829163/full#supplementary-material

REFERENCES

Bower, D. J., Gurnis, M., and Flament, N. (2015). Assimilating Lithosphere and Slab History in 4-D Earth Models. *Phys. Earth Planet. Interiors* 238, 8–22. doi:10.1016/j.pepi.2014.10.013

Cao, X., Flament, N., Li, S., and Müller, R. D. (2021). Spatio-temporal Evolution and Dynamic Origin of Jurassic-Cretaceous Magmatism in the South China Block. *Earth-Science Rev.* 217, 103605. doi:10.1016/j.earscirev.2021.103605

Christensen, U. R., and Yuen, D. A. (1985). Layered Convection Induced by Phase Transitions. *J. Geophys. Res.* 90 (Nb12), 10291–10300. doi:10.1029/JB090iB12p10291

Domeier, M., and Torsvik, T. H. (2014). Plate Tectonics in the Late Paleozoic. *Geosci. Front.* 5 (3), 303–350. doi:10.1016/j.gsf.2014.01.002

Flament, N. (2019). Present-day Dynamic Topography and Lower-Mantle Structure from Palaeogeographically Constrained Mantle Flow Models. *Geophys. J. Int.* 216 (3), 2158–2182. doi:10.1093/gji/ggy526

Fukao, Y., Obayashi, M., Nakakuki, T., and Grp, D. S. P. (2009). Stagnant Slab: A Review. *Annu. Rev. Earth Planet. Sci.* 37, 19–46. doi:10.1146/annurev.earth.36.031207.124224

Fukao, Y., and Obayashi, M. (2013). Subducted Slabs Stagnant above, Penetrating through, and Trapped below the 660 Km Discontinuity. *J. Geophys. Res. Solid Earth* 118 (11), 5920–5938. doi:10.1002/2013jb010466

Gibert, B., Seipold, U., Tommasi, A., and Mainprice, D. (2003). Thermal Diffusivity of Upper Mantle Rocks: Influence of Temperature, Pressure, and the Deformation Fabric. *J. Geophys. Res.* 108, 63–69. doi:10.1029/2002JB002108

Hu, J., Liu, L. J., Liu, L., and Zhou, Q. (2018). Reproducing Past Subduction and Mantle Flow Using High-Resolution Global Convection Models. *Earth Planet. Phys.* 2 (3), 189–207. doi:10.26464/epp2018019

Katsura, T., Yokoshi, S., Kawabe, K., Shatskiy, A., Manthilake, M. A. G. M., Zhai, S., et al. (2009). P-V-T Relations of the MgSiO3perovskite Determined by *In Situ* X-ray Diffraction Using a Large-Volume High-Pressure Apparatus. *Geophys. Res. Lett.* 36, L01305. doi:10.1029/2009GL039318

Lay, T., Hernlund, J., and Buffett, B. A. (2008). Core-mantle Boundary Heat Flow. *Nat. Geosci* 1, 25–32. doi:10.1038/ngeo.2007.44

Li, S., Suo, Y., Li, X., Zhou, J., Santosh, M., Wang, P., et al. (2019). Mesozoic Tectono-Magmatic Response in the East Asian Ocean-Continent Connection Zone to Subduction of the Paleo-Pacific Plate. *Earth-Science Rev.* 192, 91–137. doi:10.1016/j.earscirev.2019.03.003

Li, X.-Y., Zheng, J.-P., Ma, Q., Xiong, Q., Griffin, W. L., and Lu, J.-G. (2014a). From Enriched to Depleted Mantle: Evidence from Cretaceous Lamprophyres and Paleogene Basaltic Rocks in Eastern and central Guangxi Province, Western Cathaysia Block of South China. *Lithos* 184-187, 300–313. doi:10.1016/j.lithos.2013.10.039

Li, X.-Y., Zheng, J.-P., Sun, M., Pan, S.-K., Wang, W., and Xia, Q.-K. (2014b). The Cenozoic Lithospheric Mantle beneath the interior of South China Block: Constraints from Mantle Xenoliths in Guangxi Province. *Lithos* 210-211, 14–26. doi:10.1016/j.lithos.2014.09.028

Li, Z.-H., Gerya, T., and Connolly, J. A. D. (2019). Variability of Subducting Slab Morphologies in the Mantle Transition Zone: Insight from Petrological-Thermomechanical Modeling. *Earth-Science Rev.* 196, 102874. doi:10.1016/j.earscirev.2019.05.018

Liu, C.-Z., Liu, Z.-C., Wu, F.-Y., and Chu, Z.-Y. (2012). Mesozoic Accretion of Juvenile Sub-continental Lithospheric Mantle beneath South China and its Implications: Geochemical and Re-os Isotopic Results from Ningyuan Mantle Xenoliths. *Chem. Geology.* 291, 186–198. doi:10.1016/j.chemgeo.2011.10.006

Liu, L., Peng, D., Liu, L., Chen, L., Li, S., Wang, Y., et al. (2021). East Asian Lithospheric Evolution Dictated by Multistage Mesozoic Flat-Slab Subduction. *Earth-Science Rev.* 217, 103621. doi:10.1016/j.earscirev.2021.103621

Liu, S., Ma, P., Zhang, B., and Gurnis, M. (2021). The Horizontal Slab beneath East Asia and its Subdued Surface Dynamic Response. *J. Geophys. Res. Solid Earth* 126 (3), e2020JB021156. doi:10.1029/2020JB021156

Liu, X., Zhao, D., Li, S., and Wei, W. (2017). Age of the Subducting Pacific Slab beneath East Asia and its Geodynamic Implications. *Earth Planet. Sci. Lett.* 464, 166–174. doi:10.1016/j.epsl.2017.02.024

Lu, C., Grand, S. P., Lai, H., and Garnero, E. J. (2019). TX2019slab: A New P and S Tomography Model Incorporating Subducting Slabs. *J. Geophys. Res. Solid Earth* 124 (11), 11549–11567. doi:10.1029/2019JB017448

Ma, P., Liu, S., Gurnis, M., and Zhang, B. (2019). Slab Horizontal Subduction and Slab Tearing beneath East Asia. *Geophys. Res. Lett.* 46 (10), 5161–5169. doi:10.1029/2018gl081703

Ma, Q., and Xu, Y.-G. (2021). Magmatic Perspective on Subduction of Paleo-Pacific Plate and Initiation of Big Mantle Wedge in East Asia. *Earth-Science Rev.* 213, 103473. doi:10.1016/j.earscirev.2020.103473

Mao, W., and Zhong, S. (2018). Slab Stagnation Due to a Reduced Viscosity Layer beneath the Mantle Transition Zone. *Nat. Geosci* 11 (11), 876–881. doi:10.1038/s41561-018-0225-2

Matthews, K. J., Maloney, K. T., Zahirovic, S., Williams, S. E., Seton, M., and Müller, R. D. (2016). Global Plate Boundary Evolution and Kinematics since the Late Paleozoic. *Glob. Planet. Change* 146, 226–250. doi:10.1016/j.gloplacha.2016.10.002

McNamara, A. K., and Zhong, S. (2004). Thermochemical Structures within a Spherical Mantle: Superplumes or Piles. *J. Geophys. Res.* 109 (B7), B07402. doi:10.1029/2003jb002847

Meng, Q.-R. (2003). What Drove Late Mesozoic Extension of the Northern China–Mongolia Tract? *Tectonophysics* 369 (3), 155–174. doi:10.1016/S0040-1951(03)00195-1

Mitrovica, J. X., and Forte, A. M. (2004). A New Inference of Mantle Viscosity Based upon Joint Inversion of Convection and Glacial Isostatic Adjustment Data. *Earth Planet. Sci. Lett.* 225 (1-2), 177–189. doi:10.1016/j.epsl.2004.06.005

Müller, R. D., Cannon, J., Qin, X., Watson, R. J., Gurnis, M., Williams, S., et al. (2018). GPlates: Building a Virtual Earth through Deep Time. *Geochem. Geophys. Geosyst.* 19 (7), 2243–2261. doi:10.1029/2018GC007584

Müller, R. D., Zahirovic, S., Williams, S. E., Cannon, J., Seton, M., Bower, D. J., et al. (2019). A Global Plate Model Including Lithospheric Deformation along Major Rifts and Orogens since the Triassic. *Tectonics* 38 (6), 1884–1907. doi:10.1029/2018TC005462

Peng, D., Liu, L., Hu, J., Li, S., and Liu, Y. (2021a). Formation of East Asian Stagnant Slabs Due to a Pressure-Driven Cenozoic Mantle Wind Following Mesozoic Subduction. *Geophys. Res. Lett.* 48, e2021GL094638. doi:10.1029/2021GL094638

Peng, D., Liu, L., and Wang, Y. (2021b). A Newly Discovered Late-Cretaceous East Asian Flat Slab Explains its Unique Lithospheric Structure and Tectonics. *JGR Solid Earth* 126 (10), e2021JB022103. doi:10.1029/2021JB022103

Seton, M., Flament, N., Whittaker, J., Müller, R. D., Gurnis, M., and Bower, D. J. (2015). Ridge Subduction Sparked Reorganization of the Pacific Plate-Mantle System 60-50 Million Years Ago. *Geophys. Res. Lett.* 42, 1732–1740. doi:10.1002/2015GL063057

Sorokin, A. A., Zaika, V. A., Kovach, V. P., Kotov, A. B., Xu, W., and Yang, H. (2020). Timing of Closure of the Eastern Mongol-Okhotsk Ocean: Constraints from U-Pb and Hf Isotopic Data of Detrital Zircons from Metasediments along the Dzhagdy Transect. *Gondwana Res.* 81, 58–78. doi:10.1016/j.gr.2019.11.009

Sun, W., Ding, X., Hu, Y.-H., and Li, X.-H. (2007). The golden Transformation of the Cretaceous Plate Subduction in the West Pacific. *Earth Planet. Sci. Lett.* 262 (3), 533–542. doi:10.1016/j.epsl.2007.08.021

Wang, F., Zhou, X.-H., Zhang, L.-C., Ying, J.-F., Zhang, Y.-T., Wu, F.-Y., et al. (2006). Late Mesozoic Volcanism in the Great Xing'an Range (NE China): Timing and Implications for the Dynamic Setting of NE Asia. *Earth Planet. Sci. Lett.* 251 (1), 179–198. doi:10.1016/j.epsl.2006.09.007

Wang, Z., Kusky, T. M., and Capitanio, F. A. (2016). Lithosphere Thinning Induced by Slab Penetration into a Hydrous Mantle Transition Zone. *Geophys. Res. Lett.* 43 (22), 11567–11577. doi:10.1002/2016GL071186

Wang, Y., Zhou, L., Liu, S., Li, J., and Yang, T. (2018). Post-cratonization Deformation Processes and Tectonic Evolution of the North China Craton. *Earth-Science Rev.* 177, 320–365. doi:10.1016/j.earscirev.2017.11.017

Wu, F., Lin, J., Wilde, S., Zhang, X., and Yang, J. (2005). Nature and Significance of the Early Cretaceous Giant Igneous Event in Eastern China. *Earth Planet. Sci. Lett.* 233 (1-2), 103–119. doi:10.1016/j.epsl.2005.02.019

Wu, F.-Y., Yang, J.-H., Xu, Y.-G., Wilde, S. A., and Walker, R. J. (2019). Destruction of the North China Craton in the Mesozoic. *Annu. Rev. Earth Planet. Sci.* 47 (1), 173–195. doi:10.1146/annurev-earth-053018-060342

Xu, Y., Li, H., Hong, L., Ma, L., Ma, Q., and Sun, M. (2018). Generation of Cenozoic Intraplate Basalts in the Big Mantle Wedge under Eastern Asia. *Sci. China Earth Sci.* 61 (7), 869–886. doi:10.1007/s11430-017-9192-y

Xu, Z., and Zheng, Y.-F. (2017). Continental Basalts Record the Crust-Mantle Interaction in Oceanic Subduction Channel: A Geochemical Case Study from Eastern China. *J. Asian Earth Sci.* 145, 233–259. doi:10.1016/j.jseaes.2017.03.010

Yang, J., Zhao, L., Kaus, B. J. P., Lu, G., Wang, K., and Zhu, R. (2018). Slab-triggered Wet Upwellings Produce Large Volumes of Melt: Insights into the Destruction of the North China Craton. *Tectonophysics* 746, 266–279. doi:10.1016/j.tecto.2017.04.009

Yang, Y.-T. (2013). An Unrecognized Major Collision of the Okhotomorsk Block with East Asia during the Late Cretaceous, Constraints on the Plate Reorganization of the Northwest Pacific. *Earth-Science Rev.* 126, 96–115. doi:10.1016/j.earscirev.2013.07.010

Young, A., Flament, N., Maloney, K., Williams, S., Matthews, K., Zahirovic, S., et al. (2019). Global Kinematics of Tectonic Plates and Subduction Zones since the Late Paleozoic Era. *Geosci. Front.* 10 (3), 989–1013. doi:10.1016/j.gsf.2018.05.011

Zhai, M., Zhang, Y., Zhang, X., Wu, F., Peng, P., Li, Q., et al. (2016). Renewed Profile of the Mesozoic Magmatism in Korean Peninsula: Regional Correlation and Broader Implication for Cratonic Destruction in the North China Craton. *Sci. China Earth Sci.* 59 (12), 2355–2388. doi:10.1007/s11430-016-0107-0

Zhao, D., Yu, S., and Ohtani, E. (2011). East Asia: Seismotectonics, Magmatism and Mantle Dynamics. *J. Asian Earth Sci.* 40 (3), 689–709. doi:10.1016/j.jseaes.2010.11.013

Zhong, S., and Gurnis, M. (1994). Role of Plates and Temperature-dependent Viscosity in Phase Change Dynamics. *J. Geophys. Res.* 99 (B8), 15903–15917. doi:10.1029/94JB00545

Zhong, S., McNamara, A., Tan, E., Moresi, L., and Gurnis, M. (2008). A Benchmark Study on Mantle Convection in a 3-D Spherical Shell Using CitcomS. *Geochem. Geophys. Geosyst.* 9, a–n. doi:10.1029/2008gc002048

Zhu, R., and Xu, Y. (2019). The Subduction of the West Pacific Plate and the Destruction of the North China Craton. *Sci. China Earth Sci.* 62 (9), 1340–1350. doi:10.1007/s11430-018-9356-y

Zhu, R., Xu, Y., Zhu, G., Zhang, H., Xia, Q., and Zheng, T. (2012). Destruction of the North China Craton. *Sci. China Earth Sci.* 55 (10), 1565–1587. doi:10.1007/s11430-012-4516-y

Conflict of Interest: The authors declare that the research was conducted in the absence of any commercial or financial relationships that could be construed as a potential conflict of interest.

frontiers in Earth Science

ORIGINAL RESEARCH
published: 09 March 2022
doi: 10.3389/feart.2022.829300

Numerical Investigation on the Dynamic Evolution of Intra-Crustal Continental Delamination

Rui Qi[1], *Jie Liao*[1,2]*, *Xiaohui Liu*[1,2] *and Rui Gao*[1,2]*

[1]*School of Earth Sciences and Engineering, Sun Yat-Sen University, Guangzhou, China,* [2]*Southern Marine Science and Engineering Guangdong Laboratory (Zhuhai), Zhuhai, China*

Delamination often occurs in continental regions, through which process the lithospheric mantle detaches from the continental crust and sinks into the underlying asthenospheric mantle. Various modes of continental delamination are proposed, including the typical mode of delamination along the Moho and the newly proposed delamination along the mid-lithospheric discontinuity. Geological and geophysical observations reveal the possibility of an alternative mode of delamination, i.e., intra-crustal continental delamination, which is rarely studied. Using the 2D thermo-mechanical coupled geodynamical models, we systemically study the dynamic evolution of the intra-crustal continental delamination. Model results suggest that the intra-crustal continental delamination develops along the base of the upper crust, promoted by the intra-crustal decoupling, i.e., the mechanical strength decoupling between the upper and lower crust. The three physical parameters, i.e., the upper crustal thickness, the lower crustal rheology, and the initial Moho temperature all affect intra-crustal strength decoupling, and thus influence continental delamination. Combining with geological and geophysical observations, we speculate that intra-crustal continental delamination taking place along the upper and lower crustal interface is a possible way of continental destruction.

Keywords: intra-crustal continental delamination, crustal strength decoupling, geodynamical numeric modeling, intra-crustal decoupling, continental delamination

Edited by:
Zhong-Hai Li,
University of Chinese Academy of Sciences, China

Reviewed by:
Yujun Sun,
Chinese Academy of Geological Science, China
Huilin Wang,
Huazhong University of Science and Technology, China

Correspondence:
Jie Liao
liaojie5@mail.sysu.edu.cn
Rui Gao
gaorui66@mail.sysu.edu.cn

Specialty section:
This article was submitted to Structural Geology and Tectonics, a section of the journal Frontiers in Earth Science

Received: *05 December 2021*
Accepted: *24 January 2022*
Published: *09 March 2022*

Citation:
Qi R, Liao J, Liu X and Gao R (2022) Numerical Investigation on the Dynamic Evolution of Intra-Crustal Continental Delamination. Front. Earth Sci. 10:829300. doi: 10.3389/feart.2022.829300

INTRODUCTION

The destruction of continental lithosphere through delamination is often proposed. The critical conditions for the occurrence of delamination are density contrast (i.e., denser lithospheric mantle than the surrounding area) and a weak interface (Bird, 1978, 1979; Kay and Mahlburg Kay, 1993; Göğüş and Pysklywec, 2008; Faccenda et al., 2009; Burov, 2011; Krystopowicz and Currie, 2013; Magni et al., 2013; Göğüş et al., 2016; Beall et al., 2017; Göğüş and Ueda, 2018). The typical mode of continental delamination is that the relatively denser lithospheric mantle detaches and peels away from the overlying continental crust along the mechanically weak crust-mantle interface, i.e., the Moho (**Figure 1A**; Bird, 1978, Bird, 1979). Continental delamination along Moho is the most popular mode, and the proposed natural examples are the Western Mediterranean and the Eastern Anatolia (Göğüş and Pysklywec, 2008; Thurner et al., 2014). The previous geodynamical modeling studies have widely investigated this type of delamination and suggested that, for instance, a weak interface along Moho, low density of the lower crust, denser lithospheric mantle than the

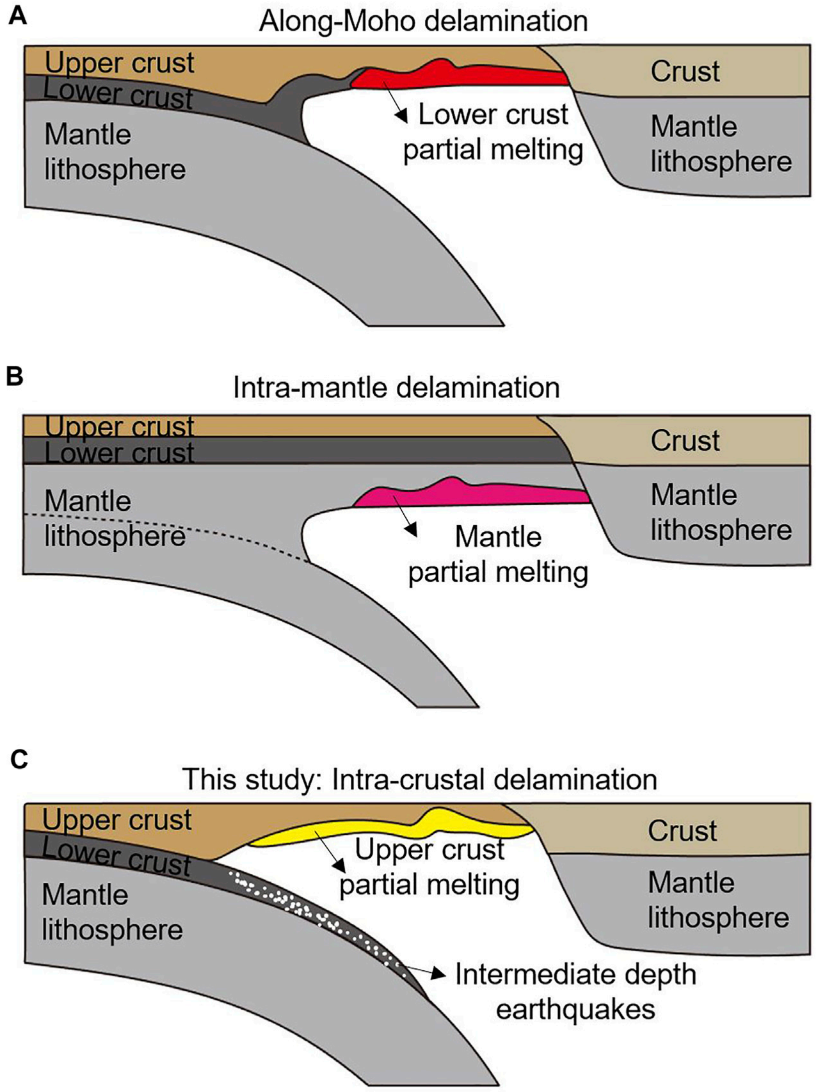

FIGURE 1 | Possible modes of continental delamination. **(A)** Along-Moho delamination. **(B)** Intra-mantle delamination. **(C)** The alternative mode of delamination: intra-crustal delamination. The earthquake data is from Fillerup et al. (2010).

asthenospheric mantle (Göğüş et al., 2016, 2011; Göğüş and Pysklywec, 2008; Li et al., 2016), low viscosity of the lower crust (Magni et al., 2013), and rapid upwelling of the partially molten mantle in the mantle wedge (Faccenda et al., 2009) are the key model parameters promoting delamination. However, in the regions where the lower crust is mechanically coupled with the underlying lithospheric mantle, the Moho may not represent a mechanical weak interface, and continental delamination may happen in different depth.

The recent studies proposed that continental delamination may happen in mid-lithospheric depth along a mid-lithospheric discontinuity (**Figure 1B**; Wang et al., 2018; Wang and Kusky, 2019). The intra-mantle delamination is proposed based on the North China Craton through geodynamical modeling (Wang et al., 2018). The modeling results indicated that the intra-mantle delamination needs smaller resultant stress and thus occurs relatively easier than that along Moho. Besides, the dynamics of intra-mantle delamination differs from the along-Moho delamination, since the former one may recycle larger amount of continental lithosphere into deep mantle (Wang et al., 2018).

The alternative scenario of delamination, termed as intra-crustal continental delamination (**Figure 1C**), is proposed in this study based on geological and geophysical observations which reveal decoupled deformation of the upper and lower crust (**Figure 2**). The possible natural examples of intra-crustal delamination are proposed in the Northern Apennines and in the southeast Carpathians (**Figure 2A**) based on the thin continental crust underneath the orogenic belt (i.e., due to the removal of the lower crust) and the subducting slabs with intermediate depth earthquakes possibly occurred in the

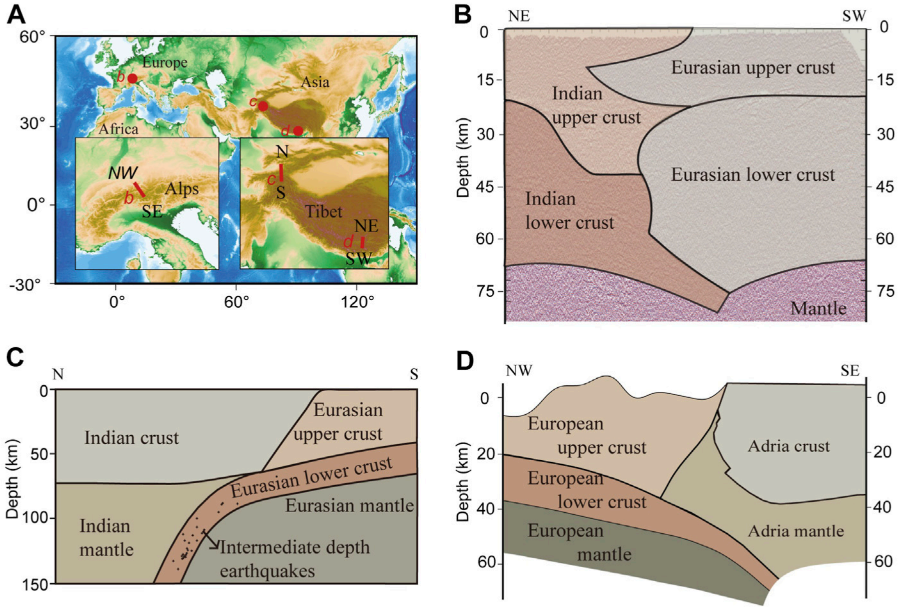

FIGURE 2 | Natural examples showing decoupled crustal deformation in collisional zones. **(A)** Locations of the Alpine orogen, the Northwestern and Southeastern Tibetan orogen. **(B–C)** Decoupled upper and lower crustal deformation in the Tibetan Plateau interpreted based on the deep seismic reflection data (Gao et al., 2016; Guo et al., 2017; Dong et al., 2020) and tele-seismic data (Schneider, 2013, 2019). **(D)** Decoupled upper and lower crustal deformation in the Alpine orogen (Schmid et al., 2017).

subducted lower crust (**Figure 1C**; Pauselli et al., 2006; Fillerup et al., 2010; Piana Agostinetti and Faccenna, 2018). The possibility of intra-crustal delamination is also supported by the widely observed intra-crustal decoupled crustal deformation (**Figure 2**). For instance, decoupled upper and lower crustal deformation is revealed by deep seismic reflection profiles in the central Himalayan Orogen (**Figures 2B,C**), where the lower crust of the Indian plate detached from the upper crust and subducted attached to the lithospheric mantle (Gao et al., 2016; Guo et al., 2017; Liang et al., 2018; Dong et al., 2020). This phenomenon is also observed in the Alpine orogeny (**Figure 2D**), where the upper crust detached from the lower crust during continental collision (Bousquet and Goff, 1997; Schmid et al., 2017). The possible reason of decoupled upper and lower crustal deformation is intra-crustal strength decoupling (Liao et al., 2017, 2018; Vogt et al., 2017, 2018), which may promote the intra-crustal delamination.

The intra-crustal delamination is a possible scenario, but its dynamic evolution remains poorly understood. In this study, we aim to systematically study the intra-crustal delamination using geodynamical numeric modeling, with specific attention paid on the influence of the controlling physical parameters. Model results are further discussed based on natural observations.

METHODS

Numerical Method

We use the thermomechanical coupled numerical code I2VIS (Gerya and Yuen, 2003, 2007) to simulate continental delamination following oceanic subduction. Assuming an incompressible media in a fully staggered grid, I2VIS uses the finite-differences and marker-in-cell techniques to solve the mass, momentum and energy conservation equations:

$$\frac{\partial v_i}{\partial x_i} = 0 \tag{1}$$

$$\frac{\partial \sigma'_{ij}}{\partial x_j} - \frac{\partial P_i}{\partial x_i} = -\rho g_i \tag{2}$$

$$\rho C_p\left(\frac{dT}{dt}\right) = \frac{\partial}{\partial x_i}\left(k\frac{\partial T}{\partial x_i}\right) + H_s + H_r + H_a + H_L \tag{3}$$

where v is velocity, $\sigma^{'}$ is the deviatoric stress tensor, P is the pressure, ρ is the density, g is the gravitational acceleration, C_p is the heat capacity, T is the temperature, k is the thermal conductivity. H_s is shear heating, H_a is the adiabatic heating, H_r is the radioactive heating with a constant value for each rock, and H_L is the latent heating included implicitly by increasing the effective heat capacity and thermal expansion of the partially crystallized/molten rocks (Burg and Gerya, 2005).

We employ visco-plastic rheology in our numerical models. The non-Newtonian viscous rheology (**Eq. 4**) depends on strain rate, pressure and temperature, where η_{ductile} is the ductile viscosity, $\dot{\varepsilon}_{\text{II}}$ is the square root of the second invariant of strain rate, A_D is the Material constants, E is the activation energy, V is the activation volume, n is the power label of the deviatoric stress, these four parameters can be determined by the experimental petrology. Yield stress (σ_{yield}) is described by a Drucker-Prager yield criterion where C is the rock cohesion and μ is the effective friction coefficient, the yielding stress σ is only depend on pressure (P). Plastic viscosity

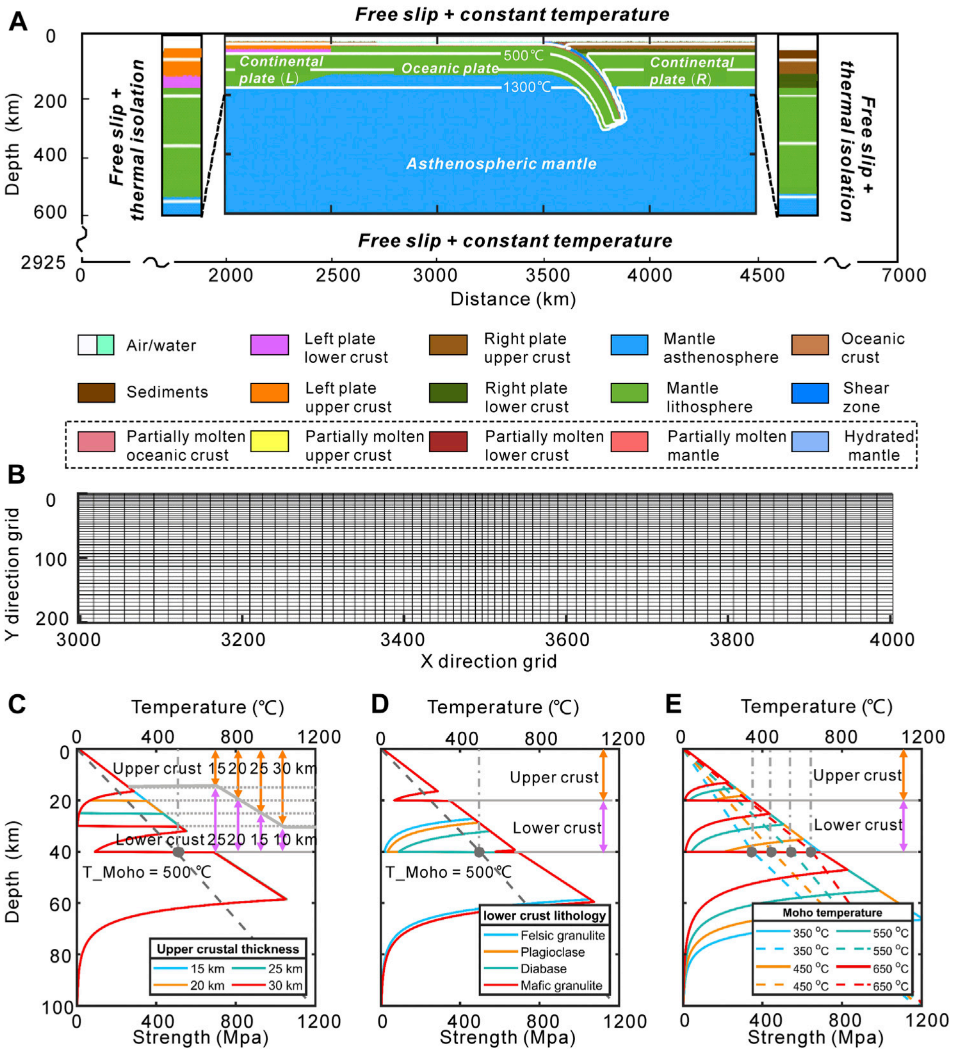

FIGURE 3 | Model setup. **(A)** Initial model configuration. A slab nose is initially imposed in the model to drive oceanic subduction. Colors in the dotted box are newly formed rocks. **(B)** Grid of a part of the model. **(C)** Lithospheric mantle strength with different crustal thickness. **(D)** Lithospheric mantle strength with different lower crustal lithology. **(E)** Lithospheric mantle strength with different Moho temperature.

(η_{plastic}) is computed based on the square root of the second invariant of strain rate ($\dot{\varepsilon}_{\text{II}}$). The effective viscosity (η_{eff}) of rocks is the minimum of the ductile viscosity and plastic viscosity (Ranalli, 1995). See further explanation of variables/symbols in **Supplementary Table S1** in the supplement (Kirby and Kronenberg, 1987; Wilks and Carter, 1990; Clauser and Huenges, 1995; Ranalli, 1995; Turcotte and Schubert, 2002; Afonso and Ranalli, 2004).

$$\eta_{\text{ductile}} = (\dot{\varepsilon}_{\text{II}})^{\frac{1-n}{n}} (A_{\text{D}})^{-\frac{1}{n}} exp\left(\frac{E+PV}{nRT}\right) \tag{4}$$

$$\sigma_{\text{yield}} = C + P\mu \tag{5}$$

$$\eta_{\text{plastic}} = \frac{\sigma_{\text{yield}}}{2\dot{\varepsilon}_{\text{II}}} \tag{6}$$

$$\eta_{\text{eff}} = \min\left(\eta_{\text{ductile}}, \eta_{\text{plastic}}\right) \tag{7}$$

We consider partial melting of rocks in the models. Partial melting of the solid rock is a function (**Eq. 8**) of temperature and pressure (Schmidt and Poli, 1998), where M is the volumetric melt fraction, T_{solidus} and T_{liquidus} are the solidus and liquids, respectively.

$$M = \begin{cases} 0 & T \leq T_{\text{solidus}} \\ \dfrac{T - T_{\text{solidus}}}{T - T_{\text{liquidus}}} & T_{\text{solidus}} < T < T_{\text{liquidus}} \\ 1 & T \geq T_{\text{liquidus}} \end{cases} \tag{8}$$

Model Setup

The initial model setup is shown in **Figure 3**. The dimension of the model box is 7,000 × 2,925 km consisting of 501 × 451

TABLE 1 | Parameters and results of the typical numerical models.

Figure	Initial moho temperature (°C)	Upper crustal thickness (km)	Lower crustal rheological flow law	Results
Figure 4, **Figure 5**, **Figure 8B**, **Figure 9B**	450	25	Mafic granulite	Intra-crustal delamination
Figure 6A, **Figure 8A**, **Figure 9A**	500	25	Felsic granulite	Along-Moho delamination
Figure 6B	600	20	Felsic granulite	Along-Moho delamination with deep depth breakoff
Figure 6C	650	20	Felsic granulite	Along-Moho delamination with shallow depth breakoff
Figure 6D, **Figure 8C**, **Figure 9C**	450	20	Felsic granulite	Continental subduction

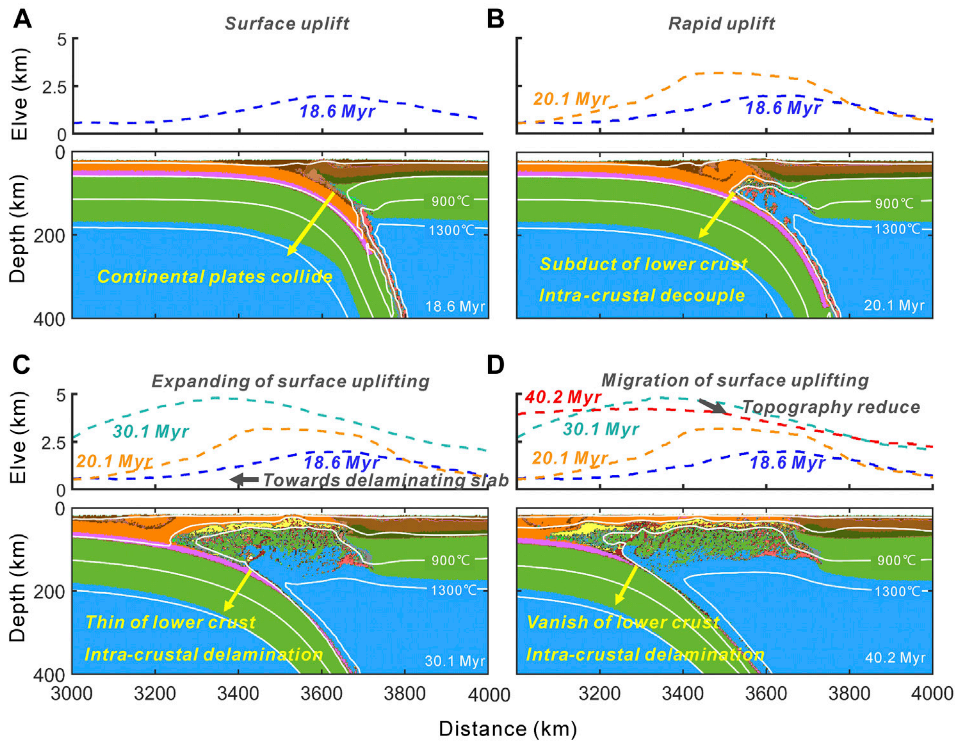

FIGURE 4 | Typical model evolution of intra-crustal delamination. **(A-D)** Snapshots shown by lithology and surface elevation. The main parameters of the continental plates: 25 and 15 km thick upper and lower crust, respectively; mafic granulite of the lower crustal lithology; and 450°C initial Moho temperature.

numerical nodes distributed nonuniformly with the highest resolution in the middle of the model domain. Grid space increases from 4 km in the middle of the model domain to 24 km on the left and right edges horizontally, and increases from 1 km on the top boundary to 12 km on the lower boundary vertically. The velocity boundary condition is free slip on all the boundaries (**Figure 3B**). The top layer is sticky air, underlain by the homogeneous crustal layer and lithospheric mantle layer (**Figure 3A**). Horizontally, the model is divided into three parts (**Figure 3A**): the left continent plate, the middle oceanic plate with a hanging slab nose driving subduction, and the right continent plate. We calculate the initial lithospheric strength (**Figures 3C–E**) using the following parameters, i.e., constant strain rate ($\dot{\varepsilon} = 1 \times 10^{-15}\ \mathrm{s}^{-1}$), effective friction coefficient ($\mu = 0.6$) and cohesion ($C = 0.7$ Mpa). The thickness of the upper continental crust may influence model evolution and its effect is systematically tested by varying its thickness (**Figure 3C**). We prescribe the rheology of wet quartzite and dry olivine for the upper crust and the mantle lithosphere, respectively. Regarding the lower crust, varied rock lithology/rheology (i.e., felsic granulite, plagioclase, diabase, and mafic granulite) are tested (**Figure 3D**).

The initial thermal state of the lithosphere is horizontally uniform with zero heat flux across the vertical boundaries. The crustal surface, Moho, and the lithosphere-asthenosphere boundary (LAB) has an initial temperature of 0°C, 450°C, and

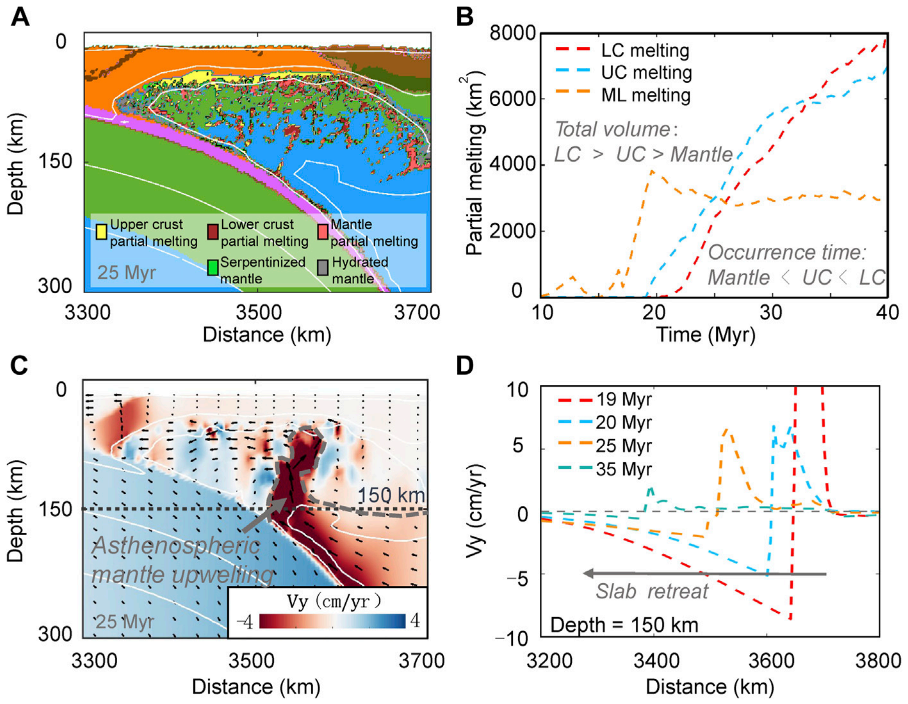

FIGURE 5 | Detailed model evolution of intra-crustal continental delamination. **(A)** Snapshots of model evolution. **(B)** Volume of lithosphere partial melting. **(C)** Snapshots of model velocity for *Y* direction. White line is temperature. Black arrows represent the magnitude and direction of the velocity. **(D)** Velocity for *Y* direction with 150 km depth in different time.

1,300°C, respectively. Temperature increases linearly in the crust and mantle lithosphere. The initial temperature along the base of the oceanic plate is around 1,009°C as a consequence to the linear temperature interpolation. We use linear temperature interpolation for the oceanic plate instead of using half space cooling model mainly because we aim to reduce sensitivity test on oceanic subduction but focus on the following collisional processes. Beneath the LAB, the initial temperature gradient is prescribed as 0.5°C/km. We also test the effect of the Moho temperature on model evolution by varying the initial values (**Figure 3E**; i.e., changing systematically from 300° to 800°C).

MODEL RESULTS

We conducted a series of numerical models with particular attention paid on investigating the effect of intra-crustal decoupling on continental delamination. The effect of various parameters (i.e., the upper crustal thickness, the lower crustal rheology, and the initial Moho temperature) is systematically tested. The model results we use in this paper is summarized in the **Table 1**.

Intra-Crustal Continental Delamination

Intra-crustal continental delamination typically occurs along the interface of the upper and lower crust, affected by intra-crustal strength decoupling, and the detailed model evolution is shown in **Figure 4**. The model evolves driven by oceanic subduction due to the initial hanging slab nose (**Figure 4A**). After a certain time, two continental plates collide, resulting in continental collision and exhumation of the upper crust (**Figure 4B**). Surface elevation increases dramatically as a consequence to the shortening and thickening of the upper crust. The lower crust subducts attached to the lithospheric mantle (**Figure 4B**). Continental delamination occurs along the upper and lower crustal interface, promoted by the mechanical decoupling between the upper and lower crust (**Figure 4C**). The subducted lower crust experiences intensive partial melting (**Figure 4C**). Besides, warm asthenosphere upwells and fills the space caused by continental delamination, which further promotes crustal partial melting beneath the upper crust (**Figures 4C,D**). Surface elevation decreases in the collisional domains and increases to the delaminated continental plate, since the upper crustal thickening is mainly located in the delaminated continental plate.

Intensive crustal and mantle partial melting is formed during the model evolution (**Figure 5A**). The lithospheric mantle first experiences partial melting due to subduction and slab dehydration (**Figure 5B**), followed by the partial melting of the upper crust due to the heating of the upwelling asthenospheric mantle (**Figures 5C,D**). New lithospheric mantle forms underneath the upper crust due to the cooling of the warm asthenospheric mantle (**Figure 5A**). Melting of the lower crust occurs later than that of the upper crust, likely due to high pressure since it subducts attached to lithospheric mantle. Partial melting of the mantle occurs much earlier than that of crust, and decays with time due to solidification (**Figure 5B**).

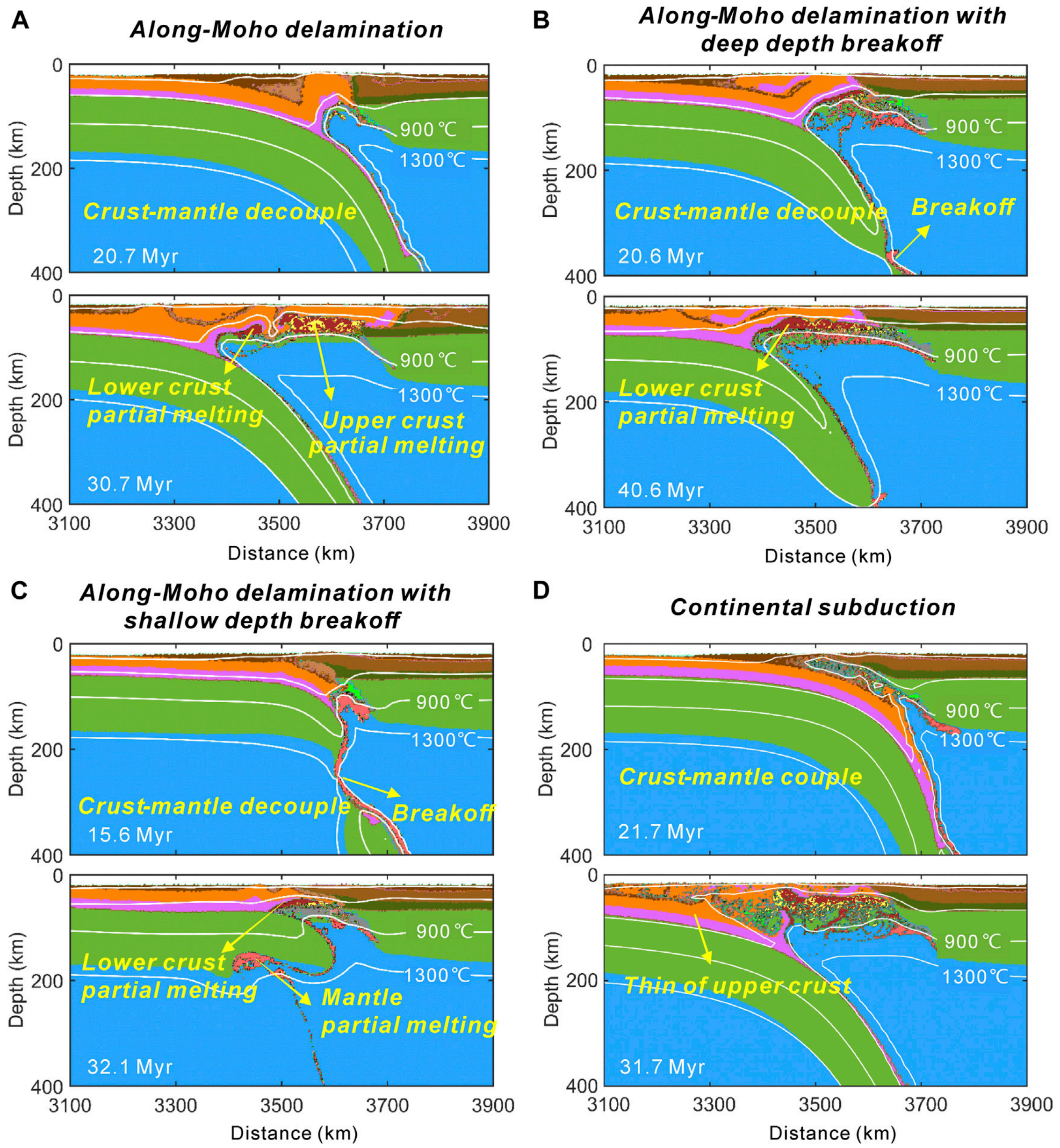

FIGURE 6 | Various types of model evolution. **(A)** Along-Moho continental delamination without slab breakoff. Main parameters used: 25 and 15 km upper and lower crustal thickness, respectively; felsic granulite of the lower crustal lithology; and 500°C initial Moho temperature. **(B–C)** Delamination with deep and shallow slab breakoff. The major changed parameters: equal thickness of 20 km of the upper and lower crust; 600°C **(B)** and 650°C **(C)** initial Moho temperature. **(D)** Continental subduction. The major changed parameters: 20 and 20 km upper and lower crustal thickness, respectively; 450°C initial Moho temperature.

Various Types of Model Evolution

Our model results also reveal the development of along-Moho delamination and continental subduction (**Figure 6**). The along-Moho continental delamination occurs favored by crust-mantle decoupling (e.g., **Figure 6A**), which is a common feature in the models with weak lower crust (due to weak rock lithology or high Moho temperature). In this type of model, subduction of the weak lower crust is retarded by the upwelling of the asthenospheric mantle, and continental delamination occurs along the Moho. As a consequence, the lower crust experience intensive partial melting earlier than that of the upper crust. Slab breakoff often occurs in this type of models mainly due to the decrease of the lithospheric strength, and the deep and shallow slab breakoff modes are recognized (**Figures 6B,C**). With the decrease in lithospheric strength (for instance, increase the initial Moho temperature), slab breakoff tends to occur at the shallow depth. Once slab breakoff happens, the dynamic evolution of continental delamination is significantly inhibited due to the loss of slab pull.

Continental subduction forms in a number of models, featured by the subduction of the entire crust, i.e., both the upper and

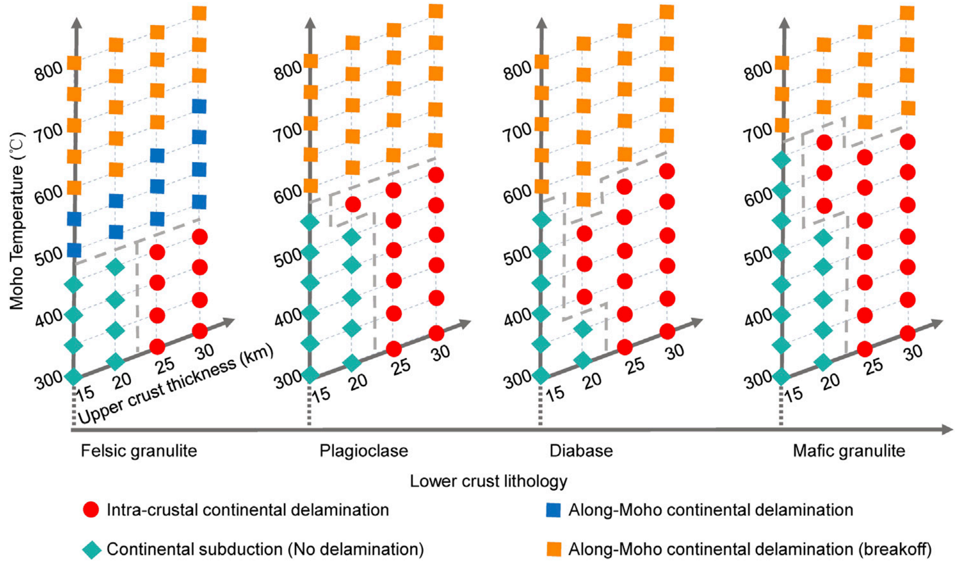

FIGURE 7 | Model results of parameter test. Blue square is along-Moho delamination with slab break off; orange rhombus is continental subduction; green triangle is along-Moho delamination; red circle is intra-crustal delamination. The grey arrow from the left to the right shows the variation of the lower crustal lithology.

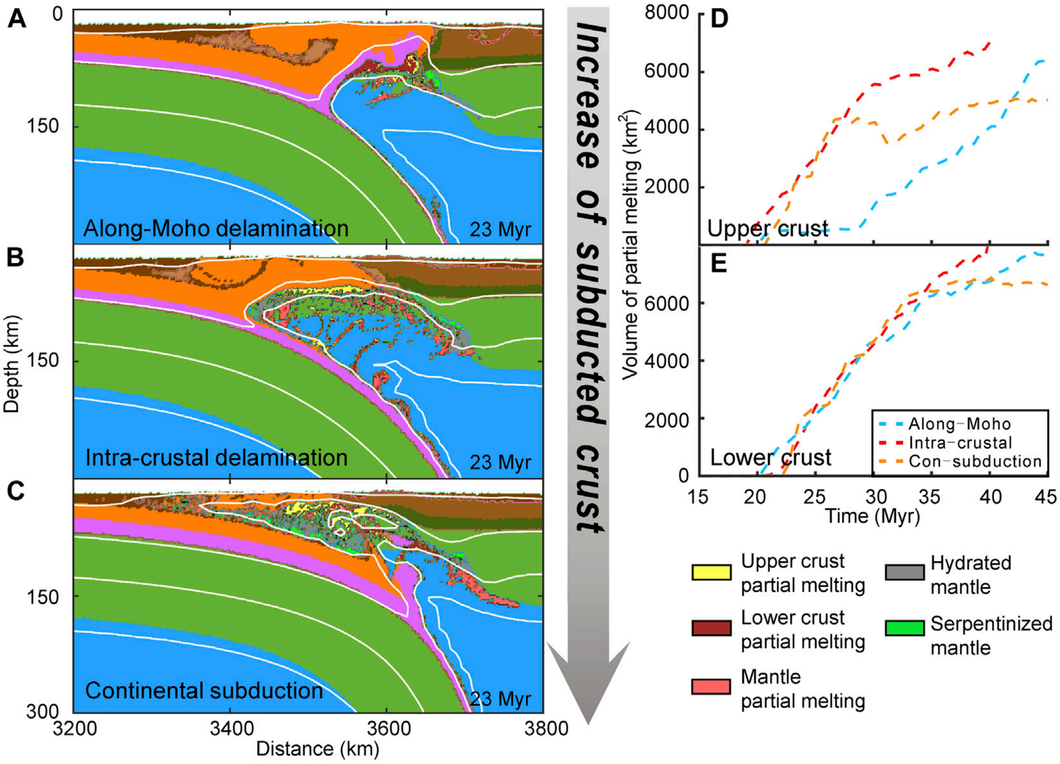

FIGURE 8 | Model comparison of the three different modes. **(A–C)** Model results shown by lithological snapshots indicating the amount of subducted crust (i.e., from no crust subducted to the entire crust subducted). Intra-crustal delamination model from **Figure 4**, along-Moho delamination model from **Figure 6A**, and continental subduction model from **Figure 6D**. **(D–E)** Partial melting of the upper crust and lower crust of the three models.

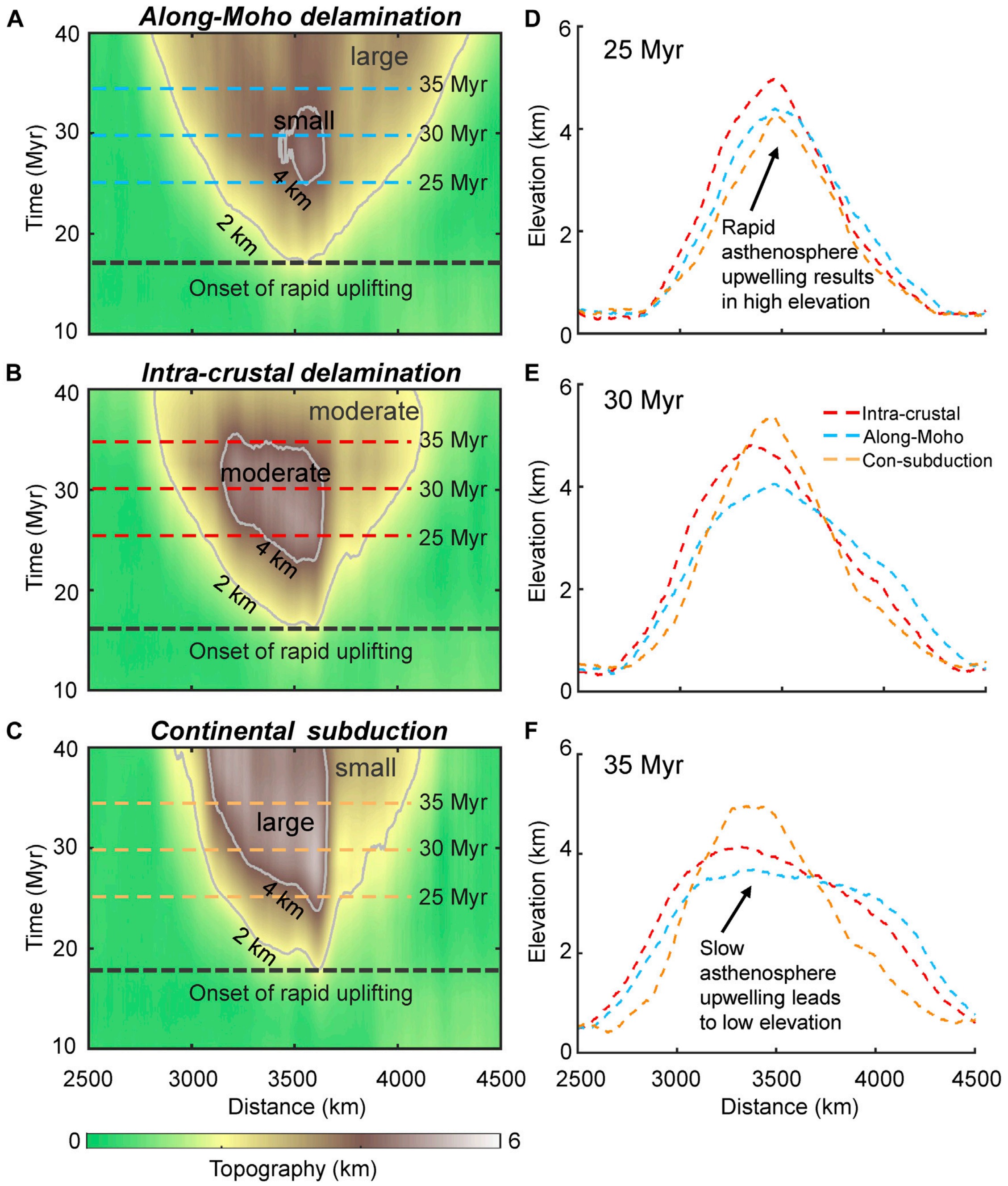

FIGURE 9 | Topography variations of the three models. **(A–C)** Temporal evolution of surface elevation of the three models. **(D–F)** Topography at 25, 30, 35 Myr for Panels **(A–C)**.

lower crust subduct attached to the lithospheric mantle (**Figure 6D**). The development of continental subduction is favored by strong lithospheric coupling i.e., both intra-crustal coupling and crust-mantle coupling (**Figure 6D**). Warm asthenospheric mantle upwells to shallow depth, intruding on top of the upper crust (**Figure 6D**). During continental subduction, the upper crust experiences intensive partial melting while melting of the lower crust is largely inhibited and postponed. Exhumation of crustal rocks is negligible in this model.

Parameter Effects on Intra-Crustal Delamination

The development of intra-crustal delamination is largely promoted by intra-crustal strength decoupling, i.e., the base

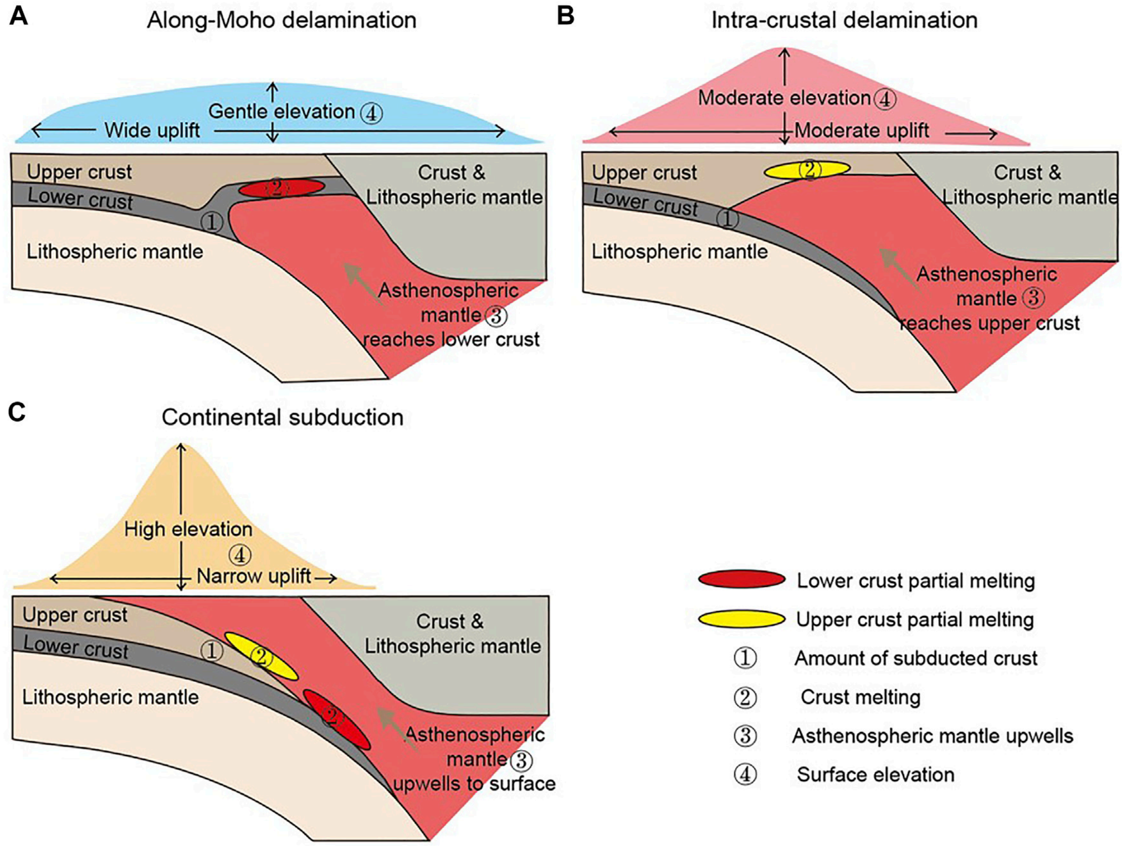

FIGURE 10 | Summarized features of these three types of models. **(A–C)** Along-Moho delamination, intra-crustal delamination and continental subduction models.

of the upper crust is mechanically weak and results in strength drop along the interface between the upper and lower crust. The major parameters affecting intra-crustal delamination are the upper crustal thickness, the lower crustal lithology and the initial Moho temperature (**Figure 7**). 1) Thick upper crust tends to promote the development of intra-crustal delamination, mainly because the lower part of the thick upper crust is mechanically weak and thus promotes intra-crustal strength decoupling. The threshold of the upper crustal thickness affecting the intra-crustal delamination is around 20 km (**Figure 7**). Decrease the upper crustal thickness results in the increase of the intra-crustal coupling, which promotes the formation of continental subduction and along-Moho delamination. 2) The initially prescribed Moho temperature is an important parameter affecting lithospheric thermal structure and rheological layering, which thus influences lithospheric dynamics (Gueydan et al., 2008; Liao et al., 2017). Model results show that initially low Moho temperature promotes the development of intra-crustal delamination. Increase the initial Moho temperature, along-Moho continental delamination becomes the dominant evolution type. Slab breakoff often happens in the along-Moho delamination models, because high initial Moho temperature results in the strength decrease of the subduction slabs, which is consistent with the previous study (Duretz et al., 2011). 3) The lower crustal lithology also affects the intra-crustal delamination. We tested four different lower crustal lithologies (i.e., felsic granulite, plagioclase, diabase, and mafic granulite). The mechanical strength increases gradually from more felsic lithology to more mafic lithology. Model results show that with more mafic lithology (e.g., mafic granulite), intra-crustal delamination occurs in much wider parameter space (**Figure 7**). The main reason is that mechanically stronger lower crust promotes crust-mantle coupling and favors intra-crustal decoupling.

DISCUSSION

Comparison of the Various Model Types

The dynamic evolution of the intra-crustal delamination model is compared to the along-Moho delamination model and the continental subduction model (**Figures 8–10**). The remarkable difference of these three models is the amount of subducted crust (**Figures 8A–C**) that increases from the along-Moho delamination model (i.e., no crust subducted)

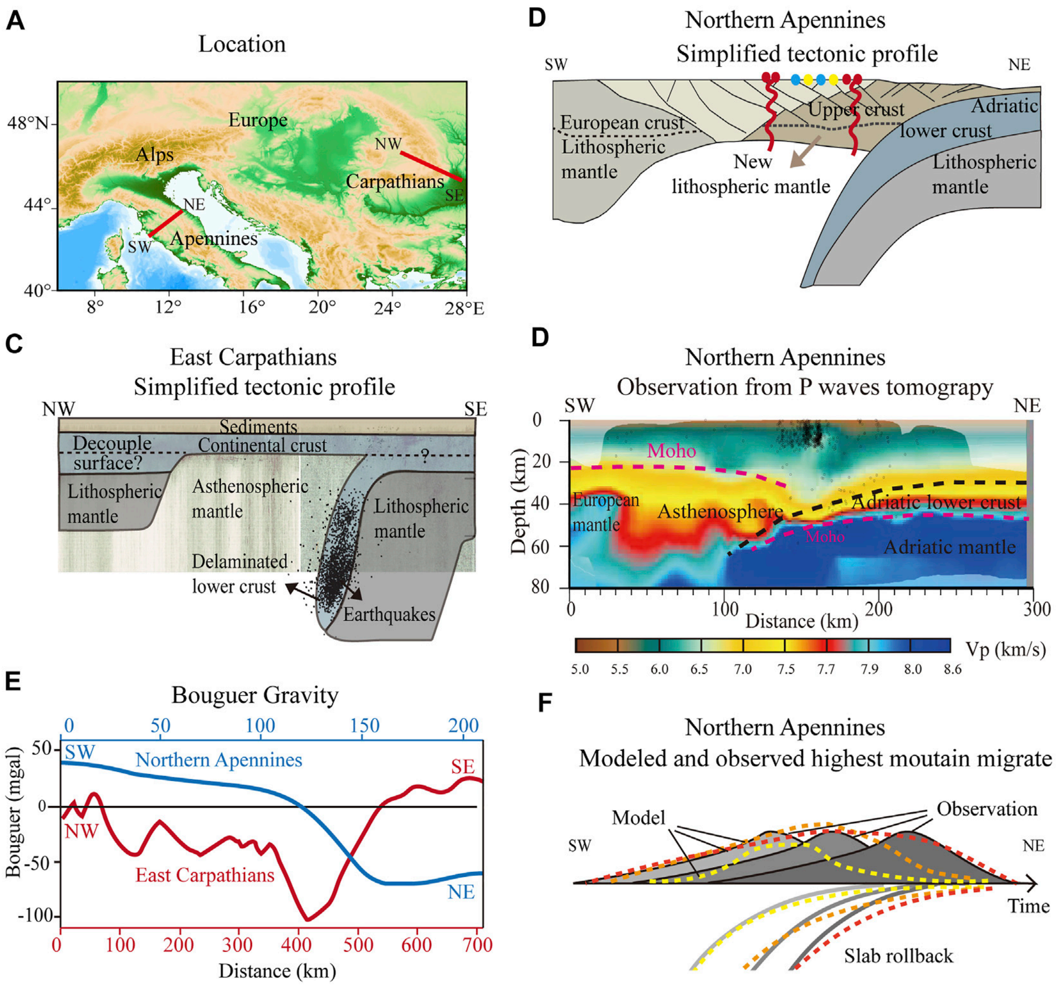

FIGURE 11 | Possible natural examples showing intra-crustal delamination. **(A)** Locations of the Northern Apennines and the East Carpathians. **(B)** Top: Simplified tectonic profile of the Northern Apennines modified from Carminati and Doglioni (2012). The red circles represent the volcanic centers containing mantle-derived magmas, and the yellow and blue circles mark the acid volcanos and plutons produced mostly by crustal anatexis, respectively (Serri et al., 1993). **(C)** Simplified tectonic profile of the East Carpathians. **(D)** *P* wave velocity of the Northern Apennines (Di Stefano et al., 2009). **(E)** Bouguer Gravity of the Northern Apennines (blue line, Carminati and Doglioni, 2012) and the East Carpathians (red line, Sperner et al., 2004). **(F)** Modeled (the colored dashed lines) and observed (the shaded area) topography migration of the Apennines controlled by slab rollback (Galli et al., 2002).

to the intra-crustal delamination model (i.e., the lower crust subducted) and continental subduction model (i.e., the entire crust subducted). As a consequence, the crustal partial melting varies among these models (**Figures 8D,E**). 1) The intra-crustal delamination model experiences the most intensive melting of the upper crust (**Figure 8D**), mainly due to the direct heating of the upwelling asthenospheric mantle along the base of the upper crust (**Figure 8B**). On the contrary, the standard along-Moho delamination model generates very limited upper crustal melting, especially in the early stage (<30 Myr), due to the isolation from the asthensopheric mantle by the lower crust (**Figure 8A**). 2) Lower crustal partial melting is first formed in the along-Moho model, but the intensity of lower crustal melting is quite similar in all these models (**Figure 8E**).

The difference in dynamic evolution of these three types of models is revealed by surface elevation (**Figure 9**). The along-Moho delamination model (**Figure 9A**) is featured by widespread surface uplifting (i.e., the large 2 km surface elevation contour) with gentle elevation (i.e., the small 4 km surface elevation contour). The continental subduction model (**Figure 9C**), however, is marked by concentrated high surface uplifting (i.e., the small 2 km elevation contour but large 4 km elevation contour). These two types of models are the two end-members, and the intra-crustal delamination model (**Figure 9B**) shows the moderate surface uplifting (i.e., both the 2 and 4 km elevation contours). The main reason influencing the surface uplift in these three models is the amount of subducted crust. The entire crust subducts in the continental subduction model, and warm asthenospheric mantle upwells to near-surface resulting in concentrated high elevation. No crust subducts in the along-Moho delamination model, and warm asthenospheric mantle upwells to Moho depth leading to widespread surface uplifting. The intra-crustal delamination model with only lower crust subducted thus forms moderate surface elevation between the two end-members. The decrease of the highest surface elevation with time (**Figures 9D–F**) is due to the decline of the warm asthenospheric mantle (**Figure 5D**).

The difference of intra-crustal delamination model from the along-Moho delamination model and the continental subduction model can be summarized by **Figure 10**. Firstly, the amount of subducted crust in the intra-crustal delamination model (i.e., the lower crust subducted) is larger than that in the along-Moho delamination model (i.e., no crust subducted) but smaller than the continental subduction model (i.e., the entire crust subducted). Secondly, upper crustal melting is a more common phenomenon in the intra-crustal delamination models than that in the other two models because the warm asthenospheric mantle contacts the upper crust directly. Thirdly, asthenospheric mantle upwells to the upper crustal depth in the intra-crustal delamination model, results in moderate surface elevation compared to the other two models. Thus, the intra-crustal delamination model is a transition mode between the along-Moho delamination model and the continental subduction model in terms of subducted crust, crustal melting, mantle upwelling and surface elevation (**Figure 10**).

Comparison With the Possible Natural Examples

The geological and geophysical observations of the Northern Apennines and the East Carpathians (**Figure 11A**) reveal the possibility of intra-crustal delamination (**Figure 11**). Firstly, the studies using high-resolution tele-seismic tomography and deep seismic reflection data revealed the possibility of intra-crustal delamination in the Northern Apennines and the East Carpathians (**Figures 11B–D**; Piana Agostinetti et al., 2002; Pauselli et al., 2006; Di Stefano et al., 2009; Fillerup et al., 2010; Giacomuzzi et al., 2011; Piana Agostinetti and Faccenna, 2018). In the Northern Apennines, the interpreted geophysical image shows that the Adriatic upper crust atop the mantle wedge and the Adriatic lower crust delaminates attached to the subducting plate (**Figure 11B**). The Adriatic upper crust undergoes intensive deformation featured by the wide-distributed faults (**Figure 11B**; Carminati et al., 2004; Faccenna et al., 2014). Another important feature is the newly formed lithospheric mantle underneath the Adriatic upper crust. The *P* wave velocity structure reveals delamination of the Adrian lower crust, and the low *Vp* anomalies deplict the upwelling of the asthenospheric mantle (**Figure 11D**). Secondly, the geochemistry study revealed metasomatized mantle in the mantle wedge with k-rich melt possibly derived from the subducted Adriatic upper crust (Serri et al., 1993), indicating the possibility of the intra-crustal delamination. Thirdly, the low Bouguer gravity (**Figure 11E**) in the Northern Apennines (Carminati and Doglioni, 2012) and East Carpathians (Sperner et al., 2004) could be affected by lithosphere upwelling as a result from lithosphere delamination. Fourthly, the morphologic study using the data of water divide analyzed the Apennines divide and the highest mountains, and suggested that the highest mountains migrated to the east, consistent with the eastward retreat of the delaminated Apennines slab in the Pliocene and Quaternary (**Figure 11F**; Galli et al., 2002). The above-mentioned features are all captured in our models (e.g., **Figures 4**, **5**, **10**).

CONCLUSION

We study systematically the dynamical evolution of intra-crustal delamination using 2D thermomechanical numeric modeling. Our model results suggest the following conclusions.

(1) Intra-crustal continental delamination is a possible way of continental destruction, facilitated by intra-crustal strength decoupling. The formation of intra-crustal continental delamination is largely promoted by thick upper crust, low Moho temperature and more mafic lower crustal lithology.
(2) Intra-crustal continental delamination differs from the standard along-Moho delamination and continental subduction in terms of the amount of subducted crust, the intense of partial melting and surface elevation.
(3) The possibility of intra-crustal continental delamination is supported by the observations of the Northern Apennines and the East Carpathians.

DATA AVAILABILITY STATEMENT

The datasets presented in this study can be found in online repositories. The names of the repository/repositories and accession number(s) can be found below: http://doi.org/10.5281/zenodo.5030906.

AUTHOR CONTRIBUTIONS

RQ: Conceptualization, Writing—Original Draft, Visualization. JL: Methodology, Writing—Review and Editing, Supervision, Resources, Conceptualization, Project administration. RG: Conceptualization, Supervision, Resources, Project administration.

FUNDING

This research is financially supported by NSFC projects (U1901214, 41974104, 91855208) and Guangdong project 2017ZT07Z066. Numerical simulations were run with the clusters of National Supercomputer Center in Guangzhou (Tianhe-II).

ACKNOWLEDGMENTS

We thank Prof. Taras Gerya for his long-standing guidance on our geodynamical modeling work. Prof. Lun Li, Dr. Hongda Liang and Dr. Xingfu Huang are thanked for their valuable suggestions on this study.

REFERENCES

Afonso, J. C., and Ranalli, G. (2004). Crustal and Mantle Strengths in continental Lithosphere: Is the Jelly sandwich Model Obsolete. *Tectonophysics* 394, 221–232. doi:10.1016/j.tecto.2004.08.006

Beall, A. P., Moresi, L., and Stern, T. (2017). Dripping or Delamination? A Range of Mechanisms for Removing the Lower Crust or Lithosphere. *Geophys. J. Int.* 210, 671–692. doi:10.1093/gji/ggx202

Bird, P. (1979). Continental Delamination and the Colorado Plateau. *J. Geophys. Res.* 84, 7561–7571. doi:10.1029/JB084iB13p07561

Bird, P. (1978). Initiation of Intracontinental Subduction in the Himalaya. *J. Geophys. Res.* 83, 4975–4987. doi:10.1029/JB083iB10p04975

Bousquet, R., Goffé, B., Henry, P., Le Pichon, X., and Chopin, C. (1997). Kinematic, thermal and Petrological Model of the Central Alps: Lepontine Metamorphism in the Upper Crust and Eclogitisation of the Lower Crust. *Tectonophysics* 273, 105–127. doi:10.1016/S0040-1951(96)00290-9

Burg, J.-P., and Gerya, T. V. (2005). The Role of Viscous Heating in Barrovian Metamorphism of Collisional Orogens: Thermomechanical Models and Application to the Lepontine Dome in the Central Alps. *J. Metamorph Geol.* 23, 75–95. doi:10.1111/j.1525-1314.2005.00563.x

Burov, E. B. (2011). Rheology and Strength of the Lithosphere. *Mar. Pet. Geology.* 28, 1402–1443. doi:10.1016/j.marpetgeo.2011.05.008

Carminati, E., and Doglioni, C. (2012). Alps vs. Apennines: The Paradigm of a Tectonically Asymmetric Earth. *Earth-Science Rev.* 112, 67–96. doi:10.1016/j.earscirev.2012.02.004

Carminati, E., Doglioni, C., and Barba, S. (2004). Reverse Migration of Seismicity on Thrusts and normal Faults. *Earth-Science Rev.* 65, 195–222. doi:10.1016/S0012-8252(03)00083-7

Clauser, C., and Huenges, E. (1995). T*Hermal Conductivity of Rocks and Minerals*., 23.

Di Stefano, R., Kissling, E., Chiarabba, C., Amato, A., and Giardini, D. (2009). Shallow Subduction beneath Italy: Three-Dimensional Images of the Adriatic-European-Tyrrhenian Lithosphere System Based on High-qualityPwave Arrival Times. *J. Geophys. Res.* 114, B05305. doi:10.1029/2008JB005641

Dong, X., Li, W., Lu, Z., Huang, X., and Gao, R. (2020). Seismic Reflection Imaging of Crustal Deformation within the Eastern Yarlung-Zangbo Suture Zone. *Tectonophysics* 780, 228395. doi:10.1016/j.tecto.2020.228395

Duretz, T., Gerya, T. V., and May, D. A. (2011). Numerical Modelling of Spontaneous Slab Breakoff and Subsequent Topographic Response. *Tectonophysics* 502, 244–256. doi:10.1016/j.tecto.2010.05.024

Faccenda, M., Minelli, G., and Gerya, T. V. (2009). Coupled and Decoupled Regimes of continental Collision: Numerical Modeling. *Earth Planet. Sci. Lett.* 278, 337–349. doi:10.1016/j.epsl.2008.12.021

Faccenna, C., Becker, T. W., Miller, M. S., Serpelloni, E., and Willett, S. D. (2014). Isostasy, Dynamic Topography, and the Elevation of the Apennines of Italy. *Earth Planet. Sci. Lett.* 407, 163–174. doi:10.1016/j.epsl.2014.09.027

Fillerup, M. A., Knapp, J. H., Knapp, C. C., and Raileanu, V. (2010). Mantle Earthquakes in the Absence of Subduction? Continental Delamination in the Romanian Carpathians. *Lithosphere* 2, 333–340. doi:10.1130/L102.1

Galli, C. S., Torrini, A., Doglioni, C., and Scrocca, D. (2002). Divide and Highest Mountains vs Subduction in the Apennines. *Studi Geol. Cam.* 1, 143–145. http://193.204.8.201:8080/jspui/handle/1336/822.

Gao, R., Lu, Z., Klemperer, S. L., Wang, H., Dong, S., Li, W., et al. (2016). Crustal-scale Duplexing beneath the Yarlung Zangbo Suture in the Western Himalaya. *Nat. Geosci* 9, 555–560. doi:10.1038/ngeo2730

Gerya, T. V., and Yuen, D. A. (2003). Characteristics-based Marker-In-Cell Method with Conservative Finite-Differences Schemes for Modeling Geological Flows with Strongly Variable Transport Properties. *Phys. Earth Planet. Interiors* 140, 293–318. doi:10.1016/j.pepi.2003.09.006

SUPPLEMENTARY MATERIAL

The Supplementary Material for this article can be found online at: https://www.frontiersin.org/articles/10.3389/feart.2022.829300/full#supplementary-material

Gerya, T. V., and Yuen, D. A. (2007). Robust Characteristics Method for Modelling Multiphase Visco-Elasto-Plastic Thermo-Mechanical Problems. *Phys. Earth Planet. Interiors* 163, 83–105. doi:10.1016/j.pepi.2007.04.015

Giacomuzzi, G., Chiarabba, C., and De Gori, P. (2011). Linking the Alps and Apennines Subduction Systems: New Constraints Revealed by High-Resolution Teleseismic Tomography. *Earth Planet. Sci. Lett.* 301, 531–543. doi:10.1016/j.epsl.2010.11.033

Göğüş, O. H., Pysklywec, R. N., Corbi, F., and Faccenna, C. (2011). The Surface Tectonics of Mantle Lithosphere Delamination Following Ocean Lithosphere Subduction: Insights from Physical-Scaled Analogue Experiments. *Geochem. Geophys. Geosyst.* 12. doi:10.1029/2010GC003430

Göğüş, O. H., Pysklywec, R. N., and Faccenna, C. (2016). Postcollisional Lithospheric Evolution of the Southeast Carpathians: Comparison of Geodynamical Models and Observations. *Tectonics* 35, 1205–1224. doi:10.1002/2015TC004096

Göğüş, O. H., and Pysklywec, R. N. (2008). Mantle Lithosphere Delamination Driving Plateau Uplift and Synconvergent Extension in Eastern Anatolia. *Geol* 36, 723. doi:10.1130/G24982A.1

Göğüş, O. H., and Ueda, K. (2018). Peeling Back the Lithosphere: Controlling Parameters, Surface Expressions and the Future Directions in Delamination Modeling. *J. Geodynamics* 117, 21–40. doi:10.1016/j.jog.2018.03.003

Gueydan, F., Morency, C., and Brun, J.-P. (2008). Continental Rifting as a Function of Lithosphere Mantle Strength. *Tectonophysics* 460, 83–93. doi:10.1016/j.tecto.2008.08.012

Guo, X., Li, W., Gao, R., Xu, X., Li, H., Huang, X., et al. (2017). Nonuniform Subduction of the Indian Crust beneath the Himalayas. *Sci. Rep.* 7, 12497. doi:10.1038/s41598-017-12908-0

Kay, R. W., and Mahlburg Kay, S. (1993). Delamination and Delamination Magmatism. *Tectonophysics* 219, 177–189. doi:10.1016/0040-1951(93)90295-U

Kirby, S. H., and Kronenberg, A. K. (1987). Rheology of the Lithosphere: Selected Topics. *Rev. Geophys.* 25, 1219. doi:10.1029/RG025i006p01219

Krystopowicz, N. J., and Currie, C. A. (2013). Crustal Eclogitization and Lithosphere Delamination in Orogens. *Earth Planet. Sci. Lett.* 361, 195–207. doi:10.1016/j.epsl.2012.09.056

Li, Z.-H., Liu, M., and Gerya, T. (2016). Lithosphere Delamination in continental Collisional Orogens: A Systematic Numerical Study. *J. Geophys. Res.* 26.

Liang, H., Jin, S., Wei, W., Gao, R., Ye, G., Zhang, L., et al. (2018). Lithospheric Electrical Structure of the Middle Lhasa Terrane in the South Tibetan Plateau. *Tectonophysics* 731-732, 95–103. doi:10.1016/j.tecto.2018.01.020

Liao, J., Gerya, T., and Malusà, M. G. (2018). 3D Modeling of Crustal Shortening Influenced by Along-Strike Lithological Changes: Implications for continental Collision in the Western and Central Alps. *Tectonophysics* 746, 425–438. doi:10.1016/j.tecto.2018.01.031

Liao, J., Gerya, T., Thielmann, M., Webb, A. A. G., Kufner, S.-K., and Yin, A. (2017). 3D Geodynamic Models for the Development of Opposing continental Subduction Zones: The Hindu Kush-Pamir Example. *Earth Planet. Sci. Lett.* 480, 133–146. doi:10.1016/j.epsl.2017.10.005

Magni, V., Faccenna, C., van Hunen, J., and Funiciello, F. (2013). Delamination vs. Break-Off: the Fate of continental Collision. *Geophys. Res. Lett.* 40, 285–289. doi:10.1002/grl.50090

Pauselli, C., Barchi, M. R., Federico, C., Magnani, M. B., and Minelli, G. (2006). The Crustal Structure of the Northern Apennines (Central Italy): An Insight by the Crop03 Seismic Line. *Am. J. Sci.* 306, 428–450. doi:10.2475/06.2006.02

Piana Agostinetti, N., and Faccenna, C. (2018). Deep Structure of Northern Apennines Subduction Orogen (Italy) as Revealed by a Joint Interpretation of Passive and Active Seismic Data. *Geophys. Res. Lett.* 45, 4017–4024. doi:10.1029/2018GL077640

Piana Agostinetti, N., Lucente, F. P., Selvaggi, G., and Di Bona, M. (2002). Crustal Structure and Moho Geometry beneath the Northern Apennines (Italy). *Geophys. Res. Lett.* 29, 60. doi:10.1029/2002GL015109

Schmid, S. M., Kissling, E., Diehl, T., van Hinsbergen, D. J. J., and Molli, G. (2017). Ivrea Mantle Wedge, Arc of the Western Alps, and Kinematic Evolution of the Alps-Apennines Orogenic System. *Swiss J. Geosci.* 110, 581–612. doi:10.1007/s00015-016-0237-0

Schmidt, M. W., and Poli, S. (1998). Experimentally Based Water Budgets for Dehydrating Slabs and Consequences for Arc Magma Generation. *Earth Planet. Sci. Lett.* 163, 361–379. doi:10.1016/S0012-821X(98)00142-3

Schneider, F. M. (2013). Seismic Imaging of Subducting continental Lower Crust beneath the Pamir. *Earth Planet. Sci. Lett.* 12. doi:10.1016/j.epsl.2013.05.015

Schneider, F. M., Yuan, X., Schurr, B., Mechie, J., Sippl, C., Kufner, S. K., et al. (2019). The Crust in the Pamir: Insights from Receiver Functions. *J. Geophys. Res. Solid Earth* 124, 9313–9331. doi:10.1029/2019JB017765

Serri, G., Innocenti, F., and Manetti, P. (1993). Geochemical and Petrological Evidence of the Subduction of Delaminated Adriatic continental Lithosphere in the Genesis of the Neogene-Quaternary Magmatism of central Italy. *Tectonophysics* 223, 117–147. doi:10.1016/0040-1951(93)90161-C

Sperner, B., Ioane, D., and Lillie, R. J. (2004). Slab Behaviour and its Surface Expression: New Insights from Gravity Modelling in the SE-Carpathians. *Tectonophysics* 382, 51–84. doi:10.1016/j.tecto.2003.12.008

Thurner, S., Palomeras, I., Levander, A., Carbonell, R., and Lee, C.-T. (2014). Ongoing Lithospheric Removal in the Western Mediterranean: Evidence from Ps Receiver Functions and Thermobarometry of Neogene Basalts (PICASSO Project). *Geochem. Geophys. Geosyst.* 15, 1113–1127. doi:10.1002/2013GC005124

Vogt, K., Matenco, L., and Cloetingh, S. (2017). Crustal Mechanics Control the Geometry of Mountain Belts. Insights from Numerical Modelling. *Earth Planet. Sci. Lett.* 460, 12–21. doi:10.1016/j.epsl.2016.11.016

Vogt, K., Willingshofer, E., Matenco, L., Sokoutis, D., Gerya, T., and Cloetingh, S. (2018). The Role of Lateral Strength Contrasts in Orogenesis: A 2D Numerical Study. *Tectonophysics* 746, 549–561. doi:10.1016/j.tecto.2017.08.010

Wang, Z., Kusky, T. M., and Capitanio, F. A. (2018). On the Role of Lower Crust and Midlithosphere Discontinuity for Cratonic Lithosphere Delamination and Recycling. *Geophys. Res. Lett.* 45, 7425–7433. doi:10.1029/2017GL076948

Wang, Z., and Kusky, T. M. (2019). The Importance of a Weak Mid-lithospheric Layer on the Evolution of the Cratonic Lithosphere. *Earth-Science Rev.* 190, 557–569. doi:10.1016/j.earscirev.2019.02.010

Wilks, K. R., and Carter, N. L. (1990). Rheology of Some continental Lower Crustal Rocks. *Tectonophysics* 182, 57–77. doi:10.1016/0040-1951(90)90342-6

Conflict of Interest: The authors declare that the research was conducted in the absence of any commercial or financial relationships that could be construed as a potential conflict of interest.

frontiers | Frontiers in Earth Science

ORIGINAL RESEARCH
published: 14 April 2022
doi: 10.3389/feart.2022.861240

Co-Evolution of Parallel Triple Subduction Systems in the New Guinea Region: A Systematic Numerical Study

Liangliang Wang [1,2], Liming Dai [1,2], Wei Gong [1,2], Sanzhong Li [1,2], Xiaodian Jiang [1,2], Hao Dong [1,2], Di Wang [1,2], Fakun Li [1,2] and Shengyao Yu [1,2]*

[1] Key Lab of Submarine Geosciences and Prospecting Techniques, Frontiers Science Center for Deep Ocean Multispheres and Earth System, MOE and College of Marine Geosciences, Ocean University of China, Qingdao, China, [2] Laboratory for Marine Mineral Resources, Qingdao National Laboratory for Marine Science and Technology, Qingdao, China

A specific configuration of the global subduction system is the parallel triple subduction. The widely accepted example of parallel triple subduction is the New Guinea region, including a northward dip at the New Britain Trench (NBT), a southward dip at the Trobriand Trough (TT), and North Solomon Trench (NST). Questions regarding the parallel triple subduction system remain largely unexplored in terms of factors controlling its initiation, duration, and dynamics. Here, we used two-dimensional numerical models to study the dynamics mechanism of the parallel triple subduction system in the New Guinea region. Four possible regimes were achieved: 1) the double subduction model, which includes the forward subduction jumping model (FSJ) and the subduction polarity reversal model (SPR) and 2) the parallel triple subduction model, which includes the tendency to the forward jumping model (TFSJ) and the tendency to polarity reversal (TSPR). By evaluating the four regimes with actual seismic data, we suggest that the pre-existing rupture and length of ocean–continent transition (OCT) determine the formation of the TT, while the formation of the NBT may be the result of the rheological strength differences between the Solomon Island Arc (SIA) and Solomon Sea Basin (SSB); the initial length of the SSB can regulate the competitive relationship between the TT and NBT, which also determines the present-day inactive state of the TT. A longer SSB makes the TT and NBT initiated independently, while a narrower SSB will allow interaction during subduction initiation of the TT and NBT.

Keywords: triple subduction system, the New Guinea region, thermal structure, numerical simulation, rheological strength differences

Edited by:
Jie Liao,
Sun Yat-sen University, China

Reviewed by:
Xin Zhou,
University of Minnesota Twin Cities,
United States
Zhensheng Wang,
China University of Geosciences
Wuhan, China

***Correspondence:**
Liming Dai
dlming@ouc.edu.cn

Specialty section:
This article was submitted to
Solid Earth Geophysics,
a section of the journal
Frontiers in Earth Science

Received: *24 January 2022*
Accepted: *03 March 2022*
Published: *14 April 2022*

Citation:
Wang L, Dai L, Gong W, Li S, Jiang X, Dong H, Wang D, Li F and Yu S (2022) Co-Evolution of Parallel Triple Subduction Systems in the New Guinea Region: A Systematic Numerical Study.
Front. Earth Sci. 10:861240.
doi: 10.3389/feart.2022.861240

1 INTRODUCTION

It is well established that the multi-subduction system is an important component of modern plate tectonics (Holt et al., 2017; Stern and Gerya, 2018; Chesley et al., 2021; Lallemand and Arcay, 2021; Zhang and Leng, 2021; Fu et al., 2022). The multi-subduction system is a complex process, including subduction initiation (SI), interactions, and dynamics of multi-subduction zones. Previous studies have focused on only two subduction systems and rarely considered more subduction zones, such as the parallel triple subduction system (Mishin et al., 2008; Jagoutz et al., 2015; Huangfu et al., 2016; Holt et al., 2017; Zhang et al., 2017; Liao et al., 2018; Yang et al., 2018; Li et al., 2019; Lyu et al., 2019;

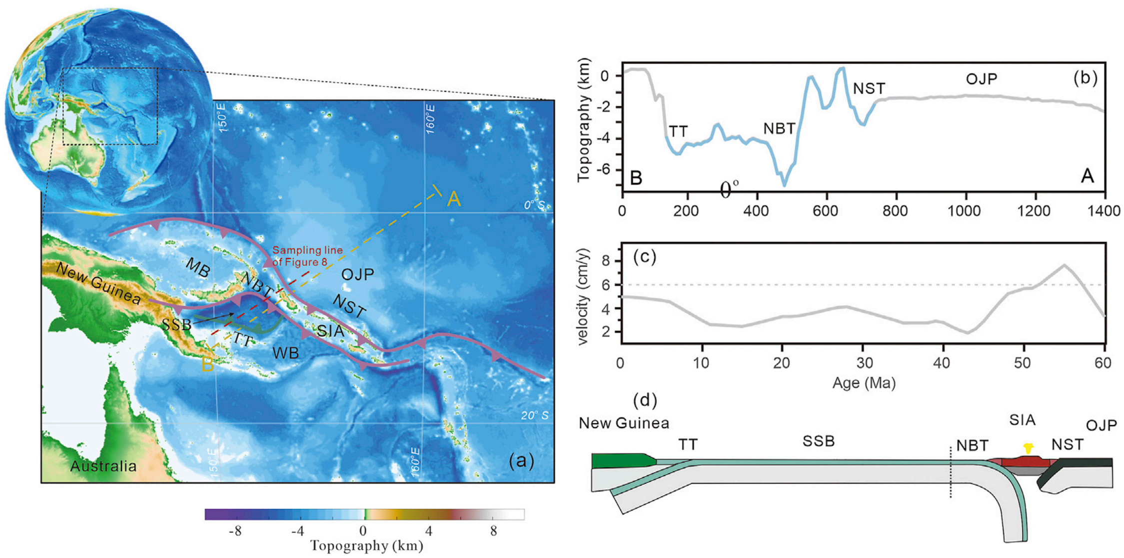

FIGURE 1 | Map of the Papua New Guinea region. **(A)** Map of the New Guinea region modified from ETOPO1. The purple line represents active or potentially active subduction zones and the green line represents dead subduction zones. **(B)** Topographic profile from ETOPO1. The sampling points are shown by orange lines in Figure.1a. **(C)** Convergence rate from Müller et al., 2019. **(D)** Conceptual schemes from Baldwin et al., 2012. NBT: the New Britain Trench; TT: Trobriand Trough; NST: North Solomon Trench. MB: Manus Basin; OJP: Ontong–Java Plateau; SIA: Solomon Island Arc; WB: Woodlark Basin.

Tao et al., 2020; Zhong and Li, 2020; Zhang and Leng, 2021). The parallel triple subduction system consists of three subduction zones that exist simultaneously, unlike the triple junction where three tectonic plates meet (Li et al., 2018). The parallel triple subduction system is a common process during the evolution of Earth, which is characteristic for both modern and ancient subduction collision zones, for example, in the Himalayan collision zone (Huangfu et al., 2018), the Central Asian Orogenic belt (Xiao et al., 2020), the active Izu–Bonin–Marianas and Ryukyu arcs (e.g. Faccenna et al., 2018), and the New Guinea region (Baldwin et al., 2012; Yang et al., 2021).

One of the modern examples is the New Britain Trench (NBT) and Trobriand Trough (TT) that resulted from the convergence of the Ontong–Java Plateau (OJP) and Solomon Island Arc (SIA) along the North Solomon Trench (NST) (Holm et al., 2016; Mann and Taira, 2004; Petterson et al., 1999; Stern, 2004; Tapster et al., 2014). The initial arrival of the OJP at the NST was at ~22 Ma (Early Miocene) (Petterson et al., 1999). Then, the TT, as a zone of conflicting subduction, is expected to have been active between ca. 20 and 10 Ma, developing the Maramuni Arc on Papua New Guinea (Hall, 2002; Baldwin et al., 2012), whereas the NBT has been proposed to fall between 14 and 8 Ma (Petterson et al., 1999; Hall, 2002; Mann and Taira, 2004; Schellart et al., 2006; Austermann et al., 2011). The available geophysical data and topography suggest that subduction at the TT is currently inactive (Abers et al., 2002; Riisager et al., 2003; Wallace et al., 2004; Holm et al., 2019), whereas the subduction in the NBT is currently active (**Figure 1B**). Previous conceptual schemes and dynamical studies have emphasized the subduction polarity reversal, that is, the NBT maybe the result of the convergence of the OJP and SIA, rarely considered the SI of the TT and the interactions between the TT and NBT (Mishin et al., 2008; Baldwin et al., 2012; Dai et al., 2018; Brandl et al., 2020; Sun et al., 2021; Zhang and Leng, 2021; Almeida et al., 2022). Thus, the formation sequence, interactions, and dynamics of the parallel triple subduction in the New Guinea region remain elusive.

In this article, we study the dynamics and stability of parallel triple subduction systems. For this purpose, we use a series of coupled thermomechanical numerical models based on finite differences and marker-in-cell techniques. These models reveal unknown processes of the oceanic plateau convergence to induce multiple subduction systems, thus providing an explanation for enigmatic geodynamic features that may have ancient multiple subduction characteristics.

2 MODEL METHODS

2.1 Numerical Modeling Method

Our two-dimensional magmatic thermodynamic model simulated collision between the OJP and SIA, which led to the initiation of subduction in the back-arc basin. The governing equations of momentum, mass, and energy conservation are solved with the I2VIS code (Gerya and Yuen, 2003). This code is based on conservative finite differences and a non-diffusive marker-in-cell technique applied on a staggered non-uniform Eulerian grid. The 4,000 km × 670 km numerical model domain is resolved with non-uniform 699 × 134 rectangular grids with the highest grid resolution of 2 km in the 1,500-km-wide and 200-km-thick subduction area of the model. We track the material properties in the different compositional layers by deploying ~7 million active Lagrangian markers. Complete

TABLE 1 | Physical parameters in the model.

Material[a]	ρ^0(kg/m^3)	Cp (J kg^{-1} K^{-1})	K (W m^{-1} K^{-1})	Hr (μWm^{-3})	Flow law	η_0 (Pa^n s)	E (kJ/mol)	V (J MPa^{-1} mol^{-1})	N	AD (MPa^{-n} s^{-1})	C (MPa)	Sin (φ_{eff})
Sticky air	1	3.3 × 10^6	200	0	10^{18}Pa s	–	–	–	–	–	–	–
Sticky water	1000	3.3 × 10^3	200	0	10^{18}Pa s	–	–	–	–	–	–	–
Sediment (solid)	2700	1000	K1	2	Wet quartzite	1.97E+17	154	0	2.3	3.20E-06	1	0.15
Upper continental crust (solid)	2700	1000	K1	1	Wet quartzite	1.97E+19	154	0	2.3	3.20E-06	20	0.15
Lower continental crust (solid)	3000	1000	K1	1	Plagioclase An75	4.80E+22	238	0	3.2	3.30E-04	20	0.45
Oceanic crust	3000	1000	K2	0.25	Plagioclase An75	4.80E+22	238	0	3.3	3.30E-04	20	0.45
Upper oceanic plateau crust (solid)	2730	1000	K2	0.25	Plagioclase An75	4.80E+22	238	0	3.3	3.30E-04	20	0.45
Middle oceanic plateau crust (solid)	2850	1000	K2	0.25	Plagioclase An75	4.80E+22	238	0	3.3	3.30E-04	20	0.45
Lower oceanic plateau crust (solid)	3030	1000	K2	0.25	Plagioclase An75	4.80E+22	238	0	3.3	3.30E-04	20	0.45
Lithosphere/dry mantle	3300	1000	K3	0.022	Dry olivine	3.98E+16	532	8	3.5	2.50E+04	40	0.6
Upper mantle of OJP	3100–3300	1000	K3	0.022	Dry olivine	3.98E+16	532	8	3.5	2.50E+04	40	0.6
Lower mantle of OJP	3100–3300	1000	K3	0.022	Dry olivine	3.98E+16	532	8	3.5	2.50E+04	40	0.6
Wet mantle (solid)	3200	1000	K3	0.022	Wet olivine	5.01E+20	470	8	4	2.00E+03	1	0.06
Mantle (Serpentinized/hydrated)	3200	1000	K3	0.022	Serpentine	3.21E+36	8.9	3.2	3.8	1.97E-33	1	0.06
Mafic underplating	3200	1000	K1	3	clinopyroxene	3.21E+36	670	0	2.7	1.56E-34	1	0.06
References[c]	1	/	2[b]	3	4	4, 5	4, 5	4, 5	4, 5	4, 5	–	–

[a] *ρ_0, reference density; Cp, specific heat capacity; k, thermal conductivity; Hr, radioactive heat; C, cohesion; sin (φ_{eff}), effective friction coefficient; η_0, reference viscosity; E, activation energy; V, activation volume; n, is the stress exponent; AD, material constant.*

[b] *K_1 = (0.64 + 807/(TK + 77))·exp.(0.00004PMPa); K2 = (1.18 + 474/(TK + 77))·exp.(0.00004PMPa); K3 = (0.73 + 1293/(TK + 77))·exp.(0.00004PMPa).*

[c] *References: 1, Bittner and Schmeling (1995); 2, Clauser and Huenges (1995); 3, Turcotte and Schubert (2003); 4, Ranalli, (1995); 5, Ranalli and Murthy (1987).*

details of the method are provided in a previous study (Gerya and Yuen, 2003).

The momentum conservation equation, incompressible continuity equation, and heat conservation equation are defined as follows:

(1) Stokes equation:

$$\frac{\partial \sigma'_{ij}}{\partial x_j} - \frac{\partial P}{\partial x_i} = g_i \rho (C, M, P, T),$$

where σ'_{ij} is the deviatoric stress tensor, g is the acceleration due to gravity, and density ρ depends on composition (C), melt fraction (M), pressure (P), and temperature (T).

(2) Conservation of mass is approximated by the incompressible continuity equation:

$$\frac{\partial V_i}{\partial X_i} = 0,$$

where V_i is the velocity vector.

(3) The heat conservation equations are

$$\rho C_p \frac{DT}{Dt} = -\frac{\partial q_i}{\partial x_i} + H,$$

$$q_i = -k(T, P, C)\frac{\partial T}{\partial x_i},$$

where DT/Dt is the full derivative of temperature with respect to time, C_p is the heat capacity, q_i is the heat flux, H represents the sum of individual heat sources (e.g. radioactive heat production, shear heating, adiabatic heating, and latent heat), and k is the thermal conductivity, which itself is a function of temperature, pressure, and composition.

The numerical model contains partial melting calculations for multiple rock types and relies on the empirically defined linear relationship between the volume ratio and temperature of partial melting as follows:

$$M = 0, T \le T_{solidus},$$

$$M = \frac{(T - T_{solidus})}{\left(T_{liquidus} - T_{solidus}\right)}, T_{solidus} < T < T_{liquidus},$$

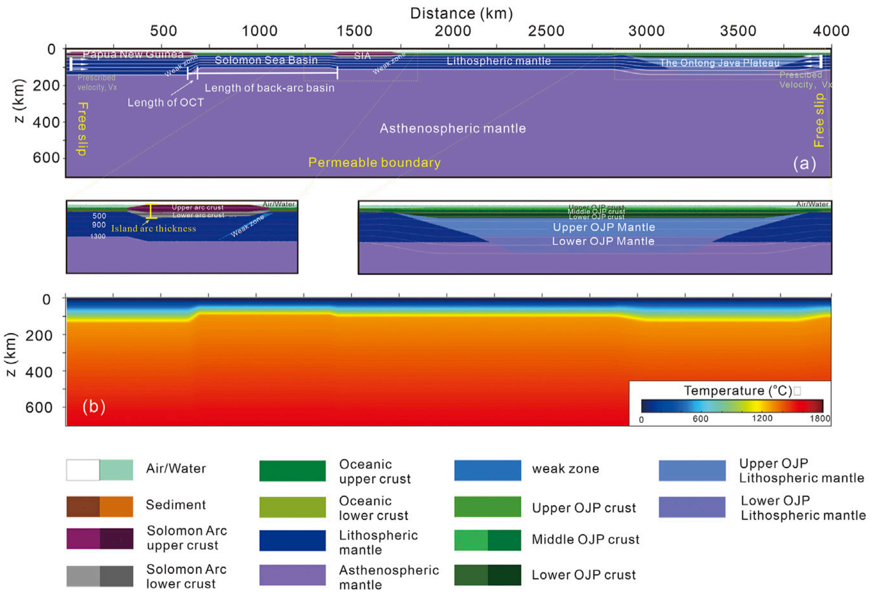

FIGURE 2 | Initial model configuration and boundary conditions. Panel **(A)** shows initial model configuration. Panel **(B)** shows the temperature field. The left inset represents a zoomed-in image of the island arc. The right inset represents anenlargement of the OJP. The isotherms (white lines) start at 100°C and are plotted at intervals of 400°C. The color key for different materials is shown at the bottom.

$$M = 1, T \geq T_{liquidus},$$

where M represents the volumetric fraction of the melt at a given temperature and $T_{solidus}$ and $T_{liquidus}$ correspond to the experimentally obtained wet solidus and dry liquidus temperatures, respectively (**Table 1**).

The rock density is dependent on the composition, melt fraction, temperature, and pressure. For partially molten rocks, the effective density obeys the following equations of state:

$$\rho_{eff} = \rho_{solid} - M\left(\rho_{solid} - \rho_{molten}\right),$$

$$\rho_{solid} = \rho_0 \left[1 - \alpha\left(T - T_0\right)\right]\left[1 + \beta\left(P - P_0\right)\right],$$

where ρ_{molten} and ρ_{solid} are the densities of molten and solid rock, respectively and ρ_0 is the standard density evaluated at $P_0 = 0.1$ MPa and $T_0 = 298$ K (**Table 1**). The thermal expansion coefficient (α) is set to $3 \times 10^{-5}\ \mathrm{K}^{-1}$, and the compressibility (β) is set to $1 \times 10^{-5}\ \mathrm{MPa}^{-1}$.

The rheology used in this study is viscoplastic. The creep flow is defined by the following equation:

$$\eta_{creep} = \left(\dot{\varepsilon}_{II}\right)^{\frac{1-n}{n}} A_D^{-\frac{1}{n}} \exp\left(\frac{E + PV}{nRT}\right),$$

where $\dot{\varepsilon}_{II}$ is the second invariant of the strain rate tensor and A_D, n, E, R, and V correspond to the material constant, stress exponent, activation energy, gas constant, and activation volume, respectively.

Plastic failure is approximated with the Drucker–Prager yield relationship (Ranalli, 1995):

$$\sigma_{yield} = C_0 + P\sin\left(\varphi_{eff}\right),$$

$$\eta_{\mathrm{plastic}} = \frac{\sigma_{yield}}{2\dot{\varepsilon}_{II}},$$

$$\eta_{eff} = \min\left(\eta_{creep}, \eta_{\mathrm{plastic}}\right),$$

where σ_{yield} is the yield stress, C_0 is cohesion, and φ_{eff} is the effective internal frictional angle. The effective viscosity (η_{eff}) of rocks is constrained by both viscous and plastic deformation, determined by the minimization of the same.

The topography changes because of erosion and sedimentation, which is defined as:

$$\frac{\partial y_{es}}{\partial t} = v_y - v_x \frac{\partial y_{es}}{\partial y} - v_s + v_e,$$

where v_s is the sedimentation rate, v_e is the erosion rate, y_{es} is the vertical position of the surface as a function of the horizontal distance, and v_x and v_y are the horizontal and vertical components of the material velocity vector at the surface, respectively. The material properties and used parameters in this study are shown in **Table 1**.

2.2 Model Geometry and Initial and Boundary Conditions

We conducted a series of numerical experiments with various island-arc crust thicknesses, back-arc basin length, and the ocean–continent transition (OCT) length and pre-existing lithospheric weakness in the OCT (**Figure 2**).

The numerical models include two domains – the left-side continent with an arc/back-arc and the right-side oceanic plate with oceanic plateau. The transition between these two domains is demarcated by a weak zone.

The plateau is 1,120 km wide and has a 26.6-km-thick oceanic crust underlain by a depleted lithospheric mantle. The oceanic plate on which the OJP resides has a normal oceanic plate thickness of 8 km (**Figure 2**). Based on seismic wave speed data, we infer that the OJP crust is divided into three layers. The oceanic plateau crust is 26.6 km thick and consists of an upper crust (a 2.66-km-thick layer of basaltic rock), a middle crust (a 5.3-km-thick layer of gabbro), and an 18.64-km-thick layer of ductile ultramafic rock (**Figure 2**). Moreover, more recent data suggest that the OJP has a thick viscous mantle root (Tharimena et al., 2016; Isse et al., 2021). Seismic and geochemical constraints reveal that the lithospheric mantle beneath the plateau may also be stratified into two layers comprising a typical oceanic lithosphere (with a thickness of 44 km) underlain by a layer that includes a component of recycled Proterozoic lithosphere (with a thickness of 44 km) (Ishikawa et al., 2004, 2011; Mann and Taira, 2004; Covellone et al., 2015; Tharimena et al., 2016; Wang et al., 2017; Wang and Kusky, 2019; Isse et al., 2021). We determined the density of the plateau and the density of each layer from the P-wave velocity structure and then further constrained the correctness of the model using Crust1.0.

Previous studies suggested that the SIA is an island arc with continental crust affinity (Tapster et al., 2014). As such, in our model, we define the SIA with continental crust properties. The arc comprises two layers: the felsic upper crust, with wet quartzite rheological properties, and the mafic lower crust which has the rheological properties of plagioclase. According to the Crust1.0 model, our model arc's crustal thickness is asymmetric. The left part has a thickness of 38 km, and the right part varies in the range of 38–42 km (**Supplementary Table S1**).

The initial thermal structure of the back-arc is defined by the plate cooling model with a plate depth of 88 km (Shi et al., 2020). The initial cooling age of the oceanic lithosphere is taken to be 30 Myr, which is similar to a previous numerical modeling study that investigated variations in oceanic–continental and intraoceanic subduction modes (Zhou et al., 2018, 2020; Li et al., 2019; Dai et al., 2020; Tao et al., 2020). The length of the back-arc basin is 650 km, 700 km, and 750 km based on plate reconstruction results (Müller et al., 2019).

The length of the OCT is 20, 30, 40, and 50 km. The OCT was either stable or with an initial 50-km-length weak zone which was probably due to large fractures based on previous speculation (Marwen et al., 2015). The continental domain comprises a 6-km-thick sedimentary layer, a 14-km-thick upper crust, a 15-km-thick lower crust, and an 85-km-thick lithospheric mantle. A thin "sticky air" layer with low density and viscosity was also applied (Crameri et al., 2012), which allowed the direct calculation of topography evolution. An asthenospheric mantle was imposed below the continental and oceanic lithosphere.

The initial temperature structure of the model varied from 0°C at the surface to 1300°C at the bottom of the lithospheric mantle (Shi et al., 2020). The initial temperature gradient of the asthenospheric mantle is ~0.5°C/km (Shi et al., 2020). The detailed compositions and temperature profile of our model are shown in **Figure 2**. The rock properties and layer thicknesses vary depending on the model parameters (**Table 1**).

We applied free-slip boundary conditions at all boundaries except for the lower boundary that is permeable (Li et al., 2016). Subduction is prescribed by the total convergence rate RT = RR + RL, where RR and RL are locally imposed constant velocities for the right and the left plates, respectively (**Figure 1C**). Thus, the total convergence rate is controlled and not the rates of individual slabs driven by slab-pull. In this series model, the initial right plate velocity is 3 cm/yr until the thick, buoyant oceanic plateau just reaches the trench. Based on previous plate reconstruction results (Müller et al., 2019), once the plateau reaches the trench, we linearly decrease the left plate velocity to 3 cm/yr, although in nature, the subduction rate is controlled by the subduction dynamics itself.

3 RESULTS

3.1 Summary of Model Results and Controlling Factors

We have run 54 model cases in total (**Supplementary Table S1**) to study the effects of the initial island-arc crust thickness, the length of the back-arc basin and the OCT, and pre-existing lithospheric weakness in the OCT (**Figure 2A**), on the evolution of parallel triple subduction systems. The numerical results are summarized as two contrasting models (**Figure 3**): 1) the double subduction model, which includes the forward subduction jumping model (FSJ) and the subduction polarity reversal model (SPR); 2) the parallel triple subduction model, which includes the tendency to the forward jumping model (TFSJ) and the tendency to polarity reversal (TSPR).

The model results showed that the pre-existing lithospheric weakness and length of the OCT are fundamental for the SI in the

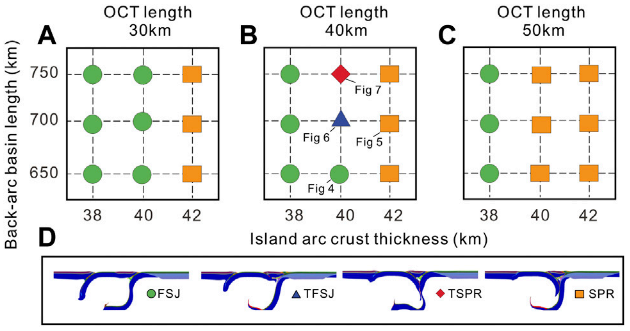

FIGURE 3 | Summary of model results. Panel **(A–C)** shows the model results with different OCT length. Green circles correspond to numerical modeling results of the forward subduction jumping model (FSJ); orange squares represent the subduction polarity reversal model (SPR); the red diamonds correspond to numerical model results that the parallel triple subduction model tends to polarity reversal (TSPR); and dark blue triangles represent that the parallel triple subduction model tends to the jumping model (TFSJ). Panel **(D)** shows the four different types of model results.

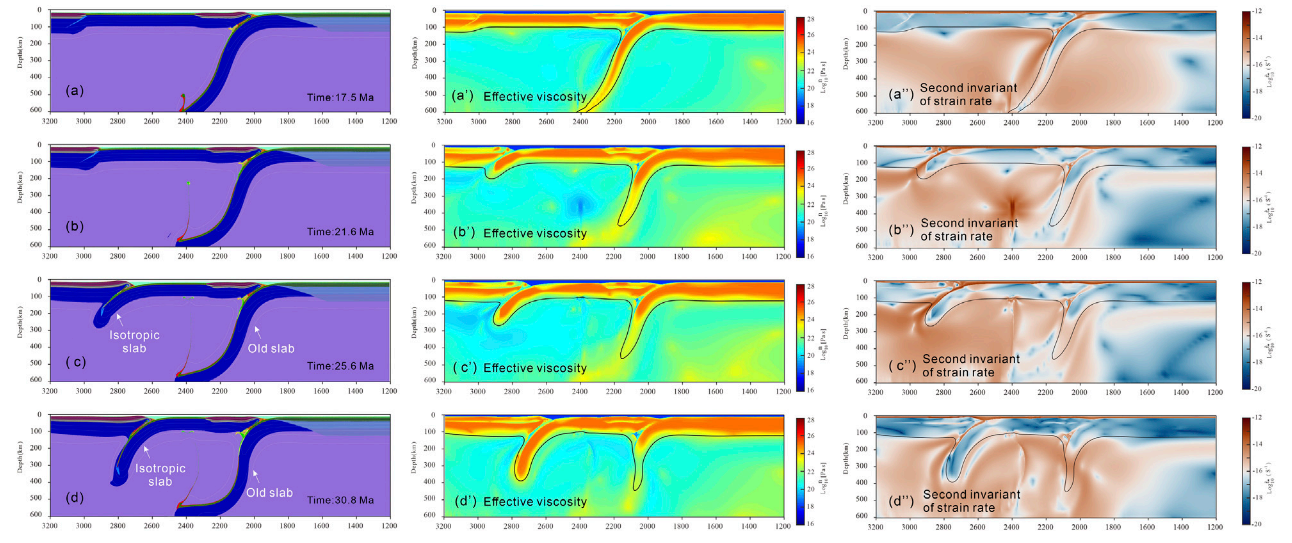

FIGURE 4 | Evolutionary process of Model 1. Panels **(A–D)**, **(a'-d')**, and **(a''-d'')** show rock composition, effective viscosity, and second invariant of the strain rate at different time steps, that is, 17.6, 21.6, 25.6, and 30.8 Ma, respectively. The color bars of viscosity and strain rate are shown on the left, while the color bar of composition is shown in **Figure 2**.

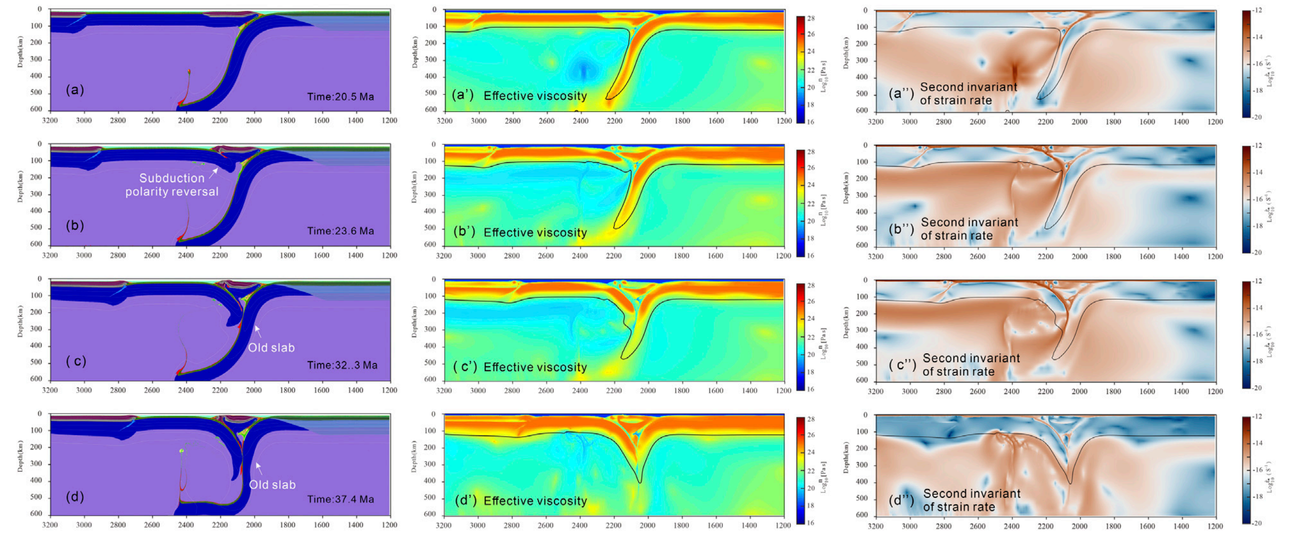

FIGURE 5 | Evolutionary process of Model 2. Panels **(A–D)**, **(a'-d')**, and **(a''-d'')** show rock composition, effective viscosity, and second invariant of the strain rate at different time steps, that is, 20.5, 23.6, 32.3 and 37.4 Ma, respectively. The color bars of viscosity and strain rate are shown on the left, while the color bar of composition is shown in **Figure 2**.

OCT (**Supplementary Table S1**; **Figure 3**). If the length of the OCT is 40 km, the results with the pre-existing lithospheric weakness in the OCT region showed that all four modes can be predicted (**Figure 3B**). Otherwise, there will only be one mode: subduction polarity reversal, if there are no pre-existing weaknesses (**Supplementary Table S1**). To further study the length of OCT importance, additional models with a narrower and longer OCT (i.e., 30 and 50 km) were used. The results indicate that a narrow OCT favors the SI in the OCT, differing from models with a 40-km-length OCT, while the longer OCT prevents the formation (**Supplementary Table S1**).

In addition, the island-arc crust thickness and length of the back-arc basin have a contribution to the results as well (**Figure 3**). The model results show that when the island-arc thickness becomes thick and the subduction mode changes from the FSJ modes to the SPR modes (**Figure 3A**). In addition, the model results with the same arc thickness of 40 km showed that when the length of the back-arc basin increases, the subduction mode changes from an FSJ

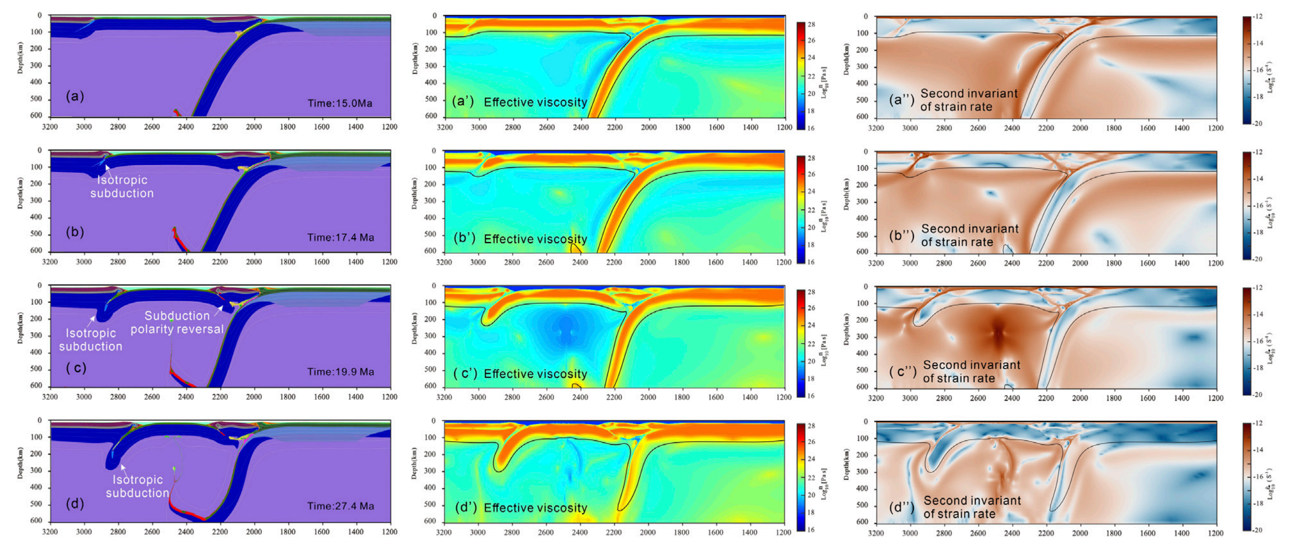

FIGURE 6 | Evolutionary process of Model 3. Panels **(A–D)**, **(a'-d')**, and **(a''-d'')** show rock composition, effective viscosity, and second invariant of the strain rate at different time steps, that is, 15.0, 17.4, 19.9 and 27.4 Ma, respectively. The color bars of viscosity and strain rate are shown on the left, while the color bar of composition is shown in **Figure 2**.

mode to a TFSJ mode and eventually, a TSPR mode (**Figure 3B**). The model results indicated that the increase in the length of the back-arc basin and the island-arc crust thickness favors the SPR (**Figure 3A**) and prevents the SI in the OCT (**Figure 3**).

3.2 The Double Subduction

3.2.1 Forward Subduction Jumping Model

Model 1 represents a typical example of forward subduction jumping model (**Figure 4**). The length of the OCT and back-arc basin and the initial thickness of the arc crust were set to 40, 650, and 40 km, respectively.

At the computational time of 17.5 Myr (**Figure 4A**), the oceanic plateau reached the subduction zone. At 21.6 Myr, the old subduction zone was blocked (**Figure 4B**). Subsequently, the OCT region begins to rupture accompanied by a high strain rate concentration under continuous compression (**Figure 4B**). After about 4 million years (Myr), under the dual effect of the continuous compression of the continental plate and obstruction of the oceanic plateau, the parallel subduction zone developed at the OCT (**Figure 4C**). After 30.8 Myr, the old subduction zone tends to break off while the newly formed subduction zone subducts to 400 km (**Figure 4D**). Thus, this model is typically characterized by the formation of forward double subduction zones and no subduction polarity reversal.

3.2.2 Subduction Zone Polarity Reversal

Model 2 represents a typical example of subduction zone polarity reversal modes (**Figure 5**). The length of the OCT and back-arc basin and the initial thickness of the arc crust were set to 40, 700, and 42 km, respectively.

In this model, the SI occurred at the island-arc and back-arc basin transitional region (IBT) which was different from the isotropic subduction model (**Figure 5**). With continuous compression, the IBT and OCT regions were accompanied by a high strain rate concentration (**Figure 5A**). At 23.6 Myr (**Figure 5B**), the IBT region begins to rupture, and the SPR begins when the oceanic plateau just reached the trench, while the concentrated strain rate in the OCT region was not sufficient to cause lithospheric rupture. With the ongoing plate convergence, the new subduction slab collided with the old subduction slab and then resulted in the slab detachment of the old slab (**Figure 5C,D**). Thus, this model is typically characterized by the formation of subduction polarity reversal and no double isotropic subduction zones.

3.3 Parallel Triple Subduction Model

3.3.1 Tendency to Subduction Jumping Model

Model 3 represents a typical example of a parallel triple subduction model with a preference for isotropic jumping modes (**Figure 6**), which has the same parameters as Model 1 except that the length of the back-arc basin increases to 700 km.

Similar to Model 1, the oceanic plate in Model 3 continuously subducted due to the right push force until the oceanic plateau reached the subduction zone. Similarly, with continuous compression, the OCT region begins to rupture, accompanied by a high strain rate concentration (**Figure 4B**). In addition, the isotropic subduction zone occurred at the OCT (**Figure 6B**). Unlike Model 1, the thickened island arc increased the rheological strength difference between the island-arc and the back-arc basin, making the SPR more easily occurring (Wang et al., 2022). Thus, at 17.4 to –19.9 Myr, the SPR occurred in the interaction region between the island-arc and the back-arc basin. However, the SPR was short-lived and maintained for about 3 Ma, resulting from the continuous subduction of the isotropic subduction zone.

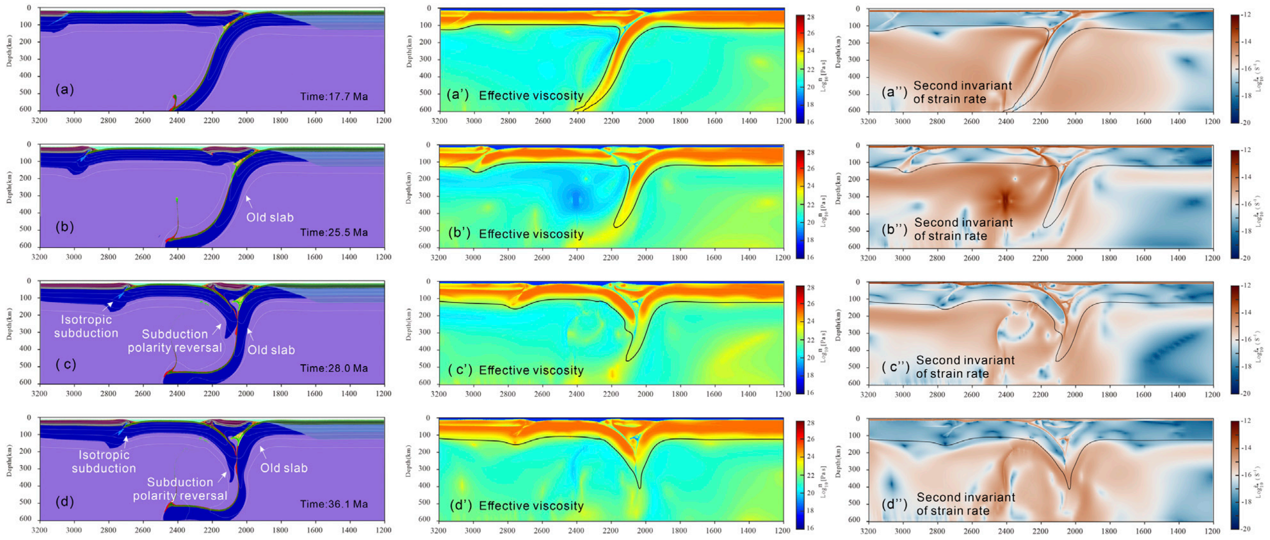

FIGURE 7 | Evolutionary process of Model4. Panels **(A–D)**, **(a'-d')**, and **(a''-d'')** show rock composition, effective viscosity, and second invariant of strain rate at different time steps, that is, 17.7, 25.5, 28.0 and 36.1 Ma, respectively . The color bars of viscosity and strain rate are shown on the left, while the color bar of composition is shown in **Figure 2**.

Thus, this model is typically characterized by the formation of parallel triple subduction, but more inclined to the subduction jumping.

3.3.2 Tendency to the Polarity Reversal Model

Model 4 represents a typical example of a parallel triple subduction model with a preference for polarity reversal modes (**Figure 7**), which has the same parameters as Model 3 except that the length of the back-arc basin increases to 750 km.

Similar to Model 3, with continuous compression, the OCT region begins to rupture, accompanied by a high strain rate concentration (**Figure 4B**). The isotropic subduction zone occurred at the OCT and subducted to about 200 km (**Figure 6B**). The SPR occurred in the interaction region between the island-arc and the back-arc basin. Contrary to Model 3, the isotropic subduction zone was short-lived, resulting from the continuous subduction of the reversal subduction. In addition, similar to case Model 2, with the ongoing plate convergence, the SPR slab collided with the old subduction slab and then resulted in the slab detachment of the old slab (**Figure 7C,D**). Thus, this model is typically characterized by the formation of parallel triple subductions, but more inclined to the SPR, which may fit best with the parallel triple subduction system in the New Guinea region (**Figure 1D**).

4 DISCUSSION

4.1 Model Results Versus Natural Data

The modeling results presented previously give new insights into the mechanisms of a parallel triple subduction system and support the interpretation of similar natural cases, such as the New Guinea region (**Figure 1**). Some studies have argued for three dipping subduction zones (**Figure 8**): north-dipping at the NBT and south-dipping at the TT and NST (Baldwin et al., 2012; Holm et al., 2019). The seismicity at the TT lacks an organized (shallow-to-deep) pattern indicative of southward subduction, and the seismic reflection images show weakly deformed sediments (Holm et al., 2016). Overall, the available geophysical data suggest that subduction in the TT is currently inactive with subduction depth being less than 200 km (Holm et al., 2019), while the subduction in the NBT is currently more seismically active (**Figure 8**).

However, previous models have discussed the SI in the TT and NBT separately and have not linked the formation of both (Marwen et al., 2015; Wang et al., 2022). The complex processes involving the onset and death of parallel triple subduction zones in the New Guinea region are resolved in our numerical model. Although Models 3 and 4 also showed the onset and death of parallel triple subduction zones, the morphology in Model 3 is not consistent with present-day seismic data, which are more active in the isotropic subduction. Model 4 fits best with the parallel triple subduction systems in the New Guinea region, including subduction depth and subduction pattern (**Figure 8**). In addition, the topography profile of Model 4 can well match the present-day topography profile (**Figure 8**).

4.2 The Role of Model Parameters

The initial island-arc crust thicknesses, length of the back-arc basin and OCT, and pre-existing lithospheric weakness in the OCT are the key driving factors for the parallel triple subduction system. The effects of the four main controlling factors are investigated in our study (**Figure 3**).

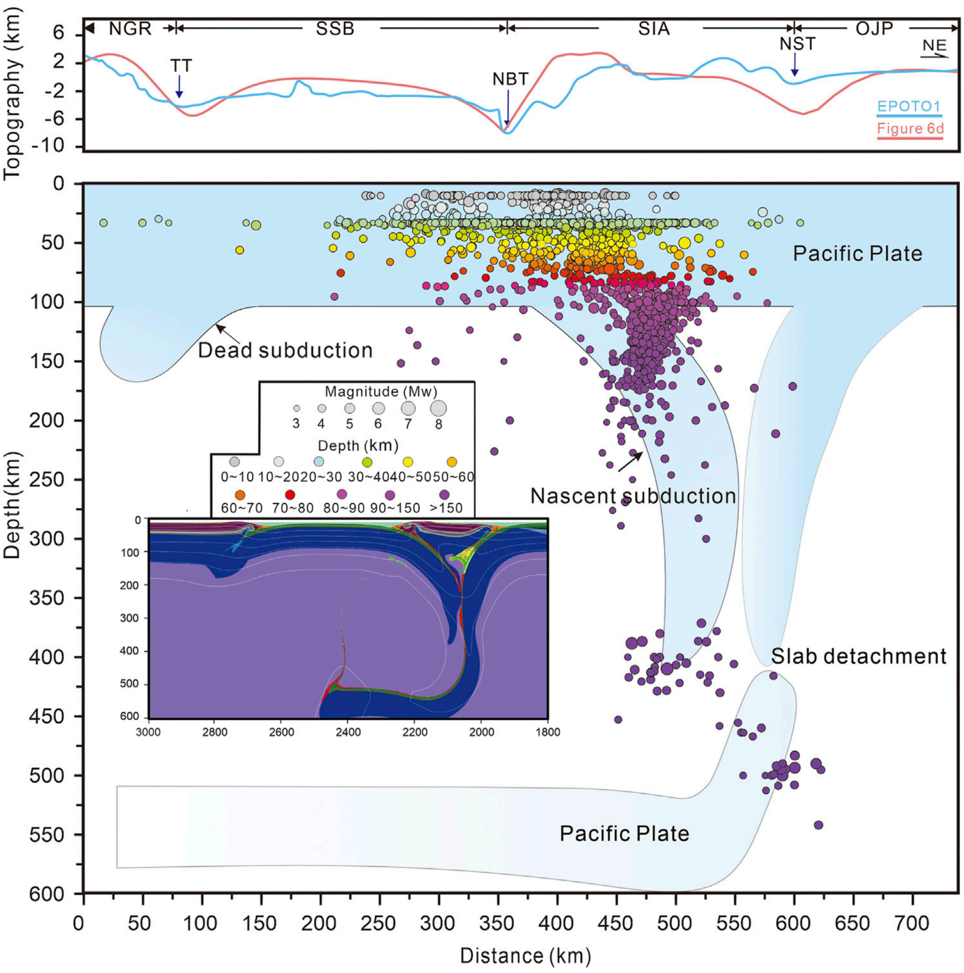

FIGURE 8 | Model results versus natural data. The topographic data in the abovementioned figure are from ETOPO1, and the seismic data in the lower figure are from Geomap (http://www.geomapapp.org). The sampling line is shown by red lines in **Figure 1A**.

Our models suggested that the weaker zones in the OCT region have provided conditions for the rupture of the continental lithosphere and propagate to form a new subduction zone along the weak zones. In addition, the narrow OCT further weakened the rheological properties of the OCT region, making the subduction in the TT more likely to occur. Our results are consistent with those of previous studies suggesting a larger fracture in the TT region (Marwen et al., 2015), which may correspond to the pre-existing lithospheric weakness in the OCT of our models.

In addition, the formation of the NBT is controlled by the rheological strength difference between the SIA and SSB (Wang et al., 2022). The increase in the thickness of the island arc can effectively increase the rheological strength difference between the island-arc and the back-arc basin, which also causes the SPR to occur more easily (Wang et al., 2022).

The length of the OCT is also an important factor for mode selection. The length of the back-arc basin does not determine the onset of the subduction in the TT and NBT, but it can regulate the competitive relationship between the two subduction zones. Assuming that the SSB is narrow, the models showed that the subduction in the TT and NBT form a strong competitive relationship under a convergence background. The formation of the TT and NBT depends on which one has a weaker rheological strength before the SI. In contrast, if the length of the back-arc basin increases, the subduction in the TT and NBT forms a weak competitive relationship, and the subductions in the TT and NBT are initiated relatively independently. Which one can form depends on whether other parameters satisfy the conditions for the SI, that is, the initial island-arc thicknesses, length of the OCT, and pre-existing lithospheric weakness in the OCT. If the conditions are satisfied on both the modes, the TT and NBT both can be formed. After the onset of subduction, the one which is more fully developed will remain active and the other one will be dead. If both subduction zones are fully developed, then an opposing subduction will be formed (Holt et al., 2017; Candioti et al., 2020).

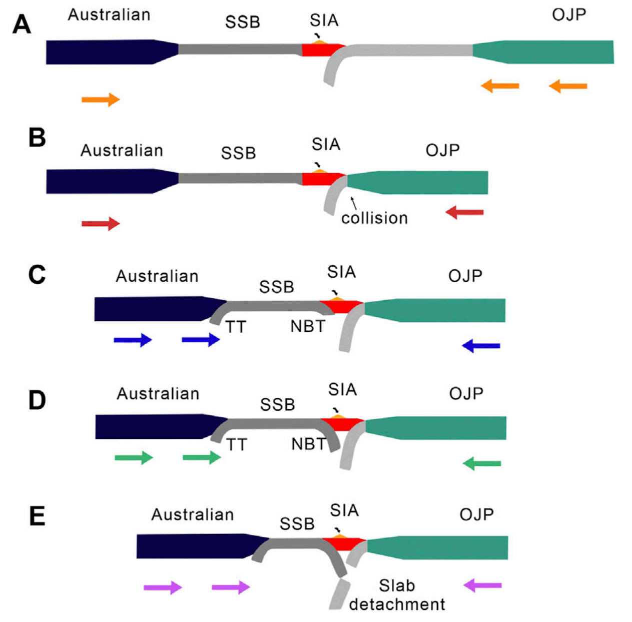

FIGURE 9 | Schematic diagram for the evolution of the New Guinea region as a sequence of stages for important events. Panel **(A–E)** represent different stages of evolution. The arrows represent the direction of plate movement.

4.3 Schematic Diagram for the Evolution of the New Guinea Region

Our numerical model results may also provide significant insight into the SI time of different subduction zones in the New Guinea subduction system. Although the present-day geological evidence has constrained the ages of the two subduction zones, the NBT (14–8 Ma) and the TT (20–10 Ma), to a certain range, there is no clear evidence for the sequence of the two subduction zones (Petterson et al., 1999; Hall, 2002; Mann and Taira, 2004; Schellart et al., 2006; Austermann et al., 2011; Baldwin et al., 2012; Holm et al., 2013). However, based on our numerical model, we propose that the NBT was formed later than the TT, and the TT began to be inactive about 3 Myr after the formation of the NBT.

Therefore, based on the latest reconstruction results (Müller et al., 2019), we suggest that the initial arrival of the OJP at the NST (NST) at ~22 Ma (Early Miocene) was termed a "soft docking" event (**Figure 9B**). In addition, the TT, as a zone of conflicting subduction, occurred first (**Figure 9C**), which leads to the arc volcanic rocks of the Papua Peninsula (Baldwin et al., 2012; Holm et al., 2019; Faccenna et al., 2021). After about 3–4 Myr, the northward NBT begins to develop. At this stage, the region progresses from the FSJ model (**Figure 4**) to the TFSJ model (**Figure 6**), while the subduction zone in the TT still dominates (**Figure 9**). Subsequently, under continuous advancing subduction, the subduction in the NBT gradually becomes the main channel for convergent stress release, and the region evolves to the TSPR model (**Figure 6**; **Figure 9D**). Then, the new slab near the island arc interacts with the old Pacific slab to result in the slab detachment of the old Pacific slab (**Figure 9E**).

5 CONCLUSION

We constructed a series of 2D thermal-mechanical numerical models to investigate the patterns and key parameters controlling the parallel triple subduction system. The model results showed that the subduction patterns can be divided into four main types: 1) the double subduction model, which includes the forward subduction jumping model (FSJ) and the subduction polarity reversal model (SPR) and 2) the parallel triple subduction model, which includes the tendency to the forward jumping model (TFSJ) and the tendency to polarity reversal (TSPR).

Our model suggested that a pre-existing weak zone in the OCT is necessary for the formation of the parallel triple subduction system, which has provided conditions for the rupture of the lithosphere. In addition, a narrower OCT favors the SI in the OCT, while a thicker island arc favors the SI in the IBT. The length of the back-arc basin does not determine the onset of the subduction in the TT and NBT, but it can regulate the competitive relationship between the two subduction zones. In addition, the onset and death of parallel triple subduction zones observed in our model can successfully explain the geological observations of multiple subductions in the New Guinea region from 25 Ma to the present day.

We suggest that the pre-existing lithospheric weakness and length of the OCT in Papua New Guinea determine the formation of the TT, whereas the formation of the NBT is controlled by the rheological strength difference between the SIA and SSB; the initial length of the SSB can regulate the competitive relationship between the TT and NBT, which also determines the present-day inactive state of the TT. If the SSB is longer, the TT and NBT are initiated independently, while a narrower SSB will allows the interaction of the TT and NBT during the SI. In addition, we explain in detail the tectonic evolution of the parallel triple subduction system in the New Guinea region based on our results.

DATA AVAILABILITY STATEMENT

The raw data supporting the conclusions of this article will be made available by the authors, without undue reservation.

AUTHOR CONTRIBUTIONS

LW wrote the manuscript. LW and LD conceptualized the study, developed the methodology, and performed the numerical simulation and validation. WG conceptualized the study. SL and XJ acquired the funding and supervised the study. HD, DW, FL and SY performed the investigation, data curation, and validation.

FUNDING

The research leading to these results has received funds from NSFC projects (Grant Nos 91958214, 91855208, 91858215, 41402172, 41688103, 42121005, and 42176064), the National Key

Technologies R&D Program (2017YFC0601401; 2017YFC0601300-01; 2016YFC0601002), Taishan Scholar Programs to Profs. SL (tspd20210305) and Yongjiang Liu (ts20190918) and Qingdao Leading innovation talents (19-3-2-19-zhc), and the Fundamental Research Funds for the Central Universities (202161011).

REFERENCES

Abers, G. A., Ferris, A., Craig, M., Davies, H., Lerner-Lam, A. L., Mutter, J. C., et al. (2002). Mantle Compensation of Active Metamorphic Core Complexes at Woodlark Rift in Papua New Guinea. *Nature* 418, 862–865. doi:10.1038/nature00990

Almeida, J., Riel, N., Rosas, F. M., Duarte, J. C., and Schellart, W. P. (2022). Polarity-reversal Subduction Zone Initiation Triggered by Buoyant Plateau Obstruction. *Earth Planet. Sci. Lett.* 577, 117195. doi:10.1016/J.EPSL.2021.117195

Austermann, J., Ben-Avraham, Z., Bird, P., Heidbach, O., Schubert, G., and Stock, J. M. (2011). Quantifying the Forces Needed for the Rapid Change of Pacific Plate Motion at 6Ma. *Earth Planet. Sci. Lett.* 307, 289–297. doi:10.1016/j.epsl.2011.04.043

Baldwin, S. L., Fitzgerald, P. G., and Webb, L. E. (2012). Tectonics of the New Guinea Region. *Annu. Rev. Earth Planet. Sci.* 40, 495–520. doi:10.1146/annurev-earth-040809-152540

Bittner, D., and Schmeling, H. (1995). Numerical Modelling of Melting Processes and Induced Diapirism in the Lower Crust. *Geophys. J. Int.* 123, 59–70.

Brandl, P. A., Hannington, M. D., Geersen, J., Petersen, S., and Gennerich, H.-H. (2020). The Submarine Tectono-Magmatic Framework of Cu-Au Endowment in the Tabar-To-Feni Island Chain, PNG. *Ore Geology. Rev.* 121, 103491. doi:10.1016/j.oregeorev.2020.103491

Candioti, L. G., Schmalholz, S. M., and Duretz, T. (2020). Impact of Upper Mantle Convection on Lithosphere Hyperextension and Subsequent Horizontally Forced Subduction Initiation. *Solid Earth* 11, 2327–2357. doi:10.5194/se-11-2327-2020

Chesley, C., Naif, S., Key, K., and Bassett, D. (2021). Fluid-rich Subducting Topography Generates Anomalous Forearc Porosity. *Nature* 595, 255–260. doi:10.1038/s41586-021-03619-8

Clauser, C., and Huenges, E. (1995). "Thermal conductivity of rocks and minerals," in *Rock physics and phase relations*Editors T. J. Ahrens (Washington, DC: American Geophysical Union), 105–126.

Covellone, B. M., Savage, B., and Shen, Y. (2015). Seismic Wave Speed Structure of the Ontong Java Plateau. *Earth Planet. Sci. Lett.* 420, 140–150. doi:10.1016/j.epsl.2015.03.033

Crameri, F., Schmeling, H., Golabek, G. J., Duretz, T., Orendt, R., Buiter, S. J. H., et al. (2012). A Comparison of Numerical Surface Topography Calculations in Geodynamic Modelling: an Evaluation of the 'sticky Air' Method. *Geophys. J. Int.* 189, 38–54. doi:10.1111/j.1365-246X.2012.05388.x

Dai, L., Li, S., Li, Z.-H., Somerville, I., Suo, Y., Liu, X., et al. (2018). Dynamics of Exhumation and Deformation of HP-UHP Orogens in Double Subduction-Collision Systems: Numerical Modeling and Implications for the Western Dabie Orogen. *Earth-Science Rev.* 182, 68–84. doi:10.1016/J.EARSCIREV.2018.05.005

Dai, L., Wang, L., Lou, D., Li, Z. H., Dong, H., Ma, F., et al. (2020). Slab Rollback versus Delamination: Contrasting Fates of Flat-Slab Subduction and Implications for South China Evolution in the Mesozoic. *J. Geophys. Res. Solid Earth* 125, 1–18. doi:10.1029/2019jb019164

Faccenna, C., Becker, T. W., Holt, A. F., and Brun, J. P. (2021). Mountain Building, Mantle Convection, and Supercontinents: Revisited. *Earth Planet. Sci. Lett.* 564, 116905. doi:10.1016/J.EPSL.2021.116905

Faccenna, C., Holt, A. F., Becker, T. W., Lallemand, S., and Royden, L. H. (2018). Dynamics of the Ryukyu/Izu-Bonin-Marianas Double Subduction System. *Tectonophysics* 746, 229–238. doi:10.1016/j.tecto.2017.08.011

Fu, D., Huang, B., Johnson, T. E., Wilde, S. A., Jourdan, F., Polat, A., et al. (2022). Boninitic Blueschists Record Subduction Initiation and Subsequent Accretion of an Arc-Forearc in the Northeast Proto-Tethys Ocean. *Geology* 50, 10–15. doi:10.1130/g49457.1

SUPPLEMENTARY MATERIAL

The Supplementary Material for this article can be found online at: https://www.frontiersin.org/articles/10.3389/feart.2022.861240/full#supplementary-material

Gerya, T. V., and Yuen, D. A. (2003). Characteristics-based Marker-In-Cell Method with Conservative Finite-Differences Schemes for Modeling Geological Flows with Strongly Variable Transport Properties. *Phys. Earth Planet. Interiors* 140, 293–318. doi:10.1016/j.pepi.2003.09.006

Hall, R. (2002). Cenozoic Geological and Plate Tectonic Evolution of SE Asia and the SW Pacific: Computer-Based Reconstructions, Model and Animations. *J. Asian Earth Sci.* 20. doi:10.1016/S1367-9120(01)00069-4

Holm, R. J., Rosenbaum, G., and Richards, S. W. (2016). Post 8 Ma Reconstruction of Papua New Guinea and Solomon Islands: Microplate Tectonics in a Convergent Plate Boundary Setting. *Earth-Science Rev.* 156, 66–81. doi:10.1016/j.earscirev.2016.03.005

Holm, R. J., Spandler, C., and Richards, S. W. (2013). Melanesian Arc Far-Field Response to Collision of the Ontong Java Plateau: Geochronology and Petrogenesis of the Simuku Igneous Complex, New Britain, Papua New Guinea. *Tectonophysics* 603, 189–212. doi:10.1016/j.tecto.2013.05.029

Holm, R. J., Tapster, S., Jelsma, H. A., Rosenbaum, G., and Mark, D. F. (2019). Tectonic Evolution and Copper-Gold Metallogenesis of the Papua New Guinea and Solomon Islands Region. *Ore Geology. Rev.* 104, 208–226. doi:10.1016/j.oregeorev.2018.11.007

Holt, A. F., Royden, L. H., and Becker, T. W. (2017). The Dynamics of Double Slab Subduction. *Geophys. J. Int.* 209, ggw496–265. doi:10.1093/gji/ggw496

Huangfu, P., Li, Z.-H., Gerya, T., Fan, W., Zhang, K.-J., Zhang, H., et al. (2018). Multi-terrane Structure Controls the Contrasting Lithospheric Evolution beneath the Western and central-eastern Tibetan Plateau. *Nat. Commun.* 9, 1–11. doi:10.1038/s41467-018-06233-x

Huangfu, P., Wang, Y., Cawood, P. A., Li, Z.-H., Fan, W., and Gerya, T. V. (2016). Thermo-mechanical Controls of Flat Subduction: Insights from Numerical Modeling. *Gondwana Res.* 40, 170–183. doi:10.1016/j.gr.2016.08.012

Ishikawa, A., Maruyama, S., and Komiya, T. (2004). Layered Lithospheric Mantle beneath the Ontong Java Plateau: Implications from Xenoliths in Alnöite, Malaita, Solomon Islands. *J. Petrol.* 45, 2011–2044. doi:10.1093/petrology/egh046

Ishikawa, A., Pearson, D. G., and Dale, C. W. (2011). Ancient Os Isotope Signatures from the Ontong Java Plateau Lithosphere: Tracing Lithospheric Accretion History. *Earth Planet. Sci. Lett.* 301, 159–170. doi:10.1016/j.epsl.2010.10.034

Isse, T., Suetsugu, D., Ishikawa, A., Shiobara, H., Sugioka, H., Ito, A., et al. (2021). Seismic Evidence for a Thermochemical Mantle Plume Underplating the Lithosphere of the Ontong Java Plateau. *Commun. Earth Environ.* 2, 1–7. doi:10.1038/s43247-021-00169-9

Jagoutz, O., Royden, L., Holt, A. F., and Becker, T. W. (2015). Anomalously Fast Convergence of India and Eurasia Caused by Double Subduction. *Nat. Geosci* 8, 475–478. doi:10.1038/NGEO2418

Lallemand, S., and Arcay, D. (2021). Subduction Initiation from the Earliest Stages to Self-Sustained Subduction: Insights from the Analysis of 70 Cenozoic Sites. *Earth-Science Rev.* 221, 103779. doi:10.1016/J.EARSCIREV.2021.103779

Li, S., Zhao, S., Liu, X., Cao, H., Yu, S., Li, X., et al. (2018). Closure of the Proto-Tethys Ocean and Early Paleozoic Amalgamation of Microcontinental Blocks in East Asia. *Earth-Science Rev.* 186, 37–75. doi:10.1016/J.EARSCIREV.2017.01.011

Li, Z.-H., Gerya, T., and Connolly, J. A. D. (2019). Variability of Subducting Slab Morphologies in the Mantle Transition Zone: Insight from Petrological-Thermomechanical Modeling. *Earth-Science Rev.* 196, 102874. doi:10.1016/j.earscirev.2019.05.018

Li, Z.-H., Liu, M., and Gerya, T. (2016). Lithosphere Delamination in continental Collisional Orogens: A Systematic Numerical Study. *J. Geophys. Res. Solid Earth* 121, 5186–5211. doi:10.1002/2016JB013106

Liao, J., Malusà, M. G., Zhao, L., Baldwin, S. L., Fitzgerald, P. G., and Gerya, T. (2018). Divergent Plate Motion Drives Rapid Exhumation of (Ultra)high Pressure Rocks. *Earth Planet. Sci. Lett.* 491, 67–80. doi:10.1016/j.epsl.2018.03.024

Lyu, T., Zhu, Z., and Wu, B. (2019). Subducting Slab Morphology and Mantle Transition Zone Upwelling in Double-Slab Subduction Models with Inward-Dipping Directions. *Geophys. J. Int.* 218, 2089–2105. doi:10.1093/gji/ggz268

Mann, P., and Taira, A. (2004). Global Tectonic Significance of the Solomon Islands and Ontong Java Plateau Convergent Zone. *Tectonophysics* 389, 137–190. doi:10.1016/j.tecto.2003.10.024

Marwen, Chaouachi., Andrzej, Falenty., Kathleen, Sell., Frieder, Enzmann., and Michael Kersten, D. H. (2015). Eduction, Extension, and Exhumation of Ultrahigh-Pressure Rocks in Metamorphic Core Complexes Due to Subduction Initiation. *Geochem. Geophys. Geosystems* 18, 1541–1576. doi:10.1002/2015GC005847.Received

Mishin, Y. A., Gerya, T. V., Burg, J.-P., and Connolly, J. A. D. (2008). Dynamics of Double Subduction: Numerical Modeling. *Phys. Earth Planet. Interiors* 171, 280–295. doi:10.1016/j.pepi.2008.06.012

Müller, R. D., Zahirovic, S., Williams, S. E., Cannon, J., Seton, M., Bower, D. J., et al. (2019). A Global Plate Model Including Lithospheric Deformation along Major Rifts and Orogens since the Triassic. *Tectonics* 38, 1884–1907. doi:10.1029/2018TC005462

Petterson, M. G., Babbs, T., Neal, C. R., Mahoney, J. J., Saunders, A. D., Duncan, R. A., et al. (1999). Geological-tectonic Framework of Solomon Islands, SW Pacific: Crustal Accretion and Growth within an Intra-oceanic Setting. *Tectonophysics* 301, 35–60. doi:10.1016/S0040-1951(98)00214-5

Ranalli, G. (1995). *Rheology of the Earth, Deformation and Flow Process in Geophysics and Geodynamics* 2nd EdnLondon, United Kingdom: Chapman & Hall.

Ranalli, G., and Murphy, D. C. (1987). Rheology Stratification of the Lithosphere. *Tectonophysics* 132, 281–295. doi:10.1016/0040-1951(87)90348-9

Riisager, P., Hall, S., Antretter, M., and Zhao, X. (2003). Paleomagnetic Paleolatitude of Early Cretaceous Ontong Java Plateau Basalts: Implications for Pacific Apparent and True Polar Wander. *Earth Planet. Sci. Lett.* 208, 235–252. doi:10.1016/S0012-821X(03)00046-3

Schellart, W. P., Lister, G. S., and Toy, V. G. (2006). A Late Cretaceous and Cenozoic Reconstruction of the Southwest Pacific Region: Tectonics Controlled by Subduction and Slab Rollback Processes. *Earth-Science Rev.* 76, 191–233. doi:10.1016/j.earscirev.2006.01.002

Shi, Y.-N., Niu, F., Li, Z.-H., and Huangfu, P. (2020). Craton Destruction Links to the Interaction between Subduction and Mid-lithospheric Discontinuity: Implications for the Eastern North China Craton. *Gondwana Res.* 83, 49–62. doi:10.1016/j.gr.2020.01.016

Stern, R. J., and Gerya, T. (2018). Subduction Initiation in Nature and Models: A Review. *Tectonophysics* 746, 173–198. doi:10.1016/j.tecto.2017.10.014

Stern, R. (2004). Subduction Initiation: Spontaneous and Induced. *Earth Planet. Sci. Lett.* 226, 275–292. doi:10.1016/j.epsl.2004.08.00710.1016/s0012-821x(04)00498-4

Sun, B., Kaus, B. J. P., Yang, J., Lu, G., Wang, X., Wang, K., et al. (2021). Subduction Polarity Reversal Triggered by Oceanic Plateau Accretion: Implications for Induced Subduction Initiation. *Geophys. Res. Lett.* 48, e2021GL095299. doi:10.1029/2021GL095299

Tao, J., Dai, L., Lou, D., Li, Z.-H., Zhou, S., Liu, Z., Li, S., Dong, H., Lan, H., Wang, L., and Li, F. (2020). Accretion of oceanic plateaus at continental margins: Numerical modeling. *Gondwana Research* 81, 390–402. doi:10.1016/j.gr.2019.11.015

Tapster, S., Roberts, N. M. W., Petterson, M. G., Saunders, A. D., and Naden, J. (2014). From Continent to Intra-oceanic Arc: Zircon Xenocrysts Record the Crustal Evolution of the Solomon Island Arc. *Geology* 42, 1087–1090. doi:10.1130/G36033.1

Tharimena, S., Rychert, C. A., and Harmon, N. (2016). Seismic Imaging of a Mid-lithospheric Discontinuity beneath Ontong Java Plateau. *Earth Planet. Sci. Lett.* 450, 62–70. doi:10.1016/j.epsl.2016.06.026

Turcotte, B., and Schubert, B. T. (2003). *Geodynamics*. Cambridge University Press Vol. 450 (2), 136–136.

Wallace, L. M., Stevens, C., Silver, E., McCaffrey, R., Loratung, W., Hasiata, S., et al. (2004). GPS and Seismological Constraints on Active Tectonics and Arc-Continent Collision in Papua New Guinea: Implications for Mechanics of Microplate Rotations in a Plate Boundary Zone. *J. Geophys. Res.* 109. doi:10.1029/2003JB002481

Wang, L., Dai, L., Gong, W., Li, S., Jiang, X., Foulger, G., et al. (2022). Subduction Initiation at the Solomon Back-Arc Basin: Contributions from Both Island Arc Rheological Strength and Oceanic Plateau Collision. *Geophys. Res. Lett.* 49, 1–11. doi:10.1029/2021gl097666

Wang, Z., Kusky, T. M., and Capitanio, F. A. (2017). Ancient Continental Lithosphere Dislocated beneath Ocean Basins along the Mid-lithosphere Discontinuity: A Hypothesis. *Geophys. Res. Lett.* 44, 9253–9260. doi:10.1002/2017GL074686

Wang, Z., and Kusky, T. M. (2019). The Importance of a Weak Mid-lithospheric Layer on the Evolution of the Cratonic Lithosphere. *Earth-Science Rev.* 190, 557–569. doi:10.1016/j.earscirev.2019.02.010

Xiao, W., Song, D., Windley, B. F., Li, J., Han, C., Wan, B., et al. (2020). Accretionary Processes and Metallogenesis of the Central Asian Orogenic Belt: Advances and Perspectives. *Sci. China Earth Sci.* 63, 329–361. doi:10.1007/s11430-019-9524-6

Yang, G., Li, Y., Tong, L., Wang, Z., Si, G., Lindagato, P., et al. (2022). Natural Observations of Subduction Initiation: Implications for the Geodynamic Evolution of the Paleo-Asian Ocean. *Geosystems and Geoenvironment* 1, 100009. doi:10.1016/J.GEOGEO.2021.10.004

Yang, S.-H., Li, Z.-H., Gerya, T., Xu, Z.-Q., and Shi, Y.-L. (2018). Dynamics of Terrane Accretion during Seaward continental Drifting and Oceanic Subduction: Numerical Modeling and Implications for the Jurassic Crustal Growth of the Lhasa Terrane, Tibet. *Tectonophysics* 746, 212–228. doi:10.1016/j.tecto.2017.07.018

Zhang, Q., Guo, F., Zhao, L., and Wu, Y. (2017). Geodynamics of Divergent Double Subduction: 3-D Numerical Modeling of a Cenozoic Example in the Molucca Sea Region, Indonesia. *J. Geophys. Res. Solid Earth* 122, 3977–3998. doi:10.1002/2017JB013991

Zhang, S., and Leng, W. (2021). Subduction Polarity Reversal: Induced or Spontaneous? *Geophys. Res. Lett.* 48, 1–11. doi:10.1029/2021GL093201

Zhong, X., and Li, Z. H. (2020). Subduction Initiation during Collision-Induced Subduction Transference: Numerical Modeling and Implications for the Tethyan Evolution. *J. Geophys. Res. Solid Earth* 125, 0–3. doi:10.1029/2019JB019288

Zhou, X., Li, Z.-H., Gerya, T. V., and Stern, R. J. (2020). Lateral Propagation-Induced Subduction Initiation at Passive continental Margins Controlled by Pre-existing Lithospheric Weakness. *Sci. Adv.* 6, 1–10. doi:10.1126/sciadv.aaz1048

Zhou, X., Li, Z.-H., Gerya, T. V., Stern, R. J., Xu, Z., and Zhang, J. (2018). Subduction Initiation Dynamics along a Transform Fault Control Trench Curvature and Ophiolite Ages. *Geology* 46, 607–610. doi:10.1130/G40154.1

Conflict of Interest: The authors declare that the research was conducted in the absence of any commercial or financial relationships that could be construed as a potential conflict of interest.

frontiers | Frontiers in Earth Science

ORIGINAL RESEARCH
published: 05 May 2022
doi: 10.3389/feart.2022.852742

How Aseismic Ridges Modify the Dynamics of Free Subduction: A 3-D Numerical Investigation

Lior Suchoy[1]*, *Saskia Goes*[1]*, *Fangqin Chen*[2] *and D. Rhodri Davies*[2]

[1]*Department of Earth Science and Engineering, Imperial College London, London, United Kingdom,* [2]*Research School of Earth Sciences, Australian National University, Canberra, ACT, Australia*

The subduction of positively buoyant features has been implicated in the development of flat and shallow dipping slabs, the formation of cusps in trench geometry, and the cessation of associated arc magmatism. However, how such buoyant anomalies influence subduction dynamics to produce these different tectonic expressions remains debated. In this paper, using a series of multi-material 3-D simulations of free subduction, we investigate how linear buoyant ridges modify subduction dynamics, in particular downgoing plate velocities, trench motions and slab morphology. We examine the sensitivity of results to downgoing plate age (affecting buoyancy and strength), ridge buoyancy and ridge location along the trench, finding that buoyant ridges can locally change slab sinking and trench retreat rates, in turn modifying the evolution of slab morphology at depth and trench shape at the surface. In all cases examined, trench retreat is reduced, or switches to trench advance, where the ridge subducts. These effects depend strongly on downgoing plate age: on young, weak plates, the change in trench shape is more localised than on old, strong plates. Slab shallowing at the ridge only occurs for young plates, while the stronger and more negatively buoyant older plates pull down the ridge at a steeper angle than the rest of the slab. On old plates, ridges located near regions of trench stagnation or advance, which typically develop in wide slabs, have a stronger effect on trench and slab shape. The combined effects of buoyant feature location, subducting plate age and overriding plate properties can result in a range of responses: from mainly trench deformation, through local slab shallowing, to the formation of a flat slab, a variation in expressions also observed on Earth.

Keywords: subduction, flat slab, slab dip, geodynamics, numerical model, aseismic ridge, buoyant ridge, trench geometry

Edited by:
Jie Liao,
Sun Yat-sen University, China

Reviewed by:
Bernhard Maximilian Steinberger,
GFZ German Research Centre for Geosciences, Germany
Carmen Gaina,
Queensland University of Technology, Australia

Correspondence:
Lior Suchoy
l.suchoy17@imperial.ac.uk
Saskia Goes
s.goes@imperial.ac.uk

Specialty section:
This article was submitted to Solid Earth Geophysics, a section of the journal Frontiers in Earth Science

Received: *11 January 2022*
Accepted: *30 March 2022*
Published: *05 May 2022*

Citation:
Suchoy L, Goes S, Chen F and Davies DR (2022) How Aseismic Ridges Modify the Dynamics of Free Subduction: A 3-D Numerical Investigation. Front. Earth Sci. 10:852742. doi: 10.3389/feart.2022.852742

1 INTRODUCTION

Buoyant features are thickened ridges and plateaus on the ocean floor that mark the surface expression of excess mantle melting. Ridges are typically elongated features with a specific orientation, whilst plateaus are often more uniform in their dimensions. Owing to their composition and thickness, they add a component of positive buoyancy to the associated lithosphere and will typically resist the subduction of this lithosphere. As a result, the subduction of buoyant features has been implicated in many irregularities of subduction tectonics, including the interruption of arc volcanism on the corresponding overriding plate (e.g., Vogt et al., 1976; Nur and Ben-Avraham, 1983; Mahlburg Kay and Mpodozis, 2002; Hu et al., 2016), uplift and compression in the overriding plate (e.g., Humphreys, 1995; Espurt et al., 2007; O'Driscoll et al., 2009) and either enhancement or suppression of seismic activity (e.g., Nur and Ben-Avraham, 1983; Gutscher et al., 1999, 2000; Kumar et al., 2016).

Although they have been widely studied, there is currently no consensus on how the subduction of buoyant features modulates subduction dynamics. It was first proposed that buoyant-feature subduction alters the shape of the trench (Vogt, 1973). The main evidence was the proximity of many features to trench cusps (e.g., the Emperor Chain at the intersection of the Aleutian and Kuril trenches, the Caroline Ridge between the Mariana and Yap trenches and the Ogasawara Ridge between the Mariana and Bonin arcs: Vogt, 1973; Vogt et al., 1976; Miller et al., 2006c; Mason et al., 2010; Rosenbaum and Mo, 2011). A proposed consequence of subduction of buoyant features is the association with low angle (i.e., "flat"), subduction (Sacks, 1983; Gutscher et al., 2000). The main examples of flat slab subduction are where the Nazca plate subducts beneath South America: the Nazca ridge is associated with the Peruvian flat slab (Gutscher et al., 2000), the Juan Fernandez ridge with the Chilean flat slab (Mahlburg Kay and Mpodozis, 2002) and the Carnegie ridge with the Ecuadorian flat slab (Gutscher et al., 1999). The Northeast Pacific hosts an example of a present-day flat slab which is associated with subduction of the plateau-like Yakutat Terrane beneath Alaska (e.g., Gulick et al., 2007). Subduction of the Palau-Kyushu ridge under Japan (Xia et al., 2021) has also been associated with low-angle subduction along the Nankai Trench, and subduction of the Emperor chain with shallow subduction under Kamchatka (Davaille and Lees, 2004). Finally, the subduction of the Shatsky Rise conjugate has been linked to past flat subduction below North America leading to the Laramide Orogeny (Atwater, 1989; Liu et al., 2010).

It is proposed that when a buoyant feature subducts, its buoyancy counteracts downgoing motion of the surrounding negatively buoyant plate, keeping it afloat (Sacks, 1983; Gutscher et al., 1999). When a full flat slab matures and develops a horizontal section that extends several hundred kilometres from the trench, the lack of mantle wedge flow between the slab and overriding plate might cause a shut-down in arc volcanism (Nur and Ben-Avraham, 1981; Isacks, 1988; Atwater, 1989). Furthermore, the release of slab fluids into the thin coupling layer between the plates may reduce seismic activity (Nur and Ben-Avraham, 1983; Kim et al., 2012; Manea et al., 2013) and the induced slab bathymetry may limit the size of large ruptures (Sparkes et al., 2010). Other studies propose that a wide upper-lower plate contact area above a shallow slab increases the potential for large inter-plate earthquakes (Corbi et al., 2017; Muldashev and Sobolev, 2020).

Although there are a number of observations supportive of a link between the subduction of buoyant features and shallow-angle or flat slab subduction (Vogt et al., 1976; Nur and Ben-Avraham, 1983; Gutscher et al., 1999; Van Hunen et al., 2002), there are also buoyant ridges and plateaus that subduct without affecting slab dip. Skinner and Clayton (2013) observed that some of the largest features subducting in the Pacific (e.g., the Magellan seamounts, Louisville ridge, Caroline ridge) are not correlated with any lower-angle subducting slab. Moreover, for some flat slab segments (most notably, Mexico, and past subduction below the Altiplano-Puna region) no candidate buoyant features have been identified to explain the anomalous subduction angle (Rosenbaum and Mo, 2011; Skinner and Clayton, 2011). In addition, a number of numerical and analogue subduction models indicate that although the subduction of buoyant features may lead to slab shallowing, by themselves they are insufficient to generate a flat slab (Van Hunen et al., 2002; Martinod et al., 2005; Gerya et al., 2009; Manea et al., 2017).

Several other mechanisms have been suggested to cause or contribute to the formation of flat or low-angle slabs. One mechanism is the active overthrusting of the upper plate, which results in forced trench retreat and can lead to a flat slab if the plate is unable to increase its sinking velocity accordingly (van Hunen et al., 2004; Currie and Beaumont, 2011; Liu and Currie, 2016). Episodes of fast convergence (> 10 cm/yr; Currie and Beaumont, 2011; Manea et al., 2017) have been proposed to have a similar flattening effect. Suction forces in the mantle wedge, although unlikely to lead to flat subduction on their own, generate an upwards force above the slab and can be enhanced by a higher viscosity mantle wedge or thick (cratonic) upper plate (van Hunen et al., 2004; Manea and Gurnis, 2007; O'Driscoll et al., 2009; Roda et al., 2011; Manea et al., 2012; Taramón et al., 2015; Schellart and Strak, 2021), thus encouraging the evolution from a low-angle to a flat slab. Another mechanism suggested to contribute to low-angle subduction is the presence of buoyant mantle support below the slab, as would be expected from a hot upwelling plume (Betts et al., 2009; Bishop et al., 2017), or as a result of slab tearing (Liu and Stegman, 2012), although this effect may be relatively small (Schellart, 2020). Finally, it has been suggested that long-lived, very wide subduction zones for which the slab is anchored in the lower mantle, can develop a shallow-dipping segment in their centre (e.g., Farallon plate) (Schellart, 2020). Most studies suggest that varying combinations of mechanisms, likely involving buoyant features, may be required to explain the observed range of low-angle and flat slab cases (van Hunen et al., 2004; Skinner and Clayton, 2013; Antonijevic et al., 2015; Hu et al., 2016).

While previous studies have modelled the subduction of buoyant features, the majority have done so in 2-D (e.g., Van Hunen et al., 2002; van Hunen et al., 2004; Gerya et al., 2009; Arrial and Billen, 2013; Schellart and Strak, 2021), which is most appropriate for simulating features with a large lateral extent. Of the 3-D studies undertaken, some focus on modelling specific subduction zones (Espurt et al., 2008; Mason et al., 2010; Hu et al., 2016). Only a few, analogue modelling, studies have systematically explored how variations in the shape and position of buoyant features affect subduction dynamics with and without an overriding plate (Martinod et al., 2005, 2013; Flórez-Rodríguez et al., 2019). These show that the relative buoyancy of a buoyant feature compared to the rest of the slab affects the extent to which it modulates subduction. Several other, numerical, 3-D models, which did not include buoyant features, examined how overriding plate thickness (Capitanio et al., 2011; Manea et al., 2012; Rodríguez-González et al., 2014; Taramón et al., 2015) and the width of the subducting plate (Schellart et al., 2007; Schellart, 2020; Chen et al., 2022) influence slab dip and can possibly cause flat subduction. In this study, we build on and complement previous work, using 3-D numerical models to investigate the effects of the relative buoyancy of buoyant features and their position along the trench. It is the first to study the effect of the age-dependent buoyancy and strength of the background subducting slabs. This study uses fully dynamic numerical simulations to simulate a subset of buoyant features, i.e., elongated, trench-perpendicular buoyant ridges, on single-plate subduction (i.e., "free subduction") to evaluate effects on trench shape and the slab dip angle. We find that the different modes of ridge subduction exhibited by our models help to explain the different expressions of subducting buoyant features around the Pacific and on the Indo-Australian plate.

2 METHODS

2.1 Modelling System

We design a series of simulations in a 3-D Cartesian domain. We use a multi-material approach to simulate subduction of a composite visco-plastic plate into a viscous mantle, with no upper plate (i.e., "free subduction"). While numerous studies demonstrate that the upper plate can affect subduction dynamics significantly (e.g. van Hunen et al., 2004; Espurt et al., 2008), its absence allows us to analyse the dynamic forcing by the subducting plate which is widely agreed to be the main driver of subduction dynamics and diversity (e.g. Forsyth and Uyeda, 1975; Goes et al., 2017). Our approach neglects the thermal evolution of the slab and associated feedbacks on density and viscosity (e.g., Garel et al., 2014; Suchoy et al., 2021). This simplification enhances numerical efficiency, allowing us to perform a systematic 3-D study across a wide parameter space. Previous studies have demonstrated that the multi-material, mechanical approach used herein captures the first-order dynamics of subduction (e.g. Bellahsen et al., 2005; Capitanio et al., 2007; Stegman et al., 2010; Chen et al., 2022).

We use Fluidity, an adaptive, unstructured mesh, finite-element, control-volume computational modelling framework (e.g., Wilson, 2009; Davies et al., 2011; Kramer et al., 2012, 2021), to solve the conservation equations of mass and momentum for an incompressible fluid under the infinite Prandtl number and Boussinesq approximations:

$$\nabla \cdot u = 0 \tag{1}$$

$$\nabla \cdot \left[\eta \left(\vec{\nabla} u + \left(\vec{\nabla} u \right)^{T} \right) \right] - \vec{\nabla} p = -g \Delta \rho \Gamma \hat{y} \tag{2}$$

$$\frac{\partial \Gamma}{\partial t} + \mathbf{u} \cdot \vec{\nabla} \Gamma = 0 \tag{3}$$

where u is the velocity, η is the dynamic viscosity, p is the pressure, g is the acceleration due to gravity, $\Delta\rho$ is the difference in density between different materials, Γ is the material volume fraction ($\Gamma = 1$ within a given material and $\Gamma = 0$ elsewhere) and $\hat{y}$ is a unit vector in the direction of gravity. We utilise an adaptive unstructured mesh of tetrahedral elements, with minimum and maximum element sizes of 3 and 300 km, respectively. This allows us to resolve fine-scale features where the gradients of velocity and viscosity are strong, whilst maintaining computational efficiency (see Davies et al., 2007, 2011, for further detail).

2.2 Reference Models

Our reference young and old "no-ridge" models (**Table 1**) follow two Cartesian model designs from Chen et al. (2022) (models W2400_young and W2400_ref, respectively). We use a domain of 4,000 × 2890 × 4,000 km^3 (length×depth×width) to simulate half the subducting plate, assuming symmetry at the centre of the plate along the long axis ($z = 0$) (**Figure 1**).

We apply a free-surface boundary condition at the top of the domain and free-slip boundary conditions at all other boundaries. The initial half-plate is 2,200 km long (in the direction of subduction), 1,200 km wide (along strike) and 45 or 70 km thick, for young or old plates, respectively. We limit lateral flow from the mantle to the section below the plate by adding a side plate with an initial gap of 22 km away from the edge of the subducting plate (e.g., Holt and Becker, 2017). A 600 km gap was prescribed between the trailing edge of the subducting plate and the domain boundary at $x = 0$. The initial slab morphology follows an arc with a radius of 250 km along the top surface, to a dip of 77° (as in Garel et al., 2014; Suchoy et al., 2021), extending to an initial depth of 200 km.

The subducting plate is composed of 3 layers with a strong isoviscous core in the centre, and visco-plastic layers at the top and bottom. The core has a viscosity 100 times η_{UM}. The visco-plastic layers have this same initial viscosity, but follow a von Mises yield criterion (e.g., OzBench et al., 2008) so that:

$$\eta_P = \begin{cases} \dfrac{\tau_{II}}{2 \cdot \dot{\varepsilon}_{II}}, & \text{if } \tau_{II} < \tau_y \\ \dfrac{\tau_y}{2 \cdot \dot{\varepsilon}_{II}}, & \text{if } \tau_{II} \geq \tau_y \end{cases} \tag{4}$$

where the second invariant of the stress tensor $\tau_{II} = 2\eta \cdot \dot{\varepsilon}_{II}$, with $\dot{\varepsilon}_{II}$ the second invariant of the strain-rate tensor and τ_y the yield stress. This rheological layering captures the concentration of slab strength in the centre of the dense plate, as expected from temperature and strain-rate dependent mantle rheology (OzBench et al., 2008; Capitanio et al., 2009; Buffett and Becker, 2012). For the old reference plate, the core is 30 km thick and the top and bottom layers are each 20 km thick, while for the young plate each layer is 15 km thick. The density of the older plate is set to be higher than that of the young plate, such that the combined densities and thicknesses of the two background plates yield a range of plate buoyancies similar to that expected for 20 and 120 Myr lithosphere from plate cooling models (e.g., McKenzie et al., 2005). We applied the same density contrast to the full thickness of the plate, i.e., only considering joint buoyancy effects of the crust and mantle lithosphere. This results in the old plate being more negatively buoyant and effectively stronger than the young plate. The upper-lower mantle boundary (ULMB) is implemented as a viscosity jump at 660 km depth, with an upper mantle viscosity, η_{UM}, of $2 \cdot 10^{20}\ Pa \cdot s$ and a lower mantle

TABLE 1 | Parameters for all model cases. H—plate thickness, W_R - ridge width (cases with side ridges effectively contain two symmetrical ridges of this width), H_C—thickness of high-viscosity core, H_P—thickness of visco-plastic layers above and below the plate core, $\Delta\rho$—excess density of plate or ridge, B_P—buoyancy of the plate per unit length, calculated as $(\Delta\rho_{P\text{-}M} \cdot W_P + \Delta\rho_{R\text{-}P} \cdot W_R) \cdot H \cdot g$, and which is positive in the direction of gravity. Model name abbreviations: NR—no-ridge, HB—high positive buoyancy, LB—low positive buoyancy, C—central ridge, S—side ridge. High and low positive buoyancy refer to ridge buoyancy relative to the rest of the plate. Central and side ridge locations pertain to a ridge at the symmetry boundary or at the centre of the half-plate, respectively (see also **Figure 1B**). Old and young refer to the age of the plate, which is assumed to affect both density and thickness (and thereby strength and buoyancy) of the plate.

Model name	H [km]	W_R [km]	H_C, H_P [km]	$\Delta\rho$ [kg/m^3]		Ridge location	B_P [10^{13} N/m]
				Plate-mantle	Ridge-plate		
NR_Old	70	-	30, 20	80	-	-	13.44
HB_C_Old	70	200	30, 20	80	-50	Centre	12.74
LB_C_Old	70	200	30, 20	80	-25	Centre	13.09
LB_S_Old	70	2 × 200	30, 20	80	-25	Side	12.74
NR_Young	45	-	15, 15	40	-	-	4.32
HB_C_Young	45	200	15, 15	40	-75	Centre	3.65
LB_C_Young	45	200	15, 15	40	-37.5	Centre	3.98
LB_S_Young	45	2 × 200	15, 15	40	-37.5	Side	3.65

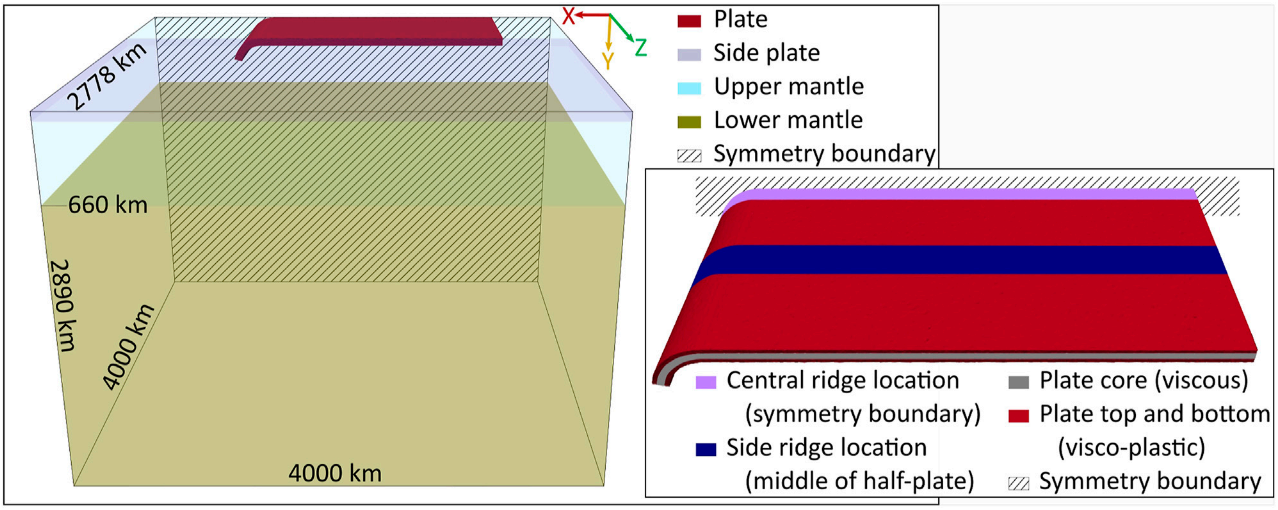

FIGURE 1 | Initial conditions of **(A)** our computational domain and **(B)** the subducting plate. See text and **Tables 1**,**2** for material properties and dimensions. We apply a free-surface boundary condition at the top of the domain, and free-slip boundary conditions elsewhere.

TABLE 2 | Parameters common to all simulations. Plate length, L_{plate}, is in the direction of subduction and plate width, W_{plate}, is along strike. Note the simulated width is half the full plate width, assuming symmetry at the centre.

Parameter	Symbol	Value
Gravitational acceleration	g	10 m/s^2
Domain length	L_{dom}	4,000 km
Domain width	W_{dom}	4,000 km
Domain depth	D_{dom}	2,890 km
Plate length	L_{plate}	2,200 km
Full plate width	W_{plate}	2,400 km
Upper-lower mantle boundary depth	D_{ULMB}	660 km
Initial plate trailing edge distance	L_{te}	600 km
Initial top of slab radius	R_S	250 km
Initial slab maximum angle from horizontal	α_S	77°
Upper mantle viscosity	η_{UM}	$2 \cdot 10^{20}$ Pa·s
Lower mantle viscosity	η_{LM}	$50 \cdot \eta_{UM}$
Plate core viscosity	η_C	$100 \cdot \eta_{UM}$
Side plate viscosity	η_{SP}	$1{,}000 \cdot \eta_{UM}$
Yield stress	τ_y	100 MPa
Mantle density	ρ_m	3,300 kg/m^3

viscosity, η_{LM}, of 50 times η_{UM}. The side plate has a viscosity of 1,000 times η_{UM}. Material properties common to all simulations are summarised in **Table 2**.

2.3 Cases With Ridges

To examine the effect of buoyant ridges (see **Table 1**), we decrease the density in a trench-perpendicular strip of the subducting plate (**Figure 1B**). We ran cases with a ridge positioned either at the centre of the plate (i.e., the symmetry edge of the half-plate, at $z = 0$) or positioned offset from the centre, in the centre of the half plate (initially centred at $z = 600$ km). The off-centre ridge cases effectively include two ridges (mirrored across the symmetry plane). The distance between these ridges is sufficiently large to allow us to investigate the effect of a single offset ridge. For off-centre ridges, we use a 200 km wide segment. For the central ridges, we use a 100 km wide segment of the plate, to represent half of a 200 km wide symmetrical ridge.

We consider 8 cases (**Table 1**). For each reference plate type (old and young), we ran a case without any ridges ("NR" or "no-

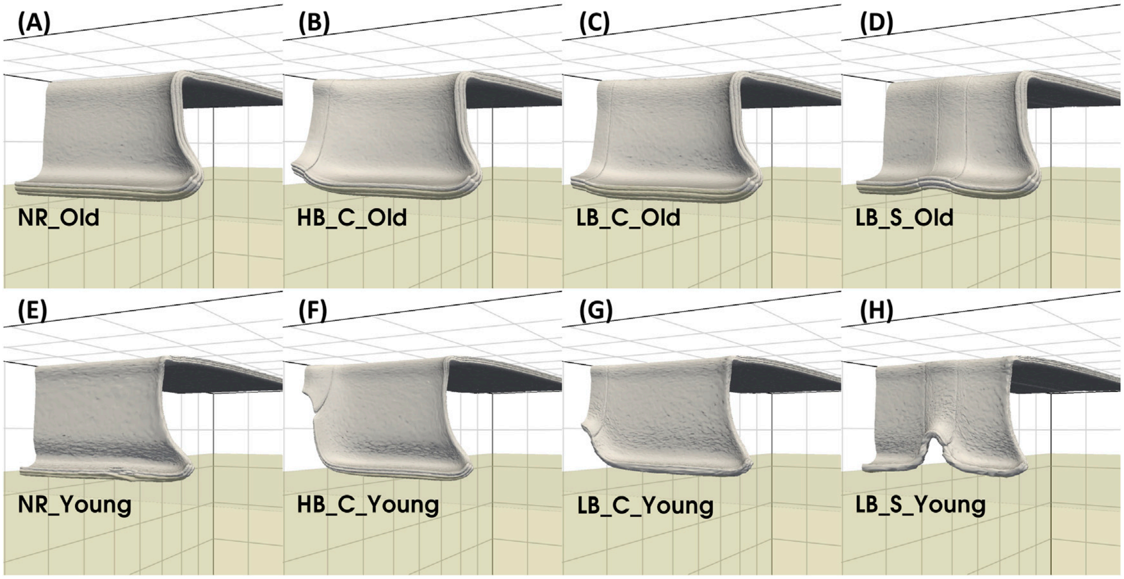

FIGURE 2 | Representative slab geometries after plates start interacting with the ULMB for all model cases. Old plate cases are presented in panels **(A–D)** at 10 Myr and young plate cases in panels **(E–H)** at 30 Myr. The lower mantle is depicted by green semi-transparent box. For scale, grey grid cells of 400 km by 400 km are shown on domain boundaries.

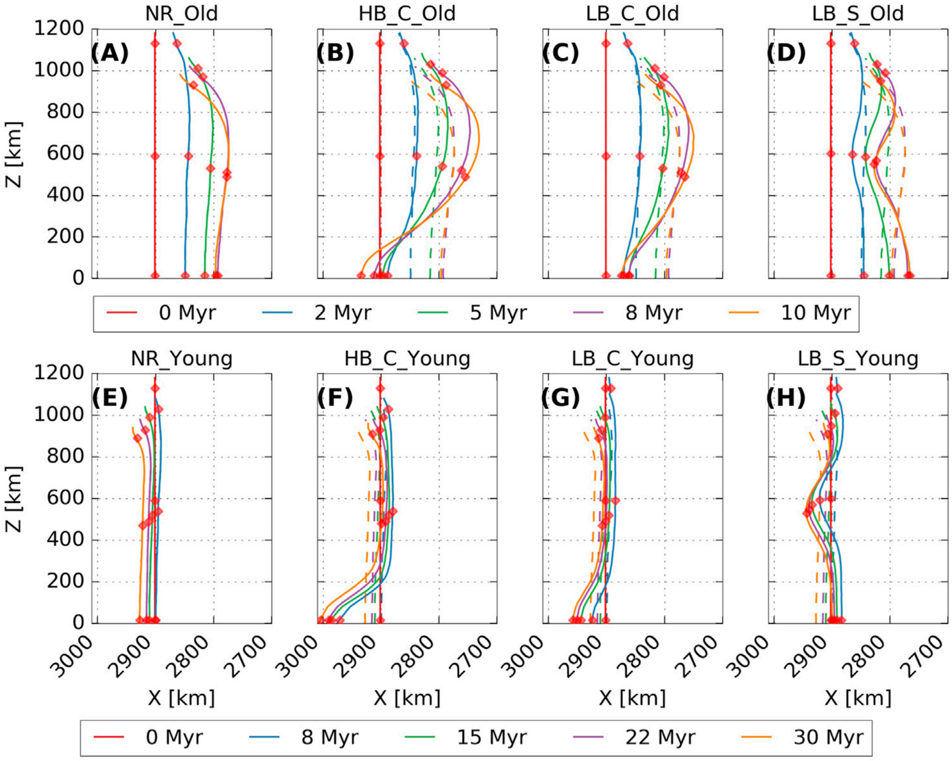

FIGURE 3 | Temporal evolution of trench shape, corresponding to the front of the plate measured at 20 km depth, for Old **(A–D)** and Young **(E–H)** models. Dashed lines in panels **(B–D)** and **(F–H)** represent the location of the trench in the corresponding reference models without a ridge (cases NR_Old and NR_Young). Red diamonds mark the location where motion of the trench and slab were measured, with results displayed in **Figures 4**,**5**. Note that the *X* and *Z* axes are differently scaled.

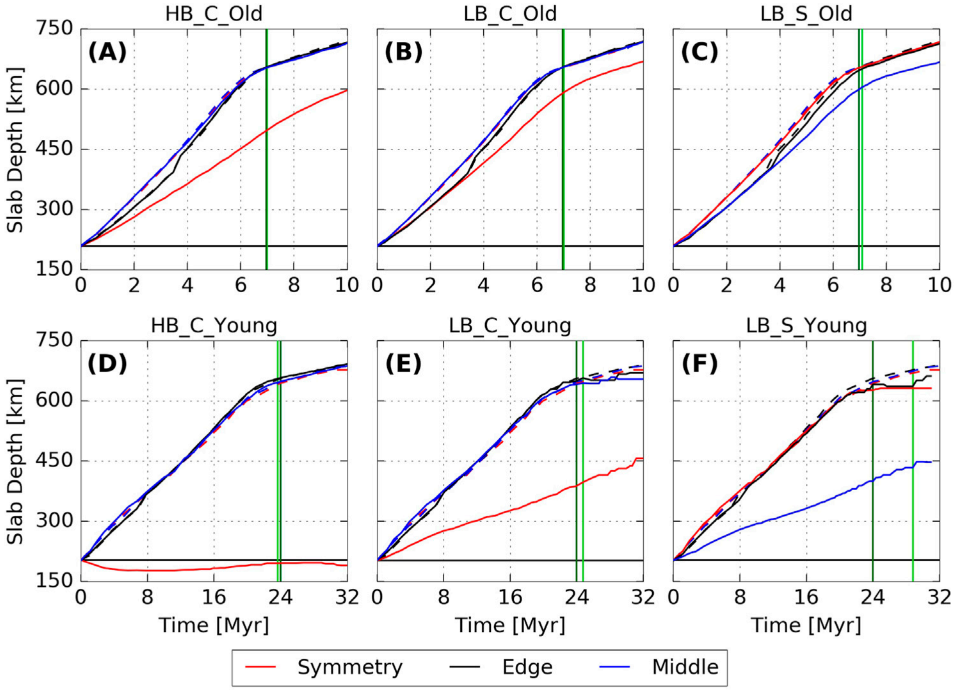

FIGURE 4 | Slab depth as a function of time for old plate models in panels **(A–C)** and young plate models in panels **(D–F)**. Dashed lines represent motions of the corresponding reference model without a ridge (cases NR_Old and NR_Young). Red lines are for measurements at the symmetry boundary [also ridge location in **(A,B, D,E)**], blue lines are for measurements in the middle of the half-plate [also ridge location in **(C,F)**] and black lines for measurements at the edge of the plate. Z-positions (along strike) where sinking was measured are marked on **Figure 3**. Vertical lines mark the time that the slab reaches ULMB (i.e. *t*660) for the ridge model (light green) and the reference cases (dark green). Solid horizontal black line corresponds to the initial depth of the slab tip at 200 km.

ridge" models, **Table 1**), as well cases with a central ridge of high and low excess positive buoyancy ("HB" and "LB" models) relative to the buoyancy of the plate (i.e., counteracting the negative buoyancy of the downgoing plate). We also ran simulations for each plate type with a low positive buoyancy ("LB" cases) ridge at the side of the plate. Based on the topography of buoyant ridges on Earth today, we chose cases that yield a typical excess relief of 0.75 and 1.5 km (relative to background plate bathymetry) to define the parameters for our low and high buoyancy ridges, respectively. We calculated what difference in buoyancy for each ridge type relative to surrounding lithosphere would yield this excess relief assuming isostatic equilibrium (following Cloos, 1993; Gutscher et al., 2000; McKenzie et al., 2005, see supplementary material for further details). We then determined the corresponding density difference over the thickness of our modelled plates and reduced it accordingly. Since the modelled young plate is thinner than the old plate, this resulted in much greater density contrast between the ridge and the young plate, compared with the old plate.

When calculating subduction diagnostics, the plate-mantle interface was delineated as the iso-surface where the mantle material volume fraction is 0.5. Snapshots of slab morphologies for all 8 cases, following interaction with the ULMB, are displayed in **Figure 2**. The trench is defined as the front edge of the plate at 20 km depth (**Figure 3**). We measure the motion and velocity of the trench and the tip of the slab at 3 points along strike: 15 km from the symmetry boundary, 50 km from the edge of the plate and at a point half way along the trench (denoted as "symmetry," "edge" and "middle," respectively). The location of the edge and the middle was calculated throughout the simulations to account for temporal changes in trench shape (red diamonds in **Figure 3**).

3 RESULTS

3.1 No Ridge Behaviour

We first discuss the behaviour of the two reference "no-ridge" models (NR_Old and NR_Young). The evolution of both is consistent with similar 2-D and 3-D models in previous studies (Funiciello et al., 2003; Schellart, 2005; Capitanio et al., 2007; Stegman et al., 2010) and includes two phases: initial sinking of the slab through the upper mantle and subsequent interaction of the slab with the lower mantle. We refer to the time of the first slab-ULMB interaction as *t*660.

In case NR_Old, the slab sinks through the upper mantle at an increasing rate, reaching the ULMB after ~7 Myr (**Figure 4A**). Over the same period, the trench retreats at rates between 1 and 3 cm/yr, depending on the position along the trench. The highest cumulative trench retreat occurs at the middle of the half-plate (~120 km in 7 Myr), with a lower value at the symmetry plane

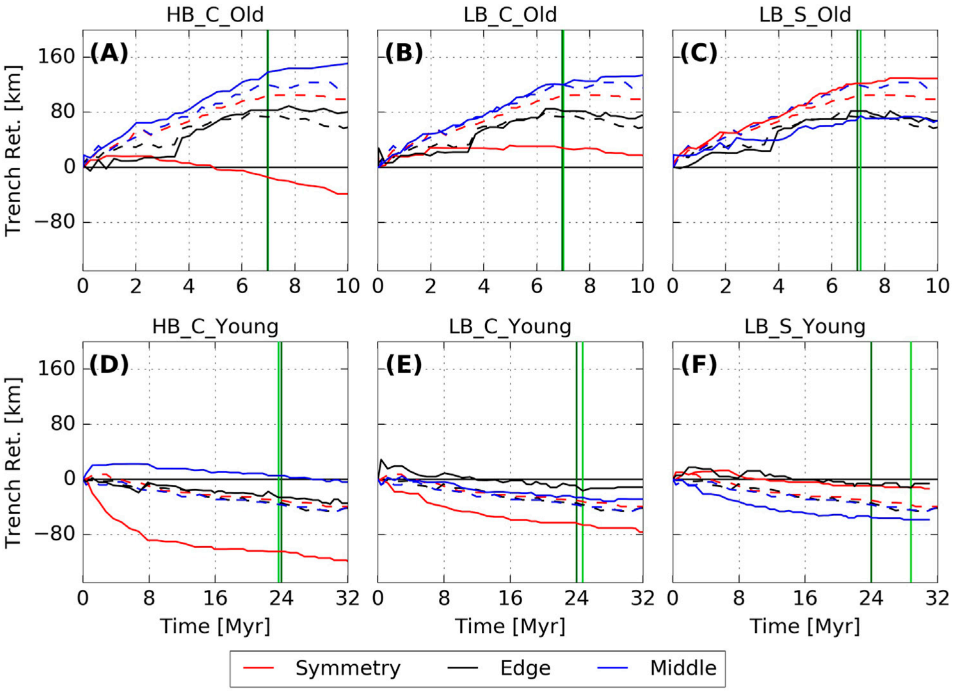

FIGURE 5 | Trench motion evolution for old plate models in panels **(A–C)** and young plate models in panels **(D–F)**, at the locations marked on **Figure 3**. Lines styles are as in **Figure 4**, i.e., solid lines are for the ridge models, and dashed lines for the corresponding reference cases. Vertical lines mark *t*660 for the ridge (light green) and no-ridge (dark green) cases. The initial location of the trench, i.e. 0 km, is marked with solid black horizontal lines.

(~100 km in 7 Myr) and the lowest value at the slab edge (~70 km in 7 Myr; **Figures 3A**, **5A**). As the slab approaches the ULMB, it flattens due to interaction with the more viscous lower mantle, which reduces the sinking velocity from an average rate of ~6.5 cm/yr before *t*660 to ~2.7 cm/yr after *t*660 (**Figure 4A**). Upon interaction with the ULMB, the trench stagnates and even advances slightly at the edge and at the symmetry boundary (**Figures 3A**, **5A**). As a result, the trench develops a "W"-shape with a stagnation point, where trench motion tends to zero, at the centre (i.e., at the symmetry boundary) surrounded by faster retreating segments, with a maximum in retreat at the middle point of the half-plate (and its symmetrical equivalent).

In case NR_Young, the slab has less negative buoyancy and, accordingly, sinks at a slower rate of ~2 cm/yr, reaching the ULMB after 24 Myr. Owing to its reduced thickness, the NR_Young plate is also weaker and, consequently, as the slab approaches the ULMB, it buckles (**Figure 2E**), as its sinking velocity reduces to ~0.5 cm/yr (**Figure 4E**). Both before and after *t*660, the trench slowly advances at a steady rate of 0.1–0.5 cm/yr (**Figure 5E**). The rate of trench advance is similar everywhere along the trench, resulting in a reasonably straight "I"-shaped trench (**Figure 3E**).

In both the young and old reference models, the shape of the trench is determined by slab-mantle interactions (Schellart et al., 2007). The difference in trench retreat along strike for the old plate is due to return flow caused by slab rollback, which creates toroidal flow cells in the mantle near the edges of the plate. When the toroidal cell is smaller than the width of the half-plate, a stagnation point emerges at the centre of the trench (Schellart et al., 2007; Schellart, 2020). Our reference old plate is wide enough for such a central stagnation point to develop (Chen et al., 2022), thereby providing an excellent basis for evaluating the effect of ridge position. Narrower old plates develop a "C"-shaped trench instead, where the centre of the slab retreats more than its sides. The young plate sinks slower, which provides more time for deformation and bending at the trench. As a result, the young plate sinks almost vertically and drives very little trench motion (e.g., Capitanio et al., 2007). The slight curvature at the edge of the plate is the result of the weak toroidal cell caused by the displacement of mantle material due to plate sinking, and overall the trench stays reasonably straight (Chen et al., 2022).

3.2 Ridge Buoyancy Effects

Next, we examine cases with ridges at the centre of the plate (i.e., at the symmetry plane), with low and high positive buoyancy relative to the downgoing plate: cases HB_C and LB_C. In all cases, the addition of a buoyant ridge results in less trench retreat, or even trench advance, at the location where the ridge impacts the trench. Compared with the NR_Old reference case, trench retreat at the centre of the plate in case LB_C_Old is reduced from ~100 km to ~30 km by *t*660 (**Figure 5B**), while in case HB_C_Old, the centre of the trench advances ~15 km by *t*660 (**Figure 5A**). In the NR_Young reference case, the centre of the trench is already advancing, and the addition of the ridge enhances this advance. For case LB_C_Young, the trench at the centre of the plate advances by ~70 km by the reference *t*660 compared with ~30 km in NR_Young case (**Figure 5E**). For the HB_C_Young case, the trench advances ~110 km by the reference *t*660 (**Figure 5D**). In both young and old plate models, trench retreat at locations away from the ridge is increased or trench advance is decreased compared to the corresponding NR case.

The sinking velocity of the slab carrying the ridge is reduced locally due to the added positive buoyancy of the ridge. Particularly in the young plate models, the local plate sinking velocity at the ridge is significantly lower than in the rest of the plate. In model HB_C_Young, the ridge has not sunk at all by the reference *t*660 (**Figure 4D**). The differential sinking rate in this model is accommodated through thinning of the slab at the side of the ridge, which could facilitate slab tearing under certain rheological parameterisations. In comparison, the less buoyant ridge in model LB_C_Young has sunk ~200 km, from its initial depth, by the reference *t*660 (**Figure 4E**). For older plate models, sinking velocity at the ridge deviates less from that in the rest of the plate. The part of the slab with the ridge has sunk ~300 km for the HB_C_Old case and ~400 km for LB_C_Old case (**Figures 4A,B**). Elsewhere along the slab, the sinking velocity remains similar to the reference case for both young and old plate models.

Previous 2-D models have demonstrated that, in free-subduction, higher slab pull and increased resistance to bending at the trench encourage trench retreat (Capitanio et al., 2007; Ribe, 2010). In our 3-D models, it is the difference between slab pull at the ridge and in the rest of the plate that drives the variable trench retreat, hindered at the ridge and enhanced elsewhere. This differential trench motion increases trench curvature, leading to the formation of a "W"-shaped trench in the young plate models and a more pronounced "W"-shape in the old plate, with more retreat at the edge of the plate than at the symmetry boundary (**Figures 3B,C,F,G**). Due to the low resistance to bending in young plates, such a "W"-shaped trench is difficult to generate by young plate subduction without along-strike buoyancy variations (Chen et al., 2022). The differential sinking between the ridge and rest of the plate also creates along-strike tension in the plate. The higher plate strength of the old plates facilitates stress transmission along strike. As a result, old plates can pull the ridge more effectively into the mantle, resulting in less along-strike variations in sinking and a smoother trench and slab shape in comparison to the corresponding young plates with ridges (**Figures 2B,C,F,G** and **Figures 3B,C,F,G**).

3.3 Ridge Location Effects

We evaluate the impact of ridge location by comparing results from models LB_C and LB_S. As for the models with a central ridge, subduction of a ridge on the side of the plate results in locally reduced trench retreat and, sometimes, induces a small amount of trench advance (**Figures 3D,H**). Although the side ridge cases effectively contain two ridges, there is no indication from the resulting trench shapes (**Figures 3D,H**) that there is an interference due to superposition of the influence of the two ridges, so these models can be used to study the effect of the subduction of a ridge offset from the slab centre.

The along-strike changes in trench motion compared to the reference cases are less for the cases with a side ridge than for the cases with a central ridge. For case LB_S_Old, the reduction in trench retreat by *t*660 is ~50 km, compared to a reduction of ~80 km for case LB_C_Old (**Figures 5B,C**). This is likely because the impact of the ridge in LB_S_Old is concentrated at the point where a ridge-free trench (case NR_Old) would retreat the most. Therefore, in this case, ridge subduction reduces the overall lateral deflection of the trench in comparison to the reference case (**Figures 3A,D**). For case LB_S_Young, the increase in trench advance relative to case NR_Young by the reference *t*660 is ~20 km, compared with ~35 km for case LB_C_Young (**Figures 5E,F**). All young plate cases with a ridge deform the trench from the straight reference shape of the NR_Young case to a curved trench with a cusp (**Figures 3E,G,H**).

As for cases with central ridges, the sinking velocity is reduced relative to the corresponding NR cases where the side ridge is subducted. The local reduction in sinking velocity is smaller for the LB_S cases than for the LB_C cases. The ridge in case LB_S_Old has sunk ~400 km by the reference *t*660, compared with ~390 km for case LB_C_Old (**Figures 4B,C**). Similarly, in LB_S_Young, the ridge has subducted ~10 km deeper by the reference *t*660 than case LB_C_Young at the same time (**Figures 4E,F**). The side-ridge cases, that effectively contain two ridges, also demonstrate that a subducting buoyant ridge can lower the overall sinking velocity of the plate if the ridge adds enough positive buoyancy. The reduction in overall sinking velocity is small, resulting in a delay of ~0.2 Myr in *t*660 in model LB_S_Old. In LB_C_Old, where the change in buoyancy is only half of that in the LB_S_Old case, the *t*660 delay is half as small, ~0.1 Myr. The effect is somewhat larger for the LB_S_Young case, where *t*660 is delayed by ~5 Myr compared with the reference NR_Young case (**Figure 4F**).

As in the cases with central ridges, a side ridge's main effect is to locally reduce trench retreat and sinking velocity. These effects are both diminished when the ridge subducts along a part of the trench that is, otherwise strongly retreating. When the ridge impacts at the side, the composite trends of the plate's tendency to retreat and the reduced trench retreat of the ridge leads to less along-strike variation in trench shape. The lower amount of along-strike bending in the LB_S cases may explain the slightly higher sinking velocities for the side ridges compared to the central ridges, as less potential energy is lost in plate deformation. Thus, our results imply that ridges that subduct along parts of the trench where trench motion is already hampered by other factors impact subduction more.

4 DISCUSSION

4.1 Buoyant Feature Subduction and the Morphology of the Trench and Slab

While 2-D models can elucidate some of the effects of buoyant feature subduction, they overestimate the buoyancy force exerted by the feature, due to the implicit assumption of infinite feature width. The full effects of the subduction of buoyant features of

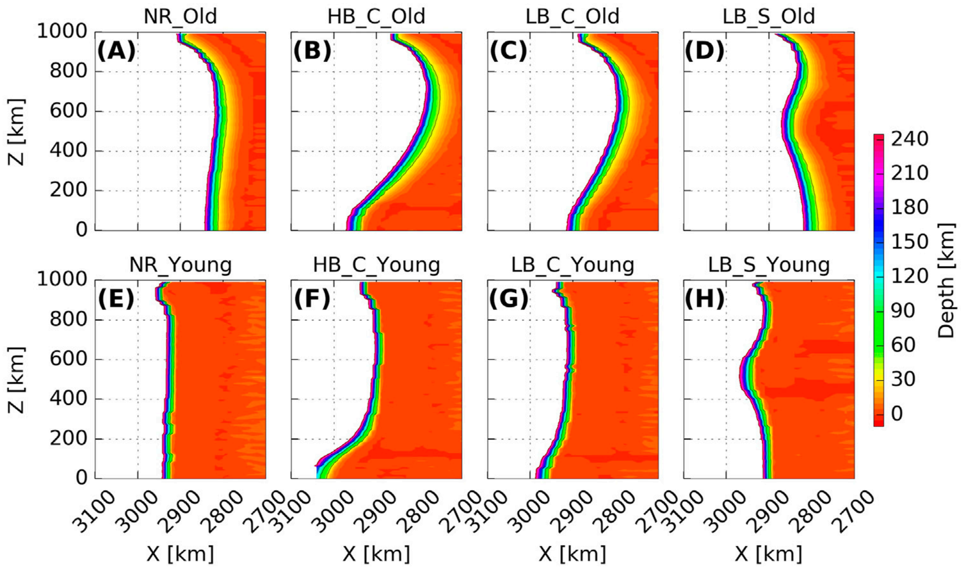

FIGURE 6 | Top-down view of final plate top surface depth above 250 km for Old **(A-D)** and Young **(E-H)** models. Coloured by depth, thereby providing an illustration of the along-strike variations in slab dip. Note that the *X* and *Z* axes are scaled differently.

limited along-strike extent can therefore only be investigated using 3-D models.

All our ridge-subduction cases lead to trench deformation, with decreased trench retreat, trench stagnation or increased trench advance where the buoyant ridges subduct. Previous 3-D models that investigated the effect of buoyant feature subduction (Martinod et al., 2005; Mason et al., 2010; Flórez-Rodríguez et al., 2019) also found that trench retreat was impeded where the buoyant feature subducts, leading to differential retreat along strike. This observation was independent of size, shape and orientation and applied to both buoyant ridges and plateaus (Martinod et al., 2005, 2013). The resulting formation of trench cusps can be offset from the position of ridge impact at the trench if the feature subducts obliquely (Martinod et al., 2013). We show that significant trench deformation occurs in both old and young plates. Plate strength and the relative buoyancy of the ridges compared to the underlying plate determine how pronounced trench deformation is. That is, trenches where a weaker young plate subducts are deformed more locally than those where a stronger old plate subducts, for the same excess ridge buoyancy.

We also find that the position of buoyant ridges along the trench affects the response of the trench and resulting slab morphology. In older plates, ridges near intrinsic trench stagnation points accentuate along-strike variations in trench shape while ridges impacting the trench at other locations lead to less pronounced curvature. Schellart (2020), in 3-D models without buoyant features, found that the central trench stagnation point can, at a late stage of subduction zone evolution, facilitate local slab shallowing. Our results suggest that the subduction of a buoyant ridge at or near such a stagnation point would further enhance such behaviour. We note that trench stagnation points can also form in response to other factors, for example, at the edge of a subducting plate, due to interaction with a side plate or existence of a triple junction, and by interaction with a thick upper plate (Capitanio et al., 2011; Jadamec and Billen, 2012).

Although it is commonly assumed that the subduction of buoyant ridges leads to a decreased slab dip (e.g., Gutscher et al., 2000), our models display a range of behaviour (**Figure 6**). In old plate cases (**Figures 6A–D**), the slab is steepened where the ridge subducts, while the dip of the slab along the rest of the plate is slightly lower than in the reference case without a ridge. Although buoyant ridges act to inhibit sinking, the older subducting plates are sufficiently strong that the pull from the rest of the plate leads to a steeper slab where the buoyant feature enters the subduction zone. In this case, the lowest dips occur where the trench retreats most. In contrast, ridges on young plates develop shallower dip angles than the surrounding plate, and the shallowing is stronger for ridges with a higher positive buoyancy (**Figures 6E–H**). In these cases, the rest of the plate is weak, and is not negatively buoyant enough to pull down the segment with the ridge. Martinod et al. (2005) found that their slabs shallowed where the buoyant feature was subducting but steepened below. Flórez-Rodríguez et al. (2019) found yet another variation in their 3-D analogue models of subduction of buoyant ridges on relatively narrow plates, where the slab shallows in the centre of the ridge but steepens on its sides. In a spherical geometry, effective resistance to plate bending at the trench is higher than in equivalent Cartesian plates (Morra et al., 2006; Mahadevan et al., 2010; Chamolly and Ribe, 2021; Chen et al., 2022). Models of spherical plates display trench and slab deformation in response to along-strike variations in slab buoyancy comparable to Cartesian models (Morra et al., 2006), and are therefore likely to respond to subduction of buoyant ridge similarly. The differences in model behaviour illustrate that the effect of buoyant features on slab dip varies depending on plate strength and relative feature buoyancy, and a range of responses are possible.

4.2 Buoyant Ridges and Low-Angle Subduction

Our results confirm that ridge subduction alone is insufficient to generate a flat slab, a finding that is, consistent with other 3-D free-subduction models (Martinod et al., 2005; Flórez-Rodríguez et al., 2019). Even in 2-D models (van Hunen et al., 2004; Gerya et al., 2009), where the buoyant features are essentially infinite in their along-strike dimension, the subduction of buoyant features alone does not generate a fully flattened slab. Instead, a number of studies have now confirmed that slab flattening requires additional mechanisms such as an upper plate that (by external forcing) overrides the lower plate faster than it can subduct (Van Hunen et al., 2002; Arcay et al., 2008; Currie and Beaumont, 2011; Martinod et al., 2013; Liu and Currie, 2016) or a thick upper plate that generates an upward suction force in the relatively high viscosity mantle wedge, which can pull a shallow-angle slab into a flat-slab geometry (Gerya et al., 2009; O'Driscoll et al., 2009; Manea et al., 2012; Rodríguez-González et al., 2012, 2014; Taramón et al., 2015; Schellart and Strak, 2021).

While upper plate forcing or thickness can result in a flat slab in the absence of buoyant feature subduction, these mechanisms have clear limitations (Hu et al., 2016). Overthrusting requires a highly forced upper plate velocity (3–5 cm/yr, e.g. van Hunen et al., 2004; Currie and Beaumont, 2011) and would usually apply to the entire upper plate, failing to localise flat subduction in bounded regions of several hundred kilometres, as is observed on Earth at present. A similar issue arises for a thickened upper plate which needs to be of a craton-like thickness (O'Driscoll et al., 2009; Manea et al., 2012; Taramón et al., 2015). While cratons comprise limited parts of the upper plate (e.g. Wyoming craton in North America; Amazonian craton in South America), they extend over scales of 1,000 km (e.g. Kusky et al., 2014, and references therein) and, therefore, can only explain very wide flat slabs. Conversely, modelling studies demonstrate that the subduction of buoyant features can aid flat slab formation, by locally reducing trench motion and slab dip (van Hunen et al., 2004; Gerya et al., 2009; Martinod et al., 2013). Thus the contribution of buoyant feature subduction can help to explain the limited lateral extent and temporal duration of flat slabs.

4.3 Buoyant Feature Subduction Styles on Earth

Together with published dynamic models, our results illustrate a number of different responses to buoyant feature subduction, both ridges and plateaus, are possible. These include three types: 1) a "trench deforming" response is an end-member in which subduction of a buoyant feature mainly deforms the trench with minor slab steepening or contortion. Our results demonstrate that this occurs when the positive buoyancy force of a buoyant ridge is low compared with overall plate strength. The upper plate in a "trench deforming" subduction style is typically thin or weak and therefore does not impede trench deformation; 2) a "slab deforming" response, in which subduction of the buoyant feature reduces slab dip locally whilst also deforming the trench. This happens when the buoyancy force associated with the feature is strong enough to locally decrease slab dip while any forcing by the upper plate does not play a significant role; 3) a "slab flattening" response, an end-member in which the slab is flattened at shallow depth over a distance of up to several hundred kilometres. This response occurs when the positive buoyancy of a feature is substantial, and it subducts under a thick, possibly advancing, upper plate. Observations of buoyant features subducting at the plate boundaries of the Pacific and Indian Oceans reflect these different expressions (see **Figure 7** and **Table 3**), although many subduction zones do have additional complexities.

The best example of "trench-deforming" buoyant-feature subduction occurs along the Izu-Bonin-Mariana (IBM) system. The two main buoyant features interacting with the IBM subduction system and impeding retreat of the Mariana trench are both located near major cusps (i.e. the Caroline ridge near the Mariana-Yap junction and the Ogasawara ridge near Bonin-Mariana junction) and these cusps are inferred to have developed when these buoyant features began interacting with the trench (Miller et al., 2006a,c; Seton et al., 2012; Xia et al., 2020). The slab below the Ogasawara Plateau is slightly steeper than adjacent slab segments subducting north and south of it (Miller et al., 2006c; Hayes et al., 2018). The Caroline Island Ridge at the southern end of Mariana is located at a clear cusp where it has reduced convergence velocity significantly and blocked subduction (Miller et al., 2006a; Xia et al., 2021). The slab on the side of the Caroline Ridge, subducting below the southern Mariana trench (Miller et al., 2006a; Zhu et al., 2019) is steep, while the part of the slab along the Yap trench may have detached in response to impingement of the Caroline Ridge (Zhang and Zhang, 2020). Another example of "trench-deforming" buoyant-feature subduction is at the southern end of the Tonga trench, where the Hikurangi Plateau appears to have served as a pivot for the rotation and migration of the Tonga-Kermadec system (Schellart and Spakman, 2012; Seton et al., 2012). Although there is some shallowing of the Hikurangi-southern Kermedec slab above 100 km, this shallowing occurs mainly north of the plateau, while below 100 km depth, the slab is steeper than further north (Reyners et al., 2011; Hayes et al., 2018). These examples all display the expected behaviour for old plates with sufficient slab pull to carry buoyant features into the trench. Rosenbaum and Mo (2011) previously noted that this behaviour is typical of the western Pacific, where subduction of buoyant features often leads to locally hampered trench retreat and to slab steepening rather than slab shallowing.

Several other buoyant features in the Pacific and Indian Oceans are associated with "slab deforming" subduction, in which both a cusp in the trench and local shallowing of the slab dip is observed. Some cases correspond to smaller features on plates of young or intermediate age (as in our young plate models), and others to larger features on older plates (similar to the models of Flórez-Rodríguez et al., 2019). The most straightforward example of "slab deforming" buoyant-feature subduction may be the Cocos ridge, which coincides with a

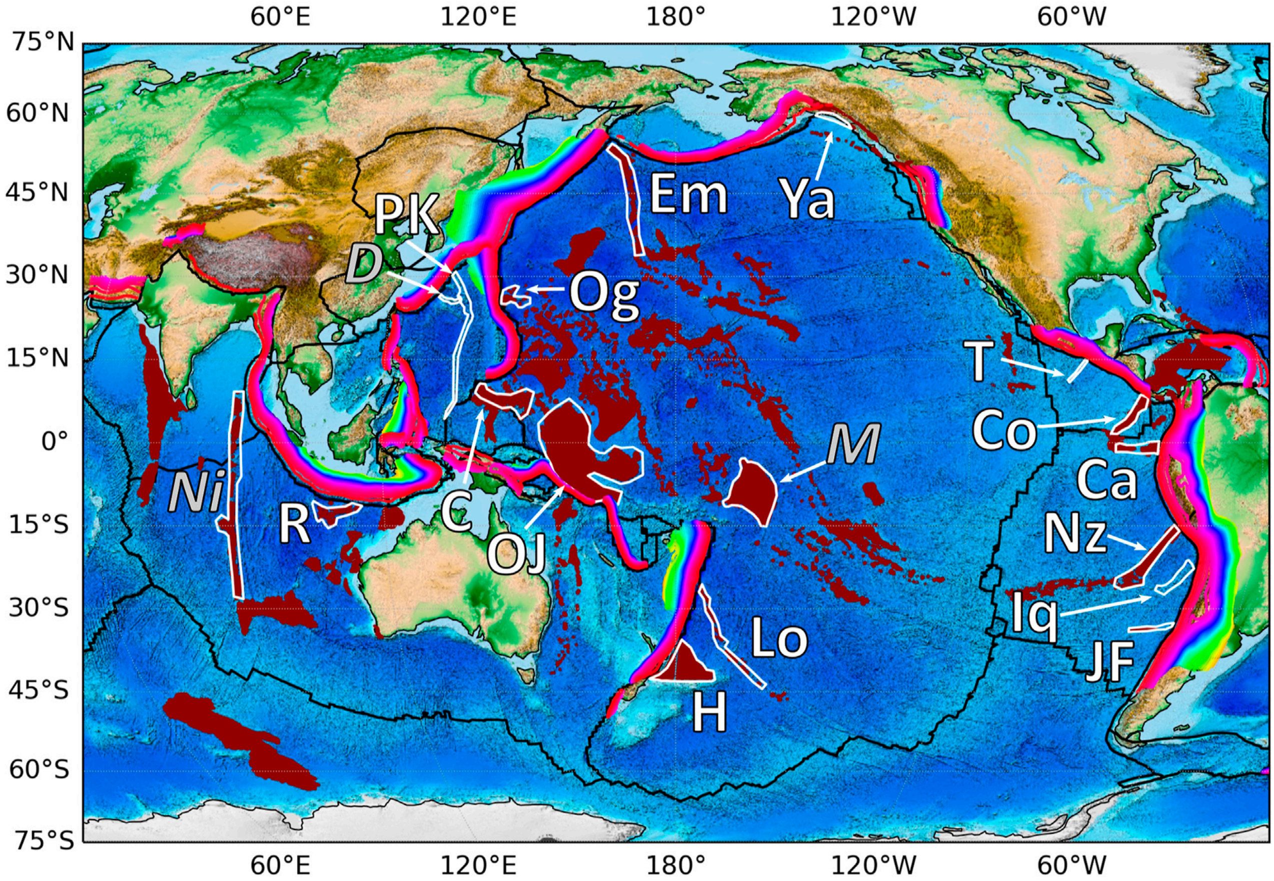

FIGURE 7 | Map of buoyant features (white outlined polygons) interacting with subduction zones in the Pacific and Indian oceans. Maroon surfaces indicate oceanic large igneous provinces (LIPs) and volcanic island chains. Slab depth contours are marked in RBG colours. Black lines indicate plate boundaries. Abbreviations for buoyant features discussed in the main text (white text): C—Caroline ridge, Ca—Carnegie ridge, Co—Cocos ridge, Em—Emperor ridge, H—Hikurangi plateau, Iq—Iquique ridge, JF—Juan-Fernandez ridge, Lo—Louisville ridge, Nz—Nazca ridge, OJ—Ontong Java plateau, Og—Ogasawara plateau, PK—Palau-Kyushu ridge, R—Roo rise, T—Tehuantepec ridge, Ya—Yakutat block. Other features (italic grey text): D—Daito ridge, M—Manihiki plateau, Ni—Ninetyeast ridge. Data from Coffin et al. (2006); Skinner and Clayton (2011); Tetreault and Buiter (2014), plate boundaries after Bird (2003), bathymetric data from Amante and Eakins (2008) and slab depth data from Hayes et al. (2018).

cusp and shallowing of the slab (Morell, 2015). Subduction of the Louisville Ridge below the Tonga trench introduces a minor cusp and some slab shallowing and contortion along the downdip projection of the obliquely subducting ridge (Bonnardot et al., 2007; Hayes et al., 2018). The Tonga-Kermadec trench is of moderate length, and might be expected to evolve to a "C" shaped trench (Schellart et al., 2007). However, the present-day shape of the Tonga-Kermadec trench is relatively straight, which may be due to early interaction between the middle of the trench, where it would have had the largest curvature, and the Louisville Ridge. This process would also account for the small size of the observed cusp where the ridge currently interacts with the Tonga-Kermadec trench. The cusp between the Japan and Kurile trench near Hokkaido is also associated with shallow slab below the island (Miller et al., 2006b; Kennett and Furumura, 2010; Hayes et al., 2018). Although there is no buoyant feature evident on the incoming plate, it has all the signatures of a recently subducted feature.

The interaction of the Ontong Java Plateau (OJP) with the South Pacific Trench is probably an extreme example of "slab deforming" style of interaction. The OJP separated from the Hikurangi plateau at ~120 Myr and from the Manihiki plateau at ~100 Myr (Taylor, 2006; Chandler et al., 2012; Seton et al., 2012) to reach the South Pacific trench at ~20 Myr (Mann and Taira, 2004; Seton et al., 2012). The impinging of the OJP on the trench hampered trench retreat and deformed the trench which, until that time, had a typical concave shape similar to the present-day Japan trench (Mann and Taira, 2004; Seton et al., 2012). The large extent of the OJP made it too buoyant to subduct, perhaps acting similarly to the ridge in model HB_C_Young. As a result, subduction in the region ceased and eventually reversed polarity (Mann and Taira, 2004).

Slab deformation due to buoyant-feature subduction may expose parts of the slab to increased stresses, which result in slab tears (e.g. models by Mason et al., 2010). This may be the case for the subduction of the Emperor ridge at the cusp between the Kamchatka and Aleutian trench, which is associated with a low

TABLE 3 | Properties of buoyant features discussed in the main text. Superscripts refer to information source.

Name	Slab shape affected	Trench deforming	Upper plate type	Subducting plate age	Comments
Hikurangi Plateau	Dip decreased above 100 km and increased below 100 km[a,b]	Yes[m,n]	Continental	Old	Near slab edge[a]
Louisville Ridge	Minor shallow dip decrease, deep contortion[a,c]	Minor[m]	Island arc	Old	Oblique subduction[c]
Ontong Java Plateau	Unsubductable[d]	Yes[d,n]	Island arc	Old	Collision resulted in subduction polarity reversal[d]
Caroline Ridge	Not subducting, S. Mariana slab steepened[e]	Yes[e]	Island arc	Old	Collison with the Yap Arc at ~20 Ma[t]
Ogasawara Plateau	Slab steepened and deformed[f]	Yes[f]	Island arc	Old	
Palau-Kyushu Ridge	Dip decreased north of ridge[a,g]	Minor[n]	Island arc	Young	Near the Boso triple junction and possible slab tear[g]
Emperor Ridge	Dip decreased[a,h]	Yes[o]	Island arc or Young oceanic	Old	Near possible slab tear[h]
Yakutat Block	Flat slab[a,i]	Yes[n]	Continental	Young	Near slab edge[a]
Tehuantepec Ridge	Flat slab[a]	Minor[p]	Continental	Young	Flat slab segment much bigger than ridge[a]
Cocos Ridge	Dip decreased significantly[j]	Minor[j]	Continental	Young	Near slab edge[a]
Carnegie Ridge	Flat slab[a,k]	Unknown	Continental	Young	Near slab edge and near the northern end of the Peruvian flat slab[a]
Nazca Ridge	Flat slab[a,k]	No[a]	Continental	Moderate	Near the southern end of the Peruvian flat slab[k]
Iquique Ridge	No effect[a]	Unknown	Continental	Moderate	
Juan-Fernandez Ridge	Flat slab[a,k]	No[a]	Continental	Moderate	
Roo Rise	Not yet subducted[a,l]	Minor[q,r]	Island arc	Old	Previous subduction of similar features implicated in slab tear[l]
Investigator Frac. Zone and Wharton Ridge	Minor local shallowing and slab contortion[a]	Minor[s]	Island Arc	Moderate	Near possible slab tear[s]

[a] *Hayes et al. (2018).*
[b] *Reyners et al. (2011).*
[c] *Bonnardot et al. (2007).*
[d] *Mann and Taira (2004).*
[e] *Miller et al. (2006a).*
[f] *Miller et al. (2006c).*
[g] *Xia et al. (2021).*
[h] *Davaille and Lees (2004).*
[i] *Gulick et al. (2007).*
[j] *Morell (2015).*
[k] *Gutscher et al. (2000).*
[l] *Hall and Spakman (2015).*
[m] *Schellart and Spakman (2012).*
[n] *Seton et al. (2012).*
[o] *Rosenbaum and Mo (2011).*
[p] *Suárez (2021).*
[q] *Kopp et al. (2006).*
[r] *Shulgin et al. (2011).*
[s] *Jacob et al. (2014).*
[t] *Lee (2004).*

slab dip angle and a possible tear (Davaille and Lees, 2004). However, this cusp may predate subduction of the Emperor chain (Seton et al., 2012), and its formation may instead have been associated with the subduction of previous, arc-related, buoyant features (e.g., Vaes et al., 2019). Another example is the Palau-Kyushu ridge, located at the cusp between the Ryukyu and Nankai trenches, which has been proposed to contribute to shallow subduction along Nankai trench, possibly with a tear near the subducting ridge (Wu et al., 2016; Pownall et al., 2017; Xia et al., 2021). The low dip of the Nankai slab may also be affected by the fact that its northern end lies at the Boso triple junction, where trench motion is limited by interaction between the Nankai, Izu and Japan trenches. In the Indian ocean, subduction of the Investigator Fracture Zone and the extinct Wharton spreading ridge coincide with a cusp in the Sumatra trench, a local slab "kink" and possible slab tear (Hall and Spakman, 2015). The excess buoyancy is likely due to subduction of the Wharton ridge, as oceanic fracture zones like Investigator are not usually associated with changes to plate buoyancy (e.g., Jacob et al., 2014). Along the Java trench, where the Roo rise is starting to deform the trench (Kopp et al., 2006; Shulgin et al., 2011), it has been suggested that past subduction of similar buoyant features is responsible for a slab tear within the Java slab (Hall and Spakman, 2015).

Flat subduction is currently observed in several subduction zones in the Eastern Pacific, under Alaska, Mexico, and South

America. In all cases, the strong westward motion of the Americas over the subducting Pacific, Cocos and Nazca plates may facilitate slab flattening (Van Hunen et al., 2002; Manea et al., 2017). In Alaska, the subduction of the Yakutat terrane occurs at a major cusp at the eastern end of the Aleutian trench and is associated with subduction of a narrow flat slab segment (Gulick et al., 2007). The Yakutat terrane subducts under a continental plate, although not of cratonic thickness, with a possible tear on the side (e.g., Daly et al., 2021). In South America, the Ecuador-Peru flat slab is associated with the subduction of the Carnegie and Nazca Ridges (which bound it from north and south) and the Chilean flat slab is associated with subduction of the Juan-Fernandez Ridge (Gutscher et al., 1999, 2000; Skinner and Clayton, 2013; Kumar et al., 2016; Bishop et al., 2017; Manea et al., 2017). The upper South American plate comprises several old platforms which may all have had thick roots, although not all persist to the present day (Feng et al., 2007). Although the Carnegie ridge interacts with the edge of the trench, where the trench motion is expected to be limited (Schellart et al., 2007), the associated Ecuador-Peru flat slab is located closer to the centre of the trench, as is the Chilean flat slab. Below the major cusp in the Andean trench, at the Bolivian Orocline, the slab is relatively steep. Although the cusp is in front of the subducting Iquique Ridge at present, it was formed before the arrival of the ridge to the trench, at 40–25 Ma (Allmendinger et al., 1997; Schepers et al., 2017). It may have formed above a previous flat slab segment which has been proposed to have existed between 40–20 Ma (Ramos and Folguera, 2009; Skinner and Clayton, 2013). A previously subducted buoyant feature may have formed the older flat slab and, aided by its location close to the centre of a long trench, have induced slab flattening. Capitanio et al. (2011) proposed that, in contrast to most trenches whose shape appears to be determined by subducting plate forcing, the recent (< 20 Ma) rise of the Andes and corresponding shape of the South American trench may be controlled by variations in thickness of the upper plate. Finally, flat subduction below Mexico is generally thought to be too wide to be induced by the buoyant Tehuantepec ridge that subducts at its southern end (Gutscher et al., 2000; Skinner and Clayton, 2011). Factors that may contribute to the formation of the Mexican flat slab include the subduction of a spreading ridge near the northern end of the plateau, a continental overriding plate, and the flat slab location just north of the boundary between the North and South American plates, where shearing due to differential movement between the Americas may result in fast moving upper plate over slow and young subducting plate.

5 CONCLUSION

We performed a set of 3-D multi-material numerical models of free subduction carrying a buoyant ridge, to investigate the role of plate age, ridge buoyancy and ridge location on trench shape and slab morphology for lower-plate controlled subduction (i.e., cases where the upper plate is young, thin or weak). Our models are the first to illustrate systematically that age-dependent slab density and viscosity can lead to different expressions of the subduction of buoyant features.

Our old-plate cases with buoyant ridges induce significant trench deformation and some steepening (rather than shallowing) of the dip angle of the subducting slab at the ridge. A similar type of "trench-deforming" response is observed in several Western Pacific subduction zones (e.g., Ogasawara Plateau on the old Pacific plate). Our young-plate cases with buoyant features generate both trench deformation and local shallowing of the subducting plate. This style of "slab-deforming" response is observed at several other locations around the Pacific, where the buoyant features are substantial enough that the background plate's pull and strength is insufficient to override the effect of local buoyancy (e.g., Cocos Ridge on the young Cocos plate). Finally, the position of the buoyant features relative to the natural slab shape, which is governed by slab width (Schellart et al., 2007; Schellart, 2020), may lead to a stronger or more subdued expression of ridge subduction. For example, the subduction of the Louisville ridge near the centre of the Tonga-Kermadec trench may explain the relatively mild expression of this ridge in slab dip and the relative straightness of the Tonga trench.

Our results, considered alongside previously published 3-D models that investigated other combinations of subducting plate buoyancy, strength and width, as well as buoyant features of various sizes and densities (Martinod et al., 2005; Mason et al., 2010; Flórez-Rodríguez et al., 2019), illustrate that a range of responses are possible for different subducting plate ages, and it is not expected that all subducting features lead to a shallowing of slab dip (Rosenbaum and Mo, 2011; Skinner and Clayton, 2011). Other studies have shown that the upper plate, if comprised of sufficiently thick continental lithosphere, can lead to further modulation of the expressions of buoyant feature subduction including the formation of flat slab segments (Manea et al., 2012; Rodríguez-González et al., 2012; Taramón et al., 2015). Our results suggest that buoyant features can play an important and varied role in shaping subduction dynamics and, particularly, on the evolution of plate boundaries, where local hampering of trench motion can induce boundary rotations and segmentation.

DATA AVAILABILITY STATEMENT

The datasets presented in this study can be found in online repositories. The names of the repository/repositories and accession number(s) can be found below: Zenodo repository; DOI: 10.5281/zenodo.5833712; URL: https://doi.org/10.5281/zenodo.5833712.

AUTHOR CONTRIBUTIONS

The ideas for this research were developed by all co-authors. Models were developed, validated and run by LS, FC and DRD. The paper was written by LS and SG, with input from DRD and FC.

FUNDING

LS was supported by the Engineering and Physical Sciences Research Council (EPSRC) (grant no. EP/N509486/1). FC was supported by an Australian Government Research Training Program (RTP) Scholarship. SG received support from Natural Environment Research Council (NERC grant NE/G004749/1). DRD acknowledges support from the Australian Research Council (ARC), under DP170100058.

ACKNOWLEDGMENTS

The MSci projects of Luke Jenkins and Kamile Rudaviciute, in collaboration with Loic Fourel, seeded the ideas developed in this paper. Numerical simulations were undertaken on the NCI National Facility in Canberra, Australia, which is supported by the Australian Commonwealth Government. The Fluidity computational modelling framework, including source code and documentation, is available from https://fluidityproject.github.io/. Authors would like to thank Stephan Kramer, Cian Wilson and Angus Gibson for support with the development and maintenance of Fluidity and two reviewers for constructive comments that helped to clarify important parts of the manuscript.

SUPPLEMENTARY MATERIAL

The Supplementary Material for this article can be found online at: https://www.frontiersin.org/articles/10.3389/feart.2022.852742/full#supplementary-material

REFERENCES

Allmendinger, R. W., Jordan, T. E., Kay, S. M., and Isacks, B. L. (1997). The Evolution of the Altiplano-Puna Plateau of the Central Andes. *Annu. Rev. Earth Planet. Sci.* 25, 139–174. doi:10.1146/annurev.earth.25.1.139

Amante, C., and Eakins, B. (2008). *Etopo1 1 Arc-Minute Global Relief Model: Procedures, Data Sources and Analysis, National Geophysical Data center, Nesdis, Noaa, Us Dept*. Boulder, CO, USA: Commerce.

Antonijevic, S. K., Wagner, L. S., Kumar, A., Beck, S. L., Long, M. D., Zandt, G., et al. (2015). The Role of Ridges in the Formation and Longevity of Flat Slabs. *Nature* 524, 212–215. doi:10.1038/nature14648

Arcay, D., Lallemand, S., and Doin, M.-P. (2008). Back-arc Strain in Subduction Zones: Statistical Observations versus Numerical Modeling. *Geochem. Geophys. Geosyst.* 9, a–n. doi:10.1029/2007GC001875

Arrial, P.-A., and Billen, M. I. (2013). Influence of Geometry and Eclogitization on Oceanic Plateau Subduction. *Earth Planet. Sci. Lett.* 363, 34–43. doi:10.1016/j.epsl.2012.12.011

Atwater, T. (1989). “Plate Tectonic History of the Northeast Pacific and Western North America,” in *The Eastern Pacific Ocean and Hawaii*. Editors E. L. Winterer, D. M. Hussong, and R. W. Decker (Boulder, Colorado, USA: Geological Society of America), Vol. N, 21–72. doi:10.1130/DNAG-GNA-N.21

Bellahsen, N., Faccenna, C., and Funiciello, F. (2005). Dynamics of Subduction and Plate Motion in Laboratory Experiments: Insights into the "plate Tectonics" Behavior of the Earth. *J. Geophys. Res.* 110, 1–15. doi:10.1029/2004JB002999

Betts, P. G., Giles, D., Foden, J., Schaefer, B. F., Mark, G., Pankhurst, M. J., et al. (2009). Mesoproterozoic Plume-Modified Orogenesis in Eastern Precambrian Australia. *Tectonics* 28, a–n. doi:10.1029/2008TC002325

Bird, P. (2003). An Updated Digital Model of Plate Boundaries. *Geochem. Geophys. Geosystems* 4. doi:10.1029/2001gc000252

Bishop, B. T., Beck, S. L., Zandt, G., Wagner, L., Long, M., Antonijevic, S. K., et al. (2017). Causes and Consequences of Flat-Slab Subduction in Southern Peru. *Geosphere* 13, 1392–1407. doi:10.1130/GES01440.1

Bonnardot, M.-A., Régnier, M., Ruellan, E., Christova, C., and Tric, E. (2007). Seismicity and State of Stress within the Overriding Plate of the Tonga-Kermadec Subduction Zone. *Tectonics* 26, a–n. doi:10.1029/2006TC002044

Buffett, B. A., and Becker, T. W. (2012). Bending Stress and Dissipation in Subducted Lithosphere. *J. Geophys. Res.* 117, a–n. doi:10.1029/2012JB009205

Capitanio, F. A., Faccenna, C., Zlotnik, S., and Stegman, D. R. (2011). Subduction Dynamics and the Origin of Andean Orogeny and the Bolivian Orocline. *Nature* 480, 83–86. doi:10.1038/nature10596

Capitanio, F. A., Morra, G., and Goes, S. (2009). Dynamics of Plate Bending at the Trench and Slab-Plate Coupling. *Geochem. Geophys. Geosyst.* 10, a–n. doi:10.1029/2008GC002348

Capitanio, F., Morra, G., and Goes, S. (2007). Dynamic Models of Downgoing Plate-Buoyancy Driven Subduction: Subduction Motions and Energy Dissipation. *Earth Planet. Sci. Lett.* 262, 284–297. doi:10.1016/j.epsl.2007.07.039

Chamolly, A., and Ribe, N. M. (2021). Fluid Mechanics of Free Subduction on a Sphere. Part 1. The Axisymmetric Case. *J. Fluid Mech.* 929, 1–32. doi:10.1017/jfm.2021.871

Chandler, M. T., Wessel, P., Taylor, B., Seton, M., Kim, S.-S., and Hyeong, K. (2012). Reconstructing Ontong Java Nui: Implications for Pacific Absolute Plate Motion, Hotspot Drift and True Polar Wander. *Earth Planet. Sci. Lett.* 331-332, 140–151. doi:10.1016/j.epsl.2012.03.017

Chen, F., Davies, D. R., Goes, S., Suchoy, L., and Kramer, S. C. (2022). How Sphericity Combines with the Age and Width of Slabs to Dictate the Dynamics and Evolution of Subduction Systems on Earth. Available at: http://www.essoar.org/doi/10.1002/essoar.10508606.1 (Accessed 03 01, 2022).doi:10.1002/essoar.10508606.1

Cloos, M. (1993). Lithospheric Buoyancy and Collisional Orogenesis: Subduction of Oceanic Plateaus, continental Margins, Island Arcs, Spreading Ridges, and Seamounts. *Geol. Soc. America Bull.* 105, 715–737. doi:10.1130/0016-7606(1993)105<0715:lbacos>2.3.co;2

Coffin, M., Duncan, R., Eldholm, O., Fitton, J. G., Frey, F., Larsen, H. C., et al. (2006). Large Igneous Provinces and Scientific Ocean Drilling: Status Quo and a Look Ahead. *Oceanog.* 19, 150–160. doi:10.5670/oceanog.2006.13

Corbi, F., Herrendörfer, R., Funiciello, F., and Dinther, Y. (2017). Controls of Seismogenic Zone Width and Subduction Velocity on Interplate Seismicity: Insights from Analog and Numerical Models. *Geophys. Res. Lett.* 44, 6082–6091. doi:10.1002/2016GL072415

Currie, C. A., and Beaumont, C. (2011). Are diamond-bearing Cretaceous Kimberlites Related to Low-Angle Subduction beneath Western North America? *Earth Planet. Sci. Lett.* 303, 59–70. doi:10.1016/j.epsl.2010.12.036

Daly, K. A., Abers, G. A., Mann, M. E., Roecker, S., and Christensen, D. H. (2021). Subduction of an Oceanic Plateau across Southcentral Alaska: High-Resolution Seismicity. *JGR Solid Earth* 126, 1–18. doi:10.1029/2021JB022809

Davaille, A., and Lees, J. M. (2004). Thermal Modeling of Subducted Plates: Tear and Hotspot at the Kamchatka Corner. *Earth Planet. Sci. Lett.* 226, 293–304. doi:10.1016/j.epsl.2004.07.024

Davies, D. R., Davies, J. H., Hassan, O., Morgan, K., and Nithiarasu, P. (2007). Investigations into the Applicability of Adaptive Finite Element Methods to Two-Dimensional Infinite Prandtl Number thermal and Thermochemical Convection. *Geochem. Geophys. Geosyst.* 8, a–n. doi:10.1029/2006GC001470

Davies, D. R., Wilson, C. R., and Kramer, S. C. (2011). Fluidity: A Fully Unstructured Anisotropic Adaptive Mesh Computational Modeling Framework for Geodynamics. *Geochem. Geophys. Geosyst.* 12, a–n. doi:10.1029/2011GC003551

Espurt, N., Baby, P., Brusset, S., Roddaz, M., Hermoza, W., Regard, V., et al. (2007). How Does the Nazca Ridge Subduction Influence the Modern Amazonian Foreland basin? *Geol* 35, 515–518. doi:10.1130/G23237A.1

Espurt, N., Funiciello, F., Martinod, J., Guillaume, B., Regard, V., Faccenna, C., et al. (2008). Flat Subduction Dynamics and Deformation of the South American Plate: Insights from Analog Modeling. *Tectonics* 27, a–n. doi:10.1029/2007TC002175

Feng, M., van der Lee, S., and Assumpção, M. (2007). Upper Mantle Structure of South America from Joint Inversion of Waveforms and Fundamental Mode Group Velocities of Rayleigh Waves. *J. Geophys. Res.* 112, 1–16. doi:10.1029/2006JB004449

Flórez-Rodríguez, A. G., Schellart, W. P., and Strak, V. (2019). Impact of Aseismic Ridges on Subduction Systems: Insights from Analog Modeling. *J. Geophys. Res. Solid Earth* 124, 5951–5969. doi:10.1029/2019JB017488

Forsyth, D., and Uyeda, S. (1975). On the Relative Importance of the Driving Forces of Plate Motion. *Geophys. J. Int.* 43, 163–200. doi:10.1111/j.1365-246X.1975.tb00631.x

Funiciello, F., Faccenna, C., Giardini, D., and Regenauer-Lieb, K. (2003). Dynamics of Retreating Slabs: 2. Insights from Three-Dimensional Laboratory Experiments. *J. Geophys. Res.* 108, 1–16. doi:10.1029/2001jb000896

Garel, F., Goes, S., Davies, D. R., Davies, J. H., Kramer, S. C., and Wilson, C. R. (2014). Interaction of Subducted Slabs with the Mantle Transition-zone: A Regime Diagram from 2-D Thermo-mechanical Models with a mobile Trench and an Overriding Plate. *Geochem. Geophys. Geosyst.* 15, 1739–1765. doi:10.1002/2014GC005257

Gerya, T. V., Fossati, D., Cantieni, C., and Seward, D. (2009). Dynamic Effects of Aseismic ridge Subduction: Numerical Modelling. *Eur. J. Mineralogy* 21, 649–661. doi:10.1127/0935-1221/2009/0021-1931

Goes, S., Agrusta, R., van Hunen, J., and Garel, F. (2017). Subduction-transition Zone Interaction: A Review. *Geosphere* 13, 644–664. doi:10.1130/GES01476.1

Gulick, S. P. S., Lowe, L. A., Pavlis, T. L., Gardner, J. V., and Mayer, L. A. (2007). Geophysical Insights into the Transition Fault Debate: Propagating Strike Slip in Response to Stalling Yakutat Block Subduction in the Gulf of Alaska. *Geol* 35, 763–766. doi:10.1130/G23585A.1

Gutscher, M.-A., Malavieille, J., Lallemand, S., and Collot, J.-Y. (1999). Tectonic Segmentation of the North Andean Margin: Impact of the Carnegie Ridge Collision. *Earth Planet. Sci. Lett.* 168, 255–270. doi:10.1016/s0012-821x(99)00060-6

Gutscher, M.-A., Spakman, W., Bijwaard, H., and Engdahl, E. R. (2000). Geodynamics of Flat Subduction: Seismicity and Tomographic Constraints from the Andean Margin. *Tectonics* 19, 814–833. doi:10.1029/1999TC001152

Hall, R., and Spakman, W. (2015). Mantle Structure and Tectonic History of SE Asia. *Tectonophysics* 658, 14–45. doi:10.1016/j.tecto.2015.07.003

Hayes, G. P., Moore, G. L., Portner, D. E., Hearne, M., Flamme, H., Furtney, M., et al. (2018). Slab2, a Comprehensive Subduction Zone Geometry Model. *Science* 362, 58–61. doi:10.1126/science.aat4723

Holt, A. F., and Becker, T. W. (2017). The Effect of a Power-Law Mantle Viscosity on Trench Retreat Rate. *Geophys. J. Int.* 208, 491–507. doi:10.1093/gji/ggw392

Hu, J., Liu, L., Hermosillo, A., and Zhou, Q. (2016). Simulation of Late Cenozoic South American Flat-Slab Subduction Using Geodynamic Models with Data Assimilation. *Earth Planet. Sci. Lett.* 438, 1–13. doi:10.1016/j.epsl.2016.01.011

Humphreys, E. D. (1995). Post-laramide Removal of the Farallon Slab, Western United States. *Geol* 23, 987–990. doi:10.1130/0091-7613(1995)023<0987:plrotf>2.3.co;2

Isacks, B. L. (1988). Uplift of the central Andean Plateau and Bending of the Bolivian Orocline. *J. Geophys. Res.* 93, 3211–3231. doi:10.1029/JB093iB04p03211

Jacob, J., Dyment, J., and Yatheesh, V. (2014). Revisiting the Structure, Age, and Evolution of the Wharton Basin to Better Understand Subduction under Indonesia. *J. Geophys. Res. Solid Earth* 119, 169–190. doi:10.1002/2013jb010285

Jadamec, M. A., and Billen, M. I. (2012). The Role of Rheology and Slab Shape on Rapid Mantle Flow: Three-Dimensional Numerical Models of the Alaska Slab Edge. *J. Geophys. Res. Solid Earth* 117, B02304. doi:10.1029/2011jb008563

Kennett, B. L. N., and Furumura, T. (2010). Tears or Thinning? Subduction Structures in the Pacific Plate beneath the Japanese Islands. *Phys. Earth Planet. Interiors* 180, 52–58. doi:10.1016/j.pepi.2010.03.001

Kim, Y., Miller, M. S., Pearce, F., and Clayton, R. W. (2012). Seismic Imaging of the Cocos Plate Subduction Zone System in central Mexico. *Geochem. Geophys. Geosyst.* 13, a–n. doi:10.1029/2012GC004033

Kopp, H., Flueh, E., Petersen, C., Weinrebe, W., Wittwer, A., and Scientists, M. (2006). The Java Margin Revisited: Evidence for Subduction Erosion off Java. *Earth Planet. Sci. Lett.* 242, 130–142. doi:10.1016/j.epsl.2005.11.036

Kramer, S. C., Davies, D. R., and Wilson, C. R. (2021). Analytical Solutions for Mantle Flow in Cylindrical and Spherical Shells. *Geosci. Model. Dev.* 14, 1899–1919. doi:10.5194/gmd-14-1899-2021

Kramer, S. C., Wilson, C. R., and Davies, D. R. (2012). An Implicit Free Surface Algorithm for Geodynamical Simulations. *Phys. Earth Planet. Interiors* 194-195, 25–37. doi:10.1016/j.pepi.2012.01.001

Kumar, A., Wagner, L. S., Beck, S. L., Long, M. D., Zandt, G., Young, B., et al. (2016). Seismicity and State of Stress in the central and Southern Peruvian Flat Slab. *Earth Planet. Sci. Lett.* 441, 71–80. doi:10.1016/j.epsl.2016.02.023

Kusky, T. M., Windley, B. F., Wang, L., Wang, Z., Li, X., and Zhu, P. (2014). Flat Slab Subduction, Trench Suction, and Craton Destruction: Comparison of the North China, Wyoming, and Brazilian Cratons. *Tectonophysics* 630, 208–221. doi:10.1016/j.tecto.2014.05.028

Lee, S.-M. (2004). Deformation from the Convergence of Oceanic Lithosphere into Yap Trench and its Implications for Early-Stage Subduction. *J. Geodynamics* 37, 83–102. doi:10.1016/j.jog.2003.10.003

Liu, L., Gurnis, M., Seton, M., Saleeby, J., Müller, R. D., and Jackson, J. M. (2010). The Role of Oceanic Plateau Subduction in the Laramide Orogeny. *Nat. Geosci* 3, 353–357. doi:10.1038/ngeo829

Liu, L., and Stegman, D. R. (2012). Origin of Columbia River Flood basalt Controlled by Propagating Rupture of the Farallon Slab. *Nature* 482, 386–389. doi:10.1038/nature10749

Liu, S., and Currie, C. A. (2016). Farallon Plate Dynamics Prior to the Laramide Orogeny: Numerical Models of Flat Subduction. *Tectonophysics* 666, 33–47. doi:10.1016/j.tecto.2015.10.010

Mahadevan, L., Bendick, R., and Liang, H. (2010). Why Subduction Zones Are Curved. *Tectonics* 29, 1–10. doi:10.1029/2010tc002720

Mahlburg Kay, S., and Mpodozis, C. (2002). Magmatism as a Probe to the Neogene Shallowing of the Nazca Plate beneath the Modern Chilean Flat-Slab. *J. South Am. Earth Sci.* 15, 39–57. doi:10.1016/S0895-9811(02)00005-6

Manea, V. C., Manea, M., and Ferrari, L. (2013). A Geodynamical Perspective on the Subduction of Cocos and Rivera Plates beneath Mexico and Central America. *Tectonophysics* 609, 56–81. doi:10.1016/j.tecto.2012.12.039

Manea, V. C., Manea, M., Ferrari, L., Orozco-Esquivel, T., Valenzuela, R. W., Husker, A., et al. (2017). A Review of the Geodynamic Evolution of Flat Slab Subduction in Mexico, Peru, and Chile. *Tectonophysics* 695, 27–52. doi:10.1016/j.tecto.2016.11.037

Manea, V. C., Pérez-Gussinyé, M., and Manea, M. (2012). Chilean Flat Slab Subduction Controlled by Overriding Plate Thickness and Trench Rollback. *Geology* 40, 35–38. doi:10.1130/G32543.1

Manea, V., and Gurnis, M. (2007). Subduction Zone Evolution and Low Viscosity Wedges and Channels. *Earth Planet. Sci. Lett.* 264, 22–45. doi:10.1016/j.epsl.2007.08.030

Mann, P., and Taira, A. (2004). Global Tectonic Significance of the Solomon Islands and Ontong Java Plateau Convergent Zone. *Tectonophysics* 389, 137–190. doi:10.1016/j.tecto.2003.10.024

Martinod, J., Funiciello, F., Faccenna, C., Labanieh, S., and Regard, V. (2005). Dynamical Effects of Subducting Ridges: Insights from 3-D Laboratory Models. *Geophys. J. Int.* 163, 1137–1150. doi:10.1111/j.1365-246x.2005.02797.x

Martinod, J., Guillaume, B., Espurt, N., Faccenna, C., Funiciello, F., and Regard, V. (2013). Effect of Aseismic ridge Subduction on Slab Geometry and Overriding Plate Deformation: Insights from Analogue Modeling. *Tectonophysics* 588, 39–55. doi:10.1016/j.tecto.2012.12.010

Mason, W. G., Moresi, L., Betts, P. G., and Miller, M. S. (2010). Three-dimensional Numerical Models of the Influence of a Buoyant Oceanic Plateau on Subduction Zones. *Tectonophysics* 483, 71–79. doi:10.1016/j.tecto.2009.08.021

McKenzie, D., Jackson, J., and Priestley, K. (2005). Thermal Structure of Oceanic and continental Lithosphere. *Earth Planet. Sci. Lett.* 233, 337–349. doi:10.1016/j.epsl.2005.02.005

Miller, M. S., Gorbatov, A., and Kennett, B. L. N. (2006a). Three-dimensional Visualization of a Near-Vertical Slab Tear beneath the Southern Mariana Arc. *Geochem. Geophys. Geosyst.* 7, a–n. doi:10.1029/2005GC001110

Miller, M. S., Kennett, B. L. N., and Gorbatov, A. (2006b). Morphology of the Distorted Subducted Pacific Slab beneath the Hokkaido Corner, Japan. *Phys. Earth Planet. Interiors* 156, 1–11. doi:10.1016/j.pepi.2006.01.007

Miller, M. S., Kennett, B. L. N., and Toy, V. G. (2006c). Spatial and Temporal Evolution of the Subducting Pacific Plate Structure along the Western Pacific Margin. *J. Geophys. Res.* 111, a–n. doi:10.1029/2005JB003705

Morell, K. D. (2015). Late M Iocene to Recent Plate Tectonic History of the Southern C Entral A Merica Convergent Margin. *Geochem. Geophys. Geosyst.* 16, 3362–3382. doi:10.1002/2015GC005971

Morra, G., Regenauer-Lieb, K., and Giardini, D. (2006). Curvature of Oceanic Arcs. *Geol* 34, 877–880. doi:10.1130/G22462.1

Muldashev, I. A., and Sobolev, S. V. (2020). What Controls Maximum Magnitudes of Giant Subduction Earthquakes? *Geochem. Geophys. Geosyst.* 21. doi:10.1029/2020GC009145

Nur, A., and Ben-Avraham, Z. (1981). "Volcanic Gaps and the Consumption of Aseismic Ridges in South America," in *Nazca Plate: Crustal Formation and Andean Convergence*. Editors L. V. D. Kulm, J. Dymond, E. J. Dasch, D. M. Hussong, and R. Roderick (Boulder, Colorado, USA: Geological Society of America), Vol. 154, 729–740. doi:10.1130/MEM154-p729

Nur, A., and Ben-Avraham, Z. (1983). Volcanic Gaps Due to Oblique Consumption of Aseismic Ridges. *Tectonophysics* 99, 355–362. doi:10.1016/0040-1951(83)90112-9

O'Driscoll, L. J., Humphreys, E. D., and Saucier, F. (2009). Subduction Adjacent to Deep continental Roots: Enhanced Negative Pressure in the Mantle Wedge, Mountain Building and continental Motion. *Earth Planet. Sci. Lett.* 280, 61–70. doi:10.1016/j.epsl.2009.01.020

OzBench, M., Regenauer-Lieb, K., Stegman, D. R., Morra, G., Farrington, R., Hale, A., et al. (2008). A Model Comparison Study of Large-Scale Mantle-Lithosphere Dynamics Driven by Subduction. *Phys. Earth Planet. Interiors* 171, 224–234. doi:10.1016/j.pepi.2008.08.011

Pownall, J. M., Lister, G. S., and Spakman, W. (2017). Reconstructing Subducted Oceanic Lithosphere by "Reverse-Engineering" Slab Geometries: The Northern Philippine Sea Plate. *Tectonics* 36, 1814–1834. doi:10.1002/2017tc004686

Ramos, V. A., and Folguera, A. (2009). Andean Flat-Slab Subduction through Time. *Geol. Soc. Lond. Spec. Publications* 327, 31–54. doi:10.1144/SP327.3

Reyners, M., Eberhart-Phillips, D., and Bannister, S. (2011). Tracking Repeated Subduction of the Hikurangi Plateau beneath New Zealand. *Earth Planet. Sci. Lett.* 311, 165–171. doi:10.1016/j.epsl.2011.09.011

Ribe, N. M. (2010). Bending Mechanics and Mode Selection in Free Subduction: A Thin-Sheet Analysis. *Geophys. J. Int.* 180, 559–576. doi:10.1111/j.1365-246X.2009.04460.x

Roda, M., Marotta, A. M., and Spalla, M. I. (2011). The Effects of the Overriding Plate thermal State on the Slab Dip in an Ocean-Continent Subduction System. *Comptes Rendus Geosci.* 343, 323–330. doi:10.1016/j.crte.2011.01.005

Rodríguez-González, J., Billen, M. I., and Negredo, A. M. (2014). Non-steady-state Subduction and Trench-Parallel Flow Induced by Overriding Plate Structure. *Earth Planet. Sci. Lett.* 401, 227–235. doi:10.1016/j.epsl.2014.06.013

Rodríguez-González, J., Negredo, A. M., and Billen, M. I. (2012). The Role of the Overriding Plate thermal State on Slab Dip Variability and on the Occurrence of Flat Subduction. *Geochem. Geophys. Geosyst.* 13, a–n. doi:10.1029/2011GC003859

Rosenbaum, G., and Mo, W. (2011). Tectonic and Magmatic Responses to the Subduction of High Bathymetric Relief. *Gondwana Res.* 19, 571–582. doi:10.1016/j.gr.2010.10.007

Sacks, I. S. (1983). The Subduction of Young Lithosphere. *J. Geophys. Res.* 88, 3355–3366. doi:10.1029/JB088iB04p03355

Schellart, W. P. (2020). Control of Subduction Zone Age and Size on Flat Slab Subduction. *Front. Earth Sci.* 8, 26. doi:10.3389/feart.2020.00026

Schellart, W. P., Freeman, J., Stegman, D. R., Moresi, L., and May, D. (2007). Evolution and Diversity of Subduction Zones Controlled by Slab Width. *Nature* 446, 308–311. doi:10.1038/nature05615

Schellart, W. P. (2005). Influence of the Subducting Plate Velocity on the Geometry of the Slab and Migration of the Subduction Hinge. *Earth Planet. Sci. Lett.* 231, 197–219. doi:10.1016/j.epsl.2004.12.019

Schellart, W. P., and Spakman, W. (2012). Mantle Constraints on the Plate Tectonic Evolution of the Tonga-Kermadec-Hikurangi Subduction Zone and the South Fiji Basin Region. *Aust. J. Earth Sci.* 59, 933–952. doi:10.1080/08120099.2012.679692

Schellart, W. P., and Strak, V. (2021). Geodynamic Models of Short-Lived, Long-Lived and Periodic Flat Slab Subduction. *Geophys. J. Int.* 226, 1517–1541. doi:10.1093/gji/ggab126

Schepers, G., Van Hinsbergen, D. J. J., Spakman, W., Kosters, M. E., Boschman, L. M., and McQuarrie, N. (2017). South-American Plate advance and Forced Andean Trench Retreat as Drivers for Transient Flat Subduction Episodes. *Nat. Commun.* 8, 1–9. doi:10.1038/ncomms15249

Seton, M., Müller, R. D., Zahirovic, S., Gaina, C., Torsvik, T., Shephard, G., et al. (2012). Global continental and Ocean basin Reconstructions since 200Ma. *Earth-Science Rev.* 113, 212–270. doi:10.1016/j.earscirev.2012.03.002

Shulgin, A., Kopp, H., Mueller, C., Planert, L., Lueschen, E., Flueh, E. R., et al. (2011). Structural Architecture of Oceanic Plateau Subduction Offshore Eastern Java and the Potential Implications for Geohazards. *Geophys. J. Int.* 184, 12–28. doi:10.1111/j.1365-246X.2010.04834.x

Skinner, S. M., and Clayton, R. W. (2011). An Evaluation of Proposed Mechanisms of Slab Flattening in Central Mexico. *Pure Appl. Geophys.* 168, 1461–1474. doi:10.1007/s00024-010-0200-3

Skinner, S. M., and Clayton, R. W. (2013). The Lack of Correlation between Flat Slabs and Bathymetric Impactors in South America. *Earth Planet. Sci. Lett.* 371-372, 1–5. doi:10.1016/j.epsl.2013.04.013

Sparkes, R., Tilmann, F., Hovius, N., and Hillier, J. (2010). Subducted Seafloor Relief Stops Rupture in South American Great Earthquakes: Implications for Rupture Behaviour in the 2010 Maule, Chile Earthquake. *Earth Planet. Sci. Lett.* 298, 89–94. doi:10.1016/j.epsl.2010.07.029

Stegman, D. R., Farrington, R., Capitanio, F. A., and Schellart, W. P. (2010). A Regime Diagram for Subduction Styles from 3-D Numerical Models of Free Subduction. *Tectonophysics* 483, 29–45. doi:10.1016/j.tecto.2009.08.041

Suárez, G. (2021). Large Earthquakes in the Tehuantepec Subduction Zone: Evidence of a Locked Plate Interface and Large-Scale Deformation of the Slab. *J. Seismol* 25, 449–460. doi:10.1007/s10950-020-09969-6

Suchoy, L., Goes, S., Maunder, B., Garel, F., and Davies, R. (2021). Effects of Basal Drag on Subduction Dynamics from 2D Numerical Models. *Solid Earth* 12, 79–93. doi:10.5194/se-12-79-2021

Taramón, J. M., Rodríguez-González, J., Negredo, A. M., and Billen, M. I. (2015). Influence of Cratonic Lithosphere on the Formation and Evolution of Flat Slabs: Insights from 3-D Time-dependent Modeling. *Geochem. Geophys. Geosyst.* 16, 2933–2948. doi:10.1002/2015GC005940

Taylor, B. (2006). The Single Largest Oceanic Plateau: Ontong Java-Manihiki-Hikurangi. *Earth Planet. Sci. Lett.* 241, 372–380. doi:10.1016/j.epsl.2005.11.049

Tetreault, J. L., and Buiter, S. J. H. (2014). Future Accreted Terranes: A Compilation of Island Arcs, Oceanic Plateaus, Submarine Ridges, Seamounts, and continental Fragments. *Solid Earth* 5, 1243–1275. doi:10.5194/se-5-1243-2014

Vaes, B., Hinsbergen, D. J. J., and Boschman, L. M. (2019). Reconstruction of Subduction and Back-Arc Spreading in the NW Pacific and Aleutian Basin: Clues to Causes of Cretaceous and Eocene Plate Reorganizations. *Tectonics* 38, 1367–1413. doi:10.1029/2018TC005164

Van Hunen, J., Van Den Berg, A. P., and Vlaar, N. J. (2002). On the Role of Subducting Oceanic Plateaus in the Development of Shallow Flat Subduction. *Tectonophysics* 352, 317–333. doi:10.1016/S0040-1951(02)00263-9

van Hunen, J., van den Berg, A. P., and Vlaar, N. J. (2004). Various Mechanisms to Induce Present-Day Shallow Flat Subduction and Implications for the Younger Earth: A Numerical Parameter Study. *Phys. Earth Planet. Interiors* 146, 179–194. doi:10.1016/j.pepi.2003.07.027

Vogt, P. R., Lowrie, A., Bracey, D. R., and Hey, R. (1976). *Subduction of Aseismic Oceanic Ridges: Effects on Shape, Seismicity, and Other Characteristics of Consuming Plate Boundaries, Vol. 172.* Boulder, Colorado, USA: Geological Society of America.

Vogt, P. R. (1973). Subduction and Aseismic Ridges. *Nature* 241, 189–191. doi:10.1038/241189a0

Wilson, C. R. (2009). *Modelling Multiple-Material Flows on Adaptive Unstructured Meshes.* Doctoral dissertation (London: Imperial College London). doi:10.25560/5526

Wu, J., Suppe, J., Lu, R., and Kanda, R. (2016). Philippine Sea and East Asian Plate Tectonics since 52 Ma Constrained by New Subducted Slab Reconstruction Methods. *J. Geophys. Res. Solid Earth* 121, 4670–4741. doi:10.1002/2016JB012923

Xia, C. L., Zheng, Y. P., Liu, B. H., Hua, Q. F., Liu, K., Ma, L., et al. (2020). Geological and Geophysical Differences between the north and South Sections of the Yap Trench-arc System and Their Relationship with Caroline Ridge Subduction. *Geol. J.* 55, 7775–7789. doi:10.1002/gj.3903

Xia, C., Zheng, Y., Liu, B., Hua, Q., Ma, L., Li, X., et al. (2021). Tectonic Implications of the Subduction of the Kyushu-Palau Ridge beneath the Kyushu, Southwest Japan. *Acta Oceanol. Sin.* 40, 70–83. doi:10.1007/s13131-021-1711-8

Zhang, J., and Zhang, G. (2020). Geochemical and Chronological Evidence for Collision of Proto-Yap arc/Caroline Plateau and Rejuvenated Plate Subduction at Yap Trench. *Lithos* 370-371, 105616. doi:10.1016/j.lithos.2020.105616

Zhu, G., Yang, H., Lin, J., Zhou, Z., Xu, M., Sun, J., et al. (2019). Along-strike Variation in Slab Geometry at the Southern Mariana Subduction Zone Revealed by Seismicity through Ocean Bottom Seismic Experiments. *Geophys. J. Int.* 218, 2122–2135. doi:10.1093/gji/ggz272

Conflict of Interest: The authors declare that the research was conducted in the absence of any commercial or financial relationships that could be construed as a potential conflict of interest.

frontiers | Frontiers in Earth Science

ORIGINAL RESEARCH
published: 09 May 2022
doi: 10.3389/feart.2022.845126

Topographic Response of Hinterland Basins in Tibet to the India–Asia Convergence: 3D Thermo-Mechanical Modeling

Pengpeng Zhang[1,2], *Lin Chen*[1]*, *Wenjiao Xiao*[1,3]* *and Ji'en Zhang*[1]

[1]*State Key Laboratory of Lithospheric Evolution, Institute of Geology and Geophysics, Chinese Academy of Sciences, Beijing, China,* [2]*Institute of Geology and Planetary Sciences, University of Chinese Academy of Sciences, Beijing, China,* [3]*Xinjiang Research Center for Mineral Resources, Xinjiang Institute of Ecology and Geography, Chinese Academy of Sciences, Urumqi, China*

A number of basins have developed in Tibet since the early stages of the India–Asia collision, and now, they have become integral parts of the Tibetan Plateau. Geophysical and geochemical data reveal that these basins are currently characterized either by strong or weak basements. However, it remains unclear how these hinterland basins evolved during the India–Asia collision and how they affected the post-collisional growth of the Tibetan Plateau. Here, we use 3D thermo-mechanical simulations to investigate the topographic response of a strength-varying hinterland basin imbedded in an orogenic plateau under the horizontal compression condition. Our results show that a strong hinterland basin experiences little deformation and develops into a lowland with respect to the surrounding plateau at the early stages of the collision. The lowland gradually shrinks and survives in the interior of the plateau for ~30–40 Myr before merging into the plateau. In contrast, a weak hinterland basin uplifts soon after the initial collision and develops into a highland after ~20 Myr of convergence. Topographic analysis reveals that the strong hinterland basin experiences an evident elevation drop after ~20–30 Myr of convergence, followed by a rapid uplift. After compiling the paleoelevation data, we proposed that the Tibetan Plateau experienced a four-stage surface uplift, which was characterized by 1) the Gangdese and central watershed highlands isolating three lowlands during the Eocene, 2) the central lowland experiencing an elevation drop of ~2000 m during the Oligocene, 3) the central lowland suffering a rapid uplift and merging into the Tibetan Plateau in the Early Miocene, and 4) the south and north lowlands rising and developing into a plateau similar to the modern Tibetan Plateau since the Middle Miocene.

Keywords: numerical modeling, Tibetan Plateau, topography, uplift history, Lunpola Basin

Edited by:
Manuele Faccenda,
Università Padova, Italy

Reviewed by:
Andrea Piccolo,
University of Bayreuth, Germany
Chenglong Deng,
Institute of Geology and Geophysics (CAS), China

****Correspondence:***
Lin Chen
chenlin@mail.iggcas.ac.cn
Wenjiao Xiao
Wj-xiao@mail.iggcas.ac.cn

Specialty section:
This article was submitted to Structural Geology and Tectonics, a section of the journal Frontiers in Earth Science

Received: *29 December 2021*
Accepted: *06 April 2022*
Published: *09 May 2022*

Citation:
Zhang P, Chen L, Xiao W and Zhang J (2022) Topographic Response of Hinterland Basins in Tibet to the India–Asia Convergence: 3D Thermo-Mechanical Modeling. Front. Earth Sci. 10:845126. doi: 10.3389/feart.2022.845126

1 INTRODUCTION

The modern Tibetan Plateau is the most extensive elevated surface on the earth, characterized by a high elevation and a flat-topped landscape. However, a number of low-elevation sedimentary basins developed in Tibet during the Cenozoic era (Kapp et al., 2005; Zhang et al., 2010; Deng and Ding, 2015; Kapp and DeCelles, 2019) (**Figure 1**). Sedimentary records and paleoelevation data reveal that

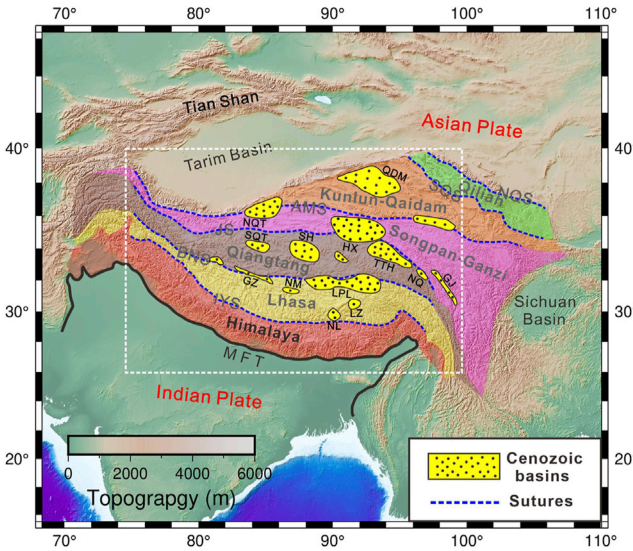

FIGURE 1 | Simplified geological map of the Tibetan Plateau. The black curve represents the main frontal thrust (MFT). The blue dashed curves delineate the suture zones, and the colored regions are different terrains within the Tibetan Plateau (Yin and Harrison., 2000). Yellow dotted areas are Paleocene–Eocene basins (Zhang et al., 2010; Zhang et al., 2013). The white dashed box outlines the area of **Figure 2A**. IYS, Indus–Yarlung suture zone; BNS, Bangong–Nujiang suture zone; JS, Jinsha suture zone; AMS, Anyimaqen–Muztagh suture zone; SQS, South Qilian suture; NQS, North Qilian suture; NL, Namling Basin; LZ, Linzhou Basin; LPL, Lunpola Basin; NM, Nima Basin; GZ, Gerze Basin; GJ, Gonjo Basin; NQ, Niangqian Basin; TTH, Tuotuohe Basin; HX, Hoh Xil Basin; SH, Shuanghu Basin; SQT, South Qiangtang Basin; NQT, North Qiangtang Basin; QDM, Qaidam Basin.

many of these basins survived for a long period of time and maintained a low elevation before merging into the Tibetan Plateau. For example, the Lunpola Basin, located in central Tibet, contains >4,000 m-thick of lacustrine sedimentary layers which deposited during the Middle Eocene to the Early Miocene (Sun et al., 2014; Fang et al., 2020). Fish and palm fossils indicate that the Lunpola Basin was in a warm and humid environment during the late Oligocene, implying an elevation <2,300 m (Wu et al., 2017; Farnsworth et al., 2018). In the neighboring Nima Basin, the sedimentary layers were deposited from the Late Cretaceous to the Early Miocene (DeCelles et al., 2007; Kapp et al., 2007), and plants fossils indicate an elevation no more than 1,000 m during the late Oligocene (Wu et al., 2017; Liu et al., 2019). In the north-central Tibetan Plateau, the Hoh Xil Basin has a series of sedimentary sequences developed from the Middle Eocene to Early Miocene (Liu et al., 2003; Wang et al., 2008), and the leaf fossils indicate an elevation less than 3,000 m during the Early Miocene (Sun et al., 2015). In contrast, there were some other basins that had uplifted and merged into the plateau soon after the India–Asia collision. For example, the sedimentary strata in the Linzhou Basin ceased to deposit during the Late Eocene (He et al., 2007; Ding et al., 2014), and the oxygen isotope indicates that the Linzhou Basin had uplifted to attain its current elevation in the Early Eocene (Ding et al., 2014).

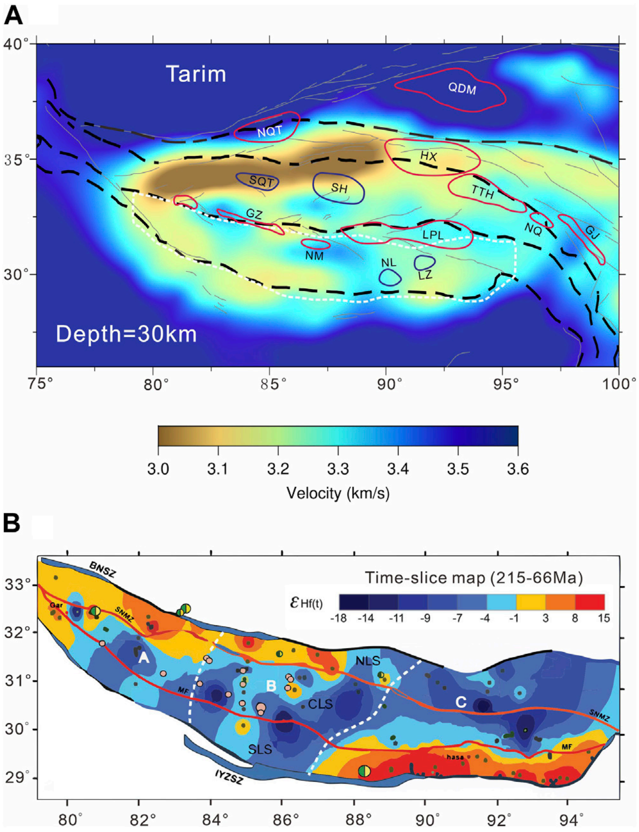

FIGURE 2 | Shear wave velocity of the crust and Hf isotopic mapping. **(A)** Shear wave velocity at a 30 km depth in the region shown in **Figure 1** (Yang et al., 2012). Red curves delineate the hinterland basins with a relatively fast velocity. Blue curves delineate the hinterland basins with a relatively slow velocity. **(B)** Hf isotopic mapping showing the spatial variation of zircon εHf(t) values for felsic igneous rocks in the Lhasa terrain (Hou et al., 2015). The region is outlined by a white dashed curve in **(A)**. SLS, southern Lhasa subterrane; CLS, central Lhasa subterrane; and NLS, northern Lhasa subterrane.

Recent geophysical investigations show that some basins inside the Tibetan Plateau have relatively high seismic velocity crusts with respect to the surroundings (Yang et al., 2012; Zhao et al., 2013; Chen M. et al., 2017; and Huang et al., 2020) (**Figure 2A**), such as the Lunpola and Nima basins, implying relatively strong basements beneath these basins. However, the others basins exhibit a low velocity anomalies in the crust (**Figure 2A**), such as the Linzhou and the Hoh Xil basins, implying soft basements beneath them. Similar differences also manifest in geochemical data. For example, the Lunpola and Nima basins in the Lhasa terrane exhibit a negative Hf isotopic ratio of felsic igneous rocks (Zhu et al., 2011; Hou et al., 2015; Hou et al., 2020), correlated with the fast velocity zones (**Figure 2B**), indicative of a strong basement underneath them. In contrast, other basins, such as the Linzhou and Namling basins, display positive Hf isotopic values (**Figure 2B**), correlated with the slow velocity zones, implying a relatively weak basement beneath them. Therefore, both the available geophysical and geochemical data suggest that the strength of the hinterland basins in Tibet varies from region to region.

Over the past several decades, a number of modeling studies have investigated the role of lateral lithospheric strength heterogeneities in the deformation pattern and growth of the orogenic plateau (England and Houseman, 1985; Cook and Royden, 2008; Dayem et al., 2009; Sokoutis and Willingshofer, 2011; Chen L. et al., 2017; Bischoff and Flesch, 2019; and Chen et al., 2020; Xie et al., 2021). These studies can be classified into two different categories: 1) weak lithosphere flanked by strong domains, and 2) strong block imbedded into a weak lithosphere. Most of these studies focus on the case of a weak domain sandwiched by a strong lithosphere (Willingshofer et al., 2005; Sokoutis and Willingshofer, 2011; Chen et al., 2020; and Xie et al., 2021). Willingshofer et al. (2005) used the lithosphere-scale analogue model to show that the strength contrast between the weak zone and surrounding lithosphere controls the scope and the shape of the collision orogen. Sokoutis and Willingshofer, (2011) demonstrated that the geometries and the decoupling degree of the weak zone play an important role in the geometric and topographic evolution of the mountain belts. Chen et al. (2020) using 3D numerical models revealed that the pre-existing weaknesses within the upper plate can alter the deformation propagation and the surface uplift pattern of the orogenic plateau. Xie et al. (2021) demonstrated that the crustal pre-existing weakness in the compressed lithosphere facilitates the local surface uplift at an early time and generates a second local surface uplift in a later time. In contrast, only a few studies investigated how the strong blocks in a weak lithosphere affect the continental deformation and surface topography (England and Houseman, 1985; Cook and Royden, 2008; Dayem et al., 2009; and Calignano et al., 2015). England and Houseman, (1985) used the thin viscous sheet model showed that the deformation is strongly concentrated around the strong crust and high mountain rise along its margins. Cook and Royden, (2008) built up a 3D numerical experiment demonstrating that the existence of a strong lower crust in the foreland slows the plateau propagation speed and develops a steep plateau margin. Dayem et al. (2009) found that the strong block's oblique orientation significantly affects the localization of shearing deformation. Calignano et al. (2015) using analogue models revealed that the depth of the strong domain strongly impacts the deformation patterns and topographic growth at the margins. In summary, these studies mainly concentrate on the deformation, localization, and surface topography induced by the lateral lithospheric strength heterogeneities. However, how the hinterland basins evolved during the India–Asia convergence and how they affected the post-collisional growth of the Tibetan Plateau remain poorly understood.

In this study, we use 3D thermo-mechanical modeling to explore the topographic response of a hinterland basin to continental collision. We focus on the topographic evolution of a strength-varying basin imbedded in an orogenic plateau which is subject to horizontal compression and its influence on the plateau growth. For simplification, we do not include all of the hinterland basins in Tibet in the model. Instead, we set a single basin to explore the basin's topographic evolution to the India–Asia collision and its influence on the growth of the Tibetan Plateau. We first describe the methodology and model setup. This is followed by presenting the simulation results of models in different situations. We then analyze the modeling results and summarize the topographic features and uplift history of basins inside the plateau. Finally, we apply the modeling results to understanding the uplift history of the Lunpola and Hoh Xil basins and discuss the growth pattern of the Tibetan Plateau.

MODELING APPROACH

Three-dimensional numerical simulations are carried out using the thermo-mechanical code I3ELVIS (Gerya, 2010). The code combines the finite difference method and the marker-in-cell technique to solve the continuity, momentum, and energy conservation equations on a staggered Eulerian grid (Gerya, 2010). It uses visco-plastic rheologies to describe the mechanical behavior of the rocks and considers thermo-mechanical properties for different rocks. These characteristics, together with an interior free surface, enable the simulation of a large-scale deformation and topographic evolution associated with continental collision.

Governing Equations

The incompressible continuity equation, which accounts for mass conservation using the Boussineq approximation, is as follows:

$$\frac{\partial v_i}{\partial x_j} = 0, \tag{1}$$

where i and j are spatial directions according to the Einstein summation convention, v_i is the component of the velocity vector, and x_j is the spatial coordinate.

Momentum conservation is governed by the three-dimensional Stokes equations, which are given as follows:

$$\frac{\partial \sigma'_{ij}}{\partial x_j} = \frac{\partial P}{\partial x_i} - g_i \rho (T, P, C, M), \tag{2}$$

where σ'_{ij} is the deviatoric stress tensor, g_i is the gravitational acceleration, and ρ is the density, which depends on temperature (T), pressure (P), composition (C), and melt fraction (M).

The heat conduction equation for the purpose of energy conservation is

$$\begin{aligned} \rho C_P \frac{DT}{Dt} &= \frac{\partial}{\partial x_i}\left(k(T,P)\frac{\partial T}{\partial x_i}\right) + H_r + H_a + H_s + H_L, \\ H_a &= T\alpha \frac{DP}{Dt}, \\ H_S &= \sigma'_{ij}\dot{\varepsilon}_{ij}, \end{aligned} \tag{3}$$

where t is time; D/Dt is the substantive time derivative; C_P is the isobaric heat capacity; k is the thermal conductivity, which is temperature and composition dependent; α is the thermal expansion; $\dot{\varepsilon}_{ij}$ is the strain rate tensor; H_r and H_s are radiogenic and shear heating; and H_a and H_L are adiabatic and latent heat production.

TABLE 1 | Material properties used in the numerical experiments.

Material	ρ_0 (kg/m^3)	K (W/m/K)	$T_{solidus}$ (K)	$T_{liquidus}$ (K)	H_L (kJ/kg)	H_r (μ W/m^3)	Flow Law	A_D (Pa^{n}S)	n	E_a (J)	V_a (J/bar)	sin(φ)	C (Mpa)
UCC	2700 (S) 2400 (M)	K1	TS1	TL1	300	1.5	WQZ	1.97×10^{17}	2.3	1.54×10^{5}	0.0	0.15	1
LCC	12,800 (S) 2500 (M)	K2	TS2	TL2	380	0.5	PL	4.80×10^{22}	3.2	2.38×10^{5}	0.0	0.15	1
Mantle	3300 (S) 2700 (M)	K3	TS3	TL3	400	0.022	DOL	3.98×10^{16}	3.5	5.32×10^{5}	0.8	0.60	1
WZ	3300 (S) 2700 (M)	K3	—	—	400	0.022	WOL	5.01×10^{20}	4.0	4.70×10^{5}	0.8	0.00	1
Ref.s	1,2	3	4,5,6,7,8	4,8	1,2	1	—	—	—	—	—	—	—

UCC, upper continental crust; LCC, lower continental crust; WZ, weak zone; S, solid; M, molten. $K1 = [0.64 + 807/(T+77)]$; $K2 = [1.18 + 474/(T+77)]$; $K3 = [0.73 + 1293/(T+77)]\times (1 + 0.00004P)$. $TS1 = 889 + 17,900/(P+54)+20,200/(P+54)^2$ at $p < 1200$ MPa, or $831 + 0.06P$ at $p > 1200$ MPa; $TL1 = 1262 + 0.09P$; $TS2 = 1327.15 + 0.0906P$; $TL2 = 1423 + 0.105P$. TS3 and TL3 follow the melting model of Katz et al. (2003). WQZ, wet quartzite; PL, Plagioclase (An75); DOL, dry olivine; WOL, Wet Olivine. 1, Turcotte and Schubert (2002); 2, Bittner and Schmeling (1995); 3, Clauser and Huenges (1995); 4, Schmidt and Poli (1998); 5, Hess (1989); 6, Hirschmann (2000); 7, Johannes (1985); 8, Poli and Schmidt (2002).

The deviatoric stress tensor σ'_{ij} is related to the effective viscosity η_{eff} and the strain rate tensor $\dot{\varepsilon}_{ij}$ via

$$\sigma'_{ij} = 2\eta_{eff}\dot{\varepsilon}_{ij}, \tag{4}$$

$$\dot{\varepsilon}_{ij} = \frac{1}{2}\left(\frac{\partial v_i}{\partial x_j} + \frac{\partial v_j}{\partial x_i}\right). \tag{5}$$

Rheology and Partial Melting

The code considers the viscous and plastic rheologies, as well as the thermomechanical properties of different rocks. The lithospheric strength is determined by a combination of ductile and brittle deformation mechanisms at a mountain building time scale. The brittle deformation follows the Drucker–Prager yield criterion, which describes the linear relationship of the material resistance on the total pressure (Ranalli, 1995):

$$\begin{aligned} \sigma_{yield} &= C_0 \cos\left(\varphi_{eff}\right) + P sin\left(\varphi_{eff}\right), \\ sin\left(\varphi_{eff}\right) &= \sin\left(\varphi_{dry}\right)(1-\lambda), \end{aligned} \tag{6}$$

$$\eta_{plastic} = \frac{\sigma_{yield}}{2\dot{\varepsilon}_{\mathrm{II}}}, \tag{7}$$

where σ_{yield} is the yield stress, P is the dynamic pressure, C_0 is the cohesion at $p = 0$, φ is the internal frictional angle (φ_{dry}) (stands for dry rocks), λ is the pore fluid pressure factor and $\dot{\varepsilon}_{\mathrm{II}}$ is the second invariant of the strain rate, and $\eta_{plastic}$ is the viscosity for plastic rheology.

The viscosity for ductile creep takes the form (Beaumont et al., 2004)

$$\begin{aligned} \eta_{ductile} &= B^* \left(\dot{\varepsilon}_{\mathrm{II}}\right)^{\left(\frac{1}{n}-1\right)} \exp\left(\frac{E_a + PV_a}{nRT}\right), \\ B^* &= f * A_D^{(-1/n)}, \end{aligned} \tag{8}$$

where E_a is the activation energy, V_a is the activation volume, n is the stress exponent, R is the gas constant, T is the absolute temperature, A_D is the material constant, and f is a pre-exponential scaling factor. The factor f is applied to scale the effective ductile viscosity calculated from the reference flow laws.

The effective viscosity (η_{eff}) is defined as the minimum value between the plastic and ductile viscosities (Ranalli, 1995):

$$\eta_{eff} = \min\left\{\eta_{plastic}, \eta_{ductile}\right\}. \tag{9}$$

Laboratory-determined flow laws of 'wet quartzite,' 'plagioclase An$_{75}$,' and 'dry olivine' are used for the continental upper crust, lower crust, and asthenospheric mantle, respectively (Ranalli, 1995). Note that a modulated 'plagioclase An$_{75}$' is used for the lower crust of the hinterland basin. The detailed rheological parameters used in this study are shown in **Table 1**. We set a lower cutoff viscosity of 10^{18} Pa s and an upper cutoff viscosity of 10^{26} Pa s for all rocks.

The degree of the partial melting of rocks is calculated by P-T–dependent solidus and liquidus curves (**Table 1**). The volumetric fraction M of the melt is assumed to linearly increase between the solidus and liquidus temperatures at a given pressure (Burg and Gerya, 2005):

$$M = \begin{cases} 0 & when\, T \le T_{solidus} \\ \dfrac{T - T_{solidus}}{T_{liquidus} - T_{solidus}} & when\, T_{solidus} < T < T_{liquidus}\,, \\ 1 & when\, T \ge T_{liquidus} \end{cases} \tag{10}$$

where $T_{solidus}$ and $T_{liquidus}$ are the solidus and liquidus temperatures of the rocks, respectively.

The effective density of partially molten rocks changes with the amount of melt fraction and P-T conditions:

$$\rho_{eff} = \rho_{solid} - M\left(\rho_{solid} - \rho_{molten}\right), \tag{11}$$

$$\rho_{P,T} = \rho_0\left[1 - \alpha(T - T_0)\right]\left[1 + \beta(P - P_0)\right], \tag{12}$$

where ρ_{solid} and ρ_{molten} are the densities of the solid and molten rock, respectively; ρ_0 is the density at $P_0 = 0.1$ MPa and $T_0 = 298$ K; and α $(3 \times 10^{-5}\mathrm{K}^{-1})$ and β $(1 \times 10^{-5}\mathrm{MPa}^{-1})$ are the thermal expansion and compressibility coefficients, respectively.

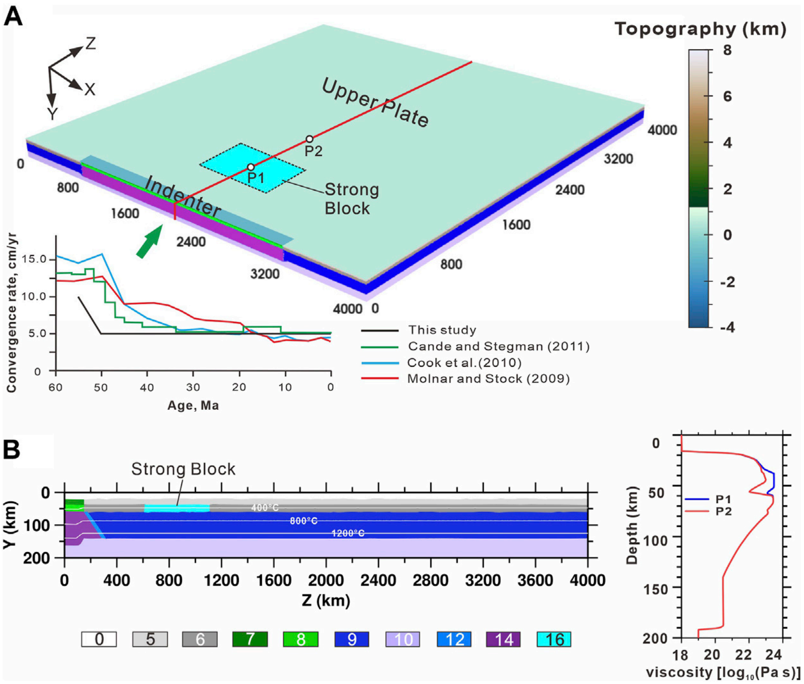

FIGURE 3 | Model setup. **(A)** the 3D model domain (4,000 × 200 × 4,000 km). The colors covering the top of the model indicate the magnitude of the topography as shown in the vertical color bar. The cyan-colored area represents the strong basin. The left bottom chart shows the convergence rate applied in this study and previous estimates (Cande and Stegman; Copley et al., 2010; Molnar and Stock, 2009). **(B)** The composition field along the section x = 2000 km, as denoted by the red line in **Figure 2A**. And viscosity contrast between strong basin and surrounding areas whose localities are shown as P1 and P2 in **(A)**. The blue curve represents the viscosity profile of the strong basin, and the red curve represents the viscosity profile of the surrounding areas. Composition numbers represent different rock types: 0- sticky air; 5- Asian upper crust; 6- Asian lower crust; 7- Indian upper crust; 8- Indian lower crust; 9- Asian lithospheric mantle; 10- asthenosphere; 12- weak zone; 14- Indian lithospheric mantle; and 16- strong lower crust of the basin.

The effects of latent heating generated by melting or crystallization are accounted for by an increased effective heat capacity (C_{pe}) and thermal expansion (α_e) (Burg and Gerya, 2005):

$$C_{pe} = C_p + Q_L\left[(\partial M/\partial T)_{P=constant}\right], \tag{13}$$

$$\alpha_e = \alpha + \rho Q_L\left[(\partial M/\partial T)_{T=constant}\right], \tag{14}$$

where C_p is the heat capacity of the solid rock and Q_L is the latent heat of the melting rock (Burg and Gerya, 2005).

Model Setup

We investigate the topographic response of a hinterland basin imbedded in the upper plate under horizontal compression condition. The computational domain is a 4000 × 200 × 4000 km (in the order of x, y, and z) Cartesian box, and is resolved by 501 × 101×501 grid points with a uniform resolution of 8 × 2 × 8 km (**Figure 3**). There are approximately 200 million Lagrangian markers randomly distributed inside the box, which are used to advect the physical properties. As Chen L. et al. (2017) demonstrated that the lower crust rheology plays an important role in the deformation of the continental lithosphere. We vary the scaling factor f (**Eq. (8)**) of the lower crust flow law to represent the different strengths of the basin inside the plateau. Previous studies indicate that the composition of the continental lower crust ranges from basaltic to andesitic (Hacker et al., 2015) and the basaltic lower crust is ~1 order of a magnitude more viscous than the andesitic lower crust (Shinevar et al., 2015). Therefore, in the reference model, we set a rectangle basin with the scaling factor f = 10, which means that the viscosity of its lower crust is 10 times higher than that of the surrounding regions. The basin is 500 × 800 km in size, and its location is varied in the study.

In the model, back and side walls are set to be free slip. We take 55 Ma as the initial continental collision time (Molnar and Stock, 2009; Hu et al., 2016), which corresponds to the onset of the model. A starting convergence rate of 10 cm/yr is imposed at the central region of the front wall (1000 < X < 3000). It gradually decreases to 5 cm/yr after 5 Ma, and is fixed at 5 cm/yr henceforth. The time-dependent convergence rate used here is generally consistent with the estimates from plate reconstructions or paleomagnetic data (Molnar and Stock, 2009; Copley et al., 2010; and Cande and Stegman, 2011) (**Figure 3A**). It should be noted that when the India–Asia collision began is still controversial. Recently, Xiao et al. (2017) proposed that the terminal India–Asia collision occurred after 14 Ma based on the anatomy of composition and tectonic nature of the Himalayas, which supports a multi-stage collision process between India and Asia. The material influx at the front boundary is limited in the central region to simulate the indentation of the Indian continent, beside which (x = 0–1000 km and x = 3000–4000 km) the free slip condition applies. To keep mass balance within the layer, a constant outflow velocity is applied at the upper boundary, which is determined by V = $(\frac{W'_x}{W_x}\ \frac{t_a}{W_z}) \times V_i$, where t_a is the thickness of the sticky air; W_x and W_z are the model widths in the x and z directions, respectively; and $W^{'}_x$ is the horizontal range on the front wall that the convergence is imposed. At the bottom boundary, an infinity-like external free slip boundary condition is imposed (Burg and Gerya, 2005). In order to simulate the quasi-free surface and hence allow for the topography development, a 20 km-thick "sticky air" layer, which is characterized by a density of 1 kg/m^3 and a viscosity of 10^{19} Pa s, is placed above the rocky model (Schmeling et al., 2008).

The initial temperature first increases linearly from 0°C at the surface to the Moho with 500°C for the indenter and 600°C for the upper plate, and then continues to increase to 1,360°C at the lithosphere base. The thermal gradient gradually changes in the transition zone between the indenter and its surrounding upper plate. The underlying asthenospheric mantle has an initial temperature gradient of 0.5°C/km. The top thermal boundary maintains a constant temperature of 0°C, and all the vertical thermal boundaries are insulating (no horizontal heat flow). At the bottom thermal boundary, an infinity-like external constant temperature condition is applied (Burg and Gerya, 2005). This implies that a constant temperature condition is satisfied at ~200 km below the model base, allowing a spontaneous adjustment of the temperature and heat flux at the bottom of the model.

Taking into account that multiple ocean closure and intercontinental suturing events occurred at the southern Asian continental margin prior to the India–Asia collision (Yin and Harrison, 2000; Kapp and DeCelles, 2019), a relatively weak plate is set to simulate the pre-collisional Asian continental margin. The Asian plate has a 40 km thick continental crust composed of a 17 km thick upper crust and a 23 km thick lower crust, and a 80 km thick lithospheric mantle. The indenter has a 35 km thick continental crust composed of a 15 km thick upper crust and a 20 km thick lower crust, and a 105 km thick lithospheric mantle, to simulate the northern moving Indian craton. In consideration of oceanic subduction before continental indentation, we set a weak zone with a dip angle of 30 in front of the indenter cutting through the entire lithosphere (**Figure 3B**). Our focus is on the topography evolution in the hinterland of the Tibetan Plateau, where the erosion and sedimentation is not as significant as that at the plateau margins. Here, we do not consider the effects of the surface processes on the topographic evolution, but we will discuss the possible limitations for simplification.

MODELING RESULTS

According to sedimentary records (**Figure 1**) and geophysical observations (**Figure 2**), we found that the basins inside the Tibetan Plateau vary in location, size, and strength. We first designed a reference model with a strong basin (f = 10) that is located 500 km north of the convergent boundary and is 500 km in width (**Table 2**). Then, we tested the influence of the basin's distance to the convergent boundary and the basin's width on the topographic response. After that, we investigated the effect of the basin strength on the uplift history and the topographic development of the plateau. In order to test the effect of the initial convergence rate on the modeling results, an additional model with a faster velocity was performed.

Reference Model

Figure 4 shows the topographic evolution of the reference model (model-1 in **Table 2**). The deformation propagates northward quickly and localizes around the borders of the strong basin soon after the convergence starts. From the cross-sections, the existence of the strong basin causes the surrounding crusts to intensely thicken and buckle, resulting in the development of a high topography around the basin. In contrast, the strong basin itself experiences little deformation and underthrusts beneath the surrounding thickened crust. As a consequence, a lowland area develops in the interior of the plateau, characterized by a notable topographic relief. As the convergence continues, the lowland gradually shrinks and migrates northward. The lowland exists in the interior of the plateau until ~46 Myr, after which it merges into the surrounding high plateau.

The lowland area displays significant topographic relief in its interior. At the early stage of the collision, topographic depressions with negative elevation developed along the margins of the strong basin and uplifted belts developed adjacently (**Figure 4**). In terms of the uplift process, the elevation of a lowland does not rise monotonously. During the convergence, the distributed width of the strong lower crust changes slightly. Here, we assume that the length of the basin's lower crust remains unchanged. This allows us to track the elevation variations of the basin's different regions (points A1, B1, C, B2, and A2) with time (**Figure 5**). The surface of the lowland uplifts progressively from the margins to the center of the strong basin. The uplift histories of different regions vary significantly, but all undergo a considerable elevation drop followed by a rapid uplift. It is noteworthy that the lowland center (Point C) maintains a constant elevation for a long period and then experiences a noticeable elevation drop, followed by a quick uplift to the elevation of the surrounding mountains (**Figure 5**).

Effects of a Strong Basin's Position

In this section, we design a group of models (models two to three in **Table 2**) to investigate the impacts of a strong basin's position on the topographic evolution of the plateau. Model-2 and model-3 are identical to the reference model, except that the distances of the strong basin to the convergent boundary are 0 and 1,000 km, respectively, instead of 500 km in the reference model. **Figure 6** shows the topographic evolution of model-2 and model-3. The strong basins in model-2 and model-3 represent the rigid basins located at the south and north Tibetan Plateau, respectively. The plateau growth patterns in model-2 and model-3 are similar to the reference model, with lowlands developing in the interior of strong basins and plateaus forming in the surrounding region.

TABLE 2 | Parameters and results of experiments.

Model	Dis (km)	Width (km)	Strength (f)	Figures	Comments
Model-1	500	500	10	4–5	Reference model
Model-2	0	500	10	6 and 7	Close to the suture
Model-3	1000	500	10	6 and 7	Further north
Model-4	500	250	10	8	Narrow basin
Model-5	500	500	2	9	Less-strong basin
Model-6	500	500	0.5	10	Weak basin
Model-7	500	500	10	11	Faster initial convergence rate

*Note that **Dis** is the distance between the strong basin and the convergent boundary, representing the strong basin's position inside the plateau.*

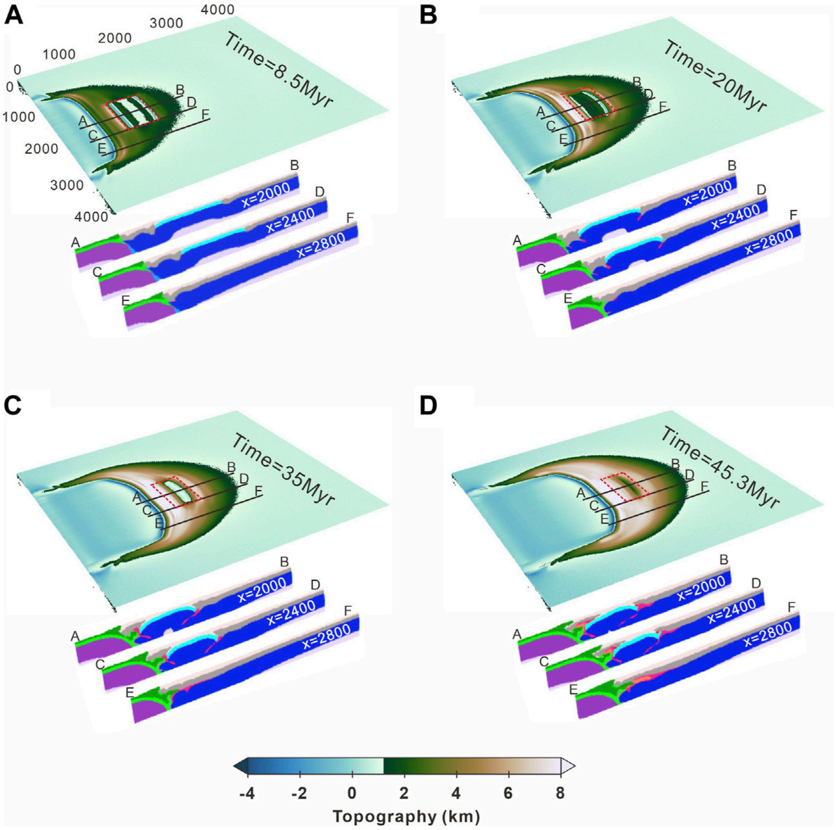

FIGURE 4 | Topographic evolution of the reference model (model-1 in **Table 2**). Snapshots showing the surface topography and slices at **(A)** 8.5 Myr **(B)**20 Myr **(C)** 35.0 Myr, and **(D)** 45.3 Myr. The red dashed rectangles outline the scope of the strong basins' lower crust. The black lines represent the different positions (x = 2,000, 2,400, and 2,800) of the slices.

Differently, the formation of the hinterland basin in model-2 occurs roughly 10 Myr earlier than that in model-3 (**Figure 6**). In addition, the time of the lowland merging into the plateau in model-2 also occurs earlier than that in model-3, at approximately 5 Myr. At 38 Myr of convergence, the lowland in model-2 has shrunk into a small residual basin, whereas the lowland in model-3 is still broad (**Figure 6**).

The topographic features in the interior of the lowland region are significantly different in the model-1, model-2, and model-3 (**Figure 7**). In model-2, the center region of the lowland has been elevated from the early stage and displays a locally positive topography. Specifically, the lowland center (Point C) in model-2 uplifts nearly 2,000 m after 20 Myr of convergence, whereas the height of the lowland center in model-1 remains unchanged until 32 Myr of convergence. In addition, in model-2, the depression formed at the south margin of the lowland is more visible and deeper than that in the reference model. In detail, the subsidence of the south depression in model-2 exceeds 3,000 m, compared to less than 2,000 m in the reference model. By contrast, the lowland in model-3 has similar topographic features to the reference model.

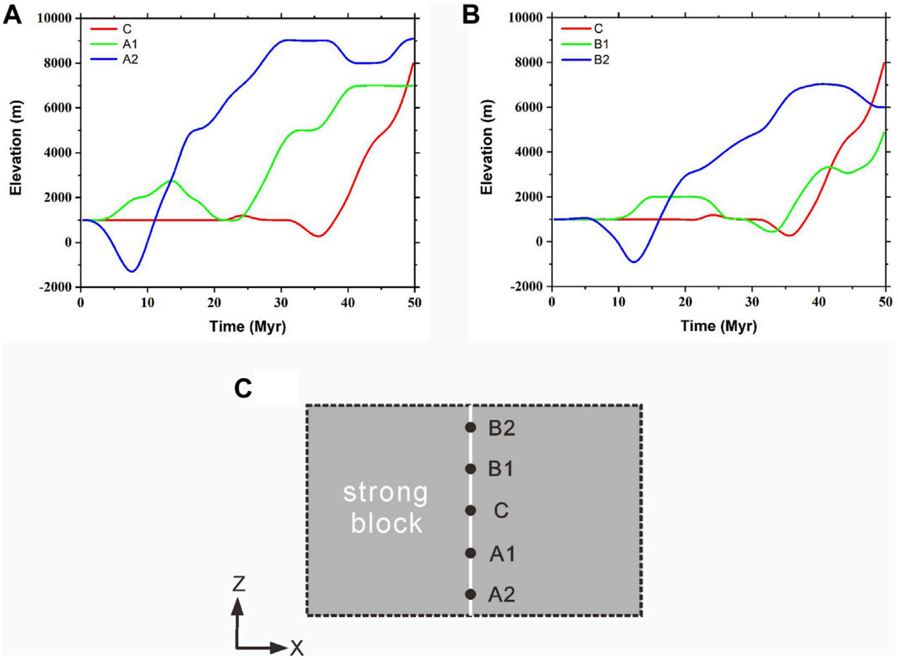

FIGURE 5 | Plots of elevation versus time for different points within the strong basin. In **(A)** and **(B)**, the red curves represent the uplift history at the center point **(C)**. The blue curves represent the uplift history of the marginal points (A2, B2). The green curves represent the uplift history at points A1 and B1 **(C)** Positions of points A1, A2, B1, B2, and C in the interior of the strong basin.

Effects of the Strong Basin's Width

Considering the fact that the hinterland basins inside the Tibetan Plateau vary in size, we designed a model (model-4, **Table 2**), in which the width of the strong basin is half that in the reference model, to investigate the effects of the strong basin's width on the topographic evolution of the plateau. **Figure 8** shows the topographic evolution and the lowland uplift history of model-4. The topographic growth pattern of model-4 is similar to that of the reference model, except that the lowland in model-4 vanishes nearly 10 Myr earlier than that in the reference model (**Figure 8A–D**). As a result, it takes only 40 Myr to form a large uniform plateau in model-4 (**Figure 8E**), instead of >45 Myr in the reference model.

The topographic features and uplift history of the lowland in model-4 are dramatically different from those observed in the reference model. The lowland center region in model-4 was elevated soon after the convergence started, rather than maintaining constant in the reference model (**Figure 8F**). To be specific, after 10 Myr of convergence, the lowland center (Point C) in model-4 had increased to a height of 3,000 m and then kept unchanged until 20 Myr. Then, the height dropped by more than 2,500 m, close to sea level after 30 Myr of convergence (**Figure 8F**). In contrast, the elevation of the lowland center in the reference model was nearly constant during the first 30 Myr. The elevation fall of the lowland center in model-4 exceeds 2,500 m, whereas this value in the reference model is less than 1,000 m.

Effects of the Basin's Strength

In this section, we designed a model with a less strong basin (f = 2, model-5 in **Table 2**) and a weak basin (f = 0.5, model-6 in **Table 2**) to test the effects of the basin's strength on the topographic expressions of the plateau. The model results showed that the less strong basin had similar effects on the topographic growth of the plateau to that produced in the reference model (**Figure 9A–E**). The lowland basin also survives in the interior of the plateau for approximately 30 Myr. However, the basin's uplift history is quite different to that in the reference model. The lowland center does not experience an elevation drop at a late stage, but keeps rising until reaching the height of the surrounding plateau (**Figure 9F**).

The topographic response to a weak basin differs significantly from that of a strong basin. In model-6, the weak basin undergoes intense deformation in the early stage of the collision and uplifts earlier than the surrounding areas, leading to the formation of a topography high in the interior of the upper plate (**Figure 10**). The highland continues to rise and maintains its size until 20 Myr. After that, it propagates southward and northward. After 30 Myr of convergence, the plateau develops a flat-surfaced morphology. This set of models illustrates that the strength of the hinterland basin is a key factor in controlling the uplift pattern of the plateau. A strong hinterland basin favors a later uplift of the plateau's interior, whereas a weak hinterland basin facilitates the formation of a topography high in the early stage of collision.

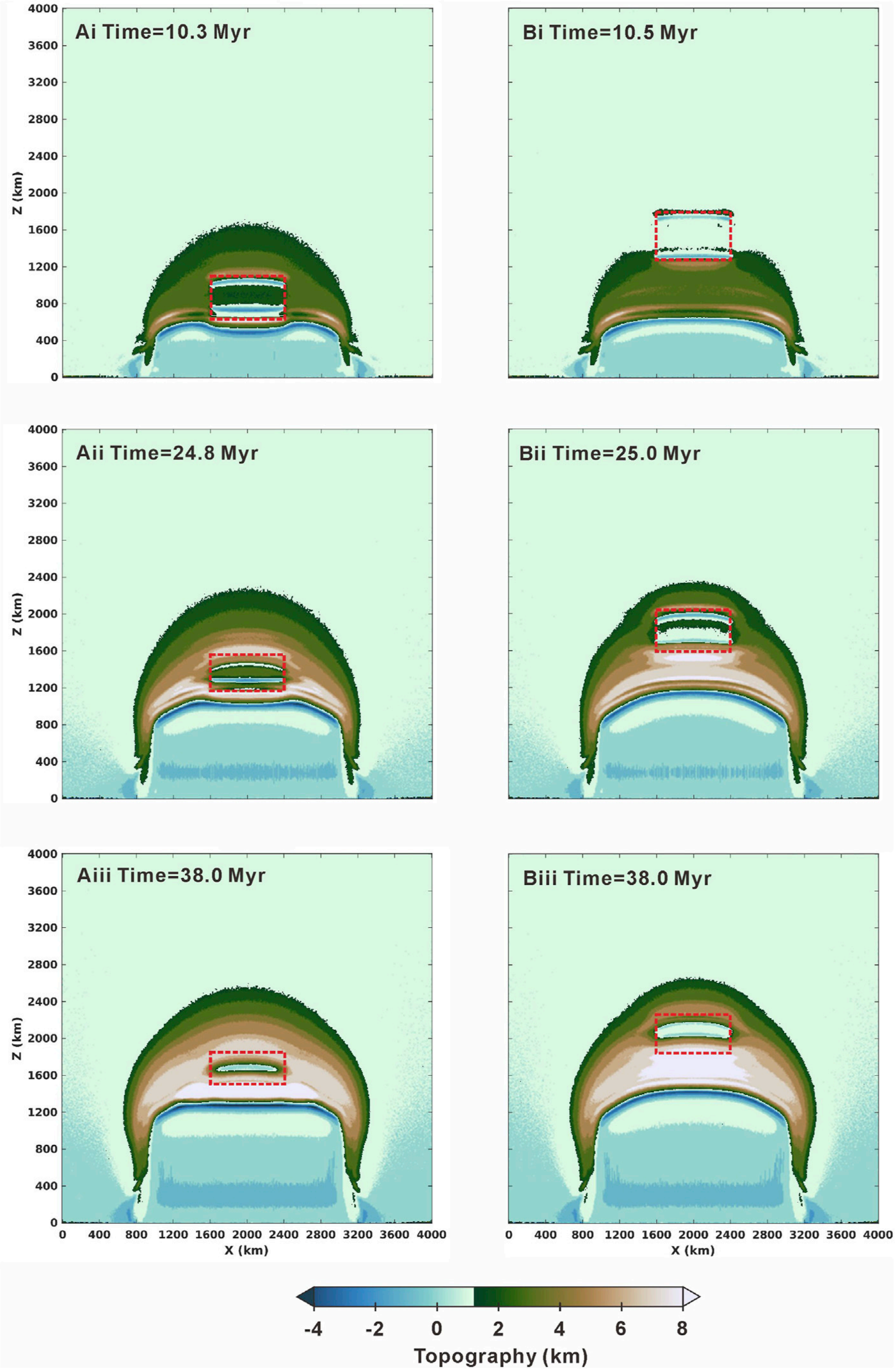

FIGURE 6 | Topographic evolution of the model-2 and model-3 (**Table 2**). Snapshots showing the surface topography of model-2 at **(Ai)** 10.3 Myr **(Aii)** 24.8 Myr, and **(Aiii)** 38.0 Myr. Snapshots showing the surface topography of model-3 at **(Bi)** 10.5 Myr **(Bii)** 25.0 Myr, and **(Biii)** 38.0 Myr. The red dashed rectangles outline the scope of the strong basins.

Effects of the Convergence Rate

Different to the aforementioned models that test the inherent properties of the basin, we perform an additional model (model-7 in **Table 2**) to test the influence of the convergence rate in the topographic response of a hinterland basin. Here, we choose the convergence rate reconstructed by Cande and Stegman (2011), in which the velocity is 13 cm/yr in the first 5 Myr and is then gradually reduces to a fixed value of 5 cm/yr after 15 Myr, keeping the other parameters the same as the reference model. The model results show that the growth pattern of the plateau and the topographic features in the interior of the lowland are similar to that in the reference model (**Figure 11A–E**). The lowland basin develops soon after the initial

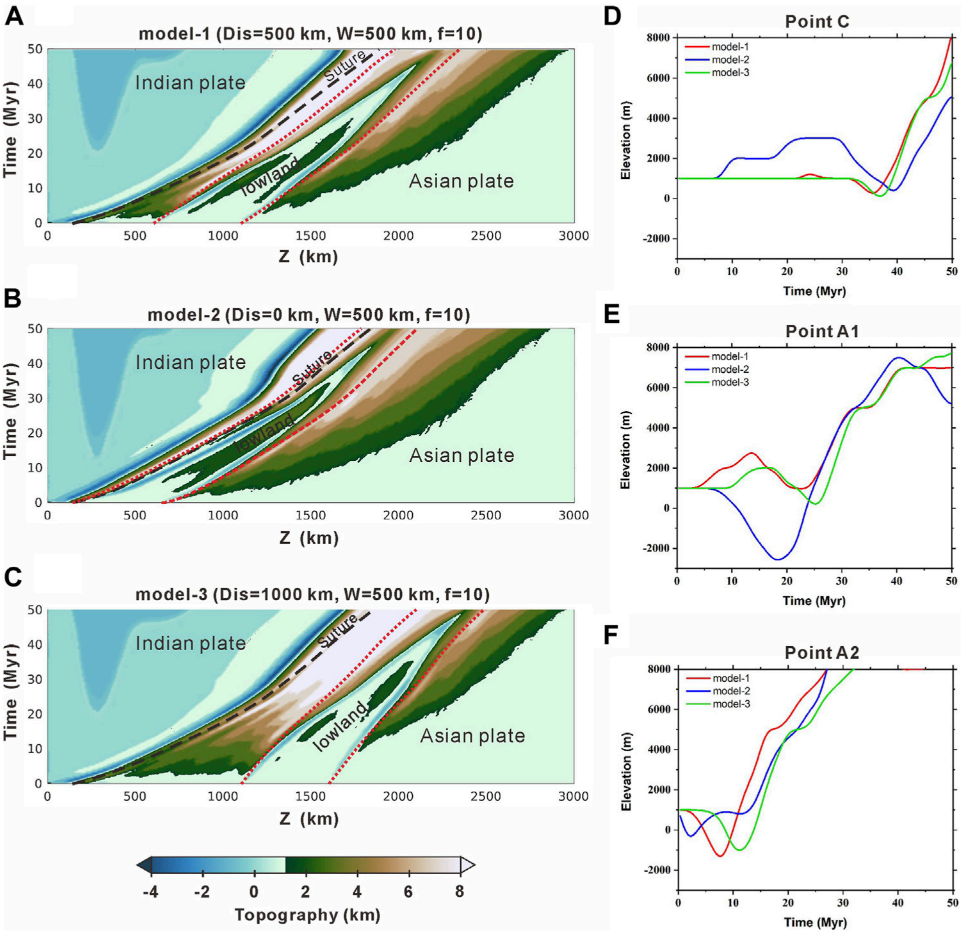

FIGURE 7 | Contrasting the topographic features among mode-1, model-2, and model-3. Topographic evolution with time along section x = 2000 km in **(A)** model-1 **(B)** model-2, and **(C)** model-3. The red dotted curves limiting the region of the strong basins and the black dashed curves represent the sutures. Uplift histories of **(D)** point C **(E)** point A1, and **(F)** point A2 in different models. Red curves show the elevation history of model-1, blue curves show the elevation history of model-2, and green curves show the elevation history of model-3.

collision and survives for ~35 Myrs in the interior of the plateau. The basin center also experiences an evident elevation drop and rapid uplift before merging into the plateau (**Figure 11F**). It is necessary to mention that the lowland basin migrates northward and shrinks more quickly due to the increased convergence amount. Also, it is worth noting that the lowland center was elevated about 1,000 m at an early stage of the basin's lifespan, which is not noticeable in the reference model (**Figure 11F**). By comparing the faster convergence model with the reference model, we can conclude that the initial convergence velocity has little influence on the major characteristics of the basin's topographic evolution and plateau growth.

DISCUSSION

Topographic Evolution of the Hinterland Basins

Our models demonstrate that the strength of the hinterland basin exerts a first-order control over the topographic evolution. The basin with a rigid basement develops into a lowland surrounded by high mountains soon after the initial collision and survives in the interior of the plateau for a long period of time (30–40 Myrs). In contrast, the basin with a soft basement uplifts quickly and reaches its current elevation after 20 Myr of the convergence. This provides an explanation to why some basins inside the Tibetan Plateau have long-term sedimentary records and keep a low elevation until the Late Oligocene, such as the Lunpola and Hoh Xil basins (Wang et al., 2008; Sun et al., 2014; Sun et al., 2015; Wu et al., 2017; and Fang et al., 2020), while some other basins ceased to deposit and have uplifted during the Eocene, such as the Linzhou and Shuanghu basins (Ding et al., 2014; Currie et al., 2016). Depending on the locations and the widths, the rigid hinterland basins display quite different lifetimes in the interior of the plateau. The time required for the formation of a lowland basin in the north Tibetan Plateau (model-3, Dis = 1000 km) delays by 10 Myr in comparison to the basin at central Tibet (model-1, Dis = 500 km). The time of merging into the plateau for the narrow basin (model-4, width = 250 km)

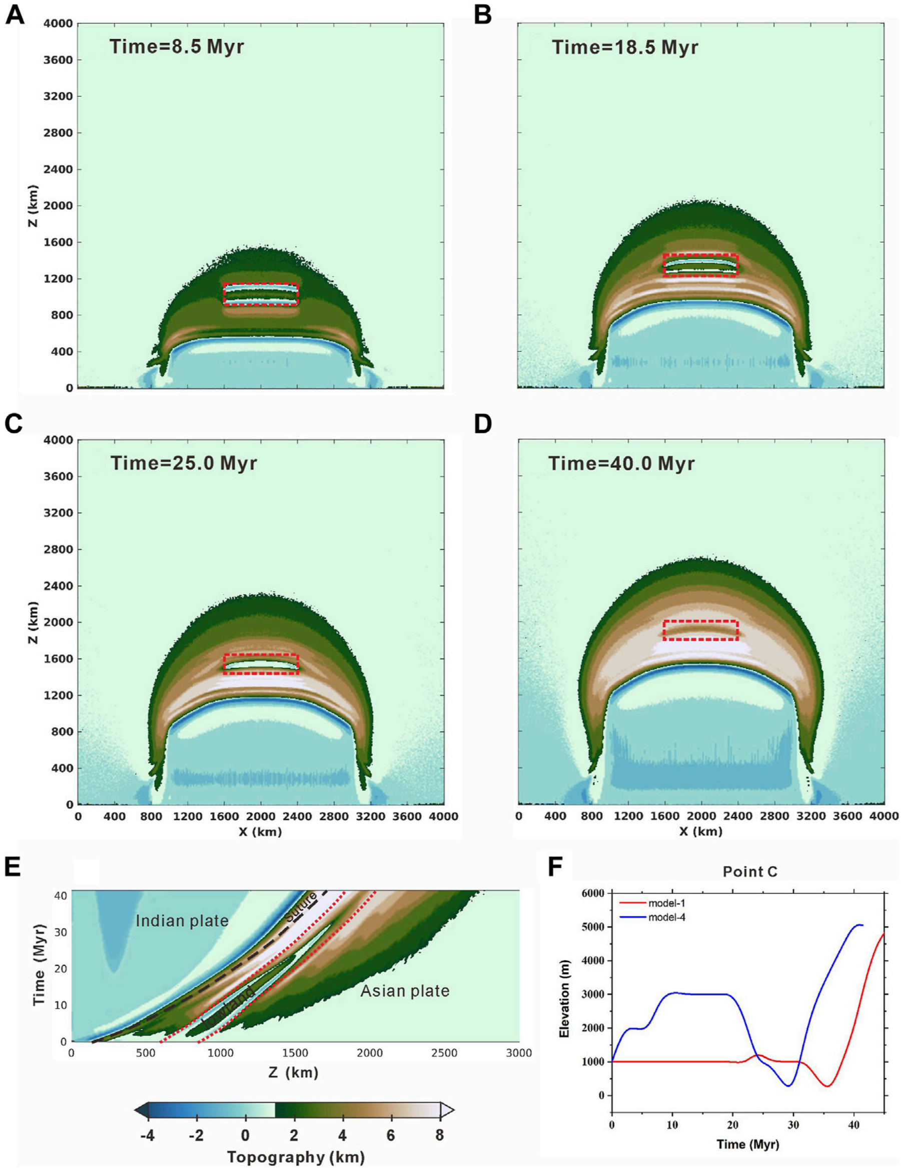

FIGURE 8 | Topographic evolution of the model-4 (**Table 2**). Snapshots showing the surface topography at **(A)** 8.5 Myr **(B)** 18.5 Myr **(C)** 25.0 Myr, and **(D)** 40.0 Myr **(E)** exhibit the topographic evolution with time along section x = 2,000 km **(F)** showing the difference of the uplift history of center point C between the reference model (red curve) and model-4 (blue curve).

is approximately 10 Myrs earlier than a vast basin (model-1, width = 500 km).

The hinterland basins also exhibit a variety of topographic features and uplift histories, depending on their locations, widths, and strengths. When the strong basin is close to the collisional zone (model-2) or is narrow (model-4), the central region rises at the early stage and then experiences an evident elevation drop at the late stage (**Figure 12**). However, when located further north (e.g., model-3), the lowland basin displays low-relief topography in the interior and the elevation keeps unchanged for a long period of time (**Figure 7D**). The topographic feature of the basin is closely related to the deep tectonic structure. Depressions and uplifted belts formed owing to the underthrusting and bending of the strong lower crust. Therefore, due to a weak surface topographic response to the bending, the less strong basin (model-5, f = 2) displays a less topographic relief in the interior (**Figure 12**). In model-2 and mode-4, the uplifted belts occur in the lowland center owing to the more intense bending and the narrowness of the strong basin, and the elevation drop is actually the result of the marginal depressions merging as the basin gradually shrinks (**Figure 12**).

Implications for the Uplift Histories of the Lunpola and Hoh Xil Basins

The Lunpola Basin is a narrow basin and is located in the northern Lhasa terrane (**Figure 1**). Geophysical observation

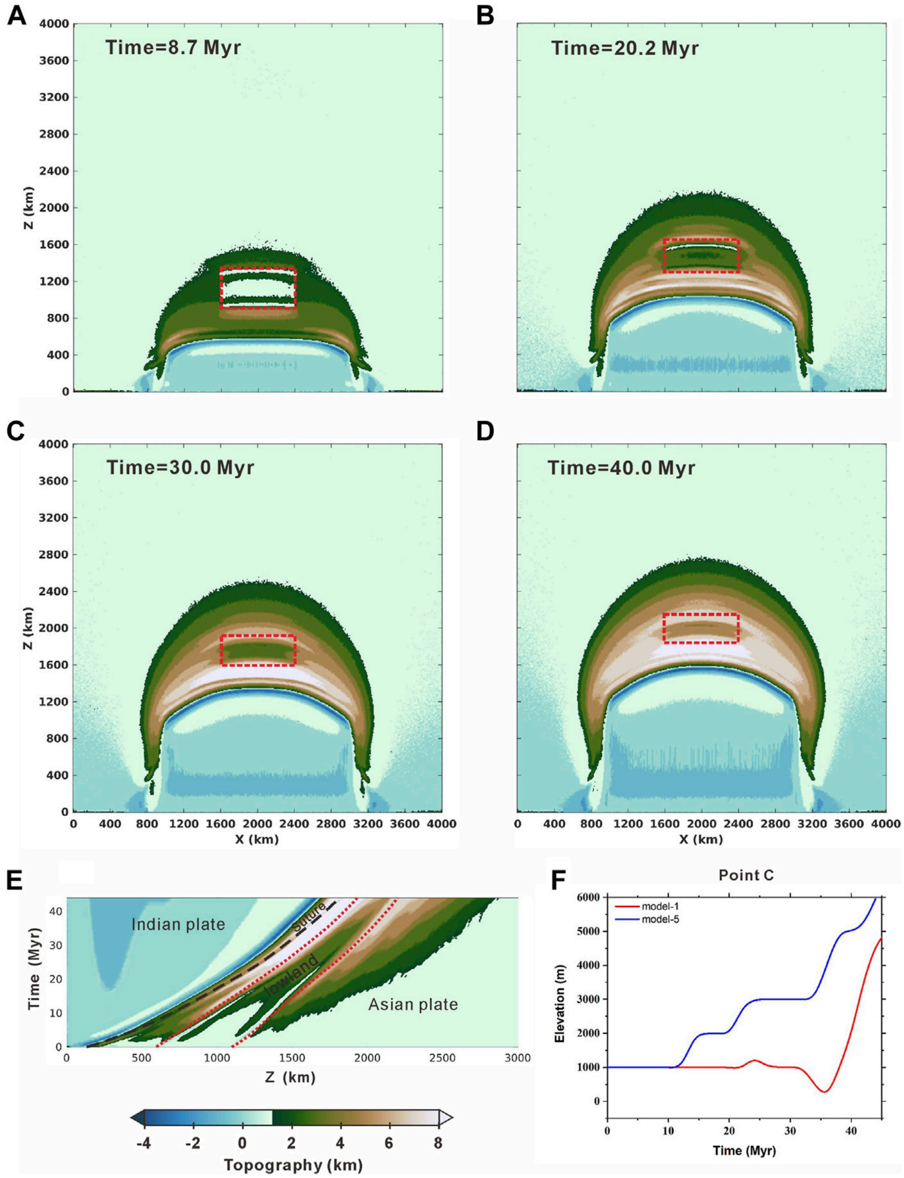

FIGURE 9 | Topographic evolution of the model-5 (**Table 2**). Snapshots showing the surface topography at **(A)**8.7 Myr **(B)** 20.2 Myr **(C)** 30.0 Myr, and **(D)**40.0 Myr **(E)** display the topographic evolution with time along section x = 2,000 km **(F)** showing the difference of uplift history of center point C between the reference model (red line) and model-5.

and geochemical data show that it is characterized by fast velocity anomalies in the crust (Yang et al., 2012) and negative Hf isotopic values of felsic igneous rocks (Hou et al., 2015; Hou et al., 2020) (**Figure 2**), which indicate that the Luopala Basin has a strong and old basement. Therefore, the uplift history of the Lunpola Basin can be compared with that of the lowland in model-4, in which the strong basin is 250 km in width and located 500 km north of the convergent boundary. A topographic analysis of model-4 shows that the basin was elevated to a medium elevation after 10 Myr of convergence and experienced a noticeable elevation drop of ~3,000 m from 20 to 30 Myr of convergence, then followed by a rapid uplift (**Figure 8F**). We compiled the paleoelevation data published over the past 2 decades in the Lunpola Basin, including oxygen isotope, hydrogen isotope, and paleontology (Rowley and Currie, 2006; Polissar et al., 2009; Sun et al., 2014; Jia et al., 2015; Wu et al., 2017; Farnsworth et al., 2018; and Fang et al., 2020) (**Figure 13A**). The estimates based on isotope data tend to predict a higher elevation, whereas fossil-based data tend to reflect lowland elevations (Spicer et al., 2021). Fossil-based data indicate that the Lunpola Basin was elevated to a medium elevation during the Eocene (50–38 Ma) and suffered an evident elevation drop during the Oligocene (38–25 Ma), and then followed by a rapid uplift in the Early Miocene (23 Ma) (**Figure 11**). The elevation fluctuation

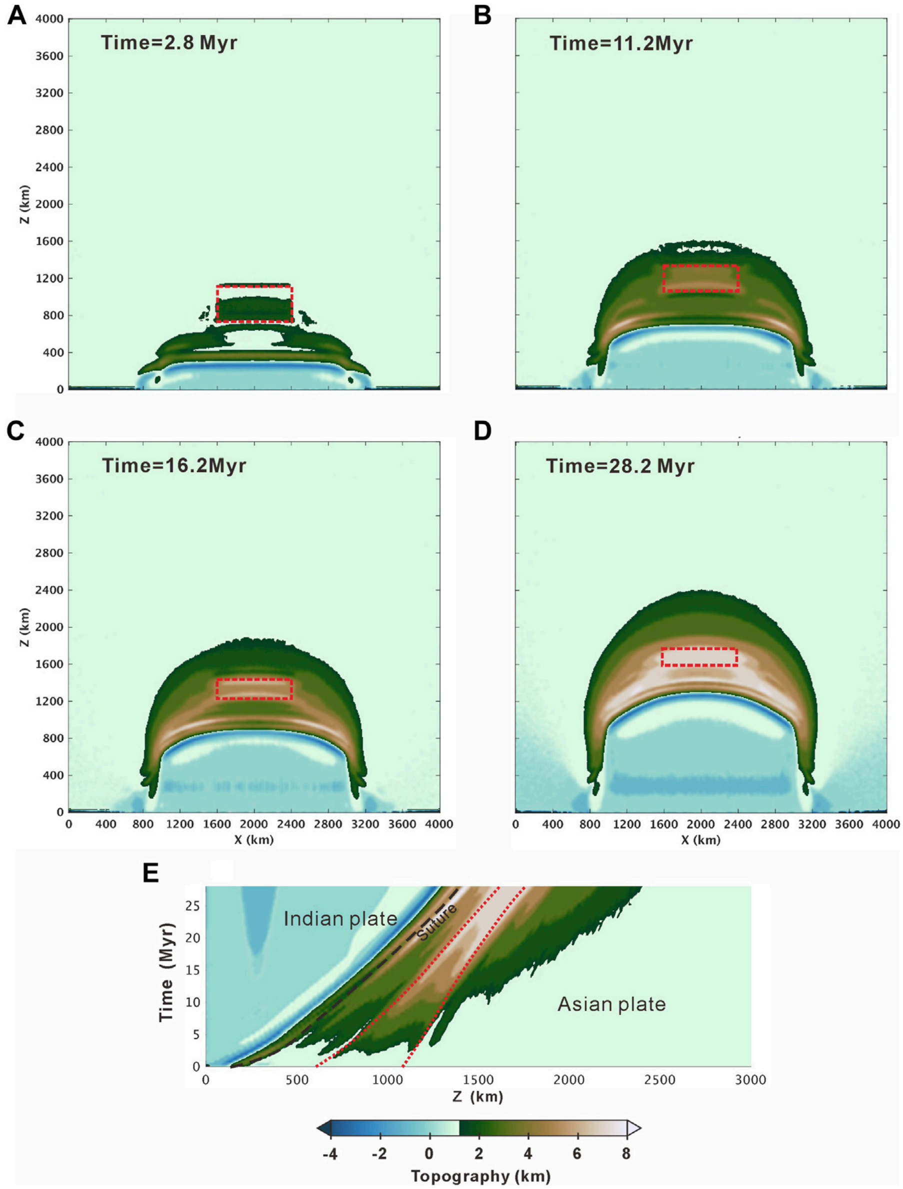

FIGURE 10 | Topographic evolution of the model-6 (**Table 2**). Snapshots showing the surface topography at **(A)**2.8 Myr **(B)** 11.2 Myr **(C)** 16.2 Myr, and **(D)** 28.2 Myr **(E)** display the topographic evolution with time along section x = 2,000 km.

of the Lunpola Basin, as revealed by fossils, is in agreement with the uplift history of the lowland center predicted by our model-4 (**Figure 13A**). In addition, the isotopic data also suggest that the Lunpola Basin had a high elevation during the Eocene and suffered a rapid uplift during the Early Miocene. Therefore, the Lunpola Basin was likely to be elevated to 2,500–3,000 m in the Middle Eocene and suffered an evident elevation fall of ~2,000 m during the Oligocene, and then experienced a rapid uplift to achieve its present height in the Early Miocene.

The Hoh Xil Basin is a large basin far from the Indus–Yarlung suture zone (IYS). Weak crustal deformation (Staisch et al., 2016) and the negative Hf isotopic feature of felsic igneous rocks (Hou et al., 2020) imply a mechanically strong basement beneath the Hoh Xil Basin. Therefore, the topographic evolution of the Hoh Xil Basin can be compared with the lowland in model-3, where the strong basin is wide and far from the collisional zone. Our results show that the lowland center in model-3 keeps a constant elevation for ~30 Myr and then experiences a slight elevation drop before the rapid uplift (**Figure 7D**). In the Hoh Xil Basin, a compilation of paleoelevation data indicates that the elevation did not change significantly throughout the Eocene (Cyr et al., 2005; Polissar et al., 2009; Miao et al., 2016; and Song et al., 2021) (**Figure 13B**). This is in accordance with the long-term unchanged elevation of the lowland center in model-3. As expected by the uplift histories of two sub-basins within the Hoh Xil Basin (Liu et al., 2016) (**Figure 13B**), the Hoh Xil Basin

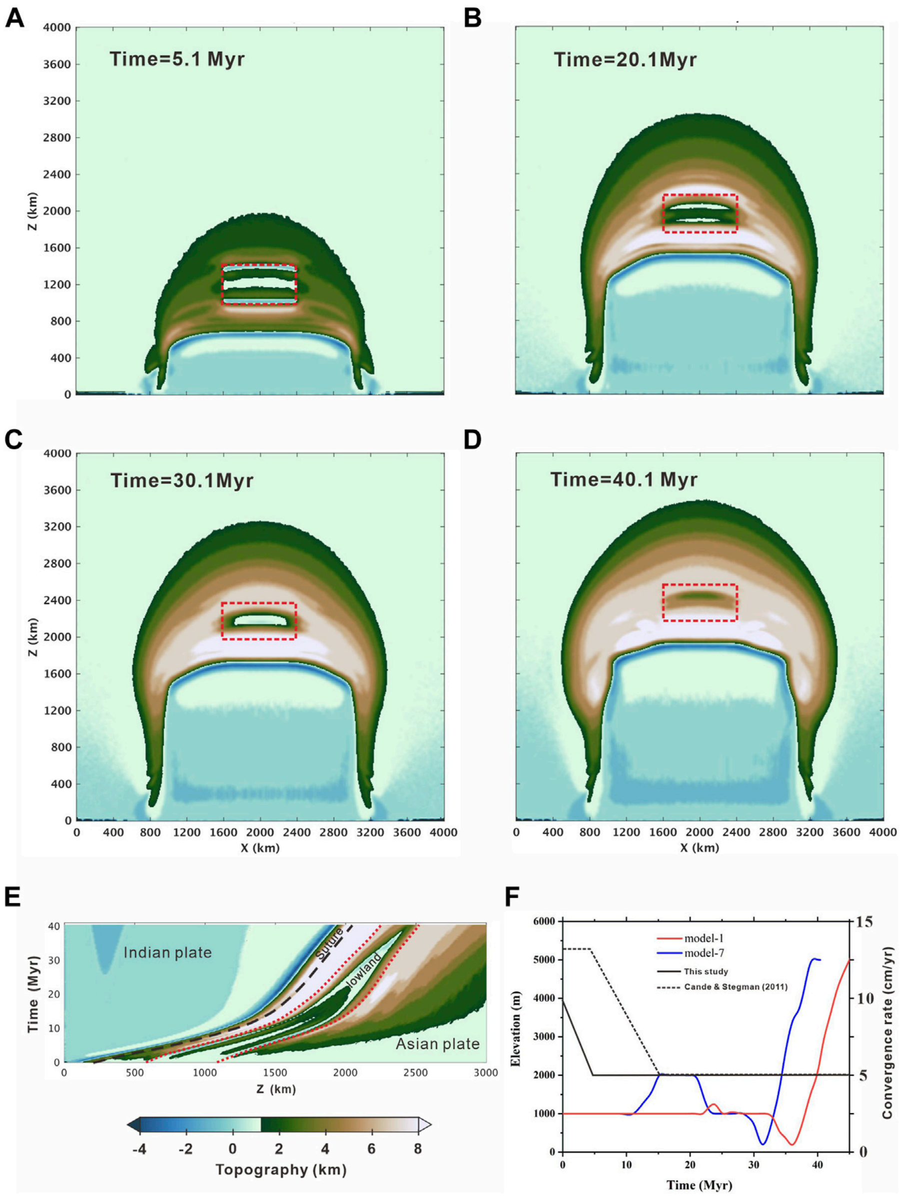

FIGURE 11 | Topographic evolution of the model-7 (**Table 2**). Snapshots showing the surface topography at **(A)** 5.1 Myr **(B)**20.1 Myr **(C)** 30.1 Myr, and **(D)** 40.1 Myr **(E)** display the topographic evolution with time along section x = 2,000 km. **(F)** showing the difference of uplift history of center point C between the reference model (red line) and model-7 (blue line).

experienced a slight elevation drop during Oligocene followed by a fast uplift in the Early Miocene. This is consistent with the late-stage elevation variation of the lowland center in model-3.

Cenozoic Uplift Process of the Tibetan Plateau

How the Tibetan Plateau uplifted is a subject of intense debate. Several hypotheses for the growth pattern of the Tibetan Plateau have been proposed, including: 1) northward stepwise uplift model (Tapponnier et al., 2001; Mulch and Chamberlain, 2006), 2) a central proto-Tibetan Plateau model (Wang et al., 2008; Wang et al., 2014), and 3) the "Central Tibetan Valley" model (Deng and Ding, 2015; Farnsworth et al., 2018; and Xiong et al., 2022). According to the stepwise uplift model, the Tibetan Plateau rises gradually from the south to the north, with the Lhasa rising by Eocene, the Qiangtang rising during the Oligocene, the Songpan–Ganzi rising during the Miocene, and the Qilian rising during the Pliocene to Quaternary (Mulch and Chamberlain, 2006). The proto-Tibetan Plateau model argues that the Lhasa and southern Qiangtang terranes were elevated into a central Tibetan highland during the Middle Eocene, and then the highland expanded to the Himalayas during the mid-Miocene, and to the Hoh Xil Basin during the Early Miocene (Wang et al.,

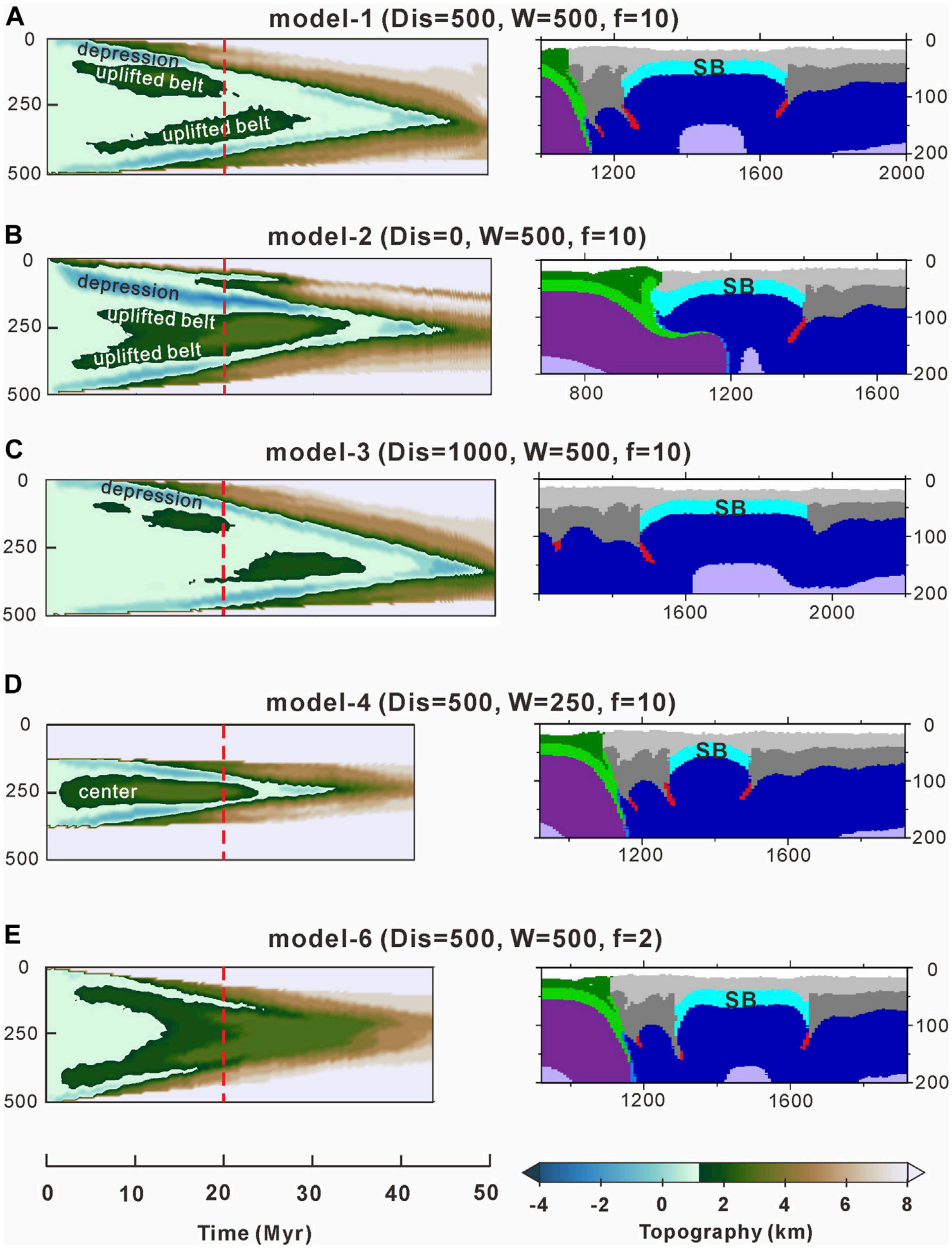

FIGURE 12 | Topographic features of the lowlands and deep structures in **(A)** model-1 **(B)** model-2 **(C)** model-3 **(D)** model-4, and **(E)** model-6. The left column exhibits the detailed topographic features of the lowland in different models. Red dashed lines highlight the time snapshot of 20 Myr. The right column shows the deep structures along section x = 2,000 km at the snapshot of 20 Myr. SB represents the strong basement of the basins. Depressions formed at the edges and uplifted belts formed adjacently due to bending of the strong lower crust. Note that a vertical exaggeration of two is used in the cross-sections of the right column.

2008; Wang et al., 2014). However, the "Central Tibetan Valley" model supports a lowland central Tibetan along the Bangong–Nujiang suture zone (BNS) sandwiched between the Gangdese and the Tanggula mountains (or central watershed) during the Early Eocene to the Late Oligocene, and then uplifted in the early Miocene (Farnsworth et al., 2018; Fang et al., 2020; Xiong et al., 2022).

Based on the predicted uplift histories of the Lunpola and Hoh Xil basins in this study and previous paleoelevation data, we propose a revised Cenozoic uplift model for the Tibetan Plateau south of the Kunlun Mountain (**Figure 14**). We subdivide the Tibetan Plateau's growth into four stages according to the surface topographic evolution. At the first stage (50–38 Ma), the Tibetan Plateau is characterized by two highlands separated by three lowlands (**Figure 14A**). Paleoelevation data from the Linzhou and Namling–Qiyug basins suggest that a high Andean-type Gangdese mountain range (~5000 m) developed in the southern Lhasa during the Early Eocene (Ding et al., 2014;

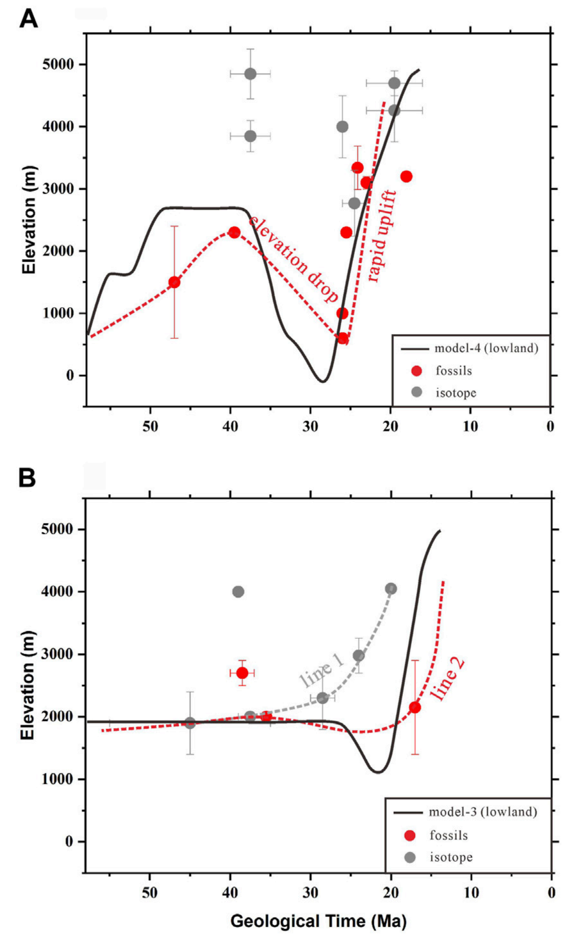

FIGURE 13 | Compilation of paleolevations data of the Lunpola Basin **(A)** Red circles are the paleoelevations of the Lunpola Basin obtained from fossils of plant, animal, and pollen (Deng et al., 2011; Sun et al., 2014; Wu et al., 2017; Liu et al., 2019; Farnsworth et al., 2018, Su et al., 2020; Fang et al., 2020; and Xie et al., 2021). Gray circles represent the paleoelevations based on the oxygen isotope (Polissar et al., 2009; Jia et al., 2015) and hydrogen isotope (Rowley and Currie, 2006; Fang et al., 2020). The red dashed curve draws the expected uplift history of the Lunpola Basin based on fossils. The black curve displays the uplift history of the lowland center in model-4 **(B)** Red circles are the paleoelevations of the Hoh Xil Basin obtained from fossils (Sun et al., 2015; Miao et al., 2016; Song et al., 2021). Gray circles represent the paleoelevations based on the oxygen isotope (Cyr et al., 2005; Quade et al., 2011; Li et al., 2020) and the hydrogen isotope (Polissar et al., 2009). Dashed curves depict the expected uplift histories of the two sub-basins in the Hoh Xil Basin based on paleoelevations. The black curve shows the tendency of the uplift history of the lowland center in model-3.

Ingalls et al., 2017). Also, the central watershed highlands were contemporaneously elevated to 4,000–5,000 m in central Qiangtang, according to the paleoelevation data of the Heihuling and Gonjo basins (Xu et al., 2013; Xiong et al., 2020). The fossil evidence indicates the existence of a lowland with an elevation of <2,000 m south of the Gangdese Mountains (Ding et al., 2017), a lowland region with an elevation of 2,500–3,000 m between the Gangdese and the central watershed highlands (Wei et al., 2016; Fang et al., 2020; Su et al., 2020), and a broad lowland region with an elevation of ~2,000 m north of the central watershed highlands during the Eocene (Miao et al., 2016; Song et al., 2021).

At the second stage (35–25 Ma), the central Tibetan lowland along the Bangong–Nujiang suture (BNS) experienced an elevation drop of ~2,000 m, forming a central Tibetan deep valley (**Figure 14B**). Plant and foraminifera fossils indicate that the elevation of the Lunpola, Nima, and Gerze basins were no more than 1,000 m during the Late Oligocene (Wei et al., 2016; Wu et al., 2017). Sedimentary records show a noticeable facie transition from lacustrine mudstones to fluvial and alluvial conglomerates and a threefold increase of the sedimentary rate in the Lunpola Basin during the Late Oligocene (Fang et al., 2020). This consolidates our prediction that the central Tibetan lowland suffered an evident subsidence during the Oligocene. However, paleoelevation data reveal that the lowland south of the Gangdese Mountains and the lowland north of the central watershed mountains remained at an elevation of ~2,000 m at this stage (Ding et al., 2017; Dai et al., 2019). The elevation drop of the central Tibetan lowland occurred soon after the reduction of the India–Asia convergence rate (Molnar and Stock, 2009; Copley et al., 2010; and Cande and Stegman, 2011). Thus, we suggest that the slow convergence rate may result in a relaxation of the lithospheric compression bending, thereby sinking the surface.

At the third stage (25–18 Ma), the central Tibetan valley suffered a rapid uplift and merged into the plateau (**Figure 14C**). Fossil evidences from plants, mammals, and fish indicate that the ecosystem of the Lunpola and Nima basins experienced a significant turnover from a warm tropical environment in the Late Oligocene to a cool climate since the Early Miocene (Deng et al., 2019; Deng et al., 2021), whereas the lowland south of the Gangdese Mountains and the lowland north of the central watershed mountains remained at a low elevation according to carbon isotopic and palaeobotanical evidences (Wang et al., 2006; Sun et al., 2015; and Li et al., 2020). Seismic evidence suggests the convective removal of thickened lithosphere under the central Tibet during the Early Miocene (Chen M. et al., 2017), implying that the lithospheric delamination and mantle upwelling may have played important roles in the uplifting of the central Tibetan valley (Xiong et al., 2022). A recent study reveals an Early Miocene transition from a cold and strong middle-lower crust to a hot and weak middle-lower crust in the Qiangtang Block (Zhang et al., 2022). This supports that the Early Miocene uplift of the central Tibetan valley was driven by the crustal flow from surrounding highlands. Thus, we suggest that the lateral crustal flow and the vertical lithospheric delamination and mantle upwelling are the primary drivers of the central Tibetan valley's rapid uplift.

At the last stage (18–0 Ma), the lowland south of the Gangdese Mountains and the lowland north of the central watershed mountains were uplifted and merged into the plateau since the Middle Miocene, forming the topography similar to the present Tibetan Plateau (**Figure 14D**). Oxygen isotopic data from the Gyirong Basin and the Thakkhola graben indicate that the Tethyan Himalaya was elevated to its current elevation by the Middle Miocene (Garzione et al., 2000; Rowley et al., 2001). Oxygen and hydrogen isotopes-based paleoelevations show that

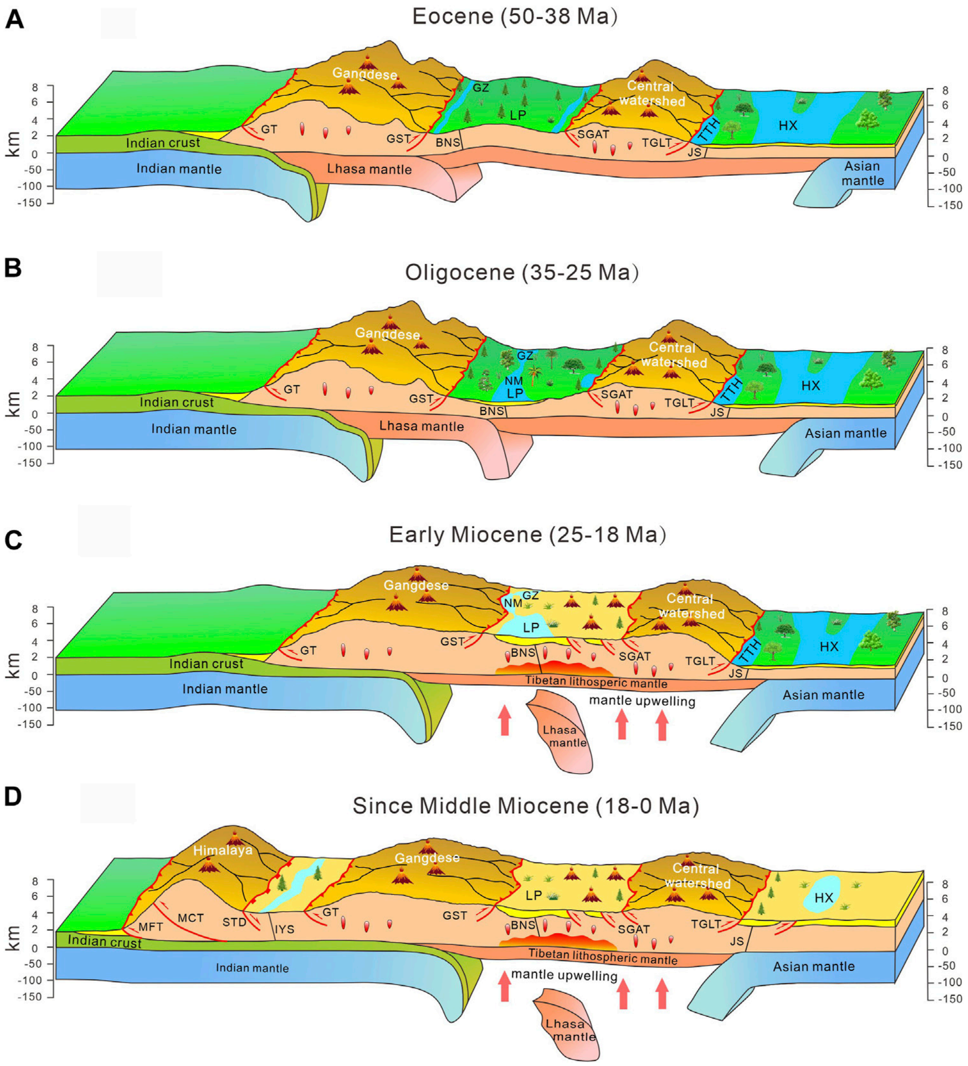

FIGURE 14 | Schematic surface uplift of the Tibetan Plateau, which can be subdivided into four stages: **(A)** two highlands, the Gangdese and central watershed mountains, were separated by three lowlands **(B)** the central Tibetan lowland along BNS experienced an elevation drop of ~2,000 m during the Oligocene **(C)** the central Tibetan lowland suffered an rapid uplift and merged into the Tibetan Plateau during the Early Miocene **(D)** the south and north lowlands were elevated and merged into the Tibetan Plateau since the Middle Miocene, forming a flat-surfaced topography similar to the modern Tibetan Plateau. GT, Gangdese Thrust; GST, Gaize-Siling Tso Thrust; SGAT, Shiquanhe-Gaize-Amdo Thrust; TGLT, Tanggula Thrust; MFT, Main Frontal Thrust; MCT, Main Central Thrust; and STD, South Tibetan Detachment.

the Hoh Xil Basin was elevated to a height of >4,000 m after the Early Miocene (Polissar et al., 2009). The small degree of shortening and the Late Oligocene cessation of deformation in the Hoh Xil Basin imply that the north Tibetan lowland may have been uplifted as a result of the crustal flow and lithospheric removal (Staisch et al., 2016; Li et al., 2017).

MODEL LIMITATIONS

The numerical models conducted in this study are incomplete in that they do not consider the surface processes, such as erosion and sedimentation. There have been a number of investigations on the coupling and feedback between tectonics and erosion for orogens (Willett, 1999; Whipple and Meade, 2004; Graveleau et al., 2012). The climate-driven erosion generally leads to a narrowing of the orogenic belts, a temporary increase in sedimentary deposition, and a persistent increase in the rate of rock exhumation (Marques and Cobbold, 2002; Persson et al., 2004; Whipple and Meade, 2004; and Cruz et al., 2010). In our simulations, ignoring the erosion process results in an abnormally high elevation of the plateau. Neglecting the sedimentation process enlarges the topographic relief between the lowland basins and their surrounding topographic highs. However, the erosion and sedimentation processes are not significant in the interior of the Tibetan Plateau, exerting limited impact on the topographic evolution of the hinterland basins.

For simplification, we set a single basin in the upper plate in the model. Yet, it is noteworthy that there are a number of basins inside Tibet before merging into the Tibetan Plateau. These basins may have an interactive impact on each other's topographic evolution. We will conduct further exploration on the basins' interaction effects in the future.

Because of the large amount of computation in the 3D numerical simulation, we did not test the influences of plastic softening and high radiogenic crust on the basin's topographic response to the continental collision. The plastic softening promotes the strain localization (Huismans and Beaumont, 2011). Chen et al. (2019) demonstrated that radioactive heating plays an important role in crustal melting, which promotes plateau expansion and crustal flow.

Despite the aforementioned simplifications, the presented 3D models can depict the first-order topographic response of the hinterland basins to the India–Asia collision.

CONCLUSION

In this article, we use 3D thermo-mechanical models to investigate the topographic response of the strong hinterland basin imbedded in a relatively weak continental lithosphere under the horizontal compression condition. The conclusions are as follows:

(1) Deformation strongly localizes around the margins of the strong basin soon after the convergence begins, while the strong basin experiences little deformation, resulting in a lowland area surrounded by topographic highs in the interior of the plateau. The central lowland progressively shrinks as the convergence continues, and eventually merges into the high plateau after ~40–50 Myr of convergence.

(2) The central lowland does not rise monotonously during plateau growth, but experiences an unexpected elevation drop after ~20–30 Myr of convergence, followed by a rapid uplift to reach the height of the surrounding plateau.

(3) A strong hinterland basin uplifts later than its surrounding regions, whereas a weak hinterland basin uplifts earlier. Our model results provide a mechanism to link the spatial distribution of hinterland basins and a diachronous uplift of the Tibetan Plateau.

(4) Based on the modeling results and paleoelevation data, we propose a revised model for the Tibetan Plateau's uplift. During the Eocene (50–38 Ma), the Gangdese Mountains and central watershed mountains have developed and isolated three lowlands. The central lowland along the BNS experienced an elevation drop of ~2,000 m during the Oligocene (35-25 Ma), then suffered a rapid uplift and merged into the Tibetan Plateau in the Early Miocene (25–18 Ma). The south and north lowlands were uplifted and merged into the plateau since the Middle Miocene (18–0 Ma).

DATA AVAILABILITY STATEMENT

The geophysical and Hf isotopic values data are available from Yang et al. (2012) and Hou et al. (2015), respectively. The paleoelevation data of the Lunpola and Hoh Xil Basin are available from Liu et al. (2016).

AUTHOR CONTRIBUTIONS

PZ conducted the work, analyzed the result data, and drafted the manuscript. LC made substantial contributions to the design of the work and revised the manuscript. WX made substantial contributions in guidance and discussion of the work and helped in revising the content. J'Z helped in analyzing the data of this work and revised the manuscript.

FUNDING

The National Natural Science of Foundation (41888101, 91955311, and 41974110) provided funds for calculating the numerical models on super computers. The Strategic Priority Research Program (B) of Chinese Academy of Sciences (XDB18030103) provided funds for participating in relatively academic meetings.

ACKNOWLEDGMENTS

The authors sincerely thank Taras Gerya for providing the I3ELVIS code. They are grateful to Xi Xu, Zhiyong Yan, Renxian Xie, Jiaxuan Tang, Shunzhi Li, Xiaona Cui, and Xiao Xiang for discussions. **Figures 3**, **4** were generated with the open-source software ParaView (http://www.paraview.org), and the rest of the figures were generated with the Generic Mapping Tools (GMT, https://www.generic-mapping-tools.org). All the models were run on the Beijing Super Cloud Computing Center, Beijing, China (http://www.blsc.cn/), on the TianHe-1A Cluster at the National Supercomputer Center, Tianjin, China, and on the Supercomputing Laboratory, IGGCAS, Beijing, China.

REFERENCES

Beaumont, C., Jamieson, R. A., Nguyen, M. H., and Medvedev, S. (2004). Crustal Channel Flows: 1. Numerical Models with Applications to the Tectonics of the Himalayan-Tibetan Orogen. *J. Geophys. Res.* 109 (B6), B06406. doi:10.1029/2003jb002809

Bischoff, S., and Flesch, L. (2019). Impact of Lithospheric Strength Distribution on India-Eurasia Deformation from 3-D Geodynamic Models. *J. Geophys. Res. Solid Earth.* 124 (1), 1084–1105. doi:10.1029/2018jb015704

Bittner, D., and Schmeling, H. (1995). Numerical Modelling of Melting Processes and Induced Diapirism in the Lower Crust. *Geophys. J. Int.* 123 (1), 59–70. doi:10.1111/j.1365-246x.1995.tb06661.x

Burg, J.-P., and Gerya, T. V. (2005). The Role of Viscous Heating in Barrovian Metamorphism of Collisional Orogens: Thermomechanical Models and Application to the Lepontine Dome in the Central Alps. *J. Metamorph. Geol.* 23 (2), 75–95. doi:10.1111/j.1525-1314.2005.00563.x

Calignano, E., Sokoutis, D., Willingshofer, E., Gueydan, F., and Cloetingh, S. (2015). Strain Localization at the Margins of strong Lithospheric Domains: Insights from Analog Models. *Tectonics.* 34 (3), 396–412. doi:10.1002/2014tc003756

Cande, S. C., and Stegman, D. R. (2011). Indian and African Plate Motions Driven by the Push Force of the Réunion Plume Head. *Nature.* 475 (7354), 47–52. doi:10.1038/nature10174

Chen, L., Capitanio, F. A., Liu, L., and Gerya, T. V. (2017). Crustal Rheology Controls on the Tibetan Plateau Formation during India-Asia Convergence. *Nat. Commun.* 8, 15992. doi:10.1038/ncomms15992

Chen, M., Niu, F., Tromp, J., Lenardic, A., Lee, C.-T. A., Cao, W., et al. (2017). Lithospheric Foundering and Underthrusting Imaged beneath Tibet. *Nat. Commun.* 8, 15659. doi:10.1038/ncomms15659

Chen, L., Liu, L., Capitanio, F. A., Gerya, T. V., and Li, Y. (2020). The Role of Pre-Existing Weak Zones in the Formation of the Himalaya and Tibetan Plateau: 3-D Thermomechanical Modelling. *Geophys. J. Int.* 221 (3), 1971–1983. doi:10.1093/gji/ggaa125

Chen, L., Song, X., Gerya, T. V., Xu, T., and Chen, Y. (2019). Crustal Melting beneath Orogenic Plateaus: Insights from 3-D Thermo-Mechanical Modeling. *Tectonophysics* 761, 1–15. doi:10.1016/j.tecto.2019.03.014

Clauser, C., and Huenges, E. (1995). Thermal Conductivity of Rocks and Minerals in *AGU Ref. Shelf Rock Physics and Phase Relations* (Washington, D. C: AGU), 3, 105–126. doi:10.1029/rf003p0105

Cook, K. L., and Royden, L. H. (2008). The Role of Crustal Strength Variations in Shaping Orogenic Plateaus, with Application to Tibet. *J. Geophys. Res.* 113 (B8), B08407. doi:10.1029/2007jb005457

Copley, A., Avouac, J.-P., and Royer, J.-Y. (2010). India-Asia Collision and the Cenozoic Slowdown of the Indian Plate: Implications for the Forces Driving Plate Motions. *J. Geophys. Res.* 115 (B3), B03410. doi:10.1029/2009jb006634

Cruz, L., Malinski, J., Wilson, A., Take, W. A., and Hilley, G. (2010). Erosional Control of the Kinematics and Geometry of Fold-And-Thrust Belts Imaged in a Physical and Numerical Sandbox. *J. Geophys. Res.* 115 (B9). doi:10.1029/2010jb007472

Currie, B. S., Polissar, P. J., Rowley, D. B., Ingalls, M., Li, S., Olack, G., et al. (2016). Multiproxy Paleoaltimetry of the Late Oligocene-Pliocene Oiyug Basin, Southern Tibet. *Am. J. Sci.* 316 (5), 401–436. doi:10.2475/05.2016.01

Cyr, A. J., Currie, B. S., and Rowley, D. B. (2005). Geochemical Evaluation of Fenghuoshan Group Lacustrine Carbonates, North-Central Tibet: Implications for the Paleoaltimetry of the Eocene Tibetan Plateau. *J. Geology.* 113 (5), 517–533. doi:10.1086/431907

Dai, J. G., Fox, M., Shuster, D. L., Hourigan, J., Han, X., Li, Y. L., et al. (2019). Burial and Exhumation of the Hoh Xil Basin, Northern Tibetan Plateau: Constraints from Detrital (U-Th)/He Ages. *Basin Res.* 32 (5), 894–915. doi:10.1111/bre.12405

Dayem, K. E., Houseman, G. A., and Molnar, P. (2009). Localization of Shear along a Lithospheric Strength Discontinuity: Application of a Continuous Deformation Model to the Boundary between Tibet and the Tarim Basin. *Tectonics.* 28 (3), a–n. doi:10.1029/2008tc002264

DeCelles, P. G., Quade, J., Kapp, P., Fan, M., Dettman, D. L., and Ding, L. (2007). High and Dry in central Tibet during the Late Oligocene. *Earth Planet. Sci. Lett.* 253 (3-4), 389–401. doi:10.1016/j.epsl.2006.11.001

Deng, T., and Ding, L. (2015). Paleoaltimetry Reconstructions of the Tibetan Plateau: Progress and Contradictions. *Natl. Sci. Rev.* 2 (4), 417–437. doi:10.1093/nsr/nwv062

Deng, T., Wang, S., Xie, G., Li, Q., Hou, S., and Sun, B. (2011). A Mammalian Fossil From the Dingqing Formation in the Lunpola Basin, Northern Tibet, and its Relevance to Age and Paleo-Altimetry. *Chin. Sci. Bull.* 57 (2–3), 261–269. doi:10.1007/s11434-011-4773-8

Deng, T., Wang, X., Wu, F., Wang, Y., Li, Q., Wang, S., et al. (2019). Review: Implications of Vertebrate Fossils for Paleo-Elevations of the Tibetan Plateau. *Glob. Planet. Change.* 174, 58–69. doi:10.1016/j.gloplacha.2019.01.005

Deng, T., Wu, F., Wang, S., Su, T., and Zhou, Z. (2021). Major Turnover of Biotas across the Oligocene/Miocene Boundary on the Tibetan Plateau. *Palaeogeogr. Palaeoclimatol. Palaeoecol.* 567, 110241. doi:10.1016/j.palaeo.2021.110241

Ding, L., Spicer, R. A., Yang, J., Xu, Q., Cai, F., Li, S., et al. (2017). Quantifying the Rise of the Himalaya Orogen and Implications for the South Asian Monsoon. *Geology.* 45 (3), 215–218. doi:10.1130/g38583.1

Ding, L., Xu, Q., Yue, Y., Wang, H., Cai, F., and Li, S. (2014). The Andean-Type Gangdese Mountains: Paleoelevation Record From the Paleocene–Eocene Linzhou Basin. *Earth Planet. Sci. Lett.* 392, 250–264. doi:10.1016/j.epsl.2014.01.045

England, P., and Houseman, G. (1985). Role of Lithospheric Strength Heterogeneities in the Tectonics of Tibet and Neighbouring Regions. *Nature.* 315 (6017), 297–301. doi:10.1038/315297a0

Fang, X., Dupont-Nivet, G., Wang, C., Song, C., Meng, Q., Zhang, W., et al. (2020). Revised Chronology of central Tibet Uplift (Lunpola Basin). *Sci. Adv.* 6 (50), eaba7298. doi:10.1126/sciadv.aba7298

Farnsworth, A., Farnsworth, A., Su, T., Spicer, R., Huang, J., Wu, F., et al. (2018). No High Tibetan Plateau until the Neogene. *Sci. Adv.* 5, eaav2189. doi:10.1130/abs/2018am-319129

Garzione, C. N., Quade, J., DeCelles, P. G., and English, N. B. (2000). Predicting Paleoelevation of Tibet and the Himalaya from N18O vs. Altitude Gradients in Meteoric Water across the Nepal Himalaya. *Earth Planet. Sci. Lette.* 183 (1-2), 215–229. doi:10.1016/s0012-821x(00)00252-1

Gerya, T. V. (2010). *Introduction to Numerical Geodynamic Modelling*. London: Cambridge Univ. Press, 338. doi:10.1017/9781316534243.022

Graveleau, F., Malavieille, J., and Dominguez, S. (2012). Experimental Modelling of Orogenic Wedges: A Review. *Tectonophysics.* 538-540, 1–66. doi:10.1016/j.tecto.2012.01.027

Hacker, B. R., Kelemen, P. B., and Behn, M. D. (2015). Continental Lower Crust. *Annu. Rev. Earth Planet. Sci.* 43 (1), 167–205. doi:10.1146/annurev-earth-050212-124117

He, S., Kapp, P., DeCelles, P. G., Gehrels, G. E., and Heizler, M. (2007). Cretaceous-Tertiary Geology of the Gangdese Arc in the Linzhou Area, Southern Tibet. *Tectonophysics.* 433 (1-4), 15–37. doi:10.1016/j.tecto.2007.01.005

Hess, P. C. (1989). *Origin of Igneous Rocks*. London: Harvard Univ. Press.

Hirschmann, M. M. (2000). Mantle Solidus: Experimental Constraints and the Effects of Peridotite Composition. *Geochem. Geophys. Geosyst.* 1, a–n. doi:10.1029/2000GC000070

Hou, Z., Duan, L., Lu, Y., Zheng, Y., Zhu, D., Yang, Z., et al. (2015). Lithospheric Architecture of the Lhasa Terrane and its Control on Ore Deposits in the Himalayan-Tibetan Orogen. *Econ. Geology.* 110, 1541–1575. doi:10.2113/econgeo.110.6.1541

Hou, Z., Zheng, Y., Lu, Z., Xu, B., Wang, C., and Zhang, H. (2020). Growth,thickening and Evolution of the Thickened Crust of the Tibet Plateau. *Acta Geologica Sinica.* 94, 2797–2815. doi:10.19762/j.cnki.dizhixuebao.2020199

Hu, X., Garzanti, E., Wang, J., Huang, W., An, W., and Webb, A. (2016). The Timing of India-Asia Collision Onset - Facts, Theories, Controversies. *Earth-Science Rev.* 160, 264–299. doi:10.1016/j.earscirev.2016.07.014

Huang, S., Yao, H., Lu, Z., Tian, X., Zheng, Y., Wang, R., et al. (2020). High-Resolution 3-D Shear Wave Velocity Model of the Tibetan Plateau: Implications for Crustal Deformation and Porphyry Cu Deposit Formation. *J. Geophys. Res. Solid Earth.* 125 (7), e2019JB019215. doi:10.1029/2019jb019215

Huismans, R., and Beaumont, C. (2011). Depth-dependent Extension, Two-Stage Breakup and Cratonic Underplating at Rifted Margins. *Nature.* 473 (7345), 74–78. doi:10.1038/nature09988

Ingalls, M., Rowley, D., Olack, G., Currie, B., Li, S., Schmidt, J., et al. (2017). Paleocene to Pliocene Low-Latitude, High-Elevation Basins of Southern Tibet: Implications for Tectonic Models of India-Asia Collision, Cenozoic Climate, and Geochemical Weathering. *GSA Bull.* 130 (1-2), 307–330. doi:10.1130/b31723.1

Jia, G., Bai, Y., Ma, Y., Sun, J., and Peng, P. a. (2015). Paleoelevation of Tibetan Lunpola basin in the Oligocene-Miocene Transition Estimated from Leaf Wax Lipid Dual Isotopes. *Glob. Planet. Change.* 126, 14–22. doi:10.1016/j.gloplacha.2014.12.007

Johannes, W. (1985). The Significance of Experimental Studies for the Formation of Migmatites in *Migmatites*. Editor J. R. Ashworth (Glasgow, U. K: Blackie), 36–85. doi:10.1007/978-1-4613-2347-1_2

Kapp, P., DeCelles, P. G., Gehrels, G. E., Heizler, M., and Ding, L. (2007). Geological Records of the Lhasa-Qiangtang and Indo-Asian Collisions in the Nima Area of central Tibet. *Geol. Soc. America Bull.* 119 (7-8), 917–933. doi:10.1130/b26033.1

Kapp, P., and DeCelles, P. G. (2019). Mesozoic-Cenozoic Geological Evolution of the Himalayan-Tibetan Orogen and Working Tectonic Hypotheses. *Am. J. Sci.* 319 (3), 159–254. doi:10.2475/03.2019.01

Kapp, P., Yin, A., Harrison, T. M., and Ding, L. (2005). Cretaceous-Tertiary Shortening, basin Development, and Volcanism in central Tibet. *Geol. Soc. America Bull.* 117 (7), 865–878. doi:10.1130/b25595.1

Katz, R. F., Spiegelman, M., and Langmuir, C. H. (2003). A New Parameterization of Hydrous Mantle Melting. *Geochem. Geophys. Geosyst.* 4 (9), a–n. doi:10.1029/2002gc000433

Li, L., Chang, H., Guan, C., Liu, W., and Cao, Y. (2020). Early Miocene Paleoaltitude of the Tuotuohe Basin, Central-Northern Tibetan Plateau and its Tectonic Implications. *Acta Geologica Sinica - English Edition* 94 (5), 1364–1372. doi:10.1111/1755-6724.14373

Li, L., Garzione, C. N., Pullen, A., Zhang, P., and Li, Y. (2017). Late Cretaceous-Cenozoic basin Evolution and Topographic Growth of the Hoh Xil Basin, central Tibetan Plateau. *GSA Bull.* 130 (3-4), 499–521. doi:10.1130/b31769.1

Liu, J., Su, T., Spicer, R. A., Tang, H., Deng, W.-Y.-D., Wu,, F.-X., et al. (2019). Biotic Interchange Through Lowlands of Tibetan Plateau Suture Zones During Paleogene. *Palaeogeogr. Palaeoclimatol. Palaeoecol.* 524, 33–40. doi:10.1016/j.palaeo.2019.02.022

Liu, X., Xu, Q., and Ding, L. (2016). Differential Surface Uplift: Cenozoic Paleoelevation History of the Tibetan Plateau. *Sci. China Earth Sci.* 59 (11), 2105–2120. doi:10.1007/s11430-015-5486-y

Liu, Z., Zhao, X., Wang, C., Liu, S., and Yi, H. (2003). Magnetostratigraphy of Tertiary Sediments from the Hoh Xil Basin: Implications for the Cenozoic Tectonic History of the Tibetan Plateau. *Geophys. J. Int.* 154 (2), 233–252. doi:10.1046/j.1365-246x.2003.01986.x

Marques, F. O., and Cobbold, P. R. (2002). Topography as a Major Factor in the Development of Arcuate Thrust Belts: Insights from Sandbox Experiments. *Tectonophysics.* 348 (4), 247–268. doi:10.1016/s0040-1951(02)00077-x

Miao, Y., Wu, F., Chang, H., Fang, X., Deng, T., Sun, J., et al. (2016). A Late-Eocene Palynological Record from the Hoh Xil Basin, Northern Tibetan Plateau, and its Implications for Stratigraphic Age, Paleoclimate and Paleoelevation. *Gondwana Res.* 31, 241–252. doi:10.1016/j.gr.2015.01.007

Molnar, P., and Stock, J. M. (2009). Slowing of India's Convergence with Eurasia since 20 Ma and its Implications for Tibetan Mantle Dynamics. *Tectonics.* 28 (3), a–n. doi:10.1029/2008tc002271

Mulch, A., and Chamberlain, C. P. (2006). The Rise and Growth of Tibet. *Nature.* 439 (7077), 670–671. doi:10.1038/439670a

Persson, K. S., Garcia-Castellanos, D., and Sokoutis, D. (2004). River Transport Effects on Compressional Belts: First Results from an Integrated Analogue-Numerical Model. *J. Geophys. Res.* 109 (B1). doi:10.1029/2002jb002274

Poli, S., and Schmidt, M. W. (2002). Petrology of Subducted Slabs. *Annu. Rev. Earth Planet. Sci.* 30 (1), 207–235. doi:10.1146/annurev.earth.30.091201.140550

Polissar, P. J., Freeman, K. H., Rowley, D. B., McInerney, F. A., and Currie, B. S. (2009). Paleoaltimetry of the Tibetan Plateau from D/H Ratios of Lipid Biomarkers. *Earth Planet. Sci. Lett.* 287 (1-2), 64–76. doi:10.1016/j.epsl.2009.07.037

Quade, J., Breecker, D. O., Daeron, M., and Eiler, J. (2011). The Paleoaltimetry of Tibet: An Isotopic Perspective. *Am. J. Sci.* 311 (2), 77–115. doi:10.2475/02.2011.01

Ranalli, G. (1995). *Rheology of the Earth: Deformation and Flow Processes in Geophysics and Geodynamics*. 2nd ed. London: Chapman & Hall.

Rowley, D. B., and Currie, B. S. (2006). Palaeo-Altimetry of the Late Eocene to Miocene Lunpola basin, central Tibet. *Nature* 439 (7077), 677–681. doi:10.1038/nature04506

Rowley, D. B., Pierrehumbert, R. T., and Currie, B. S. (2001). A New Approach to Stable Isotope-Based Paleoaltimetry: Implications for Paleoaltimetry and Paleohypsometry of the High Himalaya since the Late Miocene. *Earth Planet. Sci. Lett.* 188, 253–268. doi:10.1016/s0012-821x(01)00324-7

Schmeling, H., Babeyko, A. Y., Enns, A., Faccenna, C., Funiciello, F., Gerya, T., et al. (2008). A Benchmark Comparison of Spontaneous Subduction Models-Towards a Free Surface. *Phys. Earth Planet. Interiors.* 171 (1-4), 198–223. doi:10.1016/j.pepi.2008.06.028

Schmidt, M. W., and Poli, S. (1998). Experimentally Based Water Budgets for Dehydrating Slabs and Consequences for Arc Magma Generation. *Earth Planet. Sci. Lett.* 163, 361–379. doi:10.1016/S0012-821X(98)00142-3

Shinevar, W. J., Behn, M. D., and Hirth, G. (2015). Compositional Dependence of Lower Crustal Viscosity. *Geophys. Res. Lett.* 42 (20), 8333–8340. doi:10.1002/2015gl065459

Sokoutis, D., and Willingshofer, E. (2011). Decoupling during continental Collision and Intra-plate Deformation. *Earth Planet. Sci. Lett.* 305 (3-4), 435–444. doi:10.1016/j.epsl.2011.03.028

Song, B., Zhang, K., Han, F., Liu, Z., Ai, K., Li, S., et al. (2021). Reconstruction of the Latest Eocene-Early Oligocene Paleoenvironment in the Hoh Xil Basin (Central Tibet) Based on Palynological and Ostracod Records. *J. Asian Earth Sci.* 217, 104860. doi:10.1016/j.jseaes.2021.104860

Spicer, R. A., Su, T., Valdes, P. J., Farnsworth, A., Wu, F.-X., Shi, G., et al. (2021). Why 'the Uplift of the Tibetan Plateau' Is a Myth. *Natl. Sci. Rev.* 8 (1), nwaa091. doi:10.1093/nsr/nwaa091

Staisch, L. M., Niemi, N. A., Clark, M. K., and Chang, H. (2016). Eocene to Late Oligocene History of Crustal Shortening within the Hoh Xil Basin and Implications for the Uplift History of the Northern Tibetan Plateau. *Tectonics* 35 (4), 862–895. doi:10.1002/2015tc003972

Su, T., Spicer, R. A., Wu, F.-X., Farnsworth, A., Huang, J., Del Rio, C., et al. (2020). A Middle Eocene lowland Humid Subtropical "Shangri-La" Ecosystem in central Tibet. *Proc. Natl. Acad. Sci. U.S.A.* 117 (52), 32989–32995. doi:10.1073/pnas.2012647117

Sun, B., Wang, Y.-F., Li, C.-S., Yang, J., Li, J.-F., Li, Y.-L., et al. (2015). Early Miocene Elevation in Northern Tibet Estimated by Palaeobotanical Evidence. *Sci. Rep.* 5, 10379. doi:10.1038/srep10379

Sun, J., Xu, Q., Liu, W., Zhang, Z., Xue, L., and Zhao, P. (2014). Palynological Evidence for the Latest Oligocene−early Miocene Paleoelevation Estimate in the Lunpola Basin, central Tibet. *Palaeogeogr. Palaeoclimatol. Palaeoecol.* 399, 21–30. doi:10.1016/j.palaeo.2014.02.004

Tapponnier, P., Zhiqin, X., Roger, F., Meyer, B., Arnaud, N., Wittlinger, G., et al. (2001). Oblique Stepwise Rise and Growth of the Tibet Plateau. *Science.* 294 (5547), 1671–1677. doi:10.1126/science.105978

Turcotte, D. L., and Schubert, G. (2002). *Geodynamics*. Cambridge, U. K: Cambridge Univ. Press.

Wang, C., Dai, J., Zhao, X., Li, Y., Graham, S. A., He, D., et al. (2014). Outward-growth of the Tibetan Plateau during the Cenozoic: A Review. *Tectonophysics.* 621, 1–43. doi:10.1016/j.tecto.2014.01.036

Wang, C., Zhao, X., Liu, Z., Lippert, P. C., Graham, S. A., Coe, R. S., et al. (2008). Constraints on the Early Uplift History of the Tibetan Plateau. *Proc. Natl. Acad. Sci. U.S.A.* 105 (13), 4987–4992. doi:10.1073/pnas.0703595105

Wang, Y., Deng, T., and Biasatti, D. (2006). Ancient Diets Indicate Significant Uplift of Southern Tibet after Ca. 7 Ma. *Geol.* 34 (4), 309. doi:10.1130/g22254.1

Wei, Y., Zhang, K., Garzione, C. N., Xu, Y., Song, B., and Ji, J. (2016). Low Palaeoelevation of the Northern Lhasa Terrane during Late Eocene: Fossil Foraminifera and Stable Isotope Evidence from the Gerze Basin. *Sci. Rep.* 6, 27508. doi:10.1038/srep27508

Whipple, K. X., and Meade, B. J. (2004). Controls on the Strength of Coupling Among Climate, Erosion, and Deformation in Two-Sided, Frictional Orogenic Wedges at Steady State. *J. Geophys. Res.* 109 (F1), F01011. doi:10.1029/2003jf000019

Willett, S. D. (1999). Orogeny and Orography: The Effects of Erosion on the Structure of Mountain Belts. *J. Geophys. Res.* 104 (B12), 28957–28981. doi:10.1029/1999jb900248

Willingshofer, E., Sokoutis, D., and Burg, J.-P. (2005). Lithospheric-scale Analogue Modelling of Collision Zones with a Pre-existing Weak Zone. *Geol. Soc. Lond. Spec. Publications.* 243 (1), 277–294. doi:10.1144/gsl.sp.2005.243.01.18

Wu, F., Miao, D., Chang, M.-m., Shi, G., and Wang, N. (2017). Fossil Climbing Perch and Associated Plant Megafossils Indicate a Warm and Wet central Tibet during the Late Oligocene. *Sci. Rep.* 7 (1), 878. doi:10.1038/s41598-017-00928-9

Xiao, W., Ao, S., Yang, L., Han, C., Wan, B., Zhang, J. E., et al. (2017). Anatomy of Composition and Nature of Plate Convergence: Insights for Alternative Thoughts for Terminal India-Eurasia Collision. *Sci. China Earth Sci.* 60 (6), 1015–1039. doi:10.1007/s11430-016-9043-3

Xie, R., Chen, L., Xiong, X., Wang, K., and Yan, Z. (2021). The Role of Pre-existing Crustal Weaknesses in the Uplift of the Eastern Tibetan Plateau: 2D Thermo-Mechanical Modeling. *Tectonics.* 40 (4), TC006444. doi:10.1029/2020tc006444

Xiong, Z., Liu, X., Ding, L., Farnsworth, A., Spicer, R. A., Xu, Q., et al. (2022). The Rise and Demise of the Paleogene Central Tibetan Valley. *Sci. Adv.* 8 (6), eabj0944. doi:10.1126/sciadv.abj0944

Xiong, Z., Ding, L., Spicer, R. A., Farnsworth, A., Wang, X., Valdes, P. J., et al. (2020). The Early Eocene Rise of the Gonjo Basin, SE Tibet: From Low Desert to High forest. *Earth Planet. Sci. Lett.* 543, 116312. doi:10.1016/j.epsl.2020.116312

Xu, Q., Ding, L., Zhang, L., Cai, F., Lai, Q., Yang, D., et al. (2013). Paleogene High Elevations in the Qiangtang Terrane, central Tibetan Plateau. *Earth Planet. Sci. Lett.* 362, 31–42. doi:10.1016/j.epsl.2012.11.058

Yang, Y., Ritzwoller, M. H., Zheng, Y., Shen, W., Levshin, A. L., and Xie, Z. (2012). A Synoptic View of the Distribution and Connectivity of the Mid-crustal Low Velocity Zone beneath Tibet. *J. Geophys. Res.* 117 (B4), a–n. doi:10.1029/2011jb008810

Yin, A., and Harrison, T. M. (2000). Geologic Evolution of the Himalayan-Tibetan Orogen. *Annu. Rev. Earth Planet. Sci.* 28 (1), 211–280. doi:10.1146/annurev.earth.28.1.211

Zhang, K., Wang, G., Xu, Y., Luo, M., Ji, J., Xaio, G., et al. (2013). Sedimentary Evolution of the Qinghai-Tibet Plateau in Cenozoic and its Response to the Uplift of the Plateau. *Acta Geological Sinica* 87, 555–575. doi:10.1111/1755-6724.12068

Zhang, K.-X., Wang, G.-C., Luo, M.-S., Ji, J.-L., Xu, Y.-D., Chen, R.-M., et al. (2010). Evolution of Tectonic Lithofacies Paleogeography of Cenozoic of Qinghai-Tibet Plateau and its Response to Uplift of the Plateau. *Ear th Sci.* 35, 697–712. doi:10.3799/dqkx

Zhang, X.-Z., Wang, Q., Wyman, D., Ou, Q., Qi, Y., Gou, G.-N., et al. (2022). Tibetan Plateau Growth Linked to Crustal thermal Transitions since the Miocene. *Geology* 50 (5), 610–614. doi:10.1130/g49534.1

Zhao, L.-F., Xie, X.-B., He, J.-K., Tian, X., and Yao, Z.-X. (2013). Crustal Flow Pattern beneath the Tibetan Plateau Constrained by Regional Lg-Wave Q Tomography. *Earth Planet. Sci. Lett.* 383, 113–122. doi:10.1016/j.epsl.2013.09.038

Zhu, D.-C., Zhao, Z.-D., Niu, Y., Mo, X.-X., Chung, S.-L., Hou, Z.-Q., et al. (2011). The Lhasa Terrane: Record of a Microcontinent and its Histories of Drift and Growth. *Earth Planet. Sci. Lett.* 301 (1-2), 241–255. doi:10.1016/j.epsl.2010.11.005

Conflict of Interest: The authors declare that the research was conducted in the absence of any commercial or financial relationships that could be construed as a potential conflict of interest.

The handling editor declared a past co-authorship with one of the authors LC at time of review.

frontiers | Frontiers in Earth Science

ORIGINAL RESEARCH
published: 25 May 2022
doi: 10.3389/feart.2022.895363

Effects of Lithospheric Properties on Crustal Strain at Both Ends of Longmen Shan Orogenic Belt: Based on Numerical Simulation

Tuo Shen[1,2], Xiwei Xu[1], Yujiang Li[1], Luyuan Huang[1], E. A. Rogozhin[3], Qixin Wang[1], Wenjun Kang[1] and Xiaoqiong Lei[1]*

[1]National Institute of Natural Hazards, Ministry of Emergency Management of China, Beijing, China, [2]Department of Geophysics, School of Earth and Space Sciences, Peking University, Beijing, China, [3]Schmidt Institute of Physics of the Earth, Russian Academy of Sciences, Moscow, Russia

OPEN ACCESS

Edited by:
Zhong-Hai Li,
University of Chinese Academy of Sciences, China

Reviewed by:
Yujun Sun,
Chinese Academy of Geological Science, China
Xiaoyu Guo,
Sun Yat-Sen University, China
Zhigang Li,
Sun Yat-Sen University, China

***Correspondence:**
Xiwei Xu
xiweixu@vip.sina.com

Specialty section:
This article was submitted to Structural Geology and Tectonics, a section of the journal Frontiers in Earth Science

Received: 13 March 2022
Accepted: 02 May 2022
Published: 25 May 2022

Citation:
Shen T, Xu X, Li Y, Huang L, Rogozhin EA, Wang Q, Kang W and Lei X (2022) Effects of Lithospheric Properties on Crustal Strain at Both Ends of Longmen Shan Orogenic Belt: Based on Numerical Simulation. Front. Earth Sci. 10:895363. doi: 10.3389/feart.2022.895363

Strain partitioning and accommodation are fundamental constraints to evaluate tectonic models of orogenic plateaus. The uplift mechanism issue of the eastern Tibetan Plateau has remained a long-term focus since the last century, namely, the steep uplift of the Longmen Shan area. Several tectonic models have been proposed to describe the uplift process of the central Longmen Shan area along the eastern margin of the Tibetan Plateau. Such as upper crustal shortening, mid-crustal channel flow, and whole-crust shearing. However, these models are typically examined through vertical differences. Geophysical, geological, remote sensing and geochemistry observation data indicate that there occur not only vertical differences but also obvious horizontal differences along the Longmen Shan orogenic belt. Based on the finite element method, we employed two-dimensional profiles crossed northern and southern Longmen Shan fault to reconstruct the uplift process of the Longmen Shan orogenic belt. The mechanical properties of the lithosphere south of the Longmen Shan orogenic belt were slightly less favorable than those of the lithosphere north of the Longmen Shan orogenic belt. For the better fitting result in the southern part viscosity of lower crust is less than 10^{21} Pa·s and in the northern part viscosity of lower crust is around 10^{22} Pa·s. The uplift processes in the upper and lower crust of the Longmen Shan orogenic belt were partially decoupled. The deformation of lithosphere in the northern Longmen Shan orogenic belt is smaller than it in southern Longmen Shan orogenic belt. Due to that the rigid Ruoergai block maybe resists the formation of a weak layer or enters of weak materials to the northern Longmen Shan block, resulting in the observed difference in lithospheric properties between the northern and southern Longmen Shan blocks.

Keywords: Longmen Shan fault, viscosity, finite element method, uplift, Ruoergai block, lithosphere

INTRODUCTION

Over the past 50–55 million years, from the Indo-Asian continental collision event, the rise of the Himalayan-Tibetan Plateau has doubled the thickness of the Tibetan crust and has resulted in more than 1,400 km of plate convergence (Yin and Harrison, 2000; Ding et al., 2016; Qasim et al., 2018).

The collision between the Indian and Eurasian plates not only caused the uplift of the Tibetan Plateau but also caused eastward motion of the plateau, producing several large-scale intracontinental strike-slip fault systems (Molnar and Tapponnier, 1975; Tapponnier and Molnar, 1977). The tectonic extrusion model (Tapponnier et al., 1982, 2001) provides fundamental constraints of the uplift process of the eastern Tibetan margin (**Figure 1A**). To date, more than seven tectonic models have been published to explain the deformation and uplift process in the Longmen Shan orogenic belt area of the eastern Tibetan margin: (1) the channel flow model (Royden et al., 1997; Clark and Royden, 2000); (2) brittle upper crustal shortening (Hubbard and Shaw, 2009); (3) simple-shear deformation of the lithosphere (Yin, 2010) or crust (Guo et al., 2013); (4) pure-shear shortening and thickening of the lithosphere (Yin, 2010) with possibly decoupled upper and lower crusts (Feng et al., 2016); (5) indentation of the rigid South China crust into the weak crust of Tibet (Zhang et al., 2004); (6) uplift of Tibet associated with westernward underthrusting of the South China crust (Clark et al., 2005; Jiang and Jin, 2005); and (7) heterogeneous crustal reactivation of pre-existing weak zones (Jia D. et al., 2010; Sun et al., 2018). These models largely do not consider the effects of transverse differences in the deep lithosphere on the deformation and uplift process of the eastern Tibetan margin.

Recently, Tan suggested different exhumation rates between the northern and southern Longmen Shan orogenic belts (Tan et al., 2019). The maximum exhumation belt exhibited a 15° angle difference from the Longmen Shan thrust belt. Topographic Digital Elevation Model data (DEM data) clearly indicated that the slope differed between the northern and southern Longmen Shan orogenic belts (**Figure 1B**). Geological data (Li et al., 2012), P- and S-wave results (Lei and Zhao, 2009; Wei et al., 2017; Xin et al., 2018), magnetotelluric data (Maus et al., 2007; Sun et al., 2019), and gravity anomalies (Xu et al., 2016) suggest that the lithosphere of the Longmen Shan orogenic belt is transversely inhomogeneous. Moreover, The recent deep seismic reflection profile (Gao et al., 2014) and deep seismic sounding data (Jia S. et al., 2010) prove that there are relatively strong crystallization basement in upper crust of Ruoergai Basin. The Pn traveltime data suggest that there are high-speed crystallization basement similar to Sichuan Basin and Tarim Basin in the deep part of Ruoergai region. And some series of heat flow data also prove that the Ruoergai Basin has low heat flow value (Hu et al., 2018; An and Shi, 2007). These studies point out that the Ruoergai Basin is a relatively strong and stable block.However whether this rigid block impacts the uplift and deformation of the Longmen Shan orogenic belt in the extrusion process of the Bayan Har block remains to be investigated. As a high-risk area for earthquakes and a hot spot of plateau deformation, research on the effect of deformation and uplift due to transverse differences in the lithosphere in this region remains insufficient.

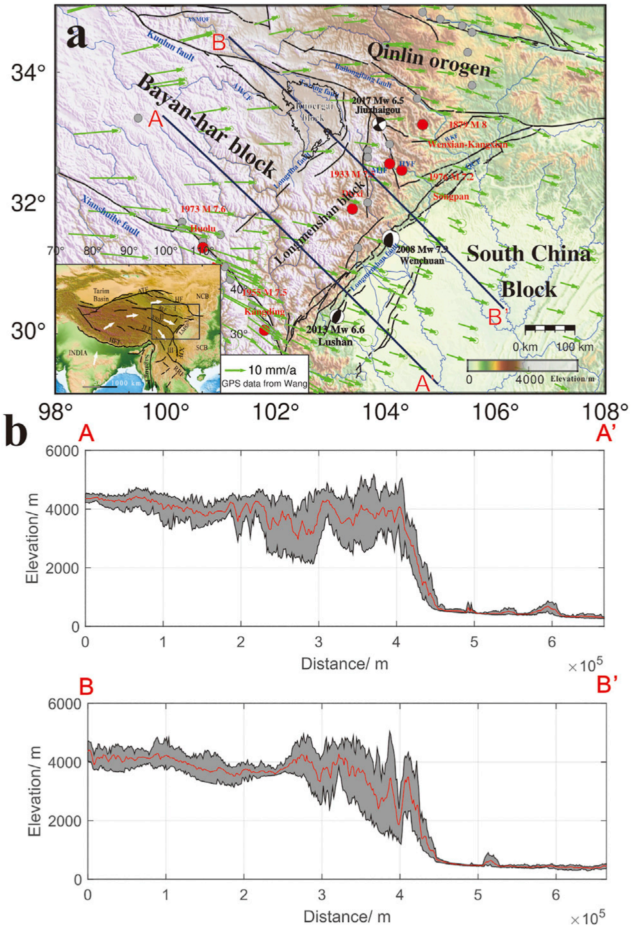

FIGURE 1 | (A). Faults and seismicity in the eastern Tibetan Plateau and neighboring regions (the location is indicated by a box in the inset). The focal mechanism solutions indicate the 2008 Mw 7.9 Wenchuan earthquake, 2013 Mw 6.6 Lushan earthquake, and 2017 Mw 6.5 Jiuzhaigou earthquake retrieved from the Global Centroid Moment Tensor (CMT) database (formerly referred to as the Harvard CMT catalog) (http://www.globalcmt.org/CMTsearch.html). The dark gray circle indicates historical events above Mw 7. The red circle indicates events above Mw 7.5 near selected faults from 1840 to 2000 (obtained from the Chinese Earthquake Administration). The green arrow is GNSS data (Wang and Shen, 2020). The dashed box indicates figure area. The area enclosed by the black line delineates the Ruoergai rigid block (Hu et al., 2018). ANMQF: Animaqing fault; AWCF: Awancang fault; HF: Haiyuan fault; HYF: Huya fault; MJF: Minjiang fault; QCF: Qingchuan fault; QLF: Qinling fault, WKF: Wenxian–Kangxian fault. The inset map demonstrated major tectonic features of the Tibetan Plateau. ATF: Altyn Tagh fault, HFT: Himalayan Frontal Thrust, JLF: Jiali fault, NCB: North China Block, RRF: Red River fault, SCB: South China Block, XJF: Xiaojiang fault, XSHF: Xianshuihe fault, I–Qaidam-Qilian Block, II–Bayan Har Block, III -Sichuan–Yunnan block. The white arrow shows the block movement direction. **(B)**. Profiles A-A'cross the southern Longmen Shan fault, and Profiles B-B′ cross the northern Longmen Shan fault. The red line indicates the average elevation. The gray range indicates the highest and lowest elevation ranges.

A large number of numerical simulation-based articles on the uplift and deformation of the Tibetan Plateau and Longmen Shan orogenic belt have been published, suggesting lithospheric rheology, which controls the deformation and gradient of the Longmen Shan uplift (Clark and Royden, 2000; Wang and He, 2012; Sun and Liu, 2018). In this study, we established two two-dimensional viscoelastic-elastoplastic profiles crossing the northern and southern Longmen Shan orogenic belts to rebuild the uplift process of the eastern Tibetan margin. Furthermore, we investigated how rheological transverse variations in the Tibetan Plateau impact lithospheric deformation and uplift of the eastern Tibetan margin. Our results indicated that the mechanical properties of the lithosphere south of the Bayan Har block are slightly less notable than those of the lithosphere north of the Bayan Har block. The uplift processes in the upper and lower crusts of the Longmen Shan orogenic belt were partially decoupled.

TECTONIC BACKGROUND

In the Eocene (50–55 Ma), the Indian continental plate started to collide with the Eurasian continental plate, and this collision event caused the uplift of the Tibetan Plateau with a very high average altitude of 4,000 m and compressional tectonics (Yin and Harrison, 2000; Ding et al., 2016; Qasim et al., 2018). Moreover, within the plateau, certain blocks experienced eastern extrusion and produced several large-scale strike-slip fault systems (Molnar and Tapponnier, 1975; Tapponnier and Molnar, 1977). The tectonic extrusion model (Tapponnier et al., 1982, 2001; Schellart et al., 2019) provides fundamental constraints of the uplift process of the eastern Tibetan margin.

Main Tectonic Blocks

The Bayan Har block in the central easternmost Tibetan Plateau is controlled by major NW-trending strike-slip faults. The eastern, northern, and southern boundaries of the Bayan Har block are the NE-trending Longmen Shan thrust, NWW-trending Kunlun fault, and Xianshuihe fault, respectively (**Figure 1**). These features are regarded as representing the southeastward extrusion route of crustal material after the Indo-Eurasian collision event. Numerous geologists have suggested that the Bayan Har block is an ancient landmass of the Sichuan block (Xu et al., 1991; Yin and Harrison, 2000). Furthermore, the Bayan Har block might have become isolated from the Sichuan block during the late Paleozoic (Zhang et al., 2004). Later, uplift of the Longmen Shan block separated the Bayan Har block from the Yangtze block.

The Ruoergai Basin is a Cenozoic basin located along the northeastern margin of the Bayan Har block. The Bayan Har block has been subjected to orogenic events related to the development of the plateau since the Cenozoic. Petroleum geologists have investigated the crustal structures of the Ruoergai Basin via seismic profiling to explore prospective oil and gas resources (Jia S. et al., 2010; Gao et al., 2014; Lei et al., 2014).

The Sichuan block occurs in the southeastern part of our study area, which is a stable basin with little seismic or tectonic activity and characterized by a high seismic velocity and low topographic relief (Burchfiel et al., 2008). This rigid Sichuan block played an important role in strain distribution and Cenozoic deformation of the southeastern part of the Tibetan Plateau (Yin, 2010).

Main Active Faults

The Longmen Shan fault forms the eastern boundary of the Tibetan Plateau It is consisted of three main faults: the Guanxian-Jiangyou fault, the Yingxiu-Beichuan fault, and the Wenchuan-Maowen fault (Zhang, 2008; Xu X. et al., 2009). From structural geometry and ages of deformation along-strike segmentation of topography and structures the Longmen Shan belt can be divided into the north Longmen Shan segment and the south Longmen Shan segment. Further, based on field investigations and interpretations of seismic sections, we can divide the Longmen Shan belt into the following two transfer zones and three segments (from northeast to southwest): the northern segment, Anxian transfer zone, central segment, Guanxian transfer zone and southern segment (Jia et al., 2006; Jin et al., 2010). The GPS data have indicated ~3 mm/a convergence and ~1 mm/a right-lateral slip along this fault, and the elevation changes from N4000 m to ~500 m within a distance of ~50 km. Associated with steep topographic changes are sharp variations in the crustal thickness and seismic velocity in the lithosphere (Burchfiel et al., 2008). Dipping angles range from ~45° to nearly vertical near the surface but gradually decrease with the depth (Burchfiel et al., 2008; Zhang, 2008; Xu Y. et al., 2009; Lin et al., 2009).

METHOD AND MODEL

In this study, we established two two-dimensional viscoelastic-elastoplastic profiles, which cross the northern Longmen Shan orogenic belt (referred to as Model N in the text) and southern Longmen Shan orogenic belt (referred to as Model S in the text) to reconstruct the uplift process of the eastern Tibetan margin (**Figure 2**). Furthermore, we investigated how rheological transverse variations in the Tibetan Plateau impacted lithospheric deformation and uplift of the eastern Tibetan margin.

The two-dimensional momentum conservation equation is:

$$\frac{\partial \sigma_{ij}}{\partial x_j} + \rho g_i = 0,\ i,\ j = 1,\ 2, \tag{1}$$

where σ_{ij} is the stress tensor ($i,\ j = 1,\ 2$), ρ is the density and g is the gravitational acceleration.

In the lower crust and mantle, we defined viscoelasticity properties. The stress is related to the strain rate and depends on the stress–strain history, so a hereditary integral is employed:

$$\sigma = 2\int_0^t G(t-\tau)\frac{de}{d\tau}d\tau + I\int_0^t K(t-\tau)\frac{d\Delta}{d\tau}d\tau, \tag{2}$$

where σ is the Cauchy stress, e is the deviatoric strain, Δ is the volumetric strain, τ is the past time, and I is the identity tensor. $G(t)$ and $K(t)$ are the Prony series shear and bulk-relaxation modulus, respectively:

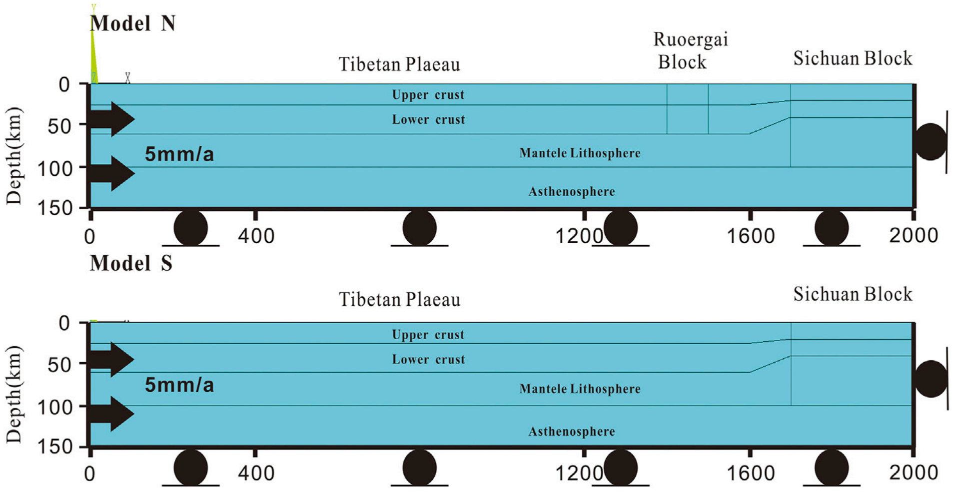

FIGURE 2 | Two two-dimensional reference models crossing the southern Longmen Shan fault (Model S) and the northern Longmen Shan fault (Model N).

TABLE 1 | Parameters for Models.

	Tibet plateau					Sichuan block (Ruoergai block)				
Layer	**Viscosity (Pa·s)**	**Young's modulus (Pa)**	**Poison ratio**	**Cohesion (MPa)**	**internal friction angle**	**Viscosity (Pa·s)**	**Young's modulus (Pa)**	**Poison ratio**	**Cohesion (MPa)**	**internal friction angle**
Upper Crust	--	7.5×10^{10}	0.25	10	15	--	1.1×10^{11}	0.25	100	15
Lower Crust	10^{21}–5×10^{22}	1.3×10^{11}	0.27	--	--	10^{23}	1.4×10^{11}	0.27	--	--
Mantle Lithosphere	10^{21}–5×10^{22}	1.6×10^{11}	0.27	--	--	10^{23}	1.7×10^{11}	0.27	--	--
Asthenosphere	10^{21}	7×10^{10}	0.27	--	--	10^{21}	7×10^{10}	0.27	--	--

Note. Constant density is used: 2,700 kg/m3 for the upper crust, 2,900 kg/m3 for the lower crust, and 3000 kg/m3 for the mantle. Ruoergai rigid Block only exist in crust.(Chen et al., 2008; Shi and Cao, 2008; Luo and Liu, 2018; Sun and Liu, 2018; Li Y. et al., 2019).

$$\begin{cases} G(t) = G_\infty + \sum_{i=1}^{n_G} G_i \exp\left(-\frac{t}{\tau_i^G}\right) \\ K(t) = K_\infty + \sum_{i=1}^{n_K} K_i \exp\left(-\frac{t}{\tau_i^K}\right) \end{cases}, \tag{3}$$

where τ_i^G is the relaxation time for each Prony component G and depends on the viscosity. G_i is the shear modulus of the ith Prony unit, while G_∞ is the long-term modulus ($t = \infty$), and n_G is the number of Prony terms. Similar behavior can be defined for the bulk relaxation modulus $K(t)$ with a separate set of n_K values of the Prony terms.

We applied the Drucker–Prager yield criterion to the elastoplastic upper crust. All the parameters are listed in **Table 1**.

These 2 profiles cross the northern and southern Longmen Shan orogenic belts. The total profile length is 2000 km, the Bayan Har block length is 1700 km, and the Sichuan block length is 300 km according to DEM data. In the plateau, the upper crust is 25 km deep, the lower crust is 60 km deep, and the lithosphere is 100 km deep. In the Sichuan block, the upper crust is 20 km deep, the lower crust is 40 km deep, and the lithosphere is 100 km deep (Jia S. et al., 2010; Gao et al., 2014; Sun and Liu, 2018; Tan et al., 2019). In the Tibetan Plateau, the thickness of the upper crust rapidly decreases from 25 to 20 km in the 1,600–1700 km section of the profile, and the thickness of the lower crust rapidly decreases from 60 to 40 km in the 1,600–1700 km section of the profile (Laske et al., 2013). In the profile, which crosses the northern Longmen Shan fault, we set the rigid Ruoergai block in the 1,400–1,500 km section of the profile (Jia S. et al., 2010; Gao et al., 2014; Lei et al., 2014). We imposed a vertical displacement of 5 mm/a on the left side of the model domain. The right side of the model domain was fixed along all directions, assuming imposed boundary conditions without vertical deviation, with the bottom defined as a free-slip boundary along the horizontal direction and a fixed boundary along the vertical direction, while the surface was defined as a free boundary (**Figure 2**). The main uplift of the Longmen Shan orogenic belt has occurred since the Cenozoic. The study of the uplift of the Longmen Shan orogenic belt should consider the preexisting topographic relief and the impact of erosion. In particular, the preexisting topographic relief affected the deformation localization within the evolving thrust wedges (Sun et al., 2016). This study does not consider the

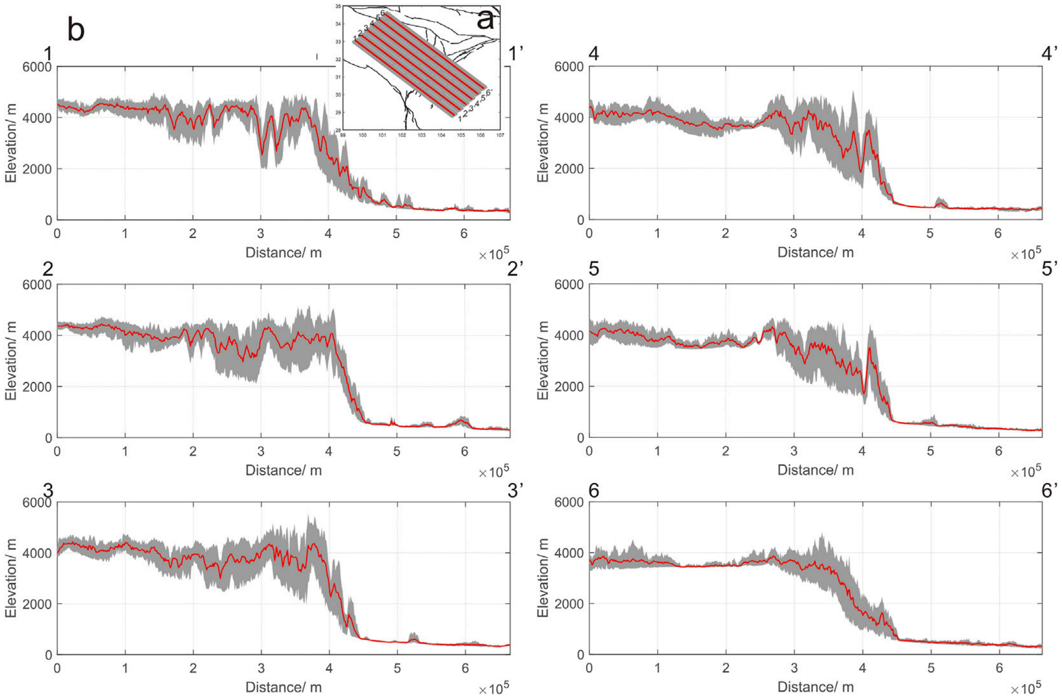

FIGURE 3 | (A) 6 profiles cross the Longmen Shan fault, every section was 500 km in length and 25 km in width. **(B)** Profiles 1-1′, 2-2′, and 3-3′ cross the southern Longmen Shan fault, and Profiles 4-4′, 5-5′, and 6-6′ cross the northern Longmen Shan fault. The red line indicates the average elevation. The gray range indicates the highest and lowest elevation ranges.

preexisting topographic relief, mainly to simplify the model, eliminate the interference of other factors, and only explore the influence of rheology on the uplift and slope of Longmen Mountain. Our modeling process encompassed 10 ten million years (Wang et al., 2012; Shen et al., 2019).

All modeling was conducted in ANSYS® finite element software. ANSYS® employs the Newton–Raphson approach to solve nonlinear problems. In this method, a load is subdivided into a series of increments applied over several steps. Prior to each solution, the out-of-balance load vector is evaluated. If the convergence criteria are not satisfied, the load vector is reevaluated, the stiffness matrix is updated, and a new solution is obtained until convergence is reached.

SIMULATION RESULTS

We extracted DEM data pertaining to 6 sections perpendicular to the Longmen Shan fault (3 sections in the north and 3 sections in the south), and every section was 500 km in length and 25 km in width (**Figure 3A**). Profiles 1-1′, 2-2′, and 3-3′ crossed the southern Longmen Shan fault, and Profiles 4-4′, 5-5′, and 6-6’ crossed the northern Longmen Shan fault. In each section, we plotted the average elevation (red line) and highest and lowest elevation ranges (gray part) (**Figure 3B**). Furthermore, we compared the DEM data of these 6 sections, and clearly shows the trend, in which the slope declined and the average elevation decreased from south to north. Thereafter, we extracted uplift data from our numerical simulated models (**Figure 4**).

We merged the modeling results with the observed DEM data to obtain data with a good fitting effect (**Figure 5**). Then we extract the curves with relatively good fitting. **Figure 6** shows the final modeling result. Profiles 1, 2, and 3 crossed the southern Longmen Shan fault, and Profiles 4, 5, and 6 crossed the northern Longmen Shan fault. We could obtain a better fitted model along Profile 1 with a lower crust viscosity of 10^{21} Pa·s and an upper mantle viscosity of 5×10^{22} Pa·s. Moreover, a lower crust viscosity of 10^{21} Pa·s and an upper mantle viscosity of 5×10^{21} Pa·s yielded a better fitting effect. Profiles 2 and 3 were more suitably fitted with a lower crust viscosity of 10^{21} Pa·s and an upper mantle viscosity of 5×10^{22} Pa·s. Moreover, the model with a lower crust viscosity of 10^{22} Pa·s and an upper mantle viscosity of 5×10^{22} Pa·s achieved a better fit. In the northern profile, we assessed Models N. In regard to Model N, we could conclude that the better fitted model along Profile 4, Profiles 5 and 6 with a lower crust viscosity 5×10^{22} Pa·s and an upper mantle viscosity 10^{22} Pa·s obtained a better fitting effect.

However, as shown in **Figure 5**, the southern profile appeared to achieve a good fitting effect, whereas the fitting effect of the northern profile was a little insufficient. Then, we further refined the viscosity coefficient in the Model N and adjusted the model across the northern Longmen Shan fault (referred to as Model AN in the text; shown as model in **Supplementary Figure S1**) for fitting purposes. We adjusted the upper crustal elasticity and

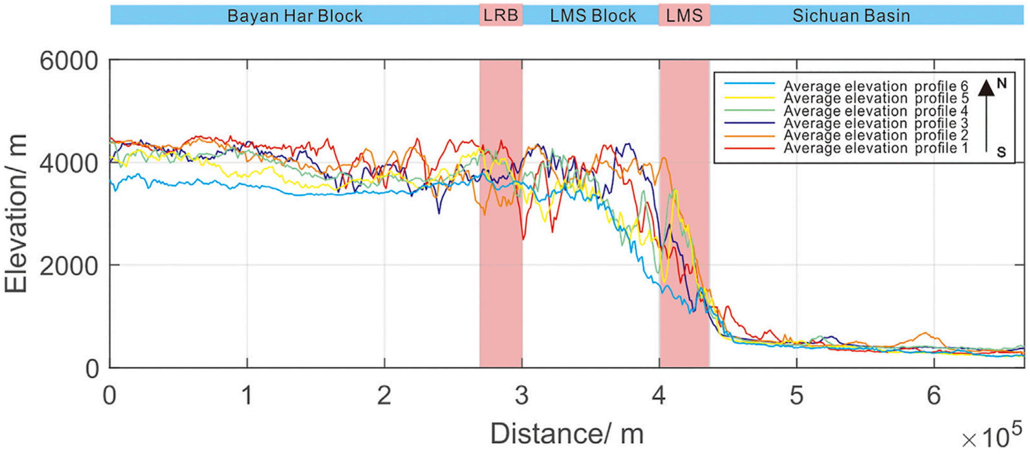

FIGURE 4 | Combination of the average altitude curves along the 6 profiles. The light blue area is the block area, and the pink area indicates the fault zone. LRB-Longriba fault; LMS-Longmen Shan fault; LMS block-Longmen Shan block (the Longmen Shan block is the area between the Longriba fault and Longmen Shan fault in the eastern part of Bayan Har block).

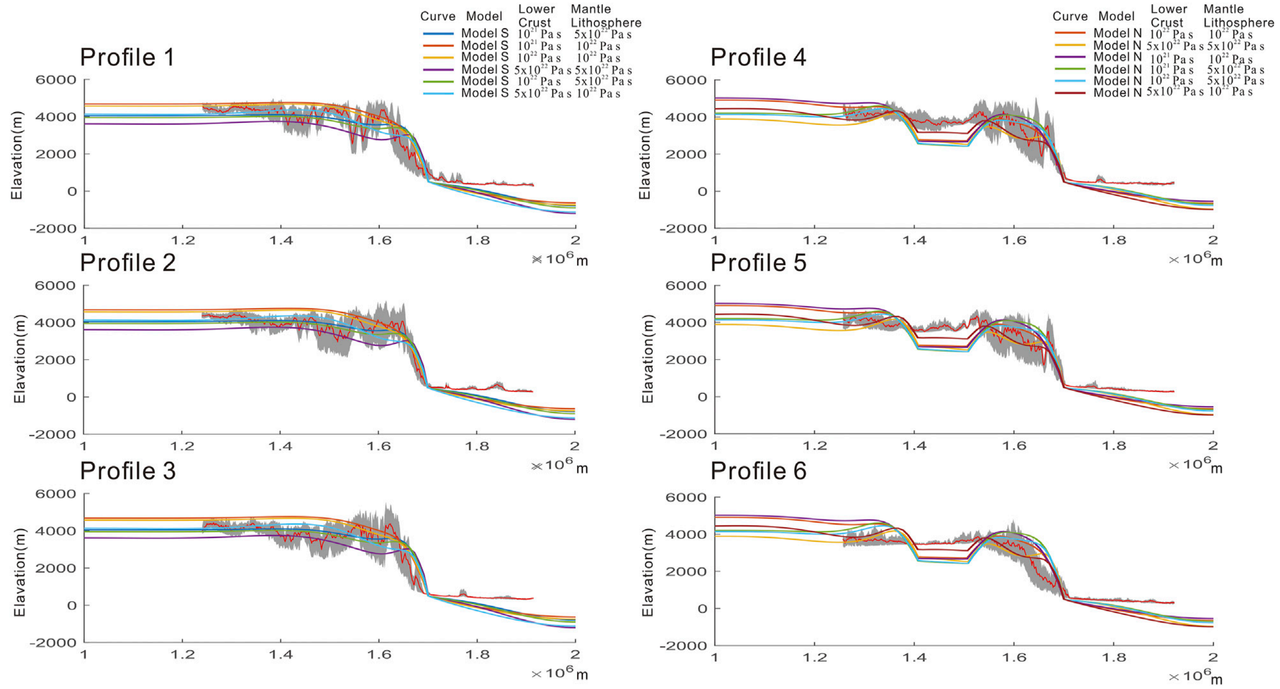

FIGURE 5 | Comparison between the simulation results and extracted DEM results. Profiles 1, 2, and 3 are the results of Model S merged with the extracted DEM profiles 1-1′, 2-2′, and 3-3′, respectively. Profiles 4, 5, and 6 are the results of Model N merged with the extracted DEM profiles 4-4′, 5-5′, and 6-6′, respectively. In the legend exhibits different the viscosity of lower crust and mantle lithosphere in the Tibet Plateau.

viscosity of lower crust of the Ruoergai block on the basis of the optimal simulation parameters (lower crust viscosity of 5 × 10^{22} Pa · s and an upper mantle viscosity of 10^{22} Pa · s or lower crust viscosity of 5 × 10^{22} Pa · s and an upper mantle viscosity of 5 × 10^{22} Pa · s), and carried out a large number of simulations. After further adjustment, we obtained a better fitting curve than that depicted of northern profiles in **Figure 5** and obtained the final result, as shown in **Supplementary Figure S2**. As shown in **Supplementary Figure S3**, we found that the curve of the slope of the modeled uplift and the altitude of plateau convergence after final uplift based on the modeling results matched the curve of the observed DEM data suitably.

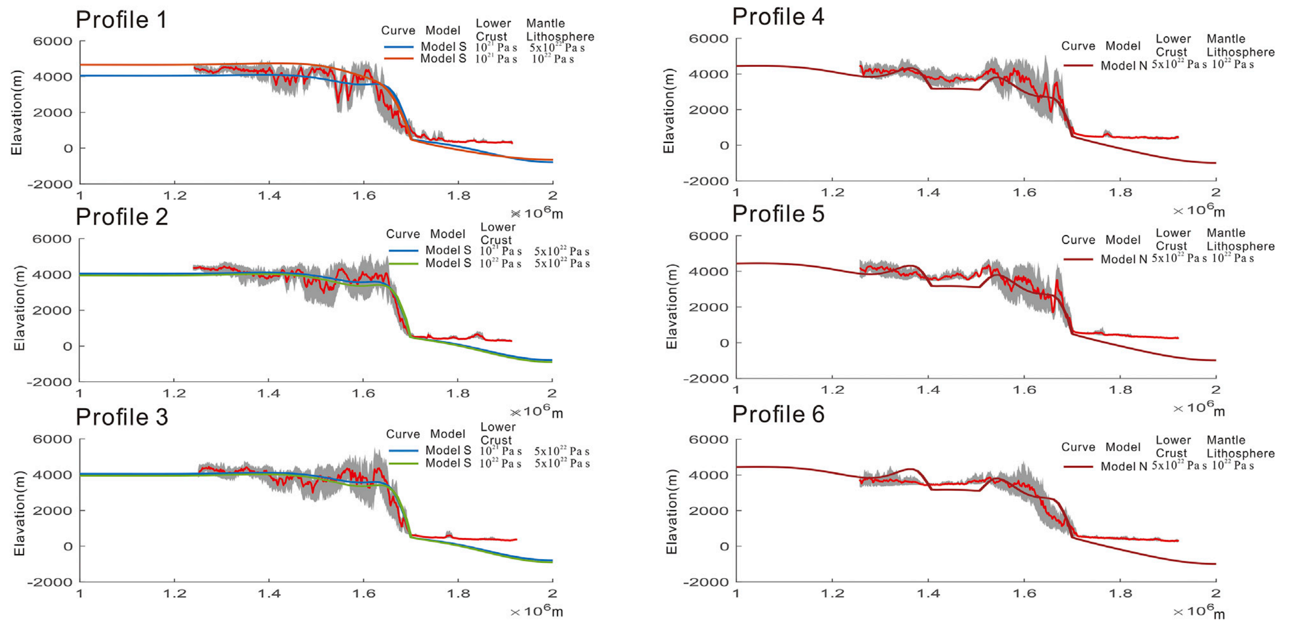

FIGURE 6 | Best fitting result from the comparison between the simulation results and DEM extraction results. Profiles 1, 2, and 3 are the results of Model S merged with the extracted DEM profiles 1-1′, 2-2′, and 3-3′, respectively. Profiles 4, 5, and 6 are the results of Model N merged with the extracted DEM profiles 4-4′, 5-5′, and 6-6′, respectively. In the legend exhibits different the viscosity of lower crust and mantle lithosphere in the Tibet Plateau.

As shown in the **Supplementary Figures S2, S3**, left profiles 4, 5, and 6 are the results of Model N merged with the extracted DEM profiles 4-4′, 5-5′, and 6-6′, respectively. Model NU1, Model NU2 and Model NU3 present Model N with weaker upper crust in Ruoergai block. Model NL present Model N with weaker lower crust in Ruoergai block. Right profiles 4, 5, and 6 are the results of Model AN (shown as model in **Supplementary Figure S1**) merged with the extracted DEM profiles 4-4′, 5-5′, and 6-6’, respectively. Model ANU1 and Model ANU2 present Model AN with weaker upper crust in Ruoergai block. The upper crust of Ruoergai block of Model NU1 has the same strength as the surrounding Bayan-Har Block. It is means that only lower crust is the strength part in the Ruoergai block Model NU1, thickness is about 35 km in the depth. The lower crust of Ruoergai block of Model NL is the same strength as the surrounding Bayan-Har Block. It is means that only upper crust is the strength part in the Ruoergai block of Model NL, thickness is about 25 km. These two profiles exhibit different uplift curve in the **Supplementary Figure S2**, which means the thickness of Ruoergai block impact the uplift result of modeling. In the legend exhibits different the viscosity of lower crust and mantle lithosphere in the Tibet Plateau. Eastern profile and Western profile exhibits in the Model AN referred Ruoergai block. (The parameter in Model NU1, Model NU2, Model NU3, Model NL, Model ANU1 and Model ANU2 shown in **Supplementary Table S1**).

In the northern profile as shown in **Supplementary Figure S3**. Left profiles 4, 5, and 6 is regarded to Model N, we could conclude that the better fitted model NU1 along Profile 4 with a lower crust viscosity 5×10^{22} Pa·s, an upper mantle viscosity 5×10^{22} Pa·s and cohesion of the upper crust in Ruoergai block is 10 MPa (It is equal to the cohesion of the upper crust of the Tibetan Plateau) obtained a better fitting effect. Profile four cross the southern margin of Ruoergai basin, the unobvious basin indicates that the strength of the upper crust here may not be large, or it may weaken as a whole. Profiles 5 and 6 were more suitably fitted model NU2 and model NU3 with a lower crust viscosity of 5×10^{22} Pa · s, an upper mantle viscosity of 10^{22} Pa · s and cohesion of the upper crust in Ruoergai block is 15–20 MPa. Right profiles 4, 5, and 6 is regarded to Model AN, result is not good as left profiles 4, 5, and 6. Regarding the AN model, the viscosity differed on both sides of the Ruoergai block. We could conclude that the improved fitted model along Profiles four and 5 with a lower crust viscosity of 10^{21} Pa·s and an upper mantle viscosity of 5×10^{22} Pa·s east of the Ruoergai block and a lower crust viscosity of 5×10^{22} Pa·s and an upper mantle viscosity of 2×10^{22} Pa·s west of the Ruoergai block achieved a better fitting effect. Profile 6 was better fitted with a lower crust viscosity of 10^{21} Pa·s and an upper mantle viscosity of 5×10^{22} Pa·s east of the Ruoergai block. Moreover, a lower crust viscosity of 5×10^{22} Pa·s and an upper mantle viscosity of 3×10^{22} Pa·s west of the Ruoergai block yielded better fitting results.

Based on our modeling results, we suggest that in the southern part of the Bayan Har block, the viscosity of the lower crust ranges from 10^{21} Pa·s–10^{22} Pa·s or is lower than 10^{21} Pa·s (in our simulations, a viscosity lower than 10^{21} Pa·s was not observed because the simulated time encompassed 10 million years), and the viscosity of the lithosphere (upper mantle) ranges from 10^{22} Pa·s–5×10^{22} Pa·s. In the northern part of the Bayan Har block, the viscosity of the lower crust is 5×10^{22} Pa·s, while the viscosity of the lithosphere (upper mantle) ranges from 10^{22} Pa·s–3×10^{22} Pa·s. Our results indicated that in the southern part of the Bayan Har block with a weaker lower crust (a weak layer or channel flow), the simulated topography better matched the real topography.

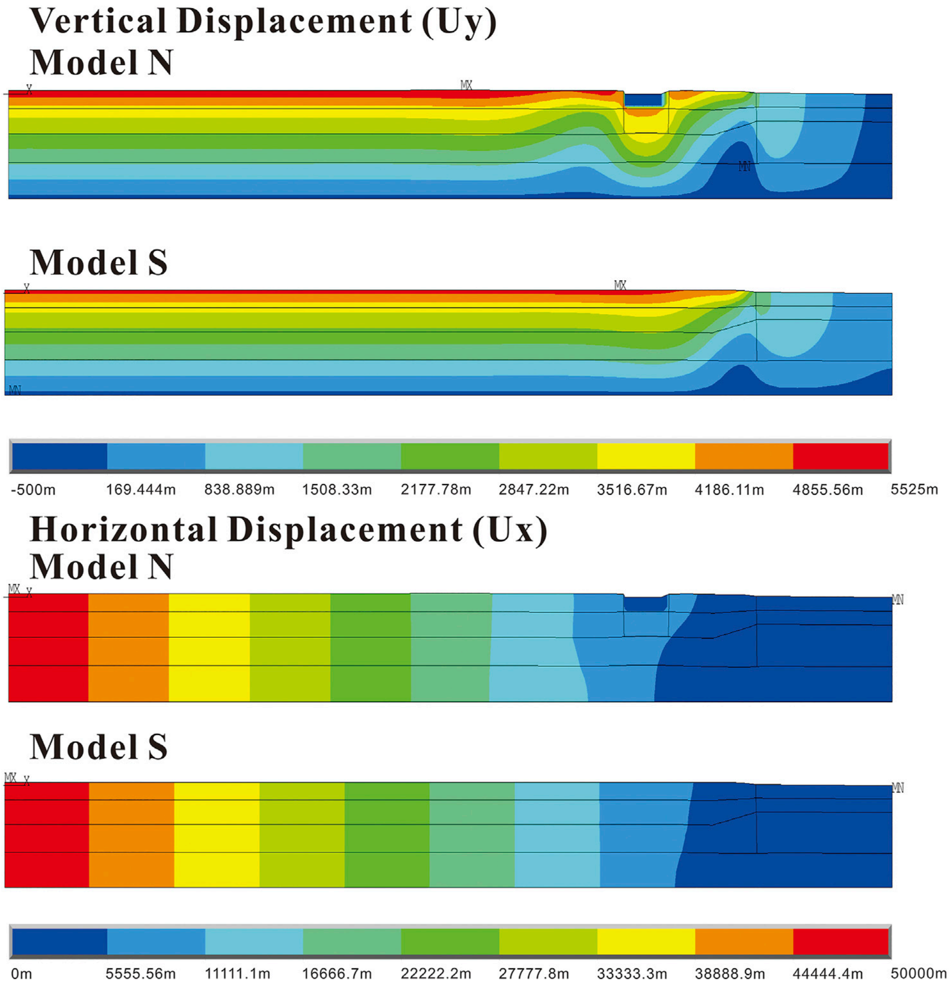

FIGURE 7 | Compared to the simulation results of displacements in Model S and Model N. The above two are the results of vertical displacement. The next two are the results of horizontal displacement. MX: Maximum displacement; MN: Minimum displacement; X: x direction.

We compare the modeling displacements result of the best fitting property. In the Model S viscosity of lower crust and mantle lithosphere (upper mantle) is 10^{21} Pa·s and 5×10^{22} Pa·s, respectively. In the Model S viscosity of lower crust and mantle lithosphere (upper mantle) is 5×10^{22} Pa·s and 10^{22} Pa·s, respectively. The node displacement in the modeling results (**Figure 7**) revealed that, due to the different crustal structures and properties, the closer to the Sichuan block, the more inconsistent the node displacement was. This suggests that the eastern Tibetan crust could be partially decoupled. Compared the result of displacements in the Model S and Model N, the horizontal and vertical displacements in the Model N is obviously smaller than it in the Model S.

DISCUSSION

The current landform is the result of the joint action of external and internal dynamic causes on the Earth's surface. In our research area, we should first exclude the factors of the difference between the northern and southern uplift processes of the Longmen Shan orogenic belt due to external dynamic reasons. In the southern Longmen Shan orogenic belt, in the hanging wall of the Wenchuan–Maoxian fault, the Xue-longbao massif yields AFT and AHe ages of ca. 2–3 Ma, and the magnitude can be measured since 10 Ma. Moreover, the highest exhumation rate is ~1 mm/a (Godard et al., 2009; Tan et al., 2017). In the northern Longmen Shan orogenic belt, the maximum exhumation rate is ~0.9 mm/a, as documented by the Pliocene cooling age (Kirby et al., 2002; Tan et al., 2019). The exhumation rate can also reflect external dynamic reasons (personal communication with Tan), which suggests that the erosion level in the northern Longmen Shan orogenic belt is lower than that in the southern Longmen Shan orogenic belt. Hence, we can exclude the factors of the difference between the northern and southern uplift processes of the Longmen Shan orogenic belt due to external dynamic reasons.

One of the most obvious differences across the north–south section of the Longmen Shan orogenic belt is the presence of a rigid Ruoergai block in the north. We defined Models S and N

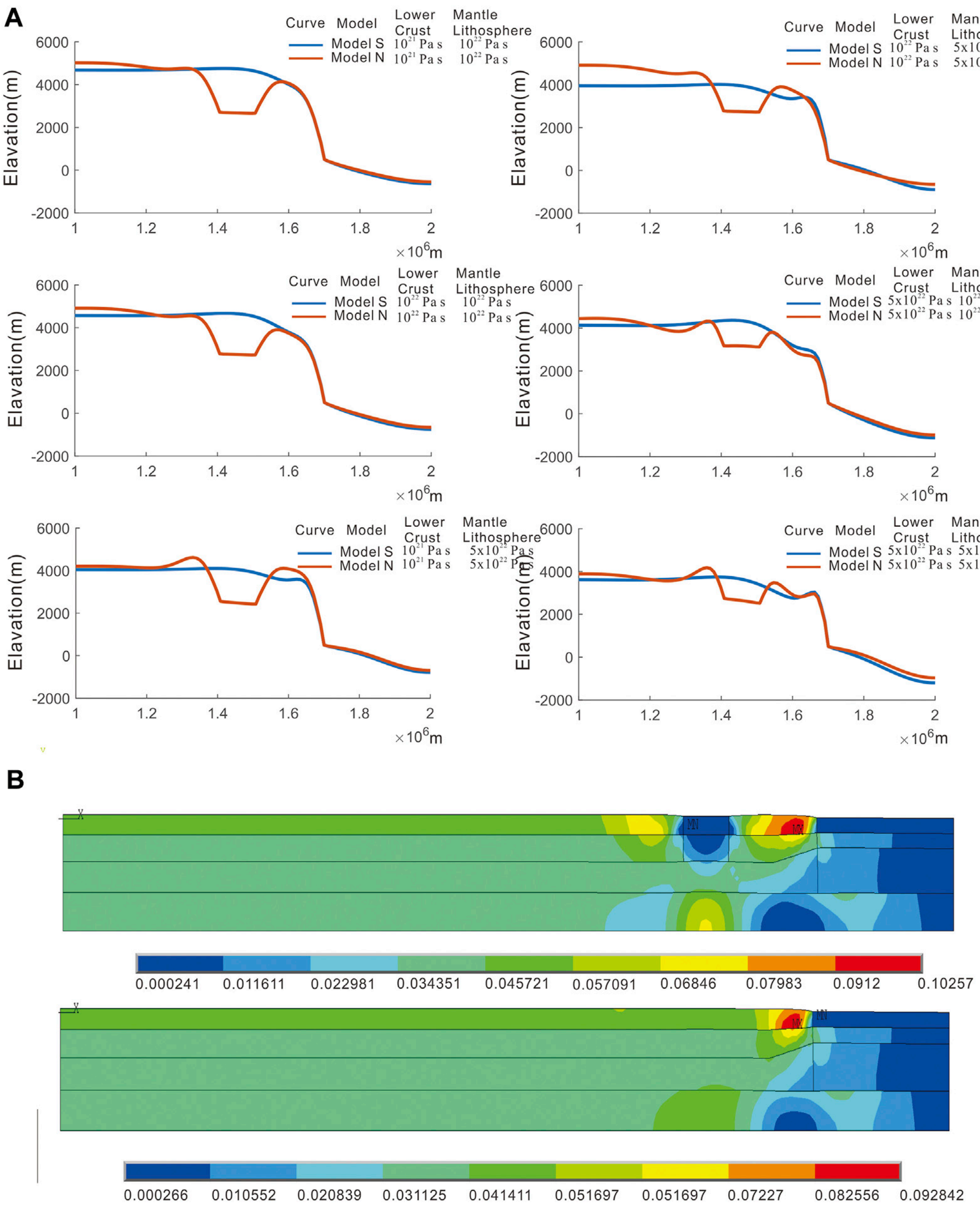

FIGURE 8 | (A) Compared to the simulation results, there is only a single variable Ruoergai rigid block. **(B)** Comparing the strain results of the simulations, there only occurs a single variable Ruoergai rigid block. MX: Maximum strain; MN: Minimum strain; X: x direction.

with the same properties, and the only difference was the occurrence of a rigid Ruoergai block in Model N. The results (**Figure 8A**) suggest that if only the lithospheric properties remain the same and only a rigid Ruoergai block occurs, it is difficult to alter the slope of the northern uplift. This could eventually lead to the final convergence height of the northern plateau exceeding that of the southern plateau. The resistance of the Ruoergai block could result in strain concentration on both sides of the rigid block, further causing more severe uplift (**Figure 8B**). The presence of the Ruoergai block is not the only reason for the different strain partitioning results in the Longmen Shan block. We could confirm that the existence of the Ruoergai block could not explain our observed results.

Through analysis of GNSS data (Gan et al., 2007; Zheng et al., 2017; Wang and Shen, 2020), the current GPS rate change across the north–south section of the Longmen Shan fault tends to remain consistent (**Figure 9**). Our GPS rate change supports the strain-partitioning model: oblique extrusion motion of eastern Tibet is partitioned dominantly by strike-slip motion on the Longriba fault and dip-slip motion for the Longmen Shan thrust belt (Ren et al., 2013; Li et al., 2018). Moreover, the local shortening rates of the piedmont and hinterland between

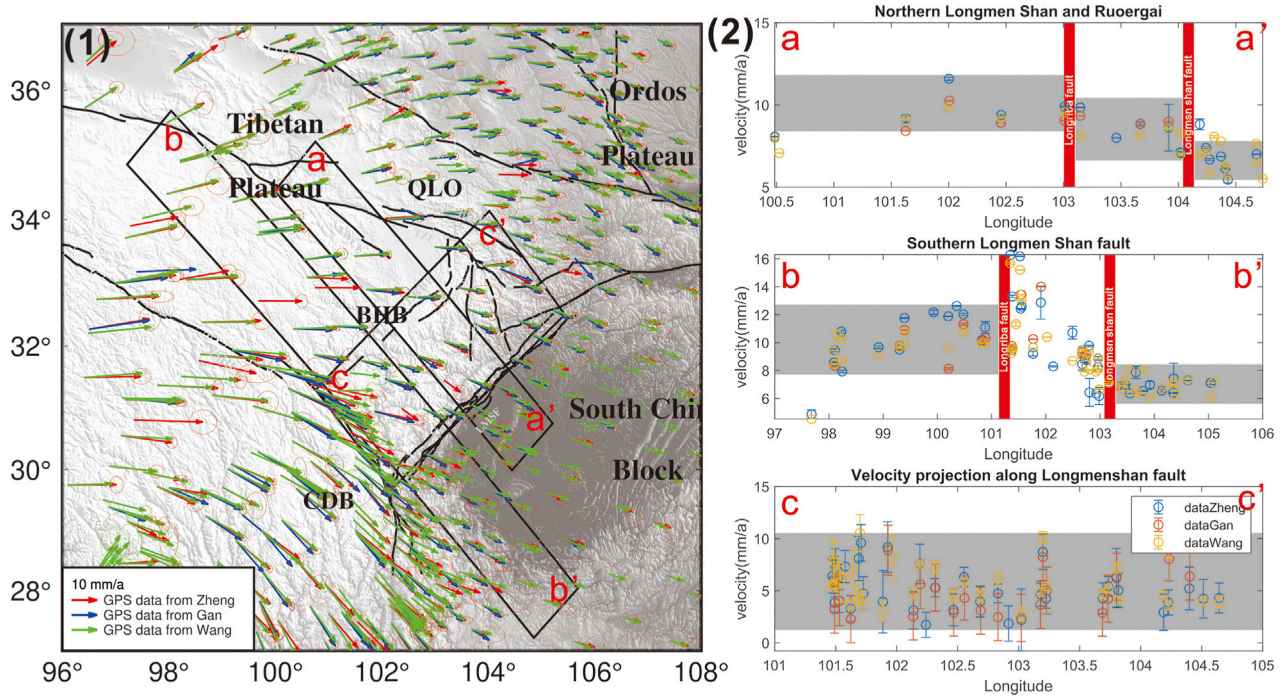

FIGURE 9 | Analysis of the GNSS extraction data. **(1)** GNSS datasets from (Gan et al., 2007; Zheng et al., 2017; Wang and Shen, 2020) visualized in the map and 3 extraction areas based on the GNSS data. **(2)** Profiles a-a', b-b' Extracted GNSS data within the box range and projected velocity field perpendicular to the Longmen Shan fault. Profile c-c' GPS data are extracted within the box, and the velocity field is projected parallel to the Longmen Shan fault. BHB: Bayan-Har Block; QLO: Qinling Orogen; CDB: Chuandian Block.

the central and the southern Longmen Shan orogenic belt are slightly different, they tend to be consistent as a whole (Li Z. et al., 2019). However, GPS data suggest that there occurs no obvious weakening along the northern profile, further there exists no notable difference in stress and strain between the northern and southern parts of the Longmen Shan fault section. Velocity in both profiles decelerate from about 11 mm/a to about 6 mm/a. Therefore, the stress–strain fields along the north–south profile perpendicular to the Longmen fault do not explain the difference in uplift between the northern and southern ends. The uplift difference between the north and South profiles is mainly caused by the vertical uplift difference under the surface. It should be caused by the different strain of the whole lithosphere mantle and the different decoupling degree of the upper crust from the lower crust.

The velocity of the surface nodes extracted from our simulation results is projected into the North-South profiles of GPS observation data (**Supplementary Figure S5**). The results show that the rate of simulation results decreases continuously from west to East, and remains stable after reaching the Sichuan block. The rate decrease in the Model N is slightly greater than that in the Model S, indicating that the Ruoergai rigid block still has a certain resistance effect in the eastern extrusion process of Bayan Har block (**Supplementary Figure S6**).

Along the Longmen Shan fault zone, the velocity component parallel to the northern end of the Longmen Shan fault zone does not significantly increase at the northern end of the Longmen Shan fault.

The advanced velocity field does not indicate that the material has been subjected to obvious northward escape. Northward motion is not the obvious reason why the northern Longman Shan uplift is weaker than the southern part.

Several studies have demonstrated that the southern Longmen Shan fault and northern Longmen Shan fault exhibit different dip angles (Xu X. et al., 2009; Shen et al., 2009) Moreover, the Moho ramp differs between the southern Longmen Shan fault and northern Longmen Shan fault (Laske et al., 2013). Therefore, we adjusted the dip angle of Model S and compared the results (shown as model in **Supplementary Figure S4**). The results indicate that the above change in dip angle affected the final uplift height, but it remained difficult to improve the uplift slope. The gentle Moho ramp will lead to more intense uplift in the north of the Longmen Shan orogenic belt. In order to obtain better fitting results, the viscosity coefficient of the lower crust is about 5×10^{22} Pa · s and the viscosity coefficient of the mantle lithospheric is 10^{22} Pa · s. This result has a stronger viscosity coefficient of the lower crust than the previous results (shown as model in **Supplementary Figures S7, S8**).

The channel flow theory gives a new explanation to the deformation and strain distribution of the Qinghai Tibet Plateau (Royden et al., 1997; Clark and Royden, 2000). A series of subsequent studies on geothermal, electromagnetic

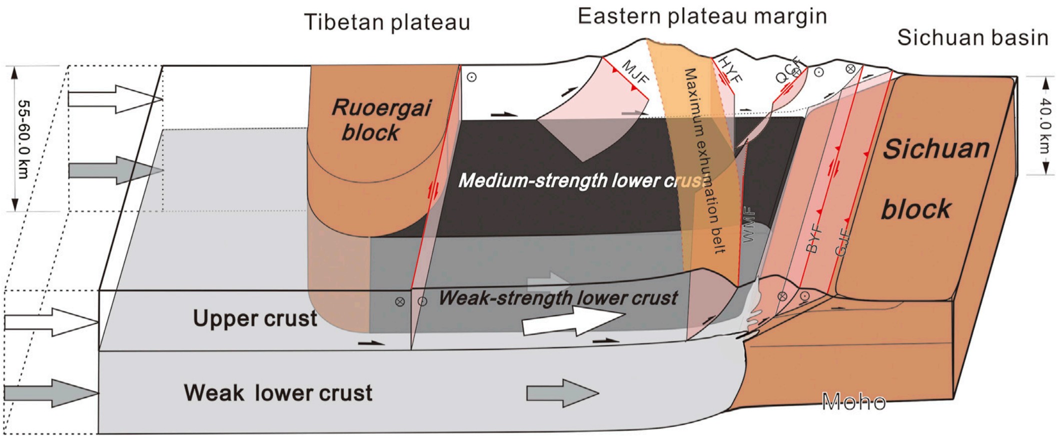

FIGURE 10 | Our conceptual tectonic models for the eastern margin of the Tibetan plateau crossed the Longmen Shan orogenic belt. The model further integrates the rigid Ruoergai block, Sichuan block and our simulation results. After imposing a uniform displacement field on the west side of the model, upper and lower crust movements are partially decoupled near the Sichuan block. Due to the weak layer in the lower crust south of the Bayan Har block, the lower crust uplifts the plateau more in the shortening process of the movement of the Bayan Har block. The red lines indicate the fault traces. The maximum exhumation belt represents the maximum uplift area (Tan et al., 2019).

and seismic wave reflection also confirmed the existence of a high temperature and low resistivity layer in the middle and lower crust of the Tibetan Plateau (Wang, 2001; Unsworth et al., 2005; Gao et al., 2009; Bai et al., 2010). Subsequently, it caused an upsurge in the study of the viscosity coefficient of the lower crust of the Tibetan Plateau. According to Clark's research, the viscosity coefficient of the middle and lower crust is 10^{16} Pa · s (Clark and Royden, 2000). A series of subsequent numerical simulation studies believe that the viscosity coefficient is from 10^{18} Pa · s to 10^{21} Pa · s (Wang and He, 2012; Bischoff and Flesch, 2018; Luo and Liu, 2018). Some series of geophysical studies have also confirmed that there is heterogeneity in the crust in this area (Wang et al., 2003; Xu Y. et al., 2009; Lei and Zhao, 2009). From the previous discussion, it can be seen that the inconsistent uplift of the North-South Longmen Shan orogenic belt may be caused by the difference of rheological properties of the middle and lower crust and upper mantle in the region. The above studies are basically consistent with the simulation results in the southern Longmen Shan orogenic belt of this paper, and this study shows that the middle and lower crust of the Longmen Shan orogenic belt in the north will be slightly larger than that in the south. Excluding all the factors above, considering our modeling results, we suggest that the obtained difference in uplift between the southern and northern Longmen Shan orogenic belts is caused by a difference in lithospheric properties. Several geophysical studies support our findings (Wang et al., 2003; Xu Y. et al., 2009; Lei and Zhao, 2009). Considering that the abovementioned existence also impacts strain partitioning in the study area, we proposed a new model (**Figure 10**).

Previous studies have pointed out that the weak lower crust may be formed by partial melting of crust at depths of 15–50 km in areas under the environment of high temperature and high pressure (Wang Q. et al., 2016). It is also pointed out that the weak lower crust has a certain fluidity, and shear action of channel flow on the upper crust caused the rapid uplift of Longmen Shan area (Clark and Royden, 2000; Bai et al., 2010). The existence of Ruoergai rigid block may resisted the weak lower crust in the process of eastward movement, further cause the weak lower crust can not effectively enter the northern lower crust of Longmen Shan orogenic belt. The simulation results show that the deformation of the lower crust in the northern Longmen Shan orogenic belt is weaker than it in the south, which may lead to the weaker partial melting of the crust and the formation of less weak materials in the lower crust of the northern Longmen Shan orogenic belt. Therefore, the rigid Ruoergai block resists the formation of a weak layer or enters the northern Longmen Shan block, resulting in the observed difference in lithospheric properties between the northern and southern Longmen Shan blocks. Moreover, the eastern Tibetan crust is partially decoupled in the shortening process of the lithosphere. Thus, the above uplift difference between the northern and southern Longmen Shan blocks is generated.

The structure of the lithospheric mantle in the eastern margin of the Tibetan Plateau is very complex. It collides with the rigid Sichuan block and also has a complex three-dimensional structure (Wang M. et al., 2016). In particular, the Longmen Shan orogenic belt produced by compression with the rigid Sichuan block, which has a low thrust angle, steep moho ramp and strong Baoxing and Pengguan Massifs in deep depth at the southern Longmen Shan orogenic belt. There is a high thrust dip angle with a dextral strike slip component, a gentle Moho ramp at the northern Longmen Shan orogenic belt (Feng et al., 2021). Further, the Bikou block is an important block which is located between the Longmen Shan fault and the Minjiang fault. Its strength is high and it has a Proterozoic basement. Bikou block, Pengguan massif and Baoxing massif have very high strength (Zhan et al., 2013; Zhao et al., 2012). Since these hard small blocks exist, the high-steep change belt can be distributed along the zone of Minjiang-southern segment of the Longmen Shan fault. Due to the shortcomings and limitations of this work, it does not completely discuss these blocks. We will further improve these points in our future work. Previous studies have also proved that the rheological heterogeneity of Longmen Shan orogenic belt determines the difference of deformation and strain distribution in the North-South section of Longmen Shan orogenic belt (Sun et al., 2019). More reasonable model is considering of the three-dimensional strength inhomogeneity. That is the key to study the geomorphology, lithospheric deformation and strain distribution. Our work explains the difference of North-South uplift of Longmen Shan orogenic belt from a new perspective. I hope to provide more thinking directions for the future research work in this area.

CONCLUSION

Based on our simulation results and relevant observation data, we obtained the following conclusions:

1. The eastern Tibetan crust is partially decoupled between the upper crust and lower crust. The deformation of lithosphere in the northern Longmen Shan orogenic belt is smaller than it in southern Longmen Shan orogenic belt.
2. The mechanical properties of the lithosphere south of the Longmen Shan orogenic belt were slightly less favorable than those of the lithosphere north of the Longmen Shan orogenic belt. For the better fitting result in the southern part viscosity of lower crust is less than 10^{21} Pa·s and in the northern part viscosity of lower crust is around 10^{22} Pa·s. The viscosity of the southern Longmen Shan block is lower than that of the northern part.
3. The presence of the Ruoergai block impacts strain partitioning in the Longmen Shan block. However, the difference in uplift between the southern and northern Longmen Shan orogenic belts is caused by a difference in lithospheric properties.
4. The Ruoergai block resists the formation of a weak layer or enters of weak materials to the northern Longmen Shan block, resulting in the abovementioned difference in lithospheric properties between the northern and southern Longmen Shan blocks. Thus, the observed uplift difference between the northern and southern Longmen Shan blocks can be explained.

DATA AVAILABILITY STATEMENT

Publicly available datasets were analyzed in this study. This data can be found here: https://doi.org/10.1029/2005JB004120 GPS Gan Weijun https://doi.org/10.1002/2017JB014465 GPS Zheng Gang https://doi.org/10.7910/DVN/C1WE3N GPS Wang Min.

AUTHOR CONTRIBUTIONS

TS conceived the study, performed numerical experiments, interpreted results and wrote the manuscript. XX, and YL help to organize ideas and experiments, further help to interpreted results. LH and YL contributed to the modeling process. QW contributed to the GPS analysis part. QW, WK, and XL contributed to the geological analysis and discussion part.

FUNDING

This work was supported by the Research Grant from the National Institute of Natural Hazards, Ministry of Emergency Management of China Research Fund (ZDJ2020-03), National Key Research and Development Project of China (2018YFC1504101), National Natural Science Foundation of China, China (grant numbers 41902217, 40802052, U2139201 & U1839204), KAUST award BAS/1/1353-01-01, ANR project ANR-005-CATT-0006 and National Institute of Natural Hazards, Ministry of Emergency Management of China Research Fund (ZDJ2017-24).

ACKNOWLEDGMENTS

We benefited from discussion with Zhou shiyong.

SUPPLEMENTARY MATERIAL

The Supplementary Material for this article can be found online at: https://www.frontiersin.org/articles/10.3389/feart.2022.895363/full#supplementary-material

REFERENCES

Bai, D., Unsworth, M. J., Meju, M. A., Ma, X., Teng, J., Kong, X., et al. (2010). Crustal Deformation of the Eastern Tibetan Plateau Revealed by Magnetotelluric Imaging. *Nat. Geosci.* 3, 358–362. doi:10.1038/ngeo830

Bischoff, S. H., and Flesch, L. M. (2018). Normal Faulting and Viscous Buckling in the Tibetan Plateau Induced by a Weak Lower Crust. *Nat. Commun.* 9. doi:10.1038/s41467-018-07312-9

Burchfiel, B. C., Royden, L. H., van der Hilst, R. D., Hager, B. H., Chen, Z., King, R. W., et al. (2008). A Geological and Geophysical Context for the Wenchuan Earthquake of 12 May 2008, Sichuan, People's Republic of China. *GSA Today* 18, 4–11. doi:10.1130/GSATG18A.1

Chen, L., Zhang, P., Lu, Y., Chen, H., Ma, H., Li, L., et al. (2008). Numerical Simulation of Loading/unloading Effect on Coulomb Failure Stress Among Strong Earthquakes in Sichuan-Yunnan Area. *Chin. J. Geophys.*, 1411–1421. *(in Chinese)*. doi:10.3321/j.issn:0001-5733.2008.05.014

Clark, M. K., and Royden, L. H. (2000). Topographic Ooze: Building the Eastern Margin of Tibet by Lower Crustal Flow. *Geology* 28, 703. doi:10.1130/0091-7613(2000)028<0703:tobtem>2.3.co;2

Clark, M. K., Bush, J. W. M., and Royden, L. H. (2005). Dynamic Topography Produced by Lower Crustal Flow against Rheological Strength Heterogeneities

Bordering the Tibetan Plateau. *Geophys. J. Int.* 162, 575–590. doi:10.1111/j.1365-246X.2005.02580.x

Ding, H., Zhang, Z., Dong, X., Tian, Z., Xiang, H., Mu, H., et al. (2016). Early Eocene (C . 50 Ma) Collision of the Indian and Asian Continents: Constraints from the North Himalayan Metamorphic Rocks, Southeastern Tibet. *Earth Planet. Sci. Lett.* 435, 64–73. doi:10.1016/j.epsl.2015.12.006

Feng, M., Qian, H., Mechie, J., An, M., Li, H., Xue, G., et al. (2021). Crustal Seismogenic Structures and Deformation Styles along the Longmen Shan Fault Belt in the Eastern Tibetan Plateau Inferred from Ambient Noise Tomography. *Tectonophysics* 798, 228689. doi:10.1016/j.tecto.2020.228689

Feng, S. y., Zhang, P. z., Liu, B. j., Wang, M., Zhu, S. b., Ran, Y. k., et al. (2016). Deep Crustal Deformation of the Longmen Shan, Eastern Margin of the Tibetan Plateau, from Seismic Reflection and Finite Element Modeling. *J. Geophys. Res. Solid Earth* 121, 767–787. doi:10.1002/2015JB012352

Gan, W., Zhang, P., Shen, Z.-K., Niu, Z., Wang, M., Wan, Y., et al. (2007). Present-day Crustal Motion within the Tibetan Plateau Inferred from GPS Measurements. *J. Geophys. Res.* 112, 1–14. doi:10.1029/2005JB004120

Gao, R., Wang, H., Zeng, L., Zhang, J., Guo, T., Li, Q., et al. (2014). The Crust Structures and the Connection of the Songpan Block and West Qinling Orogen Revealed by the Hezuo-Tangke Deep Seismic Reflection Profiling. *Tectonophysics* 634, 227–236. doi:10.1016/j.tecto.2014.08.014

Gao, X., Su, Y., Wang, W., Pei, S., and Guo, Z. (2009). Lower-crust S-Wave Velocity beneath Western Yunnan Province from Waveform Inversion of Dense Seismic Observations. *Terra Nov.* 21, 105–110. doi:10.1111/j.1365-3121.2008.00862.x

Godard, V., Pik, R., Lavé, J., Cattin, R., Tibari, B., de Sigoyer, J., et al. (2009). Late Cenozoic Evolution of the Central Longmen Shan, Eastern Tibet: Insight from (U-Th)/He Thermochronometry. *Tectonics* 28, a–n. doi:10.1029/2008TC002407

Guo, X., Gao, R., Randy Keller, G., Xu, X., Wang, H., and Li, W. (2013). Imaging the Crustal Structure beneath the Eastern Tibetan Plateau and Implications for the Uplift of the Longmen Shan Range. *Earth Planet. Sci. Lett.* 379, 72–80. doi:10.1016/j.epsl.2013.08.005

He, J., Lu, S., and Wang, W. (2013). Three-dimensional Mechanical Modeling of the GPS Velocity Field Around the Northeastern Tibetan Plateau and Surrounding Regions. *Tectonophysics* 584, 257–266. doi:10.1016/j.tecto.2012.03.025

Hu, G., Yu, L., Dong, Z., Lu, J., Li, J., Wang, Y., et al. (2018). Holocene Aeolian Activity in the Zoige Basin, Northeastern Tibetan Plateau, China. *Catena* 160, 321–328. doi:10.1016/j.catena.2017.10.005

Hubbard, J., and Shaw, J. H. (2009). Uplift of the Longmen Shan and Tibetan Plateau, and the 2008 Wenchuan (M = 7.9) Earthquake. *Nature* 458, 194–197. doi:10.1038/nature07837

Jia, D., Li, Y., Lin, A., Wang, M., Chen, W., Wu, X., et al. (2010a). Structural Model of 2008 Mw 7.9 Wenchuan Earthquake in the Rejuvenated Longmen Shan Thrust Belt, China. *Tectonophysics* 491, 174–184. doi:10.1016/j.tecto.2009.08.040

Jia, D., Wei, G., Chen, Z., Li, B., Zeng, Q., and Yang, G. (2006). Longmen Shan Fold-Thrust Belt and its Relation to the Western Sichuan Basin in Central China: New Insights from Hydrocarbon Exploration. *Bulletin* 90, 1425–1447. doi:10.1306/03230605076

Jia, S., Zhang, X., Zhao, J., Wang, F., Zhang, C., Xu, Z., et al. (2010b). Deep Seismic Sounding Data Reveal the Crustal Structures beneath Zoigê Basin and its Surrounding Folded Orogenic Belts. *Sci. China Earth Sci.* 53, 203–212. doi:10.1007/s11430-009-0166-0

Jiang, X., and Jin, Y. (2005). Mapping the Deep Lithospheric Structure beneath the Eastern Margin of the Tibetan Plateau from Gravity Anomalies. *J. Geophys. Res.* 110, B07407. doi:10.1029/2004JB003394

Jin, W., Tang, L., Yang, K., Wan, G., and Lü, Z. (2010). Segmentation of the Longmen Mountains Thrust Belt, Western Sichuan Foreland Basin, SW China. *Tectonophysics* 485, 107–121. doi:10.1016/j.tecto.2009.12.007

Kirby, E., Reiners, P. W., Krol, M. A., Whipple, K. X., Hodges, K. V., Farley, K. A., et al. (2002). Late Cenozoic Evolution of the Eastern Margin of the Tibetan Plateau: Inferences from40Ar/39Ar and (U-Th)/He Thermochronology. *Tectonics* 21, 1. doi:10.1029/2000TC001246

Laske, G., Masters, G., Ma, Z., and Pasyanos, M. (2013). Update on CRUST1. 0 A 1-degree Global Model of Earth's Crust. *Geophys. Res. Abstr.* 15, 2658.

Lei, J., Li, Y., Xie, F., Teng, J., Zhang, G., Sun, C., et al. (2014). Pn Anisotropic Tomography and Dynamics under Eastern Tibetan Plateau. *J. Geophys. Res. Solid Earth* 119, 2174–2198. doi:10.1002/2013JB010847

Lei, J., and Zhao, D. (2009). Structural Heterogeneity of the Longmenshan Fault Zone and the Mechanism of the 2008 Wenchuan Earthquake (Ms 8.0). *Geochem. Geophys. Geosyst.* 10, a–n. doi:10.1029/2009GC002590

Li, Y., Liu, M., Li, Y., and Chen, L. (2019b). Active Crustal Deformation in Southeastern Tibetan Plateau: The Kinematics and Dynamics. *Earth Planet. Sci. Lett.* 523, 115708. doi:10.1016/j.epsl.2019.07.010

Li, Z.-W., Liu, S., Chen, H., Deng, B., Hou, M., Wu, W., et al. (2012). Spatial Variation in Meso-Cenozoic Exhumation History of the Longmen Shan Thrust Belt (Eastern Tibetan Plateau) and the Adjacent Western Sichuan Basin: Constraints from Fission Track Thermochronology. *J. Asian Earth Sci.* 47, 185–203. doi:10.1016/j.jseaes.2011.10.016

Li, Z., Zhang, P., Zheng, W., Jia, D., Hubbard, J., Almeida, R., et al. (2018). Oblique Thrusting and Strain Partitioning in the Longmen Shan Fold-and-Thrust Belt, Eastern Tibetan Plateau. *J. Geophys. Res. Solid Earth* 123, 4431–4453. doi:10.1029/2018JB015529

Li, Z., Zheng, W., Zhang, P., Almeida, R., Jia, D., Sun, C., et al. (2019a). Evidence for Three Cenozoic Phases of Upper Crustal Shortening of the Xiongpo Structure in the Longmen Shan Fold-And-Thrust Belt, China: Implications for the Eastward Growth of the Eastern Tibetan Plateau. *J. Asian Earth Sci.* 179, 138–148. doi:10.1016/j.jseaes.2019.04.017

Lin, A., Ren, Z., Jia, D., and Wu, X. (2009). Co-seismic Thrusting Rupture and Slip Distribution Produced by the 2008 Mw 7.9 Wenchuan Earthquake, China. *Tectonophysics* 471, 203–215. doi:10.1016/j.tecto.2009.02.014

Luo, G., and Liu, M. (2018). Stressing Rates and Seismicity on the Major Faults in Eastern Tibetan Plateau. *J. Geophys. Res. Solid Earth* 123 (10), 968. doi:10.1029/2018jb015532

Maus, S., Sazonova, T., Hemant, K., Fairhead, J. D., and Ravat, D. (2007). National Geophysical Data Center Candidate for the World Digital Magnetic Anomaly Map. *Geochem. Geophys. Geosyst.* 8, a–n. doi:10.1029/2007GC001643

Molnar, P., and Tapponnier, P. (1975). Cenozoic Tectonics of Asia: Effects of a Continental Collision: Features of Recent Continental Tectonics in Asia Can Be Interpreted as Results of the India-Eurasia Collision. *Science* 189, 419–426. doi:10.1126/science.189.4201.419

Qasim, M., Ding, L., Khan, M. A., Jadoon, I. A. K., Haneef, M., Baral, U., et al. (2018). Tectonic Implications of Detrital Zircon Ages from Lesser Himalayan Mesozoic-Cenozoic Strata, Pakistan. *Geochem. Geophys. Geosyst.* 19, 1636–1659. doi:10.1002/2017GC006895

Ren, J., Xu, X., Yeats, R. S., and Zhang, S. (2013). Latest Quaternary Paleoseismology and Slip Rates of the Longriba Fault Zone, Eastern Tibet: Implications for Fault Behavior and Strain Partitioning. *Tectonics* 32, 216–238. doi:10.1002/tect.20029

Royden, L. H., Burchfiel, B. C., King, R. W., Wang, E., Chen, Z., Shen, F., et al. (1997). Surface Deformation and Lower Crustal Flow in Eastern Tibet. *Science* 276, 788–790. doi:10.1126/science.276.5313.788

Schellart, W. P., Chen, Z., Strak, V., Duarte, J. C., and Rosas, F. M. (2019). Pacific Subduction Control on Asian Continental Deformation Including Tibetan Extension and Eastward Extrusion Tectonics. *Nat. Commun.* 10, 12337. doi:10.1038/s41467-019-12337-9

Shen, X., Tian, Y., Zhang, G., Zhang, S., Carter, A., Kohn, B., et al. (2019). Late Miocene Hinterland Crustal Shortening in the Longmen Shan Thrust Belt, the Eastern Margin of the Tibetan Plateau. *J. Geophys. Res. Solid Earth* 124, 11972–11991. doi:10.1029/2019JB018358

Shen, Z.-K., Sun, J., Zhang, P., Wan, Y., Wang, M., Bürgmann, R., et al. (2009). Slip Maxima at Fault Junctions and Rupturing of Barriers during the 2008 Wenchuan Earthquake. *Nat. Geosci.* 2, 718–724. doi:10.1038/ngeo636

Shi, Y., and Cao, J. (2008). Lithosphere Effective Viscosity of Continental China. *Earth Sci. Front.* 15, 82–95. doi:10.1016/s1872-5791(08)60064-0

Sun, C., Jia, D., Yin, H., Chen, Z., Li, Z., Shen, L., et al. (2016). Sandbox Modeling of Evolving Thrust Wedges with Different Preexisting Topographic Relief: Implications for the Longmen Shan Thrust Belt, Eastern Tibet. *J. Geophys. Res. Solid Earth* 121, 4591–4614. doi:10.1002/2016JB013013

Sun, M., Yin, A., Yan, D., Ren, H., Mu, H., Zhu, L., et al. (2018). Role of Pre-existing Structures in Controlling the Cenozoic Tectonic Evolution of the Eastern

Tibetan Plateau: New Insights from Analogue Experiments. *Earth Planet. Sci. Lett.* 491, 207–215. doi:10.1016/j.epsl.2018.03.005

Sun, X., Zhan, Y., Zhao, L., Chen, X., Sun, J., Li, C., et al. (2019). Electrical Structure of the Kunlun-Qinling Fault System, Northeastern Tibetan Plateau, Inferred from 3-D Inversion of Magnetotelluric Data. *J. Asian Earth Sci.* 181, 103910. doi:10.1016/j.jseaes.2019.103910

Sun, Y., Li, H., and Fan, T. (2019). A Numerical Study of Lithospheric Deformation and Strain Partitioning across the Longmen Shan Orogenic Belt, Eastern Tibetan Plateau. *Tectonics* 38, 3108–3123. doi:10.1029/2019TC005512

Sun, Y., and Liu, M. (2018). Rheological Control of Lateral Growth of the Tibetan Plateau: Numerical Results. *J. Geophys. Res. Solid Earth* 123 (10), 10124–10141. doi:10.1029/2018JB016601

Tan, X.-B., Xu, X.-W., Lee, Y.-H., Lu, R.-Q., Liu, Y., Xu, C., et al. (2017). Late Cenozoic Thrusting of Major Faults along the Central Segment of Longmen Shan, Eastern Tibet: Evidence from Low-Temperature Thermochronology. *Tectonophysics* 712-713, 145–155. doi:10.1016/j.tecto.2017.05.016

Tan, X., Liu, Y., Lee, Y.-H., Lu, R., Xu, X., Suppe, J., et al. (2019). Parallelism between the Maximum Exhumation Belt and the Moho Ramp along the Eastern Tibetan Plateau Margin: Coincidence or Consequence? *Earth Planet. Sci. Lett.* 507, 73–84. doi:10.1016/j.epsl.2018.12.001

Tapponnier, P., and Molnar, P. (1977). Active Faulting and Tectonics in China. *J. Geophys. Res.* 82, 2905–2930. doi:10.1029/JB082i020p02905

Tapponnier, P., Peltzer, G., Le Dain, A. Y., Armijo, R., and Cobbold, P. (1982). Propagating Extrusion Tectonics in Asia: New Insights from Simple Experiments with Plasticine. *Geology* 10, 611–661. doi:10.1130/0091-7613(1982)10<611:PETIAN>2.010.1130/0091-7613(1982)10<611:petian>2.0.co;2

Tapponnier, P., Zhiqin, X., Roger, F., Meyer, B., Arnaud, N., Wittlinger, G., et al. (2001). Oblique Stepwise Rise and Growth of the Tibet Plateau. *Science* 294, 1671–1677. doi:10.1126/science.105978

Unsworth, M. J., Jones, A. G., Jones, A. G., Wei, W., Marquis, G., Gokarn, S. G., et al. (2005). Crustal Rheology of the Himalaya and Southern Tibet Inferred from Magnetotelluric Data. *Nature* 438, 78–81. doi:10.1038/nature04154

Wang, E., Kirby, E., Furlong, K. P., Van Soest, M., Xu, G., Shi, X., et al. (2012). Two-phase Growth of High Topography in Eastern Tibet during the Cenozoic. *Nat. Geosci.* 5, 640–645. doi:10.1038/ngeo1538

Wang, E., Meng, Q., Clark Burchfiel, B., and Zhang, G. (2003). Mesozoic Large-Scale Lateral Extrusion, Rotation, and Uplift of the Tongbai-Dabie Shan Belt in East China. *Geology* 31, 3072–3310. doi:10.1130/0091-7613(2003)031<0307:mlsler>2.0.co;2

Wang, M., Hubbard, J., Plesch, A., Shaw, J. H., and Wang, L. (2016a). Three-dimensional Seismic Velocity Structure in the Sichuan Basin, China. *J. Geophys. Res. Solid Earth* 121, 1007–1022. doi:10.1002/2015JB012644

Wang, M., and Shen, Z. K. (2020). Present-Day Crustal Deformation of Continental China Derived from GPS and its Tectonic Implications. *J. Geophys. Res. Solid Earth* 125, 8774. doi:10.1029/2019JB018774

Wang, Q., Hawkesworth, C. J., Wyman, D., Chung, S.-L., Wu, F.-Y., Li, X.-H., et al. (2016b). Pliocene-Quaternary Crustal Melting in Central and Northern Tibet and Insights into Crustal Flow. *Nat. Commun.* 7, 11888. doi:10.1038/ncomms11888

Wang, X., and He, J. (2012). Channel Flow of the Lower Crust and its Relation to Large-Scale Tectonic Geomorphology of the Eastern Tibetan Plateau. *Sci. China Earth Sci.* 55, 1383–1390. doi:10.1007/s11430-012-4391-6

Wang, Y. (2001). Heat Flow Pattern and Lateral Variations of Lithosphere Strength in China Mainland: Constraints on Active Deformation. *Phys. Earth Planet. Interiors* 126, 121–146. doi:10.1016/S0031-9201(01)00251-5

Wei, X., Jiang, M., Liang, X., Chen, L., and Ai, Y. (2017). Limited Southward Underthrusting of the Asian Lithosphere and Material Extrusion beneath the Northeastern Margin of Tibet, Inferred from Teleseismic Rayleigh Wave Tomography. *J. Geophys. Res. Solid Earth* 122, 7172–7189. doi:10.1002/2016JB013832

Xin, H., Zhang, H., Kang, M., He, R., Gao, L., and Gao, J. (2018). High-Resolution Lithospheric Velocity Structure of Continental China by Double-Difference Seismic Travel-Time Tomography. *Seismol. Res. Lett.* 90, 229–241. doi:10.1785/0220180209

Xu, X., Keller, G. R., Gao, R., Guo, X., and Zhu, X. (2016). Uplift of the Longmen Shan Area in the Eastern Tibetan Plateau: an Integrated Geophysical and Geodynamic Analysis. *Int. Geol. Rev.* 58, 14–31. doi:10.1080/00206814.2015.1055595

Xu, X., Wen, X., Yu, G., Chen, G., Klinger, Y., Hubbard, J., et al. (2009a). Coseismic Reverse- and Oblique-Slip Surface Faulting Generated by the 2008 Mw 7.9 Wenchuan Earthquake, China. *Geology* 37, 515–518. doi:10.1130/G25462A.1

Xu, Y., Huang, R.-Q., Li, Z.-W., Xu, Y., Liu, J.-S., and Liu, J.-H. (2009b). S-wave Velocity Structure of the Longmen Shan and Wenchuan Earthquake Area. *Chin. J. Geophys.* 52, 329

Xu, Z., Hou, L.-W., Wang, D.-K., and Wang, Z. (1991). Xikang-type'folds and Their Deformation Mechanism A New Fold Type in Orogenic Belts. *Reg. Geol. China* 1, 1

Yin, A. (2010). Cenozoic Tectonic Evolution of Asia: a Preliminary Synthesis. *Tectonophysics* 488, 293–325. doi:10.1016/j.tecto.2009.06.002

Yin, A., and Harrison, T. M. (2000). Geologic Evolution of the Himalayan-Tibetan Orogen. *Annu. Rev. Earth Planet. Sci.* 28, 211–280. doi:10.1146/annurev.earth.28.1.211

Zhan, Y., Zhao, G. Z., Unsworth, M., Wang, L. F., Chen, X. B., Li, T., et al. (2013). Deep structure beneath the southwestern section of the Longmenshan fault zone and seimogenetic context of the 4.20 Lushan MS7.0 earthquake. *Chinese Sci. Bull.* 58, 3467–3474. doi:10.1007/s11434-013-6013-x

Zhang, G.-W., Guo, A., and Yao, A. (2004). Western Qinling-Songpan Continental Tectonic Nodein China's Continental Tectonics. *Earth Sci. Front.* 11, 23

Zhang, P.-Z. (2008). Slip Rates and Recurrence Intervals of the Longmen Shan Active Fault Zone, and Tectonic Implications for the Mechanism of the May 12 Wenchuan Earthquake, 2008, Sichuan, China. *Chin. J. Geophys.* 51, 1066

Zhao, G., Unsworth, M. J., Zhan, Y., Wang, L., Chen, X., Jones, A. G., et al. (2012). Crustal Structure and Rheology of the Longmenshan and Wenchuan Mw 7.9 Earthquake Epicentral Area from Magnetotelluric Data. *Geology* 40 (12), 1139–1142. doi:10.1130/g33703.1

Zheng, G., Wang, H., Wright, T. J., Lou, Y., Zhang, R., Zhang, W., et al. (2017). Crustal Deformation in the India-Eurasia Collision Zone from 25 Years of GPS Measurements. *J. Geophys. Res. Solid Earth* 122, 9290–9312. doi:10.1002/2017JB014465

Conflict of Interest: The authors declare that the research was conducted in the absence of any commercial or financial relationships that could be construed as a potential conflict of interest.

frontiers | Frontiers in Earth Science

ORIGINAL RESEARCH
published: 13 June 2022
doi: 10.3389/feart.2022.919174

Overriding Lithospheric Strength Affects Continental Collisional Mode Selection and Subduction Transference: Implications for the Greater India–Asia Convergent System

Qian Li, Zhong-Hai Li* and Xinyi Zhong

Key Laboratory of Computational Geodynamics, College of Earth and Planetary Sciences, University of Chinese Academy of Sciences, Beijing, China

Edited by:
Nibir Mandal,
Jadavpur University, India

Reviewed by:
Zhonglan Liu,
University of Bremen, Germany
Liang Liu,
Chinese Academy of Sciences (CAS), China

****Correspondence:***
Zhong-Hai Li
li.zhonghai@ucas.ac.cn

Specialty section:
This article was submitted to Solid Earth Geophysics, a section of the journal Frontiers in Earth Science

Received: *13 April 2022*
Accepted: *04 May 2022*
Published: *13 June 2022*

Citation:
Li Q, Li Z-H and Zhong X (2022) Overriding Lithospheric Strength Affects Continental Collisional Mode Selection and Subduction Transference: Implications for the Greater India–Asia Convergent System. Front. Earth Sci. 10:919174. doi: 10.3389/feart.2022.919174

The India–Asia collision, starting from 55 ± 5 Ma, leads to the formation of the Himalayas and Tibetan Plateau with great gravity potential energy and large forces acting on the surrounding blocks. However, the subduction transference/jump does not occur in the southern Indian continental margin or the northern Indian oceanic plate as supposed to happen repeatedly during the preceding Tethys evolution. Instead, the continental collision and orogeny continues until present day. The total amount of convergence during the India–Asia collision has been estimated to be ~2,900–4,000 km and needs to be accommodated by shortening/extrusion of the Tibetan plate and/or subduction of the Greater Indian plate, which is a challenging issue. In order to study the collision mode selection, deformation partition, and continental mass conservation, we integrate the reconstruction-based convergence rate of the India–Asia collision into a large-scale thermomechanical numerical model and systematically investigate the effects of overriding Tibetan lithospheric strength and the amount of convergence. The model results indicate that the absence of subduction transference during the India–Asia collision may be attributed to strain localization and shortening of the rheologically weak Tibetan plate. In case of the India–Asia collision for ~50 Myr with a total convergence of ~2,900 km, the model with the intermediately weak Tibetan plate could reconcile the general deformation partition and continental mass balance of the Himalayan–Tibetan system. However, the longer period of India–Asia collision for ~55 Myr leads to significant shortening of the overriding plate that is not consistent with the Tibetan observations, in which case an oceanic basin may be required for the Greater Indian continent.

Keywords: continental collision, subduction initiation, lithospheric strength, Tibetan Plateau, numerical modeling

INTRODUCTION

The evolution of the Tethyan system has been a long-lived global geodynamic process since the early Paleozoic, which includes multiple Wilson's cycles of continental breakup, drifting, collision, and accretion, as well as the subduction initiation (SI) in the neighboring oceanic plate, i.e., subduction transference or subduction jump (Zhong and Li, 2020; and references therein). In summary, there are mainly three periods of continental terranes splitting from the Gondwana super-continent, drifting northward and finally accreted to the Eurasian continent, including the Galatian terrane, Cimmerian terranes, and Indian continent (Stampfli et al., 2013; Torsvik and Cocks, 2013; Wan et al., 2019; Zhu et al., 2021). The collision between Galatia and Eurasia induced subduction transferring into the Paleo-Tethyan Oceanic plate (Stampfli et al., 2013). Subsequently, the collision between Cimmeria with Eurasia closed the Paleo-Tethyan Ocean, leading to the SI of Neo-Tethyan Oceanic plate (Stampfli and Borel, 2002; Wan et al., 2019; Zhong and Li, 2020). Finally, when the Indian continent collided with Eurasia at about 55 ± 5 Ma, the continuous convergence created the most spectacular orogenic belt on the Earth, i.e., the Himalayan orogen and the Tibetan Plateau (**Figure 1**). However, the southern Indian continental margin and northern Indian oceanic plate have shown no signs of SI until today, which is a puzzling issue and widely debated with several mechanisms being proposed, including the resistance from the triangular shape of southern Indian continental margin, the relatively old ocean-continent transition zone with great resistance, and the continuous shortening of the overriding Tibetan Plateau (Stern, 2004; Stern and Gerya, 2018; Cloetingh et al., 1989; Zhong and Li, 2020). In a recent study by Zhong and Li (2022), systematic 3D numerical models revealed that the wedge-shaped southern Indian continental margin without proper weakness hinders its subduction initiation after the long-term India–Asia collision. In that study, the shortening and uplift of a narrowed and simplified Tibetan plate, due to the spatial resolution limit of 3D model (Zhong and Li, 2022), does not affect the subduction transference. In this study, we further investigate this issue by applying comparable spatial and temporal scales of the Tibetan Plateau, as well as the

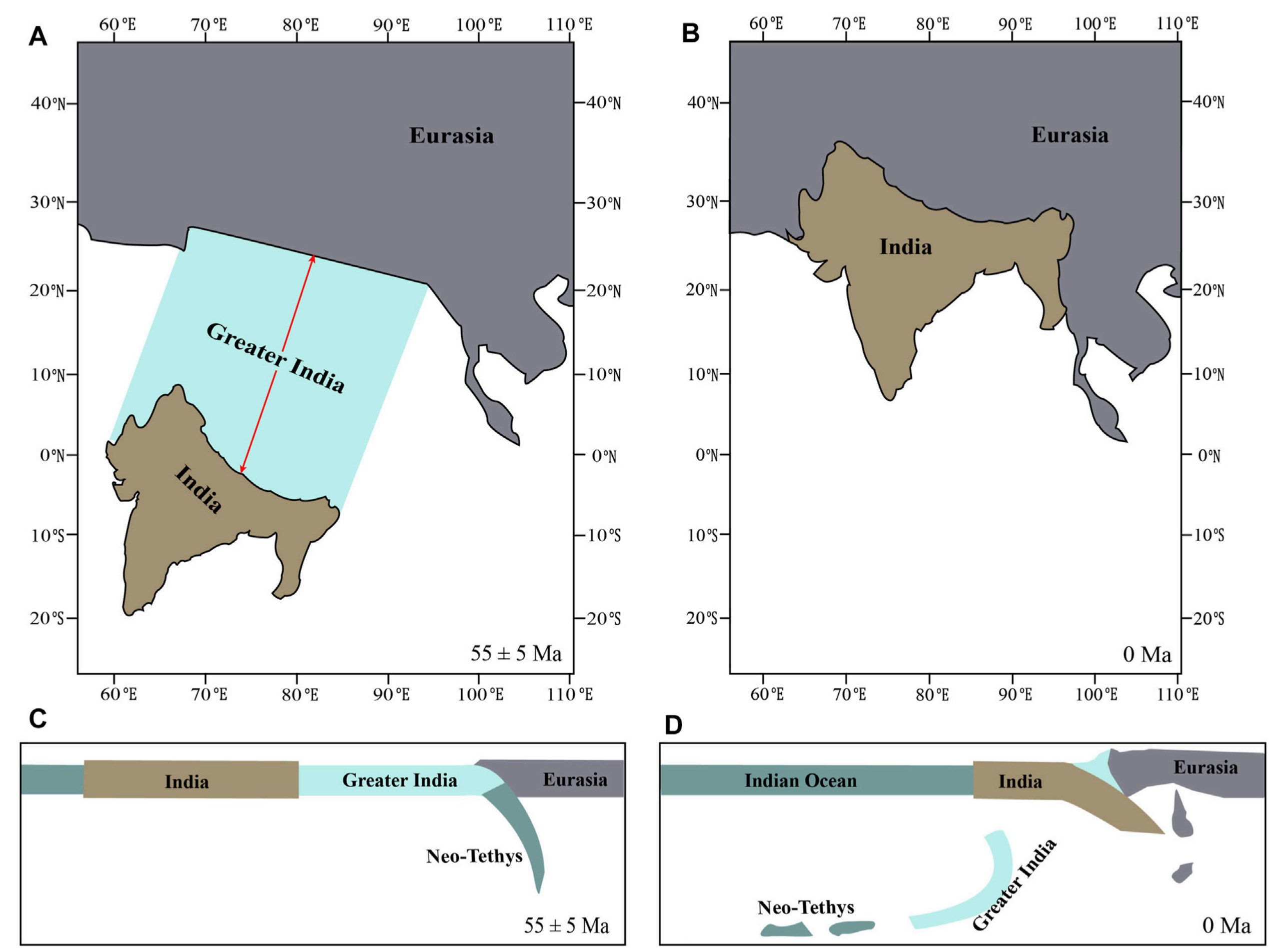

FIGURE 1 | Tectonic background and corresponding profiles of the Indo-Eurasian system at the initial collision **(A,C)** and present-day Tibetan plateau**(B,D)** (Yi et al., 2011; Ingalls et al., 2016; Wang et al., 2019; van Hinsbergen et al., 2019; Meng et al., 2019, 2020; Parsons et al., 2020).

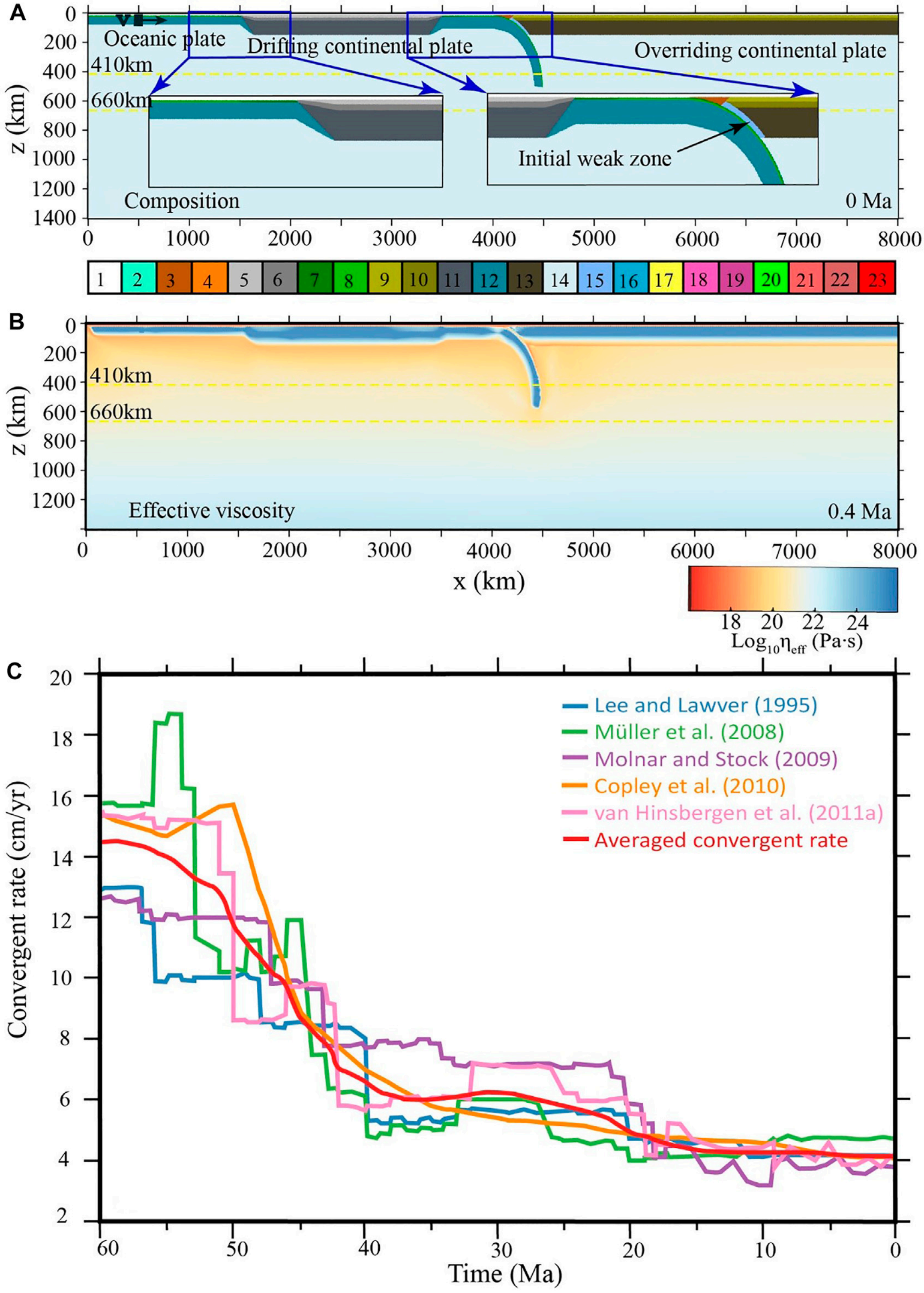

FIGURE 2 | Initial model configuration and boundary convergent rate. **(A)** Composition field with colorbar shown at the bottom: 1, stick air; 2, seawater; 3,4, sediments; 5,6, drifting continental upper and lower crust, respectively; 7,8, oceanic upper and lower crust, respectively; 9,10, overriding continental upper and lower crust, respectively; 11, drifting continental lithospheric mantle; 12, oceanic lithospheric mantle; 13, overriding continental lithospheric mantle, 14, asthenosphere, 15, hydrated mantle; 16, serpentinized mantle; 17, partially molten sediments; 18, partially molten drifting continental upper crust; 19, partially molten drifting continental lower crust; 20, partially molten oceanic crust; 21, partially molten overriding continental upper crust; 22, partially molten overriding continental lower crust; and 23, partially molten mantle. **(B)** Effective viscosity field with the colorbar shown at the bottom. The yellow dotted lines indicate the 410 and 660 km discontinuities, (*Continued*)

FIGURE 2 | with the Clapeyron slopes of phase transitions of +3 and −1 MPa/K, respectively. **(C)** The time-dependent velocity of the India–Asia convergence since 60 Ma, according to the previous plate reconstruction studies (Lee and Lawver, 1995; Müller et al., 2008; Molnar and Stock, 2009; Copley et al., 2010; van Hinsbergen et al., 2011). The red line shows the averaged convergence rate of the five reconstructions, which is further applied in the numerical model as a boundary condition as shown by a black rectangle and arrow in **(A)**.

reconstruction-based, realistic convergence rate of the India–Asia collision.

Due to the absence of collision-induced subduction transference, the continuous India–Asia convergence needs be accommodated by the shortening of the Tibetan Plateau and/or the subduction of the Greater Indian plate. The long-lasting India–Asia collision began with a relatively high convergent rate of ~14 cm/yr at ~55 Ma, and then it gradually decreases to ~4 cm/yr at the present (Lee and Lawver, 1995; Müller et al., 2008; Molnar and Stock, 2009; Copley et al., 2010; van Hinsbergen et al., 2011). With such reconstructions, the total amount of convergence since 55 ± 5 Ma will be ~2,900–4,000 km, which needs to be consumed by the Tibetan Plateau and the Indian plate (Molnar and stock, 2009; Copley at al., 2010; van Hinsbergen et al., 2011; van Hinsbergen et al., 2012; van Hinsbergen et al., 2019; Zhou and Su, 2019). Several mechanisms have been suggested for the accommodation of convergence by the Tibetan Plateau, including crustal shortening, lateral extrusion of the Indo–China block, the lower crustal flow, and surface erosion (Tapponnier et al., 1982; Gan et al., 2007; Replumaz et al., 2010; Yakovlev and Clark, 2014; Ingalls et al., 2016; Cui et al., 2021). The amount of Tibetan shortening has been widely estimated. However, the results vary significantly. The shortening of the Tibetan Plateau interior, i.e., from the Indus-Yalung suture zone in the south to the Kunlun Mountains in the north, is estimated to be about 1,100 ± 50 km (van Hinsbergen et al., 2019), which may have a large variation from 500 km (Yakovlev and Clark, 2014) to 1,700 km (Sun et al., 2012). For the northeastern Tibetan Plateau, the shortening may be about 500–600 km (e.g., Yin and Harrison, 2000). Consequently, there is still ~1,200–2,400 km left to be accommodated by the lower plate, i.e., the Greater India. Two types of models have been proposed for the consumption of the Greater Indian plate. In the first type of models, the Greater India is entirely composed of continental material. The upper part of the Greater Indian crust is detached and accumulated in the Himalayan orogeny during continental collision, whereas the lower part is subducted and recycled into the mantle. The deep subduction of such a long continental slab is a great challenge for this type of models (Ding et al., 2017; Meng et al., 2019, 2020). However, a recent study proposed that the phase-transition-induced densification of deeply subducted felsic crust below 170 km drives the continuous subduction of continental slab, i.e. Self-driven Continental Deep Subduction model (Wang et al., 2022). The other type of models assumes an oceanic basin within the Greater India, for example, the Greater Indian Oceanic Basin model (van Hinsbergen et al., 2012, 2019) or the Intra-Oceanic Arc model (Aitchison et al., 2007; Gibbons et al., 2015; Kapp and DeCelles, 2019; Martin et al., 2020). The oceanic plate within the Greater India can easily subduct and accommodate a large amount of convergence without any geodynamic difficulties in these models. However, the major problem is the lack of geological evidence for this period of oceanic subduction (Najman et al., 2010; Aitchison and Ali, 2012; Wu et al., 2014; Hu et al., 2016; Ding et al., 2017; and reference therein). In addition, the continuously decreasing convergence rate since ~55 Ma is difficult to be reconciled with the subduction of such an oceanic plate.

In this study, we aim to investigate the deformation partition and mass conservation during the long-lasting collision of the Greater India and Eurasia continent, if no oceanic basin is present within the Greater India. Notably, the models with the Greater Indian Oceanic Basin are not investigated in the current models, which require to be examined in further studies. In the previous numerical models, a constant convergent rate is generally applied to investigate the continental collision process (e.g., Kelly et al., 2016; Li et al., 2016; Liu et al., 2021). However, the northward convergent rate of the India–Asia collision has been changing significantly over time (Lee and Lawver, 1995; Müller et al., 2008; Molnar and Stock, 2009; Copley et al., 2010; van Hinsbergen et al., 2011), which may strongly affect the deformation partition and mass conservation. Consequently, a large-scale thermomechanical numerical model is integrated with the reconstruction-based plate convergence rate of the India–Asia collision, to investigate the dynamics of Himalayan and Tibetan orogeny, with paying special attention on two key issues: *1*) why the continued India–Asia collision for >50 Myr does not lead to subduction transference to the present-day Indian Ocean and *2*) if without an oceanic basin in the Greater India, how to reconcile the general deformation partition and mass conservation of the Greater India–Asia collision?

NUMERICAL MODEL SETUP

The numerical models are conducted with the code I2VIS (Gerya, 2010). The extended numerical methodologies and specific parameters (i.e. governing equations, rheological flow laws, phase transitions, hydration, and partial melting) are shown in the supporting information and following Li et al. (2019).

Initial Material and Thermal Configurations

The initial model is configured in a two-dimensional box with a spatial scale of 8,000 × 1,400 km, as shown in **Figure 2A**. The horizontal spatial resolution of the model domain is 10 km. In the vertical direction, the spatial resolution is 1 km from 0 to 200 km depth and gradually changing to 10 km downward. The total number of grids is 800 × 350. Within the model box, four plates are configured, including the spreading oceanic plate (1,500 km in length), the drifting continental plate (2,000 km in length), the subducting oceanic plate (500 km horizontally and ~800 km subducted), and the overriding continental plate (~3,800 km in length).

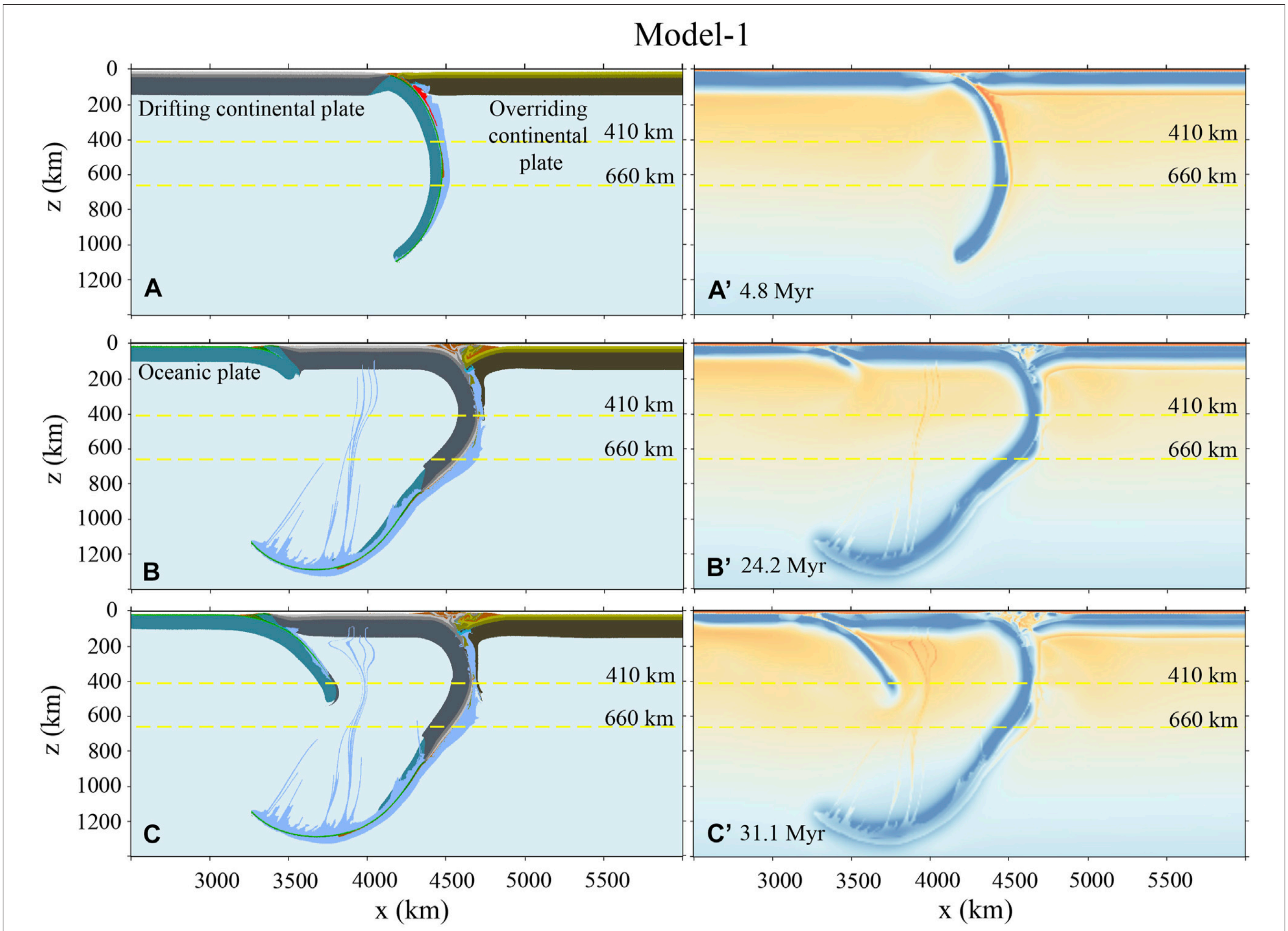

FIGURE 3 | Model-1 evolution with a strong overriding plate. The reconstruction-based convergence rate is applied from 55 Ma (**Figure 2C**). The plastic friction coefficient of the overriding lithospheric mantle is initially $\lambda \cdot \sin(\varphi) = 0.6$ and will decrease linearly to 0.1 with the accumulated plastic strain to $\varepsilon_{\text{plas}} = 1$ (**Supplementary Table S2** and **Supplementary Equation S11** in the supporting information), which is the same as that of the underthrusting Indian lithospheric mantle. **(A–C)** The composition field evolution with the corresponding colorbar is shown in **Figure 2A**. **(A'–C')** The effective viscosity evolution with the corresponding colorbar is shown in **Figure 2B**.

The oceanic lithosphere consists of a 3 km-thick upper crust, a 5 km-thick lower crust, and a lithospheric mantle with its thickness controlled by the age of the oceanic plate. The initial age of the spreading oceanic plate is set to be 30 Myr, with the corresponding lithospheric thickness of about 60 km (Turcotte and Schubert, 2002). On the other hand, the age of the horizontal section of the subducting oceanic plate is set to be 60 Myr, with the corresponding lithospheric thickness of about 86 km (Turcotte and Schubert, 2002). The age of the subducted oceanic plate is gradually changing from 60 Myr on the top to 30 Myr at the bottom, representing the slab heating during subduction. The continental lithosphere consists of an upper crust of 15 km, a lower crust of 20 km, and a lithosphere mantle of 105 km. An initial weak zone is set between the subducting oceanic plate and the overriding continental plate, which denotes a weak subduction channel. The top of the model is covered with a "sticky air" layer of 10 km (above the continental plate) or 12 km (above the oceanic plate), to simulate the free surface allowing crustal deformation (Schmeling et al., 2008). Detailed material properties of rocks are shown in **Supplementary Tables S1, S2** in the supporting information.

For the initial temperature field of the model, the continental lithosphere is configured with a constant geothermal gradient of about 9.6 K/km, which indicates a temperature of ~1623 K at the bottom of the lithosphere. On the other hand, the half-space cooling model is applied for the oceanic lithosphere (Turcotte and Schubert, 2002). The "sticky air" layer has a constant temperature of 273 K and the sublithospheric mantle has an initial thermal gradient of 0.5 K/km. For the thermal boundary conditions, the upper and lower boundaries have constant temperatures of 273 and 2248 K, respectively. The left and right boundaries are adiabatic with no horizontal heat flux.

Kinematic Boundary Conditions

The free-slip condition is applied for all the four boundaries. Plate convergence is driven by an internal pushing velocity as indicated

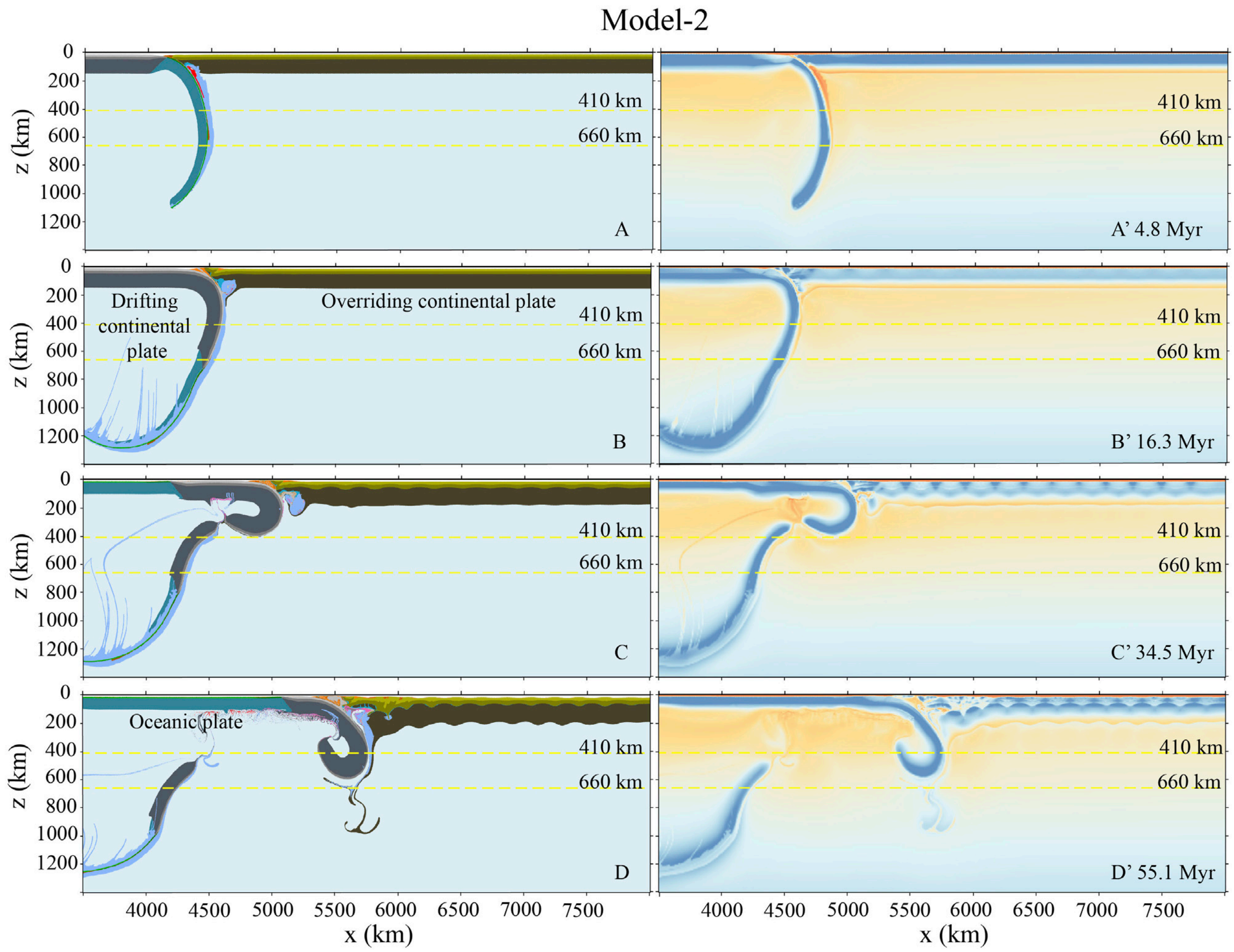

FIGURE 4 | Model-2 evolution with a decreased and uniform plastic friction coefficient of the overriding lithospheric mantle of $\lambda \cdot \sin(\varphi) = 0.1$ (**Supplementary Table S2** and **Supplementary Equation S11** in the supporting information). All the other parameters are identical to Model-1 (**Figure 3**). **(A–D)** The composition field evolution with the corresponding colorbar is shown in **Figure 2A**. **(A'–D')** The effective viscosity evolution with the corresponding colorbar is shown in **Figure 2B**.

in **Figure 2A**. In order to study the specific case of the India–Asia collision, we have compiled its convergent rate based on five independent studies of plate reconstructions and obtained an averaged time-dependent velocity evolution since 60 Ma, as shown in **Figure 2C** (Lee and Lawver, 1995; Müller et al., 2008; Molnar and Stock, 2009; Copley et al., 2010; van Hinsbergen et al., 2011). The averaged convergent rate (i.e. red line in **Figure 2C**, from either 55 and 60 Ma) is further implemented into the numerical model as an internal boundary condition as shown by the black rectangle and arrow in **Figure 2A**. The velocity patch is fixed in and moving with the spreading oceanic plate during convergence.

MODEL RESULTS

The exact time of the initial India–Asia continental collision is still in debate. However, it is generally accepted to be at about 55 ± 5 Ma, i.e. between 60 and 50 Ma (Klootwijk et al., 1992; Molnar et al., 1993; Tapponnier et al., 2001; Wang et al., 2014; Ding et al., 2016; Hu et al., 2016; Ingalls et al., 2016; Zheng and Wu, 2018). In the current model, there is a horizontal section of the oceanic lithosphere with a length of 500 km between the drifting continental plate and overriding continental plate (**Figure 2A**). With a high convergence rate of >10 cm/yr before 50 Ma (**Figure 2C**), the subduction and consumption of this oceanic section will be within 5 Myr.

In this study, two groups of models are conducted, with applying reconstruction-based convergence rate from either 55 or 60 Ma (**Figure 2C**), which indicate the onset of collision at about 50 or 55 Ma, correspondingly. In each group of models, the effects of rheological strength of the overriding continental lithospheric mantle are systematically studied with the model results shown in **Figures 3–12**. It should be noted that the overriding Tibetan lithosphere has undergone multiple stages of ocean subduction and terrane accretion before the India–Asia collision. Thus, the Tibetan lithospheric mantle could be significantly weakened by the accompanying fluid/melt

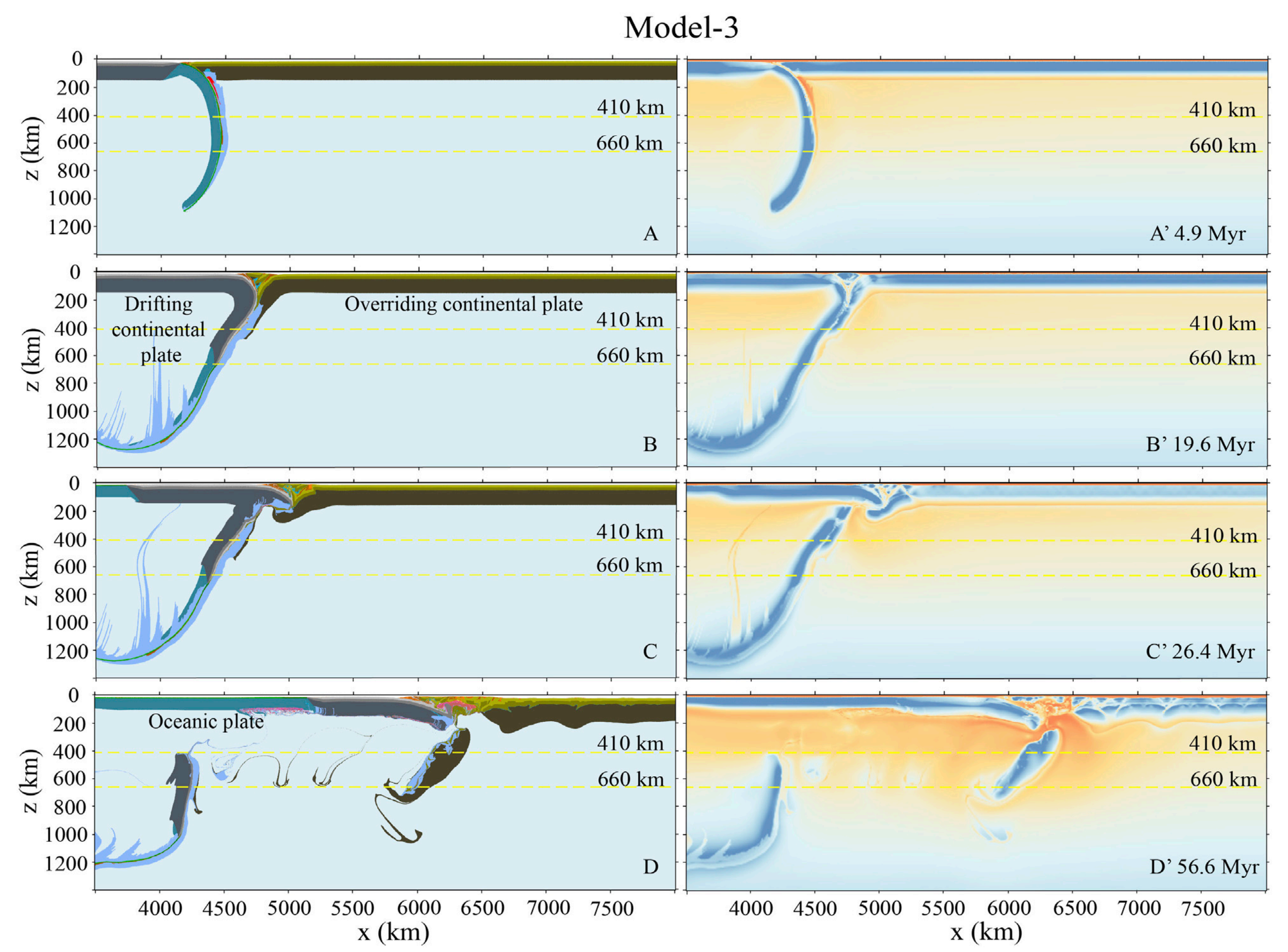

FIGURE 5 | Model-3 evolution with a further decreased plastic friction coefficient of the overriding lithospheric mantle, which is initially $\lambda \cdot \sin(\varphi) = 0.1$ and will decrease linearly to 0.01 with the accumulated plastic strain to $\varepsilon_{\text{plas}} = 1$ (**Supplementary Table S2** and **Supplementary Equation S11** in the supporting information). All the other parameters are identical to Model-2 (**Figure 4**). **(A–D)** The composition field evolution with the corresponding colorbar is shown in **Figure 2A**. **(A'–D')** The effective viscosity evolution with the corresponding colorbar is shown in **Figure 2B**.

activities, which may strongly affect the final collision dynamics (Molnar et al., 1993; Li et al., 2016, 2021; Huangfu et al., 2019). In this study, the weakness of the Tibetan plate is represented by a lower plastic friction coefficient of the overriding lithospheric mantle.

Numerical Models With India–Asia Convergence From 55 Ma

In this group of models, the plate subduction and collision is pushed by the reconstruction-based India–Asia convergence rate from 55 Ma (**Figure 2C**). With such a time-dependent convergence rate, a total amount of about 3,600 km will be achieved when the model runs for the whole 55 Myr. The Indian Continent is generally considered as a pre-Cambrian craton, which has a rheologically strong lithosphere (Replumaz et al., 2014; Jain et al., 2020). However, the overriding Tibetan lithosphere could be weakened before the final collision with the Indian Continent. In order to study the effects of overriding lithospheric strength on the continental collision mode selection and deformation partition, a series of models with variable rheological strength of overriding lithospheric mantle have been conducted.

In Model-1, the overriding continental plate is rheologically strong. The plastic friction coefficient of its lithospheric mantle is the same as the underthrusting Indian lithosphere, which was initially $\lambda \cdot \sin(\varphi) = 0.6$ and will decrease linearly to 0.1 with the accumulated plastic strain to $\varepsilon_{\text{plas}} = 1$ (**Supplementary Table S2** and **Supplementary Equation S11** in the supporting information). In this model, the continental collision occurs after convergence for ~4.8 Myr (**Figure 3A**). Subsequently, the drifting continental plate subducts following the preceding oceanic lithosphere, with the continental upper crust detached and accumulated in the orogeny (**Figure 3B**). The resistance builds gradually during the subduction of less dense continental plate, which contributes to the formation of a new subduction zone in the neighboring oceanic plate (**Figures 3B,C**). It indicates that the collision-induced subduction transference favors the

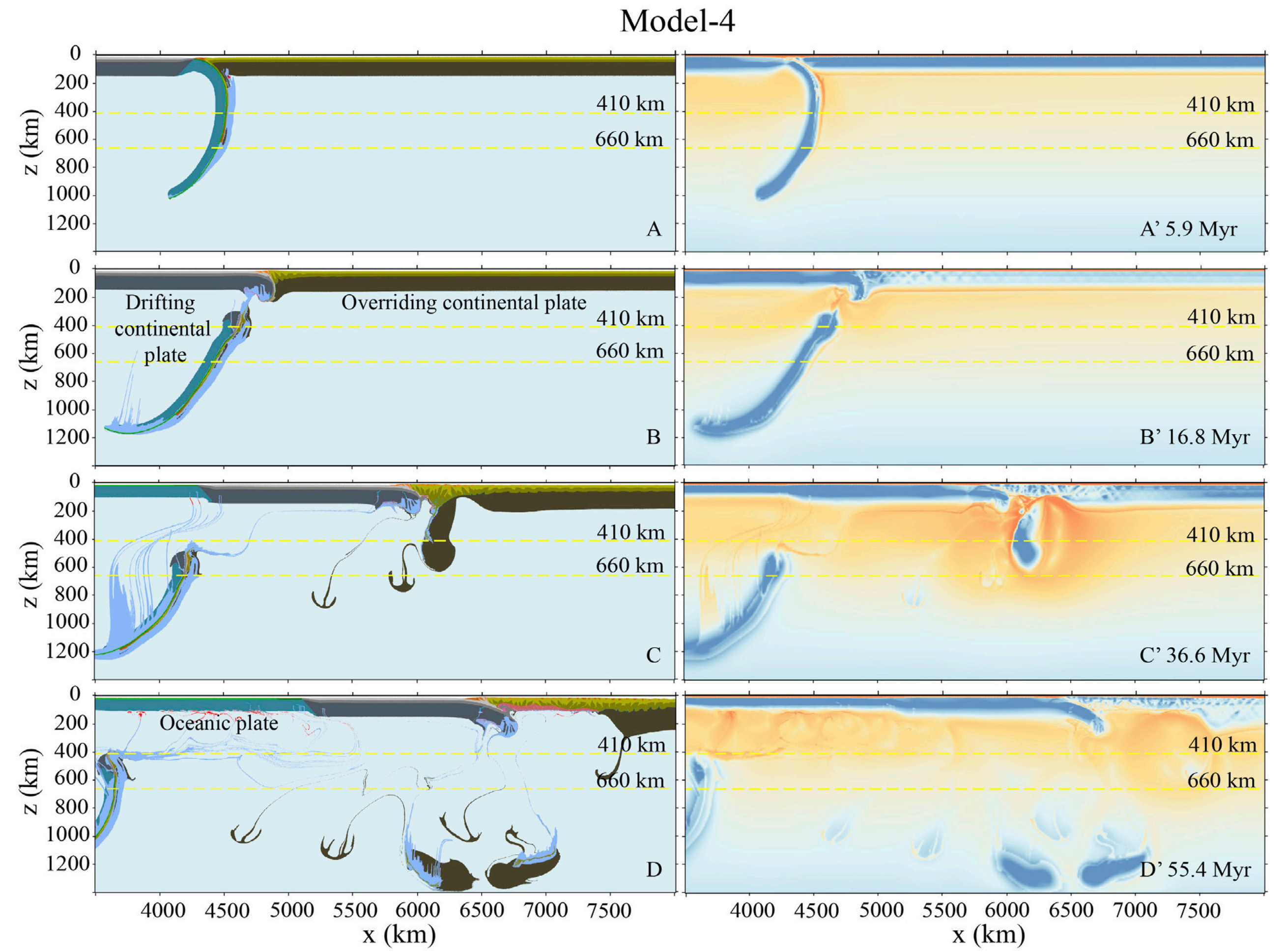

FIGURE 6 | Model-4 evolution with a further decreased and uniform plastic friction coefficient of the overriding lithospheric mantle of $\lambda \cdot \sin(\varphi) = 0.01$ (**Supplementary Table S2** and **Supplementary Equation S11** in the supporting information). All the other parameters are identical to Model-3 (**Figure 5**). **(A–D)** The composition field evolution with the corresponding colorbar is shown in **Figure 2A**. **(A'–D')** The effective viscosity evolution with the corresponding colorbar is shown in **Figure 2B**.

strong overriding plates rheologically, which leads to the strain localization in the neighboring passive margin.

In Model-2, the plastic friction coefficient of the overriding lithospheric mantle decreased to 0.1 and does not depend on the plastic strain anymore. The collision between the drifting and overriding continental plates occurs similarly at about 4.8 Myr after the initial model convergence (**Figure 4A**). Then, the drifting continental plate subducts to a depth of ~660 km at 16.3 Myr, following the sinking oceanic lithosphere (**Figure 4B**). At about 35 Myr, the slab break-off occurs in the subducted continental lithosphere, with the lower section sinking into the mantle and the upper section rolling back (**Figure 4C**). During the continuous continental subduction and collision, the overriding continental lithosphere is shortened due to its relative weakness (**Figures 4C,D**). Finally, the total convergence of ~2,900 km is achieved after the initial collision (i.e. after ~4.8 Myr) in this model, which is accommodated by overriding plate shortening of ~1,200 km, continental slab break-off of ~700 km, and continental subduction without break-off of ~1,000 km, respectively. As a result, the thickness of the overriding continental crust increases from 35 km to an average value of ~50 km, with its time-dependent evolution shown in **Supplementary Figure S1** of the supporting information.

In Model-3, the plastic friction coefficient of the overriding lithospheric mantle is decreased to $\lambda \cdot \sin(\varphi) = 0.1$ initially and further to 0.01 with accumulated plastic strain to $\varepsilon_{\text{plas}} = 1$ (**Supplementary Table S2** and **Supplementary Equation S11** in the supporting information). After the continental collision at ~4.9 Myr, the drifting continental plate subducts following the preceding oceanic plate (**Figures 5A,B**). At ~25 Myr, the slab break-off occurs in the subducted drifting continental plate, with the oceanic slab and a section of the subducted continental slab detached and sinking into the subjacent mantle. Under the continuous loading of convergence, the drifting continental plate underthrusts the overriding continental plate and drives

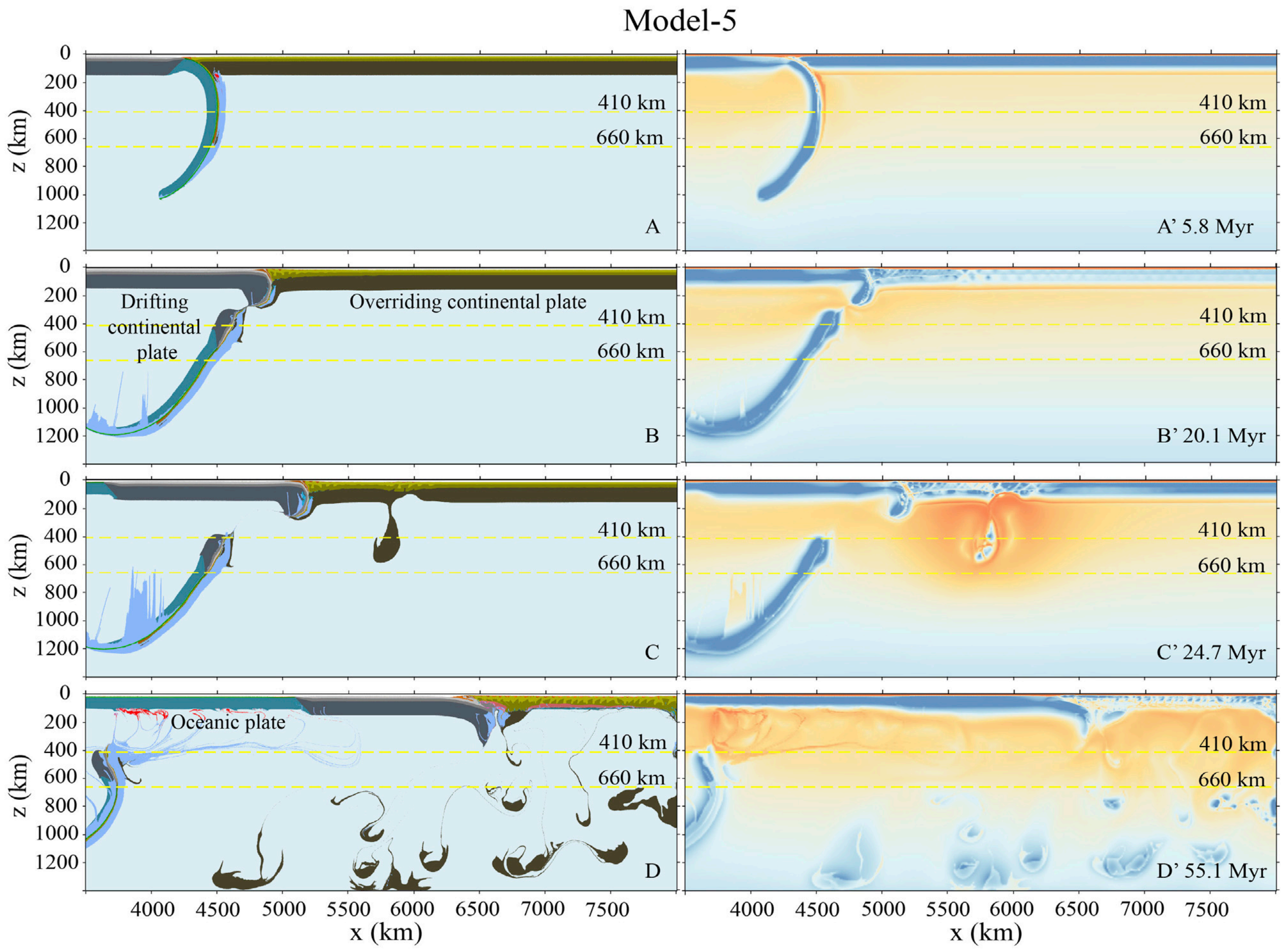

FIGURE 7 | Model-5 evolution with weakest overriding plate. The plastic friction coefficient of the overriding lithospheric mantle is initially $\lambda \cdot \sin(\varphi) = 0.01$ and will decrease linearly to 0.001 with accumulated plastic strain to $\varepsilon_{\text{plas}} = 1$ (**Supplementary Table S2** and **Supplementary Equation S11** in the supporting information). All the other parameters are identical to Model-4 (**Figure 6**). **(A–D)** The composition field evolution with the corresponding colorbar is shown in **Figure 2A**. **(A'–D')** The effective viscosity evolution with the corresponding colorbar is shown in **Figure 2B**.

significant shortening of the latter (**Figure 5C**). Finally, the delamination of the overriding lithospheric mantle is predicted at the latest stage of model evolution (**Figure 5D**). The total convergence of ~2,900 km is achieved after the initial collision (i.e., after ~4.9 Myr) in this model. The lower (Greater Indian) plate accommodates ~1,200 km, including ~500 km of the underthrusting continental plate and ~700 km of the detached continental plate. The residual convergence of ~1700 km is accommodated by the shortening of the overriding continental plate. As a result, the thickness of the overriding continental crust increases from 35 km to an average value of ~64 km, with its time-dependent evolution shown in **Supplementary Figure S1** of the supporting information.

In Model-4, the plastic friction coefficient of the overriding lithospheric mantle is further decreased to 0.01 and does not depend on the plastic strain anymore. With such a greatly weakened overriding lithosphere, the collision occurs a bit later (at ~5.9 Myr) than the previous cases (**Figures 3–5**), due to the shortening of the overriding plate during the oceanic subduction stage (**Figure 6A**). After the continental collision happens, the convergence-induced strain mostly localizes in the overriding plate, whereas the amount of continental subduction is limited. At ~10 Myr after the initial collision, the slab break-off occurs, during which a short continental slab of ~50 km is detached with the preceding oceanic slab (**Figure 6B**). Afterward, the overriding plate accommodates most of the convergence with lithospheric thickening and delamination (**Figures 6C,D**). In addition, the drifting continental plate underthrusts beneath the thickened overriding crust after the detachment of the lithospheric mantle (**Figures 6C,D**). Finally, the total convergence of the two continents after the collision is ~2,700 km. The overriding plate accommodates the majority of convergence with ~2,150 km, while the drifting continental plate absorbs the residual amount of convergence by detachment (~50 km) and subduction (~500 km) (**Table 1**). As the model evolved to ~55 Myr, the thickened overriding crust reached an averaged value of ~87 km, with its time-dependent evolution shown in **Supplementary Figure S1** of the supporting information.

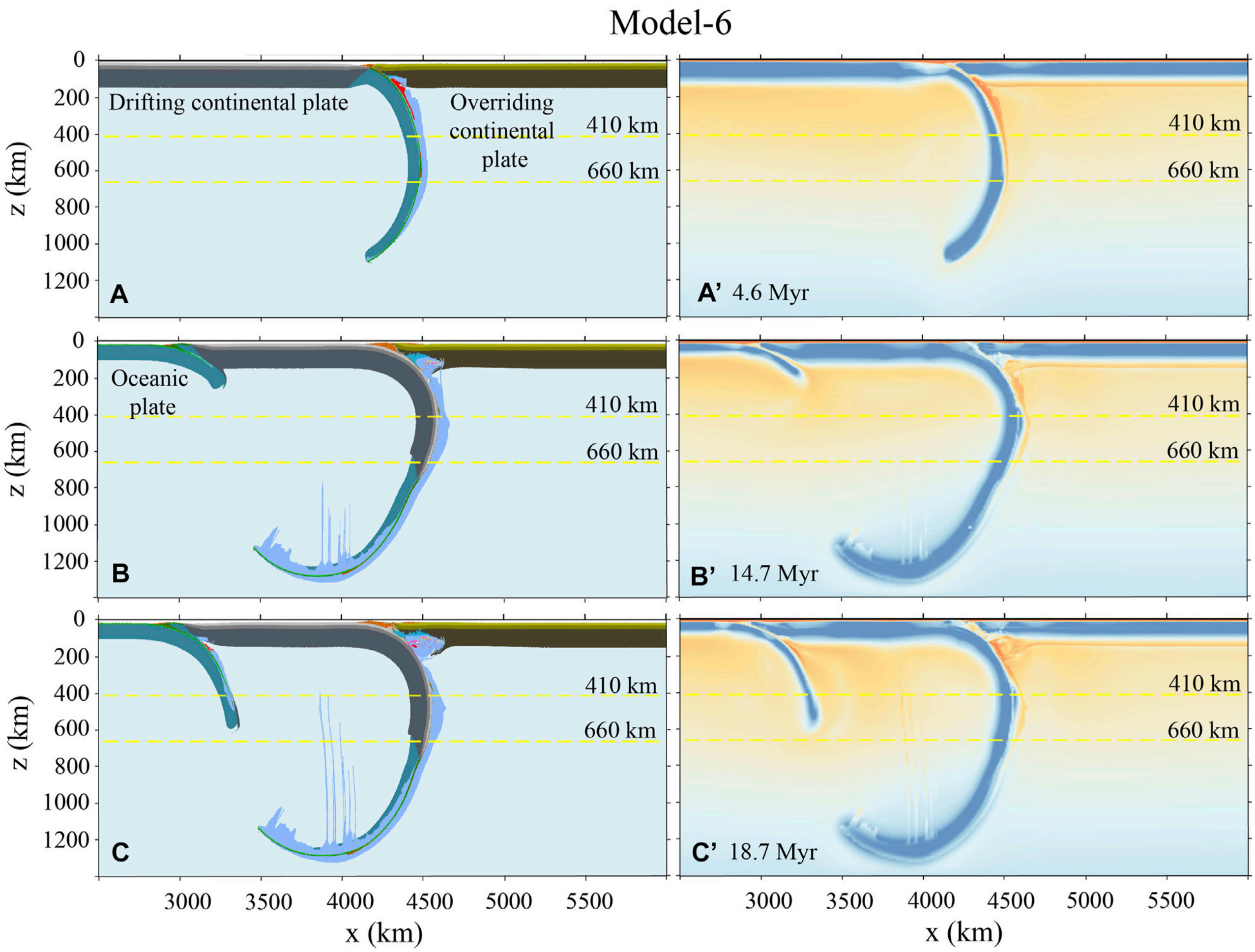

FIGURE 8 | Model-6 evolution with a strong overriding plate. The reconstruction-based convergence rate is applied from 60 Ma (**Figure 2C**). The plastic friction coefficient of overriding lithospheric mantle is initially $\lambda \cdot \sin(\varphi) = 0.6$ and will decrease linearly to 0.1 with the accumulated plastic strain to $\varepsilon_{\text{plas}} = 1$ (**Supplementary Table S2** and **Supplementary Equation S11** in the supporting information), which is the same as that of the underthrusting Indian lithospheric mantle. **(A–C)** The composition field evolution with the corresponding colorbar is shown in **Figure 2A**. **(A'–C')** The effective viscosity evolution with the corresponding colorbar is shown in **Figure 2B**.

In Model-5, with the weakest overriding plate, the plastic friction coefficient is decreased to $\lambda \cdot \sin(\varphi) = 0.01$ initially and further to 0.001 with the accumulated plastic strain to $\varepsilon_{\text{plas}} = 1$ (**Supplementary Table S2** and **Supplementary Equation S11** in the supporting information). The general evolution of this model is similar to Model-4 (**Figure 6**), with most of the convergence accommodated by the shortening of the overriding plate (**Figure 7**). The slab break-off occurs at ~20 Myr, when a short continental plate of ~100 km and the preceding oceanic slab detaches sinking into mantle (**Figure 7B**). In this model, the small-scaled delamination happens at the bottom of the overriding plate repeatedly during continuous convergence, because of the significantly weakened overriding lithospheric mantle (**Figures 7C,D**). When the model evolves to the end at ~55 Ma, the overriding lithospheric mantle is almost completely delaminated. The thickness of the crust reaches ~87 km, with its time-dependent evolution as shown in **Supplementary Figure S1** of the supporting information. The total convergence after the initial collision in this model is ~2,700 km, of which the drifting continental lithosphere takes up ~600 km including ~100 km for break-off and ~500 km for subduction without break-off. The residual convergence of ~2,100 km is absorbed by the shortening and delamination of the overriding plate (**Table 1**).

Numerical Models With India–Asia Convergence From 60 Ma

In the previous models, the plate reconstruction-based India–Asia convergence rate (**Figure 2C**) is implemented from 55 Ma. In the order for comparison, another group of models are conducted with the convergence rate from 60 Ma (**Figure 2C**). All

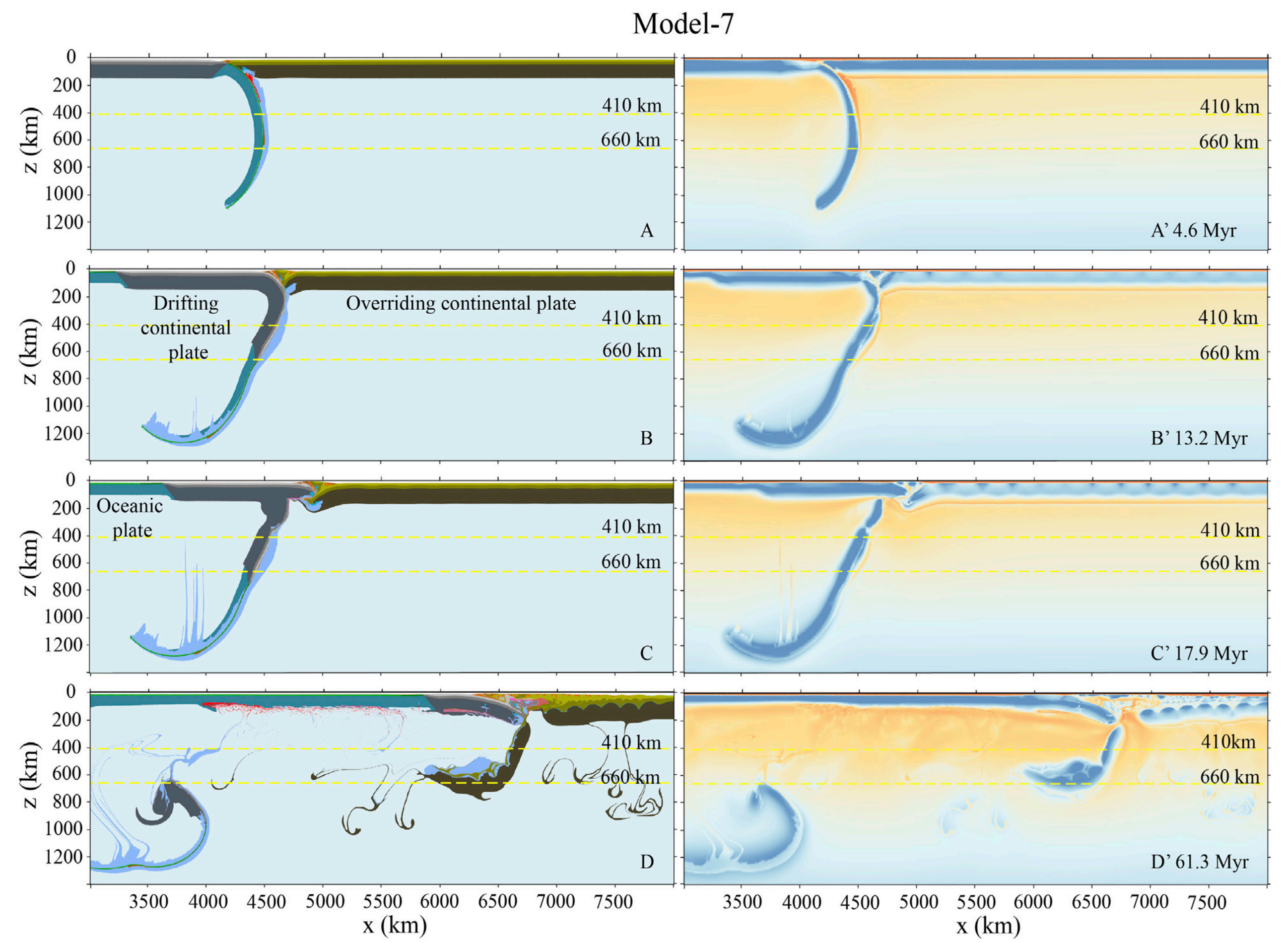

FIGURE 9 | Model-7 evolution with a decreased and uniform plastic friction coefficient of the overriding lithospheric mantle of $\lambda \cdot \sin(\varphi) = 0.1$ (**Supplementary Table S2** and **Supplementary Equation S11** in the supporting information). All the other parameters are identical to Model-6 (**Figure 8**). **(A–D)** The composition field evolution with the corresponding colorbar shown in **Figure 2A**. **(A'–D')** The effective viscosity evolution with the corresponding colorbar is shown in **Figure 2B**.

the other parameters are identical to the previous group of models.

In Model-6 (**Figure 8**), the rheological strength of all the plates are identical to Model-1 (**Figure 3**), in which the plastic friction coefficient of the strong overriding lithospheric mantle is initially $\lambda \cdot \sin(\varphi) = 0.6$ and will decrease linearly to 0.1 with the accumulated plastic strain to $\varepsilon_{plas} = 1$ (**Supplementary Table S2** and **Supplementary Equation S11** in the supporting information). The general model evolution of the current model is similar to Model-1, with collision-induced subduction transference (c.f. **Figures 3**, **8**). With a higher convergence rate, the subduction initiation occurs at about 10 Myr after the continental collision (**Figure 8**), whereas it is about 20 Myr in Model-1 with a slower convergence (**Figure 3**).

In Model-7 (**Figure 9**), the plastic friction coefficient of the overriding lithospheric mantle is extensively reduced to 0.1, similar to Model-2 (**Figure 4**). The continental collision starts at about 4.7 Myr (**Figure 9A**). Then, the drifting continental plate subducts beneath the overriding plate following the preceding oceanic slab (**Figure 9B**). The slab break-off occurs at ~17 Myr, with a long portion of subducted continental slab detached (**Figure 9C**). After the slab break-off, the strain localization changes from the subducting plate to the relatively weak overriding plate. The latter is extensively thickened accompanying lithospheric delamination (**Figure 9D**), which is similar to those in Liu et al. (2021). In this model, the total convergence after the initial collision (i.e. after ~4.7 Myr) is ~3,600 km. The lower plate takes up ~1,500 km of convergence, including ~800 km of the detached continental plate and ~700 km of the underthrusting continental plate. The convergence absorbed by the overriding continental plate is ~2,100 km, with the crust thickening from 35 km to an average value of 82 km (**Table 1**). The time-dependent evolution of the overriding crustal thickness is shown in **Supplementary Figure S2** of the supporting information.

In Model-8, the plastic friction coefficient of the overriding lithospheric mantle is decreased to $\lambda \cdot \sin(\varphi) = 0.1$ initially and further to 0.01 with the accumulated plastic strain to $\varepsilon_{plas} = 1$ (**Supplementary Table S2** and **Supplementary Equation S11** in the supporting information). In this model, the drifting

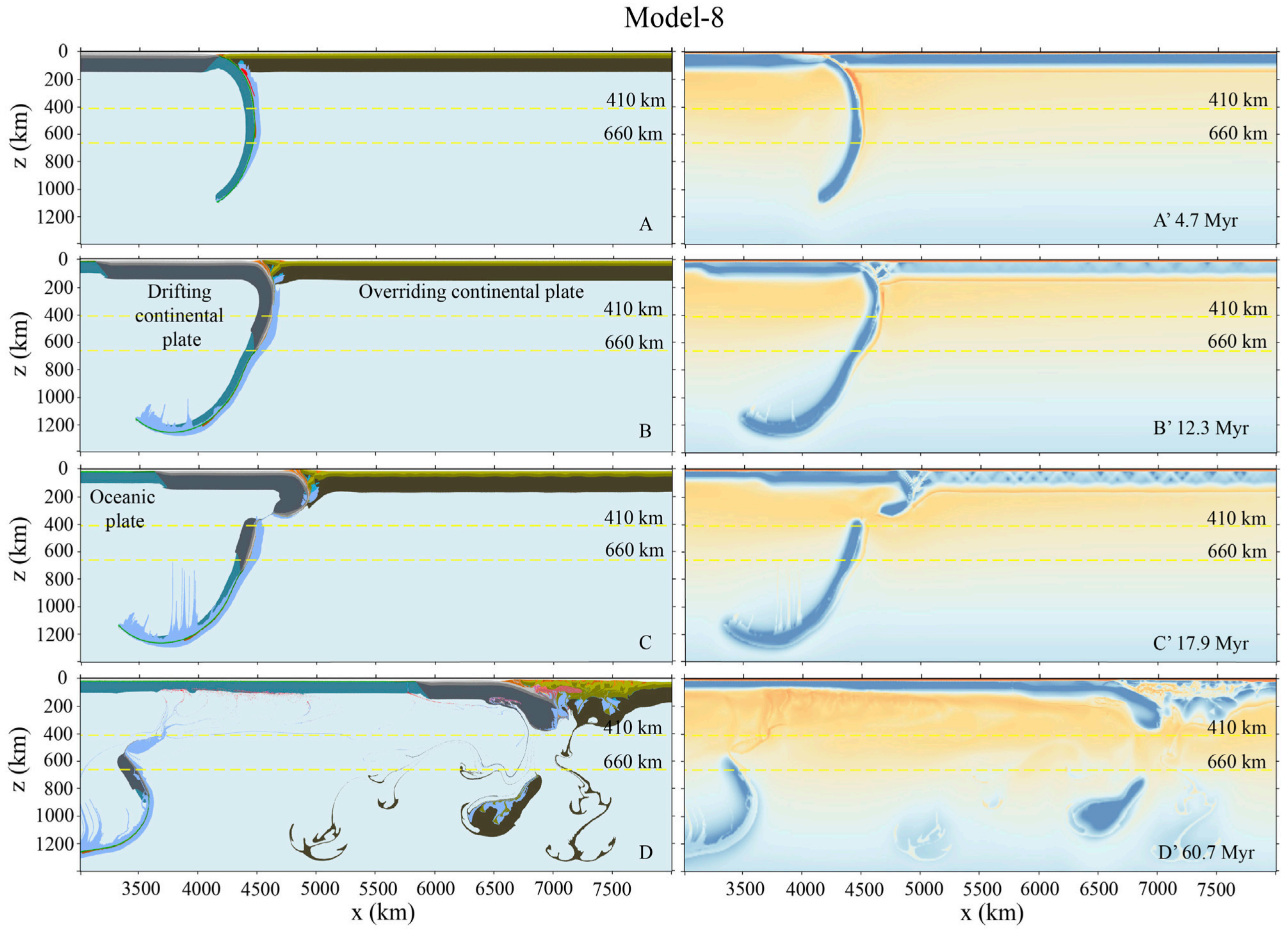

FIGURE 10 | Model-8 evolution with a further decreased plastic friction coefficient of the overriding lithospheric mantle, which is initially $\lambda \cdot \sin(\varphi) = 0.1$ and will decrease linearly to 0.01 with the accumulated plastic strain to $\varepsilon_{\text{plas}} = 1$ (**Supplementary Table S2** and **Supplementary Equation S11** in the supporting information). All the other parameters are identical to Model-7 (**Figure 9**). **(A–D)** The composition field evolution with the corresponding colorbar is shown in **Figure 2A**. **(A'–D')** The effective viscosity evolution with the corresponding colorbar is shown in **Figure 2B**.

continental plate also subducts following the subducted oceanic slab, with the slab break-off occurring at ~17 Myr (**Figure 10C**). However, the detached continental slab is much shorter than that of Model-7 in **Figure 9**. Afterward, the drifting continental plate underthrusts slightly beneath the overriding continental lithosphere. Large amount of convergence is accommodated by the shortening of overriding lithosphere, which leads to the extensive delamination of the overriding lithospheric mantle (**Figure 10D**). The total convergence after the initial collision is about 3,600 km in this model, of which ~2,400 km is accommodated by the shortening of the overriding plate. Consequently, the final thickness of the overriding crust increases to an average value of ~100 km, with the time-dependent evolution as shown in **Supplementary Figure S2**. The remaining convergence is accommodated by the detached continental plate (~800 km) and the underthrusting continental plate (~700 km), respectively (**Table 1**).

In Model-9, the overriding plate is very weak. The plastic friction coefficient of the lithospheric mantle is implemented as $\lambda \cdot \sin(\varphi) = 0.01$ (**Figure 11**). In this model, the continental subduction is limited, with slab break-off occurring very early at ~11 Myr (**Figure 11B**). Then, the convergence is mainly accommodated by the shortening of overriding continental plate and the multiple stages of lithospheric delamination (**Figures 11C,D**). When the overriding lithospheric mantle mostly delaminates, the drifting plate starts underthrusting again beneath the greatly thickened overriding crust. Finally, the thickness of the overriding crust increases to an averaged value of ~104 km, with the time-dependent evolution is shown in **Supplementary Figure S2** of the supporting information. The amount of convergence after the initial collision is about 3,400 km throughout the evolution of model, most of which (~2,400 km) is accommodated by the shortening of the overriding plate (**Table 1**).

In Model-10, the overriding lithospheric mantle is the weakest among all models, with plastic friction coefficient of $\lambda \cdot \sin(\varphi) = 0.01$ initially and further to 0.001 with the accumulated plastic strain to $\varepsilon_{\text{plas}} = 1$ (**Supplementary Table S2** and **Supplementary Equation S11** in the supporting information). The model evolution is generally consistent with that of Model-9

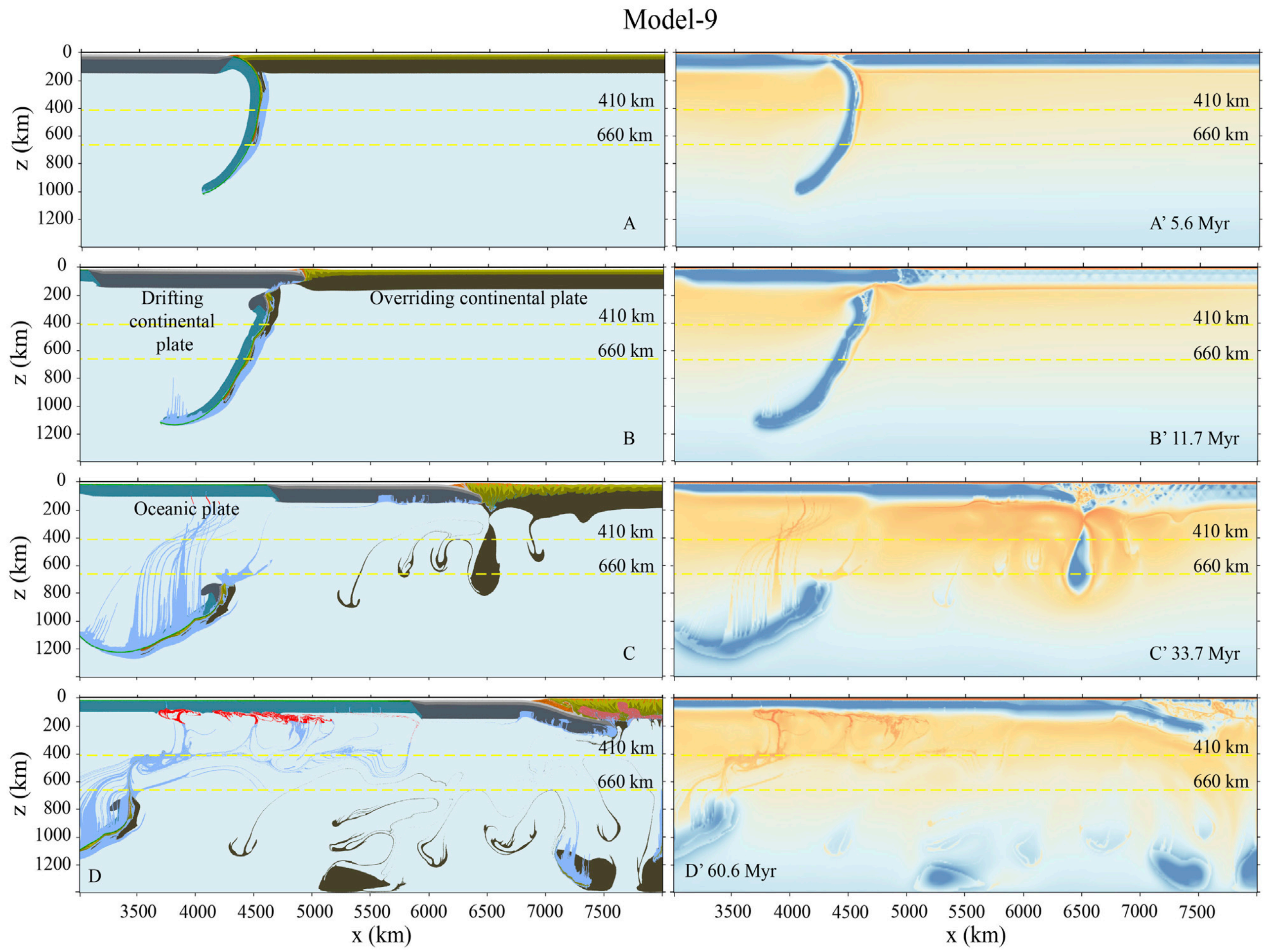

FIGURE 11 | Model-9 evolution with a further decreased and uniform plastic friction coefficient of the overriding lithospheric mantle of $\lambda \cdot \sin(\varphi) = 0.01$ (**Supplementary Table S2** and **Supplementary Equation S11** in the supporting information). All the other parameters are identical to Model-8 (**Figure 10**). **(A–D)** The composition field evolution with the corresponding colorbar is shown in **Figure 2A**. **(A'–D')** The effective viscosity evolution with the corresponding colorbar is shown in **Figure 2B**.

(**Figure 11**), with plate convergence mostly accommodated by the shortening of the overriding plate, due to its great weakness. In this model, the lithospheric delamination occurs more frequently with many small blocks of thickened lithospheric mantle detached repeatedly (**Figures 12C,D**). Finally, the average thickness of the overriding crust increases to ~127 km, with the time-dependent evolutions shown in **Supplementary Figure S2** of the supporting information. The total amount of convergence after the initial collision is about 3,400 km, which is mostly absorbed by the overriding plate. The shortening of the overriding plate accommodates an even large amount of convergence of ~2,600 km, whereas the subducting continental plate only consumes about 800 km (**Table 1**).

Summary of Model Results

Based on the numerical models, three continental collision modes are identified (**Figure 13**), including collision-induced subduction transference (Model-1 and Model-6), continuous continental deep subduction (Model-2, Model-3, Model-7, and Model-8), and overriding plate shortening and delamination (Model-4, Model-5, Model-9, and Model-10). Since the drifting (Indian) continental plate is generally considered to be strong, the collision mode selection is mainly dependent on the rheological strength of the overriding continental plate. When the overriding lithosphere is strong, the continuous convergence after collision leads to the subduction of positively buoyant continental lithosphere. The resulting resistance contributes to the subduction transference to the neighboring oceanic plate, as shown in **Figure 13A**. When the rheological strength of the overriding plate is reduced, it will accommodate a significant amount of strain during collision. Consequently, the continental subduction rate will be reduced, which will lead to continental crustal detachment and exhumation as well as the heating of sinking continental plate. Thus, the resistant force from continental subduction will be decreased, and the continental deep subduction is favored rather than the subduction transference (**Figure 13B**). The deeply subducted continental slab will finally break-off and sink into the deeper mantle.

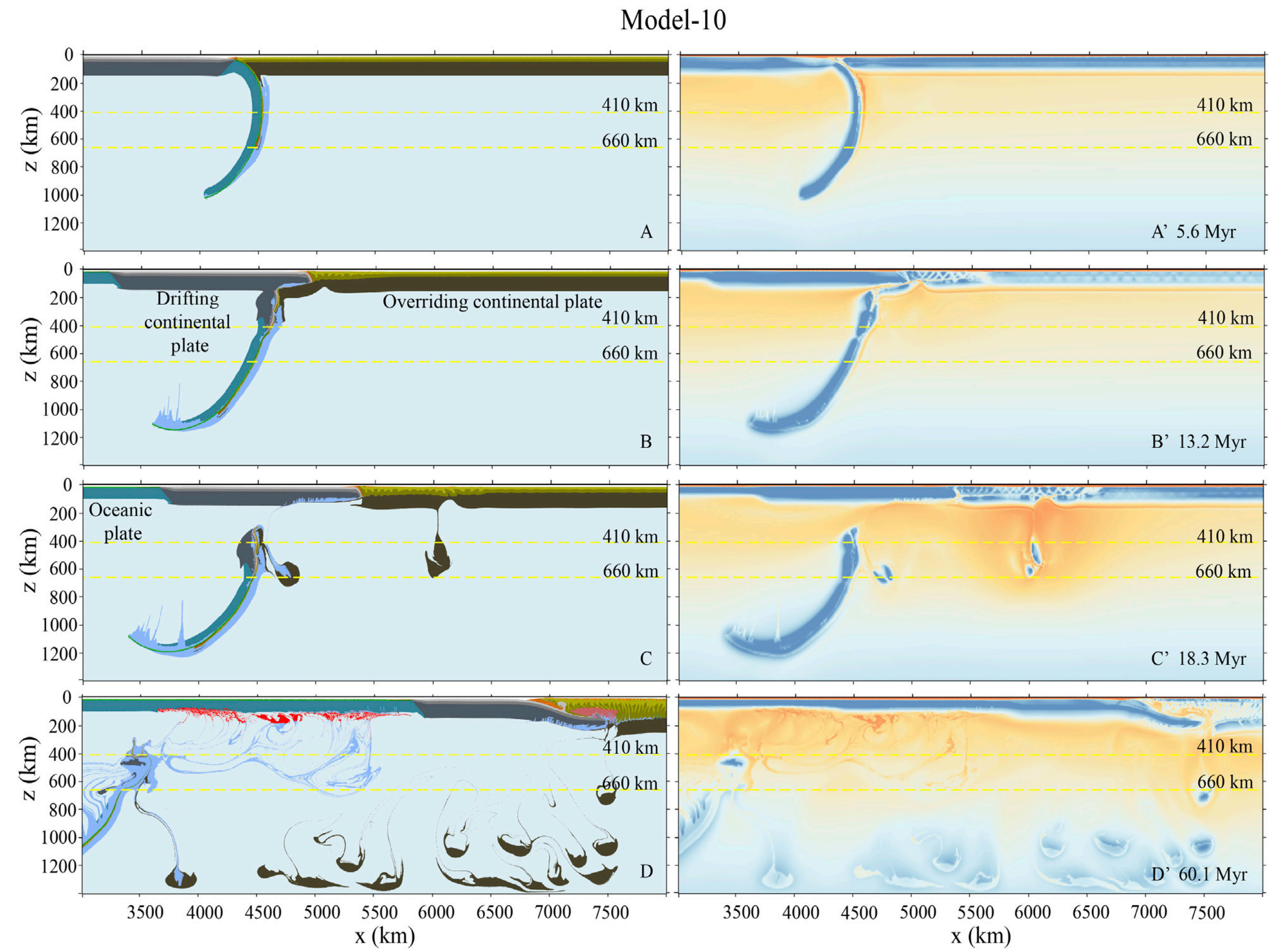

FIGURE 12 | Model-10 evolution with the weakest overriding plate. The plastic friction coefficient of the overriding lithospheric mantle is initially $\lambda \cdot \sin(\varphi) = 0.01$ and will decrease linearly to 0.001 with accumulated plastic strain to $\varepsilon_{plas} = 1$ (**Supplementary Table S2** and **Supplementary Equation S11** in the supporting information). All the other parameters are identical to Model-9 (**Figure 11**). **(A–D)** The composition field evolution with the corresponding colorbar is shown in **Figure 2A**. **(A'–D')** The effective viscosity evolution with the corresponding colorbar is shown in **Figure 2B**.

When the overriding plate is very weak, the drifting continental plate subducts following the oceanic slab and breaks off earlier at a shallow depth (~200–400 km) (**Figure 13C**). After that, most of the convergence will be absorbed by the gradual shortening of the overriding continental plate, which further contributes to lithospheric delamination and crustal thickening (**Figure 13C**). In addition, when the overriding continental plate is strong (0.6–0.1), the horizontal movement of the drifting continental plate is blocked. Therefore, the drifting continental plate tends to subduct following the oceanic slab. The continuous subduction hinders slab break-off (**Figure 13A**). In contrast, with the weak overriding continental plate, the drifting continental plate tends to move horizontally rather than subduction. Then, a strong extension is resulted between the horizontal plate and the subducted slab. Thus, the slab break-off is preferred (**Figures 13B,C**).

The different model evolution times (55 and 60 Myr) lead to contrasting amounts of convergence accommodated by the lower and upper plates, which result in different overriding crustal thicknesses (**Table 1**). However, the general continental collision mode selection is consistent, depending on the rheological strength of the overriding lithosphere (**Figure 13**).

DISCUSSION

Mechanism for the Absence of Subduction Transference During India–Asia Collision

It is generally considered that the collision of Galatian and Cimmerian terranes with Eurasia leads to SI of the Paleo-Tethyan and Neo-Tethyan Oceanic plates, respectively (Stampfli and Borel, 2002; Stampfli et al., 2013; Wan et al., 2019; Zhong and Li, 2020). However, the collision between the Indian and Eurasian plates does not result in subduction transference to the Indian Ocean, even after the long-time collision of >50 Myr. Instead, the continuous convergence

TABLE 1 | Summary of model parameters and results.

Plastic friction coefficient of the overriding lithospheric mantle	Subduction transference or not	Convergence from 55 Ma with a continental collision duration of ~50 Myrs					Convergence from 60 Ma with a continental collision duration of ~55 Myrs				
		Model	Continental break-off (km)	Continental subduction but not break-off (km)	Overriding plate shortening (km)	Final overriding crustal thickness (km)	Model	Continental break-off (km)	Continental subduction but not break-off (km)	Overriding plate shortening (km)	Final overriding crustal thickness (km)
0.6→0.1	Yes	Model-1	—	—	—	35	Model-6	—	—	—	35
0.1	No	Model-2	~700	~1,100	~1,100	~53	Model-7	~800	~700	~2,100	~82
0.1→0.01	No	Model-3	~700	~500	~1700	~70	Model-8	~300	~900	~2,400	~100
0.01	No	Model-4	~50	~500	~2,150	~87	Model-9	~100	~900	~2,400	~104
0.01→0.001	No	Model-5	~100	~500	~2,100	~87	Model-10	~100	~700	~2,600	~127

leads to the extensive shortening and delamination of the Tibetan lithosphere.

The absence of subduction transference during the India–Asia collision is an important and controversial problem. The current model results indicate that the strong overriding plate favors subduction transference to the neighboring oceanic plate after the continental collision for 10–20 Myr (**Figures 3**, **8**). In contrast, the rheological weakness of the overriding Tibetan plate before India–Asia collision may accommodate a major part of continental convergence and thus prevent the strain localization in the neighboring oceanic plate. Consequently, the subduction transference will be prohibited.

In the natural India–Asia collision system, the overriding Tibetan plateau is composed of several terranes, including Lhasa, Qiangtang, Songpan-Ganzi, Qaidam, and Qilian terranes from south to north, which have been accreted to the Eurasian Continent before the final Indian collision (Replumaz and Tapponnier, 2003). Each accretion process is following the oceanic subduction with a wide spread magmatism, as evidenced by the magmatic rocks in the Lhasa and Qiangtang terranes (Hsü et al., 1995; Li et al., 2009; Zhu et al., 2011, 2013). Based on the complex formation and evolution of the overriding Tibetan plate, its lithospheric mantle could be rheologically weaker than that of the normal cratonic lithosphere, although the absolute weakness is hard to constrain.

Finally, we propose that the weakness of the overriding Tibetan plate before India–Asia collision plays an important role in prohibiting subduction transference, which thus explains the lack of SI at the southern Indian continental margin and northern Indian oceanic plate.

Deformation Partition and Continental Mass Balance During India–Asia Collision

The continental mass conservation during the India–Asia collision is also a challenging and controversial topic. Previous evaluations and estimations suggest that there is a large amount of deficit mass in the crustal mass of the Greater Indian and Tibetan plates during the long-lasting continental collision (Capitanio et al., 2010; Replumaz et al., 2010; Yakovlev and Clark, 2014; Ingalls et al., 2016). In order to solve this problem, different type of models with assuming an oceanic basin within the Greater India has been proposed (e.g., van Hinsbergen et al., 2012, 2019). The oceanic basin subduction is applied in the model to reconcile the conservation of continental crustal mass. However, there is no geological evidence for this period of oceanic subduction (Najman et al., 2010; Aitchison and Ali, 2012; Wu et al., 2014; Hu et al., 2016; Ding et al., 2017). On the other hand, the exact time of collision has not been well-constrained. The plate reconstructions suggested an extremely high convergence rate of ~14 cm/yr between the Indian and Asian continents at ~60–50 Ma. Thus, the uncertainty in the time of initial collision for 5 Myr may lead to a deviation of 700 km in total convergence.

In the current numerical models with the India–Asia convergence from 55 Ma, i.e., continental collision for 50

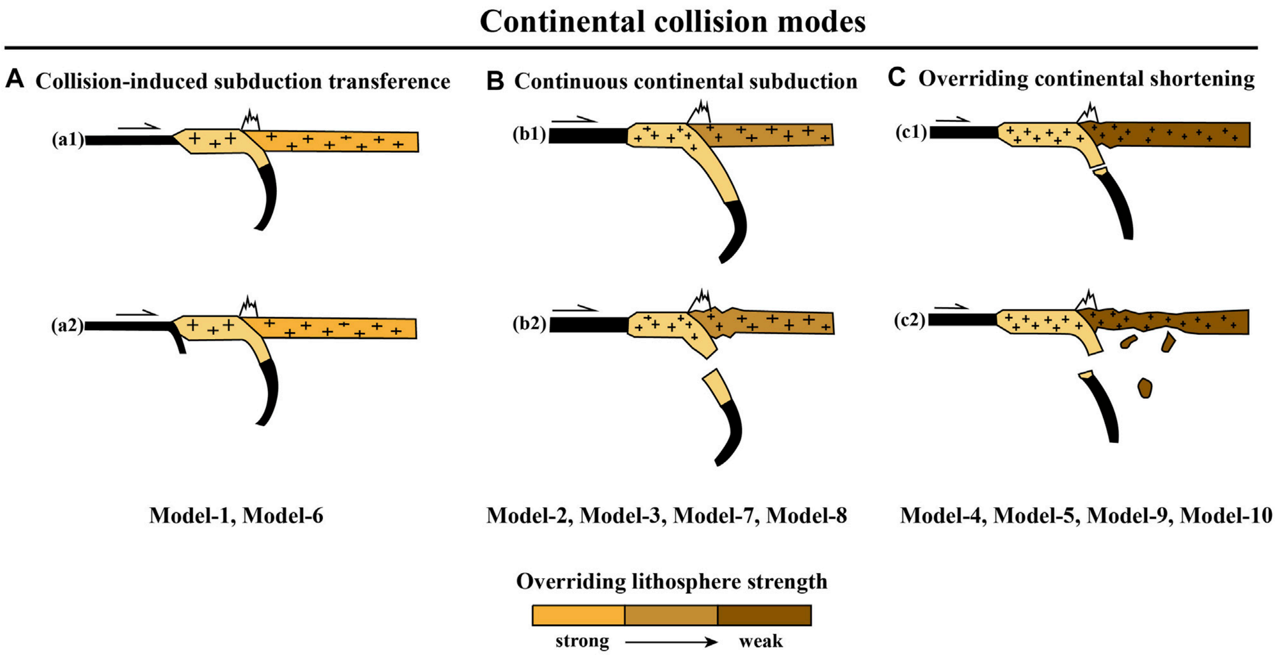

FIGURE 13 | Three collision modes dependent on the rheological strength of the overriding lithosphere. **(A)** Collision-induced subduction transference with a strong overriding plate. **(B)** Continuous continental deep subduction with intermediate strength of the overriding plate. **(C)** Overriding lithospheric shortening and delamination with a weak overriding plate.

Myr, the total convergence between India and Eurasia is about 2,700–2,900 km after the collision. A large portion of convergence (i.e., ~1,600 ± 500 km) is accommodated by the shortening of the overriding Tibetan plate, while the other portion of ~1,175 ± 625 km is consumed by the subduction and break-off of the drifting continental plate (**Table 1**). In the natural India–Asia collision system, the shortening of the overriding plate, including the northeastern portion/margin of the Tibetan plateau, may be about 1,600–1700 km (Peltzer and Tapponnier, 1988; Wang 1997; Yin and Harrison, 2000; Yin et al., 2002; Fang et al., 2007; van Hinsbergen et al., 2019). Thus, the total amount of shortening is consistent with the model (e.g., Model-3) with intermediate rheological strength of the Tibetan lithosphere (**Table 1**). In this case of Model-3, the Greater Indian plate accommodates ~1,200 km, including ~700 km of the detached continental slab and ~500 km of the subducted but not detached continental slab (**Figure 5**). It indicates that the convergence-induced deformation partition and continental mass balance can be generally reconciled with continental collision for 50 Myr, i.e. the model convergence from 55 Ma with oceanic subduction in the first ~5 Myr.

In another case with the India–Asia convergence from 60 Ma, i.e. continental collision for ~55 Myr, the amount of convergence after collision between the two continental plates is about 3,400–3,600 km. The shortening of the overriding plate has to be >2,000 km (**Table 1**), which is too large to be comparable with the observations (Peltzer and Tapponnier, 1988; Wang 1997; Yin and Harrison, 2000; Yin et al., 2002; Fang et al., 2007; van Hinsbergen et al., 2019). In addition, the resulting overriding crustal thickness is from 82 to 127 km, which is also larger than that of the present-day Tibetan Plateau (Replumaz et al., 2010; Yakovlev and Clark, 2014). Thus, in order to accommodate the excess shortening of the overriding continental plate (~1,000 km) in this case, other models are required, e.g., the Greater Indian Oceanic Basin model or the Self-driven Continental Deep Subduction model, which needs to be examined in the future study.

CONCLUSION

In this study, the reconstruction-based India–Asia convergence rate is integrated with a large-scale thermomechanical numerical model, in order to study the dynamics of continental collision mode selection and the conditions for collision-induced subduction transference, as well as the deformation partition and continental mass balance during the India–Asia collision. The main conclusions are shown below:

(1) Three collision modes are identified with variable rheological strength of the overriding plate: collision-induced subduction transference, continuous continental subduction, and overriding plate shortening and delamination.
(2) The collision between the rheologically strong continental plates favors subduction transference to the neighboring oceanic plate. In contrast, the strain localization in the weak overriding plate hinders subduction transference.

(3) If the overriding plate is too weak, it will accommodate most of the convergence, leading to extensive lithospheric thickening and repeated delamination, which is difficult for reconciling the crustal thickness of the present-day Tibetan Plateau.
(4) In case of India–Asia collision for ~50 Myr, the model with the intermediately weak overriding Tibetan plate may reconcile the general deformation partition and continental mass balance of the Himalayan–Tibetan system, without the requirement of an oceanic basin in the Greater India.
(5) The longer period of India–Asia collision for ≥55 Myr leads to significant shortening of the overriding plate that is hard to be comparable with the present-day Tibetan Plateau. The models with a Greater Indian Oceanic Basin or Self-driven Continental Deep Subduction may be required to solve the problem, which need further examinations.

DATA AVAILABILITY STATEMENT

The datasets presented in this study can be found in online repositories. The names of the repository/repositories and accession number(s) can be found at: https://doi.org/10.5281/zenodo.5814796.

AUTHOR CONTRIBUTIONS

Z-HL conceived the study. QL and XZ designed the numerical models. QL ran the models. All authors contributed to the data analysis, discussion, and writing the manuscript.

FUNDING

This work was supported by the NSFC Tethys project (91855208), the Strategic Priority Research Program (B) of Chinese Academy of Sciences (XDB42000000), and the Fundamental Research Funds for the Central Universities.

ACKNOWLEDGMENTS

Numerical simulations were run with the clusters of the National Supercomputer Center in Guangzhou (Tianhe-II).

SUPPLEMENTARY MATERIAL

The Supplementary Material for this article can be found online at: https://www.frontiersin.org/articles/10.3389/feart.2022.919174/full#supplementary-material

REFERENCES

Aitchison, J. C., and Ali, J. R. (2012). India-Asia Collision Timing. *Proc. Natl. Acad. Sci. U. S. A.* 109 (40), E2645. doi:10.1073/pnas.1207859109

Aitchison, J. C., Ali, J. R., and Davis, A. M. (2007). When and where Did India and Asia Collide? *J. Geophys. Res.* 112, B05423. doi:10.1029/2006jb004706

Capitanio, F. A., Morra, G., Goes, S., Weinberg, R. F., and Moresi, L. (2010). India-Asia Convergence Driven by the Subduction of the Greater Indian Continent. *Nat. Geosci.* 3 (2), 136–139. doi:10.1038/ngeo725

Cloetingh, S., Wortel, R., and Vlaar, N. J. (1989). On the Initiation of Subduction Zones. *Pageoph* 129 (1-2), 7–25. doi:10.1007/bf00874622

Copley, A., Avouac, J. P., and Royer, J. Y. (2010). India-Asia Collision and the Cenozoic Slowdown of the Indian Plate: Implications for the Forces Driving Plate Motions. *J. Geophys. Res.* 115, B03410. doi:10.1029/2009jb006634

Cui, Q., Li, Z.-H., and Liu, M. (2021). Crustal Thickening versus Lateral Extrusion during India-Asia Continental Collision: 3-D Thermo-Mechanical Modeling. *Tectonophysics* 818, 229081. doi:10.1016/j.tecto.2021.229081

Ding, H., Zhang, Z., Dong, X., Tian, Z., Xiang, H., Mu, H., et al. (2016). Early Eocene (C. 50 Ma) Collision of the Indian and Asian Continents: Constraints from the North Himalayan Metamorphic Rocks, Southeastern Tibet. *Earth Planet. Sci. Lett.* 435, 64–73. doi:10.1016/j.epsl.2015.12.006

Ding, L., Maksatbek, S., Cai, F., Wang, H., Song, P., Ji, W., et al. (2017). Processes of Initial Collision and Suturing between India and Asia. *Sci. China Earth Sci.* 60 (4), 635–651. doi:10.1007/s11430-016-5244-x

Fang, X., Zhang, W., Meng, Q., Gao, J., Wang, X., King, J., et al. (2007). High-resolution Magnetostratigraphy of the Neogene Huaitoutala Section in the Eastern Qaidam Basin on the NE Tibetan Plateau, Qinghai Province, China and its Implication on Tectonic Uplift of the NE Tibetan Plateau. *Earth Planet. Sci. Lett.* 258 (1-2), 293–306. doi:10.1016/j.epsl.2007.03.042

Gan, W., Zhang, P., Shen, Z. K., Niu, Z., Wang, M., Wan, Y., et al. (2007). Present-Day Crustal Motion within the Tibetan Plateau Inferred from GPS Measurements. *J. Geophys. Res.* 112, B08416. doi:10.1029/2005jb004120

Gerya, T. V. (2010). *Introduction to Numerical Geodynamic Modelling*. Cambridge: Cambridge University Press.

Gibbons, A. D., Zahirovic, S., Müller, R. D., Whittaker, J. M., and Yatheesh, V. (2015). A Tectonic Model Reconciling Evidence for the Collisions between India, Eurasia and Intra-oceanic Arcs of the Central-Eastern Tethys. *Gondwana Res.* 28 (2), 451–492. doi:10.1016/j.gr.2015.01.001

Hsü, K. J., Guitang, P., and Sengör, A. M. C. (1995). Tectonic Evolution of the Tibetan Plateau: A Working Hypothesis Based on the Archipelago Model of Orogenesis. *Int. Geol. Rev.* 37 (6), 473–508. doi:10.1080/00206819509465414

Hu, X., Garzanti, E., Wang, J., Huang, W., An, W., and Webb, A. (2016). The Timing of India-Asia Collision Onset - Facts, Theories, Controversies. *Earth-Sci. Rev.* 160, 264–299. doi:10.1016/j.earscirev.2016.07.014

Huangfu, P., Li, Z.-H., Fan, W., Zhang, K.-J., and Shi, Y. (2019). Continental Lithospheric-Scale Subduction versus Crustal-Scale Underthrusting in the Collision Zone: Numerical Modeling. *Tectonophysics* 757, 68–87. doi:10.1016/j.tecto.2019.03.007

Ingalls, M., Rowley, D. B., Currie, B., and Colman, A. S. (2016). Large-scale Subduction of Continental Crust Implied by India-Asia Mass-Balance Calculation. *Nat. Geosci.* 9 (11), 848–853. doi:10.1038/ngeo2806

Jain, A. K., Banerjee, D. M., and Kale, V. S. (2020). *Tectonics of the Indian Subcontinent: An Introduction*. Cham, Switzerland: Springer. doi:10.1007/978-3-030-42845-7_1

Kapp, P., and DeCelles, P. G. (2019). Mesozoic-Cenozoic Geological Evolution of the Himalayan-Tibetan Orogen and Working Tectonic Hypotheses. *Am. J. Sci.* 319 (3), 159–254. doi:10.2475/03.2019.01

Kelly, S., Butler, J. P., and Beaumont, C. (2016). Continental Collision with a Sandwiched Accreted Terrane: Insights into Himalayan–Tibetan Lithospheric Mantle Tectonics? *Earth Planet. Sci. Lett.* 455, 176–195. doi:10.1016/j.epsl.2016.08.039

Klootwijk, C. T., Gee, J. S., Peirce, J. W., Smith, G. M., and McFadden, P. L. (1992). An Early India-Asia Contact: Paleomagnetic Constraints from Ninetyeast Ridge, ODP Leg 121. *Geol* 20 (5), 395. doi:10.1130/0091-7613(1992)020<0395:aeiacp>2.3.co;2

Lee, T. Y., and Lawver, L. A. (1995). Cenozoic Plate Reconstruction of Southeast Asia. *Tectonophysics* 251 (1-4), 85–138. doi:10.1016/0040-1951(95)00023-2

Li, H., Xu, Z., Yang, J., Cai, Z., Chen, S., and Tang, Z. (2009). Records of Indosinian Orogenesis in Lhasa Terrane, Tibet. *J. Earth Sci.* 20 (2), 348–363. doi:10.1007/s12583-009-0029-9

Li, Z.-H., Liu, M., and Gerya, T. (2016). Lithosphere Delamination in Continental Collisional Orogens: A Systematic Numerical Study. *J. Geophys. Res. Solid Earth* 121 (7), 5186–5211. doi:10.1002/2016jb013106

Li, Z.-H., Gerya, T., and Connolly, J. A. D. (2019). Variability of Subducting Slab Morphologies in the Mantle Transition Zone: Insight from Petrological-thermomechanical Modeling. *Earth-Sci. Rev.* 196, 102874. doi:10.1016/j.earscirev.2019.05.018

Li, Z. H., Cui, Q., Zhong, X., Liu, M. Q., Wang, Y., and Huangfu, P. (2021). Numerical Modeling of Continental Dynamics: Questions, Progress and Perspectives. *Acta Geol. Sin.* 95, 238–258. doi:10.1111/1755-6724.14832

Liu, L., Liu, L., and Xu, Y. G. (2021). Intermittent Post-Paleocene Continental Collision in South Asia. *Geophys. Res. Lett.* 48, e2021GL094531. doi:10.1029/2021gl094531

Martin, C. R., Jagoutz, O., Upadhyay, R., Royden, L. H., Eddy, M. P., Bailey, E., et al. (2020). Paleocene Latitude of the Kohistan-Ladakh Arc Indicates Multistage India-Eurasia Collision. *Proc. Natl. Acad. Sci. U.S.A.* 117 (47), 29487–29494. doi:10.1073/pnas.2009039117

Meng, J., Gilder, S. A., Wang, C., Coe, R. S., Tan, X., Zhao, X., et al. (2019). Defining the Limits of Greater India. *Geophys. Res. Lett.* 46 (8), 4182–4191. doi:10.1029/2019gl082119

Meng, J., Gilder, S. A., Li, Y., Wang, C., and Liu, T. (2020). Expanse of Greater India in the Late Cretaceous. *Earth Planet. Sci. Lett.* 542, 116330. doi:10.1016/j.epsl.2020.116330

Molnar, P., and Stock, J. M. (2009). Slowing of India's Convergence with Eurasia since 20 Ma and its Implications for Tibetan Mantle Dynamics. *Tectonics* 28 (3), TC3001. doi:10.1029/2008tc002271

Molnar, P., England, P., and Martinod, J. (1993). Mantle Dynamics, Uplift of the Tibetan Plateau, and the Indian Monsoon. *Rev. Geophys.* 31 (4), 357–396. doi:10.1029/93rg02030

Müller, R. D., Sdrolias, M., Gaina, C., and Roest, W. R. (2008). Age, Spreading Rates, and Spreading Asymmetry of the World's Ocean Crust. *Geochem. Geophys. Geosyst.* 9, Q04006. doi:10.1029/2007GC001743

Najman, Y., Appel, E., Boudagher-Fadel, M., Bown, P., Carter, A., Garzanti, E., et al. (2010). Timing of India-Asia Collision: Geological, Biostratigraphic, and Palaeomagnetic Constraints. *J. Geophys. Res.* 115, B12416. doi:10.1029/2010jb007673

Parsons, A. J., Hosseini, K., Palin, R., and Sigloch, K. (2020). Geological, Geophysical and Plate Kinematic Constraints for Models of the India-Asia Collision and the Post-Triassic Central Tethys Oceans. *Earth-Sci. Rev.* 208, 103084. doi:10.1016/j.earscirev.2020.103084

Peltzer, G., and Tapponnier, P. (1988). Formation and Evolution of Strike-Slip Faults, Rifts, and Basins during the India-Asia Collision: An Experimental Approach. *J. Geophys. Res.* 93 (B12), 15085–15117. doi:10.1029/jb093ib12p15085

Replumaz, A., and Tapponnier, P. (2003). Reconstruction of the Deformed Collision Zone Between India and Asia by Backward Motion of Lithospheric Blocks. *J. Geophys. Res. Solid Earth* 108 (B6), 2285. doi:10.1029/2001jb000661

Replumaz, A., Negredo, A. M., Guillot, S., der Beek, P. V., and Villaseñor, A. (2010). Crustal Mass Budget and Recycling during the India/Asia Collision. *Tectonophysics* 492 (1-4), 99–107. doi:10.1016/j.tecto.2010.05.023

Replumaz, A., Capitanio, F. A., Guillot, S., Negredo, A. M., and Villaseñor, A. (2014). The Coupling of Indian Subduction and Asian Continental Tectonics. *Gondwana Res.* 26 (2), 608–626. doi:10.1016/j.gr.2014.04.003

Schmeling, H., Babeyko, A. Y., Enns, A., Faccenna, C., Funiciello, F., Gerya, T., et al. (2008). A Benchmark Comparison of Spontaneous Subduction Models—Towards a Free Surface. *Phys. Earth Planet. Inter.* 171 (1-4), 198–223. doi:10.1016/j.pepi.2008.06.028

Stampfli, G. M., and Borel, G. D. (2002). A Plate Tectonic Model for the Paleozoic and Mesozoic Constrained by Dynamic Plate Boundaries and Restored Synthetic Oceanic Isochrons. *Earth Planet. Sci. Lett.* 196 (1-2), 17–33. doi:10.1016/s0012-821x(01)00588-x

Stampfli, G. M., Hochard, C., Vérard, C., Wilhem, C., and vonRaumer, J. (2013). The Formation of Pangea. *Tectonophysics* 593, 1–19. doi:10.1016/j.tecto.2013.02.037

Stern, R. J., and Gerya, T. (2018). Subduction Initiation in Nature and Models: A Review. *Tectonophysics* 746, 173–198. doi:10.1016/j.tecto.2017.10.014

Stern, R. J. (2004). Subduction Initiation: Spontaneous and Induced. *Earth Planet. Sci. Lett.* 226 (3-4), 275–292. doi:10.1016/s0012-821x(04)00498-4

Sun, Z., Pei, J., Li, H., Xu, W., Jiang, W., ZhuWang, Z. X., et al. (2012). Palaeomagnetism of Late Cretaceous Sediments from Southern Tibet: Evidence for the Consistent Palaeolatitudes of the Southern Margin of Eurasia Prior to the Collision with India. *Gondwana Res.* 21 (1), 53–63. doi:10.1016/j.gr.2011.08.003

Tapponnier, P., Peltzer, G., Le Dain, A. Y., Armijo, R., and Cobbold, P. (1982). Propagating Extrusion Tectonics in Asia: New Insights from Simple Experiments with Plasticine. *Geology* 10 (12), 611. doi:10.1130/0091-7613(1982)10<611:petian>2.0.co;2

Tapponnier, P., Zhiqin, X., Roger, F., Meyer, B., Arnaud, N., Wittlinger, G., et al. (2001). Oblique Stepwise Rise and Growth of the Tibet Plateau. *Science* 294, 1671–1677. doi:10.1126/science.105978

Torsvik, T. H., and Cocks, L. R. M. (2013). Gondwana from Top to Base in Space and Time. *Gondwana Res.* 24 (3-4), 999–1030. doi:10.1016/j.gr.2013.06.012

Turcotte, D. L., and Schubert, G. (2002). *Geodynamics*. 2nd ed. New York: Cambridge Univ. Press, 456.

van Hinsbergen, D. J. J., Steinberger, B., Doubrovine, P. V., and Gassmöller, R. (2011). Acceleration and Deceleration of India-Asia Convergence since the Cretaceous: Roles of Mantle Plumes and Continental Collision. *J. Geophys. Res.* 116, B06101. doi:10.1029/2010jb008051

van Hinsbergen, D. J. J., Lippert, P. C., Dupont-Nivet, G., McQuarrie, N., Doubrovine, P. V., Spakman, W., et al. (2012). Greater India Basin Hypothesis and a Two-Stage Cenozoic Collision between India and Asia. *Proc. Natl. Acad. Sci. U.S.A.* 109 (20), 7659–7664. doi:10.1073/pnas.1117262109

van Hinsbergen, D. J. J., Lippert, P. C., Li, S., Huang, W., Advokaat, E. L., and Spakman, W. (2019). Reconstructing Greater India: Paleogeographic, Kinematic, and Geodynamic Perspectives. *Tectonophysics* 760, 69–94. doi:10.1016/j.tecto.2018.04.006

Wan, B., Wu, F., Chen, L., Zhao, L., Liang, X., Xiao, W., et al. (2019). Cyclical One-Way Continental Rupture-Drift in the Tethyan Evolution: Subduction-Driven Plate Tectonics. *Sci. China Earth Sci.* 62, 2005–2016. doi:10.1007/s11430-019-9393-4

Wang, C., Dai, J., Zhao, X., Li, Y., Graham, S. A., He, D., et al. (2014). Outward-growth of the Tibetan Plateau during the Cenozoic: A Review. *Tectonophysics* 621, 1–43. doi:10.1016/j.tecto.2014.01.036

Wang, H. Q., Ding, L., Cai, F. L., Sun, Y. L., Li, S., Yue, Y. H., et al. (2019). The Latest Jurassic Protoliths of the Sangsang Mafic Schists in Southern Tibet: Implications for the Spatial Extent of Greater India. *Gondwana Res.* 79, 248–262. doi:10.1016/j.gr.2019.10.008

Wang, E. (1997). Displacement and Timing along the Northern Strand of the Altyn Tagh Fault Zone, Northern Tibet. *Earth Planet. Sci. Lett.* 150 (1-2), 55–64. doi:10.1016/s0012-821x(97)00085-x

Wu, F.-Y., Ji, W.-Q., Wang, J.-G., Liu, C.-Z., Chung, S.-L., and Clift, P. D. (2014). Zircon U-Pb and Hf Isotopic Constraints on the Onset Time of India-Asia Collision. *Am. J. Sci.* 314 (2), 548–579. doi:10.2475/02.2014.04

Yakovlev, P. V., and Clark, M. K. (2014). Conservation and Redistribution of Crust during the Indo-Asian Collision. *Tectonics* 33 (6), 1016–1027. doi:10.1002/2013tc003469

Yi, Z., Huang, B., Chen, J., Chen, L., and Wang, H. (2011). Paleomagnetism of Early Paleogene Marine Sediments in Southern Tibet, China: Implications to Onset of the India Asia Collision and Size of Greater India. *Earth Planet. Sci. Lett.* 309, 153–165. doi:10.1016/j.epsl.2011.07.001

Yin, A., and Harrison, T. M. (2000). Geologic Evolution of the Himalayan-Tibetan Orogen. *Annu. Rev. Earth Planet. Sci.* 28 (1), 211–280. doi:10.1146/annurev.earth.28.1.211

Yin, A., Rumelhart, P. E., Butler, R., Cowgill, E., Harrison, T. M., Foster, D. A., et al. (2002). Tectonic History of the Altyn Tagh Fault System in Northern Tibet Inferred from Cenozoic Sedimentation. *Geol. Soc. Am. Bull.* 114 (10), 1257–1295. doi:10.1130/0016-7606(2002)114<1257:thotat>2.0.co;2

Zhang, L., Wang, Y., and Li, Z.-H. (2022). Where Is the Missing Felsic Crust of Greater Indian Continent? *Commun. Earth Environ.* doi:10.21203/rs.3.rs-227521/v1

Zheng, Y., and Wu, F. (2018). The Timing of Continental Collision between India and Asia. *Sci. Bull.* 63 (24), 1649–1654. doi:10.1016/j.scib.2018.11.022

Zhong, X. Y., and Li, Z. H. (2020). Subduction Initiation during Collision-induced Subduction Transference: Numerical Modeling and Implications for the Tethyan Evolution. *J. Geophys. Res. Solid Earth* 125 (2), e2019JB019288. doi:10.1029/2019jb019288

Zhong, X., and Li, Z. H. (2022). Wedge-Shaped Southern Indian Continental Margin Without Proper Weakness Hinders Subduction Initiation. *Geochem. Geophys. Geosyst.* 23, e2021GC009998. doi:10.1029/2021GC009998

Zhou, J., and Su, H. (2019). Site and Timing of Substantial India-Asia Collision Inferred from Crustal Volume Budget. *Tectonics* 38, 2275–2290. doi:10.1029/2018tc005412

Zhu, D. C., Zhao, Z. D., Niu, Y., Mo, X. X., Chung, S. L., Hou, Z. Q., et al. (2011). The Lhasa Terrane: Record of a Microcontinent and its Histories of Drift and Growth. *Earth Planet. Sci. Lett.* 301 (1-2), 241–255. doi:10.1016/j.epsl.2010.11.005

Zhu, D.-C., Zhao, Z.-D., Niu, Y., Dilek, Y., Hou, Z.-Q., and Mo, X.-X. (2013). The Origin and Pre-Cenozoic Evolution of the Tibetan Plateau. *Gondwana Res.* 23 (4), 1429–1454. doi:10.1016/j.gr.2012.02.002

Zhu, R., Zhao, P., and Zhao, L. (2021). Tectonic Evolution and Geodynamics of the Neo-Tethys Ocean. *Sci. China Earth Sci.* 65, 1–24. doi:10.1007/s11430-021-9845-7

Conflict of Interest: The authors declare that the research was conducted in the absence of any commercial or financial relationships that could be construed as a potential conflict of interest.

frontiers | Frontiers in Earth Science

TYPE Original Research
PUBLISHED 29 August 2022
DOI 10.3389/feart.2022.908234

OPEN ACCESS

EDITED BY
Manuele Faccenda,
Università Padova, Italy

REVIEWED BY
Bernhard Maximilian Steinberger,
GFZ German Research Centre for Geosciences, Germany
Andres Tassara,
University of Concepcion, Chile

*CORRESPONDENCE
Ritabrata Dasgupta,
ritabratadasgupta.rs@jadavpuruniversity.in
Nibir Mandal,
nibir.mandal@jadavpuruniversity.in

SPECIALTY SECTION
This article was submitted to Solid Earth Geophysics,
a section of the journal
Frontiers in Earth Science

RECEIVED 30 March 2022
ACCEPTED 27 July 2022
PUBLISHED 29 August 2022

CITATION
Dasgupta R and Mandal N (2022),
Trench topography in subduction zones: A reflection of the plate decoupling depth.
Front. Earth Sci. 10:908234.
doi: 10.3389/feart.2022.908234

Trench topography in subduction zones: A reflection of the plate decoupling depth

Ritabrata Dasgupta[1]* and Nibir Mandal[2]*

[1]Department of Earth System Science, Yonsei University, Seoul, South Korea, [2]Department of Geological Sciences, Jadavpur University, Kolkata, India

Subduction of lithospheric plates produces narrow, linear troughs (trench) in front of the overriding plates at the convergent boundaries. The trenches show a wide variation in their topographic characteristics, such as width, vertical depth, and bounding surface slopes. Benchmarking their controlling factors is thus a crucial step in the analysis of trench morphology. This article identifies the mechanical coupling between the subducting and overriding plates as a leading factor in modulating the topographic evolution of a trench. The maximum depth of decoupling (MDD) is used to express the degree of decoupling at the plate interface. We simulate subduction zones in computational fluid dynamic (CFD) models to show the topographic elements (maximum negative relative relief: D; fore- and hinter-wall slopes: θ_F and θ_H; opening width: W) of trenches as a function of the MDD within a range of 30–120 km. Both D and θ strongly depend on the MDD, whereas W is found to be relatively less sensitive to the MDD, implying that the narrow/broad width of a trench can change little with the plate decoupling factor. We also show that the MDD critically controls the fore-arc stress fields of a trench, switching a compressive to tensile stress transition with increasing MDD. This study finally validates the model findings with well-constrained natural trench topography.

KEYWORDS

subduction zone, trench dynamics, stress field, CFD modeling, relative relief

Introduction

Mechanical coupling between the participating lithospheric plates (subducting and overriding plates) in subduction zones regulates a range of slab-driven processes, such as earthquake generation (Scholz and Campos, 1995; Ruff and Tichelaar, 1996; Kameda et al., 2011; Lallemand et al., 2018), dehydration melting in mantle wedges (Wada and Wang, 2009; Wada et al., 2012; Lee and Wada, 2017), and overriding plate deformations (Duarte et al., 2013; Willingshofer et al., 2013; Dasgupta and Mandal, 2018). More importantly, this coupling factor plays the most decisive role in the tectonic force transfer from subducting to overriding plates under a given set of tectonic parameters, such as slab age and plate convergence velocity (Kanamori, 1971; Ruff and Kanamori, 1983). A major direction of subduction studies thus focuses on plate-interface processes that critically determine the nature as well as the degree of mechanical coupling between two convergent plates (Wada and Wang, 2009; Syracuse et al., 2010; Abers et al., 2020). It has been shown that a plate interface undergoes two sequential rheological transitions with increasing depth, a brittle-ductile transition at 20–50 km, followed by a transition to viscous coupling at ~ 70–100 km (Abers et al., 2020). The second rheological transition is assisted mainly by fluid release processes (Schmidt and Poli, 1998; Hacker, 2008), controlled by the pressure-dependent dehydration reactions of amphibole and other abundant hydrous phases in the subducting slab (Tatsumi, 1986; Wada and Wang, 2009).

Heat flow patterns in the across-trench sections of subduction zones reveal the occurrence of cold fore-arcs adjacent to hotter magmatic arc regions (England et al., 2004; Wada and Wang, 2009). Again, high-resolution P-wave tomographic analyses suggest a relatively colder, non-reworked mantle wedge beneath the fore-arc regions (Fukao et al., 1983). These geological observations warrant decoupling of the subducting slab from the overriding lithosphere at shallow levels (Abers et al., 2020). Experimental studies based on viscous rheology and petrological modeling indicate that the slab must restore its coherent, coupled interface with the ambient mantle in a deeper region (Wada et al., 2015; Cerpa et al., 2017). The dehydration reaction of hydrous phases (dominantly amphibole phase) in the subducting slabs occurs at a depth of around 110 km (Tatsumi, 1986), where the fully viscous coupling is observed to start (Wada and Wang, 2009). It is now a well-established fact that the decoupling zone has a finite areal extent down the slab dip, conventionally expressed by the term maximum depth of decoupling (MDD), which has been extensively studied in the context of various geological phenomena, such as earthquake focal distributions, arc volcanism, and exhumation of deep-crustal rocks (Arcay et al., 2007; Wada and Wang, 2009; Syracuse et al., 2010; Butler and Beaumont, 2017; Peacock and Wang, 2021). Although it is difficult to accurately measure the MDD in natural subduction zones (Syracuse et al., 2010), several studies have provided their estimates from indirect proxies, for example, the maximum depth of non-reworked colder subducting crusts (low velocity layers) using high-resolution tomographic images. Compilation of various available estimates yields the MDD in a range of 60–80 km (Wada and Wang, 2009; Abers et al., 2020), whereas cold slabs (Izu Bonin) can develop the deepest decoupling by sediment transport up to 120 km depth (Klein and Behn, 2021).

The degree of plate coupling in most cases is spatially heterogeneous, mainly due to along-trench variations of the geological settings in subduction zones, for example, the South American subduction system (Hu et al., 2021). Several studies have shown the sediment-pile thickness in a trench as one of the important factors in causing such heterogeneity (Iaffaldano et al., 2012; Behr and Becker, 2018; Hu et al., 2021). Low sediment-pile thickness gives rise to greater mechanical coupling, allowing the subducting slab to efficiently transfer the stress for deformation in the overriding plate margins (Scholz and Campos, 1995; Villegas-Lanza et al., 2016). Non-uniform plate coupling in the along-trench direction introduces several complexities in the evolution of a subduction zone. One of their significant effects is reflected in the formation of arcuate trench lines, which are widely reported from convergent tectonic settings (Iaffaldano et al., 2012; Hu et al., 2021). Also, convergent zones can give rise to differential uplift in the orogens with strongly varying seismicity patterns (Gvirtzman and Stern, 2004; Villegas-Lanza et al., 2016).

The preceding discussions suggest that plate coupling is a critical factor in controlling a range of geophysical and geological phenomena, such as earthquake mechanisms, melt generations, geothermal structures, wedge material circulations, trench arcuation, and overriding plate deformations. However, it is virtually unexplored how this factor can influence the development of negative trench topography in a subduction zone. This article focuses on subduction trenches to find the impact of plate decoupling configuration on their topographic evolution. We develop 2D computational fluid dynamic (CFD) models to replicate natural subduction zones and run a series of real-scale (both space and time) CFD simulations with varying plate decoupling conditions (up to 120 km depth, considering a wider range of possibilities). Our model results, combined with those obtained from natural trenches, provide a new insight into the role of the MDD in the development of characteristic trench topography.

Trench topography: Geometrical considerations

In subduction zones, the trenches display characteristic topography, typically defined by a linear, narrow depression between two steeply dipping bounding walls at the contact between the subducting and overriding plates (Figure 1A), termed here as foreland (FW) and hinterland (HW) walls, respectively (Figure 1B). Natural trenches (discussed later in detail) are generally asymmetric, showing unequal FW and HW slopes. We thus treat them with two independent dip angles, θ_F and θ_H, as illustrated in Figure 1B. The closing angle, that is, the downward tapering of a trench, is a characteristic topographic parameter, which is expressed as

$$\theta_T = \pi - (\theta_F + \theta_H). \quad (1)$$

θ_T is used as a measure of the closing geometry of a trench, that is, sharp (small θ_T) or blunt (large θ_T). Bathymetric profiles show a wide spread of θ_T (Figure 1A). We consider a point of surface-slope break on the subducting plate (procedure described in

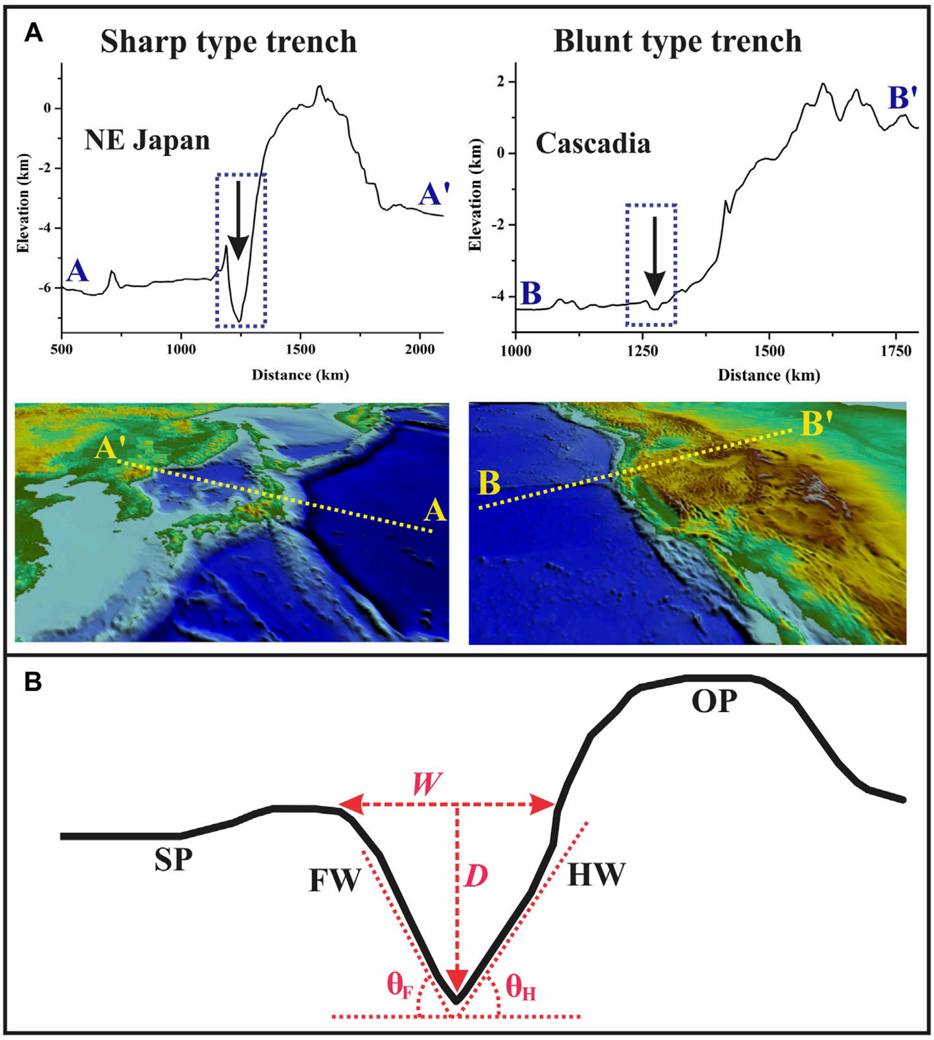

FIGURE 1
(A) Two extreme trench geometries: sharp and blunt from the North East Japan and the Cascadia subduction zones, respectively. **(B)** Geometrical parameters considered for the analysis of trench topography: trench opening width (*W*) and maximum negative relative relief (D). θ_F: fore-wall (FW) slopes on the subducting plate (SP); θ_H: hinter-wall (HW) slopes on the overriding plate (OP).

Supporting Information) and draw a horizontal line to define the trench opening width (*W*) at the ocean floor. We take the negative relative relief of the trench trough (*T*) with respect to the horizontal line drawn at A to measure the maximum vertical depth (*D*) of a trench. This topographic parameter, *D*, is used to quantitatively represent shallow and deep trenches, as observed in natural subduction zones. To characterize the trench geometry, we consider an additional parameter,

$$\lambda = \frac{W}{D}. \tag{2}$$

λ is used as a shape factor. Large λ means a wide, shallow (flat) trench, such as Cascadia, whereas low λ represents an extremely narrow, deep trench, such as the north-east Japan trench (Figure 1A). This parameter allows us to show the sensitivity of the trench morphology to the plate decoupling factor. All these geometrical parameters of trench depression are measured from simulation experiments and compared with those obtained from digital elevation models (SRTM-DEM) of selected natural subduction zones to support our interpretations.

Modeling approach

Rheological consideration

A variety of rheologies, ranging from Maxwell visco-elastic to power-law or linear viscous rheology, have been used for subduction modeling (Schmeling et al., 2008; Gerya, 2011 and references therein; Holt et al., 2015). Viscous fluid rheology provides the best rheological approximation to large-scale geodynamic processes on long time scales (million years) (McKenzie et al., 2000). In this study, we thus choose linear viscous rheology to develop subduction models to simulate the trench topography. Assuming the model fluids are incompressible, the stress *versus* strain-rate relation follows

$$\sigma_{ij} = -p\delta_{ij} + 2\eta_{ij}\dot{\varepsilon}_{ij} \tag{3}$$

where σ_{ij} and $\dot{\varepsilon}_{ij}$ are the stress and the strain rate tensors, respectively, δ_{ij} is Kronecker delta, p is the hydrostatic pressure, and η is the coefficient of viscosity. We consider a maximum viscosity value ($\eta \sim 10^{22}$ Pa·s) for the model lithosphere, rested upon the stratified mantle structure with viscosity ranging from ~10^{20} to 10^{21} Pa·s (details discussed later).

Governing equations

The computational fluid dynamic (CFD) simulations operate fundamentally on the two conservations equations: mass and momentum. Considering mass balance in an elemental fluid volume, the mass conservation equation in tensor notation follows

$$\frac{\partial \rho}{\partial t} + \frac{\partial}{\partial x_i}(\rho\, u_i) = 0, \tag{4}$$

where ρ is the density and u_i represents fluid velocity. The conservation of momentum in a viscous-fluid flow leads to

$$-\frac{\partial p}{\partial x_i} + \frac{\partial}{\partial x_j}\left[\eta\left(\frac{\partial u_i}{\partial x_j} + \frac{\partial u_j}{\partial x_i}\right)\right] + \rho X_i = \rho\frac{Du_i}{Dt}, \tag{5}$$

where p is the hydrostatic pressure, η denotes the coefficient of viscosity, and X_i represents the body force term (gravity). This is widely known as the Navier–Stokes equation. In the present case, the inertial term on the right side is neglected ($\rho\frac{Du_i}{Dt} = 0$) as the mantle flow is extremely slow, operating on million years' time scales. The equation then reduces to

$$-\frac{\partial p}{\partial x_i} + \frac{\partial}{\partial x_j}\left[\eta\left(\frac{\partial u_i}{\partial x_j} + \frac{\partial u_j}{\partial x_i}\right)\right] + \rho X_i = 0. \tag{6}$$

It is noteworthy that we ignore the effects of surface tension here because the problem concerns a large-scale fluid system.

Eqs 4, 6 were numerically solved using a finite element (FE) code (COMSOL Multiphysics ®, version 5.5) within the framework of CFD. Many earlier studies have used this CFD code to deal with different geodynamic problems, such as mantle convection (He, 2014), magma upwelling (Shahraki and Schmeling, 2012), Rayleigh-Taylor instabilities (Ruffino et al., 2016), mid-ocean ridge development (Montési and Behn, 2007), wedge melting (Lee and Kim, 2021), and plate subduction (Carminati and Petricca, 2010; Rodriguez-Gonzalez et al., 2012). To track the evolving surface of model surface topography, we implemented an arbitrary Lagrangian Eulerian (ALE) scheme, the detailed mathematical formulation of which can be seen in earlier publications (Dasgupta and Mandal, 2022 and Dasgupta et al.,2021a).

Model setup

The subduction model is conceived to represent a real-scale across-trench vertical section, 6,000 km (length) × 2,900 km (height), covering the entire lower mantle to keep the rigid bottom boundary away from the overriding plate to minimize its effects on the trench evolution (Figure 2A). A proto-subduction zone is introduced to the initial model (*cf.* Crameri et al., 2017; Dasgupta et al., 2021b), where the subducting slab (400 km length) initially dips beneath the overriding plate (OP) to form an asymmetric configuration, which is the triggering factor to set in subduction in the model (Stern and Gerya, 2018). We consider a 100-km-thick subducting slab, treated as the oceanic lithosphere, to subduct beneath a 120-km-thick overriding plate, treated as the continental lithosphere (Riel et al., 2018; Dasgupta and Mandal, 2022). Both consist of two layers: the crustal layer and the underlying mantle lithosphere (Figure 2A). Their length is chosen in the order of 3,000 km, where the trench is located at the middle point. We consider a stratified mechanical structure of the mantle part beneath the subducting and overriding lithospheric plates: a 540-km- or 520-km-thick upper mantle layer beneath oceanic and continental plates, respectively, a 60-km-thick low viscosity channel (transition zone) and a 2,200-km-thick lower mantle. The densities of the continental crust, oceanic crust, and mantle lithosphere are chosen as 2,800, 3,000, and 3,240 kg/m^3, respectively. The densities of the continental mantle lithosphere and underlying mantle in all the experiments were kept as 3,200 kg/m^3 (Dasgupta and Mandal, 2018; Dasgupta et al., 2021b).

Available rheological data provide a wide range of viscosity, from 10^{24} to 10^{21} Pa·s, for Earth's lithosphere (Zhong et al., 1996; Crameri et al., 2017; Cerpa and Arcay, 2020). The long-wavelength analysis and Monte Carlo inversion of geoid data (Hager et al., 1985; Rudolph et al., 2015) suggest that the lower-mantle viscosity is 30 times that of the upper mantle. Several geophysical studies have detected a low-viscosity layer at the base of the mantle transition zone (King, 1995; Harig et al., 2010; Weismüller et al., 2015) (Figure 2B). Based on all these estimates, we consider a depth-dependent viscosity, defined by a smooth, continuous function (up to the second-order derivative) to model the mechanical stratification, where the upper mantle is set at 10^{20} Pa·s down to a depth of 600 km, whereas the lower mantle viscosity is at 3×10^{21} Pa·s (Rudolph et al., 2015). The low-viscosity channel between 640 and 700 km is assigned a value of

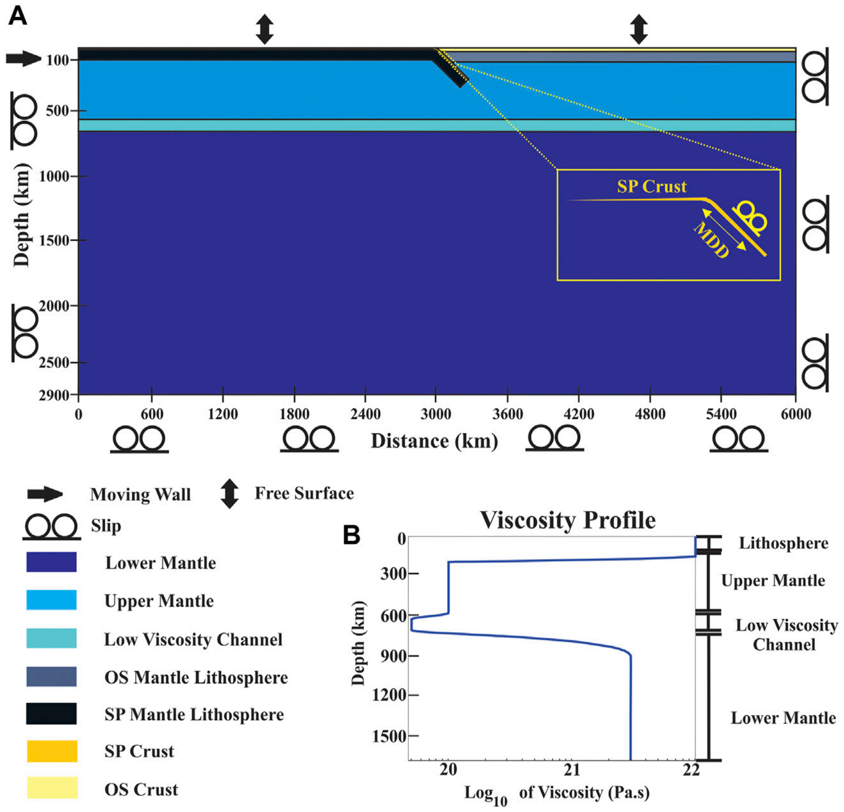

FIGURE 2
(A) Computational fluid dynamic (CFD) model setup used for trench simulations in subduction zones. An oceanic lithosphere (left) subducts beneath a continental overriding plate (right side). A proto subduction is introduced in the initial model setup to initiate the subduction process. The model dimensions, domains, and boundary conditions are explained in the lower panel. **(B)** Consideration of the initial viscosity–depth profile in the model domain. The domain divisions: upper and lower mantles with an intervening low-viscosity channel are shown in the profile.

5×10^{19} Pa·s (Kellogg et al., 1999). Using Fjeldskaar's (1994) model, we introduced a viscosity drop by an order of 10^2 across the lithospheric base (10^{22} Pa·s) to represent the upper mantle in our model. The material properties and model parameters are detailed in Supplementary Table S1.

We started our model run with a proto-subduction slab dip of 30° (measured up to a depth of 300 km), as used in much earlier modeling (François et al., 2014; Holt et al., 2015; Jadamec, 2016), imposing a free-slip boundary condition at the bottom and vertical boundaries. In a 20 Myr model simulation, we applied a horizontal velocity (2 cm/yr) at the rear slab boundaries for an initial run time of 3 Myr, and then allowed the proto-subduction to evolve spontaneously under the slab-pull action (Dasgupta et al., 2021a). The simulation run time was chosen to be relatively short (20 Myr) because the subduction topography generally tends to stabilize on a time scale <8 Myr (Zhong and Zuber, 2000; Dasgupta and Mandal, 2018; Dasgupta and Mandal, 2022). The MDD was imposed at the interface between the subducting crust and overriding lithosphere, varying its length from 30 to 120 km (Figure 2A). We chose to keep the top model boundaries under a free surface condition in order to obtain a good approximation of a free vertical movement, producing topography at the model surface (Pysklywec and Shahnas, 2003; Schmalholz, 2011; Crameri et al., 2012; Crameri et al., 2017). We used a perpetual coloring scheme (Crameri et al., 2020) to represent the data true color legends in our model setup.

Modeling results

Reference experiment

We first performed reference simulation experiments without introducing any decoupling zone to the subducting–overriding plate interface to validate the model setup chosen in this study. The reference experiment yields time-dependent velocity fields (Figure 3A), which agree well with those reported in previous numerical modeling studies. At 8 Myr of the simulation run, the

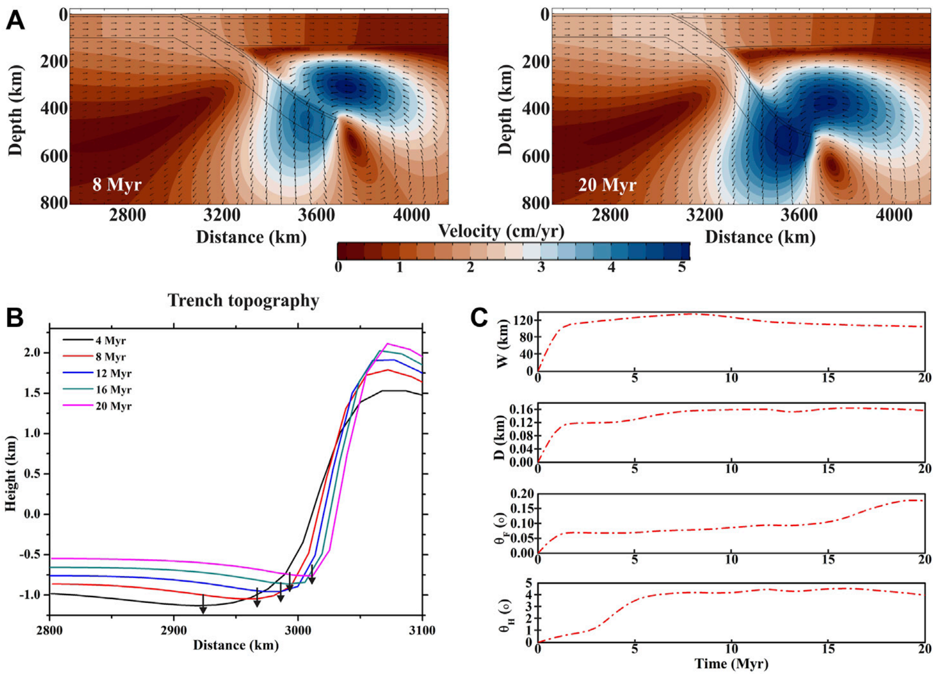

FIGURE 3
(A) Velocity fields produced in the reference experiment corresponding to model run times: 8 and 20 Myr. Note that the subducting slab creates a flow vortex in the mantle, which intensifies with time. **(B)** A time series plots of absolute topographic elevations of a trench topography in the reference model. **(C)** Temporal variations of the trench parameters: *W* (opening width), *D* (maximum negative relative relief), θ_H (HW slope), and θ_F (FW slope) presented from the reference experiment.

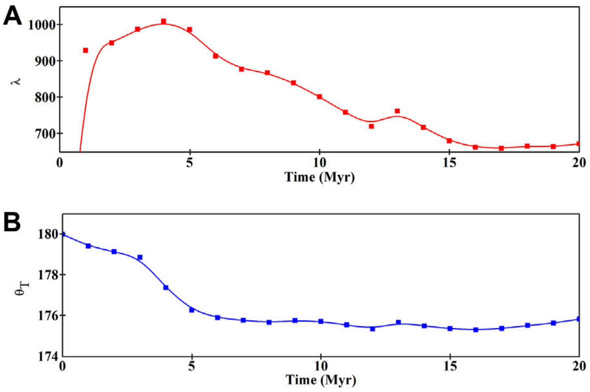

FIGURE 4
Variations of **(A)** the shape factor ($\lambda = W/D$) and **(B)** downward closing angle (θ_T) of the trench with time (results from the reference experiment).

velocity field at the subducting slab edge shows the highest magnitude of flow (5 cm/yr), mostly due to the sinking slab motion. The flow velocity becomes significantly weaker (0–1.5 cm/yr) in the upper region of the subducting slab as well as the entire overriding plate. The flow vortex at the slab edge progressively becomes more vigorous, both in the velocity magnitude and spatial extent (Figure 3A).

The model run depicts the evolution of trench topography, which is presented in Figure 3B. The trench continuously migrates forward (to the overriding plate) at a rate of 2–6 cm/yr. The model calculated topographic elements, *W*, *D*, θ_F, and θ_H, vary systematically with time (Figure 3C), but all of them tend to attain a steady state after a run time of 2–7 Myr. *W* (opening width) and *D* (maximum depth) attain stable values of 80–120 km and 0.12–0.16 km, respectively. We calculated the trench wall slopes, θ_F and θ_H, from the topographic elevation differences, the mathematical procedure of which is elaborated in Supplementary (S1). Both θ_F and θ_H are found to approach stable values of 0.07–0.1° and 3–4.5°, where θ_F is always less than θ_H (Figure 3C), implying that the fore-wall (FW) of the trench is much shallower in dip than its hinter-wall (HW). The shape factor (λ) also shows a consistent temporal variation (Figure 4A), implying an unsteady initial state of the trench geometry. In the early stage (model run time <5 Myr), λ is large (>900), but it non-linearly decreases to 673 at 20 Myr. The temporal variation of λ marks a transition from wide to narrow trench geometry with time (Figure 4A). We calculated the closing trench angle (θ_T) as a function of model run time (t) to study the evolution of the downward tapering trough geometry of a trench (Figure 4B). θ_T

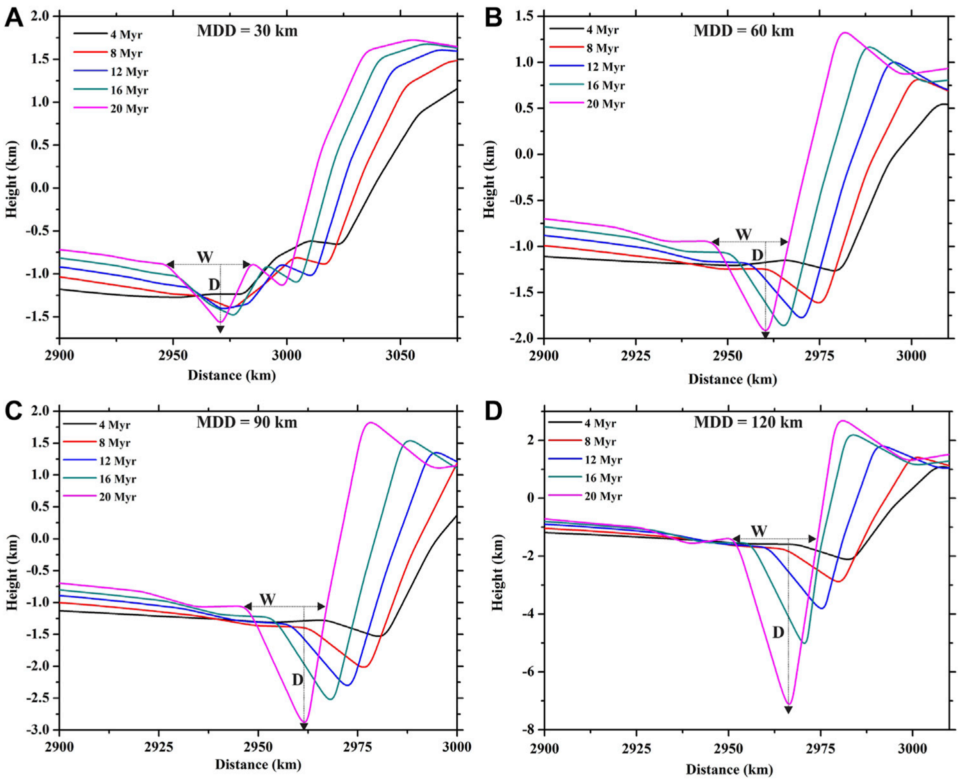

FIGURE 5
(A–D) Time series topographic profiles of subduction zones produced in CFD simulation experiments run with increasing maximum depth of decoupling (MDD): **(A)** 30 km, **(B)** 60 km, **(C)** 90 km, and **(D)** 120 km.

is found to be large (179°–178°) in the early phase (5 Myr), which decreases to ~175° after 20 Myr. The non-linear θ_T—t plot suggests that the trench attains nearly a stable taper geometry on a time scale of 15 Myr.

Experiments with varying maximum depth of decoupling

We ran a set of simulations by systematically varying the MDD (30–120 km), keeping all other model parameters constant (Supplementary Table S1) to investigate exclusively the control of plate decoupling in the geometrical evolution of trenches. These simulations yield remarkable differences in trench geometry depending on the decoupling factor MDD. It is interesting to note that they always show trench retreat (migration opposite to the subduction direction) with progressive model run time (Figure 5), irrespective of MDD values. The MDD thus hardly influences the mode of trench migration (i.e., retreat *versus* advance) in our model.

Experiments with the MDD = 30 km produced a trench with shallow negative topography (0.2–0.5 km), flanked by a flat fore-arc in the overriding plate (Figure 5A). With time, a secondary depression appears on the HW side of the trench due to the decoupling effect at shallow depths. The trenches deepened with time, and at the same time, their FW and HW slopes steepened with progressive subduction. However, the two trench walls evolve differently, where the HW develops a secondary trench depression, which is absent on the FW slope in the subducting slab. Both the major and secondary trench depressions widen and deepen at the same time, while the HW elevation continuously increases its maximum elevation with progressive subduction. At 20 Ma, the principal trench attains a maximum depth of D = 0.5 km, and the HW achieves a maximum relative relief of ~3.25 km (measured relative to the deepest trench point) at a horizontal distance of ~75 km from the trench axis.

Experiments with the MDD = 60 km show the evolution of a single trench (Figure 5B), the geometry of which markedly differs from the composite trench architecture produced in the MDD = 30 km model. The simulation on a run time of 4 Ma produces a shallow trench (D = 125 m and W = ~ 15 km) at a horizontal distance of ~35 km from the HW arc in the overriding plate (Figure 5B). The trench deepens relatively faster than its opening (W), consequently, to produce a narrow (W = ~ 20 km), deep trough topography (D = 1 km) at 20 Ma. The trench deepening is associated with a sympathetic increase in the HW elevation,

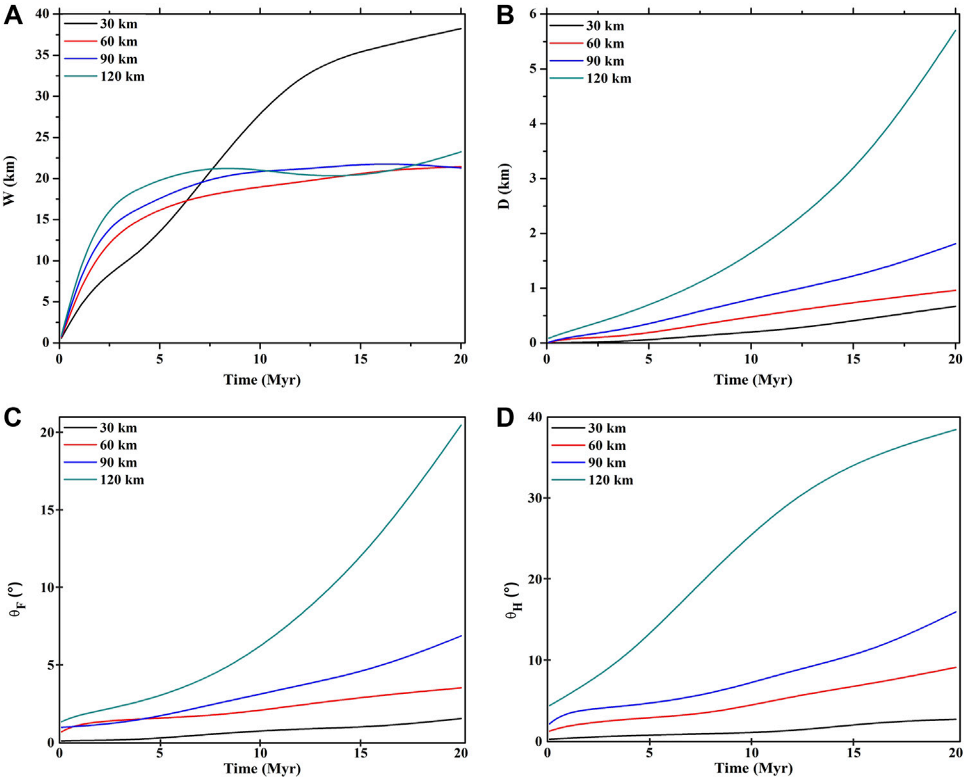

FIGURE 6
Time-dependent variations of the major topographic elements of trenches: **(A)** opening width (W), **(B)** maximum trench depth (D), **(C)** FW slopes (θF), and **(D)** HW slopes (θH). The graph colors denote MDD values used in the simulation experiments.

which eventually gives rise to an arc-like structure with a relief of ~500 m relative to the average surface topography of the overriding plate margin. In this experiment, the trench retreat is a remarkable process in the entire path of trench evolution. However, the trench hardly changes its location with respect to the HW arc. The trench is located at a distance of 25 km, which remains practically unchanged in the run time between 4 Ma and 20 Ma. The model results indicate that the hinter-wall (HW) migrates in the foreland direction to compete with the trench retreat. The trench attains a maximum relative relief (H_R: elevation difference between the trench trough and the HW arc) of ~3 km at 20 Ma. Simulation experiments with the MDD = 90 and 120 km show a similar overall trend of trench evolution but with large quantitative differences in the topographic elements, particularly trench depths (D) and locations, and their HW elevations (Figures 5C,D). For the MDD = 90 km, D = 1.8 km, which multiplies to attain an extremely large value, D = 6 km for the MDD = 120 km. The trench eventually develops a very narrow, deep trough morphology as the trench opening width, W, which is less sensitive to the MDD. The HW arc reciprocates with trench deepening, multiplying its relative topographic elevations by more than two folds, from 750 to 1,800 m. The MDD has an enormous influence on the magnitude of negative relative trench relief (H_R); for the MDD = 90 km, H_R = 4.5 km at 20 Ma, which nearly doubles to become ~10 km when the MDD = 120 km λ is consistently low for the MDD = 90 and 120 km, attaining average values of 70 and 50, respectively, after 20 Myr run time. This set of model experiments suggests that the relative relief of trenches can exceed 5 km only when the MDD is more than 90 km, which we will discuss later in the context of data from natural trenches. The trench location with respect to the HW arc topography in the overriding plate does not significantly change with the MDD.

Trench geometry: A parametric analysis

Model simulations show a complex effect of the MDD on the geometrical development of trenches, determined by their temporally varying topographic elements: opening width (W), vertical depth (D), and the bounding FW and HW slopes (θ_F) and (θ_H). We first present their time-dependent variations independently as a function of the MDD and then combine them to characterize the possible evolving trends of trenches

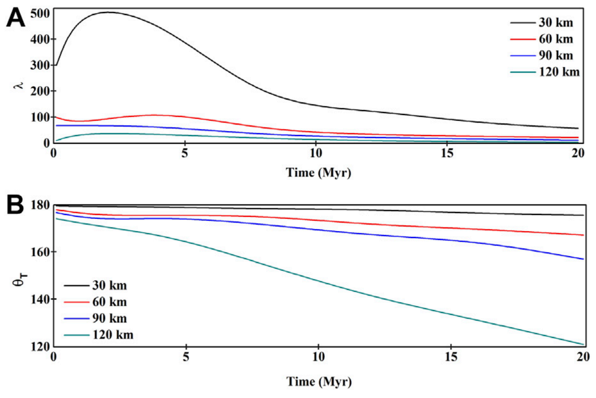

FIGURE 7
Time progression of **(A)** the shape factor (λ) and **(B)** the closing angle (θ_T) of a trench in the simulation experiments for different MDD values (indicated in the graph colors).

(Figure 6). W is found to widen with time, irrespective of MDD values chosen in the simulations (Figure 6A). However, the rate of widening at the mature stage ($\dot{W} = \frac{dW}{dt}$) varies with the MDD, and has its maximum value for the MDD = 30 km. In this case, W = 15 km at 5 Myr model run, which increases to 38 km at 20 Myr, implying an average value of $\dot{W}$ = 1.8 cm/yr. For all the other experiments (MDD = 60–120 km), W has a tendency to stabilize, implying lowering of the widening rate. For example, W = 15 km at 5 Myr, which increases to 22 km after 20 Myr. The estimates suggest $\dot{W}$ to decrease from 3 cm/yr to 0.47 mm/yr on a time span of ~15 Ma. Ultimately, the opening trench width (W) reaches almost a steady state condition in the matured stage (20 Myr) of subduction zones. In contrast, the MDD always exerts a positive effect on the trench deepening process, where a larger MDD produces greater trench depth (D), as described in the preceding section. The rate of trench deepening is found to be strongly sensitive to MDD values (Figure 6B). For the MDD = 30 km, D increases more or less linearly with time, but at a gentle gradient, that suggests trench deepening at a constant, low rate ($\dot{D}$—0.025 mm/yr). The MDD = 60 km model shows a similar linear temporal variation of D, but relatively at a steeper gradient, which yields higher $\dot{D}$ = 0.05 mm/yr. The trench deepening becomes a non-linear function of time for the MDD = 90 km, and the estimated $\dot{D}$ from this function increases from 0.05 mm/yr to 0.175 mm/yr on a time interval of 10–20 Ma. A further increase in the MDD greatly facilitates the trench deepening process to non-linearly increase D (as $\dot{D}$ increases with time). In the initial period of subduction with the MDD = 120 km, $\dot{D}$ = 0.175 mm/yr, which becomes 0.55 mm/yr at 20 Myr.

We studied the possible impacts of plate decoupling on the evolution of trench wall slopes in progressive subduction. For the MDD = 30 km, both FW and HW slopes (θ_F and θ_W) steadily increase their steepness with time, holding the following relation: $\theta_H > \theta_F$. For example, θ_F = ~ 0.7° and ~1.5°, whereas θ_H = 1° and 2.8° at 10 and 20 Ma, respectively (Figures 6C,D). An increase of the MDD causes the two trench walls to follow contrasting evolutionary trends, a nearly steady steepening of the FW, whereas a tendency of the HW to stabilize its slope on a time scale of 5–8 Ma. However, the effect of stronger plate decoupling (MDD = 60, 90, and 120 km) is hardly perceptible in the early phase of a trench; it becomes significant in the advanced stages (>10 Ma). For example, θ_F = 2 to 4.4° at 10 Myr, which increases to 4 to 20.4° at 20 Myr at an average rate of steepening, $\dot{\theta}_F$ = 0.2–1.6°/Myr. θ_H = 4 to 21° at 10 Ma, which increases at rates: $\dot{\theta}_H$ = 0.4–2.1°/Myr, reducing to 0.4–1.7°/Myr to stabilize θ_H at 8 to 38° at 20 Myr (Figures 6C,D).

The temporal changes of trench morphology (λ and θ_T) are strongly sensitive to the MDD. The shape factor (λ) yields a consistently high value for the MDD = 30 km (Figure 7A). In the initial stages (5 Myr), λ is as high as 400–500, which decreases to ~100 at 20 Myr. Increasing MDD = 60, 90, and 120 km consistently reduces λ to 100, 70, and 50 (Figure 7A). The closing geometry (θ_T) steadily narrows down with run time, irrespective of the MDD values (Figure 7B). However, the magnitude of θ_T holds an inverse relationship with the MDD.

Maximum depth of decoupling to modulate the plate-margin stress fields

A shallow MDD (30 km) favors the compressional stress field (−40 to −32 MPa) to dominate in the plate margins, leaving a weak tensile stress (10–15 MPa) regime at the shallow level (10–15 km) in the overriding plate close to the trench (Figure 8A). An increase in the MDD reduces the compressional stress regime in its spatial extent and strengthens the tensile to neutral stress regime along the decoupling zone, as observed in the simulation experiment with the MDD = 60 km (Figure 8B). However, the compressional regime (−30 to −20 MPa) remains stronger than the tensile stress regime (10–15 MPa) in terms of its magnitudes. The stress fields undergo a dramatic transformation at the MDD = 90 km, allowing the tensile regime to spatially dominate (5–10 MPa) in the overriding plate margin, where the compressional stresses (−25 to −15 MPa) localize preferentially at a deeper level (70–120 km) (Figure 8C). The tensile regime (5–10 MPa) becomes an area-wise major stress field in the overriding plate for the MDD = 120 km (Figure 8D).

Discussions

Effects of slab buoyancy

The models presented in the preceding section were run with a constant density difference ($\Delta\rho$) between the subducting slab and the ambient mantle. However, the negative buoyancy of subducting slabs can vary with the lithospheric age, as reported in

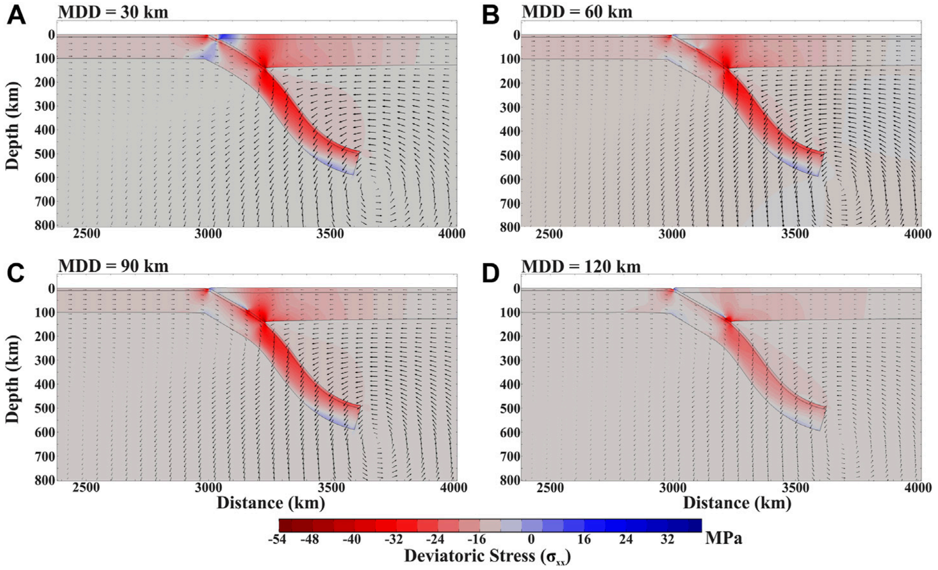

FIGURE 8
(A–D) Deviatoric stress fields of subduction zones for varying MDD in the simulation experiments. Model run time: 10 Myr. Negative and positive stress values represent compressional and extensional stresses, respectively. Arrows show the flow velocity vectors.

the existing literature (Cruciani et al., 2005; Dasgupta et al., 2021a), where the slabs become increasingly denser with age. We thus ran additional simulations to test the possible effects of increasing slab buoyancy on the trench topography by varying $\Delta\rho$ in a non-dimensional form:

$$\Delta\rho* = \frac{\rho_{slab} - \rho_{mantle}}{\rho_{slab} + \rho_{mantle}}. \tag{7}$$

$\Delta\rho*$ was varied in the range 0.003–0.01, keeping MDD = 60 km and all other parameters constant (Supplementary Table S1). It is to be noted that $\Delta\rho^*$ is a proxy for lithospheric slab ages and determines negative slab buoyancy that forces the FW of the trench to develop curvatures due to slab bending. The trenches consequently increase the degree of asymmetry of their geometry, characterized by a gradual change of θ_F, but nearly constant θ_H (Figure 9A). This transformation results in a large effective opening width (W) at high $\Delta\rho^*$, for example, $W = 16.79$ km for $\Delta\rho^* = 0.0031$, which increases to 28 km for $\Delta\rho^* = 0.0092$. The trenches at the same time steadily deepen to facilitate their relative negative relief D with increasing $\Delta\rho^*$, as shown in Figure 9B. The closing geometry (θ_T) is also sensitive to $\Delta\rho^*$ (Figure 9C), $\theta_T \sim 128^\circ$ at 20 Myr for $\Delta\rho^* = 0.0031$, which becomes <106° when $\Delta\rho^* = 0.0092$.

Topographic variations of natural trenches

Subduction zones operate as an excellent natural laboratory to produce trenches of widely varying geometries in space and time. We first consider their two extreme geometries: sharp and blunt, to discuss their quantitative morphometric differences (Supplementary Figure S1). The Cascadia subduction zone, where the Juan de Fuca plate under-thrusts against the North American plate at a rate of 3.6 cm/yr, displays a shallow, broad (blunt type) trench, flanked by a prominent accretionary prism and an elevated fore-arc, forming the Coastal Ranges. Our estimates from multiple trench normal profiles show a moderate opening width ($W \sim 28.25$ km) and a very low depth ($D \sim 0.187$ km), and thereby a large shape factor ($\lambda \sim 172.3$) of the trench (Supplementary Figure S1A). The downward closing angle (θ_T) is ~178°, satisfying the condition $\theta_F < \theta_H$. On the other hand, the Northeast Japan subduction zone, where the Pacific plate subducts under the Eurasian plate at a velocity of ~8 cm/yr, develops a sharp trench at the plate margin (Supplementary Figure S1B). This subduction zone has formed a spectacular volcanic arc complex (Honshu Volcanic Province) and a broad back-arc basin (Japan Sea). This trench shows a wider opening width ($W \sim 88.5$ km), but a deep trough ($D \sim 2.8$ km), and thereby a relatively low shape factor ($\lambda \sim 32.2$). The closing angle, $\theta_T \sim 172^\circ$, is similar to that in the Cascadian setting. The Cascadia and Japan trenches show significant differences in their hinter-wall (HW) slopes, $\theta_H = 1.2^\circ$ and 5.5°, respectively. We will now discuss diverse natural trench morphologies in the context of plate decoupling factors from five selected subduction zones with well-constrained MDD available in the literature (Supplementary Table S2). The MDD of a subduction zone is estimated from the maximum depth of non-reworked oceanic crusts and low

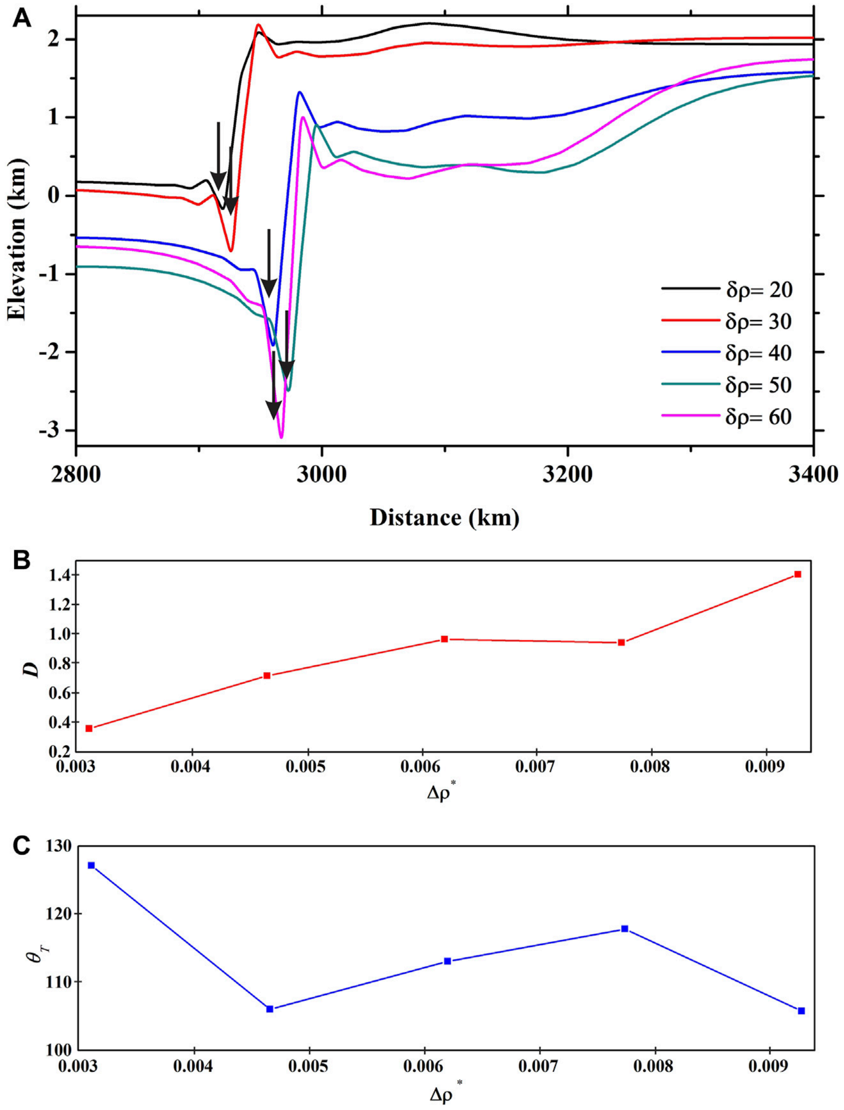

FIGURE 9
(A) Trench topography produced in CFD models for varying subducting slab buoyancy ($\Delta\rho$). Model run time: 20 Myr. MDD = 60 km. **(B)** and **(C)** Plots of the maximum depth (D) and the closing angle (θ_T) of trenches as a function of slab buoyancy ($\Delta\rho^*$).

velocity zones, revealed by high-resolution teleseismic signals (Supplementary Table S2). We choose representative trench normal sections of the subduction zones to calculate the trench topography utilizing high-resolution SRTM-DEM data (Figures 10A–E).

As discussed earlier, the Cascadian trench is shallow (D = 0.12 km), and its maximum relative relief (difference between trough and arc elevations) is H_R = 6 km (Figure 10A). Geophysical estimates suggest a low MDD (40–45 km) in this trench. Our model simulations that run with such low MDD yield closely similar topographic reliefs (Figure 5). The Nankai subduction zone shows a deeper trench (D ~ 0.2 km; Figure 10B) at the boundary between the subducting Philippines Sea plate and the Eurasian overriding plate. Interestingly, the estimated MDD in Nankai is ~60 km (Hori, 1990; Ohkura, 2000). The Cascadia and Nankai examples validate the model's predicted trench depth *versus* MDD relationship (Figure 6). The trench depressions in Alaska, Chile, and Japan subduction zones occur as sharp, narrow, and deep troughs (D ~ 2–2.8 km) (Figures 10C–E). According to the geophysical estimates, all of them have a large MDD, approximately 100–120 km (Yuan et al., 2000; Kawakatsu and Watada, 2007; Rondenay et al., 2008). The steep FW and HW slopes, and large D agree with the large MDD values. Furthermore, the Nankai subduction zone yields H_R ~ 5.5 km, whereas Chile and Japan subduction zones have

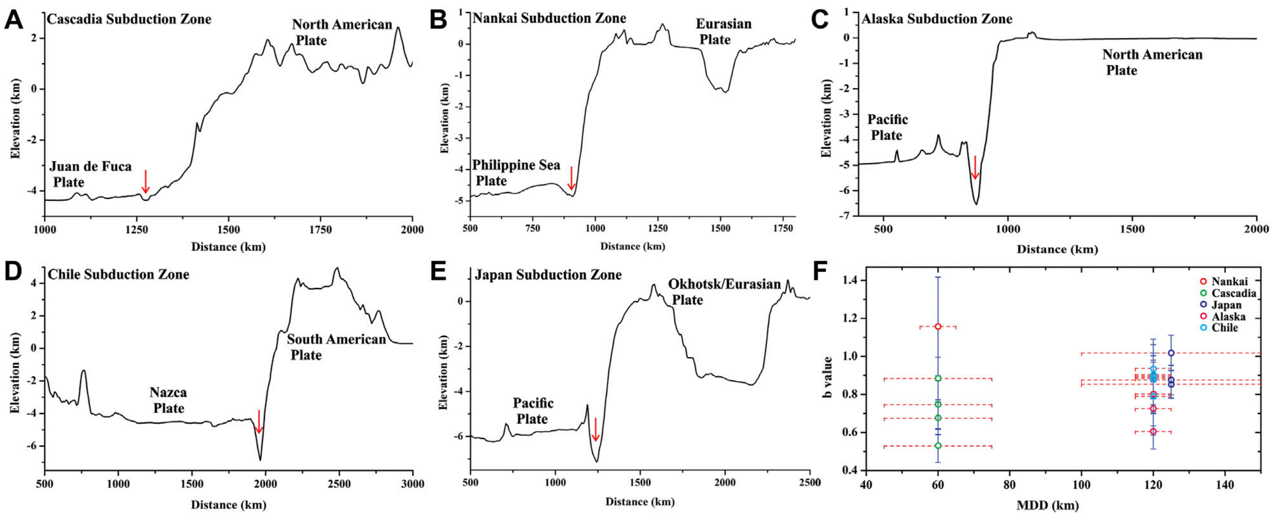

FIGURE 10
(A–E) Trench normal topographic profiles of the Cascadia, Nankai, Alaska, Chile, and Japan subduction zones with increasing trench depths. **(F)** Plots of the b-values of overriding plate earthquakes in selected natural subduction zones and their corresponding MDD values.

H_R in the range of 7.5–10 km. The relative relief (H_R) between the arc high and the trench trough thus holds a positive correlation with the MDD, as observed in the present model experiments.

The earthquake b-value (the slope of a log-normal distribution of the number of seismic events *versus* their magnitudes) estimates for the overriding plates of these subduction zones hardly provide any clear correlation with the MDD (Figure 10F). There is a general agreement that smaller b-values signify compression dominated regimes, whereas larger b-values indicate tension dominated settings (Nishikawa and Ide, 2014). Subduction zones with a low MDD yield a wide range of b-values; for example, the Cascadia subduction zone records b-value < 1, whereas the Nankai subduction zone yields b-values > 1. A similar mismatch is encountered in subduction zones with a large MDD (100–120 km). For example, the Japan and Chile subduction zones record high as well as low b-values, whereas the Alaska subduction zone, though similar in geological setting, dominantly yields low b-values. This discussion leads us to suggest that earthquake b-value estimates cannot be used solely as a proxy to detect any conclusive difference in the plate coupling dynamics.

Trench parameters: Model *versus* nature

To compare the geometrical elements of the steady-state model trench topography with natural observations, we calculated trench opening width (W), depth (D), and its wall slopes on the subducting (θ_F) and overriding (θ_H) plates. Also, the shape factor (λ) and the closing geometry (θ_T) of trenches are taken into account for the comparative analysis. Natural subduction zones generally show significant along-trench variations in their trench morphology. Keeping this heterogeneity in mind, we compiled multiple trench perpendicular sections to define a range of values for the geometrical parameters, instead of their single representative value (Supplementary Table S2). Also, previous studies suggested that plate decoupling becomes most effective in mature subduction zones (10–20 Myr old). We thus compiled the experimental data for a 10–20 Myr model run time. Figure 11A presents a synthesis of data from natural subduction zones. W is found to increase with increasing MDD values, where the Cascadia subduction zone (MDD = 60 km) and the Japan subduction zone (MDD = 125 km) yield an average W = 28 and 103 km, respectively. However, our CFD experiments yield W in a narrow range (20–40 km) for varying MDD. We find an excellent model–nature correlation in terms of their trench depths (D), where both model and natural findings suggest a steady increase of D with increasing MDD (Figure 11B). Natural subduction zones with low MDD values (45–60 km), like Cascadia and Nankai, show trenches with D ~ 0.2–0.7 km, whereas the Japan and Chile subduction zones (MDD = 100–120 km) show trenches with D ~ 2–3.8 km values. Similarly, our simulation experiments produce D ~ 0.5–1 km for MDD = 30–60 km, which increases to 2–5.5 km when MDD = 90–120 km. The effects of the MDD in different natural subduction zones are also reflected in their respective θ_F and θ_H values. The Cascadia subduction zone (MDD = 45–60 km) yields lower θ_F and θ_H (0.2–1.2° and 0.8–1.7°),

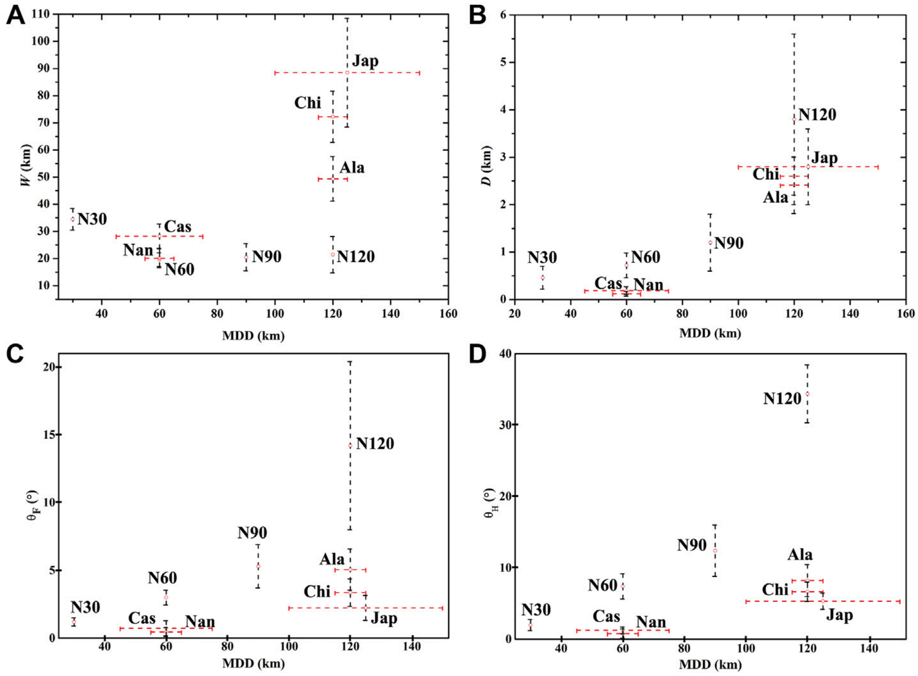

FIGURE 11
(A–D) Comparison of the trench parameters: **(A)** *W*, **(B)** *D*, **(C)** θ_F, and **(D)** θ_H of selected natural subduction zones with the model results for varying maximum depth of decoupling (MDD). N30, N60, N90, and N120 points represent numerical experiment results with 30, 60, 90, and 120 km *MDD* values, respectively. Subduction zone abbreviations: Cascadia-Cas; Nankai-Nan; Chile-Chi; Alaska-Ala; Japan-Jap.

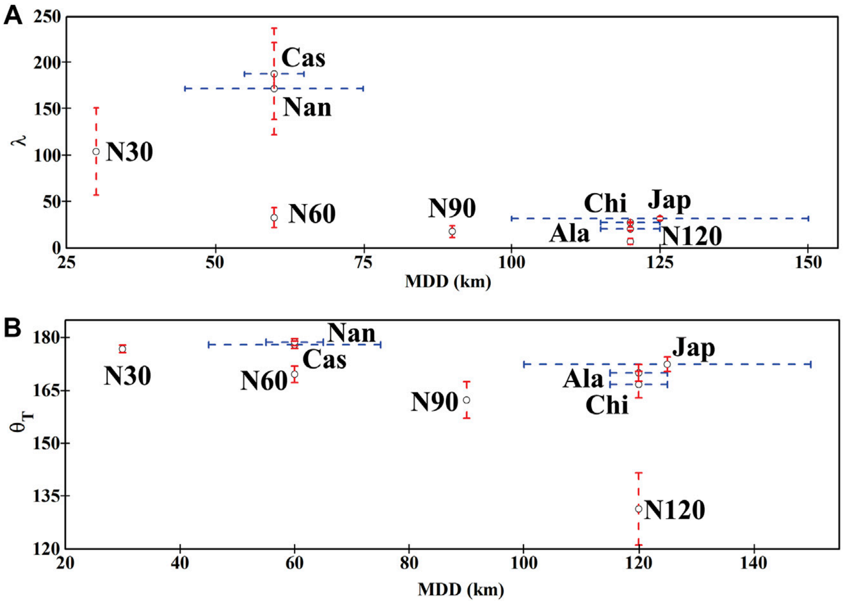

FIGURE 12
Correlations of **(A)** the shape factor (λ) and **(B)** closing angle (θ_T) *versus* MDD plots between selected natural subduction zones and the model experiments. N30, N60, N90, and N120 points represent numerical experiment results with 30, 60, 90, and 120 km *MDD* values, respectively. Subduction zone abbreviations: Cascadia-Cas; Nankai-Nan; Chile-Chi; Alaska-Ala; Japan-Jap.

whereas the Alaska subduction zone (MDD = 100–120 km) gives rise to significantly larger θ_F and θ_H (3.5–6.5°, and 6–10.5°). The simulation experiments for MDD = 30 km produce smaller θ_F and θ_H (0.9–1.5° and 1.2–2.7°), whereas those with MDD = 120 km give rise to significantly larger θ_F and θ_H (8–20.4° and 30.3–38.4°). It is interesting to note that both experimental and natural trenches always satisfy the condition $\theta_F < \theta_H$ (Figures 11C,D).

The shape factor (λ) of both natural and model trenches holds an inverse relationship with their respective MDD values (Figure 12A). The Cascadia and Nankai subduction zones, having smaller MDD values (45–60 km), yield λ in the range of 200–150. Similarly, the experiments with MDD = 30 km develop trenches with $\lambda \sim 150$–50. On the other hand, subduction zones, like Japan and Chile (MDD = 100–120 km), have $\lambda < 50$, which is similar to the experimental λ values (<30) for MDD = 120 km. The closing geometry (θ_T) that shows an inverse relation with MDD in experiments is correlated well with the natural data (Figure 12B). Subduction zones, like Cascadia (MDD = 45–60 km) and Japan (MDD = 120 km), have θ_T values of 178 and 170°, respectively. On the other hand, the MDD = 30 and 90 km models yield $\theta_T \sim 176$ and 162°, respectively.

Model limitations

The comparison of the model trench topography with nature accounts for entirely the first-order reliefs, that is, long-wavelength topographic elements attributed to tectonic processes, such as flexural deformation and mantle flows. Our model excludes a number of additional factors, for example, crustal thickening, magmatic accretion, and surface erosion/deposition of sediments that can influence the topography at varied wavelengths. In addition, the topographic features of a trench, such as its topographic slopes, can be influenced by secondary factors, like plastic rheological failure of the bounding walls and surface material transport, which are excluded in the present modeling. Due to this model limitation, some of our model calculations, especially for extreme values of MDD =120 km, probably overestimate the trench-wall slopes as compared to those calculated from natural systems. Moreover, we have modeled the lithospheric slabs and the underlying mantle, excluding the possible effects of petrological reactions such as dehydration melting and the Clapeyron slope of phase changes. Based on the available data (Ranalli, 1995), the maximum lithospheric viscosity in this model was set in the order of 10^{22} Pa·s. However, the values in cases become as high as 10^{23} Pa·s (Ribe, 2010; Garel et al., 2014). These limitations leave a scope for advancing the present model findings with a wider spectrum of rheological considerations, such as high lithospheric viscosity and complex non-linear rheology, for example, power–law.

Conclusion

1) The first-order geometry of oceanic trenches is sensitive to the maximum depth of decoupling (MDD) at the plate interface of subduction zones. Their maximum negative relative relief (D) increases with increasing MDD, where MDD = 30 and 120 km with yield mature stage D values of ~0.5 and 5.5 km, respectively. Natural subduction zones show a weakly positive correlation of trench opening width (W) with MDD, which agrees with the experimental results for a limited run time. This difference occurs possibly due to some limitation in our model. 2) The wall slopes of a trench on the subducting plate (θ_F) and the overriding plate (θ_H) steepen with increasing MDD. For example, MDD = 30 km produces a trench with θ_F = 1.5° and θ_H = 2.77°, which increase to 20.4° and 38.46°, respectively, for MDD = 120 km experiments. 3) Subduction zones develop trenches always satisfying the condition $\theta_F < \theta_H$, irrespective of their MDD. 4) Increasing negative slab buoyancy further enhances D and reduces the downward tapering angles (θ_T) of trenches, for example, $\Delta\rho^* = 0.0031$ and 0.0092 gives rise to D = 0.35, 1.4 km and θ_T = 128°, 105.4°, respectively. 5) Mechanical decoupling at the plate interface facilitates the process of trench retreat, whereas coherent coupling with initial ridge push force favors trench advancement, as revealed from the reference experiment.

Data availability statement

The original contributions presented in the study are included in the article/Supplementary Material. Further queries and data are available upon request from the corresponding author.

Author contributions

RD performed the research, analyzed the results, and wrote the manuscript. NM supervised the project, and provided guidance and support. All authors contributed to the article and approved the submitted version.

Funding

J. C. Bose Fellowship (SR/S2/JCB-36/2012) awarded to NM.

Acknowledgments

We thank Editor Manuele Faccenda and two reviewers for their thorough and constructive reviews at different stages, which substantially improved the scientific content of this study.

Discussions with Dr. Changyeol Lee and Mr. Joyjeet Sen came as additional benefits for our manuscript. NM thanks the SERB, Department of Science and Technology, India, for supporting him through the J. C. Bose Fellowship (SR/S2/JCB-36/2012). RD gratefully thanks the University Grants Commission, India, for providing him with the research fellowship [Sr No. 2061420432; Ref. No: 22/06/2014 (i) EU-V].

Conflict of interest

Publisher's note

Supplementary material

The Supplementary Material for this article can be found online at: https://www.frontiersin.org/articles/10.3389/feart.2022.908234/full#supplementary-material

References

Abers, G. A., van Keken, P. E., and Wilson, C. R. (2020). Deep decoupling in subduction zones: Observations and temperature limits. *Geosphere* 16 (6), 1408–1424. doi:10.1130/ges02278.1

Arcay, D., Tric, E., and Doin, M. P. (2007). Slab surface temperature in subduction zones: Influence of the interplate decoupling depth and upper plate thinning processes. *Earth Planet. Sci. Lett.* 255 (3-4), 324–338. doi:10.1016/j.epsl.2006.12.027

Behr, W. M., and Becker, T. W. (2018). Sediment control on subduction plate speeds. *Earth Planet. Sci. Lett.* 502, 166–173. doi:10.1016/j.epsl.2018.08.057

Butler, J. P., and Beaumont, C. (2017). Subduction zone decoupling/retreat modeling explains south Tibet (Xigaze) and other supra-subduction zone ophiolites and their UHP mineral phases. *Earth Planet. Sci. Lett.* 463, 101–117. doi:10.1016/j.epsl.2017.01.025

Carminati, E., and Petricca, P. (2010). State of stress in slabs as a function of large-scale plate kinematics. *Geochem. Geophys. Geosyst.* 11 (4). doi:10.1029/2009gc003003

Cerpa, N. G., and Arcay, D. (2020). Overriding plate velocity control on surface topography in 2-D models of subduction zones. *Geochem. Geophys. Geosyst.* 21 (4), e2019GC008900. doi:10.1029/2019gc008900

Cerpa, N. G., Wada, I., and Wilson, C. R. (2017). Fluid migration in the mantle wedge: Influence of mineral grain size and mantle compaction. *J. Geophys. Res. Solid Earth* 122 (8), 6247–6268. doi:10.1002/2017jb014046

Crameri, F., Lithgow-Bertelloni, C. R., and Tackley, P. J. (2017). The dynamical control of subduction parameters on surface topography. *Geochem. Geophys. Geosyst.* 18 (4), 1661–1687. doi:10.1002/2017gc006821

Crameri, F., Shephard, G. E., and Heron, P. J. (2020). The misuse of colour in science communication. *Nat. Commun.* 11 (1), 5444–5510. doi:10.1038/s41467-020-19160-7

Crameri, F., Tackley, P. J., Meilick, I., Gerya, T. V., and Kaus, B. J. P. (2012). A free plate surface and weak oceanic crust produce single-sided subduction on Earth. *Geophys. Res. Lett.* 39 (3). doi:10.1029/2011gl050046

Cruciani, C., Carminati, E., and Doglioni, C. (2005). Slab dip vs. lithosphere age: no direct function. *Earth Planetary Sci. Let.* 238 (3–4), 298–310.

Dasgupta, R., Mandal, N., and Lee, C. (2021a). Controls of subducting slab dip and age on the extensional versus compressional deformation in the overriding plate. *Tectonophysics* 801, 228716. doi:10.1016/j.tecto.2020.228716

Dasgupta, R., and Mandal, N. (2022). Role of double-subduction dynamics in the topographic evolution of the Sunda plate. *Geophys. J. Int.* 230, 696–713. doi:10.1093/gji/ggac025

Dasgupta, R., and Mandal, N. (2018). Surface topography of the overriding plates in bi-vergent subduction systems: A mechanical model. *Tectonophysics* 746, 280–295. doi:10.1016/j.tecto.2017.08.008

Dasgupta, R., Sen, J., and Mandal, N. (2021b). Bending curvatures of subducting plates: Old versus young slabs. *Geophys. J. Int.* 225 (3), 1963–1981. doi:10.1093/gji/ggab070

Duarte, J. C., Schellart, W. P., and Cruden, A. R. (2013). Three-dimensional dynamic laboratory models of subduction with an overriding plate and variable interplate rheology. *Geophys. J. Int.* 195 (1), 47–66. doi:10.1093/gji/ggt257

England, P., Engdahl, R., and Thatcher, W. (2004). Systematic variation in the depths of slabs beneath arc volcanoes. *Geophys. J. Int.* 156 (2), 377–408. doi:10.1111/j.1365-246x.2003.02132.x

Fjeldskaar, W. (1994). Viscosity and thickness of the asthenosphere detected from the Fennoscandian uplift. *Earth Planet. Sci. Lett.* 126, 399–410. doi:10.1016/0012-821x(94)90120-1

François, T., Burov, E., Agard, P., and Meyer, B. (2014). Buildup of a dynamically supported orogenic plateau: Numerical modeling of the Zagros/Central Iran case study. *Geochem. Geophys. Geosyst.* 15 (6), 2632–2654. doi:10.1002/2013gc005223

Fukao, Y., Hori, S., and Ukawa, M. (1983). A seismological constraint on the depth of basalt–eclogite transition in a subducting oceanic crust. *Nature* 303 (5916), 413–415. doi:10.1038/303413a0

Garel, F., Goes, S., Davies, D. R., Davies, J. H., Kramer, S. C., and Wilson, C. R. (2014). Interaction of subducted slabs with the mantle transition-zone: A regime diagram from 2-D thermo-mechanical models with a mobile trench and an overriding plate. *Geochem. Geophys. Geosyst.* 15 (5), 1739–1765. doi:10.1002/2014gc005257

Gerya, T. (2011). Future directions in subduction modeling. *J. Geodyn.* 52 (5), 344–378. doi:10.1016/j.jog.2011.06.005

Gvirtzman, Z., and Stern, R. J. (2004). Bathymetry of Mariana trench-arc system and formation of the Challenger Deep as a consequence of weak plate coupling. *Tectonics* 23 (2). doi:10.1029/2003tc001581

Hacker, B. R. (2008). H2O subduction beyond arcs. *Geochemistry, Geophysics, Geosystems* 9 (3).

Hager, B. H., Clayton, R. W., Richards, M. A., Comer, R. P., and Dziewonski, A. M. (1985). Lower mantle heterogeneity, dynamic topography and the geoid. *Nature* 313 (6003), 541–545. doi:10.1038/313541a0

Harig, C., Zhong, S., and Simons, F. (2010). Constraints on upper mantle viscosity from the flow-induced pressure gradient across the Australian continental keel. *Geochem. Geophys. Geosyst.* 11, n/a. doi:10.1029/2010gc003038

He, L. (2014). Numerical modeling of convective erosion and peridotite-melt interaction in big mantle wedge: Implications for the destruction of the North China Craton. *J. Geophysical Res. Solid Earth* 119 (4), 3662–3677.

Holt, A. F., Becker, T. W., and Buffett, B. A. (2015). Trench migration and overriding plate stress in dynamic subduction models. *Geophys. J. Int.* 201 (1), 172–192. doi:10.1093/gji/ggv011

Hori, S. (1990). Seismic waves guided by untransformed oceanic crust subducting into the mantle: The case of the kanto district, central Japan. *Tectonophysics* 176 (3-4), 355–376. doi:10.1016/0040-1951(90)90078-m

Hu, J., Liu, L., and Gurnis, M. (2021). Southward expanding plate coupling due to variation in sediment subduction as a cause of Andean growth. *Nat. Commun.* 12 (1), 7271–7279. doi:10.1038/s41467-021-27518-8

Iaffaldano, G., Di Giuseppe, E., Corbi, F., Funiciello, F., Faccenna, C., and Bunge, H. P. (2012). Varying mechanical coupling along the Andean margin: Implications for trench curvature, shortening and topography. *Tectonophysics* 526, 16–23. doi:10.1016/j.tecto.2011.09.014

Jadamec, Margarete A. (2016). Insights on slab-driven mantle flow from advances in three-dimensional modelling. *J. Geodyn.* 100, 51–70. doi:10.1016/j.jog.2016.07.004

Kameda, J., Yamaguchi, A., Saito, S., Sakuma, H., Kawamura, K., and Kimura, G. (2011). A new source of water in seismogenic subduction zones. *Geophys. Res. Lett.* 38 (22). doi:10.1029/2011gl048883

Kanamori, H. (1971). Great earthquakes at island arcs and the lithosphere. *Tectonophysics* 12 (3), 187–198. doi:10.1016/0040-1951(71)90003-5

Kawakatsu, H., and Watada, S. (2007). Seismic evidence for deep-water transportation in the mantle. *Science* 316 (5830), 1468–1471. doi:10.1126/science.1140855

Kellogg, L., Hager, B., and van der Hilst, R. (1999). Compositional stratification in the deep mantle. *Science* 283, 1881–1884. doi:10.1126/science.283.5409.1881

King, S. (1995). The viscosity structure of the mantle. *Rev. Geophys.* 33, 11. doi:10.1029/95rg00279

Klein, B. Z., and Behn, M. D. (2021). On the evolution and fate of sediment diapirs in subduction zones. *Geochem. Geophys. Geosyst.* 22 (11), e2021GC009873. doi:10.1029/2021gc009873

Lallemand, S., Peyret, M., van Rijsingen, E., Arcay, D., and Heuret, A. (2018). Roughness characteristics of oceanic seafloor prior to subduction in relation to the seismogenic potential of subduction zones. *Geochem. Geophys. Geosyst.* 19 (7), 2121–2146. doi:10.1029/2018gc007434

Lee, C., and Kim, Y. (2021). Role of warm subduction in the seismological properties of the forearc mantle: An example from southwest Japan. *Sci. Adv.* 7 (28), eabf8934. doi:10.1126/sciadv.abf8934

Lee, C., and Wada, I. (2017). Clustering of arc volcanoes caused by temperature perturbations in the back-arc mantle. *Nat. Commun.* 8 (1), 15753–15759. doi:10.1038/ncomms15753

McKenzie, D., Nimmo, F., Jackson, J. A., Gans, P. B., and Miller, E. L. (2000). Characteristics and consequences of flow in the lower crust. *J. Geophys. Res.* 11029, 11029–11046. doi:10.1029/1999jb900446

Montési, L. G., and Behn, M. D. (2007). Mantle flow and melting underneath oblique and ultraslow mid-ocean ridges. *Geophys. Res. Lett.* 34 (24), L24307. doi:10.1029/2007gl031067

Nishikawa, T., and Ide, S. (2014). Earthquake size distribution in subduction zones linked to slab buoyancy. *Nat. Geosci.* 7 (12), 904–908. doi:10.1038/ngeo2279

Ohkura, T. (2000). Structure of the upper part of the Philippine Sea plate estimated by later phases of upper mantle earthquakes in and around Shikoku, Japan. *Tectonophysics* 321 (1), 17–36. doi:10.1016/s0040-1951(00)00078-0

Peacock, S. M., and Wang, K. (2021). On the stability of talc in subduction zones: A possible control on the maximum depth of decoupling between the subducting plate and mantle wedge. *Geophys. Res. Lett.* 48 (17), e2021GL094889. doi:10.1029/2021gl094889

Pysklywec, R. N., and Shahnas, M. H. (2003). Time-dependent surface topography in a coupled crust–mantle convection model. *Geophys. J. Int.* 154 (2), 268–278. doi:10.1046/j.1365-246x.2003.01987.x

Ranalli, G. (1995). *Rheology of the Earth*. Springer Science & Business Media. ISBN 978-0-412-54670-9.

Ribe, N. M. (2010). Bending mechanics and mode selection in free subduction: A thin-sheet analysis. *Geophys. J. Int.* 180 (2), 559–576. doi:10.1111/j.1365-246x.2009.04460.x

Riel, N., Capitanio, F. A., and Velic, M. (2018). Numerical modeling of stress and topography coupling during subduction: Inferences on global vs. regional observables interpretation. *Tectonophysics* 746, 239–250. doi:10.1016/j.tecto.2017.07.023

Rodríguez-González, J., Negredo, A. M., and Billen, M. I. (2012). The role of the overriding plate thermal state on slab dip variability and on the occurrence of flat subduction. *Geochem. Geophys. Geosyst.* 13 (1). doi:10.1029/2011gc003859

Rondenay, S., Abers, G. A., and Van Keken, P. E. (2008). Seismic imaging of subduction zone metamorphism. *Geol.* 36 (4), 275–278. doi:10.1130/g24112a.1

Rudolph, M. L., Lekić, V., and Lithgow-Bertelloni, C. (2015). Viscosity jump in Earth's mid-mantle. *Science* 350 (6266), 1349–1352. doi:10.1126/science.aad1929

Ruff, L. J., and Tichelaar, B. W. (1996). *What controls the seismogenic plate interface in subduction zones?* Washington DC: American Geophysical Union Geophysical Monograph Series, 105–111. doi:10.1029/GM096p0105

Ruff, L., and Kanamori, H. (1983). Seismic coupling and uncoupling at subduction zones. *Tectonophysics* 99 (2-4), 99–117. doi:10.1016/0040-1951(83)90097-5

Ruffino, F., Gentile, A., Zimbone, M., Piccitto, G., Reitano, R., and Grimaldi, M. G. (2016). Size-selected Au nanoparticles on FTO substrate: Controlled synthesis by the Rayleigh-Taylor instability and optical properties. *Superlattices Microstruct.* 100, 418–430. doi:10.1016/j.spmi.2016.09.047

Schmalholz, S. M. (2011). A simple analytical solution for slab detachment. *Earth Planet. Sci. Lett.* 304 (1-2), 45–54. doi:10.1016/j.epsl.2011.01.011

Schmeling, H., Babeyko, A. Y., Enns, A., Faccenna, C., Funiciello, F., Gerya, T., et al. (2008). A benchmark comparison of spontaneous subduction models-Towards a free surface. *Phys. Earth Planet. Interiors* 171 (1–4), 198–223. doi:10.1016/j.pepi.2008.06.028

Schmidt, M. W., and Poli, S. (1998). Experimentally based water budgets for dehydrating slabs and consequences for arc magma generation. *Earth Planetary Science Lett.* 163 (1–4), 361–379.

Scholz, C. H., and Campos, J. (1995). On the mechanism of seismic decoupling and back arc spreading at subduction zones. *J. Geophys. Res.* 100 (B11), 22103–22115. doi:10.1029/95jb01869

Shahraki, M., and Schmeling, H. (2012). Plume-induced geoid anomalies from 2D axi-symmetric temperature-and pressure-dependent mantle convection models. *J. Geodyn.* 59, 193–206. doi:10.1016/j.jog.2012.01.006

Stern, R. J., and Gerya, T. (2018). Subduction initiation in nature and models: A review. *Tectonophysics* 746, 173–198. doi:10.1016/j.tecto.2017.10.014

Syracuse, E. M., van Keken, P. E., and Abers, G. A. (2010). The global range of subduction zone thermal models. *Phys. Earth Planet. Interiors* 183 (1-2), 73–90. doi:10.1016/j.pepi.2010.02.004

Tatsumi, Y. (1986). Formation of the volcanic front in subduction zones. *Geophys. Res. Lett.* 13 (8), 717–720. doi:10.1029/gl013i008p00717

Villegas-Lanza, J. C., Chlieh, M., Cavalié, O., Tavera, H., Baby, P., Chire-Chira, J., et al. (2016). Active tectonics of Peru: Heterogeneous interseismic coupling along the Nazca megathrust, rigid motion of the Peruvian Sliver, and Subandean shortening accommodation. *J. Geophys. Res. Solid Earth* 121 (10), 7371–7394. doi:10.1002/2016jb013080

Wada, I., Behn, M. D., and Shaw, A. M. (2012). Effects of heterogeneous hydration in the incoming plate, slab rehydration, and mantle wedge hydration on slab-derived H2O flux in subduction zones. *Earth Planet. Sci. Lett.* 353, 60–71. doi:10.1016/j.epsl.2012.07.025

Wada, I., He, J., Hasegawa, A., and Nakajima, J. (2015). Mantle wedge flow pattern and thermal structure in Northeast Japan: Effects of oblique subduction and 3-D slab geometry. *Earth Planet. Sci. Lett.* 426, 76–88. doi:10.1016/j.epsl.2015.06.021

Wada, I., and Wang, K. (2009). Common depth of slab-mantle decoupling: Reconciling diversity and uniformity of subduction zones. *Geochem. Geophys. Geosyst.* 10 (10). doi:10.1029/2009gc002570

Weismüller, J., Gmeiner, B., Ghelichkhan, S., Huber, M., John, L., Wohlmuth, B., et al. (2015). Fast asthenosphere motion in high-resolution global mantle flow models. *Geophys. Res. Lett.* 42, 7429–7435. doi:10.1002/2015gl063727

Willingshofer, E., Sokoutis, D., Luth, S. W., Beekman, F., and Cloetingh, S. (2013). Subduction and deformation of the continental lithosphere in response to plate and crust-mantle coupling. *Geology* 41 (12), 1239–1242. doi:10.1130/g34815.1

Yuan, X., Sobolev, S. V., Kind, R., Oncken, O., Bock, G., Asch, G., et al. (2000). Subduction and collision processes in the Central Andes constrained by converted seismic phases. *Nature* 408 (6815), 958–961. doi:10.1038/35050073

Zhong, S., Gurnis, M., and Moresi, L. (1996). Free-surface formulation of mantle convection—I. Basic theory and application to plumes. *Geophys. J. Int.* 127 (3), 708–718. doi:10.1111/j.1365-246x.1996.tb04049.x

Zhong, S., and Zuber, M. (2000). Long-wavelength topographic relaxation for self-gravitating planets and implications for the time-dependent compensation of surface topography. *J. Geophys. Res.* 105, 4153–4164. doi:10.1029/1999je001075

frontiers | Frontiers in Earth Science

TYPE Hypothesis and Theory
PUBLISHED 13 September 2022
DOI 10.3389/feart.2022.889907

Asthenospheric flow through the Izanagi-Pacific slab window and its influence on dynamic topography and intraplate volcanism in East Asia

Hamish Brown[1]*, Lorenzo Colli[2] and Hans-Peter Bunge[1]

[1]Department of Earth and Environmental Sciences, Ludwig-Maximilians-Universität München, Munich, Germany, [2]Department of Earth and Atmospheric Sciences, University of Houston, Houston, TX, United States

OPEN ACCESS

EDITED BY
Lijun Liu,
University of Illinois at Urbana-Champaign, United States

REVIEWED BY
Bernhard Maximilian Steinberger,
GFZ German Research Centre for Geosciences, Germany
Jiashun Hu,
Southern University of Science and Technology, China

*CORRESPONDENCE
Hamish Brown,
hbrown@geophysik.uni-muenchen.de

SPECIALTY SECTION
This article was submitted to Solid Earth Geophysics,
a section of the journal
Frontiers in Earth Science

RECEIVED 04 March 2022
ACCEPTED 27 June 2022
PUBLISHED 13 September 2022

CITATION
Brown H, Colli L and Bunge H-P (2022), Asthenospheric flow through the Izanagi-Pacific slab window and its influence on dynamic topography and intraplate volcanism in East Asia.
Front. Earth Sci. 10:889907.
doi: 10.3389/feart.2022.889907

The tectonics of East Asia are notoriously complex. Consisting of an intricate patchwork of microplates and accreted terranes, even the Cenozoic tectonic history of the region remains controversial, and many differing reconstructions have been proposed. While the exact kinematics remain poorly constrained, it is generally accepted that East Asia has been characterised by a long history of subduction and downwelling. However, numerous geological observations, at a first glance, appear to lie in stark contrast to this history. For example, seismically slow anomalies in the uppermost mantle are extensive in this region and coincide spatially with widespread intraplate volcanism since the latest Paleogene, which is seemingly at odds with the cold upper mantle and downwelling flow expected from a history of subduction. Here, we propose a solution to this paradox, in which hot asthenospheric material flows through the slab window opened by the subduction of the Izanagi-Pacific ridge during the early Cenozoic, passing from the Pacific domain into East Asia. To investigate this hypothesis, we compare several independent geological observations to the asthenospheric flow predicted by a suite of recently published global mantle circulation models. The timing and location of intraplate volcanism is compared with the predicted distribution of this hot material through time, while observations linked to uplift and erosion are compared to the changes in dynamic topography that it induces. These include the widespread late Eocene–Oligocene sedimentary hiatus in far eastern China and the regional erosion of the South China Block since the Miocene inferred from Apatite Fission Track Thermochronology studies. The westward influx of hot asthenospheric material is a robust feature in the models, being predicted regardless of the implemented Cenozoic tectonic reconstruction. However, we find that a small Philippine Sea Plate that overrides a marginal "vanished ocean" during the late Cenozoic provides an optimal fit to the geological observations considered. Flow of hot asthenospheric material through gaps in subduction has the potential to significantly affect the geodynamic and geologic history of backarc and hinterland regions, and might have been a recurring phenomenon throughout Earth's history. However, further research will be required in order to establish this.

KEYWORDS

East Asia, asthenospheric flow, dynamic topography, intraplate volcanism, slab window, ridge subduction, mantle circulation models, plate reconstructions

1 Introduction

East Asia lies at a key junction between the converging Pacific (PAC), Eurasian (EUR), and Indo-Australian (IA) plates. Characterised by several microplates, marginal seas, accreted terranes, and zones of diffuse deformation, it is generally considered to be one of the most (if not the most) tectonically complex regions on Earth. In addition to this, reconstructing even the Cenozoic tectonic history of the region has been hampered by the existence of potentially numerous small plates which have been completely subducted into the mantle, or plates which have been isolated by subduction zones from global plate circuits (Hall and Spakman, 2015; Wu et al., 2016). Consequently, extracting the first-order details of the Cenozoic tectonic history of this region from geological and seismological evidence remains an ongoing endeavour, and a variety of differing reconstructions have been proposed. Nevertheless, there exists a general consensus that the long-term convergence of PAC, EUR, and IA must have been accommodated by widespread subduction and downwelling throughout East Asia.

Given this consensus, it is understandable that geodynamic studies (at least on inter-regional scales) have focussed on downwelling slabs (e.g., Zahirovic et al., 2016), or their influence at the surface in terms of dynamic subsidence and rebound (e.g., Cao et al., 2018). However, numerous observations appear to suggest that a widespread presence of hot material in the uppermost mantle is also essential in describing the Cenozoic dynamics of this region. First of all, while global tomographic models have been crucial in identifying the distribution of subducted slabs in the East Asian mantle (e.g., Wu et al., 2016), these models also consistently reveal an extensive network of seismically slow anomalies at asthenospheric depths (e.g., Li et al., 2008; Schaeffer and Lebedev, 2013; Ma J. et al., 2019). The region may therefore be tentatively interpreted as being characterised by a largely hot upper mantle in the present day. This interpretation is corroborated by studies of present-day residual (i.e., dynamic) topography [see the recent review of Hoggard et al. (2021)], which have consistently found swells of present-day dynamic uplift throughout East Asia. Given these observations, the immediate questions arise as to when, and how, this present-day state of the mantle has developed—in a region dominated by subduction and downwelling. Regarding the first of these questions, intraplate volcanism has been widespread in East Asia since the latest Paleogene (Figure 1), potentially hinting at the arrival of this material during the late Cenozoic. The global connection between Neogene intraplate volcanism and seismically slow anomalies in the uppermost mantle was recently made explicit by the work of Ball et al. (2021), within which East Asia stood out as a prominent feature in the global picture. However, the question of how this state arose on an inter-regional scale in East Asia has not yet been tackled.

Here, we aim to reconcile the subduction-dominated environment of East Asia with its inferred hot upper mantle in the present day. We propose and investigate a new mechanism by which hot asthenospheric material from the Pacific domain can migrate into this region through pressure- and plate-driven asthenospheric flow. To test our new hypothesis, we compile geological evidence of intraplate volcanism and past changes in dynamic topography in East Asia from published literature. These observations are then compared to the asthenospheric flow predicted by the suite of global mantle circulation models published by Lin et al. (2020). The purpose of this paper is therefore twofold. First and foremost, we present a new model for the Cenozoic geodynamic development of East Asia, and substantiate it by connecting independent mantle circulation models with a wide variety of geological observations. Secondly, the comparisons made between these models and the compiled geological evidence are used to provide new constraints on the uncertain Cenozoic tectonics of the region. A map of the relevant regions and geological features for this study is shown in Figure 1 (compiled from Steinshouer et al., 1999; Chung, 1999; Ho et al., 2003; Tang et al., 2006; Choi et al., 2006; Sun et al., 2010; Gong and Chen, 2014; Liu et al., 2001; Yan Q. et al., 2018; Zheng et al., 2019).

The remainder of our paper is structured as follows. In Section 2, we introduce our hypothesis, and the inferred Mesozoic–Cenozoic dynamics on which it is based. In Section 3, we introduce the relevant tectonic reconstructions of the study region and their implementation in the circulation models of Lin et al. (2020). In Section 4, we compile four independent geological observations in East Asia, related to both intraplate volcanism and dynamic topography, and compare these with the model predictions of Lin et al. (2020). We discuss these comparisons, and bring them together under our hypothesis, in Section 5. A discussion on the limitations of the models of Lin et al. (2020) is also included. Finally, we summarise our conclusions in Section 6.

2 Asthenospheric flow through the Izanagi-Pacific slab window

The low-viscosity asthenosphere has traditionally been regarded as a passive lubricating layer to facilitate plate motion (Chase, 1979), but mounting evidence now suggests that active pressure-driven flow plays a significant role in asthenospheric dynamics. Theoretical (Weismüller et al., 2015) and observational (White and Lovell, 1997; Hartley et al., 2011; Colli et al., 2014; Parnell-Turner et al., 2014; Chen et al., 2021) constraints have found pressure-driven flow velocities of ~15–20 cm/year, which influence the motion of the overlying plates (e.g., Colli et al., 2014; Chen et al., 2021; Stotz et al., 2021). Flow in the asthenosphere is therefore thought to consist of a top-down, plate-driven component (i.e., Couette flow), and a component induced by pressure gradients in the asthenosphere (i.e., Poiseuille flow) (Höink and Lenardic, 2008; Höink and Lenardic, 2010; Höink et al., 2011; Höink et al., 2012). Given the aforementioned pressure-driven velocities, and the additional plate-driven component, it becomes apparent that asthenospheric material could potentially be transported over significant (e.g., ~4,500 km) distances within relatively short (~30 Ma) geological timescales. Combined with the late Mesozoic–Cenozoic dynamics of East Asia and the Pacific introduced below, these forms of flow provide a mechanism by which hot asthenospheric material could have migrated into East Asia during the Cenozoic.

Magnetic lineations in the western Pacific (e.g., Müller et al., 2016, and references therein) show that during the Mesozoic the Pacific plate had a conjugate plate to the northwest, termed the Izanagi plate by Woods and Davies (1982). The Mesozoic subduction of this plate has been deduced based on subduction-induced volcanism in East Asia (e.g., Charvet et al., 1994), while a break in volcanism during 56–46 Ma in Northeast Asia (Wu and Wu, 2019) reveals the subduction of the

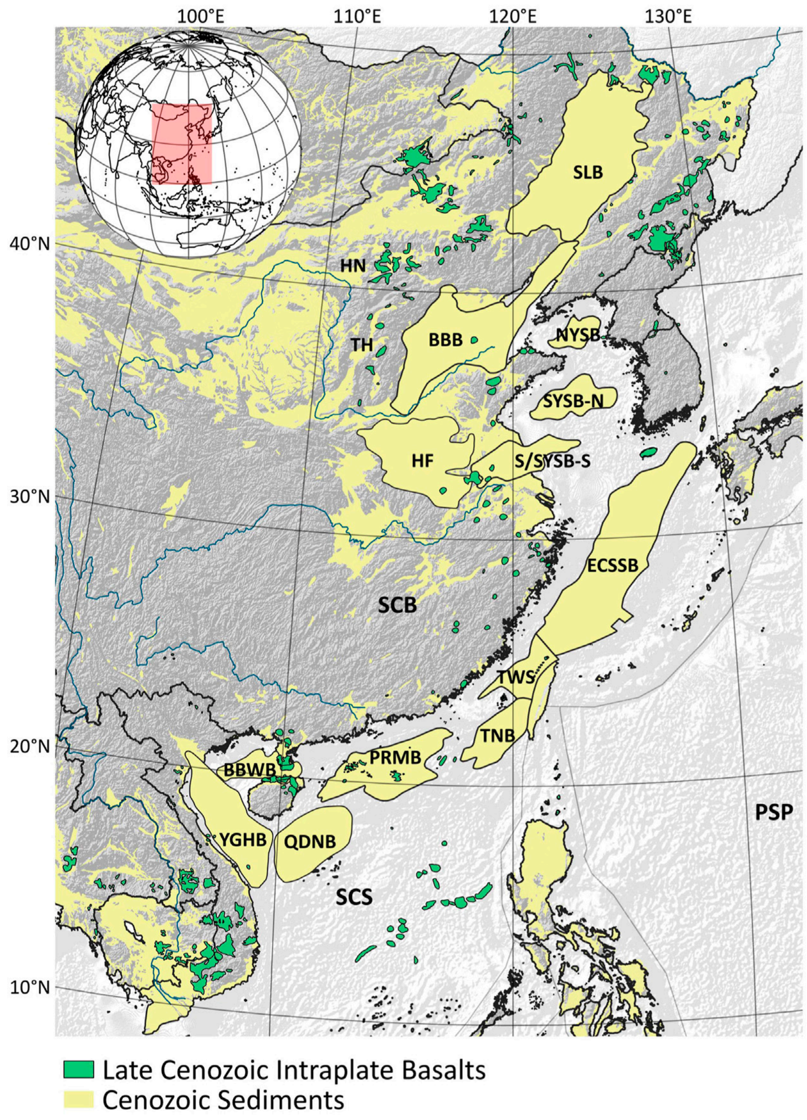

FIGURE 1
Map of the study area showing the distribution of late Cenozoic intraplate basalts considered in this study (in green) and Cenozoic sediments (in yellow), together with the outline of the main sedimentary basins mentioned in the text. Notice the scarcity of Cenozoic sediments in the South China Block. SLB, Songliao Basin; BBB, Bohai Bay Basin; NYSB, North Yellow Sea Basin; SYSB-N, South Yellow Sea Basin Northern Depression; S/SYSB-S, Subei/South Yellow Sea Basin Southern Depression; HF, Hefei Basin; ECSSB, East China Sea Shelf Basin; TWS, Taiwan Strait; TNB, Tainan Basin; PRMB, Pearl River Mouth Basin; BBWB, Beibuwan Basin; QDNB, Qiongdongnan Basin; YGHB, Yinggehai Basin; HN, Hannuoba Basalts; TH, Taihang Basalts. SCB, South China Block; SCS, South China Sea; PSP, Philippine Sea Plate.

Izanagi-Pacific ridge. The slab window opened by the subduction of this ridge would have provided a pathway for Pacific asthenosphere to flow into East Asia. A detailed reconstruction of Mesozoic–Cenozoic western Pacific tectonics, however, is hindered by the fact that most of the lithosphere that was flooring the western Pacific has since been subducted, leaving large areas with unconstrained kinematics (Müller et al., 2016). The unconstrained area can in principle be filled by a single, large Izanagi plate, inducing margin-wide ridge subduction (e.g., Seton et al., 2012). However, the accretion of intra-oceanic arcs along the Eurasian margin during the Mesozoic suggests that the large Izanagi plate may in fact have been several smaller plates, with intervening intra-oceanic subduction zones providing the accreted material (see, e.g., Lin et al., 2021, and references therein). These more complex reconstructions feature even more pathways for Pacific asthenosphere to flow into Eurasia while implying the same first-order effects on asthenospheric dynamics. We therefore centre our work on the commonly implemented large Izanagi plate and leave the implications of more complex scenarios for future investigation.

While East Asia is noted for its large-scale mantle downwelling, the Pacific domain is well-known for large-scale thermal upwelling. This is evidenced by the numerous plume-fed hotspots emanating from the Pacific LLSVP (e.g., French and Romanowicz, 2015), the influence of which at the surface is revealed by dynamic uplift inferred from tomographically-constrained geoid modelling (e.g., Richards and Hager, 1984; Richards et al., 1988) and residual topography measurements (e.g., Hoggard et al., 2017). Evidence from plume-sourced basalts found in accreted complexes on the Eurasian margin shows that this state of large-scale thermal upwelling has been present in the Pacific domain since Cretaceous times (Safonova and Santosh, 2014). One may therefore infer that the Pacific asthenosphere has been fed by hot material from the lowermost mantle since at least this time. Asthenospheric material is naturally driven from high-pressure upwellings to low-pressure subduction zones by a combination of pressure-driven Poiseuille flow and plate-driven Couette flow (Höink and Lenardic, 2010; Colli et al., 2018). Combined, these two effects provide a mechanism for the long-term transport of hot asthenospheric material to the western Pacific margin during the Cretaceous. The mantle below Eurasia has probably been characterised by even lower pressures than the western Pacific, induced by large-scale mantle downwelling (e.g., Izanagi slab, Neo- and Meso-Tethys slabs) and by the trench–arc trending pressure gradient which arises naturally by slab-induced mantle flow during subduction (sometimes referred to as trench suction, see Turcotte and Schubert, 2002). During the Mesozoic, asthenospheric flow between the Pacific/Panthalassa domain and Eurasia was likely blocked by the subducting Izanagi plate. Following the subduction of the Izanagi-Pacific ridge, however, hot material may then have flowed through the opened slab window into East Asia, and been driven further into this region by downwelling slabs during the Cenozoic. Indeed, this east–west Poiseuille flow following the subduction of the Izanagi-Pacific ridge has recently been noted, and invoked as a cause of the flat-slab subduction style of the Pacific plate (Peng et al., 2021).

Our hypothesis can be summarised as follows. During the Izanagi subduction, hot asthenospheric material was built up in the westernmost Pacific through a combination of plume- and plate-driven flow. Following the subduction of the Izanagi-Pacific ridge during the early Cenozoic, this material was then driven into East Asia by pressure-driven Poiseuille flow, induced by the large-scale mantle downwelling in this region. The migration of this material into East Asia during the late Cenozoic provides a new explanation for its inferred hot upper mantle in the present day (Section 1). A cartoon illustrating this hypothesis is shown in Figure 2.

3 Global mantle circulation models

Mantle circulation models have used kinematic reconstructions of past plate motion as a key input to overcome the initial condition problem of mantle convection. This, in turn, has allowed geodynamically-derived mantle states to be compared against a variety of geophysical and geological observations (Bunge et al., 1998; Schuberth et al., 2009a; Schuberth et al., 2009b; Nerlich et al., 2016; Zahirovic et al., 2016). But the reconstructed mantle states depend critically on the input plate kinematic model (Colli et al., 2018; Lin et al., 2020) and, as discussed above, the constant loss of ocean floor means that significant uncertainties still exist in the kinematics of subduction-dominated regions. However, advances in the resolution of seismic tomography have made it possible to "image" subducted slabs in the mantle (e.g., Li et al., 2008), providing access to new sub-surface information with which to constrain past tectonics. This has led to the development of new "slab unfolding" methods (Wu et al., 2016; Wu and Suppe, 2018), which make use of this new window into past subduction. Slabs are identified as seismically fast anomalies, and are then unfolded, and projected to their implied extent at the surface. The surface distribution of the imaged slabs can then be used to improve upon surface-based reconstructions. These methods have been applied in East Asia (Wu et al., 2016), and have shed new light on the Cenozoic history of subduction in this region. Of particular importance here are the proto-South China Sea (PSCS) and the Philippine Sea Plate (PSP), as the slab unfolding method has been used to develop new fully-kinematic plate models specifically for these plates.

3.1 Plate motion models

The PSCS, which has now been completely removed from the surface, is inferred to have subducted during the opening of the

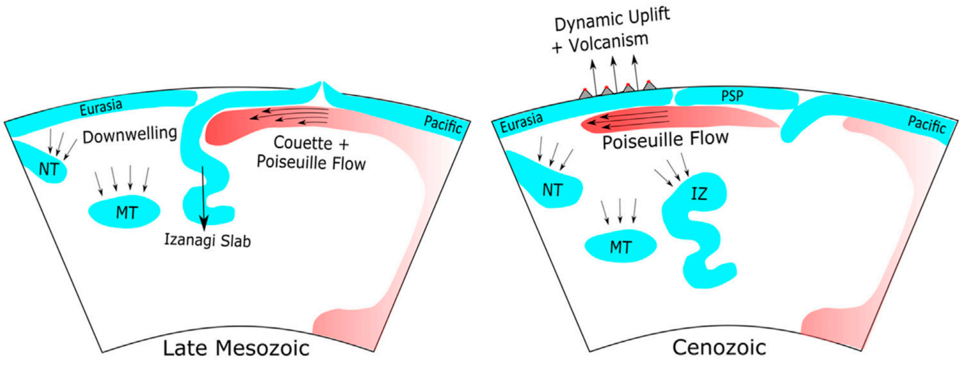

FIGURE 2
Cartoon illustrating the proposed build-up of Pacific asthenospheric material in the far western Pacific during the late Mesozoic through pressure- and plate-driven flow, and subsequent pressure-driven influx into East Asia through the Izanagi-Pacific slab window during the Cenozoic. NT, Neotethys slab; MT, Mesotethys slab; IZ, Izanagi slab; PSP, Philippine Sea Plate.

present-day South China Sea (SCS). This has been argued based both on a gap in tectonic reconstructions prior to this opening (e.g., Holloway, 1982) and the observation of fast slab-like anomalies below this region in tomographic models (e.g., Hall and Spakman, 2015). However, the details of this subduction remain uncertain. Traditionally, the PSCS has been envisioned as subducting southward below Borneo (e.g., Hall, 2002; Seton et al., 2012; Zahirovic et al., 2014). Based on slab-unfolding methods, Wu and Suppe (2018) instead argue that the PSCS subducted both northward and southward during the opening of the SCS, due to both the position of the subducted PSCS slab in the mantle and its subhorizontal orientation.

Unlike the PSCS, the PSP is still present at the Earth's surface (Figure 1). But its Cenozoic history remains uncertain due to its isolation from global plate circuits by surrounding subduction zones (see discussion in Wu et al., 2016). Due to this, vast differences exist in the proposed PSP reconstructions. A common view is that the PSP was much larger in the past, and began its current subduction along the Eurasian margin before 30 Ma (e.g., Seno and Maruyama, 1984; Xu et al., 2014; Zahirovic et al., 2014). On the other hand, based on the slab anomalies underlying the PSP in the present day, Wu et al. (2016) argue for a much smaller historic PSP, which begins subducting along the Eurasian margin at ~16 Ma. In this reconstruction, the spatial gap produced by the smaller PSP is made up by the now fully-subducted "East Asian Sea" (EAS) slabs, which have been inferred based on the imaged slabs to have subducted southward below the PSP. Therefore, under this viewpoint, the smaller PSP overrides the southward-subducting EAS slabs as it migrates northward towards its present day position. For a more detailed review of the reasoning behind these differing reconstructions, we refer the reader to the discussion of PSCS reconstructions in Lin et al. (2020) and the discussion of the PSP and EAS slabs in Wu et al. (2016) and Zahirovic et al. (2014).

3.2 Model implementations

The study of Lin et al. (2020) investigated the mantle flow predicted by differing tectonic reconstructions in East Asia. Reconstructions were assimilated as surface velocity boundary conditions in the global mantle convection code TERRA (Bunge and Baumgardner, 1995). This allows geological information about past plate motion to enter the flow, as downwellings develop at locations of plate convergence (e.g., Bunge et al., 2002). Mantle convection was modelled by solving the conservation equations for mass, momentum, and energy in the truncated anelastic liquid approximation (Jarvis and McKenzie, 1980a). Lithospheric thickness variations were generated self-consistently by solving the conservation equations with tectonic velocities and a surface temperature $T_S = 300$ K as boundary conditions. The computational domain was discretised on a regular grid based on the icosahedron, with ~80 million grid points and a minimum resolution of ~25 km. The mantle was heated from below and from within with a CMB temperature $T_{CMB} = 4{,}200$ K and a radiogenic heating rate of 6×10^{-12} W·kg^{-1}. The viscosity was assumed to be Newtonian and depends on temperature (T) and depth (d) as

$$\eta(d,T) = \eta_0 A(d) \exp\left(V^* \frac{d}{R_E - R_{CMB}} - E^* \frac{T - T_S}{T_{CMB} - T_S}\right), \quad (1)$$

where $V^* = 3.976$ and $E^* = 4.610$ are non-dimensional constants controlling the degree of depth and temperature dependence respectively. An increasing viscosity with depth is imposed by the factor $\exp[V^* d/(R_E - R_{CMB})]$, in which the depth is normalised by the mantle thickness $R_E - R_{CMB}$. The reference viscosity is $\eta_0 = 10^{22}$ Pa·s and is multiplied with a radial pre-factor $A(d)$ in order to impose a low-viscosity asthenosphere. The resulting

TABLE 1 Model naming scheme based on the implemented Cenozoic tectonic reconstruction following Lin et al. (2020).

Model Name	PSP size	PSCS subduction
Model 1a	Large	Southward
Model 1b	Large	Double-sided
Model 2a	Small	Southward
Model 2b	Small	Double-sided

maximum, minimum, and average radial viscosity profiles are reported in Supplementary Figure S1, together with the total radial pre-factor $\eta_0 A(d)$. This model rheology leads to two-sided subduction, and one-sided subduction was not forced by imposing either dipping weak plate boundaries or a prescribed dipping slab thermal structure. Slab material therefore sinks vertically unless carried passively by mantle flow.

Four different tectonic reconstructions (Models 1a, 1b, 2a & 2b) were implemented, which are designed to test different end-members of the proposed reconstructions of the PSP and the PSCS introduced above. Models labelled “a” (Models 1a & 2a) implement a southward PSCS subduction, while models labelled “b” (Models 1b & 2b) implement a double-sided PSCS subduction. Models labelled “1” (Models 1a & 1b) implement a large PSP in the style of Zahirovic et al. (2014), while models labelled with a “2” (Models 2a & 2b) implement a simplified form of the slab-unfolded model of Wu et al. (2016), featuring a small PSP that overrides a single “vanished ocean” (VO) plate. In these reconstructions, the small PSP overrides the VO plate and begins

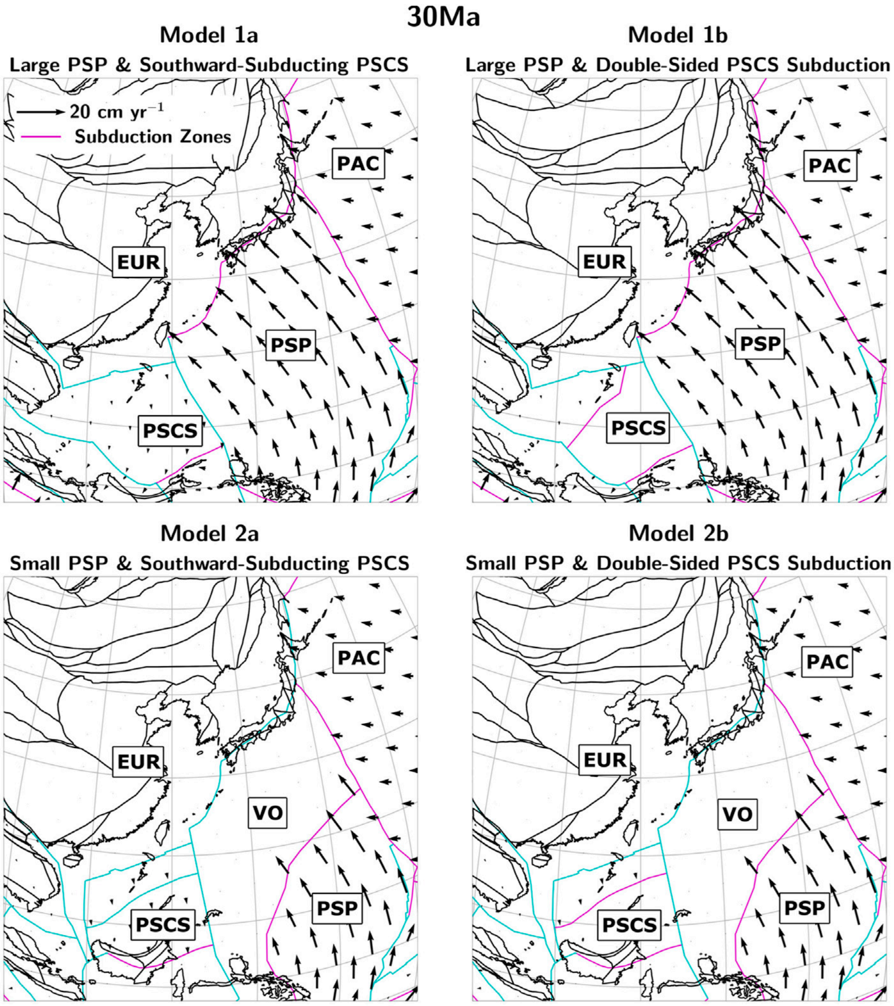

FIGURE 3
30 Ma time-step of the four late Cenozoic tectonic reconstructions used in the mantle circulation models of Lin et al. (2020). Black arrows denote plate velocities in a global moving hotspot reference frame (Matthews et al., 2016). Purple lines show the location of subduction zones, while other plate margins are drawn in light blue. EUR, Eurasian Plate; PAC, Pacific Plate; PSP, Philippine Sea Plate; VO, Vanished Ocean Plate; PSCS, proto-South China Sea Plate.

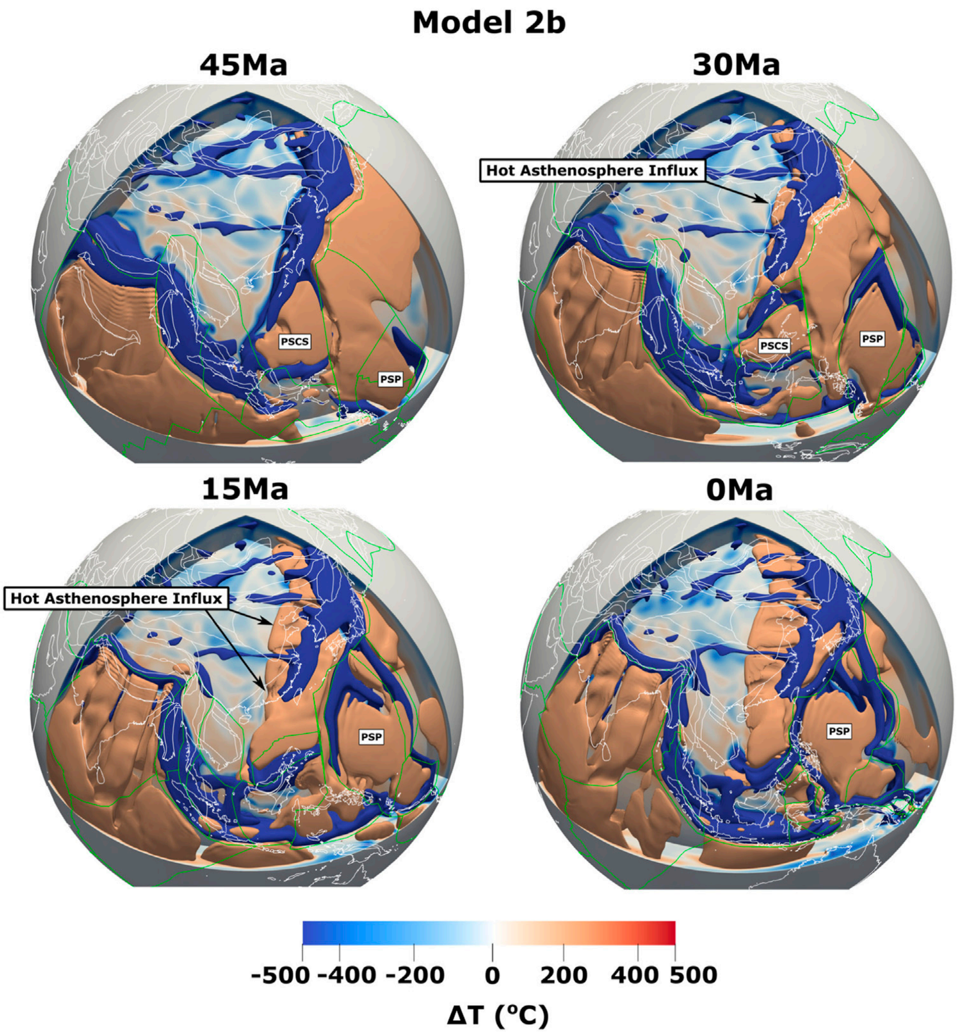

FIGURE 4
Four snapshots at 45, 30, 15, and 0 Ma from the upper mantle flow history of our preferred Model 2b (Lin et al., 2020) showing the Cenozoic influx of hot asthenospheric material through the Izanagi-Pacific slab window and its subsequent migration below East Asia. Isosurfaces of anomalous temperature (with respect to the mean radial temperature profile of the model) of −500°C and +200°C have been extracted in the upper mantle in order to highlight the downwelling slabs and influx of hot Pacific material. PSP, Philippine Sea Plate; PSCS, proto-South China Sea Plate.

its subduction along the Eurasian margin at ~12 Ma. The naming scheme for these models is summarised in Table 1. Figure 3 shows the reconstructed plate motions at 30 Ma, highlighting their key differences. The primary aim of Lin et al. (2020) was to test the present-day mantle heterogeneity predicted under each reconstruction against seismic tomography. Model 2b led to a present-day mantle state which had the highest correlation with seismic tomography, and so is our preferred reconstruction.

Prior to the assimilation of these reconstructions at 30 Ma (Models 1a & 1b) and 45 Ma (Models 2a & 2b), the reconstruction of Matthews et al. (2016) is used as a surface boundary condition on velocities since 410 Ma. A reference model implements the reconstruction of Matthews et al. (2016) for the entire 410–0 Ma timespan. All models therefore implement the subduction of a large Izanagi plate during the Mesozoic and the subduction of the Izanagi-Pacific ridge at ~55 Ma. Running these models since the Paleozoic means that an Earth-like convective planform is allowed to develop, generating vigorous plumes in the Pacific domain. Thus, a realistic hot upper mantle arises in this region during the Mesozoic. Along with the implemented Izanagi subduction and downwelling slabs in East Asia, this provides a realistic scenario in which to test our asthenospheric flow hypothesis.

The asthenospheric build-up and subsequent influx proposed in Section 2 arises under all considered reconstructions. Transects of the reference model showing the full history of this influx from 60 to 0 Ma can be found in Supplementary Figures S2–S8. Hot asthenospheric material is driven westward through the Izanagi-Pacific slab window from ~50–30 Ma, subsequently flowing laterally below East Asia during the late Cenozoic. Figure 4 shows four snapshots from the evolution of our preferred Model 2b, which implements a double-sided subduction of the PSCS and a smaller PSP. While this influx occurs under all considered tectonic reconstructions, the differences between the plate motion models described above affect how much hot material flows below East Asia, which parts of the asthenosphere are occupied by slabs, and the induced late Cenozoic dynamic topography. For further details of these models we refer the reader to Lin et al. (2020).

4 Comparisons with the geological record

4.1 Intraplate volcanism

Intraplate basaltic magmatism has been widespread in East Asia since the latest Paleogene (Figure 1), spanning from the well-known eruptions in Indochina and Hainan (e.g., Yan et al., 2008), throughout the South China Block (SCB) (e.g., Gong and Chen, 2014), and extending far northward to the Changbai mountains on the Sino-Korean border (e.g., Liu et al., 2015). These basalts are predominantly of Ocean-Island-Basalt (OIB) type (e.g., SCS and Indochina, Yan Q. et al. (2018) and references therein; SCB, Ho et al. (2003); Tan-Lu fault zone, Chung, (1999); Changbai Mountains, Liu et al. (2015); inter-regional, Kimura et al. (2018)), have moderate to high mantle potential temperatures (~1,320°C–1,440°C, see Kimura et al., 2018), and coincide spatially with seismically slow anomalies (Ball et al., 2021). Together these observations suggest that a source of hot, upwelling asthenospheric material is required in order to explain this recent phase of eruptions. We note that this doesn’t necessarily preclude a contribution from slab dehydration (e.g., Richard and Iwamori, 2010), at least for some of this magmatism.

In order to investigate a potential link between the late Cenozoic volcanism in East Asia and our asthenospheric flow hypothesis, we compare the timing and location of intraplate volcanic eruptions to the distribution of hot asthenospheric material from 30 to 0 Ma predicted by the models of Lin et al. (2020). We trace the distribution of temperature anomalies in the asthenosphere by defining the model lithosphere by the 1,300°C isotherm, and the model asthenosphere as the 200 km thick channel below this. In the case that a subducting slab is encountered (i.e., $T < 1{,}300^{\circ}$C through the asthenosphere) a default lithosphere thickness of 100 km is taken, which produces the sharp jumps near subduction zones seen in Figure 5. To avoid the influence of “drip” artefacts left over in the asthenosphere from the subduction of the Izanagi plate (see discussion of model limitations in Section 5.4), we take the mean anomalous temperature in the model asthenosphere, as this best reflects the full lateral extent of the influx of hot material. We make use of the global database of intraplate volcanic samples compiled by Ball et al. (2021). While this is primarily a database of Neogene volcanism, many Paleogene samples are also included, meaning it is suitable for the 30–0 Ma timespan considered here. Additional eruptions in the SCB, Hainan, and South Korea are taken from Gong and Chen (2014) and Arai et al. (2001). The post-rift basaltic eruptions in the PRMB have been included from the map compiled by Sun et al. (2010).

Figure 5 shows the mean anomalous temperature in the asthenosphere at 6 Ma intervals from 30 to 0 Ma, overlaid with intraplate eruptions of age within ±1.5 Ma. Given that the uncertainties in dating are often on the order of ~1 Ma although in some rare cases, were as high as ~7–10 Ma, see database of Ball et al. (2021), and the slow pace of mantle flow, this approximation is not likely to result in any spurious connections between the modelling results and mapped eruptions. Maps for the full time-series are reported in Supplementary Figures S9–S19. We briefly note that the anomalous temperature values are systematically over-estimated in the models of Lin et al. (2020), and so we simply consider the distribution of anomalously hot material through time, rather than interpreting its values.

The predicted lateral extent of hot material beneath East Asia from 30 to 0 Ma shows a good match to the distribution of intraplate volcanism during this time (Figure 5). The volcanism in NE China is matched well by all models. Moving further south, Models 2a & 2b, which implement a small PSP, predict a hot, positively buoyant asthenosphere below SE China, Taiwan, and Penghu from 24 to 0 Ma, which is consistent with the OIB-type magmatism observed here (e.g., Chung et al., 1995; Ho et al., 2003). In contrast, Models 1a & 1b, which feature a large PSP, predict predominantly downwelling, cold material in the asthenosphere below these regions, which is inconsistent with this form of magmatism. Some of the westernmost eruptions, such as the Hannuoba and Taihang basalts (HN and TH in Figure 1), are only reached a few Myrs after the onset of magmatism (cf. 24–12 Ma snapshots of Figure 5). Others, such as the eruptions in the Indochina peninsula, are not reached in any of the considered models, although the flow is typically ≲1,000 km from these eruptions. The lateral distribution of hot asthenospheric material at the present-day time-step in Figure 5 shows that this hypothesis is also able to account for the seismically slow anomalies observed in the upper mantle throughout East Asia. Here as well the modelled asthenospheric material does not match the full westward extent of the slow anomalies observed in tomographic models (e.g., Schaeffer and Lebedev, 2013) by ~1,000 km.

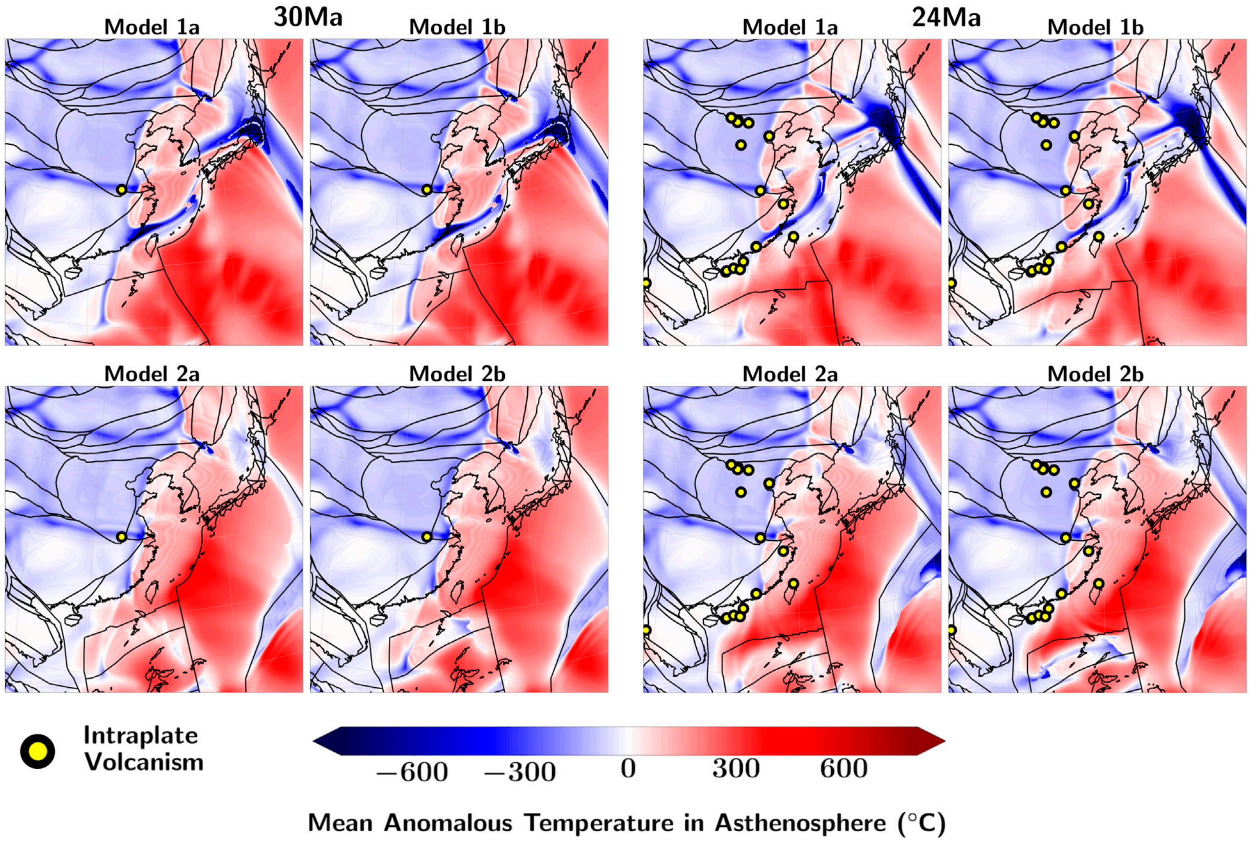

FIGURE 5
Maps of mean anomalous asthenospheric temperature predicted by the models of Lin et al. (2020) at six times from 30 to 0 Ma, with superimposed distribution of coeval intraplate volcanism (Arai et al., 2001; Sun et al., 2010; Gong and Chen, 2014; Ball et al., 2021). Note the connection between the distribution of anomalously hot material underneath the Eurasian plate and the location of intraplate volcanic eruptions, with the notable exceptions of the Hannuoba and Taihang basalts at 24–18 Ma and the eruptions in the Indochina peninsula.

4.2 Hiatus mapping

Stratigraphic data sets hold crucial information about past mantle flow. Mapping conformable and unconformable contacts on inter-regional scales can yield a proxy for the large-scale uplift and subsidence associated with dynamic topography, which may in turn be linked to convective motion in the Earth's mantle (Friedrich et al., 2018). This method of "hiatus mapping" has been carried out on the scale of single (Vibe et al., 2018; Carena et al., 2019) and multiple (Friedrich et al., 2018; Hayek et al., 2020, 2021) continents, and has provided important information on the influence of mantle flow on large-scale topographic changes since the Mesozoic. However, likely due to the potential tectonic influence of nearby subduction zones, East Asia has not been the focus of any hiatus mapping studies to date—although an inter-regional Cretaceous–Paleocene sedimentary hiatus in Southeast Asia has been noted and linked to mantle flow (Clements et al., 2011). In our preceding comparison, it was found that the proposed influx of hot asthenospheric material approximately matches the distribution of late Cenozoic intraplate volcanism in East Asia. Due to its positive buoyancy, this influx is also expected to induce a coeval dynamic uplift. We may therefore use the hiatus mapping concept to trace this uplift and compare it to the model predictions of Lin et al. (2020), allowing us to test our hypothesis against the sedimentary record over a large region.

In order to gauge large-scale topographic changes during the late Cenozoic, we make use of generalised stratigraphic columns for a group of sedimentary basins (both onshore and offshore) in eastern China. We map columns for the basins surrounding Hainan Island (Shi et al., 2011); the Pearl River Mouth Basin (PRMB, Shi et al., 2008); the Taiwan region (including both exposed strata on Taiwan Island and the rift basins in the Taiwan Strait (TWS), Lin et al., 2003; Shi et al., 2008; Huang et al., 2012); the East China Sea Shelf Basin (ECSSB, Shi et al., 2008; Wang et al., 2019); the Subei Basin (Zhou et al., 2019); the South Yellow Sea Basin (SYSB, Yang et al., 2020; Zhang R. et al., 2020); the Hefei Basin (HF, Jiaodong et al., 2012); the North Yellow Sea Basin (NYSB, Wang et al., 2017); the Bohai Bay Basin (BBB, Tang et al.,

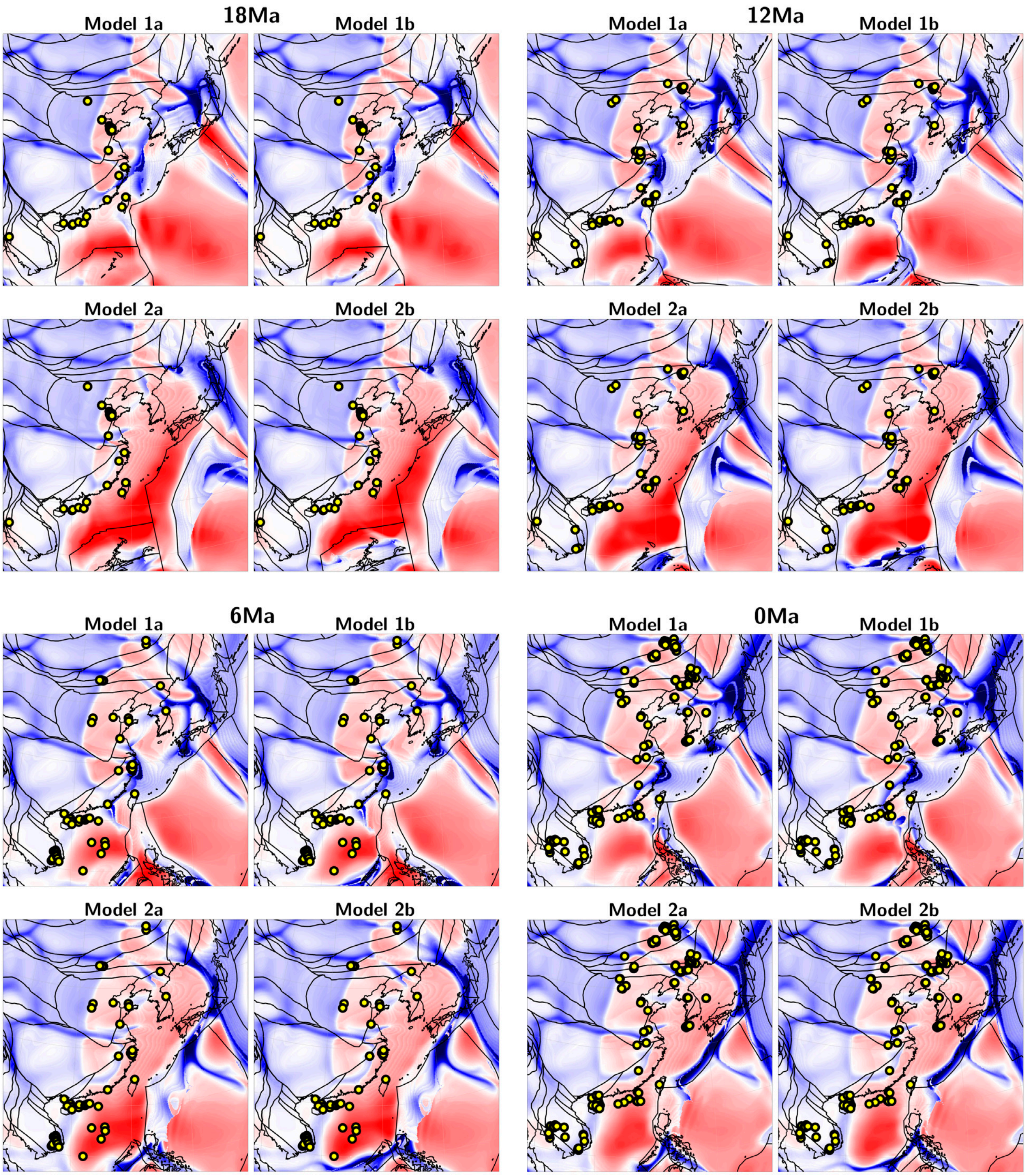

FIGURE 5
(Continued).

2019); and the Songliao Basin (SLB, Song et al., 2018). A map of these basins can be found in Figure 1.

Stratigraphic columns are mapped at the resolution of geological series (ten to a few tens of Myrs, see the definition of series as a unit of chronostratigraphy, e.g., Cohen et al., 2013; Ogg et al., 2016), given that stratigraphic columns with stages resolution were available only in a few offshore basins in eastern China. We follow the approach and terminology of Friedrich

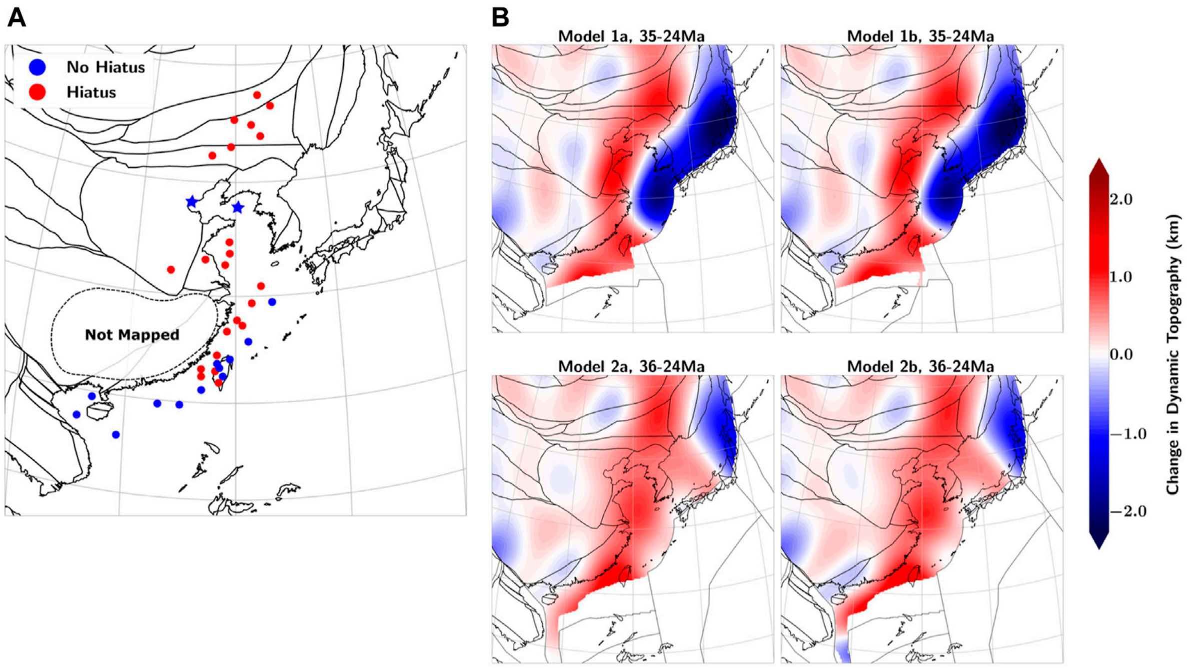

FIGURE 6
(A) Base of Miocene hiatus map for the sedimentary basins in eastern China and exposed Cenozoic strata in Taiwan. Blue stars mark the locations of Bohai Bay Basin (west) and North Yellow Sea Basin (east), which are mapped as No Hiatus but are consistent with a regional uplift event (see discussion in text). Notice that the SCB (outlined by a dashed line) is excluded from our mapping. This region is characterised by a distinct lack of Cenozoic sediments (cf. Figure 1) meaning that Cenozoic uplift events in this area can be more easily gauged via AFT thermochronology (Section 4.3). **(B)** Change in dynamic topography during the Oligocene predicted by the mantle circulation models of Lin et al. (2020).

(2019), Carena et al. (2019) and Hayek et al. (2020), Hayek et al. (2021), in which, for example, "Base of Miocene" refers to the conformable/unconformable surface below this series (i.e., Oligocene sedimentation/hiatus), and a series is marked as hiatus if and only if there are no preserved sediments of this series (i.e., missing stages within a series are not marked as hiatus). In some cases, stratigraphic columns were available for individual sub-basins and so these too have been mapped where available. Stratigraphic columns are mapped as single points, approximately central in a given basin or sub-basin. While not portraying the true scale of a given basin, this approach tends to avoid issues with intraplate deformation as stratigraphic data are reconstructed back in time to their appropriate palaeolocations. In some cases, however, we still run into issues of this kind. For example, the generalised stratigraphic columns for Taiwan Island represent exposed strata which were deposited on the continental margin during the early Cenozoic. These sediments have been significantly deformed and moved from the location where they were deposited (Suppe, 1980) during the Taiwan Orogeny since ~6.5 Ma—which is not accounted for when these points are reconstructed back in time. Due to this, the reconstructed point data will not reflect the true palaeolocations of deposition, and so this must be kept in mind when interpreting the resulting maps. Given the size of the Songliao Basin, and the lack of nearby basins, a representation of its stratigraphic column as a single point is particularly misleading (for other larger basins, stratigraphic columns for each sub-basin were available, or nearby basins filled out the surrounding space). We therefore make the choice to instead plot the generalised stratigraphic column of the Songliao Basin as a group of points—one for each sub-unit of the basin (sags and uplifts). This better represents the true area of the data used in NE China. Given that the Songliao Basin has not undergone significant deformation since the Paleocene (e.g., Song et al., 2018), the locations of the points relative to each other will have remained relatively constant throughout the late Cenozoic. This means that the reconstruction, which keeps these points fixed relative to each other, will result in a reasonable representation of their palaeolocations.

As can be seen in Figure 4, the modelled influx of hot asthenospheric material is present below far eastern China from the mid/late Eocene and flows below this region (i.e., SLB, BBB, S/SYSB, HF, ECSSB, TWS, TNB, see Figure 1) during the Oligocene. This coincides temporally with an inter-regional late Eocene–Oligocene sedimentary hiatus recorded in these basins, the exact timing of which depends somewhat on

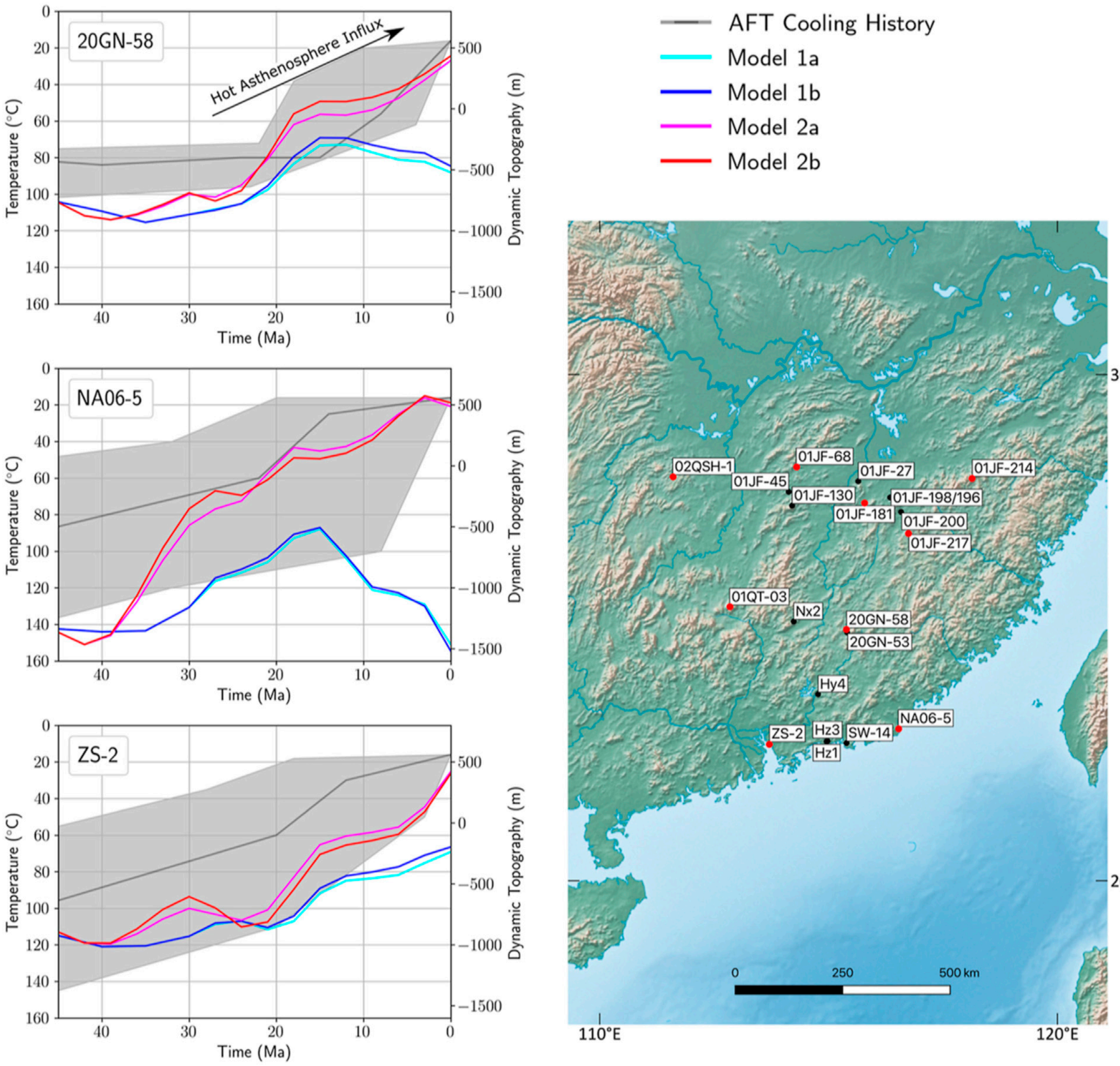

FIGURE 7
Comparison between the dynamic topography predictions of the mantle circulation models of Lin et al. (2020) and the AFT-derived cooling histories published by Wang Y. et al. (2020), Yan et al. (2009) and Li and Zou (2017). Notice the poorer fit of Models 1a & 1b, in particular for samples closer to the Ryukyu Trench. Samples included here are highlighted in red on the map of sample locations. The full set of samples is included in Supplementary Figures S13–S33.

location. To investigate the potential link between this large-scale hiatus and the inflowing Pacific material, we compare our Base of Miocene hiatus map to the modelled change in dynamic topography during the Oligocene. A comparison between our Base of Pliocene hiatus map and the predicted change in dynamic topography during the Miocene can instead be found in Supplementary Figure S20, along with an associated discussion in Supplementary Text S4.

The change in dynamic topography is calculated in a Lagrangian sense. That is, we calculate this change in the reference frame of the Eurasian plate as it moves with respect to the underlying time-dependent dynamic topography signal. The modelled asthenospheric flow predicts a broad N-S trending band of uplift during the Oligocene (Figure 6), which matches the distribution of sedimentary hiatus during this time to first-order. The BBB and NYSB (highlighted as blue stars in Figure 6) both stand out as outliers amongst the sedimentary hiatus in eastern China. It is worth noting, however, that rifting continued into the late Oligocene in these basins (Qi and Yang, 2010; Wang R. et al., 2020), and so rapid syn-rift tectonic subsidence is likely to largely

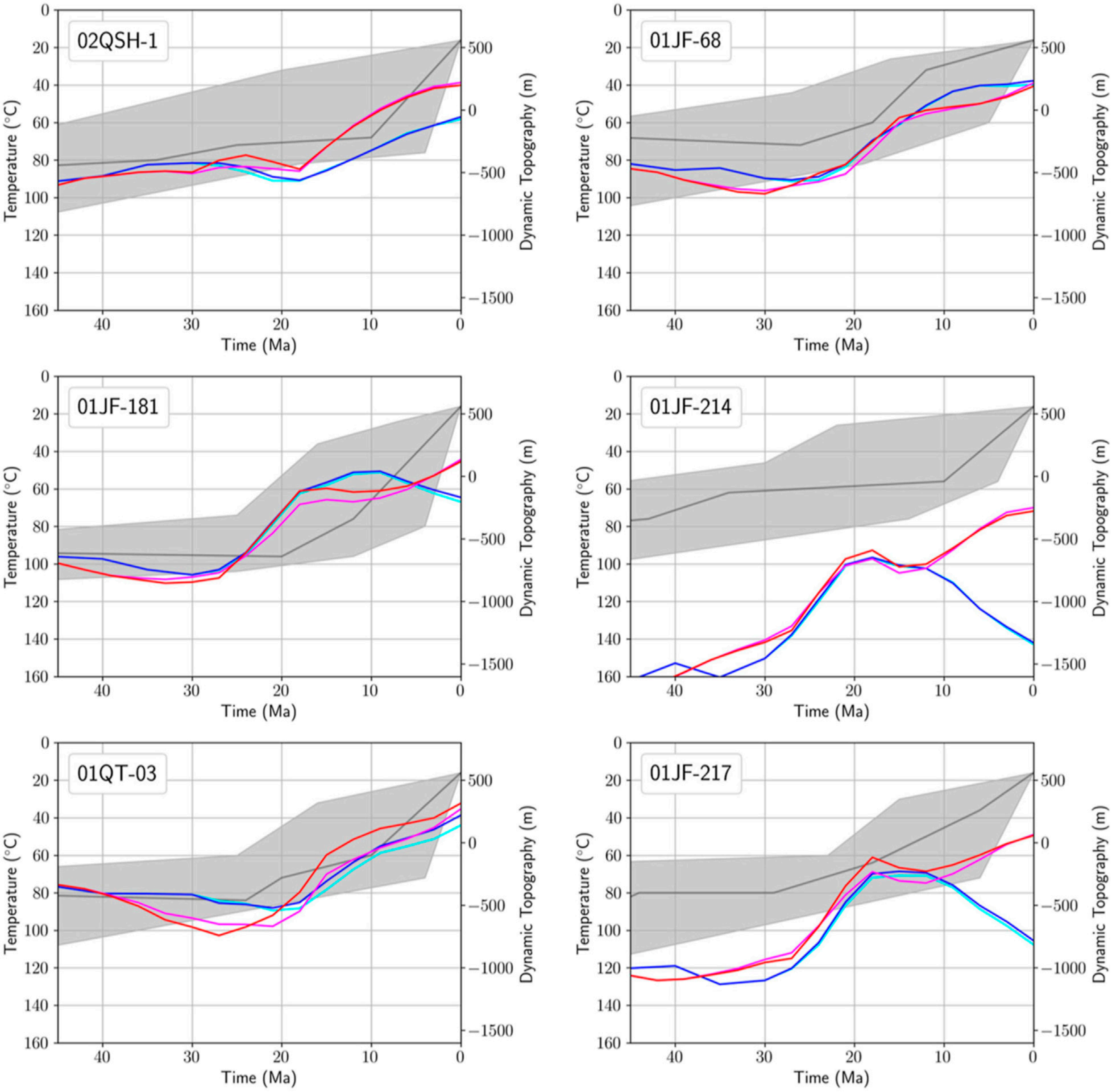

FIGURE 7
(Continued).

overwrite any dynamic topography signal in the stratigraphic record. In addition to this, while syn-rift sedimentation occurred in these basins, the late Oligocene strata are clearly eroded, and have been completely removed in some shallower parts of the basins. Indeed, this aspect of the development of the BBB has been investigated further using Apatite Fission Track Thermochronolgy (AFT), which found a rapid cooling event from 27 to 16 Ma, removing an estimated 1.5–1.8 km of sediment (Tang et al., 2019). This uplift event has been noted too in the NYSB (Wang R. et al., 2020), and while it has been attributed to tectonic compression, the stratigraphic cross-sections of the basin are also consistent with a regional uplift characteristic of dynamic topography. This uplift is thought to have continued until ~14 Ma in the NYSB (Wang R. et al., 2020). And so, while a full sedimentary hiatus was not induced in these basins, they remain consistent with the inter-regional picture of uplift and erosion during the Oligocene and early Miocene.

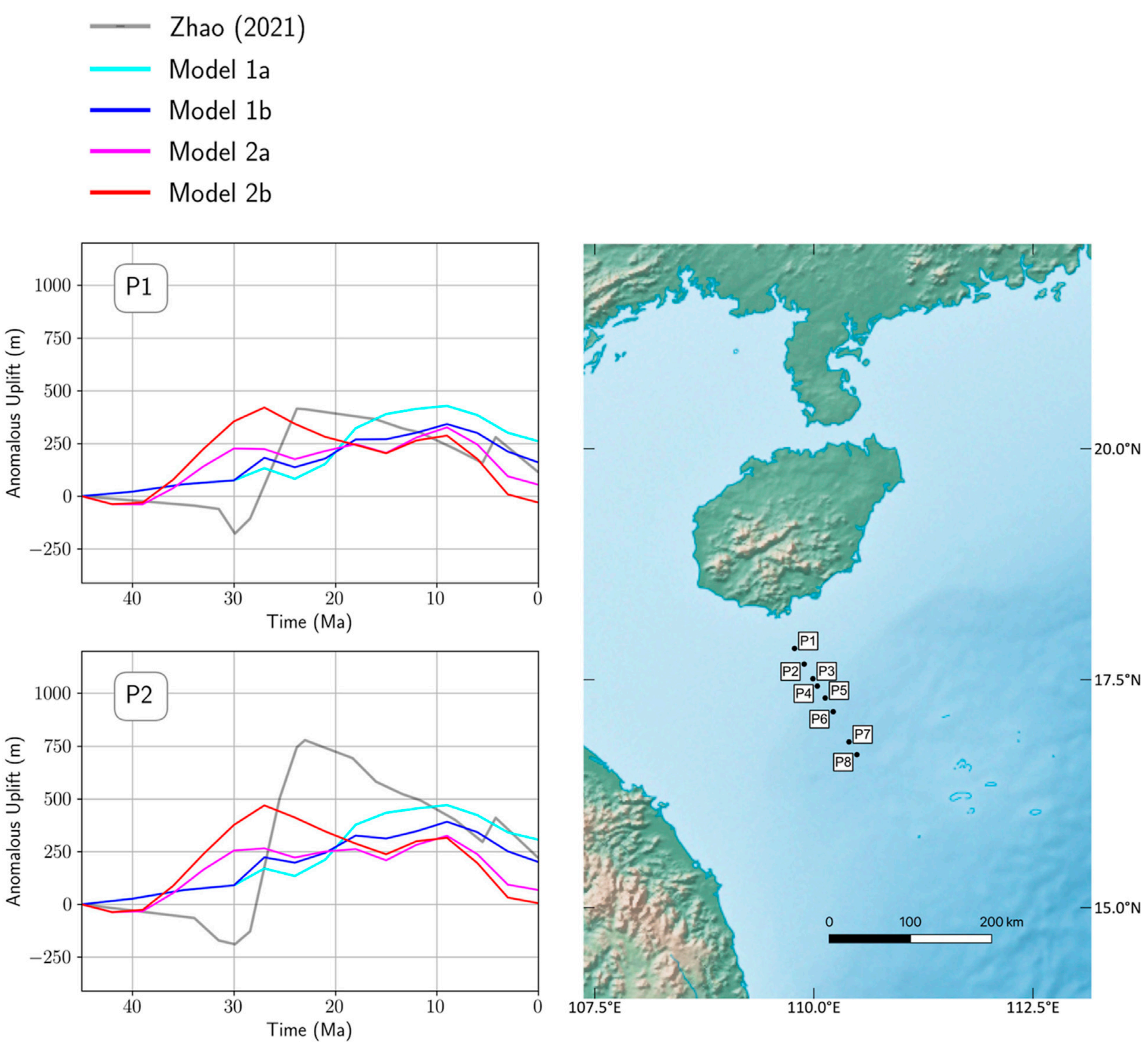

FIGURE 8
Comparison between the anomalous uplift of the QDNB from Zhao (2021) since 45 Ma with the predicted change of dynamic topography since this time predicted by the mantle circulation models of Lin et al. (2020).

Additional misfits can be found in some offshore regions, such as the eastern ECSSB and the northern margin of the SCS, in which the predicted dynamic uplift covers regions of Oligocene sedimentation. However, the early Cenozoic rifting and offshore setting of these regions means that it is somewhat less likely that a dynamic uplift will lead to a series-long sedimentary hiatus. Indeed, while a series-long hiatus has not been recorded, there nevertheless exists evidence of late Cenozoic uplift and erosion on the northern margin of the SCS (Section 5.2.3). Intense erosion has been noted too in the Taiwan region (e.g., Fuh, 2000; Shi et al., 2008), but the onset of sedimentation during the late Oligocene means that this event is not highlighted when mapping is carried out at the resolution of geological series (Figure 6).

Similarly to our comparisons with intraplate volcanism, Figure 6 shows that the downwelling induced by the large PSP of Models 1a & 1b leads to an inconsistency with the geological record. These models predict a large-scale dynamic subsidence in the ECSSB during the Oligocene, which is inconsistent with the observed sedimentary hiatus. In Models 2a & 2b, instead, the influx of hot asthenospheric material is allowed to predominate the dynamic topography signal over a larger region, leading to a consistency with the sedimentary hiatus in the ECSSB.

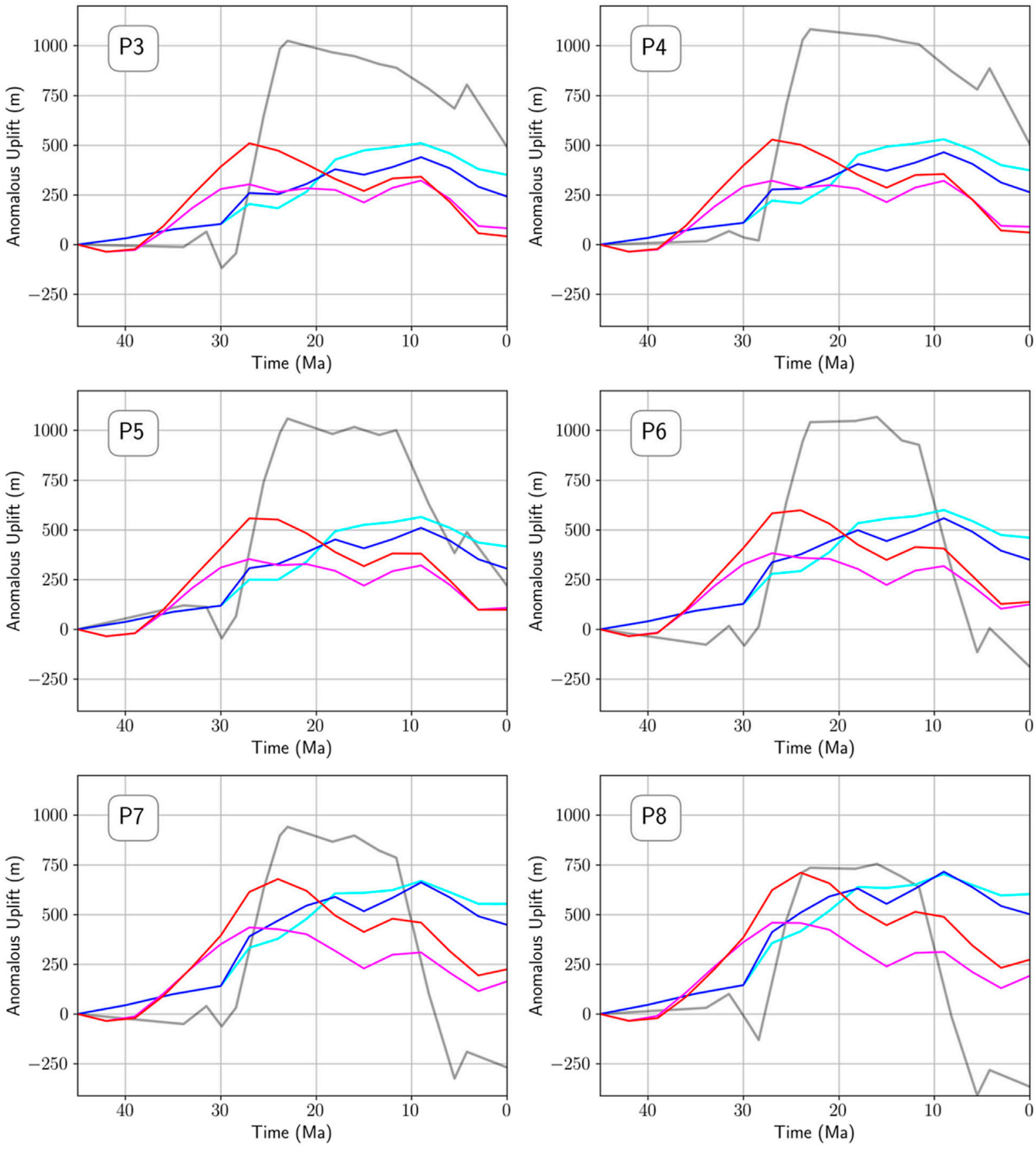

FIGURE 8
(Continued).

As can be seen in Figure 6, the SCB was excluded from our mapping. Cenozoic deposits are largely absent from this region (Figure 1), meaning that the hiatus mapping concept is not useful in gauging large-scale topographic changes during this time. Cenozoic sedimentation occurred mainly in small intermontane basins, which are not likely to be sensitive to the changes in relative sea level induced by dynamic topography. We therefore take a different approach in the SCB, which is discussed in the following section.

4.3 AFT comparisons

The SCB has garnered significant attention from thermochronological studies (e.g., Yan et al., 2009; Wang et al., 2015; Li and Zou, 2017; Su et al., 2017; Tao et al., 2019; Wang Y. et al., 2020; Qiu et al., 2020), likely due to the regional history of exhumation inferred from the widespread present-day exposure of Mesozoic and Paleozoic rocks. That this exhumation has continued into the Cenozoic is revealed by the exposure of late Cretaceous granites formed during the flat-slab subduction of the Izanagi plate (Charvet et al., 1994), indicating at least kilometre-scale erosion has occurred during the Cenozoic (Yan Y. et al., 2018). While thermochronological studies have uncovered multiple phases of heating and cooling since the beginning of the Mesozoic (Tao et al., 2019; Wang Y. et al., 2020), we focus here on the late Cenozoic cooling history of the region. This allows us to investigate the dynamic uplift expected under our hypothesis over a larger region, by filling a spatial gap in the SCB (Figure 6).

A significant rapid cooling event during the Oligocene and Miocene has been found consistently in numerous studies (see those compiled by Qiu et al., 2020), with samples covering a large (~1,000,000 km^2) region. To test whether this regional-scale erosion of the SCB during the late Cenozoic is linked to the dynamic uplift expected under our hypothesis, we compare the dynamic topography predictions of each model to the AFT-derived cooling histories published by Wang Y. et al. (2020), Yan et al. (2009), and Li and Zou, (2017). A total of 21 samples are considered, of which 9 have been reported in Figure 7 to highlight key characteristics in different regions. Clouds of "acceptable" (95% confidence limit) fits have been included to indicate the uncertainty of the AFT cooling histories. The full set of samples is included in Supplementary Figures S21–S41.

The AFT cooling histories generally show a distinct increase in cooling rate during the early Miocene (see, e.g., samples 20GN-58 and 01JF-181 in Figure 7) or late Miocene (samples 02QSH-1 and 01JF-214). In northwesterly regions (samples 02QSH-1, 01JF-68 and 01QT-03), the model predictions of dynamic topography are broadly similar, and we find a good match between the observed cooling histories and the increase in dynamic topography induced by the inflowing asthenospheric material from ~20 Ma. In easterly samples (NA06-5, 01JF-214, 01JF-217), the closer proximity to the Ryukyu Trench leads to significant differences in the model predictions based on their implementations of the PSP history. In line with our previous comparisons, we find that the large PSP implemented in Models 1a & 1b leads to a dynamic subsidence which is inconsistent with the observed cooling histories. In contrast, the smaller PSP implemented in Models 2a & 2b allows the influx of hot asthenospheric material to dominate the Neogene dynamic topography in this region, leading to a better prediction of the increased cooling rate during this time.

A key consideration to be made when interpreting this widespread cooling effect is that it occurs outside of the well-constrained Apatite Partial Annealing Zone (PAZ, 110°C–60°C). Generally, one cannot confidently interpret cooling histories below the lower bound of 60°C, due to the lack of fission track annealing below this temperature. However, we note that the samples considered often leave the PAZ at ~20–10 Ma, and given their present-day exposure at surface temperatures (~20°C), their Neogene cooling histories remain well constrained. For example, samples 20GN-58 and 01JF-181 (Figure 7) cool through the lower bound of the PAZ at ~10 Ma, and so we may infer that ~40°C of cooling has occurred since this time. Taking a lower bound on the geothermal gradient of ~20°C/km, we may then estimate ~2 km of erosion has occurred with a rate of ~0.2 km/Ma since ~10 Ma. We therefore find the recent regional cooling to be a robust effect in the derived cooling histories.

We note additionally that the predicted uplift is generally significantly lower than the eroded sediment thickness inferred from AFT cooling histories (Figure 7). For instance, the 2 km exhumation of samples 20GN-58 and 01JF-181 since 10 Ma, as estimated above, corresponds to only ~250–500 m of predicted dynamic uplift. A key reason for this is that isostatic rebound has not been accounted for in these comparisons, which provides an additional component of uplift as overlying rock is eroded. Part of this disparity may also arise due to the modelled asthenospheric influx not flowing far west enough in significant amounts, in keeping with our comparison to the magmatic record (Section 4.1). Nevertheless, we find an encouraging match between the recent regional cooling and the modelled increase in dynamic topography during the Neogene.

4.4 Anomalous uplift of the Qiongdongnan Basin

Subsidence analysis may be used to make quantitative estimations of the history of dynamic topography affecting rifted sedimentary basins. Traditionally, this is achieved by estimating strain rates during rifting, for instance by inverting the backstripped subsidence (White, 1994), and using these in conjunction with lithospheric stretching models (McKenzie, 1978; Jarvis and McKenzie, 1980b) in order to forward model the post-rift tectonic subsidence. This forward modelled tectonic subsidence may then be subtracted from the subsidence gleaned from backstripping (Sclater and Christie, 1980), in order to find the anomalous (i.e., dynamic) uplift or subsidence which has affected a given basin during its post-rift phase. A refined method of this kind has recently been proposed by Zhao (2021), which sought to remove several of the underlying assumptions of earlier methods. Zhao (2021) used fault growth rates derived from seismic cross sections to allocate the total strain of a basin, allowing spatially and temporally varying strain rates to be calculated. The use of strain rates which are independent of the backstripped subsidence means that one separates the tectonic and dynamic components of subsidence from the outset. This allows for the full (i.e., including the syn-rift phase) history of anomalous subsidence to be derived, and the tectonic subsidence due to secondary rifting phases to be accounted for. This method was applied to the Qiongdongnan Basin (QDNB), which, given its location on the northern margin of the SCS (Figure 1), provides us with an additional observation with which to test our asthenospheric flow hypothesis. Zhao (2021) found that the QDNB was anomalously uplifted by ~1 km beginning at 28.4 Ma, which decreased significantly after 11.6 Ma. Our intraplate volcanism comparisons in Figure 5 show that the influx of hot material reaches the QDNB during the Oligocene, and may therefore provide an explanation for this uplift. We therefore compare the anomalous uplift since 45 Ma with the modelled change in dynamic topography since this time. The resulting comparisons, and a map of the relevant borehole locations, is shown in Figure 8.

To first order, we find a good match between the modelled timing of dynamic uplift and subsidence affecting the QDNB and the anomalous uplift at boreholes P1–P8. The modelled uplift tends to have an earlier onset than the results of Zhao (2021) in Models 2a & 2b, and has a particularly high amplitude in Model 2b. Given the double-sided PSCS subduction in Model 2b, the northern subduction zone leads to additional downflow in the QDNB region, pulling more asthenospheric material towards the basin from the east. The northern subduction zone additionally leads to a larger initial dynamic subsidence in the QDNB, and so the rebound from this initial state following the subduction of the PSCS provides an additional component of uplift. The inflowing hot asthenospheric material comes to predominate the dynamic topography signal in this basin in all considered models during ~30–25 Ma (i.e., the dynamic topography signal becomes net positive). This timing aligns with the onset of uplift found by Zhao (2021), although the modelled amplitude of the uplift tends to fall short by ~500 m (excluding P1 and P8, in which we find an excellent match to the reconstructed amplitude). As noticed in Section 4.1, the modelled influx of asthenospheric material does not flow far west enough. This is particularly apparent in the regions of Hainan and Indochina (Figure 5), which are adjacent to the QDNB. A more vigorous influx of hot material in the geodynamic models would presumably lead to a better match to the observed amplitudes.

Another difference we observe between the results of Zhao (2021) and the model predictions of Lin et al. (2020) is the spatial variability of the dynamic uplift signal: the models predict a maximum of ~250 m of variation of the peak of uplift between the borehole locations, while subsidence analysis predicts it to be ~500 m. This may have resulted either from a lack of small-scale structure in the modelled dynamic topography, or from underlying assumptions in the analysis of Zhao (2021). At short enough wavelengths, the viscous stresses which would otherwise induce dynamic topography are instead opposed by the strength of the lithosphere. This filtering effect is modulated by the flexural rigidity of the lithosphere and is strongly wavelength-dependent (see, e.g., Turcotte and Schubert, 2002). To account for this effect, the dynamic topography predicted by the models of Lin et al. (2020) has been expressed as a spherical harmonic expansion truncated at $l_{\max} = 40$, which filters out short-scale (i.e., ≲500 km) variability. While this is a reasonable first-order approximation of lithospheric behaviour, it might filter out too much of the mantle signal, particularly in regions of young oceanic lithosphere where the flexural rigidity might be low. The analysis of Zhao (2021), on the other hand, assumes local isostasy in both the backstripping routine and the lithospheric stretching model used to forward model the tectonic subsidence. It is therefore assumed that both the sediment load and crustal thinning during rifting vary smoothly with respect to the elastic thickness of the lithosphere. If present, short-scale variability in these features leads to additional spatial variability in the derived subsidence histories (instead of being compensated via regional isostasy). The gradient in dynamic topography of ~10 m/km between boreholes P1 and P3 at ~25 Ma is particularly high, suggesting that the assumption of local isostasy might not be adequate.

5 Discussion

Several lines of evidence point towards a pervasive influence of hot asthenosperic material in East Asia during the late Cenozoic. These include the widespread intraplate volcanism since the latest Paleogene (e.g., Ball et al., 2021), extensive seismically slow anomalies at asthenospheric depths (e.g., Li et al., 2008; Schaeffer and Lebedev, 2013; Ma J. et al., 2019), and swells of present-day dynamic uplift (Hoggard et al., 2021). A westward influx of Pacific asthenospheric material through the Izanagi-Pacific slab window arises naturally in the global mantle circulation models of Lin et al. (2020), showing this to be a plausible new mechanism in explaining these observations. The comparisons presented in Section 4 show that the predicted influence of hot Pacific material during the late Cenozoic corresponds well with several independent observations throughout East Asia. These are linked to both intraplate volcanism and dynamic topography on inter-regional (Sections 4.1, 4.2), regional (Section 4.3), and local (Section 4.4) scales.

5.1 Intraplate volcanism in East Asia

A multitude of hypotheses have been proposed to explain the recent inter-regional phase of mafic volcanism in East Asia (Figures 1, 5) on smaller, regional scales. Of the mechanisms proposed, a hypothesised mantle plume below Hainan Island on the northern margin of the SCS is by far the most prevalent (e.g., Yan et al., 2008; Lei et al., 2009; Wang et al., 2012; Huang, 2014; Xia et al., 2016; Yan Q. et al., 2018; Zhang Y et al., 2020, etc.). The "Hainan plume" has been proposed to explain the basaltic eruptions in Leizhou, Hainan, Indochina and the SCS basin since the late Miocene (e.g., Yan et al., 2008), as well as the seismically slow anomalies observed below the SCS region in numerous tomographic models (e.g., Lei et al., 2009). Limited tomographic resolution in the lower mantle means it is not yet possible to conclusively prove the existence of a Hainan plume extending down to the Core Mantle Boundary (CMB), and while a seismically slow anomaly in the upper mantle appears to be a robust feature, similar anomalies are observed throughout East Asia, as discussed in Section 1. It is worth noting too that a plume in this region has not been resolved in global tomographic studies which have resolved plumes (e.g., French and Romanowicz, 2015; Hosseini et al., 2020), although it may be the case that tomographic resolution is not yet high enough to resolve the proposed Hainan plume. Additionally, the magmatic record in this region lacks the clear arrival of a plume head, which is evidenced at well-known plume locations by the formation of a Large Igneous Province (LIP) (Richards et al., 1989). The westward migration of a small plume into this region has been found to be a plausible geodynamic mechanism using mantle circulation models (Zhang and Li, 2018). As noted above, it remains unclear, though, whether the magmatic and tomographic evidence supports this hypothesis.

The lack of a clear plume signal is true, similarly, for the eruptions on inter-regional scales. In addition to the absence of LIPs, the eruptions don't show the linear age progression characteristic of plume-fed hotspots, and don't align with absolute plate motions, with contemporaneous eruptions spanning over large (~5,000 km) distances. The pattern of these eruptions (Figure 1) is instead reminiscent of those observed in the far-field of mantle upwellings, for instance in Africa (Lees et al., 2020). An east–west younging in the onset of eruptions is expected under our hypothesis, and is indeed observed in several regions. For example, the onset of volcanism in SE China and Taiwan is earlier than in Hainan, which in turn has an earlier onset than the main phase of eruptions in Indochina. This east–west younging can also be observed in NE China, with an earlier onset of volcanism in Changbai than the more westerly regions of Halaha and Dalenuor (Liu et al., 2001). However, there are clear exceptions to this trend. For instance, the onset of volcanism in Hannuoba is earlier than the more easterly eruptions in the Jiaodong peninsula, which in turn is earlier than the eruptions in the Korean peninsula. It is worth noting, however, that the study region is interspersed with offshore areas within which the magmatic record is highly biased towards the most recent eruptions. Post-rift intraplate eruptions in, for example, the ECSSB and SYSB (e.g., Yao et al., 2020) must be mapped and dated using seismic stratigraphy and borehole data due to recent sediment cover. As such, it is less likely that such eruptions have been mapped and dated accurately in the current literature. This, more generally, leads to a bias towards onshore regions. Indeed, this bias can be clearly observed in Supplementary Figures S9–S19, with the vast majority of mapped eruptions lying within onshore regions. It may therefore be the case that a clearer east–west younging will emerge as the magmatic record in these offshore regions becomes more complete.

Another prominent line of thinking invokes the influence of the Pacific slab in sourcing the intraplate volcanism (e.g., Liu et al., 2001) and underlying seismically slow anomalies (e.g., Ma J. et al., 2019) in NE China, through deep slab dehydration (e.g., Richard and Iwamori, 2010; Kuritani et al., 2019) or the interaction of the slab with a hydrous Mantle Transition Zone (MTZ) (Yang and Faccenda, 2020). While we don't necessarily preclude some contribution from these mechanisms, we note that they are not required under our hypothesis. Relatively high mantle potential temperatures (~1,380°C–1,440°C) have been noted in NE China (Kimura et al., 2018), indicating that a hot mantle source is required in this region. In addition to this, geochemical analyses have found no evidence of a typical slab-derived isotopic signature in these basalts (Chen et al., 2007; Ward et al., 2021). In any case, the distribution of seismically slow anomalies and intraplate volcanism spans far into regions which are not underlain by slabs (e.g., the SCB, see Gong and Chen, 2014; He and Santosh, 2021), suggesting that these mechanisms are not sufficient on inter-regional scales.

The asthenospheric flow hypothesis presented here unifies the inter-regional observations of intraplate OIB-type magmatism into a single picture. The approximate match observed between the timing and location of these eruptions and the models of Lin et al. (2020) shows this to be a viable new mechanism in explaining these eruptions. An open question under our hypothesis is the differing eruption volumes observed between regions—for example the low-volume eruptions observed in SE China and Taiwan compared to those observed in Indochina or NE China (Figure 1). There are many factors which may explain this disparity in future studies, such as local variations in lithospheric thickness, the influence of underlying slabs, or as noted by Lin et al. (2020), local passive return flow in the mantle—which may play a role in facilitating particularly voluminous eruptions in certain regions. Nevertheless, the correspondence we have found between the distribution of Pacific asthenospheric material and the timing and location of intraplate volcanism in East Asia provides a starting point for future investigation into the local variations observed in the erupted magmas, such as volume and geochemistry.

5.2 Topographic changes linked to asthenospheric flow

5.2.1 Far Eastern China

The dynamic uplift induced under our hypothesis is consistent with the sedimentary record over a large region. The sedimentary hiatus associated with this uplift has been noted locally under a number of names (e.g., the "Puli Event/ Orogeny" in Taiwan, the "Yuquan Movement" in the ECSSB, the "Sanduo Movement" in the SYSB, etc.), and has been commented on as an inter-regional effect (e.g., Wang R. et al., 2020), although its source has remained unclear. Due to the coeval uplift of the Tibetan plateau further west, and the proximity to the Pacific subduction zone to the east, this hiatus is sometimes attributed to a temporary change from an extensional to a compressional stress regime due to far-field effects either from the India-Asia collision (e.g., Song et al., 2018), or from an increase in the convergence rate at the Pacific subduction zone (e.g., Tang et al., 2019). However, the structures of the basins recording this hiatus inferred from seismic stratigraphy and borehole data (e.g., Lin et al., 2008; Qi and Yang, 2010; Cukur et al., 2011; Yang et al., 2016; Song et al., 2018; Yang et al., 2020) show no clear signs of compression in the sedimentary layers directly underlying the unconformity associated with this hiatus. Indeed, throughout the basins considered, the relevant unconformity truncates extensional or quiescent structures in the underlying layers, showing that structural deformation cannot be the root cause of the stratigraphic hiatus, and proving the need for inter-regional scale uplift. In addition to this, the scale (~3,000,000 km^2) of this uplift event is more characteristic of a dynamic uplift than a far-field compression such as that observed in, e.g., the Baikal rift system (Petit and Deverchere, 2006). Another consideration to be made is the eustatic sea-level drop (~50–100 m) during the Oligocene, which can look indistinguishable from dynamic uplift in the stratigraphic record (i.e., large-scale erosion with no compressional deformation). Indeed, this is observed as a clear erosional/ non-depositional signal in the hiatus maps of Hayek et al. (2020), Hayek et al. (2021). However, sonic velocity vs. depth measurements (Fuh, 2000) have found 1–3.5 km of eroded sediment thickness during the late Eocene–Oligocene erosion of the Taiwan region and the ECSSB. Similarly, as noted in Section 4.2, AFT-derived cooling histories suggest that 1.5–1.8 km of sediment was removed from the BBB from 27 to 16 Ma (Tang et al., 2019). And so, while the Oligocene sea-level drop likely contributed to this widespread erosion event, it is not sufficient in explaining the measured eroded sediment thickness. Taken together, the scale, lack of compression, and eroded sediment thickness indicate this to be a robust dynamic topography signal in the stratigraphic record.

5.2.2 The South China Block

Following the Oligocene erosion in far eastern China, the modelled hot asthenospheric material spreads further westward into the SCB during the Miocene. Along with the coeval intraplate volcanism in this region (Gong and Chen, 2014), this coincides temporally with a regional erosion event inferred from numerous AFT studies (e.g., Yan et al., 2009; Li and Zou, 2017; Wang Y. et al., 2020; Qiu et al., 2020). Recent reports by Stephenson et al. (2021) suggest the SCB to be dynamically uplifted by ~1 km at present, which is consistent with the seismically slow anomalies observed below this region (e.g., He and Santosh, 2021). Together, these observations point towards a dynamic origin of the recent regional cooling. The comparisons presented in Figure 7 show that the dynamic uplift predicted under small-PSP Models 2a & 2b provides a good match to the erosion inferred from AFT studies. Our hypothesis therefore ties together a variety of past and present-day observations in the SCB, including Neogene regional erosion (Figure 7), present-day dynamic uplift (Stephenson et al., 2021), seismically slow anomalies (e.g., He and Santosh, 2021) and intraplate volcanism (e.g., Gong and Chen, 2014).

5.2.3 The northern margin of the South China Sea

To the south of the SCB, the hot asthenospheric influx predicted by the models of Lin et al. (2020) flows westward below the northern margin of the SCS from the late Eocene to the present day (Figures 4, 5). While this region is largely dominated by syn- and post-rift tectonic subsidence during the Cenozoic, uplift events have been noted in several regions. Similarly to the observations of uplift discussed above, these also hint at the east–west progression expected under our hypothesis. At the eastern end of this region, erosion was particularly intense in Taiwan and its surrounding region from the late Eocene–late Oligocene, removing an estimated 1–3.5 km of sediment (Fuh, 2000) and generating hiatuses that span back to the Cretaceous in the Tainan Basin and the adjacent Chaoshan depression in the PRMB (Shi et al., 2008). Further westward, the subsidence analysis of Zhao (2021) found that kilometre-scale dynamic uplift affected the QDNB from the Oligocene–late Miocene. While attributed by Zhao (2021) to the dynamic influence of the Hainan plume, the first-order match between this uplift and the models of Lin et al. (2020) (Figure 8) shows that this can be explained under our asthenospheric flow hypothesis. The timing of this uplift is also consistent with thermochronological results on the adjacent Hainan Island (Shi et al., 2011). Further west still, the Yinggehai Basin shows clear evidence of erosion during the early Miocene. Cross-sections of the basin's structure (Clift and Sun, 2006) show that the ~21–16 Ma post-rift sedimentary successions are highly thinned in much of the basin, being present mainly in its central sag. Together with the lack of compressional deformation below the associated seismic reflector, this is consistent with the dynamic uplift observed in the adjacent QDNB.

The PRMB, which lies between the Tainan Basin and Hainan Island, is currently the weak link in this picture. Subsidence analyses have been applied in this basin (Xie et al., 2006; Dong et al., 2020), finding anomalous subsidence of ~1–2 km since the beginning of the Miocene. At a first glance, this is seemingly at odds with the expected dynamic uplift under our asthenospheric flow hypothesis. It is worth noting, however, that these methods contain numerous underlying assumptions which may have had a significant effect on the previously derived subsidence histories in this region. This is highlighted by the results of Zhao, (2021), in which a refined method found ~1 km of Oligocene–Miocene dynamic uplift in the QDNB, a basin in which ~1 km of Miocene dynamic subsidence was found using previous methods (Xie et al., 2006). The history of the PRMB is particularly complex, with multiple rifting phases interspersed by periods of erosion (e.g., Xie et al., 2019), followed by post-rift basaltic magmatism (e.g., Zhou et al., 2020). As such, the application of the method of Zhao, (2021) to this basin is likely to be essential in elucidating Cenozoic dynamic uplift and subsidence events in this basin. Along with the uplift events discussed above, this will lead to a more complete picture of Cenozoic dynamic topography changes on the northern margin of the SCS.

5.3 Constraints on Cenozoic tectonics

The comparisons presented in Section 4 provide new constraints on the uncertain Cenozoic tectonics of East Asia introduced in Section 3.1. The earlier onset of PSP subduction along the Eurasian margin at ~30 Ma in Models 1a & 1b leads to predominantly downwelling, cold material in the asthenosphere below SE China and the ECSSB. This downwelling corresponds poorly with the timing of OIB-type magmatism (Figure 5) and induces large-scale dynamic subsidence which is inconsistent with the observations of inter-regional uplift in far eastern China (Figure 6) and the SCB (Figure 7). In contrast, the later onset of PSP subduction at ~12 Ma in Models 2a & 2b allows a hot, positively buoyant asthenosphere to dominate over a larger region during the late Cenozoic. This provides a good fit to the observations of OIB-type magmatism and inter-regional erosion presented in Figures 5–7. The comparisons with the results of Zhao (2021) show that Models 1a & 1b provide a better fit to the onset of uplift in the QDNB (Figure 8). However, the peak of uplift predicted by Models 1a & 1b tends to come later than that found by Zhao (2021), with the latter generally lying between the peaks of Models 1a & 1b and Models 2a & 2b. As such, it is not possible to make a strong distinction between the PSP implementations based on this form of evidence. Based on Figures 5–7, we therefore find new support for the small PSP and existence of the EAS slabs proposed by Wu et al. (2016).

While the PSCS subduction style was the focus of the original study of Lin et al. (2020), it has a largely negligible effect on the asthenospheric flow considered here. This is highlighted by the minor differences between models which implement a single- (Models "a") or double-sided (Models "b") subduction of the PSCS in Figures 5–7. The location of the QDNB on the northern margin of the SCS means that we see more significant differences between the models based on their PSCS implementation in this region. However, the comparisons shown in Figure 8 indicate no clear preference for a particular reconstruction. Of Models 2a & 2b, the double-sided PSCS subduction (2b) provides a better match to the amplitude of uplift; whereas of Models 1a & 1b, the single-sided PSCS subduction (1a) provides a better match to the amplitude of uplift. And so, overall, it is not possible to make any clear distinctions between the implemented PSCS reconstructions based on the comparisons presented here.

5.4 Model limitations

Several of our comparisons in Section 4 show that the asthenospheric flow predicted by the models of Lin et al. (2020) does not flow far west enough to explain certain observations. The comparisons in Figure 5 show a ~1,000 km shortfall in matching both the westernmost volcanic eruptions considered and the present-day distribution of seismically slow anomalies (e.g., Schaeffer and Lebedev, 2013). In addition to this, Figure 8 shows that, while the models predict well the timing of uplift and subsidence of the QDNB, the influx of hot material does not reach this basin in significant enough amounts to match the amplitude of anomalous uplift found by Zhao (2021) by ~500 m.

One key limitation of these models which may reconcile this disparity in future studies is the implemented mantle viscosity profile. The asthenosphere features only a moderate (200x) viscosity drop with respect to the lithosphere, which is achieved with a gentle gradient from 50 to 250 km depth (Supplementary Figure S1). Due to limitations on the maximum per-gridpoint viscosity variations in the TERRA mantle convection code, this viscosity profile is a compromise between viscosity drop and channel thickness. These models therefore implement a relatively large viscosity in the asthenosphere, which is coupled with a temperature-dependent rheology without a yield stress. As a consequence, following the cessation of the subduction of a particular plate (e.g., the subduction of the Izanagi-Pacific ridge), slabs gradually break off at mid-asthenospheric depths, leaving large "drips" of cold slab material which hang from the lithosphere into the asthenosphere. This effect can be clearly observed in Figure 4, in which a large band of cold material is left hanging in the upper mantle at 45 Ma following the subduction of the Izanagi-Pacific ridge at 55 Ma. This can be observed, too, in Figure 5, in which the bands of cold material observed throughout China represent the drips left over from old subduction zones.

The band of slab material left over from the Izanagi subduction has a significant effect on the asthenospheric flow studied here. The inflowing material from the Pacific domain is forced to push through the base of this high-viscosity barrier and largely flows at depths of ~300–500 km (Supplementary Figures S2–S8). The blockage of this material from large parts of the low viscosity asthenosphere, as well as the intervening slab material, leads to a significant slow-down in flow velocity. Consequently, the inflowing Pacific material cannot flow far west enough during the late Cenozoic. A larger viscosity drop in the asthenosphere, making it compatible with the new constraints of ~ 10^{18}–10^{19} Pa·s (e.g., Chen et al., 2021), would also increase asthenospheric flow velocities (assuming the same pressure gradient) and may help to reconcile this issue. These limitations are highlighted by the low ~3 cm/year velocity of this influx, when compared to recent inferences of ~15 cm/year pressure-driven asthenospheric flow velocities (Hartley et al., 2011; Colli et al., 2014; Parnell-Turner et al., 2014; Chen et al., 2021). Taken together, it becomes clear that the implementation of refined viscosity profiles in the next generation of exascale-enabled mantle convection codes (e.g., TerraNeo, Bauer et al., 2020) could plausibly allow the influx of hot material reach further into East Asia during the late Cenozoic.

Another limitation of these models is the unrealistic slab morphology induced by two-sided subduction. For instance, the stagnant Pacific slab beneath East Asia (e.g., Ma J. et al., 2019) is not reproduced (Supplementary Figures S2–S8), which could have a significant effect on the predicted dynamic topography signal during the late Cenozoic (Supplementary Text S4). A variety of methods have aimed to reproduce this slab geometry using mantle circulation models (MCMs) (e.g., Mao and Zhong, 2018; Ma P. et al., 2019; Peng et al., 2021). However, these approaches have tended to come at the expense of significant additional approximations, such as the suppression of mantle upwellings. As such, it is not yet apparent whether current models can reproduce stagnant slab morphologies within an Earth-like convective planform. A conceptually simple method of generating more realistic slab behaviour is the use of a temperature-dependent viscosity coupled with a pseudo-plastic rheology (Moresi and Solomatov, 1998). The use of this rheology in MCMs produces more concentrated deformation at subduction zones, reducing the presence of "drip" artefacts, and inducing flat-slab subduction following fast trench retreat (Bello et al., 2015). Furthermore, the weak zones which arise between plates would presumably lead to more realistic slab window geometries in the uppermost mantle, which could prove vital when using MCMs to study slab window asthenospheric flow more generally. And so, while the use of a non-linear rheology comes with additional computational difficulties (e.g., Fraters et al., 2019), the self-consistent generation of realistic slab morphologies makes this an attractive option for future studies of this kind.

In any case, MCMs in general are fundamentally limited in their ability to reconstruct past mantle flow, as the initial state from which this flow is derived is unknown. This is partially overcome in MCMs by assuming an initial state, and assimilating tectonic histories as boundary conditions at the surface (Bunge et al., 2002). The models of Lin et al. (2020) illustrate nicely the utility of this technique when reconstructions are assimilated over a significant > 400 Ma timescale, as mantle upwellings are reproduced in approximately the right regions at approximately the right times. A significant improvement on this can be obtained by recasting the reconstruction of past mantle flow as an inverse problem aimed at finding an optimal initial condition via the adjoint method (Bunge et al., 2003). This approach requires as input the present-day mantle state inferred from global tomographic models, which may be used in conjunction with the adjoint equations for mantle flow (Bunge et al., 2003; Ismail-Zadeh et al., 2004; Horbach et al., 2014; Ghelichkhan and Bunge, 2016, 2018) to iteratively improve upon a "first guess" of the initial state. The assimilation of tectonic reconstructions is also required in this method to ensure convergence (Vynnytska and Bunge, 2015), and to avoid the divergent nature of chaotic mantle flow when retrodicting further back in time (Colli et al., 2015). One may therefore explicitly reconstruct the history of hot regions in the mantle inferred from tomographic models. East Asia has not been considered in any adjoint studies to date (e.g., Colli et al., 2018; Ghelichkhan et al., 2021), likely due to the significant uncertainties of the inputted tectonic histories. Following further refinement of these histories, however, the history of the seismically slow anomalies observed beneath East Asia—linked here to asthenospheric flow—may be retrodicted using these methods.

5.5 Implications for Southeast Asia

Our asthenospheric flow hypothesis has significant implications for the more southerly regions of Southeast Asia which were not considered here. Following the future model improvements discussed above, it becomes apparent that the influx of hot material studied here could flow into these region during the late Cenozoic. Due to its proximity to the Sunda Trench, Southeast Asia has traditionally been expected to be dominated by dynamic subsidence during the late Cenozoic (e.g., Wheeler and White, 2002). However, growing evidence implies the influence of hot material during this time, such as the dynamic uplift and basaltic magmatism in Borneo since the Neogene (Roberts et al., 2018), the Neogene uplift (Fyhn et al., 2009) and intraplate basalts (e.g., Yan Q. et al., 2018) in Indochina, and the seismically slow anomalies observed in the uppermost mantle throughout these regions (e.g., Schaeffer and

Lebedev, 2013). While Roberts et al. (2018) found a Neogene–present-day swell of dynamic uplift around Borneo, and dynamic subsidence in the adjacent SCS, we note that the dynamic influence at the surface of this hot material will depend on the depth, wavelength, and lateral distribution of slabs in these regions (Colli et al., 2016). Future convection models which implement refined viscosity profiles may therefore reconcile the disparity between convection models (which often predict dynamic subsidence) and observations (which find dynamic uplift) highlighted by Roberts et al. (2018).

5.6 Further applications

While we have focussed our analysis on a single ridge subduction event during the early Cenozoic, we note that the process proposed is generic. The hypothesis rests on the idea that hot asthenospheric material can be driven from high-pressure upwellings to low-pressure subduction zones by a combination of pressure- and plate-driven flow (Höink and Lenardic, 2010; Colli et al., 2018), which may then spill over into adjacent regions following ridge subduction events and the opening of slab windows. This mechanism may therefore be more widely applicable in future studies of dynamic topography and intraplate volcanism, as similar events could have occurred throughout Earth's history. Indeed, this process has been proposed in order to explain the intraplate volcanism (Zhou et al., 2018) and dynamic uplift (Zhou and Liu, 2019) in the western United States during the late Cenozoic, following the opening of tears in the Juan de Fuca slab and the Juan de Fuca-Pacific slab window. Furthermore, the asthenospheric build-up stage of this process may be invoked at circum-Pacific margins in the present day, and evidenced by seismically slow anomalies beneath subducting slabs in Japan (Ma J. et al., 2019; Bogiatzis et al., 2019), Cascadia (Hawley et al., 2016; Bodmer et al., 2018, 2020), and South America (Portner et al., 2017).

6 Conclusion

We have proposed and investigated a new component of the Cenozoic geodynamics of East Asia, whereby hot asthenospheric material from the Pacific domain flows through the Izanagi-Pacific slab window during the early Cenozoic. This mechanism provides a new explanation for the seismically slow anomalies (e.g., Schaeffer and Lebedev, 2013), late Cenozoic intraplate volcanism (Ball et al., 2021), and swells of present-day dynamic uplift (Hoggard et al., 2021) observed throughout this region. This effect arises naturally in the global mantle circulation models of Lin et al. (2020), which we have tested against a wide variety of geological observations. A good match was found between the predicted distribution of this hot material through time and the timing and location of intraplate volcanic eruptions in East Asia since 30 Ma. This influx predicts a broad band of dynamic uplift in eastern China during the Oligocene, which aligns spatially and temporally with an observed inter-regional, non-compressional sedimentary hiatus. Subsequently, the material spreads further into the SCB, inducing widespread dynamic uplift which coincides with a regional Neogene erosion event inferred from numerous AFT studies. The hot material flows below the northern margin of the SCS during the late Cenozoic, and matches the timing of anomalous uplift in the QDNB found by Zhao (2021) to first order, although the modelled amplitude of uplift tends to fall short by ~500 m. The connection found between these independent geological observations and the models of Lin et al. (2020) shows the proposed mechanism to be a viable new component in the Cenozoic geodynamic development of East Asia.

The comparisons presented here have provided new constraints on the uncertain history of the PSP. Due to its ~30 Ma onset of subduction along the Eurasian margin, the larger PSP implemented in Models 1a & 1b was found to predict large-scale mantle downwelling in eastern China during the Oligocene and Miocene. This downwelling, and the resulting dynamic subsidence, is inconsistent with observations of OIB-type magmatism and uplift during this time. In contrast, the small PSP implemented in Models 2a & 2b, which has a much later onset of subduction at ~12 Ma, allows the influx of hot asthenospheric material to dominate over a larger region during the late Cenozoic. This provides an excellent fit to the observations of uplift and intraplate volcanism considered here. We therefore find new support for tectonic reconstructions which implement a small PSP and the consequent existence of the hypothesised "East Asian Sea" slabs.

Future improvements of the implemented viscosity profile, which will be allowed by the next generation of mantle convection codes, are likely to result in this influx of hot material flowing further westward during the late Cenozoic—making up for the ~1,000 km shortfall found in this study. Along with the connections presented in this paper, this hypothesis therefore has the potential to explain a variety of observations of late Cenozoic dynamic uplift and magmatism in East Asia which were not considered here, such as the previously unexplained dynamic uplift and basaltic magmatism in Borneo since the Neogene (Roberts et al., 2018). Beyond the regional setting of Cenozoic East Asia, the geodynamic mechanism proposed here may be more widely applicable to subduction zone dynamics throughout Earth's history.

Data availability statement

The original contributions presented in the study are included in the article/Supplementary Material, further inquiries can be directed to the corresponding author.

Author contributions

Data was collated from published literature by HB under the supervision of LC. All figures were produced by HB under the supervision of LC and HPB. The initial draft of manuscript was written by HB, and was reviewed and edited by LC and HB. The manuscript was restructured and further edited following suggestions from HPB.

Funding

The initial conception of this study arose from the Master's research of HB at LMU Munich, which was funded by a scholarship from the Deutscher Akademischer Austauschdienst (DAAD). LC acknowledges funding from the State of Texas Governor's University Research Initiative (GURI).

Acknowledgments

HB sincerely thanks Bernhard Schuberth for help with extracting temperature data from the MCMs (Figure 5), and Zhongxian Zhao for kindly providing data for the anomalous uplift of the QDNB (Figure 8). LC thanks Jonny Wu, Yi-An Lin, Yiduo Liu, and John Suppe for insightful discussions on East Asian geology, tectonics and kinematics. All authors thank Jonny Wu and a reviewer for helpful comments on the manuscript.

Conflict of interest

The authors declare that the research was conducted in the absence of any commercial or financial relationships that could be construed as a potential conflict of interest.

Publisher's note

Supplementary material

The Supplementary Material for this article can be found online at: https://www.frontiersin.org/articles/10.3389/feart.2022.889907/full#supplementary-material

References

Arai, S., Kida, M., Abe, N., and Yurimoto, H. (2001). Petrology of peridotite xenoliths in alkali basalt (11 Ma) from Boun, Korea: An insight into the upper mantle beneath the east Asian continental margin. *J. Mineralogical Petrological Sci.* 96, 89–99. doi:10.2465/jmps.96.89

Ball, P., White, N., Maclennan, J., and Stephenson, S. (2021). Global influence of mantle temperature and plate thickness on intraplate volcanism. *Nat. Commun.* 12, 2045. doi:10.1038/s41467-021-22323-9

Bauer, S., Bunge, H.-P., Drzisga, D., Ghelichkhan, S., Huber, M., Kohl, N., et al. (2020). "TerraNeo—Mantle Convection Beyond a Trillion Degrees of Freedom," in *Software for Exascale Computing - SPPEXA 2016-2019. Lecture Notes in Computational Science and Engineering*. Editors H. J. Bungartz, S. Reiz, B. Uekermann, P. Neumann, and W. Nagel (Cham: Springer) 136, 569–610. doi:10.1007/978-3-030-47956-5_19

Bello, L., Coltice, N., Tackley, P. J., Müller, R. D., and Cannon, J. (2015). Assessing the role of slab rheology in coupled plate-mantle convection models. *Earth Planet. Sci. Lett.* 430, 191–201. doi:10.1016/j.epsl.2015.08.010

Bodmer, M., Toomey, D. R., Hooft, E. E., and Schmandt, B. (2018). Buoyant asthenosphere beneath Cascadia influences megathrust segmentation. *Geophys. Res. Lett.* 45, 6954–6962. doi:10.1029/2018GL078700

Bodmer, M., Toomey, D., Roering, J., and Karlstrom, L. (2020). Asthenospheric buoyancy and the origin of high-relief topography along the Cascadia forearc. *Earth Planet. Sci. Lett.* 531, 115965. doi:10.1016/j.epsl.2019.115965

Bogiatzis, P., Ishii, M., and Davis, T. A. (2019). The Dulmage–Mendelsohn permutation in seismic tomography. *Geophys. J. Int.* 218, 1157–1173. doi:10.1093/gji/ggz216

Bunge, H.-P., and Baumgardner, J. R. (1995). Mantle convection modeling on parallel virtual machines. *Comput. Phys.* 9, 207. doi:10.1063/1.168525

Bunge, H.-P., Hagelberg, C., and Travis, B. (2003). Mantle circulation models with variational data assimilation: Inferring past mantle flow and structure from plate motion histories and seismic tomography. *Geophys. J. Int.* 152, 280–301. doi:10.1046/j.1365-246x.2003.01823.x

Bunge, H.-P., Richards, M. A., Lithgow-Bertelloni, C., Baumgardner, J. R., Grand, S. P., Romanowicz, B. A., et al. (1998). Time scales and heterogeneous structure in geodynamic Earth models. *Science* 280, 91–95. doi:10.1126/science.280.5360.91

Bunge, H.-P., Richards, M., and Baumgardner, J. (2002). Mantle circulation models with sequential data assimilation: Inferring present–day mantle structure from plate motion histories. *Philosophical Trans. R. Soc. Lond. Ser. A Math. Phys. Eng. Sci.* 360, 2545–2567. doi:10.1098/rsta.2002.1080

Cao, X., Flament, N., Müller, D., and Li, S. (2018). The dynamic topography of eastern China since the latest Jurassic Period. *Tectonics* 37, 1274–1291. doi:10.1029/2017TC004830

Carena, S., Bunge, H.-P., and Friedrich, A. M. (2019). Analysis of geological hiatus surfaces across Africa in the Cenozoic and implications for the timescales of convectively-maintained topography. *Can. J. Earth Sci.* 56, 1333–1346. doi:10.1139/cjes-2018-0329

Charvet, J., Lapierre, H., and Yu, Y. (1994). Geodynamic significance of the Mesozoic volcanism of southeastern China. *J. Southeast Asian Earth Sci.* 9, 387–396. doi:10.1016/0743-9547(94)90050-7

Chase, C. G. (1979). Asthenospheric counterflow: A kinematic model. *Geophys. J. Int.* 56, 1–18. doi:10.1111/j.1365-246X.1979.tb04764.x

Chen, Y.-W., Colli, L., Bird, D. E., Wu, J., and Zhu, H. (2021). Caribbean plate tilted and actively dragged eastwards by low-viscosity asthenospheric flow. *Nat. Commun.* 12, 1603. doi:10.1038/s41467-021-21723-1

Chen, Y., Zhang, Y., Graham, D., Su, S., and Deng, J. (2007). Geochemistry of Cenozoic basalts and mantle xenoliths in Northeast China. *Lithos* 96, 108–126. doi:10.1016/j.lithos.2006.09.015

Choi, S. H., Mukasa, S. B., Kwon, S.-T., and Andronikov, A. V. (2006). Sr, Nd, Pb and Hf isotopic compositions of late Cenozoic alkali basalts in South Korea: Evidence for mixing between the two dominant asthenospheric mantle domains beneath East Asia. *Chem. Geol.* 232, 134–151. doi:10.1016/j.chemgeo.2006.02.014

Chung, S.-L., Jahn, B.-M., Chen, S.-J., Lee, T., and Chen, C.-H. (1995). Miocene basalts in northwestern Taiwan: Evidence for EM-type mantle sources in the continental lithosphere. *Geochimica Cosmochimica Acta* 59, 549–555. doi:10.1016/0016-7037(94)00360-X

Chung, S.-L. (1999). Trace element and isotope characteristics of Cenozoic basalts around the Tanlu fault with implications for the eastern plate boundary between north and South China. *J. Geol.* 107, 301–312. doi:10.1086/314348

Clements, B., Burgess, P. M., Hall, R., and Cottam, M. A. (2011). Subsidence and uplift by slab-related mantle dynamics: A driving mechanism for the late cretaceous and Cenozoic evolution of continental SE Asia? *Geol. Soc. Lond. Spec. Publ.* 355, 37–51. doi:10.1144/SP355.3

Clift, P. D., and Sun, Z. (2006). The sedimentary and tectonic evolution of the Yinggehai–Song Hong basin and the southern Hainan margin, South China Sea: Implications for Tibetan uplift and monsoon intensification. *J. Geophys. Res.* 111. doi:10.1029/2005JB004048

Cohen, K. M., Finney, S. C., Gibbard, P. L., and Fan, J.-X. (2013). The ICS international chronostratigraphic chart. *Episodes* 36, 199–204. doi:10.18814/epiiugs/2013/v36i3/002

Colli, L., Bunge, H.-P., and Schuberth, B. S. (2015). On retrodictions of global mantle flow with assimilated surface velocities. *Geophys. Res. Lett.* 42, 8341–8348. doi:10.1002/2015GL066001

Colli, L., Ghelichkhan, S., Bunge, H.-P., and Oeser, J. (2018). Retrodictions of Mid Paleogene mantle flow and dynamic topography in the Atlantic region from compressible high resolution adjoint mantle convection models: Sensitivity to deep mantle viscosity and tomographic input model. *Gondwana Res.* 53, 252–272. doi:10.1016/j.gr.2017.04.027

Colli, L., Ghelichkhan, S., and Bunge, H.-P. (2016). On the ratio of dynamic topography and gravity anomalies in a dynamic Earth. *Geophys. Res. Lett.* 43, 2510–2516. doi:10.1002/2016GL067929

Colli, L., Stotz, I., Bunge, H.-P., Smethurst, M., Clark, S., Iaffaldano, G., et al. (2014). Rapid South Atlantic spreading changes and coeval vertical motion in surrounding continents: Evidence for temporal changes of pressure-driven upper mantle flow. *Tectonics* 33, 1304–1321. doi:10.1002/2014TC003612

Cukur, D., Horozal, S., Kim, D. C., and Han, H. C. (2011). Seismic stratigraphy and structural analysis of the northern East China Sea Shelf Basin interpreted from multi-channel seismic reflection data and cross-section restoration. *Mar. Petroleum Geol.* 28, 1003–1022. doi:10.1016/j.marpetgeo.2011.01.002

Dong, M., Zhang, J., Brune, S., Wu, S., Fang, G., Yu, L., et al. (2020). Quantifying postrift lower crustal flow in the northern margin of the South China Sea. *J. Geophys. Res. Solid Earth* 125, e2019JB018910. doi:10.1029/2019JB018910

Fraters, M. R., Bangerth, W., Thieulot, C., Glerum, A., and Spakman, W. (2019). Efficient and practical Newton solvers for non-linear Stokes systems in geodynamic problems. *Geophys. J. Int.* 218, 873–894. doi:10.1093/gji/ggz183

French, S. W., and Romanowicz, B. (2015). Broad plumes rooted at the base of the Earth's mantle beneath major hotspots. *Nature* 525, 95–99. doi:10.1038/nature14876

Friedrich, A. M., Bunge, H.-P., Rieger, S. M., Colli, L., Ghelichkhan, S., Nerlich, R., et al. (2018). Stratigraphic framework for the plume mode of mantle convection and the analysis of interregional unconformities on geological maps. *Gondwana Res.* 53, 159–188. doi:10.1016/j.gr.2017.06.003

Friedrich, A. M. (2019). Palaeogeological hiatus surface mapping: A tool to visualize vertical motion of the continents. *Geol. Mag.* 156, 308–319. doi:10.1017/S0016756818000560

Fuh, S.-C. (2000). Magnitude of Cenozoic erosion from mean sonic transit time, offshore Taiwan. *Mar. Petroleum Geol.* 17, 1011–1028. doi:10.1016/S0264-8172(00)00035-0

Fyhn, M. B., Boldreel, L. O., and Nielsen, L. H. (2009). Geological development of the central and south Vietnamese margin: Implications for the establishment of the South China Sea, Indochinese escape tectonics and Cenozoic volcanism. *Tectonophysics* 478, 184–214. doi:10.1016/j.tecto.2009.08.002

Ghelichkhan, S., and Bunge, H.-P. (2018). The adjoint equations for thermochemical compressible mantle convection: Derivation and verification by twin experiments. *Proc. R. Soc. A* 474, 20180329. doi:10.1098/rspa.2018.0329

Ghelichkhan, S., and Bunge, H.-P. (2016). The compressible adjoint equations in geodynamics: Derivation and numerical assessment. *Int. J. Geomath.* 7, 1–30. doi:10.1007/s13137-016-0080-5

Ghelichkhan, S., Bunge, H., and Oeser, J. (2021). Global mantle flow retrodictions for the early Cenozoic using an adjoint method: Evolving dynamic topographies, deep mantle structures, flow trajectories and sublithospheric stresses. *Geophys. J. Int.* 226, 1432–1460. doi:10.1093/gji/ggab108

Gong, J., and Chen, J. Y. (2014). Evidence of lateral asthenosphere flow beneath the South China Craton driven by both Pacific plate subduction and the India–Eurasia continental collision. *Terra nova*. 26, 55–63. doi:10.1111/ter.12069

Hall, R. (2002). Cenozoic geological and plate tectonic evolution of SE Asia and the SW pacific: Computer-based reconstructions, model and animations. *J. Asian Earth Sci.* 20, 353–431. doi:10.1016/S1367-9120(01)00069-4

Hall, R., and Spakman, W. (2015). Mantle structure and tectonic history of SE Asia. *Tectonophysics* 658, 14–45. doi:10.1016/j.tecto.2015.07.003

Hartley, R. A., Roberts, G. G., White, N. J., and Richardson, C. (2011). Transient convective uplift of an ancient buried landscape. *Nat. Geosci.* 4, 562–565. doi:10.1038/ngeo1191

Hawley, W. B., Allen, R. M., and Richards, M. A. (2016). Tomography reveals buoyant asthenosphere accumulating beneath the Juan de Fuca plate. *Science* 353, 1406–1408. doi:10.1126/science.aad8104

Hayek, J. N., Vilacís, B., Bunge, H.-P., Friedrich, A. M., Carena, S., Vibe, Y., et al. (2020). Continent-scale hiatus maps for the Atlantic Realm and Australia since the Upper Jurassic and links to mantle flow induced dynamic topography. *Proc. R. Soc. A* 476, 20200390. doi:10.1098/rspa.2020.0390

Hayek, J. N., Vilacís, B., Bunge, H.-P., Friedrich, A. M., Carena, S., Vibe, Y., et al. (2021). Correction: Continent-scale hiatus maps for the Atlantic Realm and Australia since the Upper Jurassic and links to mantle flow-induced dynamic topography. *Proc. R. Soc. A* 477, 20210437. doi:10.1098/rspa.2021.0437

He, C., and Santosh, M. (2021). Mantle upwelling beneath the Cathaysia Block, South China. *Tectonics* 40, e2020TC006447. doi:10.1029/2020TC006447

Ho, K.-s., Chen, J.-c., Lo, C.-h., and Zhao, H.-l. (2003). ^{40}Ar–^{39}Ar dating and geochemical characteristics of late Cenozoic basaltic rocks from the zhejiang–fujian region, SE China: Eruption ages, magma evolution and petrogenesis. *Chem. Geol.* 197, 287–318. doi:10.1016/S0009-2541(02)00399-6

Hoggard, M., Austermann, J., Randel, C., and Stephenson, S. (2021). Observational estimates of dynamic topography through space and time. *Mantle Convect. Surf. expressions*, 371–411. doi:10.1002/9781119528609.ch15

Hoggard, M. J., Winterbourne, J., Czarnota, K., and White, N. (2017). Oceanic residual depth measurements, the plate cooling model, and global dynamic topography. *J. Geophys. Res. Solid Earth* 122, 2328–2372. doi:10.1002/2016JB013457

Höink, T., Jellinek, A. M., and Lenardic, A. (2011). Viscous coupling at the lithosphere-asthenosphere boundary. *Geochem. Geophys. Geosyst.* 12. doi:10.1029/2011GC003698

Höink, T., and Lenardic, A. (2010). Long wavelength convection, Poiseuilleâ "Couette flow in the low-viscosity asthenosphere and the strength of plate margins. *Geophys. J. Int.* 180, 23–33. doi:10.1111/j.1365-246X.2009.04404.x

Höink, T., Lenardic, A., and Richards, M. (2012). Depth-dependent viscosity and mantle stress amplification: Implications for the role of the asthenosphere in maintaining plate tectonics. *Geophys. J. Int.* 191, 30–41. doi:10.1111/j.1365-246X.2012.05621.x

Höink, T., and Lenardic, A. (2008). Three-dimensional mantle convection simulations with a low-viscosity asthenosphere and the relationship between heat flow and the horizontal length scale of convection. *Geophys. Res. Lett.* 35. doi:10.1029/2008GL033854

Holloway, N. (1982). North Palawan Block, Philippines—Its relation to Asian mainland and role in evolution of South China sea. *Am. Assoc. Pet. Geol. Bull.* 66, 1355–1383. doi:10.1306/03B5A7A5-16D1-11D7-8645000102C1865D

Horbach, A., Bunge, H.-P., and Oeser, J. (2014). The adjoint method in geodynamics: Derivation from a general operator formulation and application to the initial condition problem in a high resolution mantle circulation model. *Int. J. Geomath.* 5, 163–194. doi:10.1007/s13137-014-0061-5

Hosseini, K., Sigloch, K., Tsekhmistrenko, M., Zaheri, A., Nissen-Meyer, T., Igel, H., et al. (2020). Global mantle structure from multifrequency tomography using P, PP and P-diffracted waves. *Geophys. J. Int.* 220, 96–141. doi:10.1093/gji/ggz394

Huang, C.-Y., Yen, Y., Zhao, Q., and Lin, C.-T. (2012). Cenozoic stratigraphy of Taiwan: Window into rifting, stratigraphy and paleoceanography of South China Sea. *Chin. Sci. Bull.* 57, 3130–3149. doi:10.1007/s11434-012-5349-y

Huang, J. (2014). P- and S-wave tomography of the Hainan and surrounding regions: Insight into the Hainan plume. *Tectonophysics* 633, 176–192. doi:10.1016/j.tecto.2014.07.007

Ismail-Zadeh, A., Schubert, G., Tsepelev, I., and Korotkii, A. (2004). Inverse problem of thermal convection: Numerical approach and application to mantle plume restoration. *Phys. Earth Planet. Interiors* 145, 99–114. doi:10.1016/j.pepi.2004.03.006

Jarvis, G. T., and McKenzie, D. P. (1980a). Convection in a compressible fluid with infinite Prandtl number. *J. Fluid Mech.* 96, 515–583. doi:10.1017/S002211208000225X

Jarvis, G. T., and McKenzie, D. P. (1980b). Sedimentary basin formation with finite extension rates. *Earth Planet. Sci. Lett.* 48, 42–52. doi:10.1016/0012-821X(80)90168-5

Jiaodong, Z., Xuanhua, C., Qiuli, L., Chengzhai, L., Bing, L., Jie, L., et al. (2012). Mesozoic "red beds" and its evolution in the Hefei Basin. *Acta Geol. Sinica-English Ed.* 86, 1060–1076. doi:10.1111/j.1755-6724.2012.00731.x

Kimura, J.-I., Sakuyama, T., Miyazaki, T., Vaglarov, B. S., Fukao, Y., Stern, R. J., et al. (2018). Plume-stagnant slab-lithosphere interactions: Origin of the late Cenozoic intra-plate basalts on the east Eurasia margin. *Lithos* 300, 227–249. doi:10.1016/j.lithos.2017.12.003

Kuritani, T., Xia, Q.-K., Kimura, J.-I., Liu, J., Shimizu, K., Ushikubo, T., et al. (2019). Buoyant hydrous mantle plume from the mantle transition zone. *Sci. Rep.* 9, 6549. doi:10.1038/s41598-019-43103-y

Lees, M. E., Rudge, J. F., and McKenzie, D. (2020). Gravity, topography, and melt generation rates from simple 3-D models of mantle convection. *Geochem. Geophys. Geosyst.* 21, e2019GC008809. doi:10.1029/2019GC008809

Lei, J., Zhao, D., Steinberger, B., Wu, B., Shen, F., Li, Z., et al. (2009). New seismic constraints on the upper mantle structure of the Hainan plume. *Phys. Earth Planet. Interiors* 173, 33–50. doi:10.1016/j.pepi.2008.10.013

Li, C., van der Hilst, R. D., Engdahl, E. R., and Burdick, S. (2008). A new global model for P wave speed variations in Earth's mantle. *Geochem. Geophys. Geosyst.* 9 (5). doi:10.1029/2007GC001806

Li, X., and Zou, H. (2017). Late cretaceous–Cenozoic exhumation of the southeastern margin of coastal mountains, SE China, revealed by fission-track thermochronology: Implications for the topographic evolution. *Solid Earth Sci.* 2, 79–88. doi:10.1016/j.sesci.2017.02.001

Lin, A. T., Liu, C.-S., Lin, C.-C., Schnurle, P., Chen, G.-Y., Liao, W.-Z., et al. (2008). Tectonic features associated with the overriding of an accretionary wedge on top of a rifted continental margin: An example from Taiwan. *Mar. Geol.* 255, 186–203. doi:10.1016/j.margeo.2008.10.002

Lin, A., Watts, A. B., and Hesselbo, S. (2003). Cenozoic stratigraphy and subsidence history of the South China Sea margin in the Taiwan region. *Basin Res.* 15, 453–478. doi:10.1046/j.1365-2117.2003.00215.x

Lin, Y.-A., Colli, L., and Wu, J. (2021). NW Pacific-Panthalassa intra-oceanic subduction during Mesozoic times from mantle convection and geoid models (in press). *Earth Space Sci. Open Archive ESSOAr*. doi:10.1002/essoar.10506879.1

Lin, Y.-A., Colli, L., Wu, J., and Schuberth, B. S. (2020). Where are the proto-South China sea slabs? SE asian plate tectonics and mantle flow history from global mantle convection modeling. *JGR. Solid Earth* 125, e2020JB019758. doi:10.1029/2020JB019758

Liu, J.-q., Chen, S.-s., Guo, Z.-f., Guo, W.-f., He, H.-y., You, H.-t., et al. (2015). Geological background and geodynamic mechanism of Mt. Changbai volcanoes on the China–Korea border. *Lithos* 236–237, 46–73. doi:10.1016/j.lithos.2015.08.011

Liu, J., Han, J., and Fyfe, W. S. (2001). Cenozoic episodic volcanism and continental rifting in Northeast China and possible link to Japan Sea development as revealed from K–Ar geochronology. *Tectonophysics* 339, 385–401. doi:10.1016/S0040-1951(01)00132-9

Ma, J., Tian, Y., Zhao, D., Liu, C., and Liu, T. (2019). Mantle dynamics of Western pacific and east Asia: New insights from P wave anisotropic tomography. *Geochem. Geophys. Geosyst.* 20, 3628–3658. doi:10.1029/2019GC008373

Ma, P., Liu, S., Gurnis, M., and Zhang, B. (2019). Slab horizontal subduction and slab tearing beneath East Asia. *Geophys. Res. Lett.* 46, 5161–5169. doi:10.1029/2018GL081703

Mao, W., and Zhong, S. (2018). Slab stagnation due to a reduced viscosity layer beneath the mantle transition zone. *Nat. Geosci.* 11, 876–881. doi:10.1038/s41561-018-0225-2

Matthews, K. J., Maloney, K. T., Zahirovic, S., Williams, S. E., Seton, M., Mueller, R. D., et al. (2016). Global plate boundary evolution and kinematics since the late Paleozoic. *Glob. Planet. Change* 146, 226–250. doi:10.1016/j.gloplacha.2016.10.002

McKenzie, D. (1978). Some remarks on the development of sedimentary basins. *Earth Planet. Sci. Lett.* 40, 25–32. doi:10.1016/0012-821X(78)90071-7

Moresi, L., and Solomatov, V. (1998). Mantle convection with a brittle lithosphere: Thoughts on the global tectonic styles of the Earth and venus. *Geophys. J. Int.* 133, 669–682. doi:10.1046/j.1365-246X.1998.00521.x

Müller, R. D., Seton, M., Zahirovic, S., Williams, S. E., Matthews, K. J., Wright, N. M., et al. (2016). Ocean basin evolution and global-scale plate reorganization events since Pangea breakup. *Annu. Rev. Earth Planet. Sci.* 44, 107–138. doi:10.1146/annurev-earth-060115-012211

Nerlich, R., Colli, L., Ghelichkhan, S., Schuberth, B., and Bunge, H.-P. (2016). Constraining central Neo-Tethys ocean reconstructions with mantle convection models. *Geophys. Res. Lett.* 43, 9595–9603. doi:10.1002/2016GL070524

Ogg, J. G., Ogg, G., and Gradstein, F. M. (2016). "1. Introduction," in *A concise geologic time scale* (Elsevier), 1–8.

Parnell-Turner, R., White, N. J., Henstock, T., Murton, B., Maclennan, J., Jones, S. M., et al. (2014). A continuous 55-million-year record of transient mantle plume activity beneath Iceland. *Nat. Geosci.* 7, 914–919. doi:10.1038/ngeo2281

Peng, D., Liu, L., Hu, J., Li, S., and Liu, Y. (2021). Formation of East Asian stagnant slabs due to a pressure-driven Cenozoic mantle wind following Mesozoic subduction. *Geophys. Res. Lett.* 48, e2021GL094638. doi:10.1029/2021GL094638

Petit, C., and Deverchere, J. (2006). Structure and evolution of the Baikal rift: A synthesis. *Geochem. Geophys. Geosyst.* 7. doi:10.1029/2006GC001265

Portner, D. E., Beck, S., Zandt, G., and Scire, A. (2017). The nature of subslab slow velocity anomalies beneath South America. *Geophys. Res. Lett.* 44, 4747–4755. doi:10.1002/2017GL073106

Qi, J., and Yang, Q. (2010). Cenozoic structural deformation and dynamic processes of the Bohai Bay Basin province, China. *Mar. Petroleum Geol.* 27, 757–771. doi:10.1016/j.marpetgeo.2009.08.012

Qiu, L., Yan, D.-P., Tang, S.-L., Chen, F., Gong, L.-X., Zhang, Y.-X., et al. (2020). Cenozoic exhumation of the neoproterozoic sanfang batholith in South China. *J. Geol. Soc.* 177, 412–423. doi:10.1144/jgs2019-041

Richard, G. C., and Iwamori, H. (2010). Stagnant slab, wet plumes and Cenozoic volcanism in East Asia. *Phys. Earth Planet. Interiors* 183, 280–287. doi:10.1016/j.pepi.2010.02.009

Richards, M. A., Duncan, R. A., and Courtillot, V. E. (1989). Flood basalts and hot-spot tracks: Plume heads and tails. *Science* 246, 103–107. doi:10.1126/science.246.4926.103

Richards, M. A., and Hager, B. H. (1984). Geoid anomalies in a dynamic Earth. *J. Geophys. Res.* 89, 5987–6002. doi:10.1029/JB089iB07p05987

Richards, M. A., Hager, B. H., and Sleep, N. H. (1988). Dynamically supported geoid highs over hotspots: Observation and theory. *J. Geophys. Res.* 93, 7690. doi:10.1029/JB093iB07p07690

Roberts, G. G., White, N., Hoggard, M. J., Ball, P. W., and Meenan, C. (2018). A Neogene history of mantle convective support beneath Borneo. *Earth Planet. Sci. Lett.* 496, 142–158. doi:10.1016/j.epsl.2018.05.043

Safonova, I. Y., and Santosh, M. (2014). Accretionary complexes in the Asia-pacific region: Tracing archives of Ocean plate stratigraphy and tracking mantle plumes. *Gondwana Res.* 25, 126–158. doi:10.1016/j.gr.2012.10.008

Schaeffer, A., and Lebedev, S. (2013). Global shear speed structure of the upper mantle and transition zone. *Geophys. J. Int.* 194, 417–449. doi:10.1093/gji/ggt095

Schuberth, B. S., Bunge, H.-P., and Ritsema, J. (2009a). Tomographic filtering of high-resolution mantle circulation models: Can seismic heterogeneity be explained by temperature alone? *Geochem. Geophys. Geosyst.* 10. doi:10.1029/2009GC002401

Schuberth, B. S., Bunge, H.-P., Steinle-Neumann, G., Moder, C., and Oeser, J. (2009b). Thermal versus elastic heterogeneity in high-resolution mantle circulation models with pyrolite composition: High plume excess temperatures in the lowermost mantle. *Geochem. Geophys. Geosyst.* 10. doi:10.1029/2008GC002235

Sclater, J. G., and Christie, P. A. (1980). Continental stretching: An explanation of the post-mid-Cretaceous subsidence of the central North Sea basin. *J. Geophys. Res.* 85, 3711–3739. doi:10.1029/JB085iB07p03711

Seno, T., and Maruyama, S. (1984). Paleogeographic reconstruction and origin of the Philippine Sea. *Tectonophysics*. 102, 53–84. doi:10.1016/0040-1951(84)90008-8

Seton, M., Müller, R. D., Zahirovic, S., Gaina, C., Torsvik, T., Shephard, G., et al. (2012). Global continental and ocean basin reconstructions since 200 Ma. *Earth-Science Rev.* 113, 212–270. doi:10.1016/j.earscirev.2012.03.002

Shi, X., Kohn, B., Spencer, S., Guo, X., Li, Y., Yang, X., et al. (2011). Cenozoic denudation history of southern Hainan Island, South China Sea: Constraints from low temperature thermochronology. *Tectonophysics* 504, 100–115. doi:10.1016/j.tecto.2011.03.007

Shi, X., Xu, H., Qiu, X., Xia, K., Yang, X., Li, Y., et al. (2008). Numerical modeling on the relationship between thermal uplift and subsequent rapid subsidence: Discussions on the evolution of the Tainan Basin. *Tectonics* 27. doi:10.1029/2007TC002163

Song, Y., Stepashko, A., Liu, K., He, Q., Shen, C., Shi, B., et al. (2018). Post-rift tectonic history of the Songliao Basin, NE China: Cooling events and post-rift unconformities driven by orogenic pulses from plate boundaries. *J. Geophys. Res. Solid Earth* 123, 2363–2395. doi:10.1002/2017JB014741

Steinshouer, D. W., Qiang, J., McCabe, P. J., and Ryder, R. T. (1999). Maps showing geology, oil and gas fields, and geologic provinces of the Asia Pacific region. *Tech. Rep. U. S. Geol. Surv. Open-File Rep.* 97–470. doi:10.3133/ofr97470F

Stephenson, S., Hoggard, M., and White, N. (2021). "Global continental residual topography," in *EGU general assembly conference abstracts* (EGU General Assembly Conference Abstracts). doi:10.5194/egusphere-egu21-15505

Stotz, I. L., Vilacís, B., Hayek, J. N., Bunge, H.-P., and Friedrich, A. M. (2021). Yellowstone plume drives Neogene North American Plate motion change. *Geophys. Res. Lett.* 48, e2021GL095079. doi:10.1029/2021GL095079

Su, J., Dong, S., Zhang, Y., Li, Y., Chen, X., Li, J., et al. (2017). Apatite fission track geochronology of the southern hunan province across the Shi-hang belt: Insights into the Cenozoic dynamic topography of South China. *Int. Geol. Rev.* 59, 981–995. doi:10.1080/00206814.2016.1240049

Sun, Z., Zhou, D., Sun, L., Chen, C., Pang, X., Jiang, J., et al. (2010). Dynamic analysis on rifting stage of Pearl River Mouth Basin through analogue modeling. *J. Earth Sci.* 21, 439–454. doi:10.1007/s12583-010-0106-0

Suppe, J. (1980). A retrodeformable cross section of northern Taiwan. *Proc. Geol. Soc. China.* 23, 46–55.

Tang, X., Zuo, Y., Kohn, B., Li, Y., and Huang, S. (2019). Cenozoic thermal history reconstruction of the dongpu sag, Bohai Bay Basin: Insights from apatite fission-track thermochronology. *Terra nova.* 31, 159–168. doi:10.1111/ter.12379

Tang, Y.-J., Zhang, H.-F., and Ying, J.-F. (2006). Asthenosphere–lithospheric mantle interaction in an extensional regime: Implication from the geochemistry of Cenozoic basalts from Taihang mountains, north China Craton. *Chem. Geol.* 233, 309–327. doi:10.1016/j.chemgeo.2006.03.013

Tao, N., Li, Z.-X., Danišík, M., Evans, N. J., Li, R.-X., Pang, C.-J., et al. (2019). Post-250 Ma thermal evolution of the central Cathaysia Block (SE China) in response to flat-slab subduction at the proto-Western Pacific margin. *Gondwana Res.* 75, 1–15. doi:10.1016/j.gr.2019.03.019

Turcotte, D. L., and Schubert, G. (2002). *Geodynamics*. Cambridge University Press.

Vibe, Y., Friedrich, A. M., Bunge, H.-P., and Clark, S. (2018). Correlations of oceanic spreading rates and hiatus surface area in the North Atlantic realm. *Lithosphere* 10, 677–684. doi:10.1130/L736.1

Vynnytska, L., and Bunge, H.-P. (2015). Restoring past mantle convection structure through fluid dynamic inverse theory: Regularisation through surface velocity boundary conditions. *Int. J. Geomath.* 6, 83–100. doi:10.1007/s13137-014-0060-6

Wang, B., Doust, H., and Liu, J. (2019). Geology and petroleum systems of the East China Sea Basin. *Energies* 12, 4088. doi:10.3390/en12214088

Wang, F., Chen, H., Batt, G. E., Lin, X., Gong, J., Gong, G., et al. (2015). Tectonothermal history of the NE Jiangshan–Shaoxing suture zone: Evidence from ^{40}Ar/^{39}Ar and fission-track thermochronology in the Chencai region. *Precambrian Res.* 264, 192–203. doi:10.1016/j.precamres.2015.04.009

Wang, R., Shi, W., Xie, X., Wang, L., Manger, W., Busbey, A. B., et al. (2017). Lower Cretaceous lacustrine successions, North Yellow Sea Basin, eastern China: Rift basin sequence stratigraphy and stacking patterns in response to magmatic activity. *Mar. Petroleum Geol.* 88, 531–550. doi:10.1016/j.marpetgeo.2017.09.006

Wang, R., Shi, W., Xie, X., Zhang, X., Wang, L., Manger, W., et al. (2020). Coupling of strike-slip faulting and lacustrine basin evolution: Sequence stratigraphy, structure, and sedimentation in the north Yellow Sea basin (west Bay Basin offshore north Korea), eastern China. *Mar. Petroleum Geol.* 120, 104548. doi:10.1016/j.marpetgeo.2020.104548

Wang, Y., Wang, Y., Li, S., Seagren, E., Zhang, Y., Zhang, P., et al. (2020). Exhumation and landscape evolution in eastern South China since the Cretaceous: New insights from fission-track thermochronology. *J. Asian Earth Sci.* 191, 104239. doi:10.1016/j.jseaes.2020.104239

Wang, X.-C., Li, Z.-X., Li, X.-H., Li, J., Liu, Y., Long, W.-G., et al. (2012). Temperature, pressure, and composition of the mantle source region of late Cenozoic basalts in Hainan Island, SE Asia: A consequence of a young thermal mantle plume close to subduction zones? *J. Petrology* 53, 177–233. doi:10.1093/petrology/egr061

Ward, J. F., Rosenbaum, G., Ubide, T., Wu, J., Caulfield, J. T., Sandiford, M., et al. (2021). Geophysical and geochemical constraints on the origin of Holocene intraplate volcanism in East Asia. *Earth-Science Rev.* 218, 103624. doi:10.1016/j.earscirev.2021.103624

Weismüller, J., Gmeiner, B., Ghelichkhan, S., Huber, M., John, L., Wohlmuth, B., et al. (2015). Fast asthenosphere motion in high-resolution global mantle flow models. *Geophys. Res. Lett.* 42, 7429–7435. doi:10.1002/2015GL063727

Wheeler, P., and White, N. (2002). Measuring dynamic topography: An analysis of Southeast Asia. *Tectonics* 21, 4. doi:10.1029/2001TC900023

White, N. (1994). An inverse method for determining lithospheric strain rate variation on geological timescales. *Earth Planet. Sci. Lett.* 122, 351–371. doi:10.1016/0012-821X(94)90008-6

White, N., and Lovell, B. (1997). Measuring the pulse of a plume with the sedimentary record. *Nature* 387, 888–891. doi:10.1038/43151

Woods, M. T., and Davies, G. F. (1982). Late cretaceous Genesis of the kula plate. *Earth Planet. Sci. Lett.* 58, 161–166. doi:10.1016/0012-821X(82)90191-1

Wu, J., Suppe, J., Lu, R., and Kanda, R. (2016). Philippine Sea and East Asian plate tectonics since 52 Ma constrained by new subducted slab reconstruction methods. *J. Geophys. Res. Solid Earth* 121, 4670–4741. doi:10.1002/2016JB012923

Wu, J., and Suppe, J. (2018). Proto-South China Sea plate tectonics using subducted slab constraints from tomography. *J. Earth Sci.* 29, 1304–1318. doi:10.1007/s12583-017-0813-x

Wu, J. T.-J., and Wu, J. (2019). Izanagi-Pacific ridge subduction revealed by a 56 to 46 Ma magmatic gap along the Northeast Asian margin. *Geology* 47, 953–957. doi:10.1130/G46778.1

Xia, S., Zhao, D., Sun, J., and Huang, H. (2016). Teleseismic imaging of the mantle beneath southernmost China: New insights into the Hainan plume. *Gondwana Res.* 36, 46–56. doi:10.1016/j.gr.2016.05.003

Xie, X., Müller, R. D., Li, S., Gong, Z., and Steinberger, B. (2006). Origin of anomalous subsidence along the northern South China Sea margin and its relationship to dynamic topography. *Mar. Petroleum Geol.* 23, 745–765. doi:10.1016/j.marpetgeo.2006.03.004

Xie, X., Ren, J., Pang, X., Lei, C., and Chen, H. (2019). Stratigraphic architectures and associated unconformities of Pearl River Mouth Basin during rifting and lithospheric breakup of the South China Sea. *Mar. Geophys. Res.* 40, 129–144. doi:10.1007/s11001-019-09378-6

Xu, J., Ben-Avraham, Z., Kelty, T., and Yu, H.-S. (2014). Origin of marginal basins of the NW Pacific and their plate tectonic reconstructions. *Earth-Science Rev.* 130, 154–196. doi:10.1016/j.earscirev.2013.10.002

Yan, Q., Shi, X., Metcalfe, I., Liu, S., Xu, T., Kornkanitnan, N., et al. (2018). Hainan mantle plume produced late Cenozoic basaltic rocks in Thailand, Southeast Asia. *Sci. Rep.* 8, 2640. doi:10.1038/s41598-018-20712-7

Yan, Y., Yao, D., Tian, Z.-X., Huang, C.-Y., Dilek, Y., Clift, P. D., et al. (2018). Tectonic topography changes in Cenozoic East Asia: A landscape erosion-sediment archive in the South China Sea. *Geochem. Geophys. Geosyst.* 19, 1731–1750. doi:10.1029/2017GC007356

Yan, Q., Shi, X., Wang, K., Bu, W., and Xiao, L. (2008). Major element, trace element, and Sr, Nd and Pb isotope studies of Cenozoic basalts from the South China Sea. *Sci. China Ser. D-Earth. Sci.* 51, 550–566. doi:10.1007/s11430-008-0026-3

Yan, Y., Hu, X., Lin, G., Xia, B., Li, X., Patel, R. C., et al. (2009). Denudation history of South China Block and sediment supply to northern margin of the South China Sea. *J. Earth Sci.* 20, 57–65. doi:10.1007/s12583-009-0006-3

Yang, C. S., Li, S. Z., Li, G., Yang, C. Q., Yang, Y. Q., Dai, L. M., et al. (2016). Tectonic units and proto-basin of the East China Sea Shelf basin: Correlation to mesozoic subduction of the palaeo-Pacific Plate. *Geol. J.* 51, 149–161. doi:10.1002/gj.2776

Yang, F., Hu, P., Zhou, X., Zhang, R., Peng, Y., Li, X., et al. (2020). The late Jurassic to early Cretaceous strike-slip faults in the Subei-South Yellow Sea Basin, eastern China: Constraints from seismic data. *Tectonics* 39, e2020TC006091. doi:10.1029/2020TC006091

Yang, J., and Faccenda, M. (2020). Intraplate volcanism originating from upwelling hydrous mantle transition zone. *Nature* 579, 88–91. doi:10.1038/s41586-020-2045-y

Yao, Z., Li, C.-F., He, G., Tao, T., Zheng, X., Zhang, T., et al. (2020). Cenozoic sill intrusion in the central and southern East China Sea Shelf basin. *Mar. Petroleum Geol.* 119, 104465. doi:10.1016/j.marpetgeo.2020.104465

Zahirovic, S., Matthews, K. J., Flament, N., Müller, R. D., Hill, K. C., Seton, M., et al. (2016). Tectonic evolution and deep mantle structure of the eastern Tethys since the latest Jurassic. *Earth-Science Rev.* 162, 293–337. doi:10.1016/j.earscirev.2016.09.005

Zahirovic, S., Seton, M., and Müller, R. (2014). The Cretaceous and Cenozoic tectonic evolution of Southeast Asia. *Solid earth.* 5, 227–273. doi:10.5194/se-5-227-2014

Zhang, N., and Li, Z.-X. (2018). formation of mantle "lone plumes" in the global downwelling zone—a multiscale modelling of subduction-controlled plume generation beneath the South China Sea. *Tectonophysics* 723, 1–13. doi:10.1016/j.tecto.2017.11.038

Zhang, R., Yang, F., Zhao, C., Zhang, J., and Qiu, E. (2020). Coupling relationship between sedimentary basin and moho morphology in the South Yellow Sea, East China. *Geol. J.* 55, 6544–6561. doi:10.1002/gj.3821

Zhang, Y., Yu, K., Fan, T., Yue, Y., Wang, R., Jiang, W., et al. (2020). Geochemistry and petrogenesis of Quaternary basalts from Weizhou Island, northwestern South China Sea: Evidence for the Hainan plume. *Lithos* 362, 105493. doi:10.1016/j.lithos.2020.105493

Zhao, Z.-X. (2021). The deep mantle upwelling beneath the northwestern South China Sea: Insights from the time-varying residual subsidence in the Qiongdongnan Basin. *Geosci. Front.* 12, 101246. doi:10.1016/j.gsf.2021.101246

Zheng, H., Zhong, L.-F., Kapsiotis, A., Cai, G.-Q., Wan, Z.-F., Xia, B., et al. (2019). Post-spreading basalts from the Nanyue Seamount: Implications for the involvement of crustal-and plume-type components in the Genesis of the South China Sea mantle. *Minerals* 9, 378. doi:10.3390/min9060378

Zhou, Q., Liu, L., and Hu, J. (2018). Western US volcanism due to intruding oceanic mantle driven by ancient Farallon slabs. *Nat. Geosci.* 11, 70–76. doi:10.1038/s41561-017-0035-y

Zhou, Q., and Liu, L. (2019). Topographic evolution of the Western United States since the early Miocene. *Earth Planet. Sci. Lett.* 514, 1–12. doi:10.1016/j.epsl.2019.02.029

Zhou, W., Zhuo, H., Wang, Y., Xu, Q., and Li, D. (2020). post-rift submarine volcanic complexes and fault activities in the Baiyun sag, Pearl River Mouth Basin: New insights into the breakup sequence of the northern South China Sea. *Mar. Geol.* 430, 106338. doi:10.1016/j.margeo.2020.106338

Zhou, X., Jiang, Z., Quaye, J. A., Duan, Y., Hu, C., Liu, C., et al. (2019). Ichnology and sedimentology of the trace fossil-bearing fluvial red beds from the lowermost member of the Paleocene Funing Formation in the Jinhu Depression, Subei Basin, East China. *Mar. Petroleum Geol.* 99, 393–415. doi:10.1016/j.marpetgeo.2018.10.032

frontiers | Frontiers in Earth Science

TYPE Original Research
PUBLISHED 29 September 2022
DOI 10.3389/feart.2022.916189

Quantifying continental collision dynamics for Alpine-style orogens

Luuk van Agtmaal[1,2]*, Ylona van Dinther[1], Ernst Willingshofer[1] and Liviu Matenco[1]

[1]Department of Earth Sciences, Utrecht University, Utrecht, Netherlands, [2]Department of Earth Sciences, Institute of Geophysics, Swiss Federal Institute of Technology (ETH Zurich), Zurich, Switzerland

OPEN ACCESS

EDITED BY
Manuele Faccenda,
Università Padova, Italy

REVIEWED BY
Ana M. Negredo,
Complutense University of Madrid, Spain
Marta Neres,
Portuguese Institute for Sea and Atmosphere (IPMA), Portugal
O. Adrian Pfiffner,
University of Bern, Switzerland

*CORRESPONDENCE
Luuk van Agtmaal,
luuk.vanagtmaal@erdw.ethz.ch

SPECIALTY SECTION
This article was submitted to Solid Earth Geophysics,
a section of the journal
Frontiers in Earth Science

RECEIVED 08 April 2022
ACCEPTED 25 July 2022
PUBLISHED 29 September 2022

CITATION
van Agtmaal L, van Dinther Y, Willingshofer E and Matenco L (2022), Quantifying continental collision dynamics for Alpine-style orogens. *Front. Earth Sci.* 10:916189.
doi: 10.3389/feart.2022.916189

When continents collide, the arrival of positively buoyant continental crust slows down subduction. This collision often leads to the detachment of earlier subducted oceanic lithosphere, which changes the subsequent dynamics of the orogenic system. Recent studies of continental collision infer that the remaining slab may drive convergence through slab roll-back even after detachment. Here we use two-dimensional visco-elasto-plastic thermo-mechanical models to explore the conditions for post-collisional slab steepening versus shallowing by quantifying the dynamics of continental collision for a wide range of parameters. We monitor the evolution of horizontal mantle drag beneath the overriding plate and vertical slab pull to show that these forces have similar magnitudes and interact continuously with each other. We do not observe slab rollback or steepening after slab detachment within our investigated parameter space. Instead, we observe a two-stage elastic and viscous slab rebound process lasting tens of millions of years, which is associated with slab unbending and eduction that together generate orogenic widening and trench shift towards the foreland. Our parametric studies show that the initial length of the oceanic plate and the stratified lithospheric rheology exert a key control on the orogenic evolution. When correlated with previous studies our results suggest that post-detachment slab rollback may only be possible when minor amounts of continental crust subduct. Among the wide variety of natural scenarios, our modelling applies best to the evolution of the Central European Alps. Furthermore, the mantle drag force may play a more important role in continental dynamics than previously thought. Finally, our study illustrates that dynamic analysis is a useful quantitative framework that also intuitively explains observed model kinematics.

KEYWORDS
subduction, continental collision, force quantification, dynamic models, numerical modelling, mantle drag, slab pull

1 Introduction

1.1 Background

Zones of continental collision are impressive agents of plate tectonics on Earth (Dewey and Bird, 1970; Doglioni et al., 2007; Jolivet et al., 2018). Understanding the formation, evolution and dynamics of collisional orogens is important, for instance because they are often the only record of the subduction history (e.g. Celal Şengör, 1990). In a societal context, a better understanding of the processes involved in continental collision allows for a better assessment of natural hazards, including those associated with seismicity (Hubbard et al., 2016; Dal Zilio et al., 2018; Michel et al., 2021).

Based on a wealth of geological and geophysical data from natural examples, many processes and parameters involved in continental collision have been studied through both analogue and numerical modelling. For example, the degree of rheological coupling between crust and mantle influences the geometry and strain partitioning within collisional orogens (Ellis, 1996; Royden, 1996; Brun, 2002; Erdős et al., 2021), while the *lateral* decoupling across the plate interface determines where active deformation occurs (Faccenda et al., 2009; Willingshofer and Sokoutis, 2009; Luth et al., 2010; Willingshofer et al., 2013). Lateral contrasts in crustal strength at the onset of collision also influence orogen geometry, strain partitioning and deformation style (Liao and Gerya, 2017; Vogt et al., 2017; Vogt et al., 2018). However, these studies often use constant kinematic boundary conditions which might complicate explaining the *kinematics* of the system. For this reason, the *dynamics* (i.e., relative importance of driving forces) of collisional systems are less understood. Although the dynamics of subduction and slab detachment in a collisional context have been addressed by a large number of researchers (e.g. Baumann et al., 2010; Duretz et al., 2012; Duretz and Gerya, 2013; Schellart and Moresi, 2013), few studies quantify internal forces in their models (Dal Zilio et al., 2020; Candioti et al., 2021; Suchoy et al., 2021).

1.2 Slab rollback orogeny model and the Central Alps

Building on the inspirational work of Argand (1916), the Central Alps are traditionally considered as a classical collisional orogen where plate convergence is accommodated by the formation of a double-vergent orogen, in response to "head on" collision of the European downgoing plate with the Adriatic overriding plate (e.g. Schmid et al., 1996). In contrast, orogens that are controlled by subduction processes and associated slab dynamics and mantle flow display one single vergence, as well documented in the Mediterranean realm (e.g. Jolivet et al., 2003; Matenco et al., 2010; Faccenna et al., 2014; Van Hinsbergen et al., 2020; Király et al., 2021) and in the Andes, the classic subduction orogen (e.g. Barazangi and Isacks, 1979). Recently, Schlunegger and Kissling (2015) and Kissling and Schlunegger (2018) developed a new conceptual model for orogenesis in the Central Alps, referred to as the "slab rollback orogeny model (SRO)". The SRO model assigns a prominent role to the vertical pull of the European slab during collision.

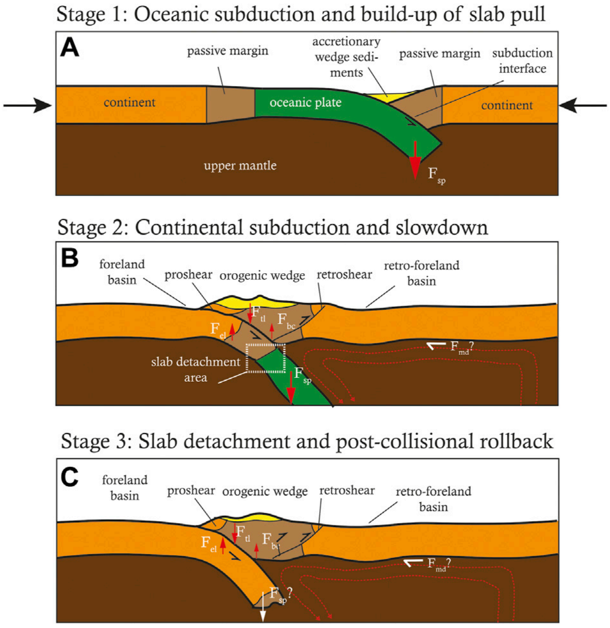

FIGURE 1
Conceptual illustration of the three stages of the slab rollback orogeny model, that is: **(A)** oceanic subduction, formation of an accretionary wedge. **(B)** Continental subduction, subduction slowdown ultimately leading to slab detachment. **(C)** Slab detachment followed by slab rebound, post-collisional slab rollback, and trench shift towards the foreland. General mantle flow patterns are drawn in red. Arrows are not to scale. Symbols: F_{sp}: slab pull, F_{el}: elastic bending resistance, F_{tl}: topographic gravitational loading, F_{bc}: buoyancy force of the light crustal root, F_{md}: mantle drag beneath the overriding plate.

In particular, the SRO model emphasises the role of vertical forces in continental collision by distinguishing between three distinct stages (Figure 1). First, negatively buoyant oceanic lithosphere subducts beneath a continental plate. As subduction progresses, the slab pull force builds up, driven by increasing volumes of cold oceanic lithosphere, whose density exceeds that of the hotter surrounding mantle. The second stage starts with the arrival of continental crust at the subduction zone (Figure 1B). As the positively buoyant continental crust subducts, the net slab pull force decreases, and consequently subduction slows down and may ultimately stop. This gives the slab time to interact with the surrounding asthenosphere, allowing intra-slab tensional stresses to build up. Eventually the slab detaches and sinks deeper into the mantle. Slab detachment marks the start of the final, third stage (Figure 1C). The SRO model proposes that after slab detachment the remaining slab still provides enough slab pull to drive convergence between the continental plates, as inferred for the Central Alps (Schlunegger and Kissling, 2015; Kissling and Schlunegger, 2018; Dal Zilio et al., 2020). This assumption is based on a number of observations in the Central Alps, primarily the isostatic disequilibrium between an exceptionally thick crustal root of ~60 km and a local, low mean surface elevation in the order of 2 km (Kissling, 1993). In fact, the thick crust would require twice the observed mean surface topography (Schlunegger and Kissling, 2015).

Key characteristics of the Central Alps further include (Schlunegger and Kissling, 2015; Kissling and Schlunegger, 2018) 1) indentation of Adriatic lower crust into the Central Alps orogenic wedge (Schmid et al., 1996), 2) a highly active retroshear in a double-vergent orogenic wedge, resulting in strong retrograde metamorphism, 3) subduction of Eurasian lower crust (and hence a deep Moho), 4) decoupling of the Eurasian upper crust from the lower crust, and 5) an orogenic wedge consisting mostly of upper crustal material. Tomographic images reveal a current position of the (continental) European slab at 100–250 km depth (Lippitsch et al., 2003; Mitterbauer et al., 2011; Sun et al., 2019; Paffrath et al., 2021). Furthermore, focal mechanism analysis shows that the retro-foreland basin of the Central Alps (i.e., the Po Basin) is under compression (Deichmann, 1992; Di Bucci and Angeloni, 2013; Singer et al., 2014). Finally, GPS measurements show that Adria (Africa) is still moving towards Europe at low rates of ~ 2–5 mm/yr (Calais et al., 2002; D'Agostino et al., 2008; Métois et al., 2015), which is much less than the ~7.9 mm/yr average advance rate for the Cenozoic as calculated from tectonic reconstructions (Dewey et al., 1989; Schmid et al., 1996; Handy et al., 2010). The subduction hinge is estimated to have retreated away from the Eurasian plate at ~ 20 mm/yr in the Paleocene, and ~10 mm/yr in the Eocene (Pfiffner, 2016).

1.3 Present work

Here we aim to assess the role and relative importance of vertical slab pull and horizontal mantle drag beneath the overriding plate. While slab pull may dominate in early stages, the question is whether the portion of a slab remaining after detachment is able to sustain convergence, or that mantle drag is an important driver of plate motions (Conrad and Lithgow-Bertelloni, 2002; Alvarez, 2010; Faccenna et al., 2013; Sternai et al., 2016; Jolivet et al., 2018). The post-collisional slab dynamics suggested by the SRO model remains not well understood, because the remaining slab is mostly continental and therefore positively buoyant. However, if some oceanic lithosphere is still attached, the net buoyancy might be enough to drive slab rollback or steepening. The idea is intriguing and requires more detailed investigation under a wide range of parameters. To analyse this problem, we run and analyse 2D thermomechanical visco-elasto-plastic lithospheric-scale numerical simulations of dynamic continental collision. We quantify the slab pull and mantle drag forces over time to assess the dynamics of continental collision in the context of the SRO model. The quantification method and accompanying post-processing scripts are described in Appendix A and available on GitHub. Our numerical simulations and the associated parametric studies target a number of critical variables and processes that are analysed in more details, such as the initial ocean length, Peierls creep, and lithospheric mantle friction.

2 Methods

2.1 Numerical methods

The simulation results were obtained using the widely used 2D geodynamic code I2ELVIS (Gerya and Yuen, 2007) with inertia activated, i.e. the seismo-thermo-mechanical version (van Dinther et al., 2013a; van Dinther et al., 2013b; van Dinther et al., 2014). This code solves the conservation of mass, momentum and energy (see Supplementary Material) on a fully staggered, Eulerian grid using a conservative finite difference scheme combined with a Lagrangian marker-in-cell technique (Gerya and Yuen, 2003). The equations are solved under assumption of flow in an incompressible medium and the extended Boussinesq approximation, i.e., only buoyancy-driven changes in density are taken into account, as are the energy contributions of adiabatic, shear, and latent heating (Christensen and Yuen, 1985; Gerya and Yuen, 2003). We refer to Gerya and Yuen (2007) for a more detailed description of the code.

2.2 Rheology

We assume that the deformation of different lithologies is governed by a visco-elasto-plastic rheology. At every time step and on each Lagrangian marker, time-dependent stress and density are calculated and interpolated to the Eulerian nodes (Gerya, 2019). The total (deviatoric) strain rate is composed of a viscous, an elastic and a plastic component:

$$\dot{\varepsilon}'_{ij} = \dot{\varepsilon}'_{ij,visc} + \dot{\varepsilon}'_{ij,el} + \dot{\varepsilon}'_{ij,pl} \tag{1}$$

The components are calculated according to (Gerya and Yuen, 2007)

$$\dot{\varepsilon}'_{ij,visc} = \frac{\sigma'_{ij}}{2\eta_{eff}} \tag{2}$$

$$\dot{\varepsilon}'_{ij,el} = \frac{1}{2G}\frac{D\sigma'_{ij}}{Dt} \tag{3}$$

TABLE 1 Rheological parameters used for the reference model. All materials have an isobaric heat capacity C_p of 1000 J/(kg K), thermal expansion α=3·10^{-5} K^{-1} and isothermal compressibility β=10^{-5} MPa^{-1} [a] Ranalli, (1995);[b] Turcotte and Schubert, (2002);[c] Rudnick and Fountain, (1995).

Material	Sediments	Continental UC	Continental LC	Oceanic UC	Oceanic LC	Mantle
Flow law	Wet quartzite	Wet quartzite	Mafic granulite	Wet quartzite	Plg/An 75%	Dry olivine
ρ_0[b] [kg/m^3]	2,600	2,750	3,000	3,000	3,300	3,300
A_d[a] [Pa^{-n}s]	1.97·10^{17}	1.97·10^{17}	1.25·10^{21}	1.97·10^{17}	4.80·10^{22}	3.98·10^{16}
E_a[a] [kJ/mol]	154	154	445	154	238	532
V_a[a] [J/bar]	1.2	0.8	0.8	0.8	0.8	0.8
n[a]	2.3	2.3	4.2	2.3	3.2	3.5
H_r[b,c] [μW/m^3]	1.5	0.25	1.5	0.25	0.25	0.022
k[a] [W/(mK)]	(0.64+807/ T+77)exp$(4 \cdot 10^{-6} P)$	(0.64+807/ T+77)exp$(4 \cdot 10^{-6} P)$	(1.18+474/ T+77)exp$(4 \cdot 10^{-6} P)$	(1.18+474/ T+77)exp$(4 \cdot 10^{-6} P)$	(1.18+474/ T+77)exp$(4 \cdot 10^{-6} P)$	(0.64+807/ T+77)exp$(4 \cdot 10^{-6} P)$
G [GPa]	25	34	34	38	38	67
μ_s	0.35–0.20	0.15	0.20	0.03	0.06	0.6
λ	0.4	0.4	0.4	0	0	0.4

$$\dot{\varepsilon}'_{ij,pl} = 0 \, \text{for} \, \sigma'_{II} < \sigma_{yield} \tag{4}$$

$$\dot{\varepsilon}'_{ij,pl} = \chi \frac{\partial \mathrm{G_{pl}}}{\partial \sigma'_{ij}} = \chi \frac{\partial \sigma'_{ij}}{2\sigma'_{II}} \text{ for } 1\sigma'_{II} = \sigma_{yield} \tag{5}$$

Here η_{eff} indicates the effective viscosity (Eq. 8) and G represents the elastic shear modulus, which relates deviatoric stresses (σ_{ij}') to (deviatoric) strain rates ($\dot{\varepsilon}'_{ij}$). The elastic component considers local variability of stress orientation due to rotation of Lagrangian markers through the objective co-rotational stress tensor ($D\sigma_{ij}'/Dt$). The plastic deviatoric strain rate follows the plastic flow rule (Gerya, 2019). The second invariant of the deviatoric stress tensor is given by $\sigma'_{II} = \sqrt{\sigma'^{2}_{xx} + \sigma'^{2}_{xy}}$ and the plastic flow potential G_{pl} is assumed to be equal to σ_{II}'. Finally, $\chi = 2\dot{\varepsilon}'_{II,pl}$ is called the plastic multiplier, which is activated when the Drucker-Prager yield criterion is reached (see Eq. 5).

The plastic yield strength is calculated following 2D Drucker-Prager plasticity and depends on cohesion C, static friction μ, the pore fluid pressure ratio P_f/P_s defined as fluid pressure P_f over solid pressure P_s, and pressure P or mean stress according to

$$\sigma_{yield} = \mathrm{C} + \mu \cdot \left(1 - \frac{P_f}{P_s}\right) \cdot P \tag{6}$$

Viscous deformation (effective viscosity η_{eff}) incorporates both diffusion and dislocation creep and is given by the harmonic average of both creep mechanisms

$$\frac{1}{\eta_{eff}} = \frac{1}{\eta_{diff}} + \frac{1}{\eta_{disl}}, \tag{7}$$

where the viscosities defined by different creep mechanisms are given by

$$\eta_{disl} = \frac{1}{2} A_d \sigma'^{1-n}_{II} \exp\left(\frac{E_{\mathrm{a}} + PV_{\mathrm{a}}}{nRT}\right) \tag{8}$$

$$\eta_{diff} = \frac{1}{2} A_d \tau_{tr}^{1-n} \exp\left(\frac{E_{\mathrm{a}} + PV_{\mathrm{a}}}{nRT}\right) \tag{9}$$

Here, A_d is the pre-exponential factor, n is the stress exponent, and E_a and V_a are the activation energy and volume, respectively, and R=8.314 J K^{-1} mol^{-1} is the universal gas constant. These parameters are experimentally determined and set for each lithology (Table 1). The threshold stress from diffusion to dislocation creep τ_{tr} is set to 30 kPa (Turcotte and Schubert, 2002), which ensures mainly dislocation creep is active. In the case of model *peierls* (Table 2), Peierls creep is added in series to the calculation of η_{eff} in (Eq. 8). This plastic deformation mechanism is active in olivine in the lithospheric mantle under high-pressure, low-temperature (HP/LT) conditions (Evans and Goetze, 1979; Katayama and Karato, 2008). It limits the plastic strength of the mantle lithosphere, and is given by

$$\eta_{Peierls} = \frac{1}{2A_{Peierls}\sigma'_{II}} \exp\left(\frac{E_a + PV_a}{nRT}\left(1 - \left(\frac{\sigma'_{II}}{\sigma_{Peierls}}\right)^p\right)^q\right) \tag{10}$$

The experimentally determined values for the material parameter $A_{Peierls}$ and the maximum plastic strength $\sigma_{Peierls}$ are 10$^{-4.4}$ Pa^{-2}s^{-1} and 9.1 GPa, respectively (Evans and Goetze, 1979). The exponents p and q are shape-and geometry-dependent parameters that are assumed to be 1 and 2 (Dal Zilio et al., 2020).

2.3 Model setup

The 2D numerical experiments were carried out in a 3,000 × 800 km^2 domain, resolved using an irregular grid of 1785 × 509 nodes. The maximum horizontal resolution of 500 m is applied between 800 ≤ x < 1,500 km and a medium-resolution zone of 2 km grid spacing is present from 1,500 ≤ x < 1850 km. A

TABLE 2 Summary of all tested parameters and their effects with respect to the reference results. The parameters discussed in detail are written in bold. Abbreviations: SVO: single-vergent orogen, qtz: quartzite, sed/UC frictional strength: ratio between brittle strength of sediments over upper continental crust at 10 MPa, LC: lower crust, LM: lithospheric mantle.

Parameter	References value	Tested values	Effects
Slab age	70 Ma	40, 50, 60, and 100 Ma	Younger slab: lower detachment depth, 100 Ma: very shallow detachment
T_{Moho}	450 °C	350 , 400, 500, 550 °C	Only 400–450 °C give consistent results in this setup
Sed/UC frictional strength	2.1	1.15, 0.79, 0.6	>>1: wide retroshear; >1: sharp retroshear: < 1: no retroshear (i.e. SVO)
LC rheology (both plates)	Mafic granulite	Plag, wet qtz	Plag: upwarped overriding LC results in SVO; qtz: early and shallow detachment following near-closure of the subduction channel
LC rheology (overriding)	Mafic granulite	Plag, wet qtz	Plag: like *ref*; qtz: decoupled behaviour of continental crust and LM
Ocean length	**610 km**	**510 km (*oc510*), 410 km (*oc410*), 310 km (*oc310*)**	**510 km: more indentation; 410 km: early UC delamination; 310 km; asthenosphere window**
LM P_f/P_s	**0.0**	**0.25 (*LM25*), 0.50 (*LM50, LMoc510*)**	**0.25: LC indentation, later detachment; 0.50: early shallow detachment, 0.50+510 km ocean: slightly early detachment**
Peierls creep	**excluded**	**Included (*peierls*)**	**Shallower, earlier detachment**
Weak zone angle	20°	15°, 25°	15°: requires longer push; 25°: promotes plate decoupling
Weak zone width	20 km	10 km, 40 km	≥20 km needed for proper subduction initiation
Decoupled boundaries	Fixed downgoing plate	Both plates free	Accelerates subduction, plate decoupling
Push velocity	10 cm/yr	1.3 cm/yr	High degree of UC and LC eduction, shallower subduction angle
Length of overriding plate	1,250 km	2,250 km	Subduction interface closes, no continental subduction, deep slab detachment, no rebound
European passive margin length	100 km	200 km	Subduction interface closes, no continental subduction, deep slab detachment, no rebound

10 km grid spacing is defined in the leftmost ($0 < x < 700$ km) and rightmost ($1900 < x < 3,000$ km) domains of the model. The resolution changes gradually between these regions. In the vertical direction, the resolution varies smoothly from 500 m ($0 \leq y \leq 100$ km) via 1 km ($103 \leq y < 300$ km) to 5 km ($345 \leq y \leq 800$ km). The temporal resolution in the thermomechanical models is 1 kyr. The side boundaries have free slip boundary conditions, while the lower boundary is open in a similar way as the modelling setups of for instance Faccenda et al. (2008) or Vogt et al. (2018).

The reference model consists of two continents separated by a 610 km long oceanic plate (Figure 2), similar to the setup of Dal Zilio et al. (2020). The continents are composed of 20 km of felsic upper crust and 15 km of strong, mafic granulite lower crust (Table 1). The oceanic crust consists of 2 km of basaltic upper crust and 8 km of gabbroic lower crust. A 20–22 km thick layer of low-density, low-viscosity, "sticky air" is present above the crust. The interface between air and crust is used to automatically calculate topography (Schmeling et al., 2008). Erosion and sedimentation are implemented using an instantaneous approach, i.e., material above a threshold level (10 km in our simulations) is converted into air, and water/air below 2 km depth is converted into layers of sediment. The continental geotherm initially has two linear segments, from 0°C at the surface to 450°C at the Moho, and on to 1,344°C at the lithosphere-asthenosphere boundary. Below this depth, temperature increases with an adiabatic gradient of 0.5°C/km. The oceanic lithosphere follows the temperature profile for a slab age of 70 Ma and a thermal diffusivity of 10^{-6} m^2/s given in the half space cooling model (Turcotte and Schubert, 2002). The lateral boundaries of the model domain are insulating.

To initiate subduction and convergence, a semi-dynamic approach (e.g. Duretz et al., 2011; van Dinther et al., 2013b; Dal Zilio et al., 2020) is applied. Such a method consists of an initial or kinematic stage in which convergence is prescribed as a boundary condition to initiate subduction. In the present study, the right continental plate is pushed toward the left at a rate of 10 cm/yr for the first 5 Myr, such that 500 km of convergence has been accommodated at the end of the initial stage (similar to e.g. Duretz et al., 2011). From this point onwards, the geodynamic system is solely driven by internal forces without externally applied kinematic boundary conditions. The high push velocity is justified, because sensitivity tests did not show major differences between 5 and 10 cm/yr. A run at 1.3 cm/yr showed similar model dynamics as well, although eduction (i.e., buoyancy-driven decoupling and flow of continental crust from the downgoing plate, Andersen et al., 1991) is more efficient (Table 2). The viscosity in the push area is increased, and stresses around it are relaxed, to minimise artificial deformation (Figure 2). Furthermore, a low viscosity zone is implemented at the right model boundary to allow the

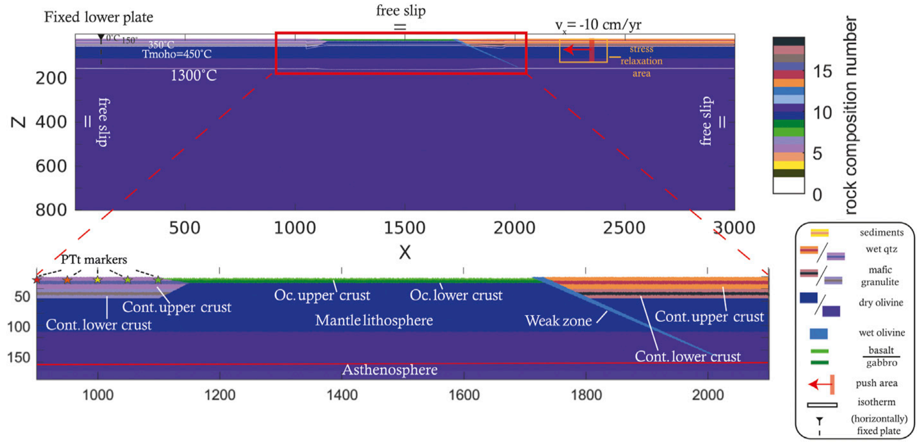

FIGURE 2
Illustration of the setup used in this study showing boundary conditions, lithological stratification and isotherms. Note that the length of the oceanic plate is varied in one of the parameter studies. Initial convergence of 10 cm/yr is applied in the red box around x = 2,300 km until 500 km of convergence has been accommodated. Stress changes are relaxed in the area indicated by the orange box around the push area to avoid artificial stresses. Finally, the initial position of five markers in the downgoing plate, used for pressure, temperature and time tracking are shown with stars.

advancing plate to decouple from the lateral boundary. This low-viscosity boundary condition is not applied on the left side of the model box to simulate a fixed downgoing plate, e.g., mimicking a stable downgoing European plate (e.g. Dewey et al., 1989; Torsvik et al., 2012).

3 Results and analysis

3.1 Reference model

3.1.1 0–5 Myr stage 1: Kinematic stage

During this first stage (Figure 1A), most of the oceanic lithosphere subducts beneath the overriding plate (Figures 3A,B, Supplementary Movies S1, S2). Sediments that were deposited on the ocean floor during the simulation are scraped off and incorporated into a large accretionary wedge-type structure that developed by predominant foreland-directed thrust imbrication (Figures 3A,B). Furthermore, pop-down structures developed near the trench due to the basal friction between the wedge and the downgoing plate against the rapidly advancing overriding plate, which acts like a back-stop. The slab dip is initially constant, but increases rapidly from 33 to 58° between 4.5 and 5.0 Myr due to a stage of back-thrusting and thickening of the accretionary wedge, which accommodates part of the convergence velocity and decreases the subduction velocity (Supplementary Movies S1, S2). During this kinematic stage, the tracked upper crustal markers are steadily buried (i.e., along a prograde burial path) (Figure 4A).

3.1.2 5–20 Myr stage 2: Collision and trench shift towards the foreland

During slab steepening, significant poloidal mantle flow is generated around the tip of the slab, initiating a counter-clockwise convection cell in the mantle wedge above the slab (Supplementary Figure S1A). Mantle is dragged down with the downgoing plate until flow rises beneath the overriding plate and moves back into the mantle wedge generating corner flow. The vertical gradient of horizontal velocity generates a strong traction beneath the overriding plate, dragging it along. This results in a significant trench-ward drag force beneath the overriding plate (positive mantle drag in Figure 6B). Therefore, the overriding plate advances rapidly as soon as the kinematic boundary condition is released at the end of the first stage. During this advance, the orogenic wedge is emplaced on the subducting continental plate (Figures 3A–D, see also Supplementary Movies S2). The frictional resistance across the pro-shear to this emplacement allows the development of a double-vergent orogenic wedge, characterised by a retroshear separating the pro-wedge from the retro-wedge (Figures 3C,D). In addition, the vertical gradient of horizontal displacement in the overriding plate results in an asymmetric retro-foreland basin. During the emplacement of the orogenic wedge, the slab pull passes its peak magnitude (in the order of $-1.6*10^{14}$ N/m, Figure 6A). What follows is a period of slow slab area growth coeval with slab heating. This leads to a net weakening of slab pull (Figure 6A), because the decrease in density contrast due to slab heating plays a more important role than the slow increase in area during this period. As a consequence of slow subduction and trench retreat, the mantle drag force beneath the overriding plate slowly

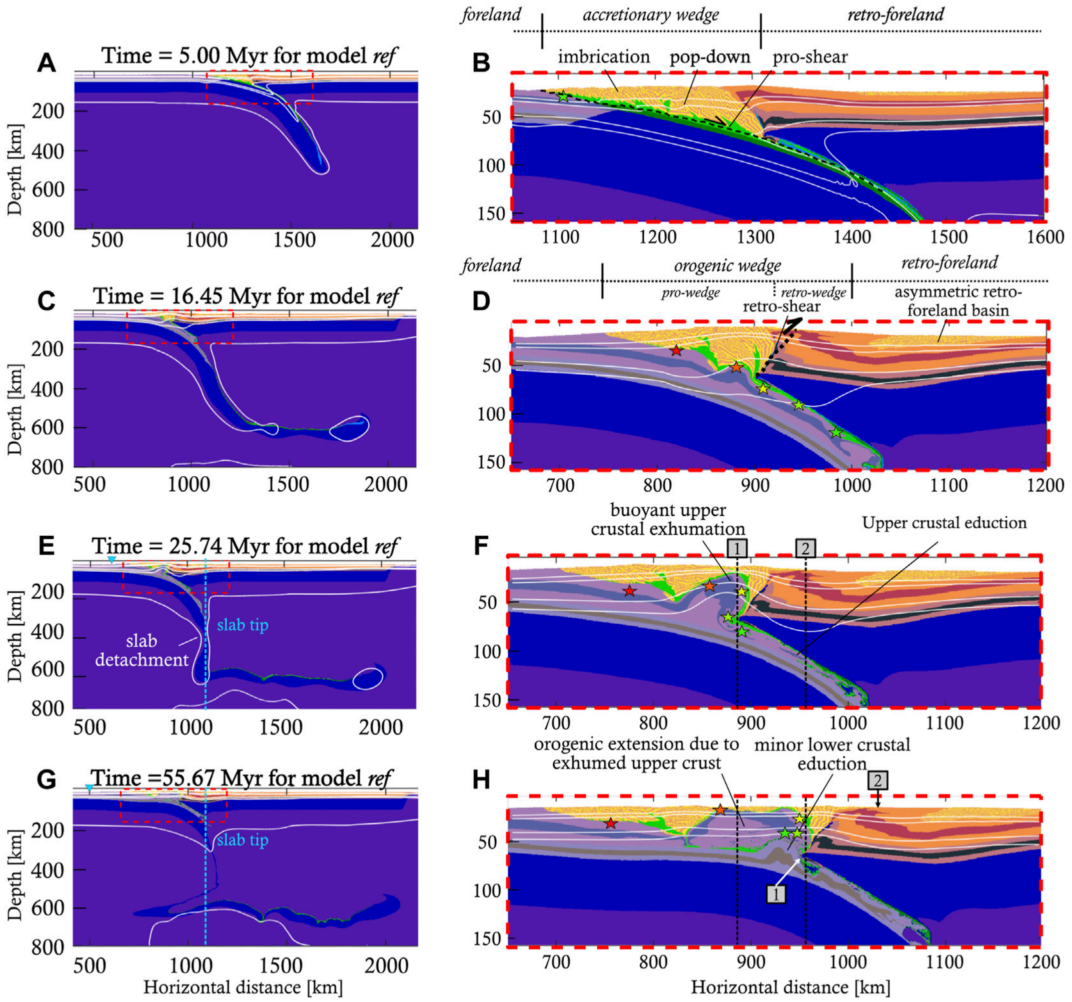

FIGURE 3
Four snapshots of the reference model at key stages of its development, showing rock composition and isotherms (100 C, 150 C, 350 C, 450 and 1300 C). In addition, PTt marker positions are shown in the same fashion as in Figure 2 **(A,B)** During the initial stage, imbricate thrusts develop, as well as pop-down structures. Prescribed oceanic subduction has just been switched off. A single-vergent orogen has developed. **(C,D)** After continental collision followed by a stage of trench shift towards the foreland, the orogen is now double-vergent. The retroshear and asymmetric retro-foreland basin are indicated. The first signs of upper crustal eduction are visible. **(E,F)** The oceanic slab has detached, resulting in slab rebound and unbending. The upper crust has almost fully educted from the subduction channel and is now exhuming, pushing the overlying material up and to the sides. **[1]** and **[2]** denote the plate boundary and the retro-wedge deformation front, respectively. The trench position is indicated with a blue triangle **(G,H)** The model has reached a quasi-steady state. The buoyant upper continental crust forms the core of the orogen. Some lower crust has started to exhume along the retroshear as well, but it is too dense to exhume further. No post-detachment slab rollback takes place, but the overriding plate has retreated by ~60 km at depth **[1]** and ~70 km at the surface **[2]**.

decreases as well (Figure 6B). Finally, heating of rocks inside the subduction channel allows the upper continental crust to educt (i.e., decouple and flow upwards) from the subducting, rheologically more heat resistant lower crust. This eduction of upper crust is clearly visible in the PTt path as an onset of retrograde marker motions, i.e., exhumation (Figure 4A).

3.1.3 20–25 Myr stage 3: Slab detachment

Around t ~ 22.5 Myr, the mantle drag force beneath the overriding plate switches from towards the trench (i.e., positive) to away from the trench (i.e., negative) (Figure 6B). The overriding plate comes to a halt, before moving to the right from t ~ 23 Myr onwards (Supplementary Movies S2). This is a result of the eduction of the upper crust of the downgoing plate in the subduction channel (Supplementary Figure S1B). The exhuming upper crust accumulates in the core of the orogen, uplifting the overlying wedge units. The orogen then becomes gravitationally unstable and starts to collapse. The previous stage of little active deformation concludes with the onset of

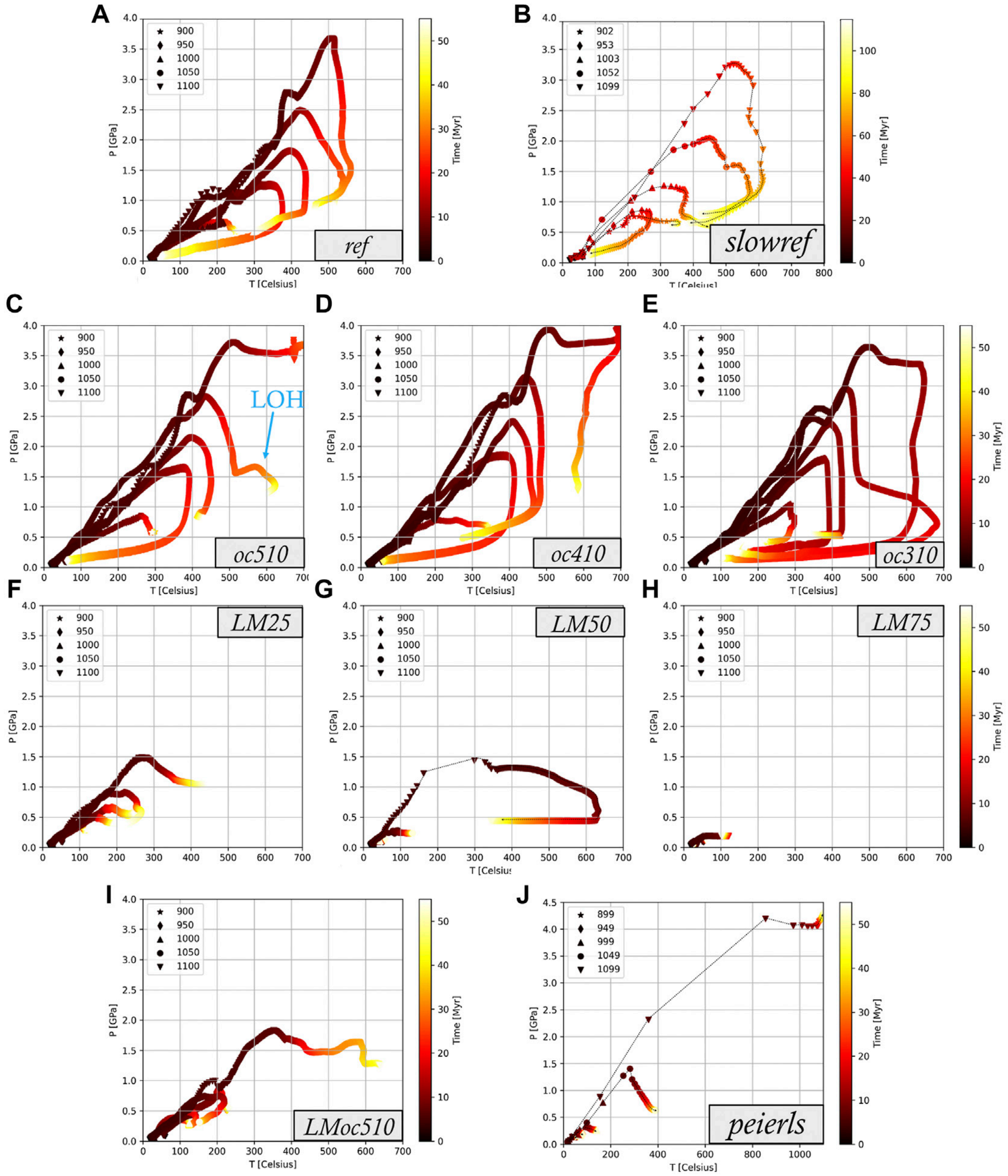

FIGURE 4
Pressure, Temperature, time (PTt) paths of models **(A)** *ref*, **(B)** *slowref*, **(C)** *oc510*, **(D)** *oc410*, **(E)** *oc310*, **(F)** *LM25*, **(G)** *LM50*, **(H)** *LM75*, **(I)** *LMoc510*, and **(J)** *peierls* (Table 2). The paths follow five markers initially located at positions x= 900–1,100 km buried >2 km deep in the continental upper crust (initial position in legend). Model *oc510* shows a late orogenic heating (LOH). Models that show early and shallow slab detachment show an immature burial-exhumation cycle (*LM50*, *LM75*, *peierls*). PTt paths for models *peierls* and *slowref* were extracted ***after*** the model run while the others were continuously tracked. Also note the different temperature and pressure axes for model *peierls* and the different time axis for model *slowref*.

gradual slab necking at $t \sim 22.5$ Myr (i.e., coinciding with the switch of mantle drag direction). Around $t \sim 25$ Myr, the oceanic slab segment detaches from the continental slab segment at a depth of ~350 km (Figure 3E).

3.1.4 25–56 Myr: Post-detachment

An immediate response of the slab to the decreased slab pull is visible (Figures 5, Figure 6A, see also Supplementary Movies S1): the slab initially unbends relatively rapidly due to elastic

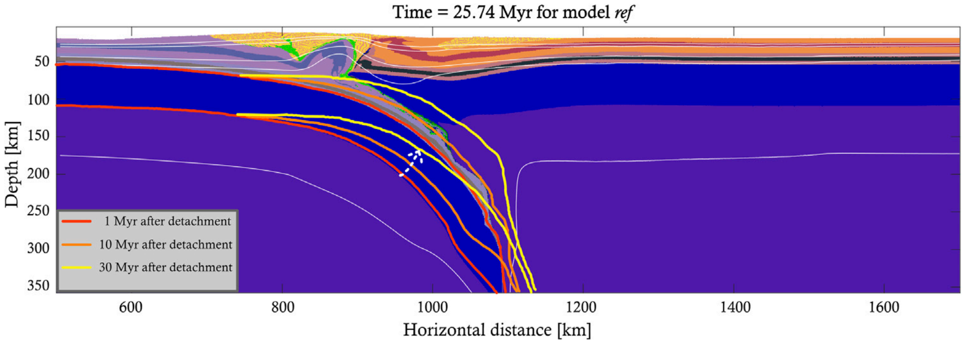

FIGURE 5
Illustration of the post-detachment slab rebound and unbending for the reference model. The slab contours at 1, 10 and 30 Myr after detachment are drawn in red, orange and yellow, respectively. The general slab motion is illustrated with a dashed white arrow.

rebound. Subsequently, slower viscous unbending is driven by the net positive buoyancy of the slab and continues for at least 30 Myr after detachment (Figures 3E,F, Figure 5, Figure 6A, Supplementary Movies S2). The buoyant rise of the slab squeezes the subduction channel, enhancing decoupling and buoyant flow of the upper crust from the subducting continent (Supplementary Movies S2). This process is often referred to as eduction (*sensu* Andersen et al., 1991). The educted continental crust is exhumed by shear reversal along the subduction channel and accumulates in the core of the orogen (Figures 3E–H). Some crustal material is still displaced along the retroshear (Figure 3F). The positively buoyant crustal material induces tensional stresses and extension in the central part of the orogenic wedge (Supplementary Figure S1B) above the exhumed crustal material by eduction, resulting in overall orogenic widening. This orogenic widening is associated with both trench retreat (i.e. the trench shifts towards the foreland) and overriding plate retreat, defined as a movement of the plate boundary (denoted by **[1]**), towards the hinterland (Figures 3E–H). Even though the elastic rebound of the previous stage uplifted the orogen to about 8 km peak elevation (3.4 km averaged from trench to edge of retro-foreland basin, Supplementary Figure S2B), the subsequent post-detachment orogenic widening flattens the peak topography to ~4 km and the average topography to 2.9 km (Supplementary Figure S1B). Due to the onset of gradual eduction of continental lower crust, the slab pull force becomes negative again around t ~ 450 Myr (Figure 6A), while the mantle drag experiences a broad, negative peak (Figure 6B) as asthenosphere replaces the educted lower crust. However, the slab pull is not strong enough to induce slab rollback. Instead, the slab remains stable while the overriding plate continues to retreat at rates decaying to <1 mm/yr at t ~ 55 Myr. No slab rollback is observed, due to the weak slab pull that is countered by a mantle drag away from the trench (Supplementary Movies S1, Figures 3, Figure 6). Instead, the slab remains in a stable position while the trench shifts to the foreland by ~100 km due to the orogenic widening (Figures 3E–H, Supplementary Figure S2B, Supplementary Movies S2).

3.2 Parameter studies

3.2.1 Ocean length

Oceanic plate length, like oceanic slab age, directly influences the amount of negatively buoyant material present in the subduction zone, and hence the slab pull magnitude. We ran three models with increasingly shorter oceanic plates compared to the 610 km in the reference model (510 km (model *oc510*), 410 km (model *oc410*) and 310 km (model *oc310*), Table 2).

The subduction and collision dynamics do not change drastically for model *oc510* (Figure 7C). Especially stage 1 and 2 are very similar (Supplementary Movies S3, Figures 8A–D). Since continental material enters the subduction zone about 350 kyr earlier, the peak slab pull is reached earlier as well, yet its magnitude is similar (Figures 7A,C, Supplementary Figure S3, $-1.45 * 10^{14}$ N/m compared to $-1.6 * 10^{14}$ N/m). In addition, the retroshear forms earlier, facilitating more efficient displacement of crustal rocks from the lubricated subduction channel upwards. This exhumation process decouples part of the overriding upper crust from its corresponding lower crust. As a result, the overriding lower crust can indent the core of the orogen more deeply (Figures 8A–D, Supplementary Movies S3). Slab detachment occurs at t ~ 24.5 Myr, very similar to the reference model. In the post-detachment stage, the same slab rebound and unbending process occurs as in the reference model. However, the lower crust of the downgoing plate does not start to educt in the final stage (Supplementary Movies S2 and Supplementary Figure S3). The final orogenic geometry resembles the reference model, including the surface topography. The orogen is ~100 km wider leading to a trench shift towards the foreland of 140 km since detachment while the overriding plate moved towards the retro-foreland (Supplementary Figure S2A,B).

In models *oc410* and *oc310*) several significant differences in orogenic evolution arise. While kinematically stage 1 is similar to the reference model, the dynamic signature (i.e., force evolution) clearly shows lower and earlier achieved peak slab pull magnitude due to a shorter oceanic slab (Figures 7E,G, Supplementary Figure S3). For such short oceanic plates, convergence is still imposed in these models when the continents collide. This disturbs the dynamic signature, such that mantle drag cannot accelerate the overriding plate. Test runs showed that without continued pushing after 300 km, an initial ocean length of 310 km is not enough to sustain subduction, but 410 km is enough. Nonetheless, for short ocean lengths the accretionary wedge does not evolve into a double-vergent orogenic wedge, since no retroshear develops. There is significantly lower shear resistance at the subduction interface, because almost all the frictionally weak, lubricating oceanic crust (Table 1) subducts (Figures 8E–H). Therefore, the entire upper crustal layer decouples from the downgoing plate and educts, allowing the overriding plate to slide off the weak subduction interface. This happens most strongly in model *oc310*, where the plates decouple (Figures 8G,H) and slab pull stays negative for the whole simulation (Figure 7G). Despite this, the PTt paths of the tracked upper crustal markers are still remarkably similar to the reference model (Figures 4A,D,E).

In summary, very short (smaller than ~400 km) oceanic plates tend to produce single-vergent orogens in this setting, while longer plate lengths are more likely to produce double-vergent orogens.

3.2.2 Peierls creep

The activation of Peierls creep weakens the mantle lithosphere of especially the downgoing plate at depth by approximately 30% (Auzemery et al., 2020) by limiting its yield stress. It is also active in the overriding plate (e.g. Duretz et al., 2011), but it has limited effects there. The activation of Peierls creep significantly influences the evolution of the orogen in the *peierls* model (Table 2), such that it cannot be readily subdivided into the three stages defined in Figure 1. There is no stage 2 (trench shift towards the foreland and slab heating), because the slab detaches much earlier and at shallower depth (t ~ 6.3 Myr at 120 km depth, Supplementary Movies S4). The reduced maximum yield stress is reached in less time, so necking, tearing, and detachment occur sooner and at shallower depths (Supplementary Figure S4). Therefore, earlier detachment is an expected consequence of the stress limiting (Duretz et al., 2011). In addition, the early, shallow slab detachment leads to a steady decrease in driving force magnitudes (Figure 7B).

After slab detachment, the rapidly subducted slab starts to unbend and educt, uplifting the orogenic wedge. Simultaneously, the overriding plate slowly slides off of the downgoing plate along the lubricated subduction interface. This generates significant extension throughout the orogen, which is largely accommodated by reactivation of the thrust faults in the pro-wedge as normal faults. The normal faults are rotated and tilted to gentler dip angles as extension progresses (Supplementary Movies S4). Extension continues until the end of the simulation at t ~ 55 Myr.

3.2.3 Lithospheric mantle friction

The frictional strength of the mantle lithosphere is often kept constant in geodynamic modelling studies, even though it makes up a significant portion of the lithosphere and thus of its strength. Our reference model assumes a dry mantle lithosphere (i.e., $P_f/P_s = 0$, as suggested in e.g. Yardley and Valley, 1997; Burov, 2011; Massonne, 2016), such that it is effectively 10 times as strong (frictionally) as the continental crust (Table 2). We explore the impact of higher pore fluid pressures ($P_f/P_s = 0.25$ (model *LM25*) and 0.50 (model *LM50*) on continental collision dynamics (Table 2). This leads to effective friction coefficients of 0.42 and 0.24, respectively, which have also been suggested for natural mantle lithosphere (Zhong and Watts, 2013).

In model *LM25* the peak forces and force evolution are quite similar to those of the reference model, but with important kinematic differences. The slab detaches 5 Myr later (~30 vs ~ 25 Myr, Figures 7A,D, Figure 9), after which the slab pull force remains positive instead of negative (Figures 7D, Figure 9). The frictional strength contrast reduction of 25% along the subduction interface increases the coupling between the downgoing and overriding plates. Moreover, the overriding plate bends more strongly, which initiates a positive feedback between burial and sedimentation, resulting in a deeper, narrower retro-foreland basin (Figures 10B,D, Supplementary Movies S6). Subsequently, the deeper lithospheric mantle scrapes off a large portion of oceanic crust during the kinematic stage, which forms a dense core beneath the orogen (Figure 10D). In turn, this dense orogenic core inhibits deep subduction of the uppermost continental crust, as well as subsequent exhumation of upper/lower continental crust along the retroshear (Figure 4F). The dense ophiolitic core also decouples the upper crust from the lower crust in the overriding plate. The topography does not flatten after detachment (Supplementary Figure S2C), because necking is slower and the elastic response is weaker, hence the uplift and orogenic widening following detachment are only minor.

In model *LM50* the significantly weakened lithospheric mantle results in slab detachment around t ~ 5.17 Myr, at a depth of ~50 km (Figure 9, Figure 10E,F) before a mature, double-vergent orogen has formed through a large rupture along the subduction interface, similar as described by Duretz et al. (2011). However, when a 50% weakened lithospheric mantle is combined with a 510 km long initial ocean (i.e., model *LMoc510,* 100 km shorter than the reference model), the downgoing plate does not detach at shallow levels. Instead, it leads to a significant amount of lower crustal indentation (Figures 10G,H). The slab detaches 5 Myr earlier than in the reference model (Figure 9). Compared to model

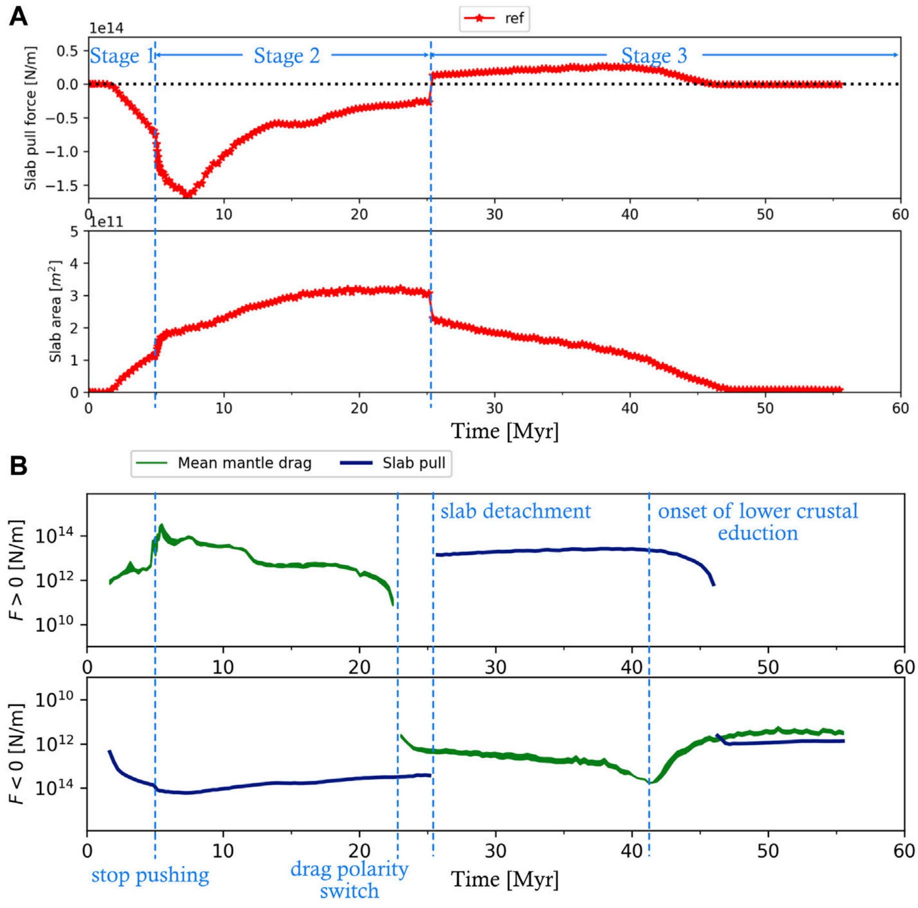

FIGURE 6
Temporal evolution of the most important forces in the model, calculated following the procedure outlined in Appendix A **(A)** Slab pull (top) and slab area (bottom). Peak slab pull is reached around t = 7.0 Myr, but peak slab area is reached right before slab detachment, which is indicated by a jump in both quantities. From 45 Myr onwards, slab pull is around 10^{12} N/m. **(B)** Evolution of the mean mantle drag force beneath the overriding plate. Slab pull is drawn for reference. The top panel displays the positive values, while the bottom panel depicts negative values. Positive values represent trenchward mantle drag and upward slab pull, and vice versa for the negative values. Note the log scale on the *y* axis.

LM25, the lithospheric mantle of the overriding plate bends more deeply, and part of the overriding plate is downwarped (Figure 10H).

The frictional strength of the lithospheric mantle thus strongly influences the burial-exhumation cycles of the downgoing plate, the timing of slab detachment and the subsequent topographic response. Moreover, reducing the frictional strength reduces the minimum wavelength of deformation in the lithospheric mantle.

3.2.4 Other parameters

The impact of numerous other parameters was explored and key outcomes are summarized (Table 2). Among them, the lower crustal rheology of the *overriding* plate has a stronger control on orogen geometry than that of the *downgoing* plate. An intermediate (plagioclase/anorthite 75%, Table 1) to strong (mafic granulite, Table 1) overriding lower crust results in a double-vergent orogen. For the downgoing plate, lower crustal subduction requires an intermediate to strong lower crustal rheology. The ratio between the frictional strength of sediments and that of the upper crust plays an important role during subduction initiation, either resulting in an upward-tilted (promoting single-vergent orogen formation) or downward-tilted (favouring a double-vergent orogen) tip of the overriding plate at the onset of collision (Table 2). A slow collision model (*slowref*) resulted in full eduction of the upper continental crust *before* slab detachment (Supplementary Figure S5A, Supplementary Movies S5) and almost full *lower* crustal eduction following slab detachment, which allows the overriding plate to revert its indented position (Supplementary Figure S5, Supplementary Movies S5). This is accompanied by significant lithospheric eduction (i.e., exhumation of the slab itself) and results in a very narrow, locked subduction interface (Supplementary Figure S5B, Supplementary Movies S5).

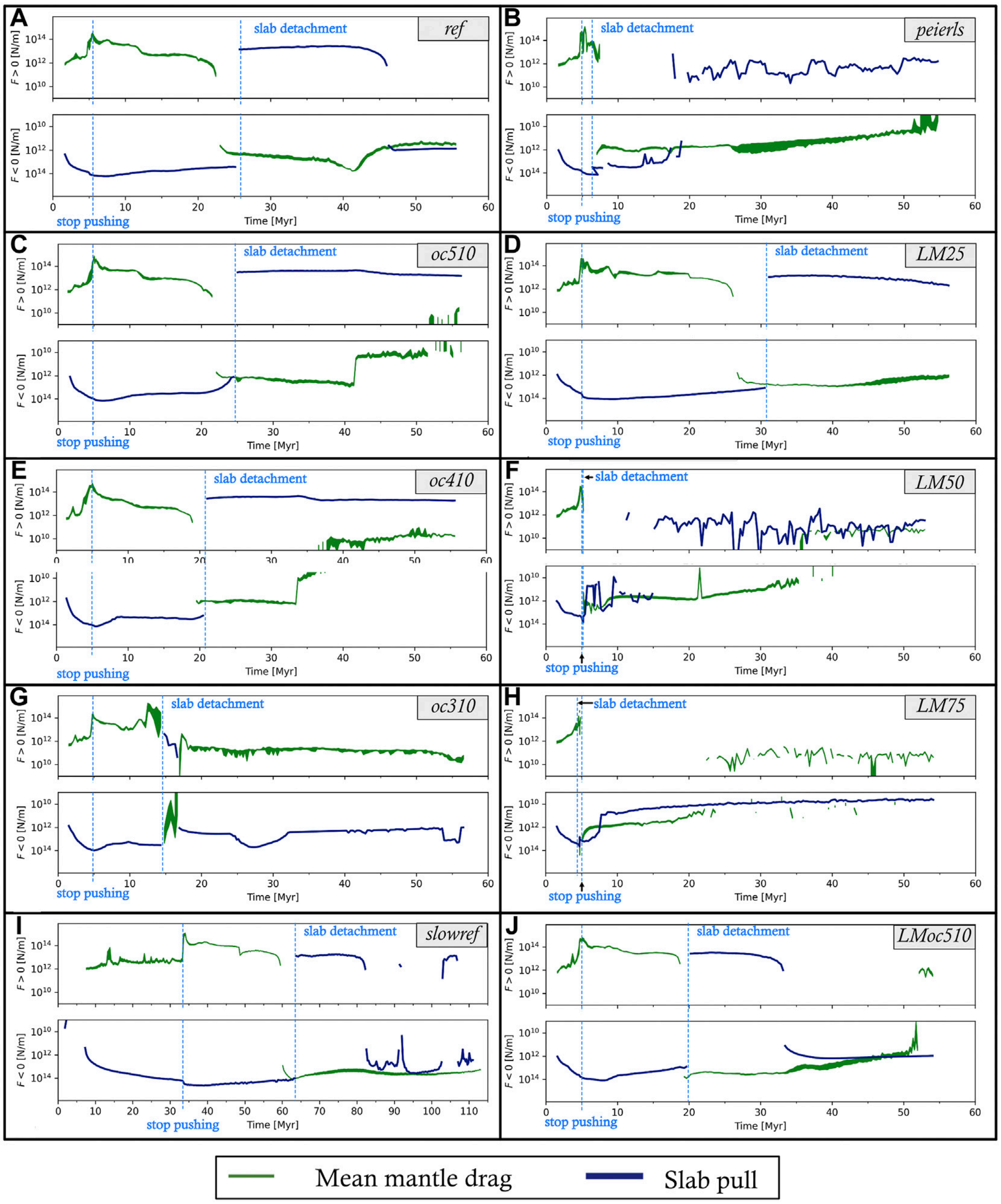

FIGURE 7
Force quantification figures for the reference model **(A)**, the oceanic length **(C,E,G)** and lithospheric mantle friction **(D,F,H,J)** parameter studies, as well as the Peierls creep **(B)** and slow-collision parameter **(I)** studies. The moment of push release and that of slab detachment are indicated on each panel. See text for further information. Note the different time axis of model *slowref*.

Furthermore, the effect of a long overriding plate was investigated with the "*reflong*" model (Table 2), where the horizontal model domain was increased by 1,000 km to 4,000 km. The overriding plate in this model is ~2,250 km long instead of ~1,250 km. During the initial stages of collision, the lithospheric mantle of the longer overriding plate locks the subduction process and the formation of an oceanic suture, preventing further continental subduction (Supplementary Figure S6C,D, Supplementary Movies S7). Therefore, no significant positively buoyant crust enters the subduction zone. The slab detaches at large depth (~350 km) at around *t* ~ 21 Myr, i.e., 4 Myr earlier than in the reference model (Supplementary Movies S1, S7). Due to the lack of positively buoyant material, the large detachment depth, and

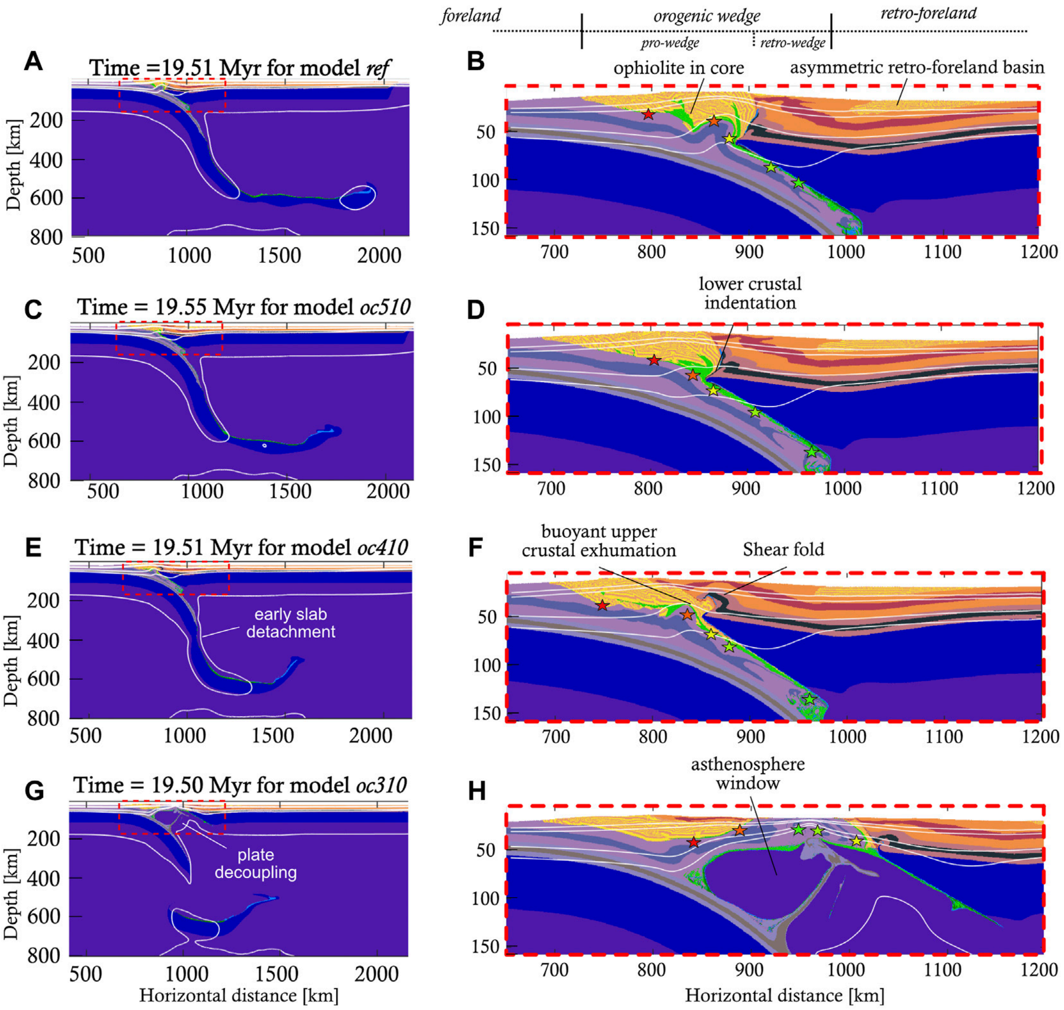

FIGURE 8
Intermediate results of the initial ocean length parameter study (Table 2), showing the differences already present at this stage. Rock composition and isotherms (100 C, 150 C, 350 C, 450 and 1300 C) are displayed and PTt markers are depicted with the usual stars. A 510 km ocean leads to more indentation of the orogen by the overriding lower crust and mantle lithosphere compared to the reference model which has a 610 km long ocean panels **(C,D)** compared to panels **(A,B)**. A 410 km long ocean leads to earlier slab detachment and a shallower retro-foreland basin. Additionally, the tip of the overriding plate has been folded into an antiformal structure **(E,F)**. When the ocean is even shorter, the plates quickly decouple **(G,H)**.

the subvertical slab position, there is no slab rebound after detachment and the model rapidly reaches a situation where tectonics ceases to be an important driver. This final tectonic quiescence is also reflected in the dynamics (Supplementary Figure S6C,D), which display a large (~-10^{14} N/m), negative slab pull and a 3 orders of magnitude weaker mantle drag. The latter is prone to changing flow direction due to its low magnitude and interaction with decoupling remnant oceanic crust (Supplementary Movies S7). This subduction channel cut-off and subsequent semi-steady state is also observed in the *thineur* model (Supplementary Figure S6E,F), in which the “European” downgoing plate has twice as long passive margins as in the reference model (Table 2). Neither of these two models display any post-detachment slab rollback.

4 Discussion

4.1 Lower crustal indentation

Deep geophysics, including reflection and refraction seismic data, constraining the deep structure of the Central Alps, have been interpreted to portray indentation of the overriding plate lower crust into the orogenic wedge (Schmid et al., 1996; Rosenberg and Kissling, 2013; Rosenberg et al., 2015). This

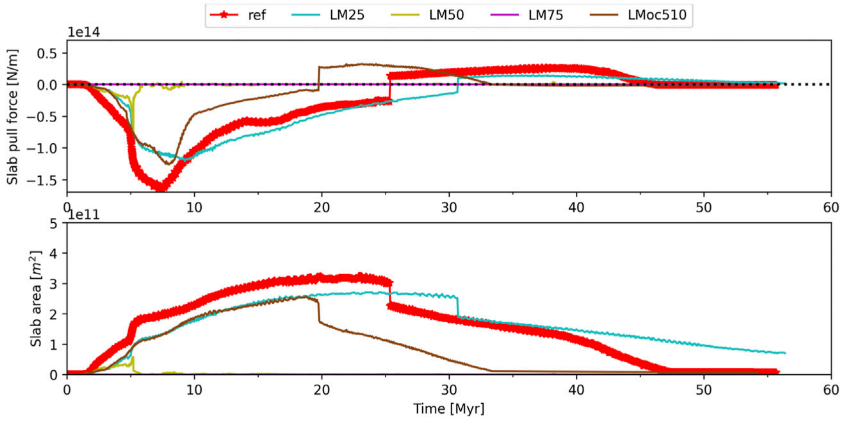

FIGURE 9
Temporal evolution of slab pull and slab area for the reference model and varying degrees of frictionally weakened lithospheric mantle (25, 50, 75, and 50% in combination with a 510 km ocean). 50% weakening or more results in slab detachment immediately after the push is stopped. Interestingly, combining 50% weakening with a slightly shorter ocean does not lead to premature slab detachment.

process leads to the emplacement of the stacked orogenic upper crust on top of the indenting downgoing plate lower crust, which in turn overlies the subducting lower crust and upper mantle of the downgoing plate (see for example plate 1 in Schmid et al., 1996). This complex geometry calls for a strong lower crust of the overriding plate, which contrasts with simple rheological models for continental crust where the lower crust is often assumed to be weaker than the upper crust (e.g. Brace and Kohlstedt, 1980; Okaya et al., 1996; Tesauro et al., 2009).

Our modelling shows that indentation by the lower crust of the overriding plate is only rarely observed, despite its strong mafic granulite rheology (Table 1). We find that lower crustal indentation occurs in two different scenarios. The first scenario involves a lower crust that behaves as a rigid indenter, for which the lower crust needs to have an intermediate to strong (e.g. plagioclase or mafic granulite) rheology. This scenario is in agreement with previous findings (Gerbault and Willingshofer, 2004; Vogt et al., 2018). We observe that this scenario of indentation is most effective when the lithospheric mantle of the overriding plate is dragged down during stage 1 (Supplementary Movies S2, S7, Figures 10A–D). The highest amount of indentation through this "active" mode of indentation is observed in model *LM25* (Supplementary Movies S6, Figures 10D, Figure 11J), which also shows the highest degree of intra-crustal decoupling and burial of the retro-foreland basin. Here, indentation occurs during the collision stage (latest stage 1, early stage 2 in Figure 1), where the accretionary wedge evolves into a double-vergent orogenic wedge. In many of our other parameter studies (not shown here) the lower crust of the overriding plate barely indents the core of the orogen.

Another scenario that leads to indentation takes place during the second and third stages (Figures 1B,C) of the model evolution. The positively buoyant, decoupled continental crust of the downgoing plate rises and flows back along the subduction channel, concentrates in the core of the orogen and uplifts the overlying units. This eduction mechanism generates orogenic widening in our models similarly to what has been described by other authors (Andersen et al., 1991; Duretz et al., 2011; Porkoláb et al., 2021). In our results this widening is more visible in the upper crustal levels, while the lower crust records lower amounts of shear reversal along the subduction plane, resulting in differential displacement between upper and lower crust. Therefore, the lower crust attains an "indented" position without actively indenting the core of the orogen, in a similar way as described for the Central Alps by Laubscher (1990), and Schmid et al. (1996). This "passive" mode of indentation is best observed in e.g. model *oc510* (Supplementary Movies S3, Figure 8D) and to a lesser extent in the reference model (Supplementary Movies S2, Figures 3D,F,H).

4.2 Slab rollback orogeny model evaluation

4.2.1 Slab detachment

The oceanic slab detaches from the downgoing plate under all parameters studied, usually at the rheological contrast between the passive margin and oceanic plate. Detachment at the passive margin is in agreement with many previous studies (e.g. Baumann et al., 2010; Baes et al., 2011; Duretz et al., 2012; Magni et al., 2012; Duretz and Gerya, 2013), which have interpreted the lateral strength contrast and crustal thickness variability at the continent-ocean transition to facilitate a localization of strain and deformation. The extensional strain from both the slab bending and the downward pull by the heavy oceanic slab is sufficient to initiate viscous necking or plastic

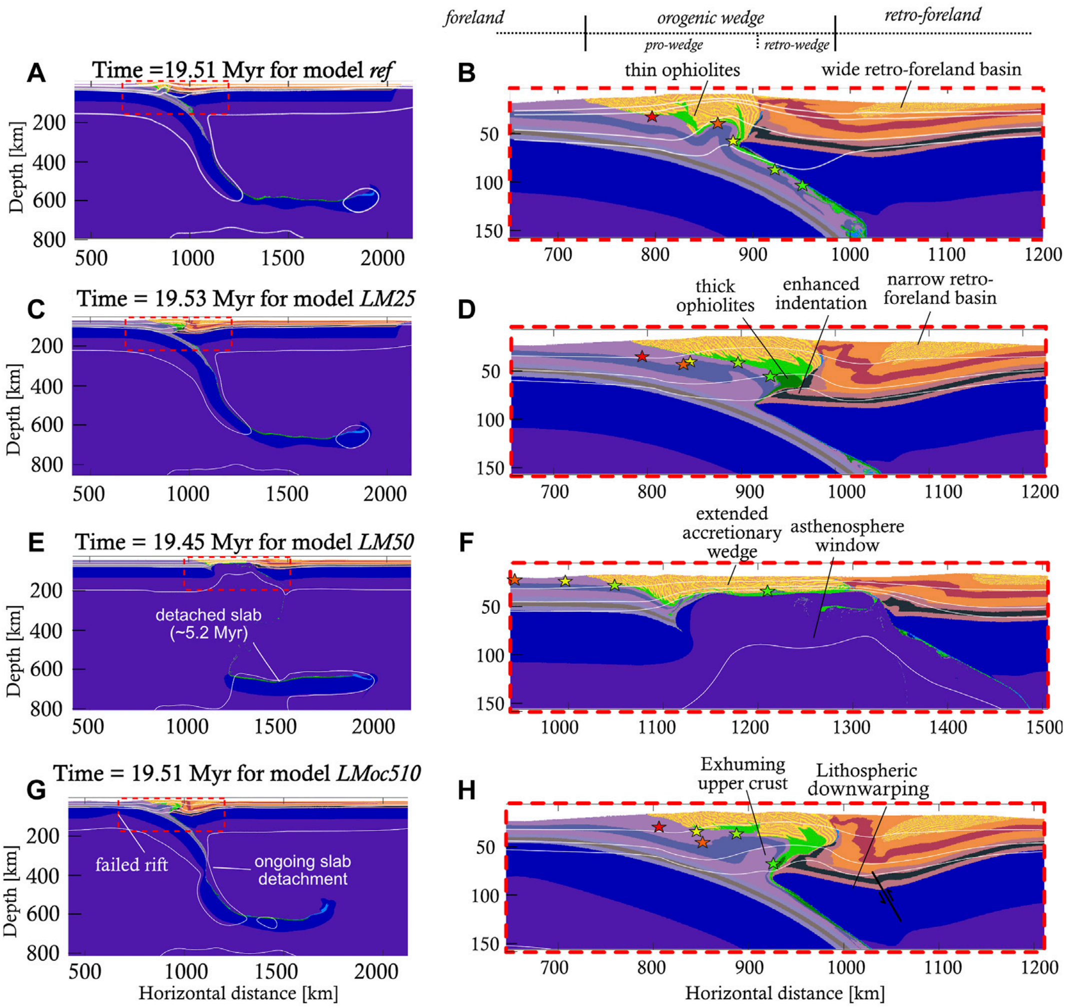

FIGURE 10
Inter-model comparison of the compositional evolution between models **(A,B)** *ref*, **(C,D)** *LM25*, **(E,F)** *LM50*, and **(G,H)** *LMoc510* during stage 2 (Figure 1), illustrating the key role of lithospheric mantle frictional strength in subduction and collision dynamics. A very weak lithospheric mantle (model *LM50*) results in premature slab detachment and rifting, but not if combined with a slightly shorter ocean (*LMoc510*).

tearing in this location (cf. Broerse et al., 2019). When the slab detaches and sinks into the mantle, it induces strong poloidal mantle flows, which interact with the orogen and take several tens of Myrs to equilibrate. The detachment depth varies from ~48 to ~600 km in our models, which is the same range observed also by the above-cited slab detachment studies (Supplementary Figure S8). Slab detachment occurs in clusters at < 200 km and >300 km depths (Supplementary Figure S8). The cluster of deep detachments mainly experiences viscous slab necking, which takes between ~1.5 and 7.0 Myr. Our models in the cluster of shallow detachments (i.e., red diamonds in Supplementary Figure S8) experience very rapid detachment (tens to a few hundred kyr) along a plastic shear zone. Both modes are also found in previous work (e.g. Sacks and Secor, 1990; Duretz et al., 2012). Duretz et al. (2012) observe that detachment through shearing is favoured when the slab dip is intermediate (35–70°). In our results shallow detachment occurs when Peierls creep is activated, when the slab is young (50 Ma) or when the lithospheric mantle is very weak (model *LM50*). If detachment happens through slow necking (model *LM25*, Supplementary Figure S2C) the orogen remains higher than when necking is faster (e.g. models *ref*, *oc510* in Supplementary Figure S2).

4.2.2 Post-detachment slab rollback

None of our modelled scenarios have resulted in either slab rollback or slab steepening after slab detachment. Instead, the slab usually rebounds upwards due to the net positive buoyancy resulting from the subducted lower crust (Figures 5, Figure 7). The slab does not rebound when no continental crust subducts (e.g. models *reflong*, *thineur*, Table 2, Supplementary Figure S6)

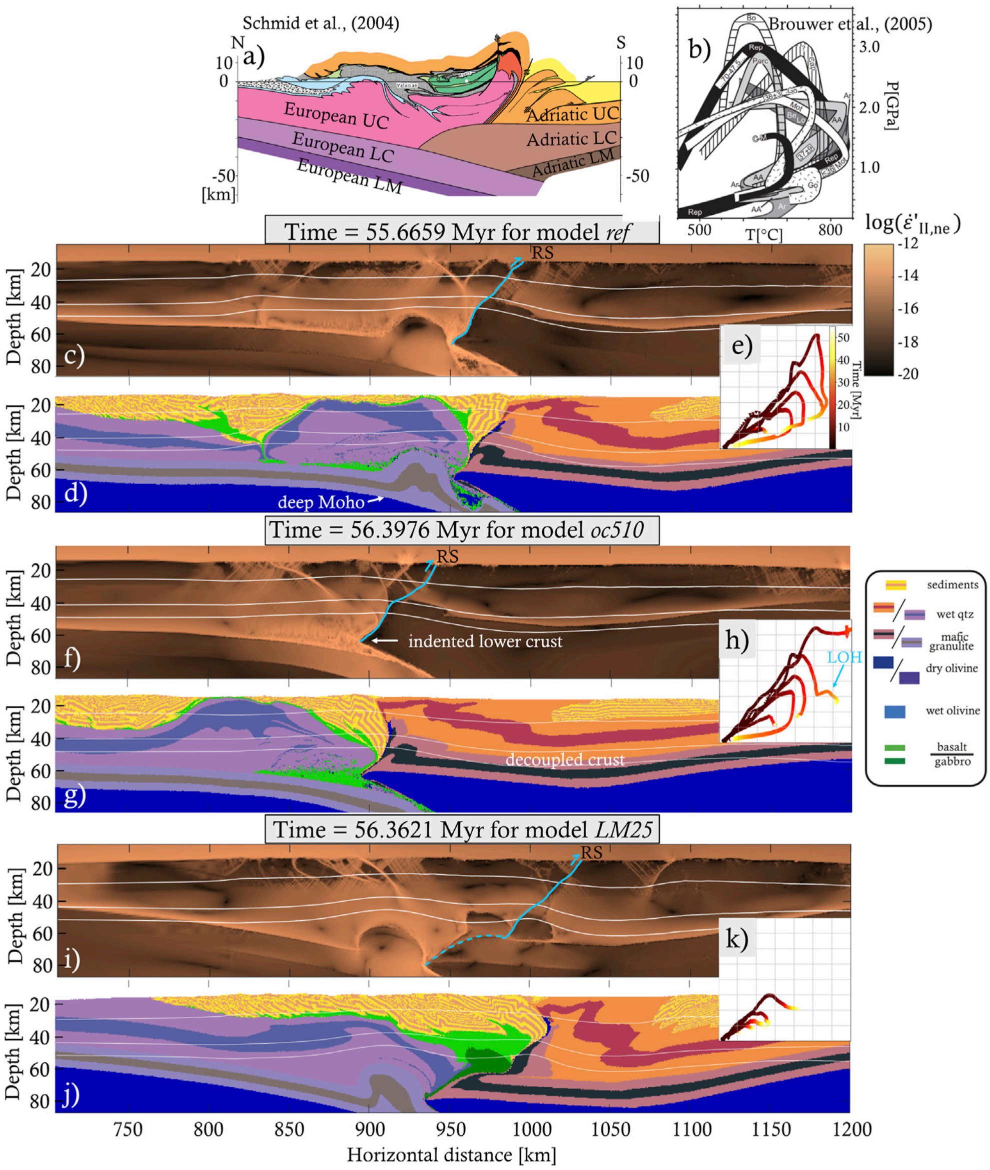

FIGURE 11
Comparison of a cross-section through the Central Alps **(A)**, modified from Schmid et al. (2004a), with composition and visco-plastic strain rate fields of models **(C,D)** *ref*, **(F,G)** *oc510* and **(I,J)** *LM25* (Table 2) at *t* ~ 56 Myr. Miniature PTt paths are shown for the models (**E,H,K**, see Figure 4) and for the Central Alps (**(B)** modified from Brouwer et al. (2005)). The trace of the retroshear **(RS)** is indicated in each model.

or when slab necking is slower than ~5 Myr (model *LM25*). Slab rebound and subsequent long-lasting slab unbending lead to eduction, which is accompanied by gravitational collapse and accumulation of exhumed crustal units in the core of the orogen. Together these processes drive orogenic widening in our models that leads to an observed trench shift towards the foreland of up to ~140 km (Supplementary Figure S2).

To instead obtain the slab steepening observed in the study of Dal Zilio et al. (2020) testing the slab rollback orogeny model, the remaining slab after detachment needs to be negatively buoyant. Negative buoyancy needs to be achieved by limiting the subduction of buoyant continental crust. Crustal subduction can be limited by a slab detachment shortly after continental collision, and when the lithospheric mantle of the overriding plate blocks crustal subduction. A comparison with the study of Dal Zilio et al. (2020) suggests that slab detachment needs to occur at the moment when 100–150 km of subduction after continental collision has occurred. Such early slab detachment at depths deeper than the passive margin would put tight constraints on the parameters that govern the strength of the downgoing plate. For instance, the continental crust would have to be stronger both frictionally and ductile, such that it resists subduction more readily. This effect is in agreement with the main differences of our model with respect to Dal Zilio et al. (2020), where a colder crust and lithosphere (a Moho temperature of 350°C compared to our 450°C) and a higher crustal friction are used. Furthermore, the plastic strength of the oceanic slab can be lowered through changes in parameters governing Peierls creep (Eq. 11), its friction, and pore fluid pressure ratio (Table 1). In addition, a lack of slab rollback may be attributed to a relatively short overriding plate, making the overriding plate more prone to move in response to changes in the stress state (e.g. Butterworth et al., 2012). However, our *reflong* model did not show post-detachment slab rollback either (Supplementary Figure S6C,D, Supplementary Movies S7). Finally, slab rollback might be facilitated by transmission of slab pull along the trench from surrounding areas where the slab has not detached yet (Duretz and Gerya, 2013), which is not accounted for by our 2D models.

4.2.3 Mantle drag

Our modelling shows that slab pull often remains positive after slab detachment for tens of millions of years, while mantle drag provides a comparable force (Figure 7). This indicates that slab pull alone cannot explain the kinematics of the collisional system. For example, the peak mantle drag generated by slab steepening in stage 1 is strong enough to emplace the orogen on top of the downgoing plate (e.g., Figure 3). Furthermore, the eduction of deeply subducted lower crust from the downgoing plate is recognisable as a broad peak in the mantle drag evolution due to asthenosphere replacing the crust (e.g. Figure 6B). The mantle drag magnitude often remains significant compared to slab pull even during stages 2 and 3. This is illustrated in Supplementary Figure S7, where the ratio of slab pull over the mantle drag is plotted over time for models *ref*, *oc510* and *LM25*. This ratio evolution can be compared with the results obtained by Candioti et al. (2021), who used the same ratio to explain crustal deformation patterns. Our observed ratio varies significantly over several orders of magnitude and is not able to explain the observed crustal deformation style (Supplementary Figure S7). This could be caused by differences in model setup and quantification methods. For example, Candioti et al. (2021) apply constant boundary velocities and use a narrower model domain (1,600 vs 3,000 km). In addition, they quantify mantle drag only on the model sides, while it is most important in the mantle wedge area in our study.

Since in most of our models neither slab pull nor mantle drag is dominant in the second and third stage (Figures 1, 3, 7), neither can be used individually to explain the behaviour of the orogen. It is the interaction between them that is most helpful in explaining the kinematics (see Section 3.1). Therefore, we propose that mantle drag could provide a useful addition to the slab rollback orogeny model.

4.3 Central Alps discussion

Our results are best applicable to the evolution of the Alps in their central sector, illustrated by the evolution of the well-studied NFP20 east transect (Figure 11A e. g. Schmid et al., 1996; Schmid et al., 2004a among others). The Central Alpine section is also the section for which the SRO model was originally proposed (Schlunegger and Kissling, 2015; Kissling and Schlunegger, 2018; Dal Zilio et al., 2020). A comparison of our models *ref*, *oc510* and *LM25* to the tectonic interpretation of this transect (Figure 11) shows numerous similarities in terms of kinematics, retroshear exhumation and indentation, as well as burial and exhumation mechanisms. The crustal thickening creates similar Moho depth geometries that reach 60–70 km beneath the orogen. The overall evolution shows significant initial burial followed by large-scale exhumation of the downgoing plate crustal material by its incorporation in the orogen and retroshear thrusting. The centrally exhumed area separates a zone of significant deformation of sediments, originally deposited on the European margin and the adjacent ocean in the fore-shear domain (foreland basin and neighbouring accretionary wedge), from highly deformed and exhumed sediments deposited originally over the oceanic and Adriatic domain in the retroshear zone (Figures 11C–G). However, the central area shows more symmetric exhumation and our models do not show far-travelled Adriatic nappes, as interpreted for the NFP20 east profile (compare Figure 11A with Figures 11D,G,J). The entire overriding plate crust is coupled by the deformation, resulting in significant exhumation in the footwall of the retroshear in a similar fashion as the post-Eocene (mostly post-Oligocene) exhumation of the Adriatic crust in the Central Alps (e.g. Rosenberg et al., 2015 among others). While models *ref* and *oc510* show only retroshear exhumation and coupling of the overriding plate crust (Figures 11C–G), model *LM25* shows an initial retroshear exhumation, followed by active indentation of the overriding plate lower crust (Figures 11I,J). The latter model is more realistic in terms of Central Alps structure evolution where the Eocene-Oligocene accretion, continental collision and retroshear exhumation along the Insubric line was followed by a post-Oligocene Adriatic indentation, although the exact age of the indentation is still debated (see discussion in Laubscher, 1990; Schmid et al., 1996; Schmid et al., 2004a; Rosenberg et al., 2015; Rosenberg et al., 2018). However, this latter *LM25* profile shows less exhumation than the NFP 20 east transect and is more similar with the NFP20 west profile (compare with Figures 3B,C in Schmid et al., 2004a). Most models show burial and exhumation curves that are similar with existing Alps PTt paths (e.g. Brouwer et al., 2005) containing high-pressure-low-temperature events during metamorphism, although peak PT conditions are underestimated in model *LM25* (Figure 4F, Figure 11K). In particular model *oc510* shows peak pressures and temperatures that are fairly similar to the ones observed in the Central Alps (Figures 4C, 11B,E). The similarity continues further in more detail, for instance the marker starting at $x = 1{,}050$ km shows late orogenic heating (LOH, Figure 11H), which is fairly similar to the interpretation of the Lepontine gneisses in the Central Alps (Brouwer et al., 2004). The average surface topography is 2.9 km for model *ref*, 3.0 km for model *oc510* and 3.7 km for model *LM25* (Supplementary Figure S2), which is in between isostatically balanced predictions and observations (e.g. Kissling, 1993). All our models predict the formation of a thick-skinned thrust wedge that affect sediments deposited far in the Adriatic hinterland (i.e., the retro-foreland basin), in a similar fashion to what is observed in the Southern Alps and their Po Plain foredeep (e.g. Pfiffner, 2016).

Our models simulate a significant slab rebound and eduction after detachment through initial elastic deformation followed by viscous unbending over tens of millions of years (Figure 5). Analysis of the final stress fields shows that the retro-*wedge* is under compression, but most of the retro-*foreland* is not (Supplementary Figure S9), which is not in agreement with observations in the Southern Alps and their foredeep where the shortening continues at present (e.g. Di Bucci and Angeloni, 2013). In our models the compression in the orogen is induced by the upper crust of the downgoing plate that accumulates within the orogen during eduction and subsequent gravitational collapse (Supplementary Figure S1B). The compression in the orogen is not transferred past the retro-wedge into the retro-foreland. Moreover, the extension in the Central Alps was parallel to the orogen, connected with the mechanics of the adjacent Western and Eastern Alps, driven by the 3D processes of oroclinal bending and lateral extrusion (Ratschbacher et al., 1991; Mancktelow, 1992; Schmid et al., 1996; Schmid and Kissling, 2000; Pfiffner, 2016), which are not available in our models due to their inherent 2D limitations. Furthermore, the topography of models is exaggerated (by 0.9–1.7 km, Supplementary Figure S2) when compared to nature, which may induce an additional component of extension driven by an increased gravitational potential. Despite these shortcomings, our modelling shows that an orogen such as the Alps requires eduction associated with extension in a theoretical cylindrical version. Such extension is orogen-perpendicular in our models, but in nature it is orogen-parallel driven by the non-cylindrical 3D processes of oroclinal bending and lateral extrusion, which in fact are the result of the interaction with the orogens located at the terminations of the Alps, i.e. the Apennines and Carpathians (e.g. Ratschbacher et al., 1991; Schmid et al., 2013; Schmid et al., 2017; Király et al., 2021).

In context of the Adria-Europe collision, the downgoing plate was not completely oceanic, but characterised by a wide, thinned continental margin, which contained a continental fragment, i.e. the Briançonnais microcontinent (Dewey et al., 1989; Stampfli et al., 1998; Schmid et al., 2004a; Handy et al., 2010; Pfiffner, 2016). It is generally accepted that the lower crust of the thinned passive margin and the Briançonnais fragment have been subducted together with the lithospheric mantle (Schmid et al., 2004a; Pfiffner, 2016). However, due to the implementation of an instantaneous erosion/sedimentation mechanism in our models, the sediment thickness on the oceanic domain is likely overestimated, partly compensating for this deficit of positively buoyant material. A qualitative comparison of the area of the orogenic wedge of the NFP20 East cross-section with the reference model shows that wedge areas and partitioning between upper crust, sediments and lower crusts are similar (Supplementary Figure S10), thus exerting buoyancy forces of similar magnitude on the system. However, we acknowledge that including a continental sliver may affect the timing and intensity of slab steepening (Brun and Faccenna, 2008), which together with poloidal mantle flow may be expected to slow down subduction. Peak slab pull and mantle drag would likely be reduced. Future studies could significantly benefit from further investigating the influence of the Briançonnais microcontinent on the subduction system.

The unbending and simultaneous eduction in our models (*sensu* Andersen et al., 1991) generate uplift and widening of the orogen, exert shear and normal strain on the subduction channel, and hence promote a rheological decoupling of upper and lower crustal rocks from the downgoing plate. Moreover, even when the slab pull attains (minor) negative values in the final stages of model evolution, it is still insufficient to induce slab rollback, as discussed above. Particularly, for the Central Alps its present-day convergence may be driven by more complex (three-dimensional) processes, such as the 3D kinematics, rotation and lateral escape associated with the Adriatic indentation, while significant oroclinal processes affected its western sector during the final phases of post-collisional evolution (Schmid et al., 2004a; Rosenberg et al., 2015).

4.4 Model limitations

The main limitation of our study is the absence of changes in the third, along-strike direction. This was necessary in order to accurately study the dynamics of this system at a high enough resolution for many different parameters. However, orogen-parallel deformation is often relevant and particularly for the Central Alps since 8 Ma (Handy et al., 2010; Krstekanić et al., 2020; Van Hinsbergen et al., 2020; Király et al., 2021). Not accounting for orogen-parallel deformation 1) overestimates topography (Gerbault and Willingshofer, 2004), 2) eliminates 3D processes from causing lower crustal indentation (e.g. Schmid and Kissling, 2000), and 3) may also explain the absence of post-detachment convergence (see Section 4.2). Besides the orogen-parallel extension discussed above, comparing our two-dimensional models to two-dimensional cross-sections neglects the right-lateral displacement along the Peri-Adriatic fault system. This means that the Adriatic margin captured in our cross-sections was located further to the east at the time of collision (Schmid et al., 1996; Pfiffner, 2016). Finally, the lack of a third dimension means that we do not account for toroidal mantle flow, which dominates during slab steepening and rollback (e.g. Schellart and Moresi, 2013). However, due to the limited post-detachment trench retreat and/or slab rollback in our study, toroidal flow is expected to have only minor effects (e.g. a slightly weaker mantle drag).

Several processes in our modelling are absent or simplified, including melting leading to volcanism (e.g. Faccenda et al., 2008; Faccenda et al., 2009) and grain size evolution (Bercovici and Ricard, 2014; Schierjott et al., 2020). Furthermore, our simplified erosion and sedimentation implementation that instantaneously removes/deposits material above/below prescribed topographic levels ignores sediment transport (e.g. Garzanti et al., 2007; Garzanti and Malusà, 2008) . However, despite the relatively high erosion level (10 km above mountain area) most models show a modest to large extent of exhumation (Figure 4). The relatively high (~3 km on average) final topography may be reduced by implementing erosion and sedimentation more accurately (as done in e.g. Malatesta et al., 2013).

5 Conclusion

We quantify continental collision dynamics in two-dimensional thermomechanical models to investigate the partitioning between slab pull and mantle drag in Alpine-style orogens under a wide range of parameters. We find that neither slab pull nor mantle drag by itself is able to explain the orogenic evolution. Our detailed comparison between the vertical slab pull and horizontal mantle drag demonstrates that these forces are in fact of similar magnitude during large parts of an orogenic cycle and interact with each other. We observe no post-detachment slab rollback or steepening in the wide parameter space explored here.

Our parameter studies show that continental collision dynamics are most strongly influenced by initial length and age of the oceanic plate, the activation of the Peierls creep mechanism, the frictional strength of the lithospheric mantle, and the lower crustal rheology of the overriding plate. These parameters affect the depth and timing of slab detachment, which dictates the post-detachment evolution of the orogenic system. Other parameters, such as convergence rate, rather influence the style of crustal deformation and burial-exhumation cycle and not the evolution of the mantle drag and slab pull forces.

The results of this study illustrate the need for quantitative analysis in numerical modelling studies. Especially in two dimensions it is straightforward to quantify forces (Appendix A). Force quantification in dynamic numerical models of continental collision allows for a more intuitive analysis of modelling results. Instead of ascribing kinematic events in the model to other motions in the model, we should use more complete quantification exemplified here to explain kinematics of the subduction-collision cycle. Moreover, it is a useful tool in the comparison of modelling results to forces acting in natural systems.

Data availability statement

Essential raw data used to make key figures are freely available at https://doi.org/10.5281/zenodo.6784339. Other raw data generated and analysed for this study will be made available by the authors on request. Post-processing scripts, the compiled model source code, initialisation files and force quantification data will be made available on www.github.com/LvAprograms/vanAgtmaaletal-2022-frontiers.

Author contributions

YD and LA conceptualised and designed the study. All authors contributed to the model setup. LA ran and analysed the models under the supervision of YD. LA wrote and ran force quantification post-processing scripts and PTt tracking/extraction algorithms. LA wrote the manuscript and all authors revised the manuscript.

Funding

ETH Zürich library: covers open access publication fees.

Acknowledgments

We warmly thank ETH Zürich for giving LA the time to write this manuscript based on his MSc thesis, since it was not part of his PhD work in the ETH+ project BECCY. In particular, we thank Taras Gerya and Luca dal Zilio for their codes. We acknowledge the very useful corrections and suggestions for improvement of Adrian Pfiffner and two reviewers that have significantly improved the quality of our research.

Conflict of interest

The authors declare that the research was conducted in the absence of any commercial or financial relationships that could be construed as a potential conflict of interest.

Publisher's note

Supplementary material

The Supplementary Material for this article can be found online at: https://www.frontiersin.org/articles/10.3389/feart.2022.916189/full#supplementary-material

References

Alvarez, W. (2010). Protracted continental collisions argue for continental plates driven by basal traction. *Earth Planet. Sci. Lett.* 296 (3–4), 434–442. doi:10.1016/j.epsl.2010.05.030

Andersen, T. B., Jamtveit, B., Dewey, J. F., and Swensson, E. (1991). Subduction and eduction of continental crust: Major mechanisms during continent-continent collision and orogenic extensional collapse, a model based on the south Norwegian Caledonides. *Terra* 3 (3), 303–310. doi:10.1111/j.1365-3121.1991.tb00148.x

Argand, E. (1916). *Sur l'arc des Alpes occidentales*. Lausanne: G. Bridel.

Auzemery, A., Willingshofer, E., Yamato, P., Duretz, T., and Sokoutis, D. (2020). Strain localization mechanisms for subduction initiation at passive margins. *Glob. Planet. Change* 195, 103323. doi:10.1016/j.gloplacha.2020.103323

Baes, M., Govers, R., and Wortel, R. (2011). Subduction initiation along the inherited weakness zone at the edge of a slab: Insights from numerical models. *Geophys. J. Int.* 184 (3), 991–1008. doi:10.1111/j.1365-246X.2010.04896.x

Barazangi, M., and Isacks, B. L. (1979). Subduction of the Nazca plate beneath Peru: Evidence from spatial distribution of earthquakes. *Geophys. J. Int.* 57 (3), 537–555. doi:10.1111/j.1365-246X.1979.tb06778.x

Baumann, C., Gerya, T. V., and Connolly, J. A. (2010). Numerical modelling of spontaneous slab breakoff dynamics during continental collision. *Geol. Soc. Lond. Spec. Publ.* 332 (1), 99–114. doi:10.1144/sp332.7

Bercovici, D., and Ricard, Y. (2014). Plate tectonics, damage and inheritance. *Nature* 508 (7497), 513–516. doi:10.1038/nature13072

Brace, W. F., and Kohlstedt, D. L. (1980). Limits on lithospheric stress imposed by laboratory experiments. *J. Geophys. Res.* 85 (B11), 6248–6252. doi:10.1029/JB085iB11p06248

Broerse, T., Norder, B., Govers, R., Sokoutis, D., Willingshofer, E., and Picken, S. J. (2019). New analogue materials for nonlinear lithosphere rheology, with an application to slab break-off. *Tectonophysics* 756, 73–96. doi:10.1016/j.tecto.2018.12.007

Brouwer, F., Burri, T., Engi, M., and Berger, A. (2005). "Eclogite relics in the central Alps: PT - evolution, Lu-Hf ages and implications for formation of tectonic mélange zones," in *Schweizerische mineralogische und petrographische mitteilungen*, 85, 147–174.

Brouwer, F., Van De Zedde, D., Wortel, M., and Vissers, R. (2004). Late-orogenic heating during exhumation: Alpine PTt trajectories and thermomechanical models. *Earth Planet. Sci. Lett.* 220 (1–2), 185–199. doi:10.1016/s0012-821x(04)00050-0

Brun, J.-P. (2002). Deformation of the continental lithosphere: Insights from brittle-ductile models. *Geol. Soc. Lond. Spec. Publ.* 200 (1), 355–370. doi:10.1144/GSL.SP.2001.200.01.20

Brun, J.-P., and Faccenna, C. (2008). Exhumation of high-pressure rocks driven by slab rollback. *Earth Planet. Sci. Lett.* 272 (1), 1–7. doi:10.1016/j.epsl.2008.02.038

Burov, E. B. (2011). Rheology and strength of the lithosphere. *Mar. Petroleum Geol.* 28 (8), 1402–1443. doi:10.1016/j.marpetgeo.2011.05.008

Butterworth, N. P., Quevedo, L., Morra, G., and Müller, R. D. (2012). Influence of overriding plate geometry and rheology on subduction. *Geochem. Geophys. Geosyst.* 13 (6). doi:10.1029/2011GC003968

Calais, E., Nocquet, J.-M., Jouanne, F., and Tardy, M. (2002). Current strain regime in the western Alps from continuous global positioning system measurements, 1996–2001. *Geol.* 30 (7), 651–654. doi:10.1130/0091-7613(2002)030<0651:csritw>2.0.co;2

Candioti, L. G., Duretz, T., Moulas, E., and Schmalholz, S. M. (2021). Buoyancy versus shear forces in building orogenic wedges. *Solid* 12 (8), 1749–1775. doi:10.5194/se-12-1749-2021

Celâl Şengör, A. M. (1990). plate tectonics and orogenic research after 25 years: A tethyan perspective. *Earth-Science Rev.* 27 (1), 1–201. doi:10.1016/0012-8252(90)90002-D

Christensen, U. R., and Yuen, D. A. (1985). Layered convection induced by phase transitions. *J. Geophys. Res.* 90 (B12), 10291–10300. doi:10.1029/JB090iB12p10291

Conrad, C. P., and Lithgow-Bertelloni, C. (2002). How mantle slabs drive plate tectonics. *Science* 298 (5591), 207–209. doi:10.1126/science.1074161

D'Agostino, N., Avallone, A., Cheloni, D., D'Anastasio, E., Mantenuto, S., and Selvaggi, G. (2008). Active tectonics of the Adriatic region from GPS and earthquake slip vectors. *J. Geophys. Res.* 113 (B12), B12413. doi:10.1029/2008JB005860

Dal Zilio, L., Kissling, E., Gerya, T., and van Dinther, Y. (2020). Slab rollback orogeny model: A test-of-concept. *Geophys. Res. Lett.* 47, e2020GL089917. doi:10.1029/2020gl089917

Dal Zilio, L., van Dinther, Y., Gerya, T. V., and Pranger, C. C. (2018). Seismic behaviour of mountain belts controlled by plate convergence rate. *Earth Planet. Sci. Lett.* 482, 81–92. doi:10.1016/j.epsl.2017.10.053

Deichmann, N. (1992). Structural and rheological implications of lower-crustal earthquakes below northern Switzerland. *Phys. Earth Planet. Interiors* 69 (3), 270–280. doi:10.1016/0031-9201(92)90146-M

Dewey, J. F., and Bird, J. M. (1970). Mountain belts and the new global tectonics. *J. Geophys. Res.* 75 (14), 2625–2647. doi:10.1029/JB075i014p02625

Dewey, J. F., and Burke, K. (1974). Hot spots and continental break-up: Implications for collisional orogeny. *Geol.* 2 (2), 57. doi:10.1130/0091-7613(1974)2<57:HSACBI>2.0.CO;2

Dewey, J. F., Helman, M., Knott, S., Turco, E., and Hutton, D. (1989). Kinematics of the Western mediterranean. *Geol. Soc. Lond. Spec. Publ.* 45 (1), 265–283. doi:10.1144/gsl.sp.1989.045.01.15

Di Bucci, D., and Angeloni, P. (2013). Adria seismicity and seismotectonics: Review and critical discussion. *Mar. Petroleum Geol.* 42, 182–190. doi:10.1016/j.marpetgeo.2012.09.005

Doglioni, C., Carminati, E., Cuffaro, M., and Scrocca, D. (2007). Subduction kinematics and dynamic constraints. *Earth-Science Rev.* 83 (3), 125–175. doi:10.1016/j.earscirev.2007.04.001

Duretz, T., and Gerya, T. (2013). Slab detachment during continental collision: Influence of crustal rheology and interaction with lithospheric delamination. *Tectonophysics* 602, 124–140. doi:10.1016/j.tecto.2012.12.024

Duretz, T., Gerya, T. V., and May, D. A. (2011). Numerical modelling of spontaneous slab breakoff and subsequent topographic response. *Tectonophysics* 502 (1–2), 244–256. doi:10.1016/j.tecto.2010.05.024

Duretz, T., Schmalholz, S., and Gerya, T. (2012). Dynamics of slab detachment. *Geochem. Geophys. Geosyst.* 13 (3), 2453. doi:10.1029/2011gc004024

Ellis, S. (1996). Forces driving continental collision: Reconciling indentation and mantle subduction tectonics. *Geol.* 24 (8), 699–702. doi:10.1130/0091-7613(1996)024<0699:fdccri>2.3.co;2

Erdős, Z., Huismans, R. S., Faccenna, C., and Wolf, S. G. (2021). The role of subduction interface and upper plate strength on back-arc extension: Application to mediterranean back-arc basins. *Tectonics* 40 (8), e2021TC006795. doi:10.1029/2021TC006795

Evans, B., and Goetze, C. (1979). The temperature variation of hardness of olivine and its implication for polycrystalline yield stress. *J. Geophys. Res.* 84 (B10), 5505–5524. doi:10.1029/jb084ib10p05505

Faccenda, M., Gerya, T. V., and Chakraborty, S. (2008). Styles of post-subduction collisional orogeny: Influence of convergence velocity, crustal rheology and radiogenic heat production. *Lithos* 103 (1–2), 257–287. doi:10.1016/j.lithos.2007.09.009

Faccenda, M., Minelli, G., and Gerya, T. (2009). Coupled and decoupled regimes of continental collision: Numerical modeling. *Earth Planet. Sci. Lett.* 278 (3–4), 337–349. doi:10.1016/j.epsl.2008.12.021

Faccenna, C., Becker, T. W., Auer, L., Billi, A., Boschi, L., Brun, J. P., et al. (2014). Mantle dynamics in the mediterranean. *Rev. Geophys.* 52 (3), 283–332. doi:10.1002/2013RG000444

Faccenna, C., Becker, T. W., Conrad, C. P., and Husson, L. (2013). Mountain building and mantle dynamics. *Tectonics* 32 (1), 80–93. doi:10.1029/2012TC003176

Garzanti, E., Doglioni, C., Vezzoli, G., and Andò, S. (2007). Orogenic belts and orogenic sediment provenance. *J. Geol.* 115 (3), 315–334. doi:10.1086/512755

Garzanti, E., and Malusà, M. G. (2008). The Oligocene Alps: Domal unroofing and drainage development during early orogenic growth. *Earth Planet. Sci. Lett.* 268 (3), 487–500. doi:10.1016/j.epsl.2008.01.039

Gerbault, M., and Willingshofer, E. (2004). Lower crust indentation or horizontal ductile flow during continental collision? *Tectonophysics* 387 (1–4), 169–187. doi:10.1016/j.tecto.2004.06.012

Gerya, T. V. (2019). *Introduction to numerical geodynamic modelling*. 2nd ed. Cambridge, United Kingdom: Cambridge University Press. doi:10.1017/9781316534243

Gerya, T. V., and Yuen, D. A. (2003). Characteristics-based marker-in-cell method with conservative finite-differences schemes for modeling geological flows with strongly variable transport properties. *Phys. Earth Planet. Interiors* 140 (4), 293–318. doi:10.1016/j.pepi.2003.09.006

Gerya, T. V., and Yuen, D. A. (2007). Robust characteristics method for modelling multiphase visco-elasto-plastic thermo-mechanical problems. *Phys. Earth Planet. Interiors* 163 (1), 83–105. doi:10.1016/j.pepi.2007.04.015

Handy, M. R., Schmid, S. M., Bousquet, R., Kissling, E., and Bernoulli, D. (2010). Reconciling plate-tectonic reconstructions of Alpine Tethys with the geological-geophysical record of spreading and subduction in the Alps. *Earth-Science Rev.* 102 (3–4), 121–158. doi:10.1016/j.earscirev.2010.06.002

Hubbard, J., Almeida, R., Foster, A., Sapkota, S. N., Bürgi, P., and Tapponnier, P. (2016). Structural segmentation controlled the 2015 Mw 7.8 Gorkha earthquake rupture in Nepal. *Geology* 44 (8), 639–642. doi:10.1130/G38077.1

Jolivet, L., Faccenna, C., Becker, T., Tesauro, M., Sternai, P., and Bouilhol, P. (2018). Mantle flow and deforming continents: From India-asia convergence to pacific subduction. *Tectonics* 37 (9), 2887–2914. doi:10.1029/2018TC005036

Jolivet, L., Faccenna, C., Goffé, B., Burov, E., and Agard, P. (2003). Subduction tectonics and exhumation of high-pressure metamorphic rocks in the Mediterranean orogens. *Am. J. Sci.* 303 (5), 353–409. doi:10.2475/ajs.303.5.353

Krstekanić, N., Matenco, L., Toljić, M., Mandic, O., Stojadinovic, U., and Willingshofer, E. (2020). Understanding partitioning of deformation in highly arcuate orogenic systems: Inferences from the evolution of the Serbian Carpathians. *Glob. Planet. Change* 195, 103361. doi:10.1016/j.gloplacha.2020.103361

Katayama, I., and Karato, S. (2008). Low-temperature, high-stress deformation of olivine under water-saturated conditions. *Phys. Earth Planet. Interiors* 168 (3–4), 125–133. doi:10.1016/j.pepi.2008.05.019

Király, Á., Funiciello, F., Capitanio, F. A., and Faccenna, C. (2021). Dynamic interactions between subduction zones. *Glob. Planet. Change* 202, 103501. doi:10.1016/j.gloplacha.2021.103501

Kissling, E. (1993). Deep structure of the Alps—what do we really know? *Phys. Earth Planet. Interiors* 79 (1), 87–112. doi:10.1016/0031-9201(93)90144-X

Kissling, E., and Schlunegger, F. (2018). Rollback orogeny model for the evolution of the Swiss Alps. *Tectonics* 37 (4), 1097–1115. doi:10.1002/2017tc004762

Laubscher, H. P. (1990). "Deep seismic data from the central Alps: Mass distributions and their kinematics," in *Mémoires de La Société Géologique de France*, 156, 335–343.

Liao, J., and Gerya, T. (2017). Partitioning of crustal shortening during continental collision: 2-D thermomechanical modeling. *J. Geophys. Res. Solid Earth* 122 (1), 592–606. doi:10.1002/2016jb013398

Lippitsch, R., Kissling, E., and Ansorge, J. (2003). Upper mantle structure beneath the Alpine orogen from high-resolution teleseismic tomography. *J. Geophys. Res.* 108 (B8), 2376. doi:10.1029/2002jb002016

Luth, S., Willingshofer, E., Sokoutis, D., and Cloetingh, S. (2010). Analogue modelling of continental collision: Influence of plate coupling on mantle lithosphere subduction, crustal deformation and surface topography. *Tectonophysics* 484 (1–4), 87–102. doi:10.1016/j.tecto.2009.08.043

Magni, V., van Hunen, J., Funiciello, F., and Faccenna, C. (2012). Numerical models of slab migration in continental collision zones. *Solid* 3 (2), 293–306. doi:10.5194/se-3-293-2012

Malatesta, C., Gerya, T., Crispini, L., Federico, L., and Capponi, G. (2013). Oblique subduction modelling indicates along-trench tectonic transport of sediments. *Nat. Commun.* 4 (1), 2456. doi:10.1038/ncomms3456

Mancktelow, N. S. (1992). Neogene lateral extension during convergence in the Central Alps: Evidence from interrelated faulting and backfolding around the Simplonpass (Switzerland). *Tectonophysics* 215 (3), 295–317. doi:10.1016/0040-1951(92)90358-D

Massonne, H.-J. (2016). Hydration of the lithospheric mantle by the descending plate in a continent–continent collisional setting and its geodynamic consequences. *J. Geodyn.* 96, 50–61. doi:10.1016/j.jog.2015.06.006

Matenco, L., Krézsek, C., Merten, S., Schmid, S., Cloetingh, S., and Andriessen, P. (2010). Characteristics of collisional orogens with low topographic build-up: An example from the Carpathians. *Terra* 22 (3), 155–165. doi:10.1111/j.1365-3121.2010.00931.x

Métois, M., D'Agostino, N., Avallone, A., Chamot-Rooke, N., Rabaute, A., Duni, L., et al. (2015). Insights on continental collisional processes from GPS data: Dynamics of the peri-Adriatic belts. *J. Geophys. Res. Solid Earth* 120 (12), 8701–8719. doi:10.1002/2015JB012023

Michel, S., Jolivet, R., Rollins, C., Jara, J., and Dal Zilio, L. (2021). Seismogenic potential of the main himalayan thrust constrained by coupling segmentation and earthquake scaling. *Geophys. Res. Lett.* 48 (13), e2021GL093106. doi:10.1029/2021GL093106

Mitterbauer, U., Behm, M., Brückl, E., Lippitsch, R., Guterch, A., Keller, G. R., et al. (2011). Shape and origin of the East-Alpine slab constrained by the ALPASS teleseismic model. *Tectonophysics* 510 (1–2), 195–206. doi:10.1016/j.tecto.2011.07.001

Okaya, N., Cloetingh, S., and Mueller, St. (1996). A lithospheric cross-section through the Swiss Alps-II. Constraints on the mechanical structure of a continent-continent collision zone. *Geophys. J. Int.* 127 (2), 399–414. doi:10.1111/j.1365-246X.1996.tb04729.x

Paffrath, M., Friederich, W., Schmid, S. M., and Handy, M. R. (2021). amp; the AlpArray and AlpArray-Swath D Working GroupImaging structure and geometry of slabs in the greater Alpine area – a P-wave travel-time tomography using AlpArray Seismic Network data. *Solid* 12 (11), 2671–2702. doi:10.5194/se-12-2671-2021

Pfiffner, O. A. (2016). Basement-involved thin-skinned and thick-skinned tectonics in the Alps. *Geol. Mag.* 153 (5–6), 1085–1109. doi:10.1017/S0016756815001090

Porkoláb, K., Duretz, T., Yamato, P., Auzemery, A., and Willingshofer, E. (2021). Extrusion of subducted crust explains the emplacement of far-travelled ophiolites. *Nat. Commun.* 12 (1), 1499. doi:10.1038/s41467-021-21866-1

Ranalli, G. (1995). *Rheology of the Earth*. Springer Science & Business Media.

Ratschbacher, L., Frisch, W., Linzer, H.-G., and Merle, O. (1991). Lateral extrusion in the eastern Alps, PArt 2: Structural analysis. *Tectonics* 10 (2), 257–271. doi:10.1029/90TC02623

Rosenberg, C. L., Berger, A., Bellahsen, N., and Bousquet, R. (2015). Relating orogen width to shortening, erosion, and exhumation during Alpine collision. *Tectonics* 34 (6), 1306–1328. doi:10.1002/2014tc003736

Rosenberg, C. L., and Kissling, E. (2013). Three-dimensional insight into Central-Alpine collision: Lower-plate or upper-plate indentation? *Geology* 41 (12), 1219–1222. doi:10.1130/g34584.1

Rosenberg, C. L., Schneider, S., Scharf, A., Bertrand, A., Hammerschmidt, K., Rabaute, A., et al. (2018). Relating collisional kinematics to exhumation processes in the Eastern Alps. *Earth-Science Rev.* 176, 311–344. doi:10.1016/j.earscirev.2017.10.013

Royden, L. (1996). Coupling and decoupling of crust and mantle in convergent orogens: Implications for strain partitioning in the crust. *J. Geophys. Res.* 101 (B8), 17679–17705. doi:10.1029/96JB00951

Rudnick, R. L., and Fountain, D. M. (1995). Nature and composition of the continental crust: A lower crustal perspective. *Rev. Geophys.* 33 (3), 267–309. doi:10.1029/95RG01302

Sandiford, M., Coblentz, D., and Schellart, W. P. (2005). Evaluating slab-plate coupling in the Indo-Australian plate. *Geology* 33 (2), 113–116.

Schellart, W. P., and Moresi, L. (2013). A new driving mechanism for backarc extension and backarc shortening through slab sinking induced toroidal and poloidal mantle flow: Results from dynamic subduction models with an overriding plate. *J. Geophys. Res. Solid Earth* 118 (6), 3221–3248. doi:10.1002/jgrb.50173

Sacks, P. E., and Secor, D. T., Jr. (1990). Delamination in collisional orogens. *Geol.* 18 (10), 999. doi:10.1130/0091-7613(1990)018<0999:DICO>2.3.CO;2

Schierjott, J. C., Thielmann, M., Rozel, A. B., Golabek, G. J., and Gerya, T. V. (2020). Can grain size reduction initiate transform faults?—insights from a 3-D numerical study. *Tectonics* 39 (10), e2019TC005793. doi:10.1029/2019TC005793

Schlunegger, F., and Kissling, E. (2015). Slab rollback orogeny in the Alps and evolution of the Swiss Molasse basin. *Nat. Commun.* 6, 8605. doi:10.1038/ncomms9605

Schmeling, H., Babeyko, A. Y., Enns, A., Faccenna, C., Funiciello, F., Gerya, T., et al. (2008). A benchmark comparison of spontaneous subduction models—towards a free surface. *Phys. Earth Planet. Interiors* 171 (1), 198–223. doi:10.1016/j.pepi.2008.06.028

Schmid, S. M., Fügenschuh, B., Kissling, E., and Schuster, R. (2004a). Tectonic map and overall architecture of the Alpine orogen. *Eclogae Geol. Helv.* 97 (1), 93–117. doi:10.1007/s00015-004-1113-x

Schmid, S. M., Kissling, E., Diehl, T., van Hinsbergen, D. J. J., and Molli, G. (2017). Ivrea mantle wedge, arc of the Western Alps, and kinematic evolution of the Alps–Apennines orogenic system. *Swiss J. Geosci.* 110 (2), 581–612. doi:10.1007/s00015-016-0237-0

Schmid, S. M., Kissling, E., and Schuster, R. (2004b). *Transects IV, V and VI: The Alps and their foreland*, 108–114.

Schmid, S. M., and Kissling, E. (2000). The arc of the Western Alps in the light of geophysical data on deep crustal structure. *Tectonics* 19 (1), 62–85. doi:10.1029/1999TC900057

Schmid, S. M., Pfiffner, O.-A., Froitzheim, N., Schönborn, G., and Kissling, E. (1996). Geophysical-geological transect and tectonic evolution of the Swiss-Italian Alps. *Tectonics* 15 (5), 1036–1064. doi:10.1029/96tc00433

Schmid, S. M., Scharf, A., Handy, M. R., and Rosenberg, C. L. (2013). The tauern window (eastern Alps, Austria): A new tectonic map, with cross-sections and a tectonometamorphic synthesis. *Swiss J. Geosci.* 106 (1), 1–32. doi:10.1007/s00015-013-0123-y

Schönborn, G. (1992). "Kinematics of a transverse zone in the southern Alps, Italy," in *Thrust tectonics* (Springer), 299–310.

Singer, J., Diehl, T., Husen, S., Kissling, E., and Duretz, T. (2014). Alpine lithosphere slab rollback causing lower crustal seismicity in northern foreland. *Earth Planet. Sci. Lett.* 397, 42–56. doi:10.1016/j.epsl.2014.04.002

Stampfli, G. M., Mosar, J., Marquer, D., Marchant, R., Baudin, T., and Borel, G. (1998). Subduction and obduction processes in the Swiss Alps. *Tectonophysics* 296 (1), 159–204. doi:10.1016/S0040-1951(98)00142-5

Sternai, P., Avouac, J.-P., Jolivet, L., Faccenna, C., Gerya, T., Becker, T. W., et al. (2016). On the influence of the asthenospheric flow on the tectonics and topography at a collision-subduction transition zones: Comparison with the eastern Tibetan margin. *J. Geodyn.* 100, 184–197. doi:10.1016/j.jog.2016.02.009

Suchoy, L., Goes, S., Maunder, B., Garel, F., and Davies, R. (2021). Effects of basal drag on subduction dynamics from 2D numerical models. *Solid* 12 (1), 79–93. doi:10.5194/se-12-79-2021

Sun, W., Zhao, L., Malusà, M. G., Guillot, S., and Fu, L.-Y. (2019). 3-D Pn tomography reveals continental subduction at the boundaries of the Adriatic microplate in the absence of a precursor oceanic slab. *Earth Planet. Sci. Lett.* 510, 131–141. doi:10.1016/j.epsl.2019.01.012

Tesauro, M., Kaban, M. K., and Cloetingh, S. A. P. L. (2009). How rigid is Europe's lithosphere? *Geophys. Res. Lett.* 36 (16), L16303. doi:10.1029/2009GL039229

Torsvik, T. H., Van der Voo, R., Preeden, U., Mac Niocaill, C., Steinberger, B., Doubrovine, P. V., et al. (2012). Phanerozoic polar wander, palaeogeography and dynamics. *Earth-Science Rev.* 114 (3), 325–368. doi:10.1016/j.earscirev.2012.06.007

Turcotte, D. L., and Schubert, G. (2002). *Geodynamics*. Cambridge, United Kingdom: Cambridge University Press.

van Dinther, Y., Gerya, T., Dalguer, L. A., Corbi, F., Funiciello, F., and Mai, P. M. (2013a). The seismic cycle at subduction thrusts: 2. Dynamic implications of geodynamic simulations validated with laboratory models. *JGR. Solid Earth* 118 (4), 1502–1525. doi:10.1029/2012jb009479

van Dinther, Y., Gerya, T. V., Dalguer, L. A., Mai, P. M., Morra, G., and Giardini, D. (2013b). The seismic cycle at subduction thrusts: Insights from seismo-thermo-mechanical models. *J. Geophys. Res. Solid Earth* 118 (12), 6183–6202. doi:10.1002/2013JB010380

van Dinther, Y., Mai, P. M., Dalguer, L., and Gerya, T. (2014). Modeling the seismic cycle in subduction zones: The role and spatiotemporal occurrence of off-megathrust earthquakes. *Geophys. Res. Lett.* 41 (4), 1194–1201. doi:10.1002/2013gl058886

Van Hinsbergen, D. J., Torsvik, T. H., Schmid, S. M., Maţenco, L. C., Maffione, M., Vissers, R. L., et al. (2020). Orogenic architecture of the Mediterranean region and kinematic reconstruction of its tectonic evolution since the Triassic. *Gondwana Res.* 81, 79–229. doi:10.1016/j.gr.2019.07.009

Vogt, K., Matenco, L., and Cloetingh, S. (2017). Crustal mechanics control the geometry of mountain belts. Insights from numerical modelling. *Earth Planet. Sci. Lett.* 460, 12–21. doi:10.1016/j.epsl.2016.11.016

Vogt, K., Willingshofer, E., Matenco, L., Sokoutis, D., Gerya, T., and Cloetingh, S. (2018). The role of lateral strength contrasts in orogenesis: A 2D numerical study. *Tectonophysics* 746, 549–561. doi:10.1016/j.tecto.2017.08.010

Willingshofer, E., and Sokoutis, D. (2009). Decoupling along plate boundaries: Key variable controlling the mode of deformation and the geometry of collisional mountain belts. *Geology* 37 (1), 39–42. doi:10.1130/g25321a.1

Willingshofer, E., Sokoutis, D., Luth, S. W., Beekman, F., and Cloetingh, S. (2013). Subduction and deformation of the continental lithosphere in response to plate and crust-mantle coupling. *Geology* 41 (12), 1239–1242. doi:10.1130/G34815.1

Wilson, J. T. (1966). Did the atlantic close and then Re-open? *Nature* 211 (5050), 676–681. doi:10.1038/211676a0

Yardley, B. W. D., and Valley, J. W. (1997). The petrologic case for a dry lower crust. *J. Geophys. Res.* 102 (B6), 12173–12185. doi:10.1029/97JB00508

Zhong, S., and Watts, A. B. (2013). Lithospheric deformation induced by loading of the Hawaiian Islands and its implications for mantle rheology. *J. Geophys. Res. Solid Earth* 118 (11), 6025–6048. doi:10.1002/2013JB010408

Appendix A Dynamic analysis

Two main forces are quantified in this research, on which the dynamic analysis is based. The first force, i.e. viscous drag along the base of the overriding plate, acts in the horizontal direction. It is referred to here as drag or mantle drag force. The second force, i.e. slab pull, acts in the vertical direction which is the expression of density differences of the subducting slab with respect to its surroundings. These forces are monitored over time so they can be linked to the kinematic evolution of the models and to examine their relative dominance.

Mantle drag is calculated here by integrating the product of the vertical gradient of horizontal velocity and the effective viscosity along the base of the overriding plate:

$$\int_{x_{trench}}^{L} \frac{\partial v_x}{\partial y} \cdot \eta_{eff} dx. \tag{A1}$$

Since both the velocity gradient and the effective viscosity are characterised by sharp variations along the base of the overriding plate, drag force is calculated between 2 km below and above the prescribed lithosphere-asthenosphere boundary of 140 km beneath the surface (e.g. 160 km on the y axis of the figures). The calculation depths are 138.25, 139.25, 140.25 and 141.25 km. Subsequently, the mean, maximum and minimum drag are averaged along the base of the overriding plate at each depth level. In the resulting figures we show the variation between these depths as shaded areas for the mean mantle drag magnitude, which looks like a thick line if the mantle drag does not vary significantly between the integration depths (Figure A1). Slab pull switches polarity during slab detachment, while mantle drag switches polarity prior to that, for example when eduction starts. We also find that a very weak (around 10^{10}–10^{11} N/m) mantle drag in a stationary orogenic system may often switch direction (e.g. Figure 6H).

Slab pull corresponds to the gravitational acceleration multiplied with the surface integral of lateral density variation:

$$g_y \iint_A (\bar{\rho}_{slab} - \bar{\rho}_{surr}) dxdy \tag{A2}$$

Where $\bar{\rho}_{slab}$ and $\bar{\rho}_{surr}$ are the horizontally averaged slab and surrounding material, i.e. mantle, densities. In practise, the slab is identified using the rock composition identifier taken from the nearest Lagrangian marker at every Eulerian node. In addition, a node is deemed part of the slab if its temperature is below the lithosphere-asthenosphere boundary temperature of 1,617.6K (see Model setup section). To detect slab detachment, the number of elements with slab temperatures is counted at each depth interval. If fewer than 100 nodes (50–70 km horizontal width) satisfy this condition, the area below that point is no longer included in the calculation. Hence, the sharp change in slab pull in the slab pull evolution figures is algorithmic and not related to the necking/shearing duration. In addition, flat-lying (detached) portions of slab at the 660 km discontinuity are not included as slab portions below 600 km are ignored. This approximation is justified as the deepest part of slab has the smallest thermal and therefore density anomaly. An example of this process is shown in Figure A2.

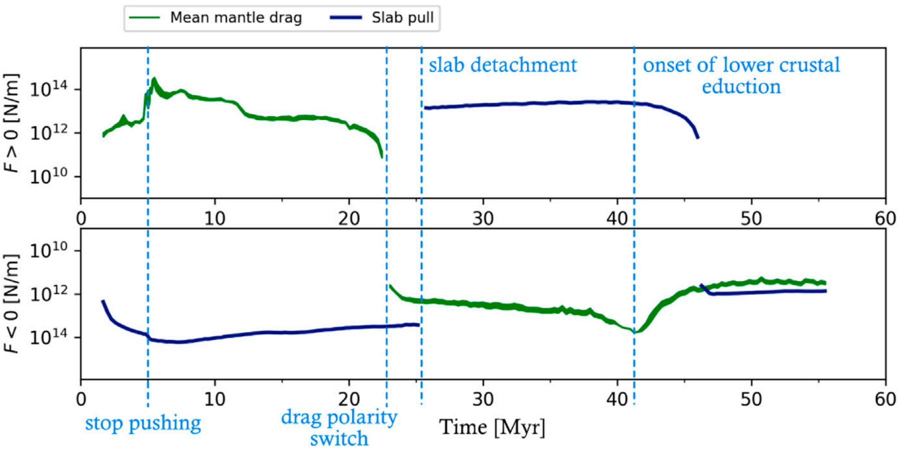

FIGURE A1
recycling of Figure 6B as a guide to the text.

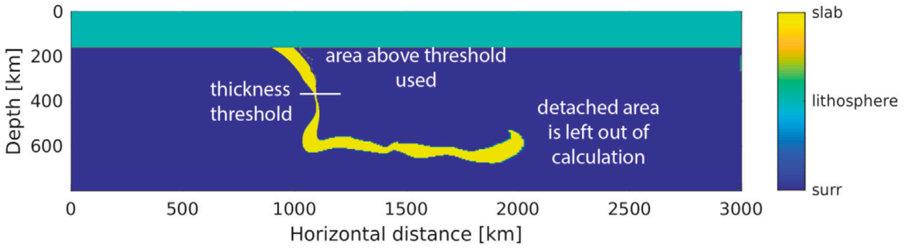

FIGURE A2
Slab identification of the slab pull calculation program for the reference model. The algorithm excludes everything below the necking level (which no longer has lithospheric temperatures) where the slab detaches, and everything above the lithosphere-asthenosphere boundary at a depth of 140 km. The resulting force estimate provides reasonable size estimates (e.g., Sandiford et al., 2005), despite these approximations.

Advantages of publishing in Frontiers

OPEN ACCESS
Articles are free to read
for greatest visibility
and readership

FAST PUBLICATION
Around 90 days
from submission
to decision

HIGH QUALITY PEER-REVIEW
Rigorous, collaborative,
and constructive
peer-review

TRANSPARENT PEER-REVIEW
Editors and reviewers
acknowledged by name
on published articles

Frontiers
Avenue du Tribunal-Fédéral 34
1005 Lausanne | Switzerland

Visit us: www.frontiersin.org
Contact us: frontiersin.org/about/contact

REPRODUCIBILITY OF RESEARCH
Support open data
and methods to enhance
research reproducibility

DIGITAL PUBLISHING
Articles designed
for optimal readership
across devices

FOLLOW US
@frontiersin

IMPACT METRICS
Advanced article metrics
track visibility across
digital media

EXTENSIVE PROMOTION
Marketing
and promotion
of impactful research

LOOP RESEARCH NETWORK
Our network
increases your
article's readership